SCIENTIFIC ACHIEVEMENTS ON MUON SCIENCE RESEARCH

AT
MUON SCIENCE LABORATORY
INSTITUTE OF MATERIALS STRUCTURE SCIENCE
HIGH ENERGY ACCELERATOR RESEARCH ORGANIZATION
(2007 ～ 2009)

EDITED BY
R. KADONO

DOCUMENT FOR EXTERNAL EVALUATION COMMITTEE

MUON SCIENCE LABORATORY IMSS-KEK
FEBRUARY 2010

List of Publications (2007 – 2009)

[1] Materials Science

< Journal Papers >

1-1.* K. Mukai, J. Sugiyama, Y. Ikedo, H. Nozaki, K. Shimomura, K. Nishiyama, K. Ariyoshi, and T. Ohzuku, "Magnetism and lithium diffusion in Li_xCoO_2 by a muon-spin rotation and relaxation (μ^+SR) technique", J. Power Sources **174** (2007) 711-715.

1-2.* H. Takeya, K. Ishida, K. Kitagawa, Y. Ihara, K. Onuma, Y. Maeno, Y. Nambu, S. Nakatsuji, D. E. MacLaughlin, A. Koda, and R. Kadono, "Spin dynamics and spin freezing behavior in the two-dimensional antiferromagnet $NiGa_2S_4$ revealed by Ga-NMR, NQR and μSR measurements", Phys. Rev. B **77** (2008) 054429(1-13).

1-3.* Risdiana, T. Adachi, N. Oki, S. Yairi, Y. Tanabe, K. Omori, Y. Koike, T. Suzuki, I. Watanabe, A. Koda, and W. Higemoto, "Cu Spin Dynamics in the Overdoped Regime of $La_{2-x}Sr_xCu_{1-y}Zn_yO_4$ Probed by Muon Spin Relaxation", Phys. Rev. B **77** (2008) 054516(1-6).

1-4.* N. Kida, M. Enomoto, I. Watanabe, T. Suzuki, and N. Kojima, "Spin Dynamics of the Charge-Transfer Phase Transition in an Iron Mixed-Valence Complex Observed Using Muon Spin Relaxation Spectroscopy", Phys. Rev. B **77** (2008) 144427(1-5).

1-5.* K. H. Satoh, S. Takeshita, A. Koda, R. Kadono, K. Ishida, S. Pyon, T. Sasagawa, and H. Takagi, "Fermi-liquid behavior and weakly anisotropic superconductivity in the electron-doped cuprate $Sr_{1-x}La_xCuO_2$", Phys. Rev. B **77** (2008) 224503(1-7).

1-6.* T. Goto, T. Suzuki, K. Kanada, T. Saito, A. Oosawa, I. Watanabe, and H. Manaka, "Muon spin relaxation detection of the soft mode toward the exotic magnetic ground state in the bond-disordered quantum spin system IPA-$Cu(Cl_{0.35}Br_{0.65})_3$", Phys. Rev. B **78** (2008) 054422(1-6).

1-7.* J. Sugiyama, Y. Ikedo, H. Nozaki, P. L. Russo, J. H. Brewer, E. J. Ansaldo, G. D. Morris, K. H. Chow, S. L. Stubbs, D. Andreica, A. Amato, T. Fujii, S. Okada, and I. Terasaki, "Comparative μ^+SR investigation of static magnetic order and anisotropy of the pure and Pb-doped $Bi_2Sr_2Co_2O_y$ layered cobalt dioxides", Phys. Rev. B **78** (2008) 094422(1-8).

1-8.* J. Sugiyama, H. Nozaki, Y. Ikedo, K. Mukai, P. L. Russo, D. Andreica, A. Amato, H. Yoshida, and Z. Hiroi, "Static magnetic order in metallic triangular antiferromagnet Ag_2MnO_2 detected by muon-spin spectroscopy", Phys. Rev. B **78** (2008) 104427(1-10).

*** *Supported by Inter-University Program Utilizing Oversea Muon Facilities***

1-9.* J. Sugiyama, K. Mukai, Y. Ikedo, P. L. Russo, H. Nozaki, D. Andreica, A. Amato, K. Ariyoshi, and T. Ohzuku, “Static magnetic order in the triangular lattice of Li_xNiO_2 ($x \leq 1$):Muon-spin spectroscopy measurements” , Phys. Rev. B **78** (2008) 144412(1-9).

1-10.* J. Sugiyama, Y. Ikedo, T. Goko, E. J. Ansaldo, J. H. Brewer, P. L. Russo, K. H. Chow, and H. Sakurai, “Complex magnetic phases of $Ca_{1-x}Na_xV_2O_4$ clarified by muon-spin spectroscopy”, Phys.l Rev. B **78** (2008) 224406(1-5).

1-11.* R. Kadono, K. Shimomura, K. H. Satoh, S. Takeshita, A. Koda, K. Nishiyama, E. Akiba, R. M. Ayabe, M. Kuba, and C. M. Jensen, “Hydrogen Bonding in Sodium Alanate: A Muon Spin Rotation Study”, Phys. Rev. Lett. **100** (2008) 026401(1-4).

1-12.* S. Kuroiwa, Y. Saura, J. Akimitsu, M. Hiraishi, M. Miyazaki, K. H. Satoh, S. Takeshita, and R. Kadono, “Multigap Superconductivity in Sesquicarbides La_2C_3 and Y_2C_3”, Phys. Rev. Lett. **100** (2008) 097002(1-4).

1-13.* S. Takeshita, R. Kadono, M. Hiraishi, M. Miyazaki, A. Koda, Y. Kamihara, and H. Hosono, “Coexistence of Supercondcutivity and Magnetism in $LaFeAs(O_{0.94}F_{0.06})$ Probed by Muon Spin Relaxation”, J. Phys. Soc. Jpn. **77** (2008) 103703(1-4).

1-14.* J. Sugiyama, M. Månsson, Y. Ikedo, T. Goko, K. Mukai, D. Andreica, A. Amato, K. Ariyoshi, and T. Ohzuku, “μSR investigation of local magnetic order in $LiCrO_2$”, Phys. Rev. B **79** (2009) 184411(1-8).

1-15. P. L. Russo, J. Sugiyama, J. H. Brewer, E. J. Ansaldo, S. L. Stubbs, K. H. Chow, R. Jin, H. Sha, and J. Zhang, “Muon spin rotation/relaxation study of Ba_2CoO_4”, Phys. Rev. B **80** (2009) 104421(1-7).

1-16.* R. Akiyama, Y. Ikedo, M. Månsson, T. Goko, J. Sugiyama ,D. Andreica, A. Amato, K. Matan, and T. J. Sato, “Short-range spin correlations in β-$LiFeO_2$ from bulk magnetization, neutron diffraction, and μSR experiments”, Phys. Rev. B **81** (2009) 024404(1-9).

1-17.* M. Hiraishi, R. Kadono, S. Takeshita, M. Miyazaki, A. Koda, H. Okabe, and J. Akimitsu, “Full Gap Superconductivity in $Ba_{0.6}K_{0.4}Fe_2As_2$ Probed by Muon Spin Rotation”, J. Phys. Soc. Jpn. **78** (2009) 023710(1-4).

1-18. M. Miyazaki, K. Yamaji, T. Yanagisawa, and R. Kadono, “Checkerboard States in the Two-Dimensional Hubbard Model with the Bi2212-Type Band”, J. Phys. Soc. Jpn. **78** (2009) 043706(1-4).

1-19.* J. Sugiyama, Y. Ikedo, O. Ofer, M. Månsson, E. J. Ansaldo, J. H. Brewer, K. H. Chow, H. Sakurai, and E. Takayama-Muromachi, “Comparative muon-spin rotation and relaxation study on the zigzag chain compounds $NaMn_2O_4$ and $Li_{0.92}Mn_2O_4$”, J. Phys. Soc. Jpn. **78** (2009) 084715(1-9).

1-20.* K. Mukai, J. Sugiyama, Y. Ikedo, P. L. Russo, D. Andreica, A. Amato, K. Ariyoshi, and T. Ohzuku, "Micro- and macroscopic magnetism in Li_xNiO_2", J. Power Sources **189** (2009) 665-668.

1-21. K. Mukai, H. Nozaki, Y. Ikedo, J. Sugiyama, K. Ariyoshi, and T. Ohzuku, "X-ray diffraction study on Li_xCoO_2 below ambient temperature", J. Power Sources **192** (2009) 684-688.

1-22. Y. Matsuo, J. Hatori, Y. Yoshida, Y. Ikedo, J. Sugiyama, and S. Ikehata, "Interrelationship between superprotonic conductivity and strain in $CsHXO_4$", Phys. Lett. A **373** (2009) 3470-3472.

1-23.* K. Ohishi, R. H. Heffner, T. U. Ito, W. Higemoto, G. D. Morris, N. Hur, E. D. Bauer, J. L. Sarrao, J. D. Thompson, D. E. MacLaughlin, L. Shu, "Development of the heavy-fermion state in Ce_2IrIn_8 and the effects of Ce dilution in $(Ce_{1-x}La_x)_2IrIn_8$", Phys. Rev. B **80** (2009) 125104(1-7).

1-24.* S. Takeshita, R. Kadono, M. Hiraishi, M. Miyazaki, A. Koda, S. Matsuishi, and H. Hosono, "Insular Superconductivity in a Co-Doped Iron Pnictide $CaFe_{1-x}Co_xAsF$", Phys. Rev. Lett. **103** (2009) 027002(1-4).

1-25.* J. Sugiyama, K. Mukai, Y. Ikedo ,H. Nozaki, M. Månsson ,and I. Watanabe, "Li diffusion in Li_xCoO_2, probed by muon-spin spectroscopy", Phys. Rev. Lett. **103** (2009) 147601(1-4).

1-26.* M. Hiraishi, R.Kadono, M. Miyazaki, S. Takeshita, Y. Taguchi, Y. Kasahara, T. Takano, T. Kishiume, and Y. Iwasa, "Anisotropic superconducting order parameter in Li-intercalated layered superconductor Li_xZrNCl", Phys. Rev. B **81** (2010) 014525(1-5).

< Proceedings >

1-27.* S. Kuroiwa, K. H. Satoh, A. Koda, R. Kadono, K. Ohishi, W. Higemoto, and J. Akimitsu, "μSR measurements on the vortex lattice of CaAlSi: Anisotropic response in magnetic penetration depth", J. Phys. Chem. Sol. **68** (2007) 2124-2128.

1-28.* H. Nozaki, M. Janoschek, B. Roessli, J. Sugiyama, L. Keller, J. H. Brewer, E. J. Ansaldo, G. D. Morris, T. Takami, and H. Ikuta, "Antiferromagnetic spin structure in $BaCoO_3$ below 15 K determined by Neutron and μ^+SR", J. Phys. Chem. Sol. **68** (2007) 2162-2165.

1-29. M. Mihara, R. Matsumiya, K. Shimomura, K. Matsuta, M. Fukuda, D. Ishikawa, J. Komurasaki, D. Nishimura, T. Nagasawa, T. Izumikawa, and T. Minamisono, "Shallow nitrogen acceptor in TiO_2 studied by β-NMR spectroscopy", Physica B **401-402** (2007) 430-432.

1-30.* N. Kojima, M. Enomoto, N. Kida, I. Watanabe, and T. Suzuki, "Ferromagnetic and Charge Transfer Phase Transitions in $[Fe^{II}Fe^{III}(dto)_3]$ (dto = $C_2O_2S_2$) Complexes Examined by Muon Spectroscopy", RIKEN Accel. Prog. Rep., **40**, v (2007).

1-31. K. Yamaji, T. Yanagisawa, M. Miyazaki, and R. Kadono, "t'- and t''-dependence of the bulk-limit superconducting condensation energy of the 2D Hubbard model", Physica C **468** (2008) 1125-1128.

1-32.* Y. Ikedo, H. Nozaki, M. Harada, J. Sugiyama, T.J. Sato, Y. Matsuo, K. Nishiyama, and J.D. Copley, "Microscopic magnetic nature of layered cobalt dioxides $\mathrm{A}_x\mathrm{CoO}_2$ with A=Li, Na, and K investigated by muon-spin rotation and relaxation", Nucl. Instr. Meth. Phys. Res. A **600** (2009) 305-308.

1-33.* Y. Ikedo, H. Nozaki, M. Harada, J. Sugiyama, T.J. Sato, Y. Matsuo, K. Nishiyama, J.S. Lord, Y. Qiu, and J.D. Copley, "Study of hydrogen diffusion in superprotonic ionic conductors, $M\mathrm{H}X\mathrm{O}_4$ by μ^+SR and QENS", Nucl. Instr. Meth. Phys. Res. A **600** (2009) 316-318.

1-34.* K. Satoh, H. Fujita, K. Katayama, H. Taniguchi, T. U. Ito, K. Ohishi, and W. Higemoto, "μSR study of an layered organic superconductor κ-(BEDT-TTF)$_4$Hg$_{2.89}$Br$_8$", Physica B **404** (2009) 597-599.

1-35.* K. Satoh, K. Sato, T. Yoshida, H. Taniguchi, T. Goko, T. U. Ito, K. Ohishi, and W. Higemoto, "μSR study of organic antiferromagnet β'-(BEDT-TTF)$_2$ICl$_2$ under high pressure", Physica B **404** (2009) 600-602.

1-36.* J. Sugiyama, H. Nozaki, K.Y. Ikedo, G.D. Morris, P.L. Russo, J.H. Brewer, E.J. Ansaldo, S. Hbert, and A. Maignan, "Complex magnetic order in quasi-one-dimensional compound $\mathrm{Ca}_3\mathrm{CoIrO}_6$", Physica B **404** (2009) 603-606.

1-37.* Y. Ikedo, J. Sugiyama, H. Nozaki, P.L. Russo, D. Andreica, A. Amato, M. Månsson, M. Shizuya, M. Isobe, and E. Takayama-Muromachi, "Paramagnetic nature of the layered cobalt dioxide with adouble rocksalt-type block", Physica B **404** (2009) 607-610.

1-38.* T. Nakano, J. Matsumoto, T. C. Duan, I. Watanabe, T. Suzuki, T. Kawamata, A. Amato, F. L. Pratt, and Y. Nozue, "Fast Muon Spin Relaxation in Ferromagnetism of Potassium Clusters in Zeolite A", Physica B **404** (2009) 630-633.

1-39.* T. C. Duan, T. Nakano, J. Matsumoto, R. Suehiro, I. Watanabe, T. Suzuki, T. Kawamata, A. Amato, F. L. Pratt, and Y. Nozue, "μSR Study on Ferromagnetic Properties of Rb Clusters Incorporated into Zeolite A", Physica B **404** (2009) 634-637.

1-40.* M. Enomoto, N. Kida, I. Watanabe, T. Suzuki, and N. Kojima, "Spin dynamics of the ferromagnetic transition in iron mixed-valence complexes, $(n\text{-}\mathrm{C}_n\mathrm{H}_{2n+1})_4\mathrm{N}[\mathrm{Fe}^{\mathrm{II}}\mathrm{Fe}^{\mathrm{III}}(\mathrm{dto})_3]$ (dto = $\mathrm{C}_2\mathrm{O}_2\mathrm{S}_2$, n=3-5) by μSR", Physica B **404** (2009) 642-644.

1-41.* Y. Ikedo, J. Sugiyama, H. Nozaki, K. Mukai, P.L. Russo, D. Andreica, A. Amato, Y. Ono, and T. Kajitani, "μSR study on delafossite $\mathrm{CuCr}_{1\text{-}x}\mathrm{Mg}_x\mathrm{O}_2$", Physica B **404** (2009) 645-648.

1-42.* Y. Ikedo, J. Sugiyama, H. Nozaki, K. Mukai, H. Itahara, P. L. Russo, D. Andreica, and A. Amato, "High pressure μSR Study on cobalt oxide spinel", Physica B **404** (2009) 652-655.

1-43.* K. Mukai, J. Sugiyama, Y. Ikedo, P. L. Russo, J. H. Brewer, E. J. Ansaldo, K. H. Chow, K. Ariyoshi, and T. Ohzuku, "Magnetic phase diagram of $Li[Mg_xMn_{2-x}]O_4$ Spinel", Physica B **404** (2009) 656-659.

1-44.* J. Sugiyama, K. Mukai, Y. Ikedo, H. Nozaki, P. L. Russo, D. Andreica, A. Amato, K. Ariyoshi, and T. Ohzuku, "Static magnetic order on the triangular antiferromagnet Li_xNiO_2 with $x \leq 1$", Physica B **404** (2009) 663-666.

1-45.* K. H. Satoh, M. Hiraishi, M. Miyazaki, S. Takeshita, A. Koda, R. Kadono, I. Yamada, K. Oka, M. Azuma, Y. Shimakawa, and M. Takano, "Effect of Zn substitution for Cu on $Ca_{2-x}Na_xCuO_2Cl_2$ near the hole concentration of 1/8 pre Cu", Physica B **404** (2009) 713-716.

1-46.* Y. Tanabe, T. Adachi, Risdiana, T. Kawamata, T. Suzuki, I. Watanabe, and Y. Koike, "Ni-Substitution Effects on Cu-Spin Correlation in $La_{2-x}Sr_xCu_{1-y}Ni_yO_4$ Relating to Hole Trapping and Stripe Pinning", Physica B **404** (2009) 717-719.

1-47.* R. Kadono, M. Hiraishi, M. Miyazaki, K. H. Satoh, S. Takeshita, S. Kuroiwa, S. Saura, and J. Akimitsu, "Magnetic response of noncentrosymmetric superconductor La_2C_3 : Effect of double-gap and spin−orbit interaction", Physica B **404** (2009) 737-739.

1-48.* N. Kase , J. Akimitsu, Y. Ishii, T. Suzuki, I. Watanabe, M. Miyazaki, M. Hiraishi, S. Takeshita, and R. Kadono, "Coexistence of superconductivity and magnetism in the Tm-based superconductor probed by muon spin relaxation", Physica B **404** (2009) 740-742.

1-49.* H. Okabe, J. Akimitsu, S. Takeshita, M. Miyazaki, M. Hiraishi, and R. Kadono, "μSR study of magnetic ground state in Mo_3Sb_7", Physica B **404** (2009) 743-745.

1-50.* K. Ohishi, R. H. Heffner, J. Spehling, G. J. MacDougall, T. U. Ito, W. Higemoto, A. Amato, D. Andreica, G. Nieuwenhuys, H. H. Klauss, G. M. Luke, J. D. Thompson, A. D. Bianchi, and Z. Fisk, "Magnetism and Superconductivity in Heavy Fermion Superconductor $CeCo(In_{0.97}Cd_{0.03})_5$", Physica B **404** (2009) 754-756.

1-51.* T. U. Ito, W. Higemoto, K. Ohishi, R. H. Heffner, N. Nishida, K. Satoh, H. Sugawara, Y. Aoki, D. Kikuchi, and H. Sato, "Possible low-energy excitations in $SmRu_4P_{12}$ probed by muon spin relaxation", Physica B **404** (2009) 761-764.

1-52.* J. Sugiyama, Y. Ikedo, H. Nozaki, K. Mukai, D. Andreica, A. Amato, M. Menetrier, D. Carlier, and C. Delmas, "Annihilation of antiferromagnetic order in $LiCoO_2$ by excess Li", Physica B **404** (2009) 769-772.

1-53.* J. Sugiyama, Y. Ikedo, H. Nozaki, P. L. Russo, J. H. Brewer, E. J. Ansaldo, G. D. Morris, K. H. Chow, D. Andreica, A. Amato, T. Fujii, S. Okada, and I. Terasaki, “Static magnetic order and anisotropy of the layered cobalt dioxides $Bi_{1.6}Pb_{0.4}Sr_2Co_2O_y$ and $Bi_2Sr_2Co_2O_y$”, Physica B 404 (2009) 773-776.

1-54.* J. Sugiyama, H. Nozaki, Y. Ikedo, K. Mukai, D. Andreica, A. Amato, H. Yoshida, and Z. Hiroi, “Static magnetic order in metallic triangular antiferromagnet Ag_2MnO_2”, Physica B **404** (2009) 777-780.

1-55.* Y. Kawasaki, T. Minami, Y. Kishimoto, T. Ohno, A. Koda, K. H. Satoh, R. Kadono, J. L. Gavilano, H. Luetkens, T. Nakajima, and Y. Ueda, “Microscopic investigation of antiferromagnetic order in A-site-ordered perovskite manganite $YBaMn_2O_6$”, Physica B **404** (2009) 781-784.

1-56.* J. Sugiyama, Y. Ikedo, P. L. Russo, T. Goko, E. J. Ansaldo, J. H. Brewer, K. H. Chow, and H. Sakurai, “Complex magnetic phases in $Ca_{1-x}Na_xV_2O_4$ with $0 \le x \le 1$”, Physica B **404** (2009) 789-792.

1-57.* Y. Ikedo, J. Sugiyama, H. Nozaki, K. Nishiyama, Y. Matsuo, and J. H. Lord, “Moun dynamics in super protpnic conductors”, Physica B **404** (2009) 798-800.

1-58.* M. Mihara, K. Shimomura, I. Watanabe, Y. Ishii, T. Suzuki, T. Kawamata, J. Komurasaki, D. Nishimura, K. Nishiyama, R. Kadono, S. Takai, and T. Nakano, “Muon spin relaxation in hydrogen tungsten bronze”, Physica B **404** (2009) 801-803.

1-59. K. Yamaji, T. Yanagisawa, M. Miyazaki, and R. Kadono, “t'- and t''-dependence of the bulk-limit superconducting condensation energy of the 2D Hubbard mode”, Physica C **469** (2009) 1125-1128.

< Review >

1-60. R. Kadono, “Future perspectives of μSR studies in condensed matter physics”, J. Phys. Chem. Sol. **68** (2007) 2052-2055.

1-61.* S. Takeshita and R. Kadono, “Competition/coexisitence of magnetism and superconductivity in iron pnictides probed by muon spin rotation”, New J. Phys. **11** (2009) 035006(1-22).

[2] Instrumentation and Technique

< Journal Papers >

2-1. S. Makimura, H. Ozaki, H. Okamura, M. Futakawa, T. Naoe, Y. Miyake, N. Kawamura, K. Nishiyama, and M. Kawai, “The present status of R&D for the muon target at J-PARC: The development of silver-brazing method for graphite”, J. Nucl. Mater. **377** (2008) 28-33.

2-2. P. Bakule, Y. Matsuda, Y. Miyake, K. Nagamine, M. Iwasaki, Y. Ikedo, K. Shimomura, P. Strasser, and S. Makimura, "Pulsed source of ultra low energy positive muons for near-surface μSR studies", Nucl. Instr. Meth. Phys. Res. B **266** (2008) 335-346.

2-3. M. J. Shirakata, H. Fujimori, Y. Irie, and T. Takayanagi, "Particle tracking study of the injection process with field interferences in a rapid cycling synchrotron", Physical Review Special Topics-Accelerators and Beams **11** (2008) 064201(1-9).

2-4. H. Imao, K. Ishida, N. Kawamura, T. Matsuzaki, Y. Matsuda, A. Toyoda, P. Strasser, M. Iwasaki, and K. Nagamine, "Preparation of ortho-para ratio controlled D_2 gas for muon-catalyzed fusion", Review of Scientific Instruments **79** (2008) 053502(1-10).

< *Proceedings* >

2-5. K. Nakahara, Y. Miyake, K. Shimomura, P. Strasser, K. Nishiyama, N. Kawamura, H. Fujimori, S. Makimura, A. Koda, K. Nagamine, T. Ogitsu, A. Yamamoto, T. Adachi, K. Sasaki, K. Tanaka, N. Kimura, Y. Makida, Y. Ajima, K.Ishida, and Y. Matsuda, "Design of the Large Acceptance Muon Beamline at J-PARC", AIP Conference Proceedings **981** (2008) 312-314.

2-6. K. Shimomura, Y. Miyake, P. Strasser, A. Koda, N. Kawamura, S. Makimura, H. Fujimori, K. Nakahara, R. Kadono, K. Ishida, J. Doornbos, W. Higemoto, K. Nishiyama, and K. Nagamine, "Status of Decay/Surface Muon Channel for the Muon Science in J-PARC", AIP Conference Proceedings **981** (2008) 381-383.

2-7. Y. Miyake, K. Nakahara, K. Shimomura, P. Strasser, N. Kawamura, A. Koda, S. Makimura, H. Fujimori, K. Nishiyama, Y. Matsuda, P. Bakule, T. Adachi, and T. Ogitsu, "Ultra Slow Muon Project at J-PARC, MUSE", AIP Conference Proceedings **1104** (2009) 47-52.

2-8. N. Kawamura, S. Makimura, K. Shimomura, P. Strasser, A. Koda, H. Fujimori, K. Nakahara, M. Kato, S. Takeshita, R. Kadono, W. Higemoto, K. Nishiyama, K. Nagamine, and Y. Miyake, "Muon Science in J-PARC", Hyperfine Interactions **194** (2009) 213–217.

2-9. Y. Miyake, K. Nishiyama, N. Kawamura, P. Strasser, S. Makimura, A. Koda, K. Shimomura, H. Fujimori, K. Nakahara, R. Kadono, M. Kato, S. Takeshita, W. Higemoto, K. Ishida, T. Matsuzaki, Y. Matsuda, and K. Nagamine, "J-PARC muon source, MUSE", Nucl. Instr. Meth. Phys. Res. A **600** (2009) 22-24.

2-10. P. Bakule, Y. Matsuda, Y. Miyake, K. Nagamine, K. Shimomura, P. Strasser, S. Makimura, and M. Iwasaki, "Prospects for ultra-low-energy muon beam at J-PARC", Nucl. Instr. Meth. Phys. Res. A **600** (2009) 35-37.

2-11. M. Harada, S. Meigo, M. Ito, E. Dantsuji, K. Takigawa, H. Takada, F. Maekawa, M. Futakawa, M. Nakamura, Y. Miyake, and Y. Ikeda, “Settlement of Materials and Life Science Experimental Facility at J-PARC”, Nucl. Instr. Meth. Phys. Res. A **600** (2009) 87-90.

2-12. N. Kawamura, S. Makimura, P. Strasser, A. Koda, H. Fujimori, K. Nishiyama, Y. Miyake, and M.L.F Muon section, “Design strategy for devices under high radiation field in J-PARC muon facility”, Nucl. Instr. Meth. Phys. Res. A **600** (2009) 114-116.

2-13. K. Nakahara, Y. Miyake, K. Shimomura, P. Strasser, K. Nishiyama, N. Kawamura, H. Fujimori, S. Makimura, A. Koda, K. Nagamine, T. Ogitsu, A. Yamamoto, T. Adachi, K. Sasaki, K. Tanaka, N. Kimura, Y. Makida, Y. Ajima, K. Ishida, and Y. Matsuda, “The super omega muon beamline at J-PARC”, Nucl. Instr. Meth. Phys. Res. A **600** (2009) 132-134.

2-14. S. Takeshita, M. Hiraishi, M. Miyazaki, A. Koda, R. Kadono, S. Y. Suzuki, Y. Yasu, M. Tanaka, Y. Matsuda, K. Ishida, and T. Matsuzaki, “Development of positron detector for μSR based on multi-pixel photoncounter”, Nucl. Instr. Meth. Phys. Res. A **600** (2009) 139-142.

2-15. S. Makimura, Y. Miyake, N. Kawamura, P. Strasser, A. Koda, K. Shimomura, H. Fujimori, K. Nishiyama, M. Kato, K. Nakahara, R. Kadono, Y. Kobayashi, J. Sagawa, T. Nakamura, M. Kaneko, H. Ozaki, H. Okamura, T. Suzuki, K. Fujimoto, and K. Kira, “Present status of construction for the muon target in J-PARC”, Nucl. Instr. Meth. Phys. Res. A **600** (2009) 146-149.

2-16. P. Strasser, Y. Miyake, N. Kawamura, S. Makimura, and K. Nishiyama, “Alignment and shields in the M2 primary proton beamline at J-PARC”, Nucl. Instr. Meth. Phys. Res. A **600** (2009) 154-156.

2-17. H. Fujimori, N. Kawamura, S. Meigo, P. Strasser, K. Nakahara, and Y. Miyake, “Radiation resistant magnets for the J-PARC muon facility”, Nucl. Instr. Meth. Phys. Res. A **600** (2009) 170-172.

2-18. W. Higemoto, K. Shimomura, Y. Kobayashi, S. Makimura, Y. Miyake, Y. Kai, and K. Sakai, “J-PARC muon control system”, Nucl. Instr. Meth. Phys. Res. A **600** (2009) 179-181.

2-19. W. Higemoto, R.H. Heffner, K. Shimomura, K. Nishiyama, and Y. Miyake, “JAEA-ASRC μSR project at J-PARC MUSE” Nucl. Instr. Meth. Phys. Res. A **600** (2009) 182-184.

2-20. K. Shimomura, A. Koda, P. Strasser, N. Kawamura, H. Fujimori, S. Makimura, W. Higemoto, K. Nakahara, K. Ishida, K. Nishiyama, K. Nagamine, and Y. Miyake, “Superconducting muon channel at J-PARC”, Nucl. Instr. Meth. Phys. Res. A **600** (2009) 192-194.

2-21. Y. Miyake, K. Shimomura, N. Kawamura, P. Strasser, S. Makimura, A. Koda, H. Fujimori, K. Nakahara, R. Kadono, M. Kato, S. Takeshita, K. Nishiyama, W. Higemoto, K. Ishida, T. Matsuzaki, Y. Matsuda, and K. Nagamine, “Birth of an intense pulsed muon source, J-PARC MUSE”, Physica B **404** (2009) 957-961.

2-22. R. Kadono, K. H. Satoh, A. Koda, K. Nishiyama, and M. Mihara, “High transverse field μSR with π/2-RF pulse spin control technique”, Physica B **404** (2009) 996-998.

2-23. S. Y. Suzuki, M. Tanaka, K. Tauchi, Y. Yasu, S. Takeshita, A. Koda, M. Hiraishi, M. Miyazaki, K. H. Satoh, R. Kadono, K. Ishida, D. Tomono, and T. Matsuzaki, “Development of a pipelined data acquisition system for μSR experiments at J-PARC”, Physica B **404** (2009) 1002-1006.

[3] Atomic and Molecular Science

< Journal Paper >

3-1. H. Imao, K. Ishida, N. Kawamura, T. Matsuzaki, Y. Matsuda, A. Toyoda, P. Strasser, M. Iwasaki, and K. Nagamine, “Density effect in *d-d* muon-catalyzed fusion with ortho- and para-enriched D_2”, Phys. Lett. B **658** (2008) 120-124.

< Proceedings >

3-2. P. Strasser, A. Taniguchi, T. Matsuzaki, K. Ishida , Y. Matsuda , S. Ohya, M. Iwasaki, and K. Nagamine, “Muon spectroscopy with trace alkaline-earth and rare-earth isotopes implanted in solid D_2”, Hyperfine Interactions 193 (2009) 121–127.

3-3. H. Imao, K. Ishida, N. Kawamura, T. Matsuzaki, Y. Matsuda, A. Toyoda, P. Strasser, M. Iwasaki, and K. Nagamine, “Density effect in *d-d* catalyzed fusion with ortho- and para-enriched deuterium”, Hyperfine Interactions **193** (2009)159–163.

[4] Others

< Journal Paper >

4-1. M. K. Kubo, H. Moriyama, Y. Tsuruoka, S. Sakamoto, E. Koseto, T. Saito, and K. Nishiyama, “Non-destructive elemental depth-profiling with muonic X-rays”, J. Radioanalytical and Nuclear Chemistry **278**(3) (2008) 777-781.

Selected 43 Papers

	TITLE	AUTHOR	JOURNAL			
				YEAR	VOL.	PAGE
< 2007 >						
1- 1*	Magnetism and lithium diffusion in Li_xCoO_2 by a muon-spin rotation and relaxation (μ^+SR) technique	K. Mukai, J. Sugiyama, Y. Ikedo, H. Nozaki, K. Shimomura, K. Nishiyama, K. Ariyoshi, and T. Ohzuku	J. Power Sources	2007	174	711
1-27*	μSR measurements on the vortex lattice of CaAlSi: Anisotropic response in magnetic penetration depth	S. Kuroiwa, K.H. Satoh, A. Koda, R. Kadono, K. Ohishi, W. Higemoto, and J. Akimitsu	J. Phys. Chem. Sol	2007	68	2124
1-29	Shallow nitrogen acceptor in TiO_2 studied by β-NMR spectroscopy	M. Mihara, R. Matsumiya, K. Shimomura, K. Matsuta, M. Fukuda, D. Ishikawa, J. Komurasaki, D. Nishimura, T. Nagasawa, T. Izumikawa, and T. Minamisono	Physica B	2007	401	430
< 2008 >						
1- 2*	Spin dynamics and spin freezing behavior in the two-dimensional antiferromagnet $NiGa_2S_4$ revealed by Ga-NMR, NQR and μSR measurements	H. Takeya, K. Ishida, K. Kitagawa, Y. Ihara, K. Onuma, Y. Maeno, Y. Nambu, S. Nakatsuji, D.E. MacLaughlin, A. Koda, and R. Kadono	Phys. Rev. B	2008	77	054429
1- 3*	Cu Spin Dynamics in the Overdoped Regime of $La_{2-x}Sr_xCu_{1-y}Zn_yO_4$ Probed by Muon Spin Relaxation	Risdiana, T. Adachi, N. Oki, S. Yairi, Y. Tanabe, K. Omori, Y. Koike, T. Suzuki, I. Watanabe, A. Koda, and W. Higemoto	Phys. Rev. B	2008	77	054516
1- 5*	Fermi-liquid behavior and weakly anisotropic superconductivity in the electron-doped cuprate $Sr_{1-x}La_xCuO_2$	K.H. Satoh, S. Takeshita, A. Koda, R. Kadono, K. Ishida, S. Pyon, T. Sasagawa, and H. Takagi	Phys. Rev. B	2008	77	224503
1-11*	Hydrogen Bonding in Sodium Alanate: A Muon Spin Rotation Study	R. Kadono, K. Shimomura, K.H. Satoh, S. Takeshita, A. Koda, K. Nishiyama, E. Akiba, R.M. Ayabe, M. Kuba, and C.M. Jensen	Phys. Rev. Lett.	2008	100	026401
1-12*	Multigap Superconductivity in Sesquicarbides La_2C_3 and Y_2C_3	S. Kuroiwa, Y. Saura, J. Akimitsu, M. Hiraishi, M. Miyazaki, K.H. Satoh, S. Takeshita, and R. Kadono	Phys. Rev. Lett.	2008	100	097002
1-13*	Coexistence of Supercondcutivity and Magnetism in $LaFeAs(O_{0.94}F_{0.06})$ Probed by Muon Spin Relaxation	S. Takeshita, R. Kadono, M. Hiraishi, M. Miyazaki, A. Koda, Y. Kamihara, and H. Hosono	J. Phys. Soc. Jpn.	2008	77	103703
2- 1	The present status of R&D for the muon target at J-PARC: The development of silver-brazing method for graphite	S. Makimura, H. Ozaki, H. Okamura, M. Futakawa, T. Naoe, Y. Miyake, N. Kawamura, K. Nishiyama, and M. Kawai	J. Nucl. Mater.	2008	377	28
2- 2	Pulsed source of ultra low energy positive muons for near-surface μSR studies	P. Bakule, Y. Matsuda, Y. Miyake, K. Nagamine, M. Iwasaki, Y. Ikedo, K. Shimomura, P. Strasser, and S. Makimura	Nucl. Instr. Meth. Phys. Res. B	2008	266	335
2- 3	Particle tracking study of the injection process with field interferences in a rapid cycling synchrotron	M.J. Shirakata, H. Fujimori, Y. Irie, and T. Takayanagi	Physical Review Special Topics-Accelerators and Beams	2008	11	064201
2- 4	Preparation of ortho-para ratio controlled D_2 gas for muon-catalyzed fusion	H. Imao, K. Ishida, N. Kawamura, T. Matsuzaki, Y. Matsuda, A. Toyoda, P. Strasser, M. Iwasaki, and K. Nagamine	Review of Scientific Instruments	2008	79	053502
3- 1	Density effect in *d-d* muon-catalyzed fusion with ortho- and para-enriched D_2	H. Imao, K. Ishida, N. Kawamura, T. Matsuzaki, Y. Matsuda, A. Toyoda, P. Strasser, M. Iwasaki, and K. Nagamine	Phys. Lett. B	2008	658	120
4- 1	Non-destructive elemental depth-profiling with muonic X-rays	M.K. Kubo, H. Moriyama, Y. Tsuruoka, S. Sakamoto, E. Koseto, T. Saito, and K. Nishiyama	J. Radioanalytical and Nuclear Chemistry	2008	278	777

	TITLE	AUTHOR	JOURNAL		
			YEAR	VOL.	PAGE
< 2009 >					
1-17*	Full Gap Superconductivity in $Ba_{0.6}K_{0.4}Fe_2As_2$ Probed by Muon Spin Rotation	M. Hiraishi, R. Kadono, S. Takeshita, M. Miyazaki, A. Koda, H. Okabe, and J. Akimitsu	J. Phys. Soc. Jpn. 2009	78	023710
1-24*	Insular Superconductivity in a Co-Doped Iron Pnictide $CaFe_{1-x}Co_xAsF$	S. Takeshita, R. Kadono, M. Hiraishi, M. Miyazaki, A. Koda, S. Matsuishi, and H. Hosono	Phys. Rev. Lett. 2009	103	027002
1-33*	Study of hydrogen diffusion in superprotonic ionic conductors, $M\mathrm{H}X\mathrm{O}_4$ by μ^+SR and QENS	Y. Ikedo, H. Nozaki, M. Harada, J. Sugiyama, T.J. Sato, Y. Matsuo, K. Nishiyama, J.S. Lord, Y. Qiu and J.D. Copley	Nucl. Instr. Meth. Phys. Res. A 2009	600	316
1-45*	Effect of Zn substitution for Cu on $Ca_{2-x}Na_xCuO_2Cl_2$ near the hole concentration of 1/8 per Cu	K.H. Satoh, M. Hiraishi, M. Miyazaki, S. Takeshita, A. Koda, R. Kadono, I. Yamada, K. Oka, M. Azuma, Y. Shimakawa, and M. Takano	Physica B 2009	404	713
1-47*	Magnetic response of noncentrosymmetric superconductor La_2C_3 : Effect of double-gap and spin–orbit interaction	R. Kadono, M. Hiraishi, M. Miyazaki, K.H. Satoh, S. Takeshita, S. Kuroiwa, S. Saura, and J. Akimitsu	Physica B 2009	404	737
1-48*	Coexistence of superconductivity and magnetism in the Tm-based superconductor probed by muon spin relaxation	N. Kase, J. Akimitsu, Y. Ishii, T. Suzuki, I. Watanabe, M. Miyazaki, M. Hiraishi, S. Takeshita, and R. Kadono	Physica B 2009	404	740
1-49*	μSR study of magnetic ground state in Mo_3Sb_7	H. Okabe, J. Akimitsu, S. Takeshita, M. Miyazaki, M. Hiraishi, and R. Kadono	Physica B 2009	404	743
1-55*	Microscopic investigation of antiferromagnetic order in A-site-ordered perovskite manganite $YBaMn_2O_6$	Y. Kawasaki, T. Minami, Y. Kishimoto, T. Ohno, A. Koda, K.H. Satoh, R. Kadono, J.L. Gavilano, H. Luetkens, T. Nakajima, and Y. Ueda	Physica B 2009	404	781
1-58*	Muon spin relaxation in hydrogen tungsten bronze	M. Mihara, K. Shimomura, I. Watanabe, Y. Ishii, T. Suzuki, T. Kawamata, J. Komurasaki, D. Nishimura, K. Nishiyama, R. Kadono, S. Takai, and T. Nakano	Physica B 2009	404	801
2- 8	Muon Science in J-PARC	N. Kawamura, S. Makimura, K. Shimomura, P. Strasser, A. Koda, H. Fujimori, K. Nakahara, M. Kato, S. Takeshita, R. Kadono, W. Higemoto, K. Nishiyama, K. Nagamine and Y. Miyake	Hyperfine Interactions 2009	194	213
2- 9	J-PARC muon source, MUSE	Y. Miyake, K. Nishiyama, N. Kawamura, P. Strasser, S. Makimura, A. Koda, K. Shimomura, H. Fujimori, K. Nakahara, R. Kadono, M. Kato, S. Takeshita, W. Higemoto, K. Ishida, T. Matsuzaki, Y. Matsuda and K. Nagamine	Nucl. Instr. Meth. Phys. Res. A 2009	600	22
2-10	Prospects for ultra-low-energy muon beam at J-PARC	P. Bakule, Y. Matsuda, Y. Miyake, K. Nagamine, K. Shimomura, P. Strasser, S. Makimura, and M. Iwasaki	Nucl. Instr. Meth. Phys. Res. A 2009	600	35
2-11	Settlement of Materials and Life Science Experimental Facility at J-PARC	M. Harada, S. Meigo, M. Ito, E. Dantsuji, K. Takigawa, H. Takada, F. Maekawa, M. Futakawa, M. Nakamura, Y. Miyake, and Y. Ikeda	Nucl. Instr. Meth. Phys. Res. A 2009	600	87
2-12	Design strategy for devices under high radiation field in J-PARC muon facility	N. Kawamura, S. Makimura, P. Strasser, A. Koda, H. Fujimori, K. Nishiyama, Y. Miyake, and M.L.F Muon section	Nucl. Instr. Meth. Phys. Res. A 2009	600	114
2-13	The super omega muon beamline at J-PARC	K. Nakahara, Y. Miyake, K. Shimomura, P. Strasser, K. Nishiyama, N. Kawamura, H. Fujimori, S. Makimura, A. Koda, K. Nagamine, T. Ogitsu, A. Yamamoto, T. Adachi, K. Sasaki, K. Tanaka, N. Kimura, Y. Makida, Y. Ajima, K. Ishida, and Y. Matsuda	Nucl. Instr. Meth. Phys. Res. A 2009	600	132

	TITLE	AUTHOR	JOURNAL		
			YEAR	VOL.	PAGE
2-14	Development of positron detector for μSR basedonmulti-pixel photoncounter	S. Takeshita, M. Hiraishi, M. Miyazaki, A. Koda, R. Kadono, S. Y. Suzuki, Y. Yasu, M. Tanaka, Y. Matsuda, K. Ishida, and T. Matsuzaki	Nucl. Instr. Meth. Phys. Res. A		
			2009	600	139
2-15	Present status of construction for the muon target in J-PARC	S. Makimura, Y. Miyake, N. Kawamura, P. Strasser, A. Koda, K. Shimomura, H. Fujimori, K. Nishiyama, M. Kato, K. Nakahara, R. Kadono, Y. Kobayashi, J. Sagawa, T. Nakamura, M. Kaneko, H. Ozaki, H. Okamura, T. Suzuki, K. Fujimoto, and K. Kira	Nucl. Instr. Meth. Phys. Res. A		
			2009	600	146
2-16	Alignment and shields in the M2 primary proton beamline at J-PARC	P. Strasser, Y. Miyake, N. Kawamura, S. Makimura, and K. Nishiyama	Nucl. Instr. Meth. Phys. Res. A		
			2009	600	154
2-17	Radiation resistant magnets for the J-PARC muon facility	H. Fujimori, N. Kawamura, S. Meigo, P. Strasser, K. Nakahara, and Y. Miyake	Nucl. Instr. Meth. Phys. Res. A		
			2009	600	170
2-18	J-PARC muon control system	W. Higemoto, K. Shimomura, Y. Kobayashi, S. Makimura, Y. Miyake, Y. Kai, and K. Sakai	Nucl. Instr. Meth. Phys. Res. A		
			2009	600	179
2-19	JAEA-ASRC μSR project at J-PARC MUSE	W. Higemoto, R.H. Heffner, K. Shimomura, K. Nishiyama, and Y. Miyake	Nucl. Instr. Meth. Phys. Res. A		
			2009	600	182
2-20	Superconducting muon channel at J-PARC	K. Shimomura, A. Koda, P. Strasser, N. Kawamura, H. Fujimori, S. Makimura, W. Higemoto, K. Nakahara, K. Ishida, K. Nishiyama, K. Nagamine, and Y. Miyake	Nucl. Instr. Meth. Phys. Res. A		
			2009	600	192
2-21	Birth of an intense pulsed muon source, J-PARC MUSE	Y. Miyake, K. Shimomura, N. Kawamura, P. Strasser, S. Makimura, A. Koda, H. Fujimori, K. Nakahara, R. Kadono, M. Kato, S. Takeshita, K. Nishiyama, W. Higemoto, K. Ishida, T. Matsuzaki, Y. Matsuda, and K. Nagamine	Physica B		
			2009	404	957
2-22	High transverse field μSR with $\pi/2$-RF pulse spin control technique	R. Kadono, K. H. Satoh, A. Koda, K. Nishiyama, and M. Mihara	Physica B		
			2009	404	996
2-23	Development of a pipelined data acquisition system for μSR experiments at J-PARC	S.Y. Suzuki, M. Tanaka, K. Tauchi, Y. Yasu, S. Takeshita, A. Koda, M. Hiraishi, M. Miyazaki, K.H. Satoh, R. Kadono, K. Ishida, D. Tomono, and T. Matsuzaki	Physica B		
			2009	404	1002
3- 2	Muon spectroscopy with trace alkaline-earth and rare-earth isotopes implanted in solid D_2	P. Strasser, A. Taniguchi, T. Matsuzaki, K. Ishida, Y. Matsuda , S. Ohya, M. Iwasaki, and K. Nagamine	Hyperfine Interactions		
			2009	193	121
3- 3	Density effect in *d-d* catalyzed fusion with ortho- and para-enriched deuerium	H. Imao, K. Ishida, N. Kawamura, T. Matsuzaki, Y. Matsuda, A. Toyoda, P. Strasser, M. Iwasaki, and K. Nagamine	Hyperfine Interactions		
			2009	193	159
< 2010 >					
1-26*	Anisotropic superconducting order parameter in Li-intercalated layered superconductor Li_xZrNCl	M. Hiraishi, R.Kadono, M. Miyazaki, S. Takeshita, Y. Taguchi, Y. Kasahara, T. Takano, T. Kishiume, and Y. Iwasa	Phys. Rev. B		
			2010	81	014525

Contents

< 2007 >

< 2008 >

< 2009 >

< 2010 >

Available online at www.sciencedirect.com

ScienceDirect

ELSEVIER

Journal of Power Sources 174 (2007) 711–715

JOURNAL OF POWER SOURCES

www.elsevier.com/locate/jpowsour

Short communication

Magnetism and lithium diffusion in Li_xCoO_2 by a muon-spin rotation and relaxation (μ^+SR) technique

Kazuhiko Mukai [a,*], Jun Sugiyama [a], Yutaka Ikedo [a], Hiroshi Nozaki [a], Koichiro Shimomura [b], Kusuo Nishiyama [b], Kingo Ariyoshi [c], Tsutomu Ohzuku [c]

[a] *Toyota Central Research and Development Laboratories, Inc., Nagakute, Aichi 480-1192, Japan*
[b] *High Energy Accelerator Research Organization (KEK), Tsukuba, Ibaraki 305-0801, Japan*
[c] *Department of Applied Chemistry, Graduate School of Engineering, Osaka City University (OCU), Osaka 558-8585, Japan*

Abstract

Microscopic magnetism of the electrochemically Li-deintercaleted Li_xCoO_2 powders has been investigated by muon-spin rotation and relaxation (μ^+SR) spectroscopy in the temperature (T) range between 10 and 300 K. Weak transverse-field μ^+SR measurements indicate that localized moments appear in $LiCoO_2$ below 60 K, while both $Li_{0.53}CoO_2$ and $Li_{0.04}CoO_2$ are paramagnetic even at 10 K. Zero-field μ^+SR measurements for the samples with $x = 0.53$ and 0.04 show that the field distribution width (Δ) due to randomly oriented nuclear magnetic moments of ^7Li and ^{59}Co decreases monotonically with increasing T up to 250 K, and then it decreases steeper (increasing slope ($d\Delta/dT$)) above 250 K. Because the muon hopping rate (ν) is almost T independent for $Li_{0.53}CoO_2$ below 300 K, the decrease in Δ suggests that the time scale of Li^+ diffusion in Li_xCoO_2 is within a microsecond scale.

Keywords: Lithium-ion battery; $LiCoO_2$; Muon-spin rotation and relaxation (μ^+SR); Magnetism; Diffusion

1. Introduction

Lithium cobalt dioxide, $LiCoO_2$ has been extensively studied as a positive electrode material for Li-ion batteries over the past decade. According to ^7Li NMR [1] and magnetic susceptibility (χ) measurements [2], the electronic configuration of Co^{3+} in $LiCoO_2$ is in its low-spin state (t_{2g}^6), suggesting the absence of magnetic transitions at low temperatures (T). Sugiyama et al. [3], however, reported the appearance of localized moments below 65 K and long-range antiferromagnetic (AF) order below 30 K by muon-spin rotation and relaxation (μ^+SR) experiments, which is very sensitive to the local magnetic order. This suggests that either partial spin state transition ($t_{2g}^6 \rightarrow t_{2g}^5 e_g^1$) or a charge seperation ($2Co^{3+} \rightarrow Co^{2+} + Co^{4+}$) occurs below 65 K for $LiCoO_2$. However, such AF order was not observed for the Li_xCoO_2 samples with $x = 0.95$ and 0.70 [3]. Further Li^+ deintercalation induces structural phase transitions from the rhombohedral ($R\bar{3}m$) to the monoclinic ($C2/m$) phase at $0.5 \le x \le 0.55$ [4], and then O3 to O1 at $x \le 0.25$ [5,6]. This leads to the question on the correspondence between magnetism and crystal structures particularly for the Li_xCoO_2 with $x \le 0.55$.

In order to examine the relation between magnetism and structure in Li_xCoO_2, μ^+SR experiments for the samples with $x = 0.53$ and 0.04 are carried out because only μ^+SR detects the magnetic transition of Li_xCoO_2 with $x \ge 0.7$. Again, μ^+SR is a powerful technique to detect both static and dynamic internal magnetic fields of nuclear and electronic origin, and it gives essential information for understanding magnetic properties on a microscopic scale [7]. Recently, it is found that μ^+SR provides useful information on Li^+ mobility by detecting change in nuclear dipole fields as was reported for $LiMn_2O_4$ and related materials [8,9]. In this paper, we report μ^+SR results on microscopic magnetism for Li_xCoO_2 and discuss the relation between magnetism and structure together with Li^+ diffusion.

2. Experimental

A stoichiometric $LiCoO_2$ was prepared from $LiOH{\cdot}H_2O$ and $CoCO_3$ as described previously [4]. Starting materials were well

---

* Corresponding author.
E-mail address: e1089@mosk.tytlabs.co.jp (K. Mukai).

0378-7753/$ – see front matter © 2007 Elsevier B.V. All rights reserved.
doi:10.1016/j.jpowsour.2007.06.111

mixed and pressed into pellets (23 mm diameter and ∼5 mm thickness). The pellets were heated at 900 °C for 12 h in air. The sample was characterized by powder X-ray diffraction (XRD) and electrochemical measurements.

The Li_xCoO_2 samples for μ^+SR experiments were prepared by an electrochemical reaction in non-aqueous Li cells. In order to avoid μ^+SR signals from conducting carbon and binder, the electrodes were made of only the $LiCoO_2$ powder (a disc with 23 mm diameter and ∼0.3 mm thickness). The electrolyte used was 1 M $LiPF_6$ dissolved in ethylene carbonate (EC)/diethyl carbonate (DEC) (1/1, v/v) solution.

μ^+SR requires low-energy muons, so that they stop in samples within 100–200 mg cm^{-2} depth. High intensity beams are produced by high-energy (>500 MeV) proton accelerators. The muon beams are distinguishable by their time structure. Paul Scherrer Institut (PSI) in Switzerland and Tri-University Meson Facility (TRIUMF) in Canada are both *continuous wave* facilities, while high energy accelerator research organization (KEK) in Japan and Rutherford Appleton Laboratory (RAL) in the UK are sources of *pulsed* muon beam. The *continuous wave* facilities are suitable for the detection of larger magnetic fields and fast relaxing signals. The *pulsed* muon beam facilities are ideal for studying relatively slow relaxation, such as muon diffusion. In this study, we focused on the both local magnetism and muon diffusion, so that we have performed the μ^+SR experiments in the surface muon channel (π_A port) in KEK.

Each Li-deintercalated sample electrochemically prepared was packed in a sealed aluminum sample cell in a He-filled glove-box, and then placed on the silver sample holder in a cryostat. μ^+SR spectra were measured in a zero-field (ZF-), longitudinal-field (LF-) and weak transverse-field (wTF-) mode in the T range between 10 and 300 K. The orientations of external magnetic field are parallel for LF-, and perpendicular for wTF-, respectively, to the initial direction of muon-spin polarization.

After the μ^+SR experiments, the Li-cells were re-fabricated using the Li-deintercalated samples and their open circuit voltages (OCV) were measured in order to examine whether or not one-to-one correspondence μ^+SR signal and structure holds via electrochemical data. Magnetic susceptibility χ was measured using a superconducting quantum interference device (SQUID) magnetometer (MPMS, Quantum Design) in the T range between 5 and 400 K under magnetic field H = 10 kOe. Other sets of experimental conditions are given in Section 3.

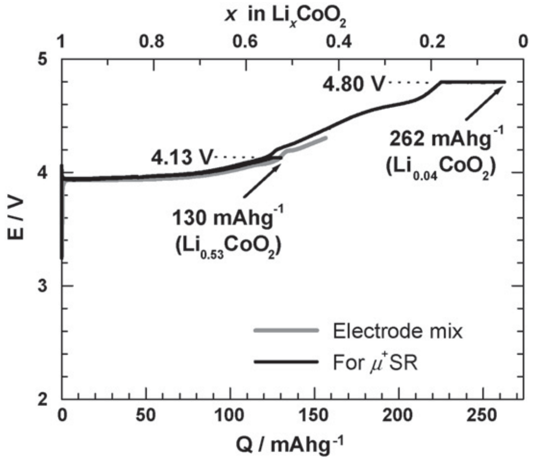

Fig. 1. Charge curves of Li/$LiCoO_2$ cells operated at a rate of 0.72 mA cm^{-2} at 25 °C. At 4.13 (or 4.8 V), the cell was potentiostatically charged totally for 3 days. The charge curve of the cell using the electrode mix, which consists of 88 wt.% $LiCoO_2$, 6 wt.% conductive carbon and 6 wt.% binder, is also shown for comparison. The Li composition was calculated from Q and theoretical capacity (274 mAh g^{-1}) based on one-electron transfer per formula weight of $LiCoO_2$.

3. Results and discussion

3.1. Characterization of Li_xCoO_2

$LiCoO_2$ was identified as a layered structure (a = 2.814 Å, c = 14.049 Å) with a space group symmetry of $R\bar{3}m$, in which cobalt- and lithium-ions were, respectively, located at the octahedral 3a and 3b sites in a cubic close-packed oxygen array. Fig. 1 shows the charging curves $E(Q)$ of Li/$LiCoO_2$ cells operated at a rate of 0.72 mA cm^{-2} (ca. 6 mA g^{-1}) at 25 °C. The values of x for the present Li_xCoO_2 samples with x = 0.53 and 0.04 were calculated from the theoretical capacity of 274 mAh g^{-1} assuming one-electron transfer per formula weight of $LiCoO_2$ and 100% of coulombic efficiency. Electrochemical charge was carried out up to 4.13 or 4.8 V at which the cell was potentiostatically charged totally for 3 days. The operating voltage (E) for 0 to 70 mAh g^{-1} is almost constant, and then the $E(Q)$ curve monotonically increases in voltage as a function of Q. Two minor changes in the slope of the $E(Q)$ curve are observed around 125 mAh g^{-1} and 200 mA g^{-1}. The former corresponds to the phase transition from the $R\bar{3}m$ to the $C2/m$ phase [4], and the latter shows the change in oxygen packing from the O3 to the O1 [5,6]. These $E(Q)$ curves for the electrodes prepared without the addition of conducting carbon and binder are almost the same to those of usual electrode mix as seen in Fig. 1. After the whole

Table 1
The Li/Co ratio of the Li_xCoO_2 samples and open circuit voltages (OCV) of the Li/Li_xCoO_2 cells before and after the μ^+SR and χ measurements

Li/Co (EC)	OCV (μ^+SR)		OCV (χ) (∼150 h[a])	Li/Co (ICP-AES) (∼180 h[a])
	Before (0 h[a])	After (∼12 h[a])		
0.53	4.13 V	4.11 V	4.08 V	0.50
0.04	4.43 V	4.38 V	4.41 V	0.12

ICP-AES analysis was carried out after the whole measurements: that is, ∼1 week later after the initial electrochemical charge (EC). The Li/Co ratio of the $LiCoO_2$ sample is 1.02.

[a] Time after the charge.

μ^+SR and χ measurements, the composition of the samples was determined by an induction coupled plasma-atomic emission spectral (ICP-AES) analysis. The samples were washed with acetone and dried. The results are summarized in Table 1. The Li/Co ratio calculated by an electrochemical measurement is usually different from that by an ICP-AES analysis mainly due to the decomposition of the electrolyte especially at higher voltage than 4.5 V. The Li/Co ratios for the present samples are thus estimated to be within $0.50 \leq x \leq 0.53$ and $0.04 \leq x \leq 0.12$ in Li_xCoO_2. Although the structural analysis of these samples was not performed, the $E(Q)$ curves and the value of OCV support that the sample with $0.50 \leq x \leq 0.53$ is the monoclinic phase [4] and with the $0.04 \leq x \leq 0.12$ the O1 phase [5,6]. In this paper, the Li/Co ratios calculated from electrochemical data were used.

3.2. Micro- and macroscopic magnetism of Li_xCoO_2

In order to examine the existence/absence of magnetic phase transitions and/or volume fraction of magnetic phases, wTF-μ^+SR spectra were measured in magnetic field of ~20 Oe for the Li_xCoO_2 samples with $x = 1$, 0.53, 0.04. The T dependence of wTF-μ^+SR time spectra are shown in Fig. 2 for the $x = 0.53$ sample at 100 and 10 K. Open circles indicate the given experimental data and solid lines the fitting result using the function of

$$A_0 P_{\mathrm{TF}}(t) = A_{\mathrm{TF}} \exp(-(\lambda t)^{\beta}) \cos(\omega_{\mu} t + \varphi) \tag{1}$$

where A_0 is the empirical initial muon asymmetry, $P_{\mathrm{TF}}(t)$ the muon-spin depolarization function, ω_μ the muon Larmor frequency in the applied field, φ the initial phase of the precession, A_{TF} and λ are, respectively, the asymmetry and the exponential relaxation rate of the oscillation caused by the external wTF and β is the power of the exponential relaxation. The asymmetry indicates muon-spin depolarization by the local magnetic fields in the sample. If the sample has weak internal fields, such as due to paramagnetism or nuclear magnetism, A_{TF} is independent of T. Conversely, ferromagnetic or antiferromagnetic order generates in the sample, A_{TF} decreases in proportion to the volume of the magnetic phases. Therefore, $A_{\mathrm{TF}}(T)$ curve is very useful to know the magnetic transition and the volume fraction of the magnetic phase.

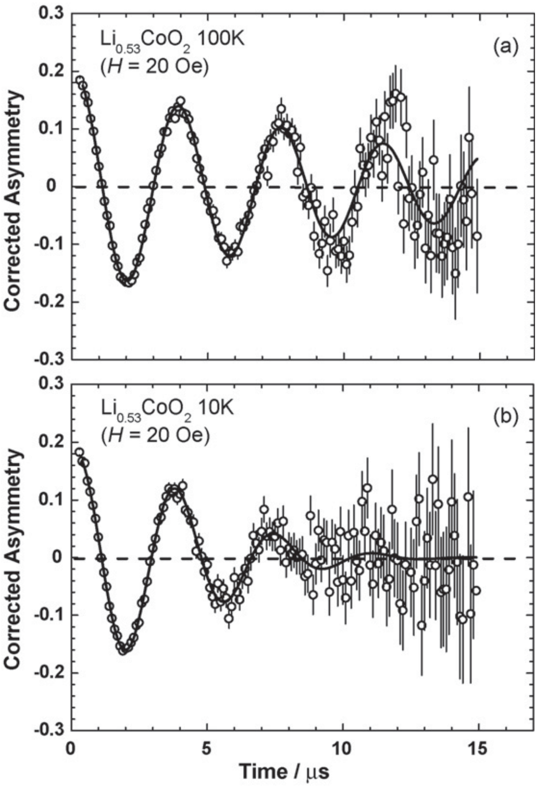

Fig. 2. wTF-μ^+SR time spectra for the Li_xCoO_2 sample with $x = 0.53$ at: (a) 100 K and (b) 10 K. Open circles and solid lines indicate the experimental data and the fitting result using Eq. (1), respectively. The orientation of the external magnetic field (transverse-field) is perpendicular to the initial direction of muon-spin polarization. A clear oscillation due to the external field is observed both 100 and 10 K. Although the bottom spectrum shows a larger relaxation than that of top, the initial amplitude does not change with T. This indicates $Li_{0.53}CoO_2$ is paramagnetic at 10 K.

Fig. 3 shows the T dependence of A_{TF} for the samples with $x = 1$, 0.53 and 0.04. The normalized A_{TF} (N_{ATF}) is defined by $[A_{\mathrm{TF}}(100\,\mathrm{K}) - A_{\mathrm{TF}}(T)]/A_{\mathrm{TF}}(100\,\mathrm{K})$. When T decreases from 100 K, N_{ATF} for the $x = 1$ sample is almost constant (~1) down to 60 K, and then drops with further decreasing T. This clearly indicates that the sample is approximately 100% paramagnetic above 60 K, and enters into a magnetic phase below 60 K. The volume fraction of the magnetic phase is ca. 13% at 10 K, as reported previously [3]. The magnetic Co^{3+} ($S = 1$) in the CoO_5 square-based pyramid was observed in non-stoichiometric compounds, such as $Li_{1.08}CoO_2$ [10]. However, the existence of the change in voltage around $x = 1/2$ in the $E(Q)$ curve in Fig. 1 suggests that the present sample is the stoichiometric $LiCoO_2$, because the change around $x = 1/2$ is a characteristic of stoichiometric $LiCoO_2$ [4]. Since the low-spin Co^{3+} (t_{2g}^6) ions are non-magnetic, the origin of this magnetism is probably due to a partial spin state transition ($t_{2g}^6 \rightarrow t_{2g}^5 e_g^1$) [11] or a charge seperation reaction ($2Co^{3+} \rightarrow Co^{2+} + Co^{4+}$) as already reported [3]. For the Li-deintercalated samples, N_{ATF} is almost constant over an entire T range for the $x = 0.53$ and 0.04 samples, indicating absence of magnetic order even at 10 K.

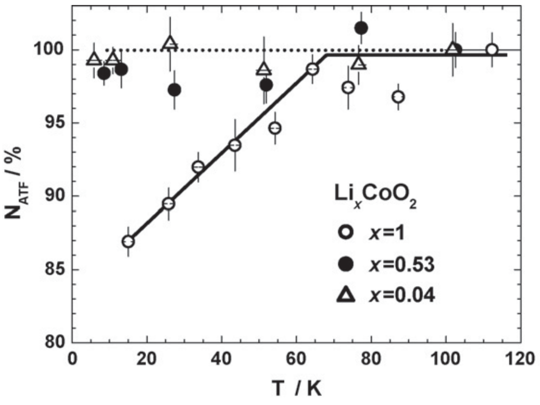

Fig. 3. Temperature dependence of the normalized asymmetry ($N_{A_{\mathrm{TF}}}$) for the samples with $x = 1$, 0.53 and 0.04. Data were obtained by fitting the wTF-μ^+SR spectra using Eq. (1). N_{ATF} is defined as $[A_{\mathrm{TF}}(100\,\mathrm{K}) - A_{\mathrm{TF}}(T)]/A_{\mathrm{TF}}(100\,\mathrm{K})$.

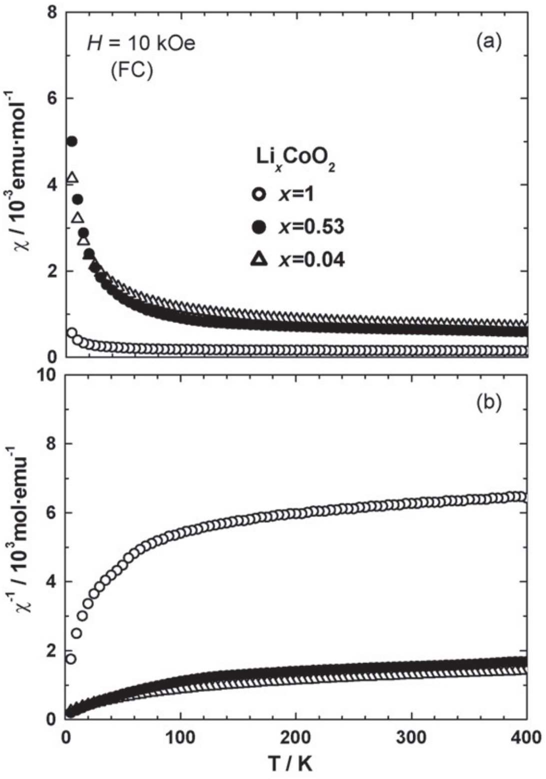

Fig. 4. (a) χ and (b) χ^{-1} as a function of temperature for the Li$_x$CoO$_2$ samples with $x = 0$, 0.53 and 0.04, measured in field-cooling (FC) mode with $H = 10$ kOe.

Fig. 4 shows (a) the $\chi(T)$ and (b) $\chi^{-1}(T)$ curves for the three samples. The $\chi(T)$ curve was measured in field-cooling (FC) mode with $H = 10$ kOe. After the μ^+SR experiment, the OCV of the cell were 4.11 V for the $x = 0.53$ sample and 4.38 V for $x = 0.04$, respectively. These values are 0.02–0.05 V lower than those measured before the μ^+SR experiment. The $\chi(T)$ curve for the $x = 1$ sample shows paramagnetic behavior down to 5 K. On the other hand, the $\chi(T)$ curves for both $x = 0.53$ and 0.04 samples are almost T independent down to 100 K, indicating a Pauli paramagnetic behavior. This is consistent with the insulator to metal transition induced by the decrease in Li at $x = 0.95$ [12]. The magnetic transition around 170 K for the $x = 0.95$, 0.70 [3] or 0.5 [2] samples, is not observed in the present two samples. As seen in Figs. 3 and 4, $x = 0.53$ and 0.04 samples are paramagnetic even at 10 K, confirming the lack of magnetic order both macro- and microscopically. This also supports that there is no direct correlation between phase transition and magnetism for the $x \leq 0.55$ samples.

Fig. 5 shows the T dependence of ZF-μ^+SR time spectra for the $x = 0.53$ sample at 300, 250, 200 and 10 K. Solid lines represent the fitting results obtained using the dynamic Kubo-Toyabe function $G^{\mathrm{DGKT}}(t, \Delta, \nu)$ due to randomly oriented nuclear magnetic moments [13];

$$A_0 P(t) = A_{\mathrm{KT}} G^{\mathrm{DGKT}}(t, \Delta, \nu) + A_{\mathrm{BG}} \tag{2}$$

where A_{KT} and A_{BG} are, respectively, the asymmetries of dynamic Kubo-Toyabe component and background signals mainly from the silver sample cell, Δ the static width of the local fields at the disordered sites and ν is the muon hopping or field fluctuation rate. When $\nu = 0$, $G^{\mathrm{DGKT}}(t, \Delta, \nu)$ is the static Gaussian Kubo-Toyabe function $G^{\mathrm{KT}}(t, \Delta)$ given by

$$G^{\mathrm{KT}}(t, \Delta) = \frac{1}{3} + \frac{2}{3}(1 - \Delta^2 t^2)\exp\left(\frac{-\Delta^2 t^2}{2}\right) \tag{3}$$

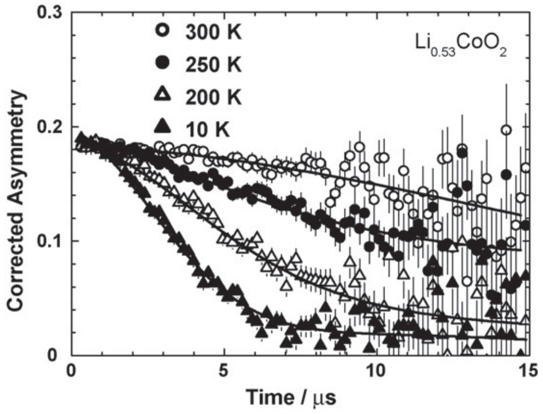

Fig. 5. ZF-μ^+SR time spectra for the Li$_x$CoO$_2$ sample with $x = 0.53$ at 300, 250, 200 and 10 K. Solid lines represent the results of fitting using Eq. (2).

As seen in Fig. 5, neither fast relaxation nor rotation is observed in these spectra, indicating that muon-spin is depolarized mainly by nuclear moments of ^{7}Li (4.20 μ_N) and ^{59}Co (5.25 μ_N).

Fig. 6 shows the T dependence of (a) Δ and (b) ν for the $x = 1$, 0.53 and 0.04 samples. Although Δ and ν for LiCoO$_2$ are

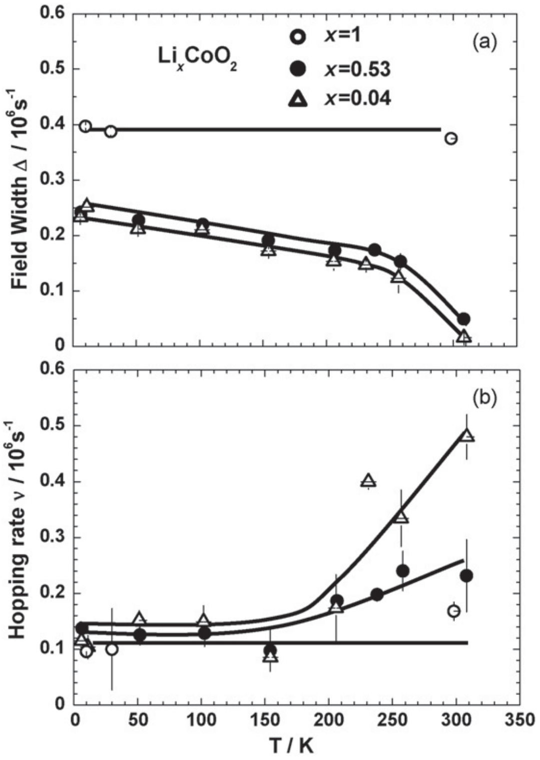

Fig. 6. Temperature dependence of (a) field distribution width Δ and (b) muon hopping rate ν for the Li$_x$CoO$_2$ samples with $x = 1$, 0.53 and 0.04. Both Δ and ν were estimated by fitting the ZF- and LF-μ^+SR time spectra using Eq. (2).

virtually independent of T, Δ for the $x<1$ samples decreases gradually with increasing T up to 250 K, and then decreases more rapidly. This may be a similar phenomenon to motional narrowing of the ^{7}Li NMR line shape at ∼400 K [14]. Considering the measurement accuracy of ν, the $\nu(T)$ curve for the $x = 0.53$ sample is almost T independent even at $T > 200$ K. The rapid decrease in Δ above 250 K would therefore correlate with the change in Li^+ diffusion as already reported for $LiMn_2O_4$ and related materials [8,9]. On the contrary, ν increases rapidly above 250 K for the $x = 0.04$ sample when T increases. This means that muon diffusion in the lattice begins above 250 K. Since ν is almost T independent for both $Li[Li_{0.04}Mn_{1.96}]O_4$ and $Li_{0.2}[Li_{0.04}Mn_{1.96}]O_4$ [8], the difference in the $\nu(T)$ curves between $Li_{0.04}CoO_2$ and $Li_{0.2}[Li_{0.04}Mn_{1.96}]O_4$ is probably due to the difference in "ion channel", i.e., two-dimensional channel in $LiCoO_2$ versus three-dimensional channel consisting of one-dimensional tunnels in $LiMn_2O_4$.

As stated above, μ^+SR is an effective tool to characterize lithium insertion materials in terms of both magnetic behavior and Li^+-ions dynamics. In this paper, we have reported the results on μ^+SR experiments for the Li_xCoO_2 samples with $x = 0.53$ and 0.04. In order to determine the full phase diagram of Li_xCoO_2, further μ^+SR experiments are necessary in particular for the $0.5 \leq x \leq 0.7$ samples. Such experiments are still in progress in our research group.

Acknowledgements

We wish to thank Mr. S. Kohno of OCU for preparing sample of $LiCoO_2$ and Mr. Y. Kondo of Toyota Central R&D Labs., Inc. for measuring ICP-AES analysis. We also appreciate Prof. J.H. Brewer of University of British Columbia and Prof. E.J. Ansaldo of TRIUMF for fruitful discussions.

References

[1] M. Ménétrier, A. Rougier, C. Delmas, Solid State Commun. 90 (1994) 439–442.
[2] S. Kikkawa, S. Miyazaki, M. Koizumi, J. Solid State Chem. 62 (1986) 35–39.
[3] J. Sugiyama, H. Nozaki, J.H. Brewer, E.J. Ansaldo, G.D. Morris, C. Delmas, Phys. Rev. B 72 (2005) 144424.
[4] T. Ohzuku, A. Ueda, J. Electrochem. Soc. 141 (1994) 2972–2977.
[5] G.G. Amatucci, J.M. Tarascon, L.C. Klein, J. Electrochem. Soc. 143 (1996) 1114–1123.
[6] L. Liu, L. Chen, X. Huang, X.-Q. Yang, W.-S. Yoon, H.S. Lee, J. McBreen, J. Electrochem. Soc. 151 (2004) A1344–A1351.
[7] J.H. Brewer, Encyclopaedia Appl. Phys. 11 (1994) 23–53 (and references cited therein).
[8] C.T. Kaiser, V.W.J. Verhoeven, P.C.M. Gubbens, F.M. Mulder, I. de Schepper, A. Yaouanc, P. Dalmas de Réotier, S.P. Cottrell, E.M. Kelder, J. Schoonman, Phys. Rev. B 62 (2000) R9236–R9239.
[9] M.J. Ariza, D.J. Jones, J. Roziere, J.S. Lord, D. Ravot, J. Phys. Chem. B 107 (2003) 6003–6011.
[10] S. Levasseur, M. Ménétrier, Y. Shao-Horn, L. Gautier, A. Audemer, G. Demazeau, A. Largetew, C. Delmas, Chem. Mater. 15 (2003) 348–354.
[11] M. Mikami, M. Yoshimura, Y. Mori, T. Sasaki, R. Funabashi, M. Shikano, Jpn. J. Appl. Phys. 42 (2003) 7383–7386.
[12] M. Ménétrier, I. Saadoune, S. Levasseur, C. Delmas, J. Mater. Chem. 9 (1999) 1135–1140.
[13] R.S. Hayano, Y.J. Uemura, J. Imazato, N. Nishida, T. Yamazaki, R. Kubo, Phys. Rev. B 20 (1979) 850–859.
[14] K. Nakamura, H. Ohno, K. Okamura, Y. Michihiro, I. Nakabayashi, T. Kanashiro, Solid State Ionics 135 (2000) 143–147.

Journal of Physics and Chemistry of Solids 68 (2007) 2124–2128

JOURNAL OF
PHYSICS AND CHEMISTRY
OF SOLIDS

www.elsevier.com/locate/jpcs

μSR measurements on the vortex lattice of CaAlSi: Anisotropic response in magnetic penetration depth

S. Kuroiwa[a,]*, K.H. Satoh[b], A. Koda[b,c], R. Kadono[b,c], K. Ohishi[d],
W. Higemoto[d], J. Akimitsu[a]

[a] *Department of Physics and Mathematics, Aoyama-Gakuin University, Sagamihara, Kanagawa 229-8558, Japan*
[b] *School of High Energy Accelerator Science, The Graduate University for Advanced Studies, Tsukuba 305-0801, Japan*
[c] *Institute of Materials Structure Science, High Energy Accelerator Research Organization (KEK), Tsukuba 305-0801, Japan*
[d] *Advanced Science Research Center, Japan Atomic Energy Agency (JAEA), Tokai 319-1195, Japan*

Abstract

The vortex state defined by two characteristic length scales, magnetic penetration depth (λ) and coherence length (ξ), in a layered hexagonal superconductor CaAlSi was probed using muon spin rotation. From preliminary analysis using modified London model, we found that the in-plane λ increases with increasing magnetic field while inter-plane λ is almost independent of magnetic field. The presence of field-induced quasiparticle excitation manifested in the field dependence of λ suggests that CaAlSi has an anisotropic gap structure (nodes/dips or multi-gapped).

Keywords: A. Superconductors

Recently, Sagayama et al. reported detailed crystal structure of a layered hexagonal superconductor CaAlSi (CAS), where they found two types of multi-stacked structures having either a clear five-fold (5*H*-CAS, T_c~5.7 K) or six-fold (6*H*-CAS, T_c~7.8 K) superlattice along the *c*-axis [1]. Meanwhile, we reported on the so-called clean-CAS that has only flat AlSi layers with Al and Si atoms being distributed regularly in the hexagonal plane without superstructure (1*H*-CAS, T_c~6.5 K) [2]. Interestingly, the T_c and many other transport properties depend on the superstructured periodicity. For these three phases, therefore, we have conducted μSR measurements using single crystal specimens to clarify the relationship between superstructured periodicity and superconducting property from microscopic viewpoint.

The detailed single crystal growth condition and superconducting properties in 6*H*-, 5*H*- and 1*H*-CAS were described elsewhere [2]. μSR measurements under a high transverse field (TF) were carried out on the M15 beamline of TRIUMF, Canada. Single crystalline samples with a dimension of $7 \times 7\,\mathrm{mm}^2$ were loaded to a He gas-flow cryostat with their *c*- or *a*-axis parallel to the applied magnetic field. Each measurement was performed under field-cooling process to minimize the disorder of flux line lattice (FLL) due to the pinning of vortices.

Since we can reasonably assume that muons stop randomly in the FLL, the muon spin precession signal, $P_z(t)$, provides the random sampling of the internal field distribution $B(\mathbf{r})$, $P_z(t) = \exp(-\sigma_p^2 t^2)\int_{-\infty}^{\infty} n(B)\exp(\mathrm{i}\gamma_\mu Bt + \phi)$ with $n(B) = \langle \delta(B - B(\mathbf{r}))\rangle_r$, where σ_p is the rate of additional relaxation due to the random flux pinning, $n(B)$ is the spectral density for the internal field defined as a spatial average ($\langle \cdots \rangle_r$) of the delta function over a unit cell of FLL, γ_μ is the muon gyromagnetic ratio, and ϕ is the initial phase of rotation [3]. These equations indicate that the real amplitude of the Fourier transformed muon precession signal corresponds to $n(B)$. Fig. 1 shows the fast Fourier transform (FFT) spectra in 6*H*-, 5*H*- and 1*H*-CAS at 2.0 K under several applied fields with respective field orientation. Note that the spectra for the field parallel to the *c*-axis are characterized by the broader line width

---

*Corresponding author. Tel.: +81 42 759 6545; fax: +81 42 759 6287.
E-mail address: kuro@phys.aoyama.ac.jp (S. Kuroiwa).

0022-3697/$ - see front matter © 2007 Elsevier Ltd. All rights reserved.
doi:10.1016/j.jpcs.2007.08.048

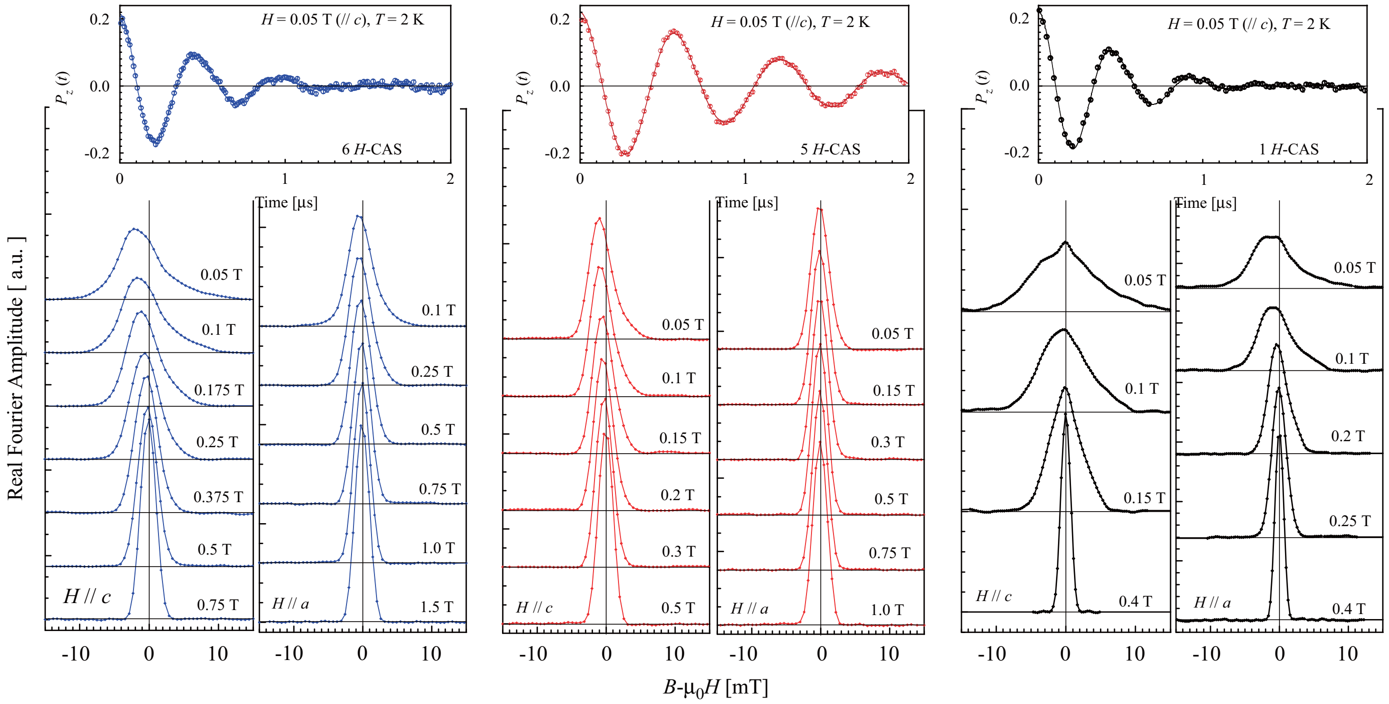

Fig. 1. The real amplitude of the fast Fourier transform (FFT, raw data) of the time spectra under several magnetic fields parallel to the crystalline c- or a-axis in $6H$-, $5H$- and $1H$-CAS. The insets show examples of μSR time spectra at 2 K under 0.05 T ($H\|c$), where solid curves represent fitting result using a model described in the text.

compared with those for $H\|a$ in all three phases, suggesting the presence of anisotropy in the penetration depth. The small peak near $B\text{-}\mu_0H = 0$ in $1H$-CAS is due to a background signal caused by muons missing at the sample.

We employed the modified London model for uniaxial superconductors (with z being the symmetric axis parallel to the crystalline c-axis) to reconstruct the two-dimensional field profile from the one-dimensional $n(B)$ measured by TF–μSR [4]. When the external field (μ_0H) is parallel to one of the crystalline axes, the field profile $B(\mathbf{r})$ is given by

$$B(\mathbf{r}) = B_0 \sum_{\mathbf{K}} \frac{\mathrm{e}^{-\mathbf{K}\cdot\mathbf{r}}\mathrm{e}^{-K^2\xi_v^2}}{1 + K_x^2\lambda_{ab}^2 + K_y^2\lambda_{xx}^2}, \qquad (1)$$

where B_0 ($\approx \mu_0H$) is the average internal field, $\mathbf{K}$ is the translation momentum of the vortex reciprocal lattice $\mathbf{K} = l\mathbf{u} + m\mathbf{v}$ ($l, m = 0, \pm1, \pm2\ldots$), λ_{ab} is the effective in-plane London penetration depth, $\lambda_{xx} = \lambda_{ab}$ for $H\|c$ and $\lambda_{xx} = \lambda_c$ for $H\|a$ ($a\|x$) with λ_c being the penetration depth along the c-axis, and ξ_v the Gaussian cutoff parameter. As a preliminary analysis, we adopted an approximation in Eq. (1) that $1/(1 + K_x^2\lambda_{ab}^2 + K_y^2\lambda_c^2) \simeq 1/(1 + K^2\lambda_{H\|a}^2)$ while $\lambda_{ab} \equiv \lambda_{H\|c}$. In the first-round analysis, we found that the triangular FLL without nonlocal correction [5] would be enough to reproduce the observed spectra. The possible fluctuation of reciprocal vectors was considered by introduced a mean width for the long range FLL distortion (σ_{lm}) as $\mathbf{K} = l(1 + \delta_l)\mathbf{u} + m(1 + \delta_m)\mathbf{v}$ with the probability

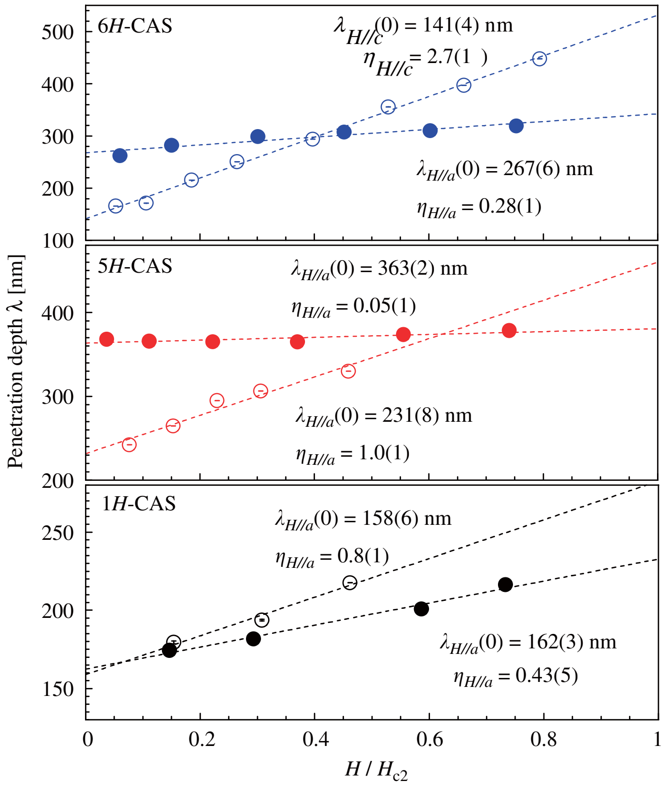

Fig. 2. Magnetic penetration depth ($\lambda_{H\|i}$, i = a and c) in $6H$-, $5H$- and $1H$-CAS as a function of H/H_{c2}. Dashed lines represent the result of fitting using $\lambda_{H\|i}(h) = \lambda_{H\|i}[1 + \eta_{H\|i} \cdot h]$.

distribution function $P(\delta_k) \propto \exp(-\delta_k^2/\sigma_{lm}^2)$. Here, we note that this yielded the best fit result with $\sigma_{lm}{\sim}0$ for 1*H*-CAS. The analysis was made in the time domain to avoid the statistical uncertainty. Typical examples of the TF–μSR time spectra are shown in the insets of Fig. 1 together with the results of fitting analysis based on the least square method using Eq. (1). A more detailed fitting analysis without the approximation mentioned above is now in progress.

Fig. 2 shows the $\lambda_{H\|i}$ for an applied field parallel to the *i*-axis ($i = a$ and c) as a function of H/H_{c2} normalized by upper critical fields at the measurement temperature. Interestingly, we observed the gradual increase of $\lambda_{H\|c}$ with increasing fields while $\lambda_{H\|a}$ depends only slightly on the applied field. It should be noted that the anisotropy of $\lambda(0)$ in 6*H*- and 5*H*-CAS is estimated to be about 1.6–1.8 while it is very small (~1) in 1*H*-CAS, which justifies the presumption that there is a correlation between the FLL ground state and superstructured periodicity.

Fig. 3 shows the field dependence of the vortex core radius, ρ_v, and cutoff parameter, ξ_v. Here, ρ_v is defined as a radial distance from the vortex center at which the supercurrent density $j(\mathbf{r})$, given by the Maxwell's relation $j(\mathbf{r}) = |\nabla \times B(\mathbf{r})|$, reaches its maximum value. Ichioka et al. reported that theoretical calculation predict the shrinkage of ρ_v due to the vortex-vortex interaction as shown in Fig. 3 [6]. The field dependence of ρ_v is a measure for the quasiparticle density of states (DOS) per each vortex, where the total DOS for the bulk specimen $N(H)$ is proportional to $\pi\rho_v^2 H \propto H^\beta$ with $\beta = 1$ for the rigid vortex core (the factor H is the number of vortices per unit area). The dashed curves in Fig. 3 show the fitting result using this form $\rho_v = \rho_0 h^{(\beta_{H\|i}-1)/2}$, and the estimated $\beta_{H\|i}$ are listed in Fig. 3. Interestingly, $\beta_{H\|i}$ in 1*H*-CAS are

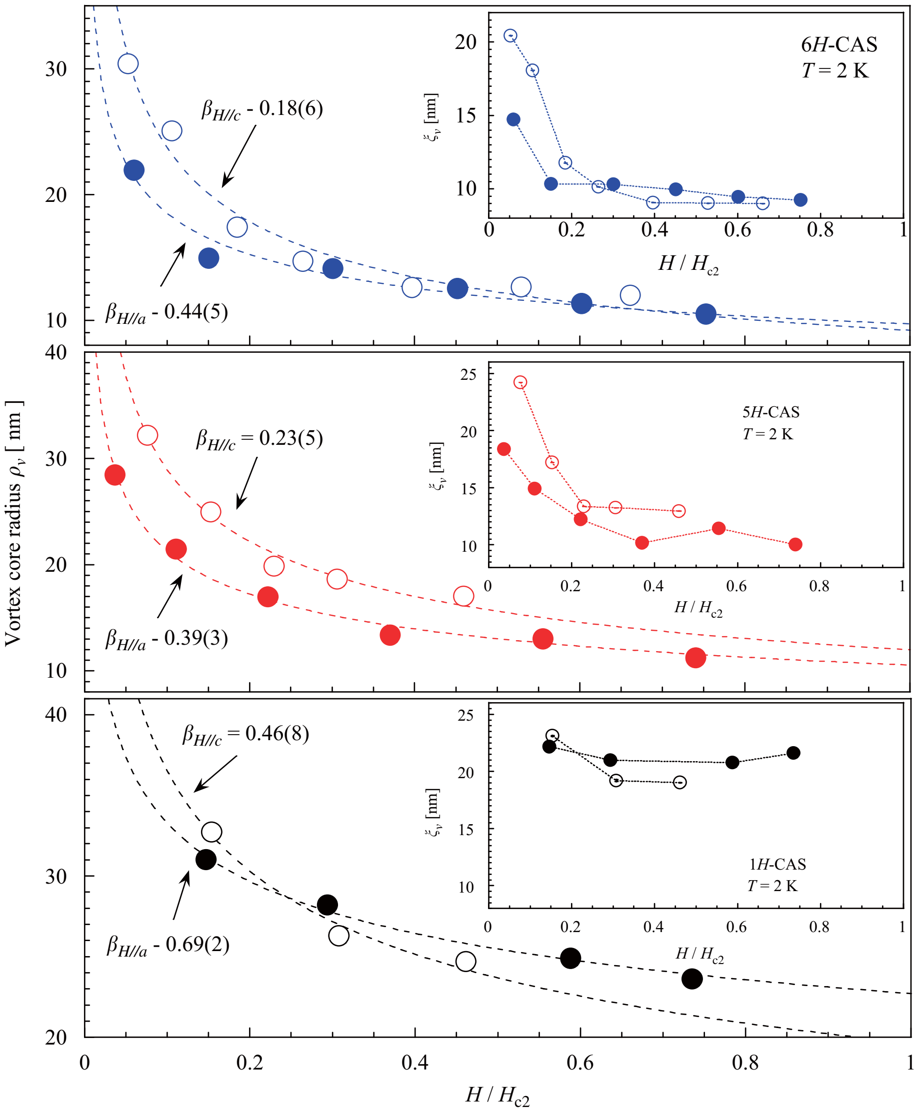

Fig. 3. The field dependence of the vortex core radius (ρ_v) and cutoff parameter (ξ_v, inset). For the dashed curves, see the text. Dotted lines in the insets are guide for the eye.

qualitatively consistent with that in a recent calculation assuming s-wave pairing for $T/T_c = 0.5$ ($\beta = 0.67$). On the other hand, the smaller value of $\beta_{H\parallel i}$ in superstructured specimens compared with that in 1H-CAS may be related with the quasiparticle excitations outside the vortex cores. Meanwhile, ξ_v in 6H- and 5H-CAS shows a steep decrease with increasing field while that in 1H-CAS is almost independent of fields expected for the conventional single band superconductor. The value of ξ_v at lower field in the respective phases are in good agreement with the Ginzburg–Landau coherence length $\xi_{\rm GL}$ (see Ref. [2]). As shown in Fig. 4, $\sigma_{\rm p}$ exhibits a gradual decrease with increasing field. This behavior can be explained by the stronger overlap of flux lines at higher field region. We point out here that the random pinning force in 1H-CAS is extremely stronger than that in superstructured specimens, whose origin remains to be clarified. Meanwhile, we observed clear enhancement of σ_{lm} at lower fields parallel to the c-axis while no such behavior was found for the case of $H\parallel a$. This seems to be related with the softening of the compression modulus C_{11}–C_{66} for the FLL at lower magnetic fields. It is generally known that the elastic property of FLL is provided by the compression modulus C_{11}–C_{66}, shear modulus C_{66} and tilt modulus C_{44}. The field dependence of these modulus over the field region far from the lower critical field H_{c1} is then

$$C_{11} \simeq C_{44} \simeq \frac{H_{c2}^2}{8\pi} h^2, \quad C_{66} \simeq \frac{0.13}{\kappa^2} \frac{H_{c2}}{8\pi} (1 - h^2),$$

where κ is the GL-parameter. Here, the relationship between a field-independent vortex pinning force F_p, C_{ij} and σ_{lm} is described by the Hooke's law, $F_p \propto C_{ij}\sigma_{lm}$, which leads to $\sigma_{lm} \propto F_p/C_{ij} \sim g/(h - h_0)^2$, where g is the effective inverse force constant and h_0 is the offset parameter. As is found in the insets, the h dependence of σ_{lm} is well described by this relation. Therefore, σ_{lm} is related to the long range distortion induced by random compression/tilting of vortices.

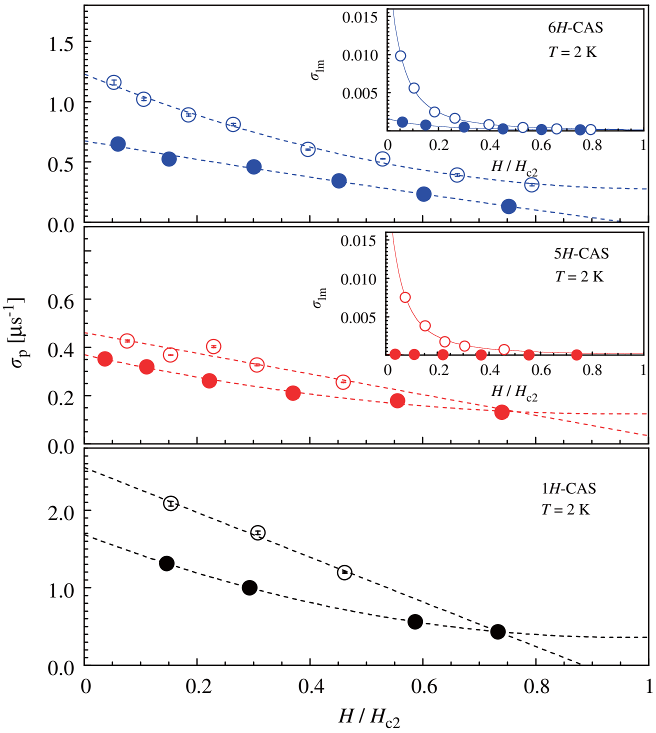

Fig. 4. The field dependence of $\sigma_{\rm p}$ and σ_{lm} at 2 K. These dashed lines are intended to guide for eyes. Fitting result by $\sigma_{lm} \propto g/(h - h_0)^2$ is shown as solid curves in insets figure.

Finally, we discuss the origin of gradual enhancement of λ with increasing field as shown in Fig. 2. It is now being established that the low energy quasiparticle excitation manifested in the field-gradient of $\lambda(h)$ can provide a measure for the anisotropy of superconducting order parameter [4]. In the FLL state, the shift in the quasiparticle energy spectrum, $\varepsilon = \hat{p} \cdot \hat{v}_s$, due to the semi-classical Doppler shift around vortex cores gives rise to the field-induced quasiparticle excitation, where $\hat{p}$ is the quasiparticle momentum and $\hat{v}_s$ is the supercurrent velocity. In the case of order parameter with a nodal or anisotropic structure (including multigap), the Cooper pair with a gap energy of less than ε can be broken by Doppler shift, leading to an enhancement of λ. In order to assess the magnitude of low-lying quasiparticle excitation, we performed fitting analysis for the data in Fig. 2 using the following linear relation, $\lambda_{H\parallel i}(h) = \lambda_{H\parallel i}(0)[1 + \eta_{H\parallel i} \cdot h]$, where η represents the strength of the pair breaking effect. The estimated values of $\lambda_{H\parallel i}(0)$ and $\eta_{H\parallel i}$ in the respective phases are displayed in Fig. 2. For all phases in CAS, $\eta_{H\parallel c}$ is comparable to those in YNi$_2$B$_2$C [7], KOs$_2$O$_6$ [8] and MgB$_2$ [9] (i.e., $\eta = 0.97$, 2.58 and 1.27, respectively) in which point nodes or two-gap is strongly suggested by other experiments [10,11]. On the other hand, the gradient of $\lambda_{H\parallel a}(h)$ is extremely small compared with that of $\lambda_{H\parallel c}(h)$. Since the Doppler shift is far smaller than the gap energy in a typical situation for the isotropic gap, no such enhancement of $\lambda(h)$ is expected for the conventional s-wave pairing (i.e., $\eta \ll 1$). Therefore, it is suggested from the field dependence of $\lambda_{H\parallel i}$ that an anisotropic structure (nodes/dips or multi gapped) is present in the order parameter along the direction normal to the c-axis, while a full-gap is anticipated for a direction perpendicular to the a-axis.

In summary, we have performed μSR measurements under high TF in the single crystal of CAS with a variety of superstructure, and extracted the characteristic length scale of superconductivity by mapping out the local field distribution in the FLL. For three crystalline phases, it is inferred from the presence of low-lying quasiparticle excitation indicated by the gradient of effective penetration depth that the order parameter in CAS has an anisotropic or multi-gapped structure.

We are grateful to the μSR staff of TRIUMF for their technical support. This work was partially supported by a Grant-in-Aid for Scientific Research on Priority Areas from the Ministry of Education, Culture, Sports , Science and Technology of Japan.

References

[1] H. Sagayama, et al., J. Phys. Soc. Jpn 75 (2006) 043713.
[2] S. Kuroiwa, et al., Phys. Rev. B 74 (2006) 014517.
[3] E.H. Brandt, Phys. Rev. B 37 (1988) 2349.
[4] R. Kadono, et al., J. Phys. Condens Matter 16 (2004) 2631.
[5] V.G. Kogan, et al., Phys. Rev. B 55 (1997) R8693.
[6] M. Ichioka, et al., Phys. Rev. B 59 (1999) 184.
[7] K. Ohishi, et al., Phys. Rev. B 65 (2002) 0140505 (R).
[8] A. Koda, et al., J. Phys. Soc. Jpn 74 (2005) 1678.
[9] K. Ohishi, et al., J. Phys. Soc. Jpn 72 (2003) 29.
[10] T. Yokoya, et al., Phys. Rev. Lett. 85 (2000) 4952.
[11] K. Izawa, et al., Phys. Rev. Lett. 89 (2002) 137006.

Available online at www.sciencedirect.com
ScienceDirect
ELSEVIER
Physica B 401–402 (2007) 430–432
PHYSICA B
www.elsevier.com/locate/physb

Shallow nitrogen acceptor in TiO_2 studied by β-NMR spectroscopy

M. Mihara[a,*], R. Matsumiya[a], K. Shimomura[b], K. Matsuta[a], M. Fukuda[a], D. Ishikawa[a], J. Komurasaki[a], D. Nishimura[a], T. Nagasawa[a], T. Izumikawa[c], T. Minamisono[d]

[a]*Department of Physics, Graduate School of Science, Osaka University, 1-1 Machikaneyama, Toyonaka, Osaka 560-0043, Japan*
[b]*Institute of Material Structure Science, KEK, Tsukuba 305-0301, Japan*
[c]*Radioisotope Center, Niigata University, Niigata 951-8510, Japan*
[d]*Fukui University of Technology, Fukui 910-8505, Japan*

Abstract

The local electronic structure of substitutional nitrogen impurity in rutile TiO_2 was studied by means of the β-NMR technique. A short-lived β emitter ^{12}N ($I = 1$, $T_{1/2} = 11\,ms$) was implanted into a rutile single crystal as a probe nucleus to detect double-quantum NMR spectrum. The result shows the existence of a small hyperfine interaction at low temperatures due to paramagnetic states localized at oxygen substitutional site, which suggests that a substitutional nitrogen atom acts as a shallow acceptor in rutile TiO_2.

PACS: 76.60.−k; 61.72.Ww; 71.20.Nr; 71.55.−i

Keywords: Shallow acceptor; TiO_2; Implantation; β-NMR

---

1. Introduction

Nitrogen impurities are expected to be one of the key dopants in TiO_2 to facilitate its use as a visible light responsive photocatalyst, since the photocatalitic activity in nitrogen-doped TiO_2 has been shown under visible light irradiation [1,2]. Substitutional nitrogen doping for oxygen in TiO_2 is thought to cause the band-gap narrowing, and to shift the optical response from ultraviolet to visible light range [2]. So far, there have not been sufficient experimental studies of the electronic structure of the nitrogen-doped TiO_2. An isolated substitutional nitrogen atom is expected to form an acceptor level in the band-gap of TiO_2. According to the hydrogen-like impurity model, Bohr radius a^* and binding energy E_b^* of a hole at an acceptor center is renormalized by the dielectric constant ε and the hole effective mass m_h^* as $a^* = \varepsilon/(m_h^*/m_e)a_0$ and $E_b^* = (13.6\,eV) \times (m_h^*/m_e)/\varepsilon^2$, respectively, where m_e is free electron mass and a_0 is the Bohr radius of hydrogen in vacuum. In case of rutile TiO_2, large dielectric constants $\varepsilon = 111$ and 257 along *a*- and *c*-axis, respectively, at low temperatures [3] might give a significant large a^* and small E_b^*, so that quite a small hyperfine constant due to large volume of the paramagnetic acceptor center might be observed at low temperatures. Studies of the electronic structure and the characteristics of such an acceptor center are of importance in understanding the properties of doped samples with various range of impurity concentration. The experimental studies on the electronic structure of paramagnetic shallow acceptor centers in semiconductors have been done by the electron-nuclear-double-resonance (ENDOR) and the negative muon spin rotation (μSR) techniques. The former was applied to a shallow boron acceptor in SiC [4] and the latter to an aluminum acceptor in Si [5]. In addition to these techniques, the β-NMR technique is also useful for the direct observation of such microscopic properties of isolated impurities, because of the extremely high sensitivity of NMR detection. In the present study, we have measured the double-quantum (DQ) NMR spectra of a short lived nucleus ^{12}N ($I = 1$, $T_{1/2} = 11\,ms$) implanted into a single crystal of rutile TiO_2

---

[*] Corresponding author. Tel.: +81 6 6850 5536; fax: +81 6 6850 5535.
E-mail address: mihara@vg.phys.sci.osaka-u.ac.jp (M. Mihara).

0921-4526/$ - see front matter © 2007 Elsevier B.V. All rights reserved.
doi:10.1016/j.physb.2007.08.204

by means of the β-NMR technique, in order to observe the hyperfine interactions of the substitutional ^{12}N nucleus with the surrounding electronic state.

2. Experimental

The experimental method is similar to the previous one [6]. The short-lived β-emitter ^{12}N was produced through the ^{10}B(^{3}He,n)^{12}N reaction. The ^{3}He beam of 3.0 MeV with an intensity of 10–15 μA from the 5 MV Van de Graaff accelerator at Osaka University was used to bombard the 90% enriched ^{10}B target which was prepared by the vacuum evaporation on a 0.5-mm-thick Al backing. The ^{12}N nuclei ejected from the target at angles in between 12° and 28° relative to the ^{3}He-beam direction was selected with a collimator to obtain nuclear spin polarization of ~20%. The polarized ^{12}N nuclei were implanted into a single crystal of rutile TiO$_2$ within a static magnetic field $B_0 = 0.5\,\mathrm{T}$ applied parallel to the polarization direction. The crystalline c-axis was set parallel to B_0. Two sets of plastic-scintillation-counter telescopes were located above and below the sample relative to the reaction plane to detect the asymmetry in the β-ray angular distribution. A radiofrequency (rf) magnetic field B_1 was applied perpendicular to B_0 to induce resonance which was detected by polarization change monitored via the β-ray asymmetry.

From the previous β-NMR studies on ^{12}N in rutile, two lattice locations with different electric field gradients (EFG) were identified as the oxygen substitutional site and the octahedral interstitial site [7]. So in the present case, the DQ transition between substrates $m = -1$ and $+1$ will be observed as a sharp single NMR line in the middle of a pair of single-quantum transition frequencies $\nu_{-1\leftrightarrow 0}$ and $\nu_{+1\leftrightarrow 0}$ under a strong external magnetic field, which is useful to search a small internal field B_{int} due to the hyperfine interaction. The frequency for the DQ transition ν_{DQ} in case of nuclear spin $I = 1$ is described as follows, considering the second-order shift due to the quadrupole interaction under a strong magnetic field B ($= B_0 + B_{\mathrm{int}}$):

$$\nu_{\mathrm{DQ}} = \nu_{\mathrm{L}} + \left(\frac{1}{8}\right)\left(\frac{\nu_{\mathrm{Q}}^2}{\nu_{\mathrm{L}}}\right)\{\sin^2\theta(3\cos^2\theta + 1) + \frac{2}{3}\eta\cos^2\varphi\sin^4\theta + \frac{1}{4}\eta^2(4 - 3\cos^2 2\varphi\sin^4\theta)\}, \quad (1)$$

where $\nu_{\mathrm{L}} = \gamma_{\mathrm{n}}B/2\pi$, the Larmor frequency with the nuclear gyromagnetic ratio γ_{n}; $\nu_{\mathrm{Q}} = (3/4)eqQ/h$ with the electric field gradient (EFG) q and the nuclear quadrupole moment Q, and the asymmetry parameter η of EFG. θ and φ are Euler angles of the EFG relative to the external field B_0. Using known values of eqQ/h and η for the substitutional site as $eqQ/h = 469\,\mathrm{kHz}$ and $\eta = 0.37$ at room temperature [7]; $\nu_{\mathrm{DQ}} = 1749\,\mathrm{kHz}$ is expected at $B_0 = 0.5\,\mathrm{T}$ for the present crystal orientation, $c \| B_0$, giving $\theta = \varphi = 90°$ [8]. For the interstitial site, $\nu_{\mathrm{DQ}} = {\sim}2040\,\mathrm{kHz}$ is estimated from $eqQ/h = 2888\,\mathrm{kHz}$ and $\eta = 0.038$, which is far from the DQ frequency for the substitutional site.

3. Results and discussion

The DQ NMR spectra of ^{12}N in TiO$_2$ at temperatures of 18, 105 and 280 K are shown in Fig. 1. The rf field B_1 of ~2.5 mT with the frequency modulation of ±1 kHz and the duration of 6 ms was applied to induce the DQ transition. The spectrum at 280 K shows a sharp NMR line and its frequency is consistent with the above estimation for the oxygen substitutional site, so that this resonance corresponds to the diamagnetic component of the substitutional nitrogen.

As the temperature decreases, the diamagnetic fraction decreases at 18 K and other components than the narrow diamagnetic line emerge with frequencies shifted to both sides by up to ~20 kHz from the diamagnetic line. The fraction of this broad component in the spectrum is about 40% of the total fraction deduced by integrating the spectrum over the observed frequency range. The total fraction at 18 K is nearly the same as that at 280 K. However, about 30% of the total fraction is missing at 105 K. In the spectrum at 18 K, resonances are observed even at lower frequencies than the Larmor frequency $\nu_{\mathrm{L}} = 1742\,\mathrm{kHz}$ at $B_{\mathrm{int}} = 0$, which cannot be explained without considering the existence of a negative internal field B_{int} because the second-order shift must be always positive. The chemical shift for the nitrogen case is ~400 ppm [8] which is too small to affect the present spectrum. The possibility of the single-quantum transition with tiny quadrupole interaction is ruled out because, if that is true, a distinct double quantum peak with the

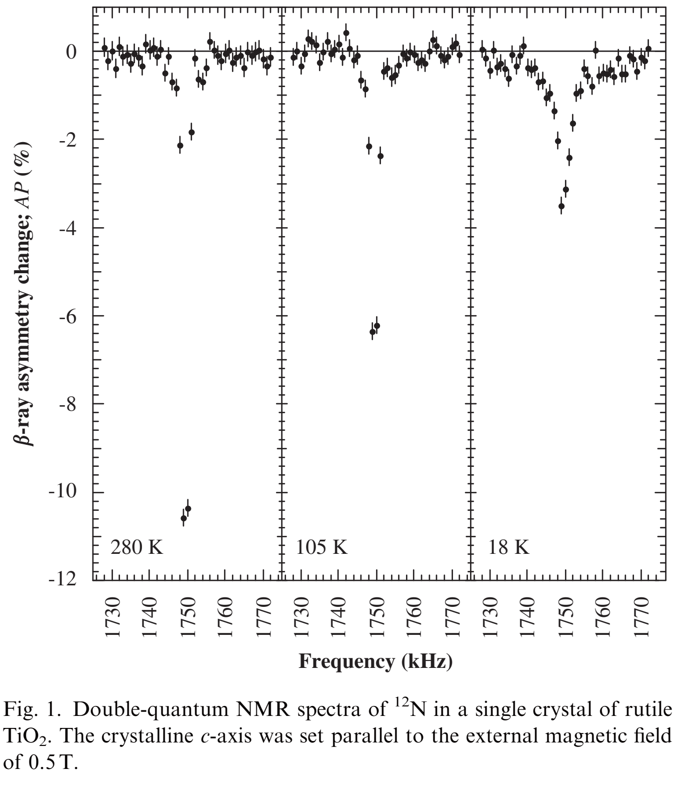

Fig. 1. Double-quantum NMR spectra of ^{12}N in a single crystal of rutile TiO$_2$. The crystalline c-axis was set parallel to the external magnetic field of 0.5 T.

second order shift $\sim\nu_Q^2/\nu_L$ of nearly zero should be observed at around 1742 kHz. This result suggests the existense of paramagnetic states formed by a nitrogen acceptor at low temperatures. If we accept this picture, the broad component at the higher frequency side can also be considered to be due to the paramagnetic states with the opposite direction of electron spin relative to that for the lower frequency component. From the observed NMR line shift, the hyperfine constant is estimated as $\sim10^{-4}$ times smaller than the vacuum hydrogen value. This result is similar to that of μSR studies on some semiconductors showing extremely small hyperfine constants for muonium (Mu) compared to the vacuum Mu value (10^{-3} to 10^{-4} times) due to formation of shallow donor levels [9].

In summary, the DQ NMR of ^{12}N in a single crystal of rutile TiO_2 was performed by means of the β-NMR technique and quite a small hyperfine field was observed at 18 K. This result suggests that the substitutional nitrogen atom for oxygen acts as a shallow acceptor in rutile TiO_2. In order to clarify the electronic structure of the nitrogen acceptor center, further experimental studies such as more precise temperature dependence of the DQ spectrum are in progress.

Acknowledgments

The present work was partly supported by the Murata Science Foundation and the grant-in-aid for Scientific Research Program of the Japan Society for the Promotion of Science.

References

[1] S. Sato, Chem. Phys. Lett. 123 (1986) 126.

[2] R. Asahi, T. Morikawa, T. Ohwaki, K. Aoki, Y. Taga, Science 293 (2001) 269.

[3] R.A. Parker, Phys. Rev. 124 (1961) 1719.

[4] A. van Duijn-Arnold, J. Mol, R. Verberk, J. Schmidt, Phys. Rev. B 60 (1999) 15829.

[5] T.N. Mamedov, V.N. Gorelkin, A.V. Stoikov, Phys. Part. Nucl. 33 (2002) 519.

[6] M. Mihara, S. Kumashiro, H. Fujiwara, R. Matsumiya, K. Matsuta, Y. Nakashima, Y.N. Zheng, M. Ogura, T. Sumikama, T. Nagatomo, K. Minamisono, M. Fukuda, T. Izumikawa, T. Minamisono, Physica B 376–377 (2006) 955.

[7] T. Minamisono, K. Sato, H. Akai, S. Takeda, Y. Maruyama, K. Matsuta, M. Fukuda, T. Miyake, A. Morishita, T. Izumikawa, Y. Nojiri, Z. Naturforsch 53a (1998) 293.

[8] C. Brevard, P. Granger, in: Handbook of High Resolution Multinuclear NMR, Wiley/Interscience, New York, 1981, pp. 90–91.

[9] S.F.J. Cox, J. Phys.: Condens. Matter 15 (2003) R1727.

PHYSICAL REVIEW B **77**, 054429 (2008)

Spin dynamics and spin freezing behavior in the two-dimensional antiferromagnet NiGa$_2$S$_4$ revealed by Ga-NMR, NQR and μSR measurements

Hideo Takeya,[1] Kenji Ishida,[1,*] Kentaro Kitagawa,[1,2] Yoshihiko Ihara,[1] Keisuke Onuma,[1] Yoshiteru Maeno,[1]
Yusuke Nambu,[1,2] Satoru Nakatsuji,[1,2] Douglas E. MacLaughlin,[3] Akihiko Koda,[4] and Ryosuke Kadono[4]
[1]*Department of Physics, Graduate School of Science, Kyoto University, Kyoto 606-8502, Japan*
[2]*Institute for Solid State Physics, University of Tokyo, Kashiwa 277-8581, Japan*
[3]*Department of Physics, University of California, Riverside, California 92521-0413, USA*
[4]*Meson Science Laboratory, Institute of Materials Structure Science, High Energy Accelerator Research Organization (KEK), 1-1 Oho, Tsukuba, Ibaraki 305-0801, Japan*

(Received 8 October 2007; published 21 February 2008)

We have performed ^{69,71}Ga nuclear magnetic resonance (NMR), nuclear quadrupole resonance (NQR), and muon spin rotation and resonance on the quasi-two-dimensional antiferromagnet NiGa$_2$S$_4$, in order to investigate its spin dynamics and magnetic state at low temperatures. Although there exists only one crystallographic site for Ga in NiGa$_2$S$_4$, we found two distinct Ga signals by NMR and NQR. The origin of the two Ga signals is not fully understood, but possibly due to stacking faults along the c axis which induce additional broad Ga NMR and NQR signals with different local symmetries. We found the spin freezing occurring at T_f, at which the specific heat shows a maximum, from a clear divergent behavior of the nuclear spin-lattice relaxation rate $1/T_1$ and nuclear spin-spin relaxation rate $1/T_2$ measured by Ga-NQR as well as the muon spin relaxation rate λ. The main sharp NQR peaks exhibit a stronger tendency of divergence, compared with the weak broader spectral peaks, indicating that the spin freezing is intrinsic in NiGa$_2$S$_4$. The behavior of these relaxation rates strongly suggests that the Ni spin fluctuations slow down towards T_f, and the temperature range of the divergence is anomalously wider than that in a conventional magnetic ordering. A broad structureless spectrum and multicomponent T_1 were observed below 2 K, indicating that a static magnetic state with incommensurate magnetic correlations or inhomogeneously distributed moments is realized at low temperatures. However, the wide temperature region between 2 K and T_f, where the NQR signal was not observed, suggests that the Ni spins do not freeze immediately below T_f, but keep fluctuating down to 2 K with the MHz frequency range. Below 0.5 K, all components of $1/T_1$ follow a T^3 behavior. We also found that $1/T_1$ and $1/T_2$ show the same temperature dependence above T_f but different temperature dependence below 0.8 K. These results suggest that the spin dynamics is isotropic above T_f, which is characteristic of the Heisenberg spin system, and becomes anisotropic below 0.8 K.

DOI: 10.1103/PhysRevB.77.054429 PACS number(s): 75.40.Gb, 76.60.−k, 75.50.Lk

I. INTRODUCTION

Recently, vigorous theoretical and experimental studies have been performed on various compounds with geometrically frustrating lattices.[1] Among such compounds, a two-dimensional (2D) triangular lattice is quite intriguing because it is the simplest and most fundamental structure. Quite recently, a new quasi-2D triangular antiferromagnet NiGa$_2$S$_4$ was discovered as the first example of a bulk low-spin antiferromagnet with an exact triangular lattice.[2] NiGa$_2$S$_4$ is a layered compound with the central NiS$_2$ block layers of edge-sharing NiS$_6$ octahedra and top and bottom sheets of GaS$_4$ tetrahedra (Fig. 1). These slabs are stacked along the c axis and connected with each other by a weak van der Waals force. Since the NiS$_2$ layers are effectively decoupled, and the Ni-Ni distance along the c axis is more than three times longer than the Ni-Ni distance along the a axis, NiGa$_2$S$_4$ has been regarded as a nearly ideal 2D triangular system. The electronic configuration of magnetic Ni^{2+} ($3d^8$) ions is t_{2g}^6, e_g^2 ($S=1$). Despite strong antiferromagnetic interactions (the Weiss temperature $\theta_W \simeq -80$ K), it was reported that no long-range magnetic order is detected down to 0.35 K by susceptibility, specific-heat, and neutron-diffraction measurements.[2] Instead, incommensurate short-range order with nanoscale correlation, whose wave vector is $\boldsymbol{q}=(\eta,\eta,0)$ with $\eta=0.158\sim 1/6$, was revealed by the neutron diffraction. In addition, a quadratic temperature dependence of the specific heat below 4 K indicates the presence of coherent gapless linearly dispersive modes at low temperatures, although the bulk measurements show a small

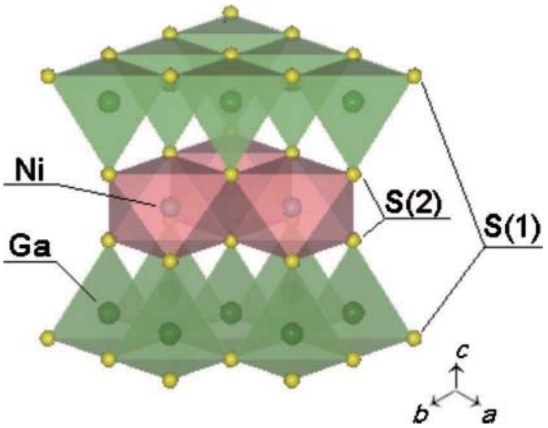

FIG. 1. (Color online) Crystal structure of NiGa$_2$S$_4$. The lattice constants are $a=3.624$ Å, $c=11.996$ Å.

anomaly around 10 K ($=T_f$) Ref. 2. However, the origin of the T^2 dependence of the specific heat (C) has not been understood yet.

In this paper, we report the results of Ga nuclear-magnetic-resonance (NMR) and nuclear-quadrupole-resonance (NQR) measurements on $NiGa_2S_4$, which have been performed in order to investigate from a microscopic viewpoint the origin of the anomaly at $T_f=10$ K, spin dynamics at low temperatures, and the magnetic ground state. We also report the results of muon-spin-rotation and relaxation (μSR) measurements, which detect the slow dynamics beyond the NMR limitation. We found that the nuclear spin-lattice relaxation rate $1/T_1$, nuclear spin-spin relaxation rate $1/T_2$, and the muon spin relaxation rate λ all exhibit a clear divergence in approaching from above $T_f \sim 10$ K. In addition, a broad structureless Ga-NQR spectrum and inhomogeneous distribution of T_1 were observed below 2 K. These results strongly suggest that the Ni moments freeze out below T_f and give rise to inhomogeneous internal fields at the Ga sites below 2 K. Moreover, it was found that the spin dynamics is isotropic above T_f, which is shown from the identical temperature dependence of $1/T_1$ and $1/T_2$. Isotropic spin dynamics is considered to be characteristic of the Heisenberg spin system. The different temperature dependence was observed at low temperatures between $1/T_1$ and $1/T_2$: $1/T_1$ follows a T^3 dependence below 0.5 K, and $1/T_2$ is almost linear in T below 2 K. The different temperature dependence suggests anisotropic spin dynamics at low temperatures.

II. EXPERIMENT

Polycrystalline and single-crystal samples of $NiGa_2S_4$ were synthesized as described in the literature.[2] Powder x-ray measurements at room temperature and neutron diffraction measurements in the temperature range between 1.5 and 300 K confirmed that $NiGa_2S_4$ retains the trigonal crystal structure down to 1.5 K with $P\bar{3}m1$ symmetry.[2] Three samples (polycrystalline and as-grown single crystalline samples of nominal $NiGa_2S_4$, and a polycrystalline sample of $NiGa_2S_{4.04}$) were used in the measurements. The same batch of polycrystalline $NiGa_2S_4$ used in the neutron diffraction[2] was measured in the present NQR experiments, and the single crystal was used in NMR. Since NQR results (NQR spectrum and $1/T_1$) are essentially the same in the three samples, we consider that the NQR results are determined by the intrinsic magnetic properties, which are not affected by a spurious impurity phase.

The NMR and NQR measurements were performed on two Ga isotopes [^{69}Ga ($I=3/2$): $^{69}\gamma=10.219$ MHz/10 kOe and $^{69}Q=0.19\times10^{-24}$ cm^2, ^{71}Ga ($I=3/2$): $^{71}\gamma=12.984$ MHz/10 kOe and $^{71}Q=0.16\times10^{-24}$ cm^2, where γ and Q are the gyromagnetic ratio and the electric quadrupole moment, respectively]. NMR and NQR spectra $1/T_1$ and $1/T_2$ were measured by Ga spin-echo signals in the temperature range of 75 mK–200 K. Zero-field and longitudinal-field μSR measurements in the temperature range of 1.8–250 K were performed at the πA-port of the Meson Science Laboratory at KEK in Tsukuba, Japan. The powder sample was attached to a silver "cold plate" by GE varnish. A ^{4}He gas flow cryostat was used for the μSR measurements.

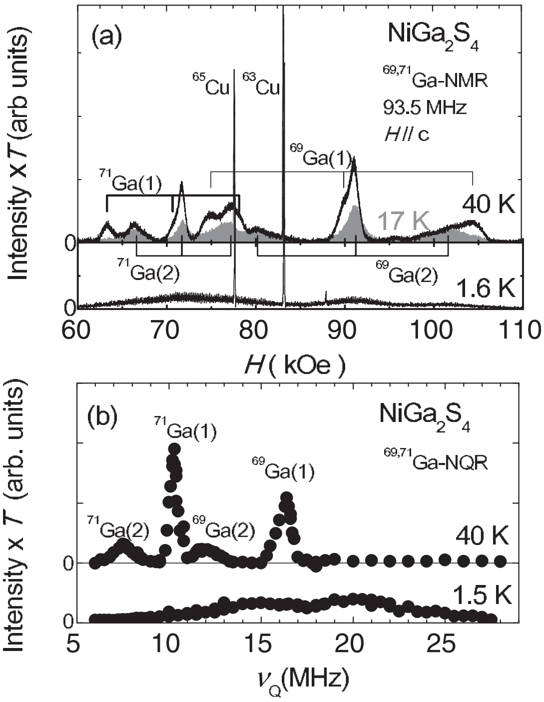

FIG. 2. (a) ^{69,71}Ga-NMR spectra from single-crystal $NiGa_2S_4$ at 40 K (curve in upper part), 17 K (gray area), and 1.6 K (lower part). NMR intensity normalization, i.e., taking into account difference in the T_2 relaxation rate (T_2 correction) has not been made. The resonant frequency is 93.5 MHz and the magnetic field is applied along the c axis. The time between first and second pulses to observe spin echo is 30 μsec. The ^{63,65}Cu signals are from an NMR coil. (b) ^{69,71}Ga-NQR spectra after T_2 correction at 40 and 1.5 K using polycrystalline samples. NQR intensity is normalized by temperature.

III. EXPERIMENTAL RESULTS

A. NMR and NQR spectra

NMR spectra of a single-crystalline $NiGa_2S_4$ were obtained by sweeping the external field. Figure 2(a) displays the Ga-NMR spectra against the field at 40, 17, and 1.6 K. Here, the NMR frequency is fixed at 93.5 MHz and the external magnetic field is applied parallel to the c axis.

In general, NMR spectra for nuclear spin $I(=3/2)$ show three peaks, which are composed of an intense central peak arising from the $1/2 \leftrightarrow -1/2$ transition and two satellite peaks from $3/2 \leftrightarrow 1/2$ and $-1/2 \leftrightarrow -3/2$ transitions when an electric field gradient exists at the observed nucleus site. Since $NiGa_2S_4$ has one crystallographic Ga site surrounded by four S atoms, which forms a GaS_4 tetrahedron, three peaks should be observed for each of the ^{69}Ga and ^{71}Ga nuclei. However, the spectrum at 40 K exhibits asymmetric center peaks and two asymmetric satellite peaks, indicative of the existence of two Ga sites [Ga(1) and Ga(2) sites] with

TABLE I. The quadrupole parameters for ^{69,71}Ga(1) and ^{69,71}Ga(2) derived from the peak position of the NMR and NQR spectra. The ratio of quadrupole moment of Ga isotopes which corresponds to that of NQR resonance frequency is $^{69}Q/^{71}Q = ^{69}\nu_Q/^{71}\nu_Q = 1.589$.

	ν_z (MHz)	ν_{Q} (MHz)	η
^{69}Ga(1)	15.87	16.26	0.39
^{69}Ga(2)	10.95	11.97	0.77
^{71}Ga(1)	10.05	10.25	0.35
^{71}Ga(2)	6.95	7.54	0.73

different EFGs. With decreasing temperature, the intensity of the NMR signals from the Ga(1) site decreases, and NMR signals from only one Ga site were observed at 17 K as shown by the dark gray area in Fig. 2(a). It should be noted that measurement of T_2 on NMR spectra was needed in order to discuss the intrinsic intensity ratio of the two Ga sites. By further cooling, all NMR signals disappeared below $T_{\mathrm{f}} \sim 10$ K, and an extremely broad NMR spectrum reappears below 2 K as shown in the bottom of Fig. 2(a). The extremely broad Ga-NMR spectrum strongly suggests the occurrence of static magnetism with inhomogeneous internal field well below T_{f}.

The existence of two Ga sites with different electric field gradients (EFGs), which was indicated by the Ga NMR, was confirmed by the NQR measurement. Ga-NQR spectra from a polycrystalline sample were obtained by measuring the spin-echo intensity as a function of frequency. Unlike the NMR, the NQR spectrum for the $I=3/2$ nuclei should consist of a single peak of the $\pm 1/2 \leftrightarrow \pm 3/2$ levels. We observed two intense peaks with narrow width and two weak peaks with broad width as shown in Fig. 2(b). The frequency ratio of two intense peaks (16.5 MHz/10 MHz) is nearly the same as that of two weak peaks (12.5 MHz/7.5 MHz), which is equal to the ratio of the nuclear quadrupole moment ($^{69}Q/^{71}Q=1.589$). This indicates that there are two sets of distinct NQR signals, and reveals the existence of two Ga sites with different EFGs in $\mathrm{NiGa_2S_4}$. From the separation between two satellite peaks in the NMR spectra at 40 K, we deduced the NQR frequency along the principal axis (c axis) of the EFG at the Ga site (ν_z). We evaluated the asymmetry parameter $\eta=(\nu_y-\nu_x)/\nu_z$ using the relation

$$\nu_{\mathrm{Q}} = \nu_{\mathrm{z}}\sqrt{1+\frac{1}{3}\eta^2},$$

where ν_Q is the NQR resonance frequency in Fig. 2(b). The values of ν_{Q}, ν_{z}, and η are listed in Table I.

It is noted that two Ga NQR signals are observed, even though there exists only one crystallographic site for Ga in perfect $\mathrm{NiGa_2S_4}$. From careful inductively coupled plasma (ICP) and scanning electron microscope (SEM) measurements,[3] it was revealed that S occupation is ~3.96, suggesting that the S deficiency is at most ~1%, and that the configuration of the triangular structure is rather good. At present, the origin of the two Ga sites is not identified, but we point out that possible inclusion of different stacking units, closely related to the structure of $\mathrm{NiGa_2S_4}$, might give rise to an additional Ga site with a different EFG. A tiny amount of sulfur deficiency and/or disorder is considered to exist in the "outer" sulfur layer, which is shown by S(1) in Fig. 1. It is considered that the sulfur deficiency and/or disorder is more easily introduced in the outer S(1) layer than in the inner S(2) layers which are coupled strongly with $\mathrm{Ni^{2+}}$ ions and form the $\mathrm{NiS_2}$ block layer. The fraction of the two Ga sites estimated from the Ga-NQR intensity at 40 K, which is normalized by $1/T_2$ values, is Ga(1):Ga(2) $=0.78:0.22$. If we assume that the Ga(2) NQR is ascribed to the Ga site which is influenced by the sulfur deficiency at the S(1) site, we estimate that the S(1) deficiency is approximately 7% from the intensity ratio of two Ga NQR signals because one S(1) deficiency gives an influence to three Ga atoms in the low concentration limit. However, this possibility might be excluded from the ICP result. Instead, we consider that the stacking faults along the c axis, which result in a different stacking unit from the bulk $\mathrm{NiGa_2S_4}$, might be the origin of the Ga(2) site. In any case, the linewidth of the Ga(2) NQR signal is twice broader than that of the Ga(1) signal, it is reasonably considered that the Ga(1) signal arises from the Ga site with the regular crystal structure, and the Ga(2) signal arises from the Ga site with disorder and/or defects in the structure. This assignment is consistent with the fact that η at the Ga(2) (~0.75) is larger than η at the Ga(1) (~0.37).

The NQR-signal intensity at both Ga sites decreases with decreasing temperature and the NQR signals disappear around $T_{\mathrm{f}} \sim 10$ K, indicative of a magnetic anomaly. On further cooling, enormously broad NQR spectra were observed as in the NMR spectra below 2 K. Since no obvious structure was found in the spectra, it is inferred that the internal field at the Ga sites is widely distributed in a static magnetic state at low temperatures. Such a magnetic state is discussed in Secs. IV B and IV C.

B. Knight shift

Next, we show the temperature dependence of the Knight shift (K) measured at the central peaks of the Ga-NMR spectrum. In the K estimation, the shift originating from the second-order quadrupole interaction was subtracted. Figure 3 displays the temperature dependence of $K(T)$ for ^{71}Ga(1) and ^{71}Ga(2), along with the behavior of the bulk susceptibility normalized by the behavior of the Knight shift above 100 K.[2] In general, $K(T)$ is decomposed as

$$K(T) = K_{\mathrm{spin}}(T) + K_{\mathrm{orb}},$$

where $K_{\mathrm{spin}}(T)$ and K_{orb} are the spin and orbital parts of the Knight shift, respectively. K_{spin} is related to the bulk susceptibility $\chi(T)$ originating from the Ni spins as

$$K_{\mathrm{spin}}(T) = \frac{A_{\mathrm{hf}}}{N_{\mathrm{A}}\mu_{\mathrm{B}}}\chi(T),$$

where A_{hf}, N_{A}, and μ_{B} are the hyperfine coupling constant between the Ga-nuclear spin and Ni-3d spins, Avogadro's

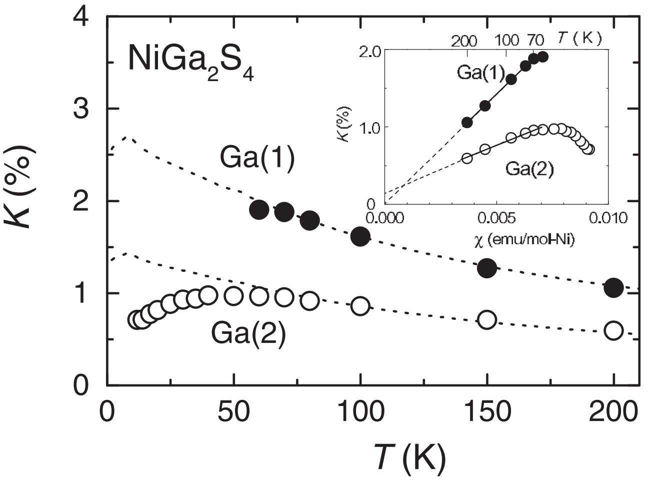

FIG. 3. Temperature dependence of the Knight shift K for ^{71}Ga(1)(●) and ^{71}Ga(2)(○) sites. The dotted curves in the main panel give the temperature dependence of susceptibility χ normalized to K above 100 K. Inset: K vs χ plot for the two ^{71}Ga sites. Dotted lines are the linear fits between 70 and 200 K.

number, and the Bohr magneton, respectively. K_{orb} is related to the Van Vleck susceptibility, which is temperature independent in general.

As shown in Fig. 3, the Knight shift at both sites follows the bulk susceptibility above 80 K. The hyperfine coupling constant A_{hf} at both sites $[17.70 \pm 0.20$ (kOe/μ_B) for Ga(1), 7.67 ± 0.36 (kOe/μ_B) for Ga(2)$]$ was evaluated from the slopes in the K-χ plot displayed in the inset of Fig. 3. However, K at the Ga(1) site could not be measured below 50 K due to the decrease of the NMR-signal intensity, and K at the Ga(2) site deviates from the temperature dependence of $\chi(T)$ below 80 K. The Knight shift probing the microscopic susceptibility decreases although the bulk susceptibility continues to increase. It seems that a precursor of the magnetic anomaly starts below 80 K. This corresponds well to the Weiss temperature obtained from $\chi(T)$. We point out that a similar deviation of $K(T)$ from $\chi(T)$ at low temperatures was observed in a number of geometrically frustrated spin systems such as $SrCr_8Ga_4O_{19}$ (SCGO),[4] $Ba_2Sn_2ZnCr_{7p}Ga_{10-7p}O_{22}$,[5] and $FeSc_2S_4$.[6] In these compounds, the possibility of spin singlet state and/or gapped state with the defectlike contribution has been suggested. However, such possibilities are not applicable to the present case because the divergence of $1/T_1$, which is discussed later, suggests a magnetic ground state. In the magnetic state, there exist static moments giving rise to inhomogeneous internal fields at the Ga sites. The different temperature dependence between microscopic and macroscopic spin susceptibilities in the highly frustrated compounds, which are probed with NMR and bulk susceptibility, respectively, remains unclear, and deserves to be understood theoretically.

C. Nuclear spin-lattice and spin-spin relaxation rate, $1/T_1$ and $1/T_2$

The nuclear spin-lattice relaxation rate (longitudinal rate) $1/T_1$ was measured by the saturation-recovery method with

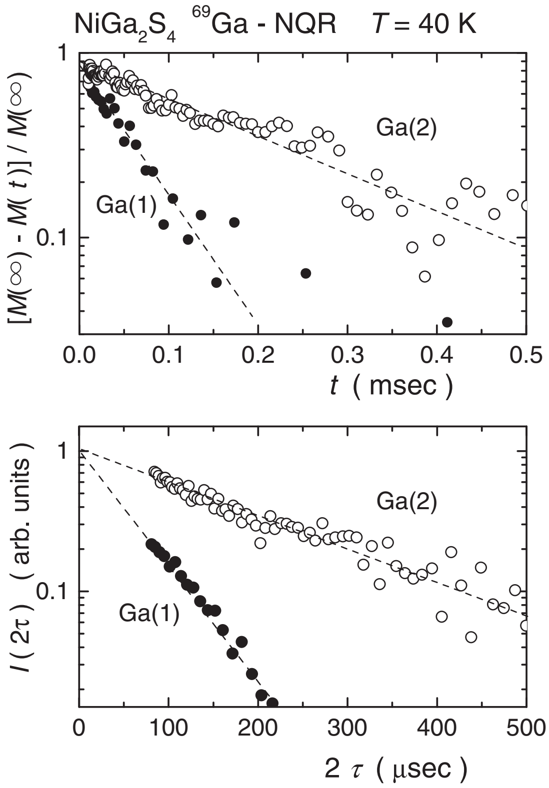

FIG. 4. (a) Recovery curves $m(t)$ derived from the ^{69}Ga nuclear magnetization at two Ga sites [^{69}Ga(1)(●) and ^{69}Ga(2)(○)] by changing the time interval between a saturation pulse and first pulse. Single component of T_1 was derived at two sites. (b) Decay curve $I(2\tau)$ from the ^{69}Ga nuclear magnetization obtained by changing the duration time τ between first and second pulses. The decay curves are consistently fitted by an exponential function $[I(2\tau) \propto \exp(-2\tau/T_2)]$.

saturation pulses. Above T_f, the recovery curve $m(t)$ of the nuclear magnetization $M(t)$ at time t after the saturation pulses, which is defined by $m(t) = [M(\infty) - M(t)]/M(\infty)$, is consistently fitted by the $m(t) \propto \exp(-3t/T_1)$ at both Ga sites as shown on a semilogarithmic scale in Fig. 4(a). Thus a single T_1 component was determined above 10 K. The nuclear spin-spin relaxation rate (transverse rate) $1/T_2$ was measured by recording the spin-echo intensity $I(2\tau)$ by changing the time separation τ between the $\pi/2$ (first) and π (second) pulses. $I(2\tau)$ was well fitted by the relation of $I(2\tau) \propto \exp(-2\tau/T_2)$ at both Ga sites as shown in Fig. 4(b). Here, the pulse length of a $\pi/2$ is approximately 5 μsec.

Between T_f and 2 K the NQR signals are not observed due to the extremely short T_1 and T_2. This is due to the critical slowing down of the spin fluctuations to the NQR frequency scale, which results in the rapid spin relaxation. On further cooling, a broad NQR spectra in Fig. 2(b) was observed below 2 K. The $m(t)$ exhibits the multicomponent behavior, which is characterized by the upward curve as shown in Fig. 5(a). The $m(t)$ is consistently fitted by the relation $m(t) \propto \exp(-\sqrt{3t/\tilde{T}_1})$ in Fig. 5(a). This is shown by the straight line in the semilog plot between $m(t)$ and $\sqrt{t}$. This relation is often observed when $1/T_1$ is inhomogeneously

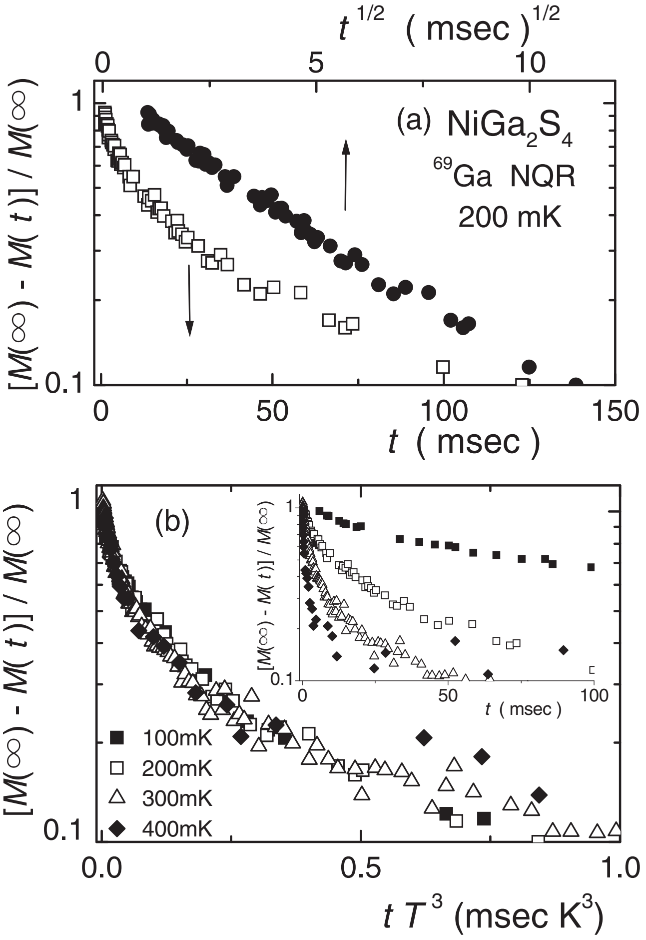

FIG. 5. (a) Relaxation curves $m(t)$ plotted at 200 mK against t (bottom axis, black circles) and $\sqrt{t}$ (top axis, open circles), where t is the time between the saturation pulse and the first spin-echo pulse. (b) Several recovery curves at several temperatures far below T_f plotted against tT^3, where T is the temperature. The inset of Fig. 5(b) shows the same recovery curves plotted against t.

distributed due to the presence of the relaxation center, e.g., an amount of doped magnetic impurities and/or crystal imperfection.[7] In such a case, $1/\widetilde{T}_1$ is normally adopted as $1/T_1$. On the other hand, it was found that $I(2\tau)$ follows the same $I(2\tau)\propto\exp(-2\tau/T_2)$ relation even below T_f. The inset of Fig. 6 shows the plot of the $I(2\tau)$ against 2τ at 76, 220, and 485 mK. Thus single-component $1/T_2$ was determined down to the lowest temperature.

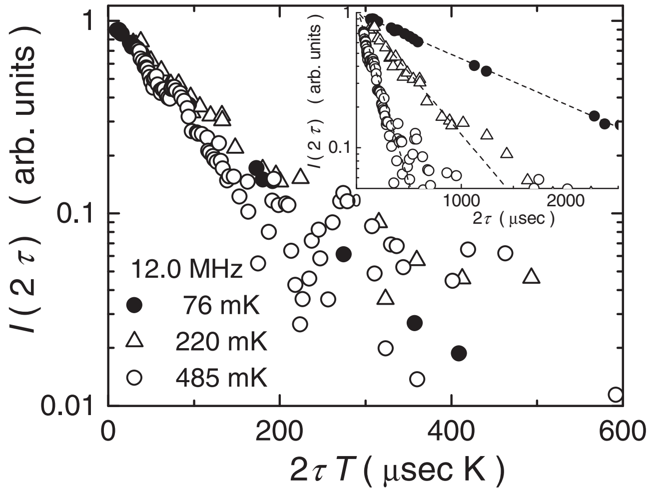

FIG. 6. Ga-NQR decay curves $I(2\tau)$ of $NiGa_2S_4$ are plotted against $2\tau T$ at various temperatures far below T_f. The inset shows the same decay curves plotted against t.

The temperature dependences of $1/T_1$, $1/\widetilde{T}_1$, and $1/T_2$ determined by the above fitting procedures are displayed in Figs. 7(a) and 7(b), together with the temperature dependence of the integrated NQR intensity multiplied by temperature, which is normalized to the value at 100 K [Fig. 7(c)]. A T_2 correction has been made for the estimation of the NQR intensity in Fig. 7(c), and we assume that T_2 is independent of frequency below 2.5 K. Figures 7(a) and 7(b) display the temperature dependence of $1/T_1$ and $1/T_2$ measured at the two ^{69}Ga sites above 10 K, $1/\widetilde{T}_1$ measured at various frequencies, and $1/T_2$ at 12 MHz, respectively. The ratio of $1/T_1$ between the two isotopes at high temperatures is $(1/^{69}T_1)/(1/^{71}T_1)=0.67\pm0.05$, which is in good agreement with the ratio of gyromagnetic ratio $(^{69}\gamma/^{71}\gamma)^2=0.62$. This indicates that $1/T_1$ is dominated by the magnetic interaction with the electrons, not by the electric quadrupole interaction. Above 80 K, $1/T_1$ of ^{69}Ga(1) is nearly constant, which is often observed in a localized-moment system when the temperature is higher than the exchange energy between the localized moments. Below 80 K, as shown in Fig. 7(a), $1/T_1$ gradually increases with decreasing temperature, and correspondingly the intensity of the NQR signal decreases. Such behavior is considered as a precursor of the spin freezing of Ni-3d spins. If we compare the temperature dependence of $1/T_1$ at the two Ga sites, ^{69}Ga(1) and ^{69}Ga(2) sites, the magnitude of $1/T_1$ at the Ga(1) site is three times larger than $1/T_1$ at the Ga(2) site. It should also be noted that the onset temperature of the divergent behavior below about 80 K is higher at the Ga(1) site than at the Ga(2) site. From the comparison of the temperature dependence of $1/T_1$ at the two Ga sites, we conclude that the magnetic anomaly seen in T_f is an intrinsic nature of $NiGa_2S_4$, because the Ga(1) site possesses a narrower NQR spectrum, indicative of the homogeneous site. If T_f were induced by inhomogeneity of the sample, such as sulfur disorder and/or stacking faults, $1/T_1$ at the Ga(2) site, where larger inhomogeneity is suggested by the NQR spectrum, would show the magnetic precursor from higher temperatures. Obviously, this is not the case. A similar difference between the Ga(1) and Ga(2) sites, which indicates that the magnetic anomaly at T_f is intrinsic in $NiGa_2S_4$, was also observed in $1/T_2$ and NQR-intensity results as shown in Figs. 7(b) and 7(c).

As noted above, in the temperature range between 10 and 2 K, the NQR signal was not observed due to the extremely short T_1 and T_2 beyond the limit of the NMR measurement. Below 2 K, the relaxation rate is distributed inhomogeneously in the low-temperature region. This multicomponent T_1 behavior is often observed in the spin-glass[8] and Kondo-disordered systems.[9] $1/\widetilde{T}_1$ determined from $m(t)\propto\exp(-\sqrt{3t/\widetilde{T}_1})$ decreases strongly with decreasing temperature as

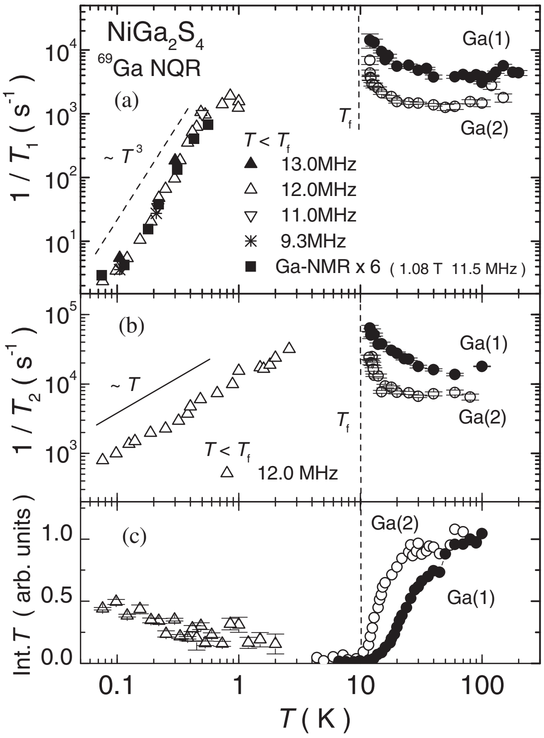

FIG. 7. (a) Temperature dependence of nuclear spin-lattice relaxation rate $1/T_1$. $1/T_1$ was measured at ^{69}Ga(1)(●), ^{69}Ga(2)(○) site above T_f. Below 1 K, $1/\widetilde{T}_1$ was derived from the fitting of $m(t)$ measured at four frequencies in a range between 9.5 and 13 MHz. Solid squares give $1/\widetilde{T}_1$ measured at 1.08 T with resonant frequency of 11.5 MHz. $1/T_1$ for NMR is normalized for the difference in the matrix elements (see text). (b) Temperature dependence of nuclear spin-spin relaxation rate $1/T_2$. Below 2.5 K, $1/T_2$ was measured at 12 MHz in the broad NQR spectrum affected by the inhomogeneous internal fields. Decay curves below 2.5 K are consistently fitted by a single exponential function down to a lowest temperature as shown in Fig. 6 although $1/T_1$ is widely distributed as shown in Fig. 5(b). (c) Temperature dependence of integrated intensities of spin echo after T_2 correction. Below 2.5 K, we assume that T_2 is independent of frequency.

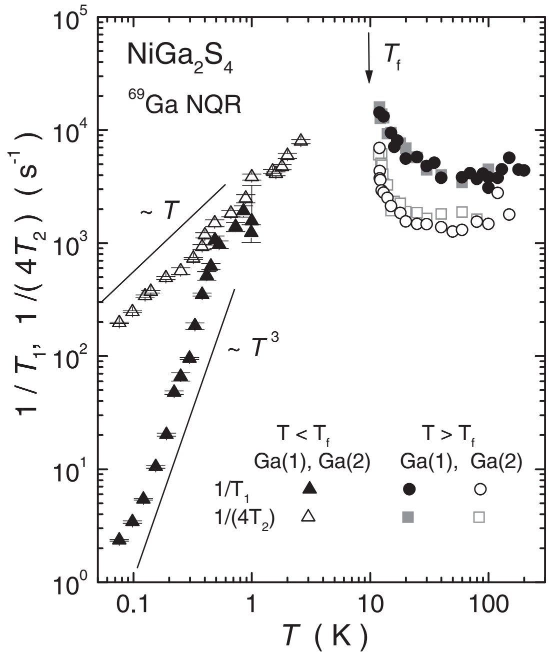

FIG. 8. Temperature dependence of the NQR relaxation rate $1/T_1$ and $1/(4T_2)$ at ^{69}Ga(1) and ^{69}Ga(2) sites.

shown in Fig. 7(a). Here, $\widetilde{T}_1/3$, the time when $m(t)$ decays to $1/e$, is regarded as a characteristic value of T_1 in multicomponent T_1. $1/\widetilde{T}_1$ was measured at several NQR frequencies from 9.5 and 28 MHz at 1.5 K, but the values of $\widetilde{T}_1$ do not change so much in this frequency range. The temperature dependence of $1/\widetilde{T}_1$ below 2 K is shown in Fig. 7(a) in the frequency range between 9.3 and 13 MHz, and is independent of the frequency. $1/\widetilde{T}_1$ measured in 10 kOe shows the same temperature dependence as that in zero field, although the value of $1/\widetilde{T}_1$ in 10 kOe is approximately six times smaller than $1/\widetilde{T}_1$ in zero field. This is due to the difference of the matrix elements of the transition probability.

We found that $1/\widetilde{T}_1$ is proportional to T^3 between 0.8 and 0.1 K. It should be noted that, although the spin dynamics is highly inhomogeneous, the T^3 dependence holds in all $1/T_1$ components, because the experimental data of $m(t)$ at several temperatures below 0.5 K lie on the same curve when plotted against tT^3 as shown in Fig. 5(b). Therefore the T^3 dependence of $1/\widetilde{T}_1$ is intrinsic behavior at low temperatures in NiGa$_2$S$_4$. Temperature dependence of $1/\widetilde{T}_1$ is discussed in Sec. IV.

Figure 7(b) shows temperature dependence of $1/T_2$. $1/T_2$ at both Ga sites also diverges at T_f, but $1/T_2$ at the Ga(1) site has larger values and starts to diverge at a higher temperature, which is in agreement with the $1/T_1$ results. Below 2.5 K, $1/T_2$ follows a T-linear temperature dependence down to the lowest temperature as shown from the plot of $I(2\tau)$ against $2\tau T$ at several temperatures in the main panel of Fig. 6. The large $1/T_2$ values and the strong temperature dependence of $1/T_2$ that follows $1/T_1$ behavior above T_f indicate that $1/T_2$ is not determined by the nuclear dipole interaction, but by the T_1 process. We found that the ratio of T_2/T_1 in NiGa$_2$S$_4$ is 4.2 ± 0.2 above T_f. We show temperature dependence of $1/T_1$ and $1/T_2$ divided by 4 in Fig. 8. It should be noted that $1/(4T_2)$ follows quantitatively the same temperature dependence as $1/T_1$ above T_f for both Ga sites, and that different temperature dependence is observed in $1/\widetilde{T}_1$ and $1/(4T_2)$ below 0.8 K. In general, $1/T_1$ ($1/T_2$) measured with the NQR spectra are affected by the spin dynamics perpendicular (parallel) to the principal axis of EFG. Therefore it is considered that spin dynamics is isotropic above T_f, but becomes anisotropic below 0.8 K. We suggest that the isotropic spin dynamics, characterized by the Heisenberg spin system, are slowing down and changed to the anisotropic ones below 0.8 K, where the in-plane spin dynamics is suppressed by the static magnetism, but the out-of-plane spin dynamics remains active and is proportional to temperature. Detailed temperature dependences above and below T_f are discussed in Sec. IV.

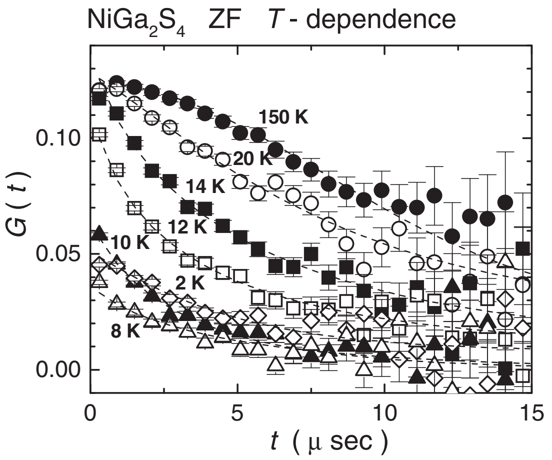

FIG. 9. Zero-field μSR asymmetry relaxation functions $G(t)$ in NiGa$_2$S$_4$ at various temperatures. The dotted curves are fits to the power exponential form $G(t)=A\ \exp[-(\lambda t)^{\beta}]$.

D. Muon spin rotation and relaxation

Muon spin rotation and relaxation (μSR) experiments are particularly suitable for detecting *slow* spin dynamics with an extremely high relaxation rate beyond the NMR experimental limitation. Therefore NMR and μSR are complementary to each other. Detailed μSR measurements in the temperature range between 2 K and T_f are published in the literature.[10] Here we concentrate on the zero-field μSR (ZF-μSR) experiments carried out at the Meson Science Laboratory KEK.

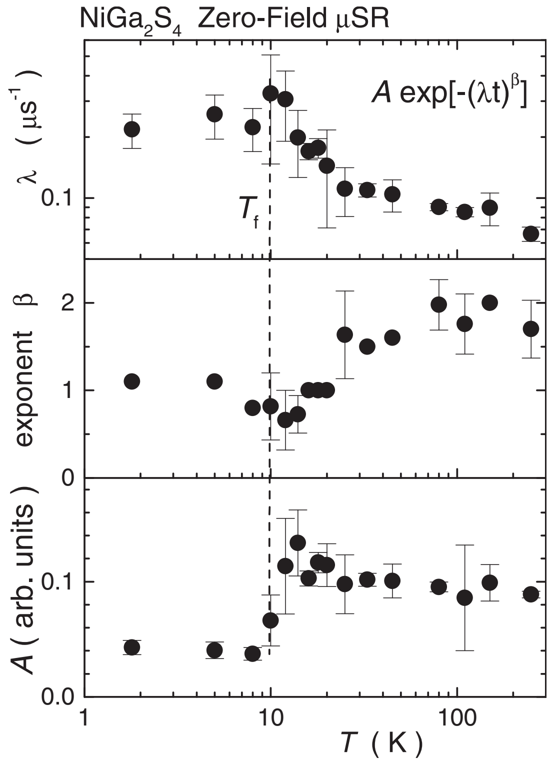

FIG. 10. Temperature dependence of (a) μSR relaxation rate (λ), (b) exponent β, and (c) asymmetry A derived from the fitting of zero-field asymmetry by $G(t)=A\ \exp[-(\lambda t)^{\beta}]$.

Figure 9 shows the ZF μSR asymmetry relaxation function $G(t)$ in NiGa$_2$S$_4$ at various temperatures. The relaxation function is gradually changing from Gaussian to Lorentzian by approaching T_f. The experimental asymmetry data were fitted to the "power exponential" form

$$G(t) = A\ \exp[-(\lambda t)^{\beta}],$$

where A is the initial muon decay asymmetry, λ is a generalized relaxation rate, and the exponent β interpolates between exponential (β=1) and Gaussian (β=2) limits. This form is suitable for characterizing spin dynamics, i.e., Gaussian (exponential) function suggests that muons see static (dynamics) magnetic fields during their lifetimes ($\sim$2.2 μs). $\beta > 1$ indicates an intermediate dynamics between two limits, and $\beta < 1$ suggests inhomogeneous dynamics with multicomponents.

The relaxation rate λ, exponent β, and asymmetry A are plotted against temperature in Fig. 10. Above 100 K, λ is small and β is close to 2. Both indicate that the nuclear dipole effect is dominant in the relaxation. With decreasing temperature, β gradually decreases from 2 to 1, and λ increases, although A is nearly constant down to T_f. These results indicate that μSR can detect the slow spin dynamics which is beyond the NMR limitation, since the NMR intensity gradually decreases in this temperature range. λ shows a distinct peak at $T_f \sim 10$ K, below which the asymmetry A decreases to approximately 1/3 of the values above T_f. As evident from Fig. 9, the so-called "1/3 tail" is lifted up at 2 K, which indicates that the static field along the implanted muon direction appears at least 2 K. In general, the muon spin polarization function below T_f is characterized by rapid depolarization of 2/3 of the initial polarization, followed by slow dynamic relaxation of the remaining 1/3 component. This is a characteristic signature of a highly disordered magnetic state in which the moments are quasistatic on the time scale of the muon lifetime.[11] In the present measurement, the rapid depolarization could not be detected due to the high inhomogeneity of the static moments, but the 1/3 component was detectable. It is considered from the residual asymmetry below T_f that almost the entire region in the sample is in the magnetic state.

It should be noted that relaxation of the 1/3 tail was observed at T=2 K. Therefore strong relaxation demonstrates the existence of slow dynamics even below T_f, which is consistent with the experimental fact that the Ga NQR spectrum is not observed down to 2 K. The present μSR measurements suggest that magnetic fluctuations of Ni spins are gradually slowing down below 80 K, and that the inhomogeneous static field appears at the implanted muon site at low temperatures. However, fluctuations of the Ni spins remain strong even far below T_f. Spin dynamics is discussed in the next section on the basis of NMR and μSR relaxation behavior.

IV. DISCUSSION

A. Spin dynamics above T_f

In this section, we discuss spin dynamics in NiGa$_2$S$_4$ in the paramagnetic state, which are revealed by $1/T_1$ and $1/T_2$

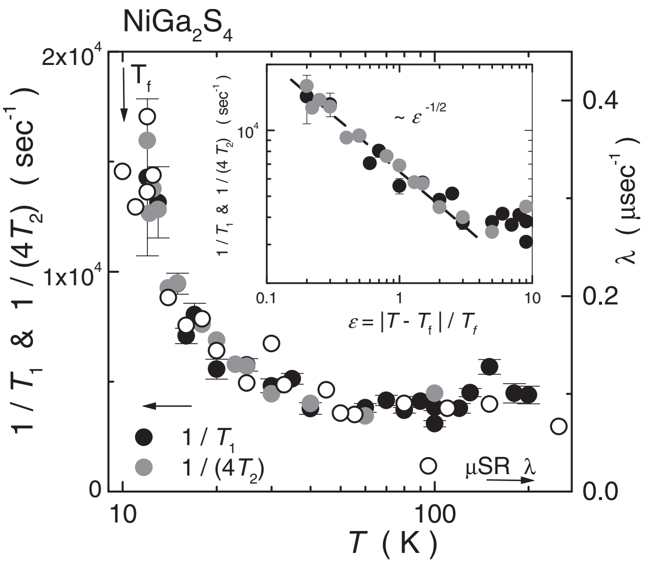

FIG. 11. Temperature dependence of $1/T_1$ and $1/(4T_2)$ of the Ga(1) NQR spectra, and μSR relaxation rate λ. The inset shows the plot of $1/T_1$ and $1/(4T_2)$ against $(T-T_f)/T_f$.

at the Ga(1) site, because the Ga(1) is considered to be more homogeneous than the Ga(2) site from the narrower NQR spectrum shown in Fig. 2(b). Above T_f, $1/T_1$ and $1/(4T_2)$ behave quantitatively the same as shown in Figs. 8 and 11, and λ derived from the μSR experiments also follows the same temperature dependence. At temperatures higher than 80 K, $1/T_1$ and $1/(4T_2)$ are nearly constant due to local-moment fluctuations by the exchange interaction between the Ni spins. Below 80 K, $1/T_1$ and $1/(4T_2)$ start to diverge towards T_f. As seen in the inset of Fig. 11, the divergent behavior of $1/T_1$ and $1/(4T_2)$ is approximately fitted by

$$1/T_{1,2} \propto \varepsilon^{-\nu}$$

with $\varepsilon=(T-T_f)/T_f$, and T_f and ν are estimated to be $T_f = 10.3 \pm 1.0$, and $\nu = 0.45 \pm 0.10$. According to theoretical prediction, ν is 0.3 and 0.8 in 3D and 2D Heisenberg systems, respectively.[12] $\nu \sim 0.5$ suggests that a magnetic anomaly might occur due to weak interactions along the c axis, since magnetic order is not realized at a finite temperature in the 2D Heisenberg system. It should be noted that the critical divergence of the relaxation rate was observed over an unusually wide temperature range $0.2 < \varepsilon < 3$, in which the 2D short-range correlation is highly developed. This is in marked contrast with the ordinary critical behavior in the 2D Heisenberg system,[12] for which the critical divergence is limited to the vicinity of T_N ($\varepsilon < 0.5$). Such a remarkable divergent behavior persisting over a wide temperature range seems to be one of the key features of the 2D triangular lattice, because similar critical behavior over wide temperature ranges was reported in LiCrO$_2$ and HCrO$_2$ with 2D triangular lattices.[13,14]

In addition, it was found that $1/(4T_2)$ shows quantitatively the same temperature dependence as $1/T_1$. This indicates that the spin dynamics is isotropic. When the nuclear dipole interaction is negligibly small, there is the relation between $1/T_1$ and $1/T_2$ measured with the NQR signal arising from the $\pm 1/2 \leftrightarrow \pm 3/2$ of $I=3/2$ transitions:[21,22]

$$\frac{1}{T_1} = G_{\perp}(\omega),$$

$$\frac{1}{T_2} = \frac{1}{2} G_z(0) + \frac{5}{2} G_{\perp}(\omega).$$

Here, $G_\alpha(\omega)$ is the spectral density of the longitudinal ($\alpha = z$) and transverse ($\alpha = \perp$) components of the fluctuating local field,[23] and is given by

$$G_\alpha(\omega) = \frac{\gamma^2}{2} \int_{-\infty}^{\infty} \langle \delta H_\alpha(t) \delta H_\alpha(0) \rangle \exp(i\omega t) dt,$$

where γ is the gyromagnetic ratio, and $\delta H_z(t)$ $[\delta H_\perp(t)]$ is the longitudinal (transverse) component of the fluctuating local field. If we assume an exponential correlation function,

$$\langle \delta H_\alpha(t) \delta H_\alpha(0) \rangle = \langle (\delta H_\alpha)^2 \rangle \exp\left(\frac{-|t|}{\tau_c} \right),$$

using the correlation time τ_c of the fluctuation, $1/T_1$ and $1/T_2$ are expressed as follows:

$$\frac{1}{T_1} \propto \gamma^2 \langle (\delta H_\perp)^2 \rangle \frac{\tau_c}{1 + (\omega \tau_c)^2},$$

$$\frac{1}{T_2} \propto \frac{1}{2} \gamma^2 \langle (\delta H_z)^2 \rangle \tau_c + \frac{5}{2} \gamma^2 \langle (\delta H_\perp)^2 \rangle \frac{\tau_c}{1 + (\omega \tau_c)^2}.$$

As seen in the equations, $1/T_1$ and $1/T_2$ are determined by the dimensionless value of $\omega\tau_c$, and are proportional to τ_c ($1/\omega^2 \tau_c$) in the case of $\omega\tau_c \ll 1$ ($\omega\tau_c \gg 1$). When τ_c becomes longer due to the slowing down of the Ni spins with approaching T_f, the relaxation rates at once increase with a maximum at $\omega\tau_c = 1$ and then decrease with decreasing temperature. The experimental facts that $1/T_2 \sim 4(1/T_1)$ and both show quantitatively the same temperature dependence to each other imply that the magnetic fluctuations are in the regime $\omega\tau_c \ll 1$ and isotropic, and that the relation between $\delta H_\perp$ and δH_z is $\langle (\delta H_z)^2 \rangle \sim 3 \langle (\delta H_\perp)^2 \rangle$ in the temperature region above T_f. The relaxation behaviors are consistent with the Heisenberg spin system.

With decreasing temperature, magnetic fluctuations are slowing down below 80 K, and seem to be static below T_f. Now, we discuss the temperature dependence of the correlation time $\tau_c(T)$ of the magnetic fluctuations quantitatively using the experimental data for $1/T_1$ and $A_{\rm hf}$ at the Ga(1) site and magnetic susceptibility χ. In the case when the nuclear spin-lattice relaxation rate at the Ga site is dominated by magnetic fluctuations of the Ni localized spins, $1/T_1$ is expressed as follows:

$$\frac{1}{T_1} = z \frac{\gamma_n^2 k_B T}{2\mu_B^2} \lim_{\omega \to 0} \sum_q [A(q)]^2 \frac{\chi''(q,\omega)}{\omega},$$

where $z(=3)$ is the number of the nearest neighbor Ni sites to a Ga site, $A(q)$ is the q-dependent hyperfine coupling constant at a Ga site from a Ni spin, and $\chi''(q,\omega)$ is the dynami-

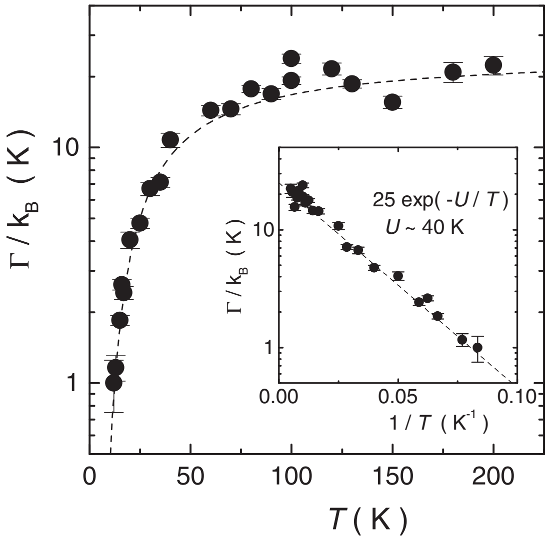

FIG. 12. Temperature dependence of the characteristic energy of the spin fluctuations $\Gamma(T)/k_{\mathrm{B}}$ (see text). The inset shows the plot of $\Gamma(T)/k_{\mathrm{B}}$ against $1/T$.

cal susceptibility and the sum is over the Brillouin zone. At temperatures much higher than T_{f}, the spin dynamics is determined by independent Ni moments, and the local-moment ($q=0$) susceptibility is given by

$$\chi_L(\omega) = \frac{\chi_0(T)}{1 - i\omega\tau_c(T)},$$

where χ_0 is the magnetic susceptibility per Ni atom (emu/Ni atom).

We consider that $A(q)$ and the dynamical susceptibility are isotropic because $1/T_1$ and $1/(4T_2)$ show nearly the same behavior in this temperature region, and take $A(q) \sim A_{\mathrm{hf}}/z = 17.7/3 = 5.9$ (kOe/μ_B). Then $1/T_1$ is described in the regime of $\omega\tau_c \ll 1$ as

$$\frac{1}{T_1} = 3\frac{\gamma_n^2 k_{\mathrm{B}} T}{\mu_{\mathrm{B}}^2} A_{\mathrm{hf}}^2 \chi_0(T)\tau_c(T).$$

Therefore the characteristic energy of the spin fluctuations Γ/k_{B}, which corresponds to $\hbar/[\tau_c(T)k_{\mathrm{B}}]$, is given by

$$\Gamma/k_{\mathrm{B}} = \hbar/[\tau_c(T)k_B] = 3\frac{(\gamma_n A_{\mathrm{hf}})^2\hbar}{\mu_B^2}\chi_0(T)T_1T$$
$$= 1.4 \times 10^5 T_1 T \chi_0 N_{\mathrm{A}} \ (\mathrm{K}).$$

Figure 12 shows the temperature dependence of $\Gamma(T)/k_{\mathrm{B}} = \hbar/[\tau_c(T)k_{\mathrm{B}}]$. $\Gamma(T)/k_B$ is constant above 100 K with the value of $\Gamma(T)/k_{\mathrm{B}} \sim 20$ K. This is in good agreement with the exchange interaction J between Ni spins, which is estimated to be $J \sim 20$ K from the relation

$$J = \frac{3k_{\mathrm{B}}\theta_W}{z' S(S+1)},$$

where we use the Weiss temperature θ_W of -80 K and the number of the nearest neighbor Ni sites for a Ni ion z' of 6.

It was found that $\Gamma(T)/k_{\mathrm{B}}$ shows thermally activated decrease below 100 K, described by the relation of

$$\Gamma(T)/k_{\mathrm{B}} = A \exp(-U/T).$$

From the inset of Fig. 12, A and U are estimated to be 25 and 40 K, respectively. Here, U corresponds to a binding energy of the local spin configuration determined by J. In general, we expect from the temperature dependence of $1/T_1$ that magnetic correlation length $\xi(T)$ develops exponentially with decreasing temperature, because $\Gamma(T)$ is related to $\xi(T)$ as $\Gamma(T) \propto [c/\xi(T)]^n$ in the Heisenberg spin system. However, neutron experiments showed that the $\xi(T)$ remains a couple of lattice constants even at 1.5 K.[2] It seems that $\Gamma(T)$ is not directly related to $\xi(T)$ in $\mathrm{NiGa_2S_4}$. Alternatively, we point out that the similar thermally activated behavior was reported in ESR studies on 2D triangular compounds of $\mathrm{LiCrO_2}$ and $\mathrm{HCrO_2}$,[13] and in NMR studies on a Heisenberg *kagomé* lattice antiferromagnet $\mathrm{KFe_3(OH)_6(SO_4)_2}$.[15] Particularly, Ajiro *et al.*[13] pointed out that the activation energy U in $\mathrm{LiCrO_2}$ and $\mathrm{HCrO_2}$ takes a universal value equivalent to $U = (2.7 \pm 0.3)JS^2 = 4k_{\mathrm{B}}T_{\mathrm{KM}}$, where T_{KM} is a critical temperature for a Kosterlitz-Thouless-type phase transition. In the 2D triangular spin system, the possibility of the "Z_2 vortex state" has been suggested.[16] Vortices related to the topologically stable defects appear at higher temperatures and start to couple to each other below T_{KM}. If we apply the above analyses to $\mathrm{NiGa_2S_4}$, $U \sim 40$ K corresponds to $U \sim 2JS^2 = 4k_{\mathrm{B}}T_{\mathrm{f}}$. This relation is quite different with that observed in dilute-alloy spin glasses.[17] In these compounds, the correlation time τ_c obeys the Arrhenius law $\tau_c = \tau_0 \exp(E_a/k_{\mathrm{B}}T)$ with a very large activation energy $E_a \sim 20k_{\mathrm{B}}T_{\mathrm{g}}$. This indicates that the freezing behavior is observed near T_g and the spins slow down immediately. We point out that the freezing behavior observed in $\mathrm{NiGa_2S_4}$ is different from the canonical spin-glass systems, and suggest the possibility that the "Z_2 vortex" transition occurs in $\mathrm{NiGa_2S_4}$. It is feasible that T_{f} is regarded as T_{KM} in $\mathrm{NiGa_2S_4}$.

We point out that the spin dynamics in $\mathrm{NiGa_2S_4}$ possesses the novel 2D spin character, discussed in the 2D Heisenberg compounds for nearly two decades.[13] As discussed above, it was revealed that some kind of magnetic correlations start to develop below $|\theta_{\mathrm{W}}| \sim 80$ K, which is far above T_{f}, and continue to grow down to T_{f}. The development of magnetic correlations over a wide temperature range and the occurrence of a magnetic anomaly well below θ_{W} seem to be characteristic of frustrated magnetism, but it is still unclear what kind of magnetic correlations are developing below θ_{W}. The magnetic correlations developing in the frustrated systems is an interesting issue to be studied from experimental and theoretical points of view.

B. Ga-NQR Spectrum below 2 K

As shown in Fig. 2(b), a broad and structureless spectrum was observed at 1.5 K. This spectrum indicates the presence of inhomogeneous static magnetic fields at the Ga sites. When the internal magnetic field appears at a Ga nuclear site below T_{f} with the electric quadrupole interaction, the Zeeman interaction from the internal fields is added to the total

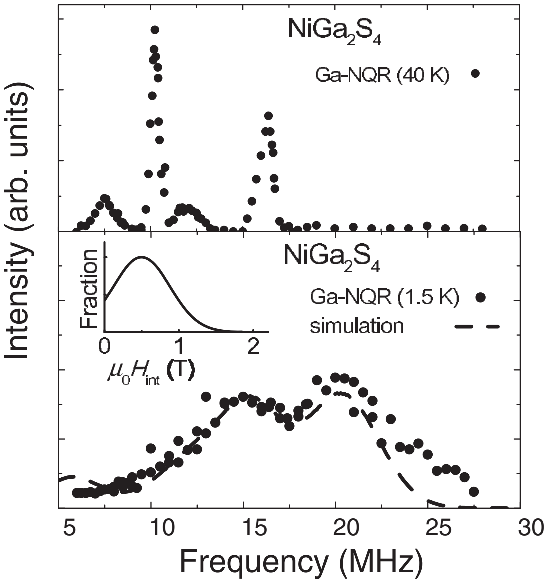

FIG. 13. ^{69,71}Ga-NQR spectra at 40 K (upper panel) and at 1.5 K (bottom panel). The broad spectrum in the bottom figure is approximately reproduced by the presence of inhomogeneous internal fields pointing along the c axis. The distribution of the internal fields is shown in the inset of the bottom figure.

nuclear Hamiltonian. The Zeeman interaction is expressed as

$$\mathcal{H}_{\rm Z} = -\gamma_{\rm n}\hbar \boldsymbol{I}\cdot\boldsymbol{H}_{\rm int},$$

where $\gamma_{\rm n}$ is the Ga nuclear gyromagnetic ratio and $\boldsymbol{H}_{\rm int}$ is the internal field at the Ga nuclear site. The structureless broad spectrum is approximately reproduced by using the inhomogeneous internal field at the Ga nuclear site, as shown in the inset of Fig. 13. The average and distribution width of the internal field at the Ga site are approximately 0.5 and 0.5 T, respectively, and the calculated Ga-NQR spectrum is shown by the dotted line in the bottom figure of Fig. 13. In the calculation, we assume that the inhomogeneous internal field has only a c-axis component for simplicity. $\boldsymbol{H}_{\rm int}$ arises mainly from the transferred hyperfine field and the dipolar field from the Ni ions, which is expressed as

$$\boldsymbol{H}_{\rm int} = \sum_i \frac{A_{\rm hf}}{N_{\rm A}\mu_B}\boldsymbol{m}_i - \sum_i \frac{1}{\boldsymbol{r}_i^3}\left\{\boldsymbol{m}_i + \frac{3\boldsymbol{r}_i(\boldsymbol{r}_i\cdot\boldsymbol{m}_i)}{\boldsymbol{r}_i^2}\right\},$$

where m_i is the magnetic moment at the ith Ni site and r_i is the vector connecting the Ga site to the ith Ni site. The average value of the ordered moments is estimated to be $\sim 1.0\mu_B$ from the first term of the right-hand side in the equation above. It is difficult to estimate accurately the ordered moments and the magnetic structure from such a broad spectrum, since the magnitude of the dipolar fields highly depends strongly on the orientations of the moments.

C. Spin dynamics below $T_{\rm f}$

Since an extremely broad signal was observed below 2 K, it is concluded that the static magnetic fields are present below 2 K. However, over the wide temperature range below $T_{\rm f}$, slow spin dynamics remains as probed by NQR and μSR. Taking into account the multi-exponential behavior in the relaxation curves at low temperatures, it is concluded that a 2D inhomogeneous magnetic state is realized in this compound.

We found that the spin dynamics becomes anisotropic below 0.8 K from the different temperature dependence of $1/T_1$ and $1/(4T_2)$ as shown in Fig. 8. $1/T_1$ follows a T^3 dependence in the temperature range between 0.5 and 0.1 K, and this T^3 dependence holds for all the spin dynamics detected by the Ga NQR as discussed above. On the other hand, $1/(4T_2)$ shows a T-linear dependence below 1 K. If we take into account that $1/T_1$ and $1/(4T_2)$ probe spin dynamics along different directions, we can conclude that $G_\perp(\omega)$ and $G_z(0)$ show the T^3 and T-linear dependence, respectively. It is noteworthy that isotropic spin dynamics above $T_{\rm f}$ change to anisotropic ones below 0.8 K.

In the following, we discuss the temperature dependence of $1/T_1$ below $T_{\rm f}$ on the basis of a conventional two-magnon process in a triangular Heisenberg antiferromagnet. $1/T_1$ determined by the two-magnon process was discussed by Moriya,[18] and was extended to the triangular lattice by Maegawa.[19] $1/T_1$ by this process is expressed as

$$\frac{1}{T_1} = \frac{\pi}{2}\gamma_e\gamma_n\hbar\sum_{i,j} G_{ij}\int_{\omega_0}^{\omega_{\rm m}}\left\{1+\left(\frac{\omega_{\rm m}}{\omega}\right)^2\right\} \times \frac{e^{\hbar\omega/k_{\rm B}T}}{(e^{\hbar\omega/k_{\rm B}T}-1)^2}N(\omega)^2 d\omega,$$

where γ_e is the electronic gyromagnetic ratio, $G_{i,j}$ is a geometrical factor. $\omega_{\rm m}$ is the maximum frequency of the spin wave, ω_0 is the spin-anisotropy energy related to the internal field at the Ni sites, and $N(\omega)$ is the state density of magnons. If we assume the long-wavelength approximation, $N(\omega)$ in the 3D and 2D spin waves is

$$N(\omega) = \begin{cases} \dfrac{3\omega\sqrt{\omega^2-\omega_0^2}}{(\omega_{\rm m}^2-\omega_0^2)^{3/2}} & \text{three-dimensional} \\ \dfrac{\omega}{2\pi\omega_{\rm ex}^2 a^2} & \text{two-dimensional,} \end{cases}$$

where $\omega_{\rm ex}$ is the exchange frequency between the Ni spins. Using $N(\omega)$, the temperature dependence of $1/T_1$ determined by the 3D and 2D spin waves is given by

$$\left(\frac{1}{T_1}\right)_{\rm 3D} \propto T^5\int_{T_0/T}^{T_{\rm m}/T}\left\{x^2-\left(\frac{T_0}{T}\right)^2\right\}\left\{x^2+\left(\frac{T_{\rm m}}{T}\right)^2\right\}\frac{e^x}{(e^x-1)^2}dx$$

and

$$\left(\frac{1}{T_1}\right)_{\rm 2D} \propto T^3\int_{T_0/T}^{T_{\rm m}/T}\left\{x^2+\left(\frac{T_{\rm m}}{T}\right)^2\right\}\frac{e^x}{(e^x-1)^2}dx,$$

respectively. Here, $T_{\rm m}=\hbar\omega_{\rm m}/k_{\rm B}$ and $T_0=\hbar\omega_0/k_{\rm B}$. The temperature dependences of $(1/T_1)_{\rm 3D}$ and $(1/T_1)_{\rm 2D}$ are calculated using $T_m\sim|\theta_{\rm W}|=80$ K, and $T_0=0.4$ K, which are shown in Fig. 14 by dotted and solid curves, respectively.

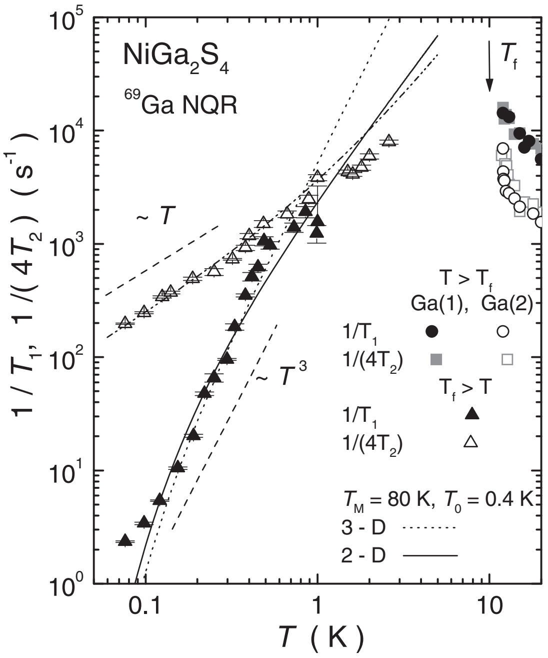

FIG. 14. Temperature dependence of $1/T_1$ calculated by the 3D and 2D spin-wave models are compared with the experimental data (see text).

$1/T_1$ data in the temperature range below 1 K are roughly reproduced by both calculations using the gap magnitude of T_0=0.4 K, however, a deviation between the calculation and $1/T_1$ data is observed below 0.15 K. The deviation is considered to be due to the distribution of T_0, which is suggested from the inhomogeneous internal field as discussed in Sec. IV B. It seems that the 2D model is more suitable for interpreting the whole temperature dependence below T_f, because the deviation between the data and the 3D calculation above 1 K is more significant than that in the 2D one. $1/T_1$ from the 3D model is approximately a T^3 dependence above 1 K, which is incompatible with the experimental result. The 2D spin-wave model seems to be consistent with the T^2 dependence observed in specific-heat experiments above 0.35 K,[2] which suggests the existence of linearly dispersive modes. We point out that the 2D spin-wave model also gives the ω-linear density of states.

The temperature dependence of $1/(4T_2)$ is consistently interpreted by the dominant T-linear $G_z(0)$ and the small T^3 dependence from the $G_\perp(\omega)$ contribution discussed above. $1/(4T_2)$ below 1 K is approximately expressed by

$$\frac{1}{4T_2} = 2.5 \times 10^3 T(\mathrm{K}^{-1}\ \mathrm{s}^{-1}) + \frac{1}{2}\mathrm{G}_\perp(\omega),$$

which is shown by a dotted curve in Fig. 14.

In the Heisenberg triangular magnet with the 120° spin structure, there are three kinds of low-energy excitation modes, viz. swinging fluctuations in the *xy* plane, rotational fluctuations around one of the moment directions, and vertical deviation from the *xy* plane (see Fig. 4 in Ref. 19). It is considered that the lowest excitation mode is the swinging fluctuation, because the fluctuation conserves energy.[19] Taking into account that NiGa$_2$S$_4$ has an incommensurate short-range correlation with $\boldsymbol{q}$ close to $(1/6,1/6,0)$, which is a 60° spin structure,[2] it is reasonable to consider that NiGa$_2$S$_4$ has magnetic fluctuations similar to those in the triangular compounds. It should be noted that the out-of-plane dynamics is homogeneous although the in-plane dynamics is inhomogeneously distributed. It is considered that the out-of-plane dynamics is related to the lowest excitation, which is the swinging fluctuation in the *xy* plane, because the swinging fluctuation gives rise to $\langle S_z(t)S_z(0)\rangle$. However, it is difficult to identify what kinds of magnetic fluctuations are associated with the in-plane and out-of-plane spin dynamics at the Ga site. To determine the origin of the temperature dependence in $G_\perp(\omega)$ and $G_z(0)$, a theoretical study of the magnetic fluctuations with a 60° spin structure is desired.

One of the characteristic features of the $1/T_1$ results on NiGa$_2$S$_4$ is that $1/T_1$ retains a large value down to 1 K, i.e., far below T_f, which is also indicated by the μSR relaxation rate in Fig. 10. The large value of $1/T_1$ is related to the fact that the NQR spectrum affected by the inhomogeneous static field cannot be observed between 2 K and T_f. In an ordinary magnetic transition and spin glass ordering, $1/T_1$ shows a divergence at the magnetic ordering temperature T_M and decreases abruptly below T_M, and then the internal field emerges. Contrastingly, in NiGa$_2$S$_4$, $1/T_1$ is too short to be measured by the Ga-NQR measurements down to 2 K $(\sim T_f/5)$. This indicates that the magnetic fluctuations are not quenched abruptly but gradually decrease or stay constant down to 2 K.

Another characteristic feature of the $1/T_1$ behavior is that the enhancement of $1/T_1$ does not start just above T_f but at 80 K, which is far above T_f. Such behavior of $1/T_1$ suggests that the release of the magnetic entropy at T_f is small. It is considered that the gradual decrease of the magnetic entropy is the reason why the anomaly of the specific heat at T_f is so broad that the anomaly seems to be different from ordinary magnetic ordering. We point out that the small change of the entropy at the magnetic anomaly is one of the characteristic features of frustrated magnetism, because a similar broad maximum in the specific-heat results is often observed in not only in triangular compounds[14,20] but also in *kagomé* compounds.[24,25]

Furthermore, there remains a question to be understood when we interpret the temperature dependence of $1/T_1$ on the basis of the spin-wave model. As reported from the neutron experiment, the magnetic correlation length in NiGa$_2$S$_4$ is short with only six lattice constants even at 1.5 K, which makes NiGa$_2$S$_4$ resemble more conventional spin glasses than the long-range ordered 2D AF magnet. The presence of the spin wave seems to be unrealistic in such a short-range ordered compound. In addition, the spin-wave model is considered to have a significant field dependence of $1/T_1$, which seems to contradict the field insensitive $C(T)$.[2]

However, we point out that a similar situation was observed in SCGO,[24] in which the magnetic correlation length is only two times that of inter-Cr spacing[26] but specific heat

$C(T)$ varies as T^2 at low temperatures.[24] In addition, the similar slowing down of the Cr spin fluctuations when approaching to the susceptibility-cusp temperature $T_g \sim 3.5$ K was reported from the μSR and Ga-NMR measurements.[4,27] It is considered that the linear dispersion indicated from the specific-heat behavior does not imply the presence of the long correlation length. We suggest the possibility of a cluster glass, which might be consistent with all existing results except for the field insensitive behavior of $C(T)$. The spin-wave excitations arise inside the cluster and the clusters freeze out independently. It is considered that the size of the cluster might be approximately six lattice constants. The persisting spin fluctuations below T_{f} might be associated with the spins at the cluster boundaries. To examine this scenario, ac susceptibility measurements and theoretical studies of the field dependence of $N(\omega)$ in the frustrated systems are highly desired.

Quite recently, Tsunetsugu and Arikawa pointed out that spin nematic order can explain the experimental facts of absence of the magnetic long-range order, a power-law behavior $C \sim T^2$, and the incommensurate wave vector $\boldsymbol{q} \sim (1/6, 1/6, 0)$.[28] The order parameters of the spin nematic order are not related to ordinary static spin dipole moments, but related to anisotropy of spin fluctuations. The present results of $1/T_1 \sim T^3$ and the anisotropic spin fluctuations below T_{f} seems to be consistent with the spin nematic order. However, it is a crucial point whether the spin freezing behavior accompanied by the internal magnetic fields below 2 K, observed by the NMR NQR, and μSR measurements, is consistent with their scenario.

On the other hand, Kawamura and Yamamoto studied the ordering of the classical Heisenberg antiferromagnet on the triangular structure with bilinear and biquadratic interactions.[29] They suggested a topological phase transition at a finite temperature driven by topological vortices although the spin correlation length remains finite even below the transition point. They pointed out that the magnetic anomaly at T_{f} in NiGa$_2$S$_4$ might originate from a vortex-induced topological transition related to Z_2 vortices.[29] In their vortex scenario, the magnetic-correlation time does not truly diverge at T_{f}, but only grows sharply at T_{f} exceeding the experimental time scale, and remains short over a wide temperature range below T_{f}. Correspondingly, magnetic-correlation length ξ is short and remains finite in this temperature range, and the onset of the magnetic long-range order, which is characterized by the exponential divergence of ξ, is observed only at still lower temperatures.[29] The magnetic properties revealed with the present NQR, μSR, and neutron experiments above 2 K seem to be consistent with the above vortex transition. In addition, if the temperature for long-range order in the vortex scenario is considered to be ~ 2 K, the observation of spin-wave-like excitations similar to those in a long-range ordered 2D antiferromagnet can be understood. To examine this vortex scenario, the neutron experiments below 2 K are highly desired.

V. CONCLUSION

We have performed ^{69,71}Ga-NMR/NQR and μSR measurements on the triangular antiferromagnet NiGa$_2$S$_4$. NMR and NQR spectra above T_{f} indicate the existence of two Ga sites with different local symmetries, although there exists only one crystallographic site in perfect NiGa$_2$S$_4$. The intensity ratio of two NQR peaks is approximately 4: 1 and the linewidth of the intense peak is narrower than the other. At present, the origin of the two NQR peaks is not fully understood, but it is speculated that a tiny amount of sulfur disorder and/or planar defects such as stacking faults might induce the different Ga site.

$1/T_1$ and $1/T_2$ were measured at both Ga sites and divergent behavior of $1/T_1$ and $1/T_2$ was observed at T_{f} at both Ga sites. It was found that $1/T_1$ and $1/T_2$ show the same temperature dependence above T_{f}, indicative of isotropic spin dynamics in the rapid-motion limit. The observed isotropic spin dynamics is considered to be characteristic of a Heisenberg spin system. With decreasing temperature, magnetic correlations start to develop below $-\theta_{\mathrm{W}} \sim 80$ K, which is far above T_{f}. Spin fluctuations continue to slow down below $-\theta_{\mathrm{W}}$, and become nearly static below $T_{\mathrm{f}}=10$ K, where the specific heat $C(T)$ shows a broad maximum. The remarkable divergence of $1/T_1$ and $1/T_2$, which is observed over wide temperature range between θ_{W} and T_{f}, is characteristic of frustrated systems, because geometrical frustration suppresses the magnetic anomaly down to low temperatures.

However, the wide temperature region between T_{f} and 2 K, where the NQR signal was not observed, suggests that the Ni spins do not freeze immediately below T_{f}, but keep fluctuating down to 2 K with the MHz frequency range. Below 0.5 K, all components of $1/T_1$ follow a T^3 behavior. Below T_{f}, we found a broad spectrum and an inhomogeneous distribution of T_1 in NMR and NQR measurements. These results indicate the freezing of magnetic moments and the emergence of inhomogeneous static magnetism below 2 K. These are also suggested from the μSR experiments. The relaxation rates decrease below T_{f}, and $1/T_1$ follows a T^3 dependence below 0.8 K, and the overall temperature dependence of $1/T_1$ is roughly interpreted by the 2D spin-wave model. In addition, on the basis of the observed difference in the temperature dependence of $1/T_1$ and $1/T_2$, the spin dynamics is interpreted to become anisotropic below 0.8 K. These experimental results strongly suggest that short-range magnetic order with incommensurability and/or inhomogeneous static moments is realized below T_{f}, which is consistent with the neutron experiments. We suggest that the ω-linear dispersion implied from the specific-heat measurements is understood as a consequence of the inhomogeneous magnetic fields due to the inhomogeneous short-range magnetic order. The spin dynamics in the short-range ordered state, which is considered to be field insensitive, and the magnetic correlations developing below 80 K are interesting issues in frustrated magnetism to be further studied from theoretical and experimental points of view.

ACKNOWLEDGMENTS

We thank S. Maegawa, N. Büttgen, M. Takigawa, S. Fujimoto, and H. Kawamura for valuable discussions. This work was partially supported by CREST of the Japan Science and Technology Agency (JST) and the 21 COE program on "Center for Diversity and Universality in Physics" from MEXT of Japan, and by Grants-in-Aid for Scientific Research from the Japan Society for the Promotion of Science (JSPS) (Grants No. 16340111 and No. 18340102), MEXT (Grant No. 16076209), and the U.S. National Science Foundation (Grant No. 0422674).

---

*kishida@scphys.kyoto-u.ac.jp

[1] A. P. Ramirez, in *Handbook of Magnetic Materials*, edited by K. J. H. Buschow (Elsevier Science, Amsterdam, 2001).

[2] S. Nakatsuji, Y. Nambu, H. Tonomura, O. Sakai, S. Jonas, C. Broholm, H. Tsunetsugu, Y. Qiu, and Y. Maeno, Science **309**, 1697 (2005).

[3] S. Nakatsuji and Y. Nambu (private communications).

[4] P. Mendels, A. Keren, L. Limot, M. Mekata, G. Collin, and M. Horvatic, Phys. Rev. Lett. **85**, 3496 (2000).

[5] D. Bono, P. Mendels, G. Collin, and N. Blanchard, Phys. Rev. Lett. **92**, 217202 (2004).

[6] N. Büttgen, A. Zymara, C. Kegler, V. Tsurkan, and A. Loidl, Phys. Rev. B **73**, 132409 (2006).

[7] M. R. McHenry and B. G. Slbernagell, Phys. Rev. B **5**, 2958 (1972).

[8] N. J. Curro, P. C. Hammel, B. J. Suh, M. Hücker, B. Büchner, U. Ammerahl, and A. Revcolevsche, Phys. Rev. Lett. **85**, 642 (2000).

[9] D. E. MacLaughlin, O. O. Bernal, R. H. Heffner, G. J. Nieuwenhuys, M. S. Rose, J. E. Sonier, B. Andraka, R. Chau, and M. B. Maple, Phys. Rev. Lett. **87**, 066402 (2001).

[10] D. E. MacLaughlin, R. H. Heffner, S. Nakatsuji, Y. Numbu, K. Onuma, Y. Maeno, K. Ishida, O. O. Bernal, and L. Shu, J. Magn. Magn. Mater. **310**, 1300 (2007).

[11] R. Kubo and T. Toyabe, in *Magnetic Resonance and Relaxation*, edited by R. Blinc (North-Holland, Amsterdam, 1967), p. 810.

[12] H. Benner and J. P. Boucher, in *Magnetic Properties of Layered Transition Metals Compounds*, edited by L. J. de Jongh (Kluwer Academic Publishers, Dordrecht, 1990).

[13] Y. Ajiro, H. Kikuchi, S. Sugiyama, T. Nakashima, S. Shamoto, N. Nakayama, M. Kiyama, N. Yamamoto, and Y. Oka, J. Phys. Soc. Jpn. **57**, 2268 (1988).

[14] L. K. Alexander, N. Büttgen, R. Nath, A. V. Mahajan, and A. Loidl, Phys. Rev. B **76**, 064429 (2007).

[15] M. Nishiyama, S. Maegawa, T. Inami, and Y. Oka, Phys. Rev. B **67**, 224435 (2003).

[16] H. Kawamura and S. Miyashita, J. Phys. Soc. Jpn. **53**, 4138 (1984).

[17] Y. J. Uemura, T. Yamazaki, D. R. Harshman, M. Senba, and E. J. Ansalda, Phys. Rev. B **31**, 546 (1985).

[18] T. Moriya, Prog. Theor. Phys. **16**, 23 (1956).

[19] S. Maegawa, Phys. Rev. B **51**, 15979 (1995).

[20] A. Olariu, P. Mendels, F. Bert, B. G. Ueland, P. Schiffer, R. F. Berger, and R. J. Cava, Phys. Rev. Lett. **97**, 167203 (2006).

[21] R. E. Walstedt, Phys. Rev. Lett. **19**, 146 (1967).

[22] T. Auler, P. Butaud, and J. A. Gillet, J. Phys.: Condens. Matter **8**, 6425 (1996).

[23] C. P. Slichter, *Principles of Magnetic Resonance*, third edition (Springer, New York, 1989), Chap. 5.

[24] A. P. Ramirez, G. P. Espinosa, and A. S. Cooper, Phys. Rev. Lett. **64**, 2070 (1990).

[25] K. Matsuno, T. Katsufuji, S. Mori, M. Nohara, A. Machida, Y. Moritomo, K. Kato, E. Nishibori, M. Takata, M. Sakata, K. Kitazawa, and H. Takagi, Phys. Rev. Lett. **90**, 096404 (2003).

[26] C. Broholm, G. Aeppli, G. P. Espinosa, and A. S. Cooper, Phys. Rev. Lett. **65**, 3173 (1990).

[27] Y. J. Uemura, A. Keren, K. Kojima, L. P. Le, G. M. Luke, W. D. Wu, Y. Ajiro, T. Asano, Y. Kuriyama, M. Mekata, H. Kikuchi, and K. Kakurai, Phys. Rev. Lett. **73**, 3306 (1994).

[28] H. Tsunetsugu and M. Arikawa, J. Phys. Soc. Jpn. **75**, 083701 (2006).

[29] H. Kawamura and A. Yamamoto, J. Phys. Soc. Jpn. **76**, 073704 (2007).

PHYSICAL REVIEW B **77**, 054516 (2008)

Cu spin dynamics in the overdoped regime of $La_{2-x}Sr_xCu_{1-y}Zn_yO_4$ probed by muon spin relaxation

Risdiana,* T. Adachi,† N. Oki, S. Yairi, Y. Tanabe, K. Omori, and Y. Koike
Department of Applied Physics, Graduate School of Engineering, Tohoku University, 6-6-05 Aoba, Aramaki, Aoba-ku, Sendai 980-8579, Japan

T. Suzuki and I. Watanabe
Advanced Meson Science Laboratory, RIKEN Nishina Center, 2-1 Hirosawa, Wako 351-0198, Japan

A. Koda
Muon Science Laboratory, Institute of Materials Structure Science, High Energy Accelerator Research Organization (KEK-IMSS), 1-1 Oho, Tsukuba 305-0801, Japan

W. Higemoto
Advanced Science Research Center, Japan Atomic Energy Agency (JAEA), 2-4 Shirane, Shirakata, Tokai, Naka, Ibaraki 319-1195, Japan

(Received 18 February 2007; revised manuscript received 15 October 2007; published 26 February 2008)

Muon-spin-relaxation measurements have been performed for partially Zn-substituted $La_{2-x}Sr_xCu_{1-y}Zn_yO_4$ with $y=0-0.10$ in the overdoped regime up to $x=0.30$. In the 3% Zn-substituted samples up to $x=0.27$, exponential-like depolarization of muon spins has been observed at low temperatures, indicating a Zn-induced slowing down of the Cu spin fluctuations. The depolarization rate decreases with increasing x, and almost no fast depolarization of muon spins has been observed for $x=0.30$ where superconductivity disappears. The present results suggest that there is no quantum critical point at $x\sim0.19$. These results are discussed in terms of the stripe-pinning model and the phase-separation model.

DOI: 10.1103/PhysRevB.77.054516 PACS number(s): 74.62.Dh, 74.72.Dn, 76.75.+i, 74.25.Ha

I. INTRODUCTION

The effects of nonmagnetic impurities on the Cu spin dynamics have been one of the central issues in research on high-T_c superconductivity. It is widely recognized that local magnetic moments due to Cu spins are induced by nonmagnetic Zn in the underdoped regime[1] and that superconductivity is strongly suppressed by Zn.[2] In the overdoped regime, on the other hand, Panagopoulos *et al.* have performed muon-spin-relaxation (μSR) measurements in Zn-substituted $La_{2-x}Sr_xCu_{1-y}Zn_yO_4$ with $y=0.05$ and have found a Zn-induced slowing down of the Cu spin fluctuations for $x<0.19$ while not for $x\geqslant0.19$, pointing out the existence of a quantum critical point (QCP) at $x\sim0.19$.[3]

Dynamical stripe correlations of spins and holes have attracted great interest in relation to the mechanism of high-T_c superconductivity.[4,5] It is well known that dynamical stripe correlations tend to be pinned and statically stabilized not only by the characteristic structure of the tetragonal low-temperature structure (space group $P4_2/ncm$) in the La-214 system but also by Zn impurities.[6–9] So far, impurity effects on the Cu spin dynamics and superconductivity have been investigated from zero-field (ZF) μSR measurements in the underdoped regime of $La_{2-x}Sr_xCu_{1-y}Zn_yO_4$ with $x\leqslant0.15$.[10–16] It has been found that fluctuations of Cu spins around Zn exhibit a slowing down due to the pinning of the dynamical stripes by Zn, leading to the formation of a static stripe order and the destruction of superconductivity around Zn. This is an interpretation called a stripe-pinning model. Similar effects of Zn on the Cu spin fluctuations have been observed in the underdoped regime of $Bi_2Sr_2Ca_{1-x}Y_x(Cu_{1-y}Zn_y)_2O_{8+\delta}$ (Refs. 17 and 18) and $YBa_2Cu_{3-2y}Zn_{2y}O_{7-\delta}$ (Ref. 19) as well. The static stripe order is regarded as competing with the superconductivity. On the other hand, the dynamical stripe correlations may play an important role in the appearance of superconductivity. In fact, theoretical models on the mechanism of superconductivity based upon the dynamical stripe correlations have been proposed.[20] If this is the case, similar effects of Zn must be observed not only in the underdoped regime but also in the overdoped regime where superconductivity appears.

In this paper, we investigate effects of Zn on the Cu spin dynamics from μSR measurements in the overdoped regime of $La_{2-x}Sr_xCu_{1-y}Zn_yO_4$ with $0.15\leqslant x\leqslant0.30$ and $0\leqslant y\leqslant0.10$ in order to elucidate whether or not a QCP exists at $x\sim0.19$ and to investigate the validity of the stripe-pinning model in the overdoped regime of $La_{2-x}Sr_xCuO_4$.

II. EXPERIMENT

Polycrystalline samples of $La_{2-x}Sr_xCu_{1-y}Zn_yO_4$ with $0.15\leqslant x\leqslant0.30$ and $0\leqslant y\leqslant0.10$ were prepared by the ordinary solid-state reaction method. Raw materials of dried La_2O_3, $SrCO_3$, CuO, and ZnO powders were mixed in a stoichiometric ratio and prefired in air at 750 °C for 3 h, followed by a prefiring at 900 °C for 12 h. The prefired materials were reground and pressed into pellets of 10 mm in diameter and sintered in air at 750 °C for 3 h, followed by sintering at 1050 °C for 24 h with repeated regrinding. The as-grown samples were annealed in flowing gas of O_2 at 500 °C for 72 h. All of the samples were checked by powder x-ray diffraction measurements to be single phase. Electrical

1098-0121/2008/77(5)/054516(6)

resistivity measurements were also carried out to check the quality of the samples, which was found to be good.

The ZF-μSR measurements were performed at low temperatures down to 0.3 K at the RIKEN-RAL Muon Facility at the Rutherford-Appleton Laboratory in the UK and at lower temperatures down to 0.02 K at the KEK-MSL in Japan using a pulsed positive surface muon beam. The asymmetry parameter $A(t)$ at a time t was defined as $A(t)=[F(t)-\alpha B(t)]/[F(t)+\alpha B(t)]$, where $F(t)$ and $B(t)$ are total muon events counted by the forward and backward counters, respectively, and α is the calibration factor reflecting the relative counting efficiencies between the forward and backward counters.

III. RESULTS

It is known that muons with positive charges injected in a high-T_c copper oxide tend to stop near oxygen ions.[21] In $La_{2-x}Sr_xCuO_4$, it is well established that muons tend to stop only near the so-called apical oxygen ion just above Cu.[22] Therefore, muons stopping near the apical oxygen ion feel strong internal fields from the CuO_2 plane when the Cu spin fluctuations exhibit a slowing down at low temperatures.

Figure 1 shows the ZF-μSR time spectra of $La_{2-x}Sr_xCu_{1-y}Zn_yO_4$ with $x=0.20$ and $0 \leq y \leq 0.10$. At high temperatures above 1 K, all the spectra show Gaussian-like depolarization due to dipole fields induced by randomly oriented nuclear spins, indicating a fast fluctuating state of Cu spins beyond the μSR time window (10^{-6}–10^{-11} s). At 0.3 K, the Gaussian-like depolarization is still observed for $y=0$ and 0.01. On the other hand, the muon spin depolarization becomes fast for $y=0.02$ and 0.03 so that exponential-like depolarization is observed. This indicates slowing down of the Cu spin fluctuations, as in the case of the underdoped regime.[10–16] Even at 0.3 K, however, no muon spin precession corresponding to the formation of any coherent magnetic order is observed. In the heavily Zn-substituted sample with $y=0.10$, no fast depolarization of muon spins is observed, indicating that the Cu spins again fluctuate fast beyond the μSR time window. This is explained as being due to the spin dilution through the large amount of substitution of nonmagnetic Zn, namely, due to the destruction of the spin correlation, as in the case of the underdoped regime.[10–16]

Figure 2 shows the ZF-μSR time spectra of the 3% Zn-substituted $La_{2-x}Sr_xCu_{1-y}Zn_yO_4$ with $0.15 \leq x \leq 0.30$ and $y=0.03$ at low temperatures down to 0.3 K. The reason why the 3% Zn-substituted samples are taken is that the Zn-induced slowing down of the Cu spin fluctuations is most observable in the overdoped regime as well as in the underdoped regime.[10–16] Focusing on the spectra at 0.3 K, the exponential-like depolarization is still observed with increasing x up to $x=0.27$, indicating the slowing down of the Cu spin fluctuations. The depolarization becomes weak with increasing x, and almost no fast depolarization of muon spins is observed for $x=0.30$ where superconductivity disappears. As for $x=0.15$, both the very fast depolarization in a short-time region below 1 μs and the almost flat spectrum above 1 μs suggest the existence of a disordered static magnetic ground state. It is noted that similar spectra have been observed in underdoped $La_{2-x}Sr_xCuO_4$ and $Y_{0.8}Ca_{0.2}Ba_2Cu_3O_6$ with p (the hole concentration per Cu)=0.09 (Ref. 23) and $(Ca_xLa_{1-x})(Ba_{1.75-x}La_{0.25+x})Cu_3O_y$ (Ref. 24).

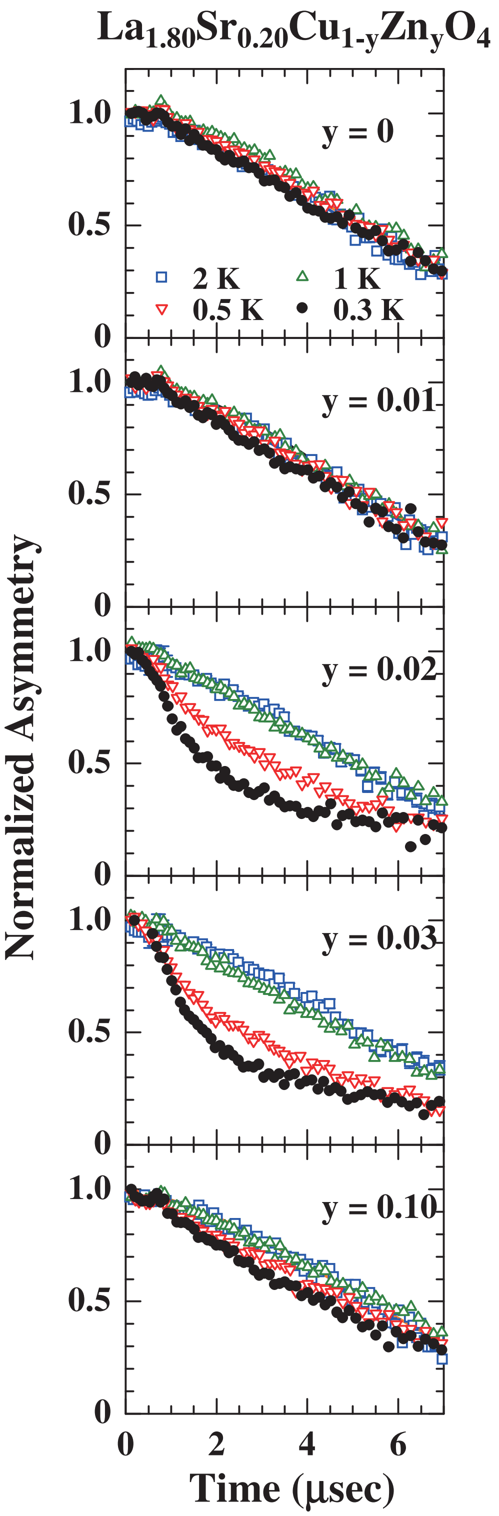

FIG. 1. (Color online) ZF-μSR time spectra of $La_{1.80}Sr_{0.20}Cu_{1-y}Zn_yO_4$ with various y values at low temperatures down to 0.3 K.

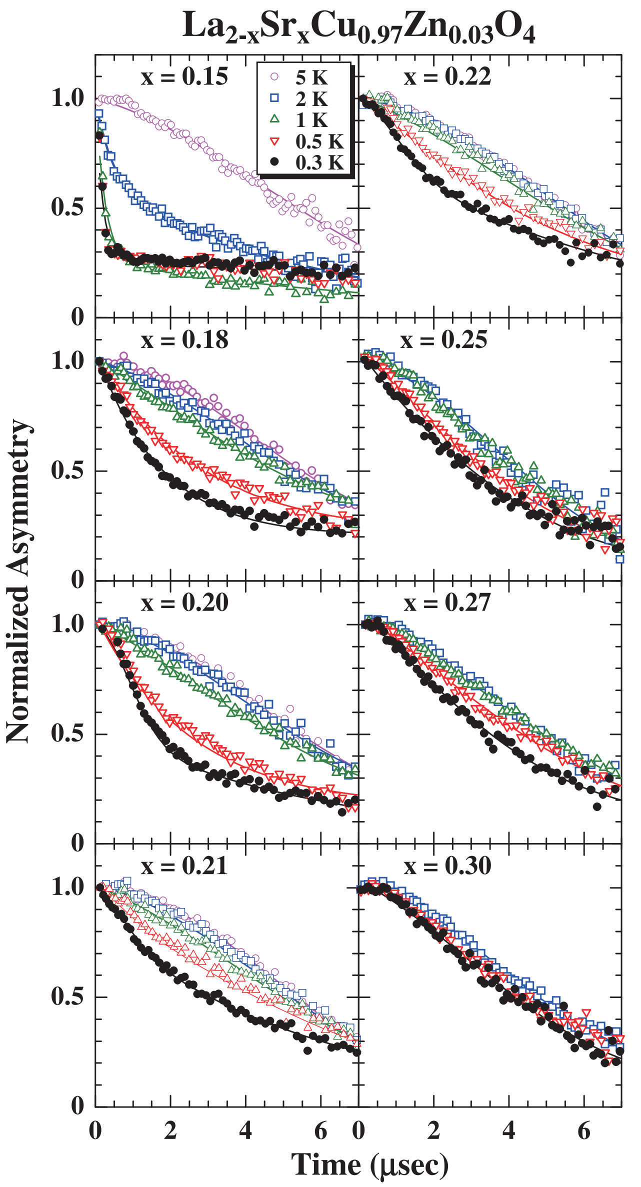

FIG. 2. (Color online) ZF-μSR time spectra of $La_{2-x}Sr_xCu_{0.97}Zn_{0.03}O_4$ with $0.15 \leqslant x \leqslant 0.30$ at low temperatures down to 0.3 K. Solid lines indicate the best-fit results using $A(t) = A_0 e^{-\lambda_0 t} G_Z(\Delta, t) + A_1 e^{-\lambda_1 t}$.

In order to obtain detailed information on the Cu spin dynamics, the time spectra were analyzed using the following two-component function:

$$A(t) = A_0 e^{-\lambda_0 t} G_Z(\Delta, t) + A_1 e^{-\lambda_1 t}. \tag{3.1}$$

The first term represents the slowly depolarizing component in a region where the Cu spins fluctuate fast beyond the μSR time window. The A_0 and λ_0 are the initial asymmetry and the depolarization rate of the slowly depolarizing component, respectively. The $G_Z(\Delta, t)$ is the static Kubo-Toyabe function with a distribution width Δ of nuclear-dipole fields at the muon site.[25] The second term represents the fast depolarizing component in a region where the Cu spin fluctuations slow down. The A_1 and λ_1 are the initial asymmetry and the depolarization rate of the fast depolarizing component, respectively. The time spectra are well fitted with Eq. (3.1), as shown by solid lines in Fig. 2. In the fitting, the value of A_0+A_1 was kept constant at all measured temperatures.

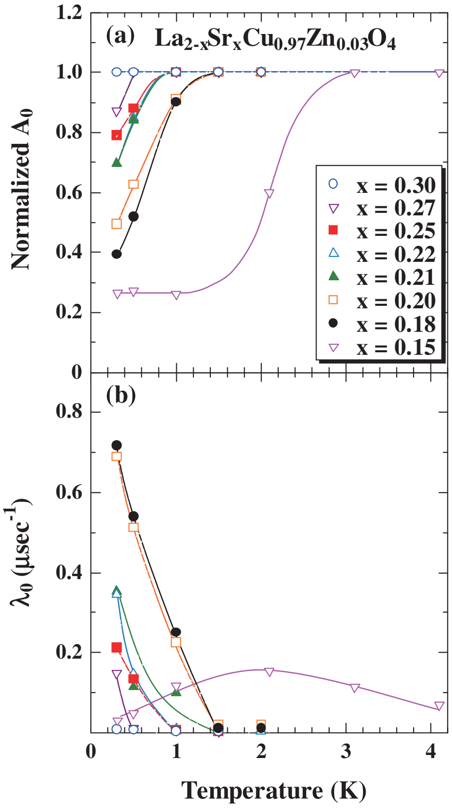

FIG. 3. (Color online) (a) Temperature dependence of the initial asymmetry of the slowly depolarizing component, A_0, for $La_{2-x}Sr_xCu_{0.97}Zn_{0.03}O_4$ with $0.15 \leqslant x \leqslant 0.30$. Values of A_0 are normalized by those obtained at high temperatures. Lines are to guide the reader's eye. (b) Temperature dependence of the depolarization rate of the slowly depolarizing component, λ_0, for $La_{2-x}Sr_xCu_{0.97}Zn_{0.03}O_4$ with $0.15 \leqslant x \leqslant 0.30$. Lines are to guide the reader's eye.

Figure 3(a) shows the temperature dependence of A_0 for the 3% Zn-substituted $La_{2-x}Sr_xCu_{0.97}Zn_{0.03}O_4$ with various x values. Values of A_0 are normalized by those obtained at high temperatures. It is found that A_0 decreases with decreasing temperature at low temperatures for $0.15 \leqslant x \leqslant 0.27$. The temperature where A_0 starts to decrease decreases with increasing x and the decrease in A_0 disappears at $x=0.30$. The decrease in A_0 means the appearance of the fast depolarizing component due to the slowing down of the Cu spin fluctuations. As for $x=0.15$, the A_0 value is saturated at low temperatures to be roughly 1/3, suggesting the existence of a disordered static magnetic ground state.

Figure 3(b) shows the temperature dependence of λ_0 for the 3% Zn-substituted $La_{2-x}Sr_xCu_{0.97}Zn_{0.03}O_4$ with various x values. Values of λ_0 increase with decreasing temperature at low temperatures for $0.18 \leqslant x \leqslant 0.27$. It is found that λ_0 at the lowest temperature of 0.3 K decreases with increasing x, suggesting that the degree of the slowing down of the Cu

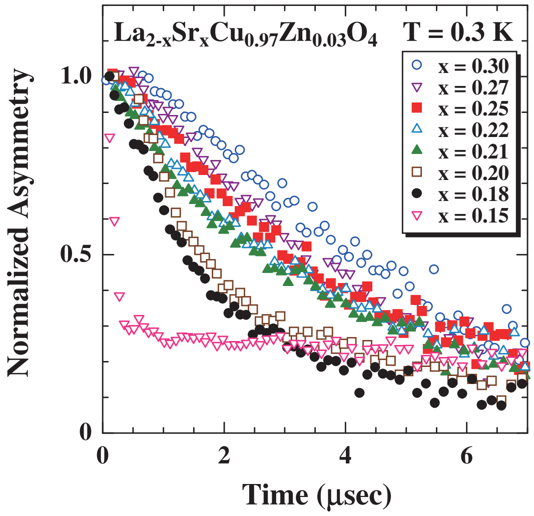

FIG. 4. (Color online) ZF-μSR time spectra of $La_{2-x}Sr_xCu_{0.97}Zn_{0.03}O_4$ with $0.15 \leqslant x \leqslant 0.30$ at 0.3 K.

spin fluctuations is weakened with increasing x. As for $x = 0.15$, λ_0 exhibits a peak at 2 K where A_0 rapidly decreases. This is a typical behavior of λ_0 in the case of the existence of a static magnetism.[11]

IV. DISCUSSION

The most important feature in the present results is that the fast muon spin depolarization due to the Zn-induced slowing down of the Cu spin fluctuations is observed in the overdoped regime where superconductivity appears, though the muon spin depolarization becomes weak with increasing x. This is clearly seen in Fig. 4. Quantitatively speaking, the normalized value of A_0 increases little by little with increasing x, as shown in Fig. 5(a). It reaches the unity at $x = 0.30$, indicating that the Cu spins fluctuate very fast with shorter periods than the μSR time window. The superconductivity disappears at $x \geqslant 0.30$,[26] as shown in Fig. 5(c). These results are compatible with the stripe-pinning model. That is, it is possible that the dynamical stripe correlations exist in the whole superconducting regime and disappear in the normal-state regime of $x \geqslant 0.30$. Therefore, it is possible that the dynamical stripe correlations play an important role in the appearance of superconductivity. The present results are supported by the low-energy inelastic neutron-scattering experiment in the overdoped regime of $La_{2-x}Sr_xCuO_4$ by Wakimoto *et al.*[27] They have reported that the maximum value of the integrated dynamic spin susceptibility of the incommensurate magnetic peaks corresponding to the dynamical stripe correlations decreases linearly with increasing x for $x \geqslant 0.25$ and disappears at $x = 0.30$. It is noted that the existence of Zn-induced local moments[1] does not conflict with the stripe-pinning model. It is because, even in the stripe-ordered state pinned by Zn, the spin correlation is locally destroyed in the nearest neighborhood of Zn, producing local magnetic moments around Zn.[28]

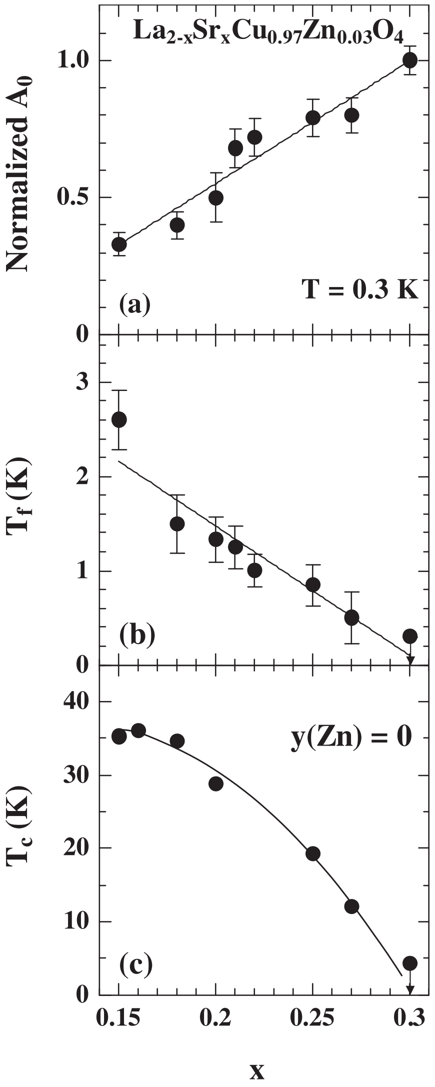

FIG. 5. (a) The initial asymmetry of the slowly depolarizing component, A_0, for $La_{2-x}Sr_xCu_{0.97}Zn_{0.03}O_4$ with $0.15 \leqslant x \leqslant 0.30$ at 0.3 K. Values of A_0 are normalized by those obtained at high temperatures. (b) T_f, defined as the temperature where the ZF-μSR time spectrum starts to deviate from the Gaussian-like to exponential-like behavior for $La_{2-x}Sr_xCu_{0.97}Zn_{0.03}O_4$ with $0.15 \leqslant x \leqslant 0.30$. (c) The superconducting transition temperature T_c, defined at the midpoint of the resistive transition for the Zn-free $La_{2-x}Sr_xCuO_4$ (Ref. 26).

The existence of a QCP in the phase diagram of temperature versus p for the high-T_c superconductors is one of interesting issues in recent years.[29,30] Panagopoulos *et al.*[3] have reported the existence of a QCP at $x \sim 0.19$ from the μSR results that no Zn-induced slowing down of the Cu spin fluctuations was observed in the overdoped regime above $x = 0.19$ for 5% Zn-substituted $La_{2-x}Sr_xCu_{0.95}Zn_{0.05}O_4$. As mentioned above, however, the 5% substitution of Zn is too much for the slowing down of the Cu spin fluctuations to be observed. In our μSR results of the 3% Zn-substituted samples, there is no large difference between above and below $x = 0.19$. Accordingly, it is concluded that no QCP exists at $x \sim 0.19$.

Figure 5(b) shows the x dependence of T_f, defined as the temperature where the ZF-μSR time spectrum starts to deviate from the Gaussian-like to exponential-like behavior for the 3% Zn-substituted $La_{2-x}Sr_xCu_{0.97}Zn_{0.03}O_4$ with $0.15 \leq x \leq 0.30$. The value of T_f gradually decreases with increasing x and tends to be zero at $x=0.30$. Therefore, it is possible that QCP is located at $x=0.30$ rather than $x=0.19$.

Next, we discuss the reason for the decrease of the depolarization rate of muon spins with increasing x. There are two possible reasons. One is due to the weakening of the correlation between Cu spins on account of the increase of holes. As well known, a hole incorporated at an oxygen site in the CuO_2 plane forms a Zhang-Rice singlet together with a Cu spin, producing a spin defect. Therefore, the increase of holes may weaken the Cu spin correlation in the overdoped regime, leading to a decrease of the muon spin depolarization rate with increasing x. The other reason is due to the decrease of the superconducting volume fraction with increasing x in the overdoped regime. First, this has been suggested from transverse-field μSR measurements in the overdoped regime of $Tl_2Ba_2CuO_{6+\delta}$, because the superconducting carrier density divided by the effective mass, n_s/m^*, has been found to decrease with increasing p.[31,32] Recently, the decrease of the superconducting volume fraction with increasing x has been confirmed by Tanabe *et al.*[33,34] and Adachi *et al.*[35] from magnetic-susceptibility measurements in the overdoped regime of $La_{2-x}Sr_xCuO_4$. Accordingly, it is plausible that a phase separation into superconducting and normal-state regions takes place in the high-T_c copper oxides. As the Cu spin correlation is regarded as being very weak in the normal-state region, the Zn-induced slowing down of the Cu spin fluctuations may occur only in the superconducting region. Therefore, the muon spin depolarization rate may decrease with the progressive decrease of the superconducting volume fraction with increasing x in the overdoped regime. It is a forthcoming issue to determine which reason is plausible.

V. SUMMARY

We have investigated the Cu spin dynamics from ZF-μSR measurements in the overdoped regime of $La_{2-x}Sr_xCu_{1-y}Zn_yO_4$ with $0.15 \leq x \leq 0.30$ and $0 \leq y \leq 0.10$. In the 3% Zn-substituted samples with $0.15 \leq x \leq 0.30$ and $y=0.03$, exponential-like depolarization of muon spins has been observed at 0.3 K, indicating a Zn-induced slowing down of the Cu spin fluctuations. Almost no fast depolarization of muon spins has been observed for $x=0.30$ where the superconductivity disappears. The present results suggest that no QCP exists at $x \sim 0.19$. Moreover, the present results are compatible with the stripe-pinning model and the phase-separation model. That is, it is possible that the dynamical stripe correlations exist in the whole superconducting regime and that they play an important role in the appearance of superconductivity.

ACKNOWLEDGMENTS

We would like to thank K. Hachitani and H. Sato for their technical support in the μSR measurements. We are also grateful to K. Nagamine and K. Nishiyama for their continuous encouragement. This work was partly supported by Joint Programs of the Japan Society for the Promotion of Science, by a TORAY Science and Technology Grant, and by a Grant-in-Aid for Scientific Research from the Ministry of Education, Culture, Sport, Science and Technology, Japan.

---

[*] Present address: Department of Physics, Faculty of Mathematics and Natural Sciences, Padjadjaran University, Jl. Raya Bandung-Sumedang Km. 21 Jatinangor, West Jawa, Indonesia 45363.

[†] Corresponding author: adachi@teion.apph.tohoku.ac.jp

[1] A. V. Mahajan, H. Alloul, G. Collin, and J. F. Marucco, Phys. Rev. Lett. **72**, 3100 (1994).

[2] Y. Maeno and T. Fujita, Physica C **153-155**, 1105 (1988).

[3] C. Panagopoulos, A. P. Petrovic, A. D. Hillier, J. L. Tallon, C. A. Scott, and B. D. Rainford, Phys. Rev. B **69**, 144510 (2004).

[4] J. M. Tranquada, B. J. Sternlieb, J. D. Axe, Y. Nakamura, and S. Uchida, Nature (London) **375**, 561 (1995).

[5] J. M. Tranquada, J. D. Axe, N. Ichikawa, Y. Nakamura, S. Uchida, and B. Nachumi, Phys. Rev. B **54**, 7489 (1996).

[6] Y. Koike, S. Takeuchi, H. Sato, Y. Hama, M. Kato, Y. Ono, and S. Katano, J. Low Temp. Phys. **105**, 317 (1996).

[7] Y. Koike, S. Takeuchi, Y. Hama, H. Sato, T. Adachi, and M. Kato, Physica C **282-287**, 1233 (1997).

[8] T. Adachi, T. Noji, H. Sato, Y. Koike, T. Nishizaki, and N. Kobayashi, J. Low Temp. Phys. **117**, 1151 (1999).

[9] C. M. Smith, A. H. Castro Neto, and A. V. Balatsky, Phys. Rev. Lett. **87**, 177010 (2001).

[10] I. Watanabe, T. Adachi, K. Takahashi, S. Yairi, Y. Koike, and K. Nagamine, Phys. Rev. B **65**, 180516(R) (2002).

[11] I. Watanabe, T. Adachi, K. Takahashi, S. Yairi, Y. Koike, and K. Nagamine, J. Phys. Chem. Solids **63**, 1093 (2002).

[12] I. Watanabe, T. Adachi, S. Yairi, Y. Koike, and K. Nagamine, Physica B **326**, 305 (2003).

[13] T. Adachi, I. Watanabe, S. Yairi, K. Takahashi, Y. Koike, and K. Nagamine, J. Low Temp. Phys. **131**, 843 (2003).

[14] T. Adachi, S. Yairi, K. Takahashi, Y. Koike, I. Watanabe, and K. Nagamine, Phys. Rev. B **69**, 184507 (2004).

[15] T. Adachi, S. Yairi, Y. Koike, I. Watanabe, and K. Nagamine, Phys. Rev. B **70**, 060504(R) (2004).

[16] Y. Koike, T. Adachi, N. Oki, Risdiana, M. Yamazaki, T. Kawamata, T. Noji, K. Kudo, N. Kobayashi, I. Watanabe, and K. Nagamine, Physica C **426-431**, 189 (2005).

[17] I. Watanabe, M. Akoshima, Y. Koike, and K. Nagamine, Phys. Rev. B **60**, R9955 (1999).

[18] I. Watanabe, M. Akoshima, Y. Koike, S. Ohira, and K. Nagamine, Phys. Rev. B **62**, 14524 (2000).

[19] M. Akoshima, Y. Koike, I. Watanabe, and K. Nagamine, Phys. Rev. B **62**, 6761 (2000).

[20] For example, see, S. A. Kivelson, I. P. Bindloss, E. Fradkin, V. Oganesyan, J. M. Tranquada, A. Kapitulnik, and C. Howald, Rev. Mod. Phys. **75**, 1201 (2003).

[21] S. B. Sulaiman, N. Sahoo, S. Srinivas, F. Hagelberg, T. P. Das, E.

Torikai, and K. Nagamine, Hyperfine Interact. **79**, 901 (1993).

[22] B. Nachumi, Y. Fudamoto, A. Keren, K. M. Kojima, M. Larkin, G. M. Luke, J. Merrin, O. Tchernyshyov, Y. J. Uemura, N. Ichikawa, M. Goto, H. Takagi, S. Uchida, M. K. Crawford, E. M. McCarron, D. E. MacLaughlin, and R. H. Heffner, Phys. Rev. B **58**, 8760 (1998).

[23] Ch. Niedermayer, C. Bernhard, T. Blasius, A. Golnik, A. Moodenbaugh, and J. I. Budnick, Phys. Rev. Lett. **80**, 3843 (1998).

[24] A. Kanigel, A. Keren, Y. Eckstein, A. Knizhnik, J. S. Lord, and A. Amato, Phys. Rev. Lett. **88**, 137003 (2002).

[25] Y. J. Uemura, T. Yamazaki, D. R. Harshman, M. Senba, and E. J. Ansaldo, Phys. Rev. B **31**, 546 (1985).

[26] Y. Koike, A. Kobayashi, T. Kawaguchi, M. Kato, T. Noji, Y. Ono, T. Hikita, and Y. Saito, Solid State Commun. **82**, 889 (1992).

[27] S. Wakimoto, H. Zhang, K. Yamada, I. Swainson, H. Kim, and R. J. Birgeneau, Phys. Rev. Lett. **92**, 217004 (2004).

[28] In the overdoped regime, to our knowledge, there have been no reports of the existence of Zn-induced local moments to date. However, based on the present results that the Zn-induced slowing down of the Cu spin fluctuations was observed, it is guessed that Zn tends to induce local moments even in the overdoped regime, though the size of moments decreases with an increase of x.

[29] J. L. Tallon and J. W. Loram, Physica C **349**, 53 (2001).

[30] S. Uchida, Solid State Commun. **126**, 57 (2003).

[31] Y. J. Uemura, A. Keren, L. P. Le, G. M. Luke, W. D. Wu, Y. Kubo, T. Manako, Y. Shimakawa, M. Subramanian, J. L. Cobb, and J. T. Markert, Nature (London) **364**, 605 (1993).

[32] Ch. Niedermayer, C. Bernhard, U. Binninger, H. Glückler, J. L. Tallon, E. J. Ansaldo, and J. I. Budnick, Phys. Rev. Lett. **71**, 1764 (1993).

[33] Y. Tanabe, T. Adachi, T. Noji, and Y. Koike, J. Phys. Soc. Jpn. **74**, 2893 (2005).

[34] Y. Tanabe, T. Adachi, T. Noji, H. Sato, and Y. Koike, in *Low Temperature Physics: Proceedings of the 24th International Conference on Low Temperature Physics - LT24*, edited by Y. Takano, S. P. Hershfield, S. O. Hill, P. J. Hirschfeld, and A. M. Goldman, AIP Conf. Proc. No. 850 (AIP, Melville, NY, 2006), p. 419.

[35] T. Adachi, Y. Tanabe, T. Noji, H. Sato, and Y. Koike, Physica C **445-448**, 14 (2006).

PHYSICAL REVIEW B **77**, 224503 (2008)

Fermi-liquid behavior and weakly anisotropic superconductivity in the electron-doped cuprate $Sr_{1-x}La_xCuO_2$

Kohki H. Satoh,[1,*] Soshi Takeshita,[2] Akihiro Koda,[1,2] Ryosuke Kadono,[1,2] Kenji Ishida,[3] Sunsen Pyon,[4]
Takao Sasagawa,[4,†] and Hidenori Takagi[4]
[1]*Department of Materials Structure Science, The Graduate University for Advanced Studies, Tsukuba, Ibaraki 305-0801, Japan*
[2]*Institute of Materials Structure Science, High Energy Accelerator Research Organization, Tsukuba, Ibaraki 305-0801, Japan*
[3]*Department of Physics, Graduate School of Science, Kyoto University, Kyoto 606-8502, Japan*
[4]*Department of Advanced Materials Science, University of Tokyo, Kashiwa, Chiba 277-8561, Japan*
(Received 14 September 2007; revised manuscript received 26 March 2008; published 9 June 2008)

The microscopic details of flux-line lattice state studied by muon spin rotation are reported in an electron-doped high-T_c cuprate superconductor, $Sr_{1-x}La_xCuO_2$ (SLCO) (x=0.10–0.15). A clear sign of phase separation between magnetic and nonmagnetic phases is observed, where the effective magnetic penetration depth [$\lambda \equiv \lambda(T,H)$] is determined selectively for the latter phase. The extremely small value of $\lambda(0,0)$ and corresponding large superfluid density ($n_s \propto \lambda^{-2}$) is consistent with the presence of a large Fermi surface with carrier density of $1+x$, which suggests the breakdown of the "doped Mott insulator" even at the "optimal doping" in SLCO. Moreover, a relatively weak anisotropy in the superconducting order parameter is suggested by the field dependence of $\lambda(0,H)$. These observations strongly suggest that the superconductivity in SLCO is of a different class from hole-doped cuprates.

DOI: 10.1103/PhysRevB.77.224503 PACS number(s): 74.25.Qt, 74.72.−h, 76.75.+i

The question whether or not the mechanism of superconductivity in electron-doped (n-type) cuprates is common to that in hole-doped (p-type) cuprates is one of the most interesting issues in the field of cuprate superconductors, which is yet to be answered. This "electron-hole symmetry" has been addressed by many experiments and theories since the discovery of n-type cuprate superconductors.[1] In the theoretical models assuming strong electronic correlation where the infinitely large on-site Coulomb interaction ($U \rightarrow \infty$) leads to the Mott insulating phase for the half filled band, the correlation among the doped carriers is projected into the t-J model in which the mechanism of superconductivity does not depend on the sign of charge carriers.[2,3] This is in marked contrast to the models starting from Fermi-liquid (=normal metal) state, where such symmetry is irrelevant to their basic framework.[4] Experimentally, recent advent in crystal-growth techniques and that in experimental methods for evaluating their electronic properties triggered detailed measurements on n-type cuprates, reporting interesting results suggesting certain differences from p-type ones, such as the observation of a commensurate spin fluctuations in neutron-scattering study or the nonmonotonic d-wave superconducting order parameter in angle-resolved photoelectron spectroscopy (ARPES) measurement.[5,6]

The effective magnetic penetration depth (λ) is one of the most important physical quantities directly related to the superfluid density (n_s),

$$\frac{1}{\lambda^2} = \frac{n_s e^2}{m^* c}, \tag{1}$$

which is reflected in the microscopic field profile of the flux-line lattice (FLL) state in type II superconductors. Considering that the response of n_s against various perturbations strongly depends on the characters of the Cooper pairing, the comparison of n_s between two types of carriers might serve as a testing ground for the electron-hole symmetry. However, the study of FLL state in n-type cuprates such as T'-phase RE_2CuO_4 compounds (RE=Nd, Pr, Sm, etc.) is far behind that in p-type cuprates because of strong random local fields from rare-earth ions which mask information of CuO_2 planes regarding both superconductivity and magnetism against magnetic probes such as muon. In this regard, infinite-layer structured $Sr_{1-x}La_xCuO_2$ (SLCO) is a suitable compound for detailed muon spin relaxation and rotation (μSR) study of electron-doped systems, as it is free from magnetic rare-earth ions.

A recent μSR study on SLCO with x=0.10 ($T_c \simeq 40$ K) reported a relatively large $n_s \propto \lambda_{ab}^{-2}$ [$\lambda_{ab}(T \rightarrow 0) \sim 116$ nm] as compared to p-type cuprates,[7] strongly suggesting that n-type cuprates belong to a different class in view of the n_s versus T_c relation.[8] On the other hand, another μSR study showed the appearance of a spin-glass-like magnetism over a wide temperature range including superconducting phase,[9] which might have also affected the result of Ref. 7. In this paper, we demonstrate by μSR measurements under both zero field (ZF) and high transverse field (HTF) that SLCO exhibits a phase separation into magnetic and nonmagnetic phases, where the superconductivity occurs predominantly in the latter. Our measurement made it feasible to evaluate λ reliably as it was selectively determined for the nonmagnetic phase of SLCO.

Meanwhile, the pairing symmetry of order parameter, which is one of the most important issues in discussing the electron-hole symmetry, still remains controversial in n-type cuprates. A number of groups reported s-wave symmetry in SLCO,[10,11] which is in marked contrast to the $d_{x^2-y^2}$ symmetry well established in p-type cuprates. The pairing symmetry can be examined by measuring the temperature and/or field variation of $\lambda(T,H)$ as an *effective* value observed by μSR: it reflects the change in $n_s \equiv n_s(T,H)$ due to quasiparticle excitation and/or nonlocal effect associated with anisotropic or-

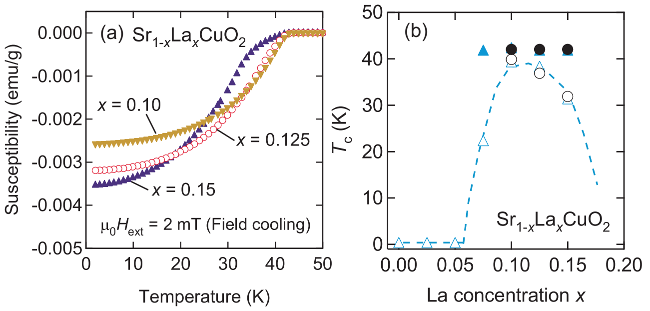

FIG. 1. (Color online) (a) Magnetic susceptibility of SLCO with x=0.10, 0.125, and 0.15 under 20 G. (b) La concentration dependence of T_c. The closed symbols show T_{conset} and the open symbols show T_{cbulk}, respectively. An earlier result (Ref. 15) (triangles) is also quoted for comparison. The dashed line is guide for the eyes.

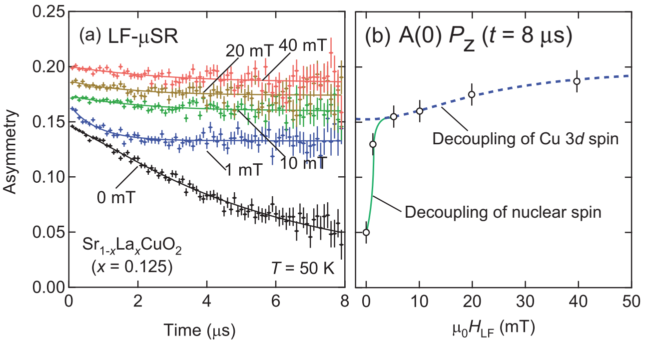

FIG. 3. (Color online) (a) LF-μSR spectra in the sample with x=0.125. (b) Two kinds of decoupling behavior at 50 K. The dashed line is fitting curb by Eq. (2)

der parameter.[12,13] Here, we show evidence that the order parameter in SLCO is not described by simple isotropic s-wave pairing nor that of pure $d_{x^2-y^2}$.

Powder samples of SLCO (x=0.10, 0.125, and 0.15) were prepared by high-pressure synthesis under 6 GPa at 1000 °C. They were confirmed to be of single phase by powder x-ray diffraction, where a small amount of $\text{LaCuO}_{2.5}$ phase (LCO2.5, less than a few percent) was identified. The length of a and c axes showed almost linear change with x, indicating successful substitution of Sr with La for carrier doping.[14] As displayed in Fig. 1(a), the susceptibility (χ_0) measured by superconducting quantum interference device magnetometer implies that the onset of superconductivity is nearly 42 K and least dependent on x, whereas the bulk T_c determined by the maximum of $d\chi_0/dT$ varies with x [see Fig. 1(b)], which reproduces earlier results.[15,16] The x dependence of bulk T_c suggests that the sample is close to the optimal doping for x=0.1.

The μSR experiment was performed on the M15 beamline at TRIUMF (Vancouver, Canada), where measurements under ZF and longitudinal field (LF) were made to investigate magnetic ground state of SLCO. Subsequently, those under a HTF (up to 6 T) were made to study the FLL state in detail. In ZF and LF measurements, a pair of scintillation counters (in backward and forward geometry relative to the initial muon polarization that was parallel to the beam direction) were employed for the detection of positron emitted preferentially to the muon polarization upon its decay. In HTF measurements, sample was at the center of four position counters placed around the beam axis, and initial muon spin polarization was perpendicular to the muon beam direction so that the magnetic field can be applied along the beam direction without interfering with beam trajectory. A veto countersystem was employed to eliminate background signals from the muons that missed the sample, which was crucial for samples available only in small quantities such as those obtained by high-pressure synthesis. For the measurements under a transverse field, the sample was field-cooled to the target temperature to minimize the effect of flux pinning.

Figure 2(a) shows ZF-μSR spectra for the sample with x=0.125, where no spontaneous muon precession is observed as sample is cooled down to 2 K. Instead, fast muon spin depolarization can be identified between $0<t<0.2$ μs, which develops with decreasing temperature. LF-μSR spectra in Fig. 3(a) show that the depolarization is quenched in two steps as a function of field strength, at first near a few millitesla due to nuclear magnetic moments and second around 10^1 mT. The asymptotic behavior of $P_z(t)$ under random local fields H (with an isotropic mean square, $\langle H_x^2\rangle = \langle H_y^2\rangle = \langle H_z^2\rangle = \frac{1}{3}\langle H^2\rangle$) as a function of external magnetic field H_{LF} is approximately given by the following equation:

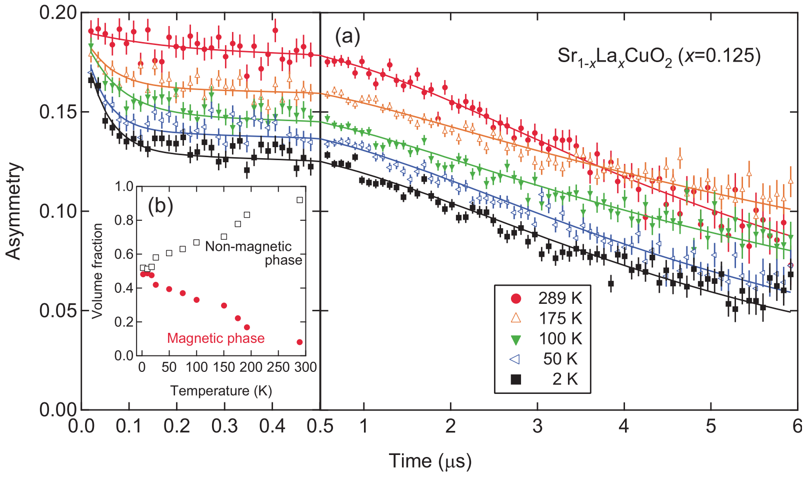

FIG. 2. (Color online) (a) ZF-μSR spectra in the sample with x=0.125. Inset (b) is temperature dependence of the volume fraction of magnetic and nonmagnetic phases.

$$P_z(t \to \infty) \approx \frac{H_{\mathrm{LF}}^2 + \langle H_z^2 \rangle}{H_{\mathrm{LF}}^2 + \langle H^2 \rangle} = \frac{H_{\mathrm{LF}}^2 + \frac{1}{3}\langle H^2 \rangle}{H_{\mathrm{LF}}^2 + \langle H^2 \rangle}, \tag{2}$$

and we estimated the magnitude of $\sqrt{\langle H^2 \rangle} \equiv \bar{H}_{\mathrm{int}}$ from the behavior of $P_z(t \to \infty)$ as 39(3) mT [the best fit with Eq. (2) is shown in Fig. 3(b)]. This is consistent with the fast initial depolarization rate estimated by $\gamma_\mu \bar{H}_{\mathrm{int}} = 33(3)$ MHz (where $\gamma_\mu = 2\pi \times 135.53$ MHz/T is the muon gyromagnetic ratio). The origin of $\bar{H}_{\mathrm{int}}$ can be uniquely attributed to the localized moment of Cu atoms, where the effective moment size is $0.15(1)\mu_B$. The almost negligible depolarization for the asymptotic component implies that spin-fluctuation rate is much smaller than $\gamma_\mu \bar{H}_{\mathrm{int}}$ at 50 K. Thus, ZF/LF-μSR results strongly suggest that the sample that exhibits superconductivity has also static magnetic phase. The magnetic region enlarges to a halfway partition at low temperature [as seen in Fig. 2(b)]. We note that a common tendency was observed for $x=0.10$ and 0.15.

In HTF-μSR, each pair of counters (right-left, upward-downward) observes time-dependent muon spin polarization, $\hat{P}(t)$, projected to the x or y axis perpendicular to the beam direction (with a relative phase shift of $\pi/2$). Inhomogeneity of magnetic-field distribution $B(\mathbf{r})$ leads to depolarization due to the loss of phase coherence among muons probing different parts of $B(\mathbf{r})$. Using a complex notation, $\hat{P}(t)$ is directly provided using the spectral density distribution for the internal field, $n(B)$,

$$\hat{P}(t) = P_x(t) + iP_y(t) = \int_{-\infty}^{\infty} n(B) e^{i(\gamma_\mu B t - \phi)} dB, \tag{3}$$

where $n(B)$ is defined as a spatial average ($\langle\ \rangle_r$) of the delta function,

$$n(B) = \langle \delta[B - B(\mathbf{r})] \rangle_r, \tag{4}$$

and ϕ is the initial phase of muon spin rotation. Then, the real part of fast Fourier transform (FFT) of μSR time spectrum corresponds to $n(B)$, namely,

$$n(B) = \Re \int_{-\infty}^{\infty} \hat{P}(t) e^{-i(\gamma_\mu B t - \phi)} dt. \tag{5}$$

Figure 4 shows the real amplitudes obtained by the FFT of HTF-μSR spectra, which contain information on $n(B)$. The narrow central peak (labeled A) is the signal from muons stopped in a nonmagnetic (and/or nonsuperconducting) phase where the frequency is equal to that of the external field ($\mu_0 H_{\mathrm{ext}} = 6$ T) with a linewidth determined by random nuclear dipolar fields besides the effect of limited time window ($0 \le t \le 6$ μs). A broad satellite peak (labeled B) appears on the positive side of the central peak, when temperature is lowered below 300 K. This corresponds to the fast depolarization in time domain. The ZF/LF-μSR spectra in Figs. 2 and 3 demonstrate that this satellite comes from a magnetic phase in which quasistatic random magnetism of Cu electron spins develops.

While the FFT spectra were useful to examine the overall feature of $n(B)$, the actual data analysis was carried out in time domain using the χ^2-minimizing method. As inferred by Fig. 4, the μSR spectra in the normal state can be reproduced by a sum of two Gaussian dumping signals,

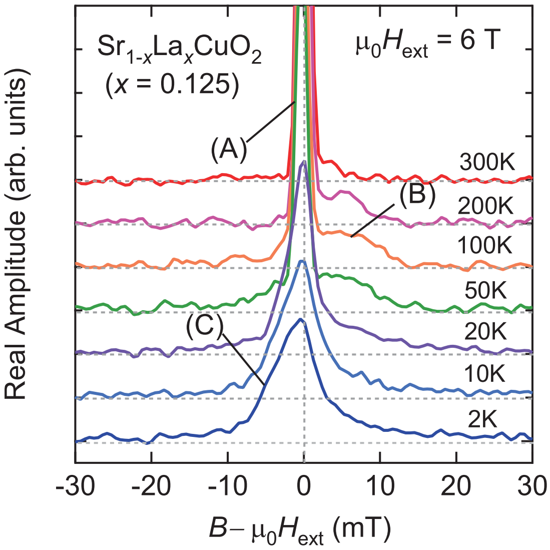

FIG. 4. (Color online) Fast Fourier transform of HTF-μSR spectra under 6 T [after filtering the artifacts due to a finite time window for transform ($0 \le t \le 6$ μs)]. The peaks labeled A, B, and C correspond to nonmagnetic and/or nonsuperconducting, magnetic, and FLL phases, respectively.

$$\hat{P}_n(t) = \sum_{k=1}^{2} f_k \int_{-\infty}^{\infty} n_k(B) e^{i(\gamma_\mu B t - \phi)} dB = \sum_{k=1}^{2} f_k \exp(-\sigma_k^2 t^2/2) e^{i(\omega_k t - \phi)}, \tag{6}$$

where f_k is the relative yield proportional to the fractional volume of each phase, σ_k is the linewidth, and $\omega_k = \gamma_\mu \bar{B}_k$, with $\bar{B}_k$ being the mean value of local magnetic field following a Gaussian distribution,

$$n_k(B) = (\sqrt{2\pi}\sigma_k)^{-1} \exp[-\gamma_\mu^2 (B - \bar{B}_k)^2 / 2\sigma_k^2].$$

It is inferred from the χ^2-minimizing fit of the time spectra by Eq. (6) that the volume fraction of magnetic phase increases toward low temperature monotonously in place of nonmagnetic phase and becomes nearly a half at 50 K. This is clearly not due to the LCO2.5 impurity phase, considering the small volume fraction of LCO2.5 and its known Néel temperature (~125 K).[17] The magnetic volume fraction is independent of H_{ext} at 50 K where the sample is in the normal state. Thus, the appearance of the satellite peak demonstrates the occurrence of a phase separation into magnetic and nonmagnetic domains in the normal state of SLCO.

Taking the result in the normal state into consideration, we analyzed the μSR spectra in the superconducting phase. In the FLL state of type II superconductors, one can reasonably assume that muon stops randomly over the length scale of vortex lattice and serves to provide a random sampling of inhomogeneity due to FLL formation. In the modified-

London (m-London) model, $B(\mathbf{r})$ is approximated as a sum of magnetic inductions from isolated vortices,

$$B_v(\mathbf{r}) = B_0 \sum_{\mathbf{K}} \frac{e^{-i\mathbf{K}\cdot\mathbf{r}}}{1 + K^2\lambda^2} F(K, \xi_v),$$

where $\mathbf{K}$ are the vortex reciprocal-lattice vectors, B_0 ($\simeq \mu_0 H_{\rm ext}$) is the average internal field, $\lambda \equiv \lambda(T,H)$ is the effective London penetration depth depending on temperature and field, and $F(K,\xi_v) = \exp(-K^2\xi_v^2/2)$ is a nonlocal correction term with ξ_v ($\simeq \xi$) being the cutoff parameter for the magnetic-field distribution; the Gaussian cutoff generally provides satisfactory agreement with data. The density distribution $n(B)$ in this case is characterized by the Van Hove singularity originating from the saddle points of $B_v(\mathbf{r})$ with a negative shift primarily determined by λ and that corresponds to the peak (seen as a shoulder) labeled C in Fig. 4. Thus, the signal from the FLL state can be readily separated from other phases at large $H_{\rm ext}$ as they exhibit different frequency shifts with each other. The FFT spectra below T_c also indicate that the domain size of the superconducting phase is much greater than that determined by λ.

It is known that the m-London model is virtually identical to the Ginzburg-Landau (GL) model for large $\kappa = \lambda/\xi$ (ξ is the GL coherence length) and at low magnetic fields ($H_{\rm ext}/H_{c2} < 0.25$, with H_{c2} being the upper critical field).[18,19] Meanwhile, according to a reported value of the upper critical field for SLCO ($\mu_0 H_{c2} = 12$ T, in Ref. 20), the field range of the present measurements ($0 \leq \mu_0 H_{\rm ext} \leq 6$ T) might exceed the above mentioned boundary, and thus the use of the GL model would be more appropriate. However, the m-London model has certain advantages over the GL model in practical application to the analysis: for example, we can avoid further complexity of analysis due to introduction of the field-dependent effective coherence length.[12] We also stress that the discrepancy in the analysis results has been studied in detail between these two models, and now it is well established that m-London model exhibits a systematic tendency of slight overestimation of λ at higher fields due to a known cause.[12,19] The discussion on the present result will be made below considering this tendency.

Another uncertainty comes from the fact that the FLL symmetry in SLCO is not known at this stage, and it might even depend on the magnitude of external field as has been found in some other cuprates.[21,22] However, since we do not observe any abrupt change in line shape nor the increase in χ^2 in the fits (irrespective of model) associated with the alteration of FLL symmetry with varying field,[23,24] we can reasonably assume that the FLL symmetry remains the same throughout entire field range. Moreover, the observed line shape is perfectly in line with the hexagonal FLL, without showing any sign of squared FLL (e.g., a large spectral weight at the lower field side of the central peak in the absence of nonlocal effect[25] or an enhanced weight at the central peak associated with the strong nonlocal effect[24]). Therefore, the FLL symmetry has been assumed to be hexagonal in the following analysis.

The μSR spectra in the FLL state were analyzed by fit analysis using

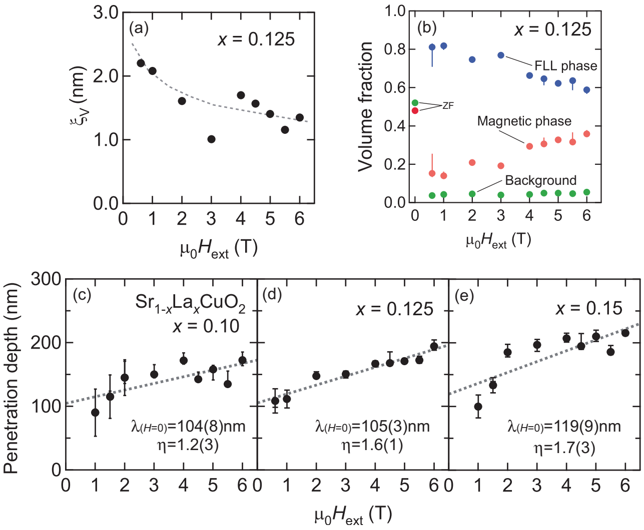

FIG. 5. (Color online) (a) Field dependence of cutoff parameter and (b) volume fraction of each phase at 2 K for the sample with $x = 0.125$, where dashed curves are guide for the eyes. [(c)–(e)] Field dependence of effective penetration depth at 2 K for $x = 0.10$, 0.125, and 0.15, respectively. The dashed lines are a linear fit (see text).

$$\hat{P}(t) = \hat{P}_v(t) + \hat{P}_n(t), \tag{7}$$

$$\hat{P}_v(t) \equiv f_v e^{-\sigma_p^2 t^2} \int n_v(B) e^{i(\gamma_\mu B t - \phi)} dB, \tag{8}$$

$$n_v(B) = \langle \delta[B - B_v(\mathbf{r})] \rangle_r, \tag{9}$$

where f_v is the volume fraction of FLL phase, σ_p represents the contribution from the distortion of FLL due to vortex pinning and that due to nuclear random local fields, and $\hat{P}_n(t)$ is that defined in Eq. (6). The parameters including f_v, λ, ξ_v, σ_p, f_k, σ_k, and ω_k were determined by the χ^2-minimization method with good fits as inferred from the value of reduced χ^2 close to unity. (More specifically, in order to reduce the uncertainty for the analysis of data below T_c, ω_k was fixed to the value determined by the data above T_c.) The magnitude of line broadening due to vortex pinning (σ_p) was relatively small (typically 30%–40% of the frequency shift for the shoulder C in Fig. 4). This was partly due to relatively short λ and associated large asymmetry in $n(B)$, and thereby the correlation between these parameters turned out to be small except at lower fields ($\mu_0 H_{\rm ext} \leq 1$ T) where the spectra exhibit stronger relaxation due to greater linewidth of $n(B)$ and stronger vortex pining (leading to larger σ_p).

Figure 5(a) shows a decreasing tendency of ξ_v with increasing field, which is understood as a shrinkage of vortex core due to vortex-vortex interaction.[19] Figure 5(b) shows the field dependence of fractional yield for each phase at 2 K. With increasing field, the FLL phase appears to be transformed into the magnetic phase. However, it must be noted that there is a discontinuous change between ZF (~50%) and HTF-μSR (~60%–80%). Since no field dependence is observed for the volume fraction in the normal state (T

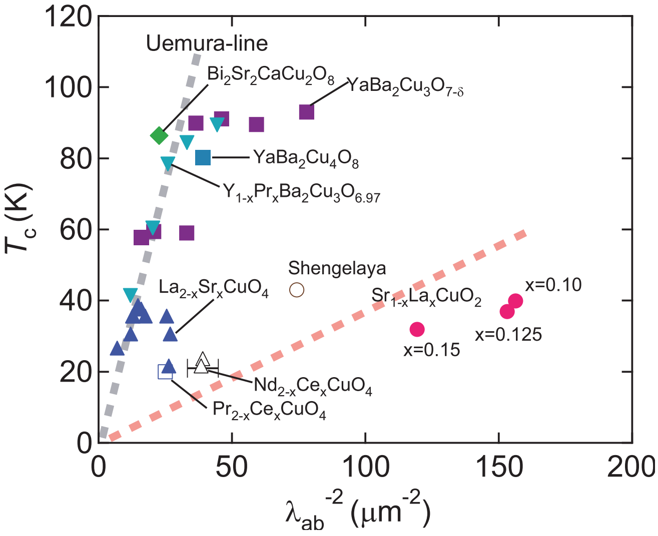

FIG. 6. (Color online) T_c vs λ^{-2} for various cuprate superconductors. The closed circles represent our result, whereas the open circle is that of Ref. 7. The open squares and triangles are for other n-type cuprates (Refs. 33–35), closed upward triangles for $La_{2-x}Sr_xCuO_4$ (Refs. 29 and 36–38) and downward ones for $Y_{1-x}Pr_xBa_2Cu_3O_{6.97}$ (Ref. 39). The square symbols for $YBa_2Cu_3O_y$ and diamond for $Bi_2Sr_2CaCu_2O_8$ (Refs. 40–43).

$\sim$50 K), the reduction of the magnetic fraction at lower fields is attributed to the overlap of magnetic domains with vortex cores: the magnetic domains would serve as pinning centers for vortices more effectively at lower fields due to the softness of FLL. The increase in magnetic fraction with increasing field is then readily understood as a result of decreasing probability for vortices to overlap with random magnetic domains at higher fields because the relative density of vortices as well as the rigidity of FLL would increase. This also suggests that the mean domain size of the magnetic phase is considerably smaller than the FLL spacing (=69 nm at 0.5 T).

Figures 5(c)–5(e) show the field dependence of λ in each compounds. While the London penetration depth is a physical constant uniquely determined by local electromagnetic response, λ in our definition [Eq. (1)] is a variable parameter, as n_s depends on temperature (T) and external magnetic field (H). Therefore, we introduce an effective penetration depth, $\lambda(T,H)$, with an explicit reference to T and H dependence. It is clear in Figs. 5(c)–5(e) that $\lambda(H)=\lambda(2\ \text{K},H)$ tends to increase with increasing external field. Here, one may further notice a tendency that $\lambda(H)$ increases more steeply below $\sim$2 T in the case of $x=0.10$ and 0.15. However, these points at lower fields are also associated with larger error bars probably because of the stronger depolarization in the time domain. The value extrapolated to $\mu_0 H_{\text{ext}}=0$ [$\lambda(0)$] is estimated by a linear fit with a proper consideration of the uncertainty associated with these errors, and the result is indicated in Fig. 5. These values (104–119 nm) turn out to be significantly shorter than the earlier result[7] (hereafter, the in-plane penetration depth λ_{ab} is approximated by an equation $\lambda \simeq 1.3\lambda_{ab}$, according to Ref. 26). In qualitative sense, however, our result supports the earlier suggestion of a large discrepancy for SLCO from the quasilinear relation between T_c and n_s observed over a wide variety of p-type cuprates.[8] The anomaly becomes more evident when they are mapped to the T_c vs λ^{-2} plot, as shown in Fig. 6. They are far off the line followed by the data of p-type cuprates, suggesting that n-type SLCO belongs to a class of superconductors different from that of p-type cuprates.

It is well established that the carrier concentration, p, of p-type cuprates nearly corresponds to that of the doping value x while $x \leq 0.20$.[27] In contrast, a recent ARPES measurement on an n-type cuprate, $Nd_{2-x}Ce_xCuO_{4\pm\delta}$, has revealed that small electron pockets ($p \simeq x$) observed for $x=0.04$ sample are replaced by a large Fermi surface (corresponding to $p \simeq 1+x$) for $x=0.10$ and 0.15 samples.[28] When m^* is assumed to be comparable with that of p-type cuprate ($m^* \simeq 3m_e$), n_s can be estimated using Eq. (1), yielding 1.3×10^{22} cm^{-3} in SLCO with $x=0.125$ [where $\lambda(0)$ is determined with the best accuracy]. This corresponds to $p \geq 0.70$, and an order of magnitude larger than that of p-type cuprates.[19,29] A better correspondence to $p \simeq 1+x=1.125$ would be attained when $m^* \simeq 4.8m_e$. Thus, the present result is yet another evidence for a large Fermi surface in SLCO. This is also in line with some recent experimental results for n-type superconductors. For example, resistivity (ρ) in the normal state shows a Fermi-liquid-like temperature dependence ($\rho \propto T^2$) common to ordinary metals,[30] and a metallic Korringa law has been revealed by NMR study under high magnetic fields.[31] These observations coherently suggest that the n-type cuprates cannot be regarded as the doped Mott insulators, but they might be better understood as in the normal Fermi-liquid state already at the optimal doping ($x \sim 0.1$).

The increase in λ with increasing external field is a clear sign that the superconducting order parameter is not described by that of simple isotropic s-wave paring for single-band electrons.[12] One of the possible origins for the field dependent λ is the presence of nodal structure in the order parameter [$|\Delta(\mathbf{k})|=0$ at particular $\mathbf{k}$] that leads to the field-induced quasiparticle excitation due to the quasiclassical Doppler shift.[32] The quasiparticle energy spectrum is shifted by the flow of supercurrent around vortex cores to an extent $\delta E = m\mathbf{v}_F \cdot \mathbf{v}_s$, where $\mathbf{v}_F$ and $\mathbf{v}_s$ are the Fermi velocity and superfluid velocity, respectively. This gives rise to the pair breaking for $|\Delta(\mathbf{k})| < \delta E$ and associated reduction of n_s. The presence of nodes also leads to a nonlocal effect in which λ is affected by the modification of supercurrent near the nodes where the coherence length $\xi_0(\mathbf{k}) = \hbar v_F / \pi\Delta(\mathbf{k})$ exceeds the local London penetration depth.[44] For the comparison of magnitude for the field-induced effect, we use a dimensionless parameter η deduced by fitting data in Fig. 5 using $\lambda(h)=\lambda(0)[1+\eta h]$ with $h=H/H_{c2}$. Provided that η is dominated by the presence of gap nodes, the magnitude of η at lower fields is roughly proportional to the phase volume of the Fermi surface where $|\Delta(\mathbf{k})| < \delta E$. As seen in Fig. 5, η in SLCO is definitely greater than zero irrespective of x, taking values between 1.2 and 1.7. It is noticeable that these values are considerably smaller than $\eta \simeq 6$ ($\mu_0 H_{\text{ext}} < 2$ T) observed in $YBa_2Cu_3O_{6.95}$ (YBCO) that has a typical $d_{x^2-y^2}$-wave gap symmetry. The situation remains true even when one considers (i) the nonlocal effect that tends to reduce η at high magnetic fields ($\eta \simeq 2$ for $\mu_0 H_{\text{ext}} > 2$ T) (Ref. 45) and (ii) a possible overestimation of λ at higher fields due to the extended use of the *m*-London model that also leads to the overestimation of η [e.g., η based on the *m*-London model is greater than that on the GL model by 0.23(7) in $NbSe_2$ (Ref. 19) and 0.6(2) in YB_6 (Ref. 12)].

Interestingly, the relatively small value of η is in line with the recent suggestion by ARPES measurement on another *n*-type superconductor, $Pr_{0.89}LaCe_{0.11}CuO_4$ (PLCCO), which the order parameter $\Delta(k,\psi)$ has a steeper gradient at the nodes along azimuthal (ψ) direction than that for the $d_{x^2-y^2}$ symmetry.[6] Since the phase volume satisfying $|\Delta(\mathbf{k})| < \delta E$ is inversely proportional to $d|\Delta(k,\psi)|/d\psi$ at the node, we have

$$\eta \propto \left(\frac{d|\Delta(k,\psi)|}{d\psi} \right)^{-1}_{\psi(|\Delta|=0)}. \qquad (10)$$

Assuming a situation similar to PLCCO and that η observed in YBCO represents a typical value for $d_{x^2-y^2}$-wave gap, our result suggests that the gradient $d|\Delta(k,\psi)|/d\psi$ in SLCO is 1.2(3)–5.0(3) times greater than that at the node of $d_{x^2-y^2}$-wave gap. However, it is clear that further assessments by other techniques that are more sensitive to the symmetry of the order parameters are necessary to discuss the details of gap structure in SLCO.

In conclusion, it has been revealed by the present μSR study that a phase separation occurs in an electron-doped cuprate superconductor, $Sr_{1-x}La_xCuO_2$ (x=0.10, 0.125, and 0.15), where nearly half of the sample volume exhibits magnetism having no long-range correlation while the rest remains nonmagnetic. The superconductivity occurs predominantly in the nonmagnetic domain, where the effective magnetic penetration depth evaluated by using a modified-London model is much shorter than that of other *p*-type cuprates. This suggests a large carrier density corresponding to $1+x$ and accordingly the breakdown of the Mott insulating phase in SLCO and other *n*-type cuprates even at their optimal doping. The field dependence of λ suggests that the superconductivity of SLCO is not described by single-band *s*-wave pairing. The magnitude of the dimensionless parameter, η ($\propto d\lambda/dH$), is qualitatively in line with nonmonotonic *d*-wave superconducting gap observed in other *n*-type cuprates.

We would like to thank the staff of TRIUMF for technical support during the μSR experiment and Takano-group of ICR-Kyoto University (M. Takano, Y. Shimakawa, M. Azuma, I. Yamada, and K. Oka) for useful advice concerning sample preparation. This work was partially supported by the Grant-in-Aid for Creative Scientific Research and the Grant-in-Aid for Scientific Research on Priority Areas by the Ministry of Education, Culture, Sports, Science and Technology, Japan.

---

*ksatoh@post.kek.jp
†Present address: Materials and Structures Laboratory, Tokyo Institute of Technology.

[1] H. Takagi, S. Uchida, and Y. Tokura, Phys. Rev. Lett. **62**, 1197 (1989).

[2] F. C. Zhang and T. M. Rice, Phys. Rev. B **37**, 3759 (1988).

[3] For the recent review, see, for example, P. W. Anderson, P. A. Lee, M. Randeria, T. M. Rice, N. Trivedi, and F. C. Zhang, J. Phys.: Condens. Matter **16**, R755 (2004).

[4] For the recent review, see for example, T. Moriya and K. Ueda, Adv. Phys. **49**, 555 (2000).

[5] K. Yamada, K. Kurahashi, T. Uefuji, M. Fujita, S. Park, S.-H. Lee, and Y. Endoh, Phys. Rev. Lett. **90**, 137004 (2003).

[6] H. Matsui, K. Terashima, T. Sato, T. Takahashi, M. Fujita, and K. Yamada, Phys. Rev. Lett. **95**, 017003 (2005).

[7] A. Shengelaya, R. Khasanov, D. G. Eshchenko, D. Di Castro, I. M. Savić, M. S. Park, K. H. Kim, S.-I. Lee, K. A. Müller, and H. Keller, Phys. Rev. Lett. **94**, 127001 (2005).

[8] Y. J. Uemura, L. P. Le, G. M. Luke, B. J. Sternlieb, W. D. Wu, J. H. Brewer, T. M. Riseman, C. L. Seaman, M. B. Maple, M. Ishikawa, D. G. Hinks, J. D. Jorgensen, G. Saito, and H. Yamochi, Phys. Rev. Lett. **66**, 2665 (1991).

[9] K. M. Kojima, K. Kawashima, M. Fujita, K. Yamada, M. Azuma, M. Takano, A. Koda, K. Ohishi, W. Higemoto, R. Kadono, and Y. J. Uemura, Physica B (Amsterdam) **374-375**, 207 (2006).

[10] C.-T. Chen, P. Seneor, N.-C. Yeh, R. P. Vasquez, L. D. Bell, C. U. Jung, J. Y. Kim, M.-S. Park, H.-J. Kim, and S.-I. Lee, Phys. Rev. Lett. **88**, 227002 (2002).

[11] Z. Y. Liu, H. H. Wen, L. Shan, H. P. Yang, X. F. Lu, H. Gao, M.-S. Park, C. U. Jung, and S.-I. Lee, Europhys. Lett. **69**, 263 (2005).

[12] R. Kadono, S. Kuroiwa, J. Akimitsu, A. Koda, K. Ohishi, W. Higemoto, and S. Otani, Phys. Rev. B **76**, 094501 (2007).

[13] R. Kadono, J. Phys.: Condens. Matter **16**, S4421 (2004).

[14] G. Er. S. Kikkawa, F. Kanamaru, Y. Miyamoto, S. Tanaka, M. Sera, M. Sato, Z. Hiroi, M. Takano, and Y. Bando, Physica C **196**, 271 (1992).

[15] K. Kawashima, M.S. thesis (unpublished).

[16] S. Karimoto, K. Ueda, M. Naito, and T. Imai, Physica C **378-381**, 127 (2002).

[17] R. Kadono, H. Okajima, A. Yamashita, K. Ishii, T. Yokoo, J. Akimitsu, N. Kobayashi, Z. Hiroi, M. Takano, and K. Nagamine, Phys. Rev. B **54**, R9628 (1996).

[18] E. H. Brandt, Phys. Rev. B **37**, 2349 (1988).

[19] J. E. Sonier, J. H. Brewer, and R. F. Kiefl, Rev. Mod. Phys. **72**, 769 (2000).

[20] V. S. Zapf, N.-C. Yeh, A. D. Beyer, C. R. Hughes, C. H. Mielke, N. Harrison, M. S. Park, K. H. Kim, and S.-I. Lee, Phys. Rev. B **71**, 134526 (2005).

[21] S. P. Brown, D. Charalambous, E. C. Jones, E. M. Forgan, P. G. Kealey, A. Erb, and J. Kohlbrecher, Phys. Rev. Lett. **92**, 067004 (2004).

[22] R. Gilardi, J. Mesot, A. Drew, U. Divakar, S. L. Lee, E. M. Forgan, O. Zaharko, K. Conder, V. K. Aswal, C. D. Dewhurst, R. Cubitt, N. Momono, and M. Oda, Phys. Rev. Lett. **88**, 217003 (2002).

[23] R. Kadono, K. H. Satoh, A. Koda, T. Nagata, H. Kawano-

Furukawa, J. Suzuki, M. Matsuda, K. Ohishi, W. Higemoto, S. Kuroiwa, H. Takagiwa, and J. Akimitsu, Phys. Rev. B **74**, 024513 (2006).

[24] K. Ohishi, K. Kakuta, J. Akimitsu, W. Higemoto, R. Kadono, J. E. Sonier, A. N. Price, R. I. Miller, R. F. Kiefl, M. Nohara, H. Suzuki, and H. Takagi, Phys. Rev. B **65**, 140505(R) (2002).

[25] C. M. Aegerter, S. H. Lloyd, C. Ager, S. L. Lee, S. Romer, H. Keller, and E. M. Forgan, J. Phys.: Condens. Matter **10**, 7445 (1998).

[26] V. I. Fesenko, V. N. Gorbunov, and V. P. Smilga, Physica C **176**, 551 (1991).

[27] Y. Fukuzumi, K. Mizuhashi, K. Takenaka, and S. Uchida, Phys. Rev. Lett. **76**, 684 (1996).

[28] N. P. Armitage, F. Ronning, D. H. Lu, C. Kim, A. Damascelli, K. M. Shen, D. L. Feng, H. Eisaki, Z.-X. Shen, P. K. Mang, N. Kaneko, M. Greven, Y. Onose, Y. Taguchi, and Y. Tokura, Phys. Rev. Lett. **88**, 257001 (2002).

[29] G. Aeppli, R. J. Cava, E. J. Ansaldo, J. H. Brewer, S. R. Kreitzman, G. M. Luke, D. R. Noakes, and R. F. Kiefl, Phys. Rev. B **35**, 7129 (1987).

[30] C. H. Wang, L. Huang, L. Wang, Y. Peng, X. G. Luo, Y. M. Xiong, and X. H. Chen, Supercond. Sci. Technol. **17**, 469 (2004).

[31] G.-Q. Zheng, T. Sato, Y. Kitaoka, M. Fujita, and K. Yamada, Phys. Rev. Lett. **90**, 197005 (2003).

[32] G. E. Volovik, Pis'ma Zh. Eksp. Teor. Fiz. **58**, 457 (1993) [JETP Lett. **58**, 469 (1993)].

[33] C. C. Homes, R. P. S. M. Lobo, P. Fournier, A. Zimmers, and R. L. Greene, Phys. Rev. B **74**, 214515 (2006).

[34] A. A. Nugroho, I. M. Sutjahja, A. Rusydi, M. O. Tjia, A. A. Menovsky, F. R. de Boer, and J. J. M. Franse, Phys. Rev. B **60**, 15384 (1999).

[35] C. C. Homes, B. P. Clayman, J. L. Peng, and R. L. Greene, Phys. Rev. B **56**, 5525 (1997).

[36] G. M. Luke, Y. Fudamoto, K. Kojima, M. Larkin, J. Merrin, B. Natumi, Y. J. Uemura, J. E. Sonier, T. Ito, K. Oka, M. de Andrade, M. B. Maple, and S. Uchida, Physica C **282-287**, 1465 (1997).

[37] T. Schneider and H. Keller, New J. Phys. **6**, 144 (2004).

[38] C. Panagopoulos, J. R. Cooper, T. Xiang, Y. S. Wang, and C. W. Chu, Phys. Rev. B **61**, R3808 (2000).

[39] C. L. Seaman, J. J. Neumeier, M. B. Maple, L. P. Le, G. M. Luke, B. J. Sternlieb, Y. J. Uemura, J. H. Brewer, R. Kadono, R. F. Kiefl, S. R. Krietzman, and T. M. Riseman, Phys. Rev. B **42**, 6801 (1990).

[40] W. N. Hardy, D. A. Bonn, D. C. Morgan, R. Liang, and K. Zhang, Phys. Rev. Lett. **70**, 3999 (1993).

[41] J. E. Sonier, D. A. Bonn, J. H. Brewer, W. N. Hardy, R. F. Kiefl, and R. Liang, Phys. Rev. B **72**, 146501 (2005).

[42] Y. J. Uemura, V. J. Emery, A. R. Moodenbaugh, M. Suenaga, D. C. Johnston, A. J. Jacobson, J. T. Lewandowski, J. H. Brewer, R. F. Kiefl, S. R. Kreitzman, G. M. Luke, T. Riseman, C. E. Stronach, W. J. Kossler, J. R. Kempton, X. H. Yu, D. Opie, and H. E. Schone, Phys. Rev. B **38**, 909 (1988).

[43] H. Keller, W. Kündig, I. M. Savić, H. Simmler, B. Stäuble-Pümpin, M. Warden, D. Zech, P. Zimmermann, E. Kaldis, J. Karpinski, S. Rusiecki, J. H. Brewer, T. M. Riseman, and J. W. Schneider, Physica C **185189**, 1089 (1991).

[44] M. H. S. Amin, I. Affleck, and M. Franz, Phys. Rev. B **58**, 5848 (1998).

[45] J. E. Sonier, J. H. Brewer, R. F. Kiefl, G. D. Morris, R. I. Miller, D. A. Bonn, J. Chakhalian, R. H. Heffner, W. N. Hardy, and R. Liang, Phys. Rev. Lett. **83**, 4156 (1999).

Hydrogen Bonding in Sodium Alanate: A Muon Spin Rotation Study

R. Kadono,[1,2] K. Shimomura,[1] K. H. Satoh,[2] S. Takeshita,[1] A. Koda,[1,2] K. Nishiyama,[1] E. Akiba,[3]
R. M. Ayabe,[4] M. Kuba,[4] and C. M. Jensen[4]

[1]*Institute of Materials Structure Science, High Energy Accelerator Research Organization (KEK), Tsukuba, Ibaraki 305-0801, Japan*
[2]*Department of Materials Structure Science, The Graduate University for Advanced Studies, Tsukuba, Ibaraki 305-0801, Japan*
[3]*Energy Technology Research Institute, National Institute of Advanced Industrial Science and Technology, Tsukuba, Ibaraki 305-8568, Japan*
[4]*Department of Chemistry, University of Hawaii at Manoa, Honolulu, Hawaii 96822-2275, USA*

(Received 15 January 2007; revised manuscript received 9 April 2007; published 15 January 2008)

We have detected the occurrence of hydrogen bonding involving an interstitial positive muon situated between hydrogen atoms of two independent alanate anions in sodium alanate ($NaAlH_4$). Ti doping, which is known to dramatically improve the hydrogen cycling performance of $NaAlH_4$, reduces the kinetic barrier of the transition of the muon from the muon-dialanate state to a mobile interstitial state. This observation strongly suggests that hydrogen bonding is the primary bottleneck for hydrogen release or uptake in sodium alanate, which might be common to other complex hydrides.

DOI: 10.1103/PhysRevLett.100.026401 PACS numbers: 71.55.−i, 76.75.+i, 82.33.−z

Complex hydrides are one of the most promising hydrogen storage materials to have emerged in recent years. Many complex hydrides have a high hydrogen weight percentage; thus, their potential as hydrogen storage materials has long been recognized. However, they are generally characterized by extremely slow hydrogen cycling kinetics. Thus they were precluded from consideration as practical onboard hydrogen carriers until Bogdanović's discovery of the remarkable effect of transition metal dopants on the kinetics of the hydrogen cycling process [1], $NaAlH_4 \leftrightarrow \frac{1}{3}Na_3AlH_6 + \frac{2}{3}Al + H_2 \leftrightarrow NaH + Al + \frac{3}{2}H_2$. This breakthrough marked the beginning of a new era in the development of metal hydrides as hydrogen storage materials. Prior to this finding, hydrogen cycling in a highly ionic, saline material under moderate conditions was considered to be impossible. In light of Bogdanović's findings, the search for materials with the right combination of high hydrogen capacity, rapid kinetics below 100 °C, and favorable thermodynamic parameters is no longer restricted to hydrogen absorbing metals and alloys.

Recently, it has been found that the phenomenon of kinetic enhancement upon transition metal doping extends to other hydrogen storage materials. For example, investigators have recently found that this phenomenon extends to the reversible dehydrogenation of $LiNH_2$ [2]. This new, expanded frontier of hydrogen storage materials can be expected to continue to yield promising results. Despite this progress, a material with the right combination of properties that is required for practical viability in vehicular applications has still not been developed. A better understanding of the fundamental basis of the enigmatic, solid state kinetic enhancement of reversible dehydrogenation in the doped materials would be invaluable to the effort to develop improved hydrogen storage materials.

The microscopic details of how transition metal doping enhances hydrogen cycling kinetics is still unknown. A major component of research on alanate based materials has been directed towards gaining a fundamental understanding of the nature of the dopants and the structural effects they exert on complex hydrides. We previously conducted solid state ^1H nuclear magnetic resonance (NMR) studies which showed that the introduction of Ti dopants into $NaAlH_4$ enhances a population of highly mobile hydrogen in the hydride [3]. This conclusion is reinforced by the observation of a $\sim$10 cm^{-1} shift of the frequency of the Al-H stretch that is observed upon doping the hydride [4]. Further information about the effects of doping on the hydrogen in the hydride was obtained in a recent study of $NaAlH_4$ by anelastic spectroscopy [5]. These studies resulted in the detection of point defects that are formed during the dehydrogenation of the doped hydride [6]. Measurements on samples of the doped hydride at subambient temperatures revealed a dynamic process involving a very mobile species. At 70 K, a highly mobile entity performs about 5×10^3 jumps/s corresponding to an activation energy of 0.126 eV (=1460 K). Deuterium isotope studies have shown these entities involve hydrogen [6].

The technique of muon spin rotation (μSR) has been widely applied to the study of local electronic structure of hydrogen atoms. It is well established that a positively charged muon (μ^+) behaves as a light isotope of a proton or hydrogen upon its implantation in matter, where it resides at the interstitial site(s) to minimize the electrostatic energy. The electronic structure of a muon-electron bound state (a muonic analog of a hydrogen atom, called *muonium*) is identical to that of hydrogen except a small correction due to the difference of reduced mass ($\sim$0.5%). Thus, the implanted muon simulates the state of interstitial hydrogen on the atomic scale and provides information on the local structure of hydrogen isotopes which is highly complementary to that of the on site hydrogens obtained by neutron scattering and ^1H NMR. As shown below, the positive muon also serves as a sensitive probe of the internal magnetic fields at interstitial site(s). This is partially due to its large gyromagnetic ratio ($\gamma_\mu/2\pi =$ 135.53 MHz/T, which is 3.183 times that of ^{1}H). This allows us to investigate the local atomic configuration around the muon by probing the magnitude of local magnetic fields from *nuclear* magnetic moments.

The experiments were performed on the M15 beam line at TRIUMF (Canada) and the πM3 beam line at PSI (Switzerland) which, respectively, provide a beam of nearly 100% spin-polarized positive muons. Conventional μSR measurements were carried out on the powder specimens of pure and Ti-doped sodium alanate. The Ti-doped material was prepared by the mechanical milling method [7,8] in which the hydride was combined with 2 mol % TiF_3 and ball milled under an argon atmosphere in a stainless steel bowl. The obtained powder ($\sim$0.5 g) was wrapped with a thin aluminum foil ($\simeq$15 μm) and then sealed with a thin polymer sheet under an argon atmosphere to prevent oxidation of samples. A muon beam with an energy of 4 MeV (corresponding to the stopping range of $\sim$150 mg/cm^2) was irradiated on the sample loaded on a He gas-flow cryostat, and time-dependent muon spin polarization was monitored by measuring the energetic μ-e decay positrons emitted preferentially along the muon spin direction.

Figure 1 shows the time evolution of positron decay asymmetry $A(t)$ under a zero-field condition, where $A(t)$ is proportional to the instantaneous muon polarization $\vec{P}(t)$ projected along the z axis parallel to the initial muon beam direction, $A(t) = A_0 P_z(t)$, with A_0 ($\simeq$0.18 for PSI data and $\simeq$ 0.26 for TRIUMF data) being the instrumental asymmetry. A_0 at PSI was small because $\vec{P}(0)$ was tilted by nearly 45° from the z axis. In both undoped and Ti-doped samples, the time evolution of $A(t)$ observed near 5 K is characterized by a Gaussian damping that is overlapped with sinusoidal oscillation. While such a spontaneous oscillation of muon spin in magnetic materials is a sign of magnetic order, it is clearly not the case considering that sodium alanate is a nonmagnetic insulator. The only possible origin of the oscillation is the formation of a local atomic cluster consisting of a μ^+ and a small number ($\leq$2) of nearby atoms having nuclear magnetic moments. One of the classical examples is the F^--μ^+-F-($F\mu F^-$) complex observed in alkali metal fluorides, where the two ^{19}F nuclei (spin $I = 1/2$) exert a well-defined magnetic dipolar field on a muon and thereby the muon exhibits coherent spin precession [9]. The $F\mu F^-$ state is a muonic analogue of hydrogen difluoride (F-H-F^-) that is known as a prototype of strong hydrogen bonding [10]. Observation of the $F\mu F^-$ state in NaF naturally leads to the possibility that alanate substitutes the role of fluorine to form an AlH_4^- μ^+-AlH_4^- bonding state in $NaAlH_4$, where the nearest two nuclei are those of hydrogen atoms. As shown below, this speculation turns out to be a quantitatively reasonable model for understanding the local atomic configuration for the interstitial muon.

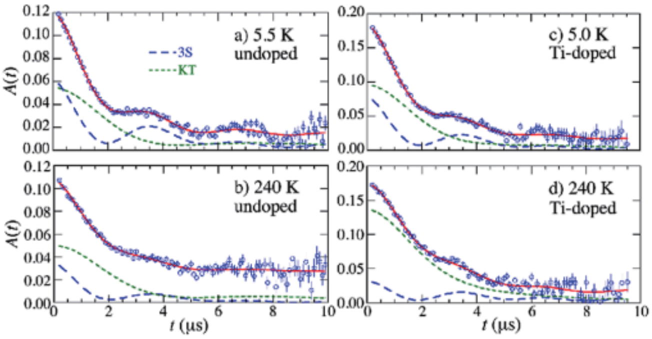

FIG. 1 (color online). Time-dependent μ-e decay asymmetry ($\propto$ muon polarization) observed in undoped (a),(b) and Ti-doped (c),(d) $NaAlH_4$, respectively, at about 5 and 240 K under zero external field. The full polarization corresponds to $\sim$0.18 for (a),(b) (PSI data), and $\sim$0.26 for (c),(d) (TRIUMF data). Solid curves are those obtained by fitting analysis using the model described in the text, where contributions of $G_{3S}(t)$ and $G_{KT}(t)$ are displayed by broken curves.

Assuming a static collinear geometry with μ^+ at the center of the line joining two other nuclear spins ($I = 1/2$), the time evolution of muon polarization as a cubic average is calculated by solving a simple three-spin model to yield

$$G_{3S}(t) = \tfrac{1}{6}\{3 + \cos(\sqrt{3}\omega_d t) + \alpha_+ \cos(\beta_+ \omega_d t) + \alpha_- \cos(\beta_- \omega_d t)\}, \qquad (1)$$

where $\alpha_\pm = 1 \pm 1/\sqrt{3}$, $\beta_\pm = (3 \pm \sqrt{3})/2$, and ω_d is the dipolar interaction frequency

$$\omega_d = 2\gamma_\mu \gamma_I / r^3, \qquad (2)$$

with γ_I and r, respectively, being the gyromagnetic ratio of nuclear spin ($\gamma_I/2\pi = 42.58$ MHz/T for ^{1}H) and the distance between μ^+ and the nucleus [9]. The observed time evolution also suggests that a considerable fraction of implanted muons are subjected to a local field characterized by the Gaussian distribution, leading to depolarization described by the Kubo-Toyabe relaxation function [$G_{KT}(t)$] under zero external field [11]. In addition, a stationary (undamped) component emerges in the undoped specimen at higher temperatures [see Fig. 1(b)]. Considering those three components, the time spectra in Fig. 1 are analyzed by a model relaxation function,

$$A(t) = f_d A_0 [f e^{-\Lambda t} G_{3S}(t) + g G_{KT}(t; \Delta, \nu) + h], \qquad (3)$$

where f_d is the fractional yield of the μ^+ state, f and g are relative yield of the muon-dialanate state and that described by $G_{KT}(t)$ (with $f + g + h \equiv 1$), Λ is the damping rate of the dialanate signal, Δ is the Gaussian linewidth, and ν is the hopping frequency of the muon. As shown in Fig. 1, the fitting analysis by the above model function using the χ^2-minimization method provides perfect agreement with the observed spectra. The deduced parameter values are shown in Figs. 2 and 3 with correlated errors obtained by scanning over the multidimensional χ^2 contour. We also examined the possibility of a muon bound to a single nuclear spin, such as monoalanate (μ^+-AlH_4^-) or μ-H bound state (a H_2 molecule with one of the protons substituted by μ^+), where the time evolution of muon polarization in two-spin system is described by $G_{2S}(t) = \frac{1}{6}\{1 + \cos\omega_d t + 2\cos(\frac{1}{2}\omega_d t) + 2\cos(\frac{3}{2}\omega_d t)\}$ [12]. The best fit by Eq. (3) with $G_{2S}(t)$ substituting for $G_{3S}(t)$ yields nearly twice as large χ^2 as that with $G_{3S}(t)$, indicating that the observed μSR spectra is best explained by the muon-dialanate configuration.

Among parameters introduced in Eq. (3), those shown in Fig. 2 do not show significant difference between undoped and Ti-doped cases, whereas the fractional yields (f and g) exhibit a different tendency in the Ti-doped sample as displayed in Fig. 3. More specifically, the population of $G_{3S}(t)$ is shifted to $G_{KT}(t)$ ($\propto g$) with increasing temperature in the Ti-doped sample, while it is shifted to an undamped component ($\propto h = 1 - f - g$) with considerably higher characteristic temperature for activation. As shown in Fig. 3, a simple activation model, $f(T) = f_0[1 + \tau_0\nu_a\exp(-E_a/kT)]^{-1}$, provides reasonable description of the observed T dependence, where τ_0 refers to the intrinsic mean resident time, ν_a to the attempt frequency, and E_a to the activation energy. Curve fitting analysis yields $E_a/k \simeq$ 756(86) K (from f and h) and $\simeq$251(42) K (from f and g) for undoped and Ti-doped samples, respectively.

In the present model, the nearest neighboring (NN) nuclei seen from the muon in the dialanate state are one H atom of each NN alanates (the C site in Fig. 3), and thereby the muon-H bond length is deduced from Eq. (2). It is inferred from Fig. 2(a) that $r \simeq 1.43$–1.46 Å in both undoped and Ti-doped samples over most of the present temperature region, indicating that the distance between H atoms in the AlH_4^--μ^+-AlH_4^- bonding is 2.86–2.92 Å. This is slightly longer than the distance of H atoms between the neighboring alanates (~2.2 Å), suggesting that the bonding is associated with a slight deformation of the alanate units.

The second component described by the Kubo-Toyabe relaxation function is attributed to the muons located at the octahedral interstitial sites (the O site in Fig. 3), where the muon is surrounded by six ^{1}H, three ^{23}Na, and three ^{27}Al NN nuclei. The estimated linewidth Δ from these NN nuclei is ~0.33 μs^{-1}, which is slightly smaller than those deduced from the present data (0.4–0.5 μs^{-1}). This discrepancy, however, may be readily explained by a small (5%–10%) local shrinkage of the alanate cage around the muon, or slight shift of the muon position towards negatively charged alanate ions. Interestingly, the hopping rate at the O site shows very little dependence on the Ti doping, where $\nu \simeq 2$–4×10^5 s^{-1}. Since ν is related to the macroscopic diffusion rate by the expression $D = \frac{1}{2}a_0^2\nu$ for the jump between O sites in a fcc lattice (with a_0 being the unit cell length $\simeq 5$ Å), we have $D \simeq 2.5$–5×10^{-10} cm^2 s^{-1}. This is comparable to typical rates for hydrogen diffusion in fcc metals over the relevant temperature region [13].

Compared with the above two components, the origin of the undamped component ($\propto h$) is not clear at this stage. Considering that all the elements in $NaAlH_4$ have nuclear magnetic moments that are comparable with each other, the absence of spin relaxation or precession strongly suggests that muons in this state are subject to fast spin

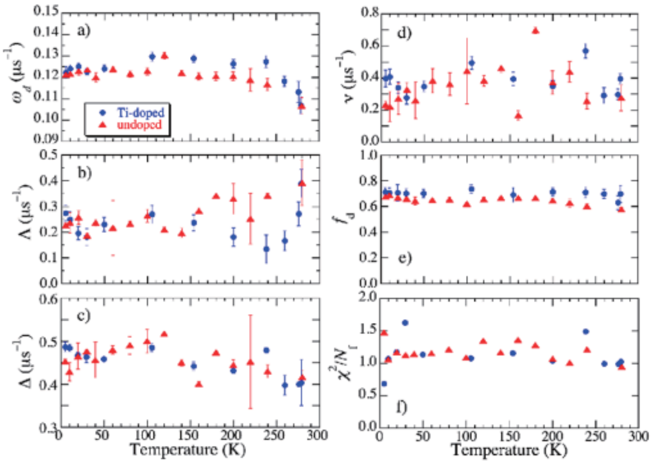

FIG. 2 (color online). Temperature dependence of (a) ω_d, (b) Λ, (c) Δ, (d) ν, and (e) f_d extracted from μSR spectra using χ^2-minimization fits. The value of reduced χ^2 is also shown in (f). For the fractional yields (f and g), see Fig. 3.

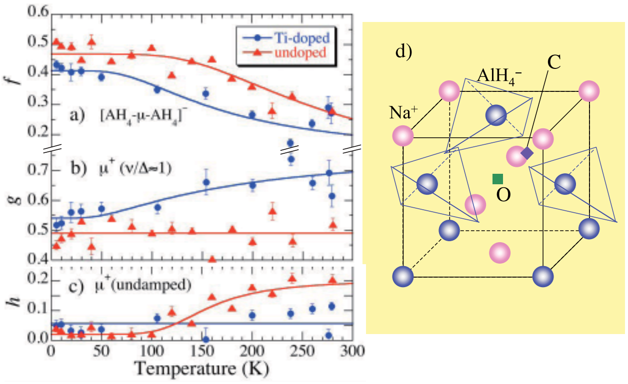

FIG. 3 (color online). Temperature dependence of the fractional yield for (a) muon-dialanate state (f), (b) muons at the O site (g), and (c) undamped state (h), where $f + g + h \equiv 1$. Solid curves represent the best fit to a simple activation model shown in the text. (d) Crystal structure of $NaAlH_4$ where half of the unit cell is displayed. Dark gray (blue) (Al) and light gray (pink) (Na) atoms occupy the vertices of a fcc lattice, and tetrahedra represent the alanate ions (AlH_4^-) in which the corners are occupied by H (those at the bottom are not shown for clarity). Possible muon (and H) sites are marked by the diamond (labeled C, forming a collinear AlH_4^--μ^+-AlH_4^- hydrogen bond) and by the square (labeled O, an octahedral interstitial site).

dynamics irrespective of the local atomic configuration around the muon.

We also note that a small fraction of muons ($1 - f_d \simeq 0.2$–0.3) loses its initial polarization immediately upon implantation. The polarization is recovered by applying a magnetic field parallel to the initial muon polarization, where the characteristic field for recovery suggests that the loss is caused by the muonium formation with a hyperfine coupling of ~420 MHz. Unfortunately, we were not able to observe the muonium state directly by μSR measurement under a transverse field. This is currently attributed to the loss of phase coherence during the muonium formation (epithermal) process, as it is suggested by the absence of temperature dependence in f_d.

Finally, we discuss the implications of our study of implanted muons. It is most likely that the local atomic structure of the muon is common to that of interstitial H atoms in $NaAlH_4$. This is analogous to the conclusion of the previous studies of alkali fluorides. Thus, our result provides direct evidence for the interaction of interstitial hydrogen with a hydrogen atom of two AlH_4^- anions—a new example of hydrogen bonding. This bonding interaction has been found for both undoped and Ti-doped $NaAlH_4$. The character of the resulting species could lie anywhere on the continuum between AlH_4^--H^+-AlH_4^- and AlH_3^--H_3^--AlH_3. Relatively large binding energy involved in hydrogen bonding suggests that it is the primary bottleneck for hydrogen kinetics in $NaAlH_4$, which might be common to other complex hydrides currently considered as hydrogen storage materials.

Provided that the free energy of interstitial muons is different between C and O sites, the nonzero populations of implanted muons at both sites below ~10^2 K strongly suggest that they are determined by statistical filling of those states that are separated by a kinetic barrier (E_a). (Otherwise, most of the implanted muons must be found at a site having the lowest free energy.) Therefore, our observations suggest that Ti doping serves to reduce the kinetic barrier for the transition from C site to O site. This naturally leads to the hypothesis that H^+-dialanate state is the bottleneck for the hydrogen kinetics which is improved by reducing the barrier for the transition of hydrogen to the mobile O site. It is likely that the hydrogen dialanate leads to generation of the off-stoichiometric units observed by the recent anelastic spectroscopy study [6].

The reduction of E_a is associated with a change in the final state from "undamped" to that of the O-site muon. This might imply that long-range diffusion of the μ^+ (and H^+) over the O sites is important for the efficient generation of Na_3AlH_6. The undamped state observed in the undoped sample might not contribute to such long-range diffusion. Then, the fast spin dynamics in the undamped state may be attributed to that of locally confined motion.

It must be stressed that the information derived from implanted muons corresponds to that in the dilute limit of the interstitial hydrogen. Therefore, the present result should be understood in the context of dehydrogenation of $NaAlH_4$ at its early stage. Further μSR studies of $NaAlH_4$ at different stages of dehydrogenation over a wider temperature range would be useful to clarify the complete picture of the hydrogen process in $NaAlH_4$.

We would like to thank the staff of TRIUMF and PSI for their technical support during the μSR experiment. This work was partially supported by KEK-MSL Inter-University Program for Overseas Muon Facilities and a Grant-in-Aid for Creative Scientific Research and from the Ministry of Education, Culture, Sports, Science and Technology of Japan. The support by the Office of Hydrogen, Fuel Cells and Infrastructure Technologies of the U.S. Department of Energy is also acknowledged.

[1] B. Bogdanovic and M. Schwickardi, J. Alloys Compd. **253**, 1 (1997).
[2] T. Ichikawa, S. Isobe, N. Handada, and H. Fujii, J. Alloys Compd. **365**, 271 (2004).
[3] C. M. Jensen, D. Sun, B. Lewandowski, K. K. Kumashiro, W. P. Niemczura, D. Morales-Morales, and Z. Wang, in Proceedings of the 2001 U.S. DOE Hydrogen Program Review, Baltimore, MD, 2001 (unpublished).
[4] S. Gomes, G. Renaudin, H. Hagemann, K. Yvon, M. P. Sulic, and C. M. Jensen, J. Alloys Compd. **390**, 305 (2005).
[5] O. Palumbo, R. Cantelli, A. Paolone, S. S. Srinivasan, and C. M. Jensen, J. Phys. Chem. B **109**, 1168 (2005).
[6] O. Palumbo, A. Paolone, R. Cantelli, C. M. Jensen, and M. Sulic, J. Phys. Chem. B **110**, 9105 (2006).
[7] R. A. Zidan, S. Takara, A. G. Hee, and C. M. Jensen, J. Alloys Compd. **285**, 119 (1999); C. M. Jensen and R. A. Zidan, U.S. Patent No. 6,471,935 (2002).
[8] C. Weidenthaler, A. Pommerin, M. Felderhoff, B. Bogdanovic, and F. Schüth, Phys. Chem. Chem. Phys. **5**, 5149 (2003).
[9] J. H. Brewer, S. R. Kreitzman, D. R. Noakes, E. J. Ansaldo, D. R. Harshman, and R. Keitel, Phys. Rev. B **33**, 7813 (1986).
[10] G. A. Jeffery, *An Introduction to Hydrogen Bonding* (Oxford University Press, New York, 1997).
[11] R. S. Hayano, Y. J. Uemura, J. Imazato, N. Nishida, T. Yamazaki, and R. Kubo, Phys. Rev. B **20**, 850 (1979).
[12] K. Nishiyama, S. W. Nishiyama, and W. Higemoto, Physica (Amsterdam) **326B**, 41 (2003).
[13] See, for example, Yu. Fukai, *The Metal-Hydrogen System* (Springer, Berlin, 1993).

Multigap Superconductivity in Sesquicarbides La_2C_3 and Y_2C_3

S. Kuroiwa,[1] Y. Saura,[1] J. Akimitsu,[1] M. Hiraishi,[2] M. Miyazaki,[2] K. H. Satoh,[2] S. Takeshita,[3] and R. Kadono[2,3]

[1]*Department of Physics and Mathematics, Aoyama Gakuin University, Sagamihara, Kanagawa 229-8558, Japan*
[2]*Department of Materials Structure Science, The Graduate University for Advanced Studies, Tsukuba, Ibaraki 305-0801, Japan*
[3]*Institute of Materials Structure Science, High Energy Accelerator Research Organization, Tsukuba, Ibaraki 305-0801, Japan*

(Received 26 September 2007; published 6 March 2008)

A complex structure of the superconducting order parameter in Ln_2C_3 (Ln = La, Y) is demonstrated by muon spin relaxation measurements in their mixed state. The muon depolarization rate $[\sigma_v(T)]$ exhibits a characteristic temperature dependence that can be perfectly described by a phenomenological double-gap model for nodeless superconductivity. While the magnitude of two gaps is similar between La_2C_3 and Y_2C_3, a significant difference in the interband coupling between those two cases is clearly observed in the behavior of $\sigma_v(T)$.

DOI: 10.1103/PhysRevLett.100.097002 PACS numbers: 74.70.Ad, 74.25.Jb, 76.75.+i

The revelation of high-temperature superconductivity in magnesium diboride (MgB_2, with a critical temperature $T_c \simeq 39$ K) has stimulated renewed interest in other boride and carbide superconductors as an alternative path to novel superconductors with an even higher T_c [1]. Sesquicarbides (Ln_2C_3, Ln = La, Y) are among such compounds reported in the early literature; they exhibit superconductivity at relatively high critical temperatures ($T_c \simeq 6$–11 K) and their T_c's strongly depend on their carbon composition [2–4]. Recently, we have found a new superconducting phase in Y_2C_3 that exhibits a much higher T_c (~18 K) comparable with A-15 compounds [5]. This discovery has attracted further attention to the relationship between structural details and superconductivity in sesquicarbide systems. However, despite various attempts [6–9], little is known so far about the details of superconducting order parameters in La_2C_3 and Y_2C_3 from a microscopic viewpoint.

A recent study on the temperature dependence of the nuclear spin-lattice relaxation rate in Y_2C_3 has suggested the occurrence of a multiple superconducting gap with s-wave symmetry in a sample having $T_c = 15.7$ K [10]. While a similar electronic structure would be expected for La_2C_3 [9], a report on the specific heat measurement suggests single-gap superconductivity in a specimen with $T_c \approx 13.4$ K [11]. In any case, the real nature of superconductivity in Y_2C_3 and La_2C_3, including a potential difference between the two systems, still remains largely unclear.

The muon spin rotation (μSR) technique is a useful microscopic tool for probing the quasiparticle (QP) density of states available for the thermal- or field-induced excitation in the mixed state of type II superconductors [12,13]. The muon depolarization rate in the mixed state is predominantly determined by the magnetic penetration depth (λ) that is controlled by the superfluid density. Since the latter is reduced by the QP excitation, the effective value of λ serves as a monitor of the QP excitation. In this Letter, we present the result of μSR measurements on polycrystalline samples of La_2C_3 ($T_c \sim 11$ K) and Y_2C_3 ($T_c \sim 15$ K), where a clear sign of double-gap superconductivity is observed in the temperature dependence of the muon depolarization rate. They also provide the first clear case for the double-gap model, where the magnitude of coupling between electronic bands responsible for superconductivity is explicitly examined. Our result establishes a coherent description of multiple band or gap superconductivity in this sesquicarbide system.

For the Ln_2C_3 samples, starting materials were prepared by the arc melting method using a mixture of La/Y (99.9%) and C (graphite, 99.99%) with stoichiometric composition of sesquicarbide. The obtained Y-C alloys were placed into a BN cell in a dry box under an argon gas atmosphere, and polycrystalline Y_2C_3 was synthesized by elevating temperature to 1300–1400 °C for 30 min under a high pressure of 5 GPa using cubic-anvil-type equipment. For the polycrystalline La_2C_3, the La-C alloys obtained by the arc melting were pressed into pellets in a sealed Ta tube, and sintered at 1000 °C for 200 h under a high vacuum condition of 3.0×10^{-5} Torr, followed by a slow cooling process to ambient temperature at a rate of 5 °C/h.

The powder x-ray diffraction patterns for both specimens could be indexed as a sesquicarbide phase with the space group of $I\bar{4}3d$. In La_2C_3, nearly 10% of LaC_2 was observed as a minor phase besides that of the sesquicarbide, while Y_2C_3 was found to be in a single phase. LaC_2 behaves as a normal metal above 2 K and only causes a background in the μSR signal in the superconducting phase. The lattice constants of La_2C_3 and Y_2C_3 were determined to be approximately $a = 8.808(5)$ Å and 8.238(5) Å, respectively, which are in good agreement with those reported previously [11,14–16]. Unfortunately, the precise stoichiometry of carbon has not been determined. Therefore, the chemical composition in this Letter refers only to a nominal value. Heat capacity and ac and dc magnetic susceptibilities were measured using MPMSR2 and PPMS (Quantum Design Co., Ltd.).

Figure 1 shows the temperature dependence of dc susceptibility under zero-field cooling in La_2C_3 and Y_2C_3. In

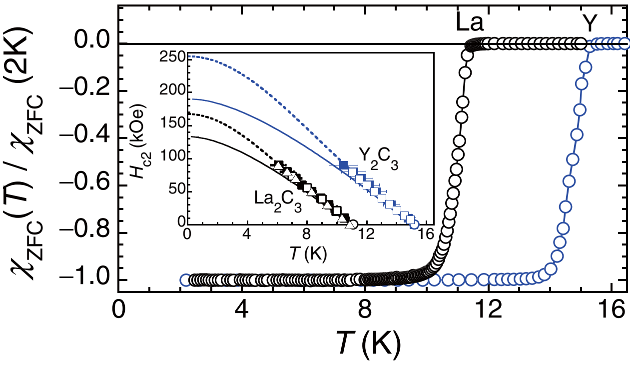

FIG. 1 (color online). Temperature dependence of dc magnetic susceptibility at 10 Oe in La_2C_3 and Y_2C_3 normalized by the value at 2 K. Inset shows magnetic field (H) vs temperature (T) phase diagram. The triangle, circle, and square symbols indicate data determined by heat capacity and dc and ac magnetic susceptibility measurements, respectively. The open and closed symbols show data obtained from T and H scan, respectively. The solid and dashed curves correspond to the WHH relation and the GL model, respectively.

both cases, clear diamagnetic signals are observed below T_c ($\simeq$11.2 K and 15.2 K, respectively). As shown in the inset, $H_{c2}(T)$ exhibits almost linear dependence on temperature, which differs significantly from the Werthamer-Helfand-Hohenberg (WHH) relation [17]. The enhancement of $H_{c2}(T)$ from the WHH prediction is due to the strong electron-phonon coupling rather than the anisotropic Fermi surface or localization effect [11]. We can extract $H_{c2}(0)$ without much uncertainty using the Ginzburg-Landau (GL) theory, $H_{c2}(T) = H_{c2}(0)[1 - (T/T_c)^2]/[1 + (T/T_c)^2]$, where $H_{c2}(0) = \Phi_0/2\pi\xi_{\mathrm{GL}}^2$, Φ_0 is the flux quantum, and ξ_{GL} is the GL-coherence length [18]. The best fit using the above equation yields $H_{c2}(0) =$ 167(3) and 256(7) kOe for La_2C_3 and Y_2C_3, respectively.

A conventional μSR experiment was performed on the M15 beam line of TRIUMF, Canada. The polycrystalline samples were loaded on a sample holder (a scintillator serving as a muon veto counter, with a sample dimension of 7 × 7 mm^2) and placed into a He gas-flow cryostat, to which a 100% spin-polarized muon beam with a momentum of 29 MeV/c was irradiated to collect 1.5×10^7 decay positron events for each spectrum (taking about 1.5 h). Each measurement was performed under a field-cooling process to minimize the effect of flux pinning, and field fluctuation was kept within 10^{-4} of the applied field.

Since we can reasonably assume that muons stop randomly on the length scale of the flux-line lattice (FLL), the muon spin precession signal, $\hat{P}(t)$, provides the random sampling of the internal field distribution $B(\mathbf{r})$,

$$\hat{P}(t) = \int_{-\infty}^{\infty} n(B)\cos(\gamma_\mu B t + \phi)dB, \qquad (1)$$

$$n(B) = \langle \delta[B - B(\mathbf{r})]\rangle_{\mathbf{r}}, \qquad (2)$$

where γ_μ is the muon gyromagnetic ratio ($=2\pi \times$ 13.553 MHz/kOe), $n(B)$ is the spectral density for the internal field defined as a spatial average ($\langle\,\rangle_{\mathbf{r}}$) of the delta function, and ϕ is the initial phase of rotation. These equations indicate that the real amplitude of the Fourier transformed muon spin precession signal corresponds to $n(B)$ (except corrections for additional relaxation due to other origins; see below). In the case of a relatively large magnetic penetration depth ($\lambda \geq 3000$ Å), $n(B)$ can be well approximated by a simple Gaussian field profile, yielding $\hat{P}(t) \simeq \exp(-\sigma^2 t^2/2)\cos(\gamma_\mu \bar{B} t + \phi)$, where $\sigma = \gamma_\mu \sqrt{\langle [B - B(\mathbf{r})]^2\rangle} \propto \lambda^{-2}$ and $\bar{B} \simeq H$ is the mean field. Here, it must be stressed that λ is an *effective* magnetic penetration depth susceptible to the quasiparticle excitation.

Figure 2 shows the time-dependent muon-positron decay asymmetry at 2 K in La_2C_3 and Y_2C_3 with their fast Fourier transform (FFT) displayed in the inset. The FFT spectral linewidth in the normal state ($T > T_c$) is determined by the small random local fields from nuclear moments and a limited μSR time window ($\simeq$8 μs), while that in the superconducting state is further broadened by the formation of FLL and associated inhomogeneous local field distribution [$B(\mathbf{r})$]. The solid curves in the main panels are the best fits of the data in the time domain, assuming two components of the Gaussian damping,

$$A\hat{P}(t) = \sum_{i=1}^{2} A_i \exp\left(-\frac{\sigma_i^2 t^2}{2}\right)\cos(\gamma_\mu B_i t + \phi_i), \qquad (3)$$

where the ith component refers to the contribution from superconducting ($i = 1$) and normal ($i = 2$) phases, A_i is the partial asymmetry ($\sum_i A_i = A$), σ_i is the relaxation rate, and $\gamma_\mu B_i$ is the central frequency for the respective components. The model yields good fits to data, as indicated by the reasonably small values of reduced chi square: χ^2/N_f is mostly less than 1.7 for La_2C_3 and 1.3 for Y_2C_3, with N_f being the number of degrees of freedom. Considering that σ_2 represents the relaxation due to the nuclear magnetic

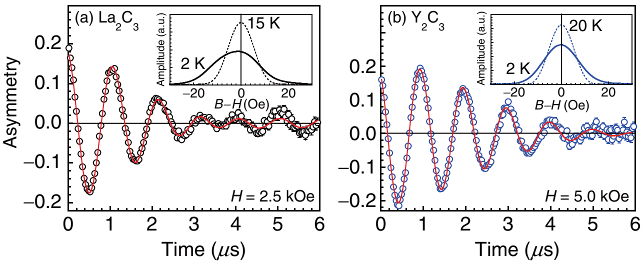

FIG. 2 (color online). Time revolution of muon-positron decay asymmetry in (a) La_2C_3 and (b) Y_2C_3 at 2 K under a transverse field of 2.5 kOe and 5.0 kOe, respectively, displayed in a rotating-reference-frame frequency of (a) 33 MHz and (b) 66.8 MHz. The respective insets show the fast Fourier transform at 2 K (solid lines) and above T_c (dashed lines).

moment (i.e., $\sigma_2 = \sigma_n$), the net relaxation rate in the superconducting state is expressed as $\sigma_1^2 = \sigma_n^2 + \sigma_v^2$, where the second term comes from $n(B)$ in the FLL state and it is proportional to the superfluid density [19]. From the fitting analysis, the superconducting volume fractions $[= A_1/(A_1 + A_2)]$ at 2 K are estimated to be ≈ 0.91 and 0.98 in La_2C_3 and Y_2C_3, respectively, where the former value is in good agreement with the fractional yield estimated by the x-ray analysis (with the rest corresponding to LaC_2 in the normal state).

Figure 3 shows the temperature dependence of σ_v for La_2C_3 at 2.5 kOe and Y_2C_3 at 5.0 kOe, where the fields are chosen to be reasonably away from the lower critical field (the field dependence at the relevant field range is shown for La_2C_3). It is interesting to note that the data of La_2C_3 exhibit a shoulderlike structure near 4 K, indicating clear deviation from the behavior predicted for single-gap BCS superconductors. The effect of flux pinning as a possible origin of such a structure is ruled out by the fact that σ_1 at 2 K is almost independent of the applied field below 30 kOe [see the inset of Fig. 3(a)]. According to the theories that consider multiband superconductivity [20–22], such an inflection is expected to occur in the systems consisting of two superconducting bands that are weakly coupled. The behavior of σ_v below ~4 K is then attributed to the band with a smaller gap energy. To our knowledge, this is the first unambiguous example of double-gap superconductivity with extremely week interband coupling.

Compared with La_2C_3, no strong anomaly is observed in the case of Y_2C_3. However, while the superfluid density (and hence σ_v) is predicted to be virtually independent of temperature for $T/T_c \leq 0.4$ in the single-gap BCS model, a clear variation of σ_v with temperature is observed below 6 K. This is another sign that the order parameter of Y_2C_3 has an anisotropic structure. Considering the present result in La_2C_3 and previous NMR studies [10], we can attribute the T dependence of σ_v also to the double-gap superconductivity. This is further supported by a recent first-principles calculation [23], where it is suggested that the Fermi surface of Y_2C_3 consists of three hole bands (0.12, 0.15, and 0.88/eV unit cell spin) and one electron band (2.73/eV unit cell spin) that arise mainly from the hybridized orbitals of Y d and C-C antibonding π^* states. Such large differences in the density of states and Fermi velocities between hole and electron bands might lead to the opening of two superconducting gaps in the different parts of the Fermi surface.

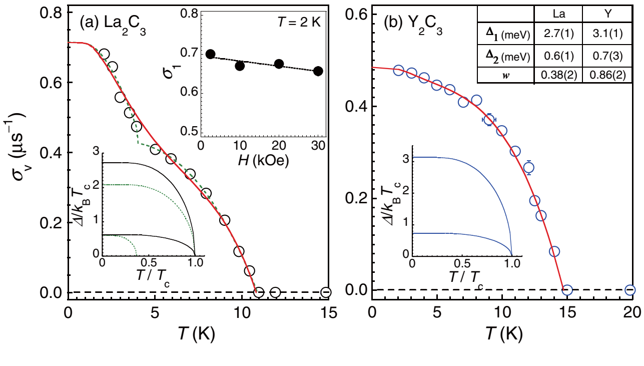

FIG. 3 (color online). Temperature dependence of the muon spin relaxation rate for (a) La_2C_3 at 2.5 kOe and (b) Y_2C_3 at 5.0 kOe. Error bars (not shown) are smaller than the symbol size. Solid and dashed curves indicate the result of the fitting analysis using the double-gap model described in the text. Insets show the relaxation rate in the superconducting state (σ_1) as a function of the magnetic field for La_2C_3 (a) and the order parameters $[\Delta(T)/k_BT_c]$ for the respective cases.

The origin of difference in the temperature dependence of σ_v between La_2C_3 and Y_2C_3 is understood by considering the difference in the interband coupling strength between these two compounds. For quantitative discussion, the data in Fig. 3 are analyzed using a phenomenological double-gap model with s-wave symmetry [24,25],

$$\sigma(T) = \sigma(0) - w\delta\sigma(\Delta_1, T) - (1 - w)\delta\sigma(\Delta_2, T),$$

$$\delta\sigma(\Delta, T) = \frac{2\sigma(0)}{k_BT}\int_0^\infty f(\epsilon, T)[1 - f(\epsilon, T)]d\epsilon,$$

$$f(\epsilon, T) = (1 + e^{\sqrt{\epsilon^2 + \Delta(T)^2}/k_BT})^{-1},$$

where Δ_i ($i = 1$ and 2) is the energy gap at $T = 0$, w is the relative weight for $i = 1$, k_B is the Boltzmann constant, $f(\epsilon, T)$ is the Fermi distribution function, and $\Delta(T)$ is the standard BCS gap energy. The solid curves in Fig. 3 are the best fit results obtained by using the above double-gap model with the parameters listed in Table I. For La_2C_3, a simplified model (dashed curve) assuming two independent superconducting bands was also tested against the data, which turned out to exhibit a slightly better agreement than that described by using the above model [yielding $2\Delta_1/k_BT_c = 4.5(3)$ and $2\Delta_2/k_BT_c = 1.3(3)$]. This might suggest that the above model may not necessarily be a good approximation for the case of weak interband coupling.

TABLE I. Superconducting properties of La_2C_3 and Y_2C_3 determined from the present experiment, where those obtained from the double-gap analysis correspond to the solid curves in Fig. 3.

	La_2C_3	Y_2C_3
Transverse field (kOe)	2.5	5.0
T_c (K)	10.9(1)	14.7(2)
$\sigma_v(0)$ (μs^{-1})	0.71(3)	0.48(2)
$\lambda(0)$ (Å)	3800(100)	4600(100)
w	0.38(2)	0.86(2)
$\Delta_1(0)$ (meV)	2.7(1)	3.1(1)
$\Delta_2(0)$ (meV)	0.6(1)	0.7(3)
$2\Delta_1/k_BT_c$	5.6(3)	4.9(3)
$2\Delta_2/k_BT_c$	1.3(3)	1.1(5)

The superconducting parameters deduced from the present experiment are summarized in Table I. Here, we calculated the magnetic penetration depth $\lambda(0)$ using the formula $\sigma_v(0)[\mu s^{-1}] = 4.83 \times 10^4(1 - H/H_{c2}) \times [1 + 3.9(1 - H/H_{c2})^2]^{1/2}/\lambda^2(0)$ [nm] [19,26]. The gap parameter $2\Delta/k_BT_c$ of Y_2C_3 is in reasonable agreement with that deduced by NMR (i.e., $2\Delta/k_BT_c = 5$ and 2) [10], again supporting the present double-gap scenario. We also find that $2\Delta/k_BT_c$ for the two respective bands of La_2C_3 are comparable with those of Y_2C_3. Thus, it appears that the superconductivity of La_2C_3 and Y_2C_3 share the common features of strong electron-phonon coupling and s-wave symmetry, which is in line with the previous heat capacity results [11].

Provided that there is a significant difference in the interband coupling between La_2C_3 and Y_2C_3, the observed difference in the relative weight (w) between two gaps might also be connected with the interband coupling. Furthermore, considering that the double-gap features tend to be suppressed by the localization (scattering) effect, one might suspect that such a difference in w may arise from that in the quality of the specimen. In this regard, we have to note that the Y_2C_3 samples were obtained only in a polycrystalline form using high pressure synthesis and that their short annealing time might have resulted in a quality less than that of La_2C_3. At this stage, we presume it unlikely that the present result has been strongly affected by the localization effect, considering that the electronic mean free path measured using the microwave cavity perturbation technique is much longer than ξ_{GL} for the sample prepared under the same condition [27]. However, it would be certainly helpful to study the influence of sample quality (and chemical stoichiometry as well) in the future to elucidate the details of the localization effect on the double-gap behavior.

Finally, let us point out the noncentrosymmetric effect in superconductivity. In the case of a sesquicarbides system with the $I\bar{4}3d$ group symmetry, an asymmetric spin-orbit interaction can be approximated by the Dresselhaus-type interaction. When the order of magnitude of a superconducting gap is comparable to that of the spin-orbit band splitting, the original isotropic gap structure is modulated by a magnetic field to have a point node, because the anisotropic Pauli depairing effect can occur in the specific part of the momentum space [28]. This may lead to an unusual field-induced quasiparticle excitation, and a detailed μSR study on the field dependence of magnetic penetration depth is currently in progress to examine the proposed scenario.

In summary, we performed a μSR experiment on Ln_2C_3 (Ln = La, Y) to clarify the structure of a superconducting order parameter through the temperature dependence of quasiparticle excitation reflected in the muon depolarization rate, $\sigma_v(T)$ in the mixed state. We showed that $\sigma_v(T)$ exhibits a characteristic of double gap in the superconducting order parameter, with a marked variation in the temperature dependence between La and Y compounds that is attributed to the difference in the interband coupling. The gap parameters for two respective bands were deduced using the phenomenological double-gap model and were found to be comparable between La and Y compounds, which is consistent with the occurrence of a strong-coupling superconductivity with s-wave symmetry in both the systems.

We thank the TRIUMF staff for technical support during the μSR experiment. The experiment was partially supported by the KEK-MSL Inter-University Program for Oversea Muon Facilities and the Grant-in-Aid for Scientific Research on Priority Area from the Ministry of Education, Culture, Sports, Science and Technology of Japan. One of the authors (S. K.) acknowledges the support of the JSPS.

[1] J. Nagamatsu *et al.*, Nature (London) **410**, 63 (2001).
[2] A. L. Giorgi, High Temp. Sci. **19**, 127 (1985).
[3] M. C. Krupka *et al.*, J. Less-Common Met. **19**, 113 (1969).
[4] A. Simon and Th. Gulden, Z. Anorg. Allg. Chem. **630**, 2191 (2004).
[5] G. Amano *et al.*, J. Phys. Soc. Jpn. **73**, 530 (2004).
[6] T. L. Francavilla and F. L. Carter, Phys. Rev. B **14**, 128 (1976).
[7] B. Cort *et al.*, J. Low Temp. Phys. **54**, 149 (1984).
[8] T. Nakane *et al.*, Appl. Phys. Lett. **84**, 2859 (2004).
[9] J. S. Kim *et al.*, Current Appl. Phys. **6**, 897 (2006).
[10] A. Harada *et al.*, J. Phys. Soc. Jpn. **76**, 023704 (2007).
[11] J. S. Kim *et al.*, Phys. Rev. B **76**, 014516 (2007).
[12] J. E. Sonier *et al.*, Rev. Mod. Phys. **72**, 769 (2000).
[13] R. Kadono *et al.*, Phys. Rev. B **76**, 094501 (2007).
[14] V. I. Novokshonov, Russ. J. Inorg. Chem. **25**, 375 (1980).
[15] T. Mochiku *et al.*, Physica (Amsterdam) **426C**, 421 (2005).
[16] X. Wang *et al.*, Phys. Rev. B **72**, 064520 (2005).
[17] N. R. Werthamer *et al.*, Phys. Rev. **147**, 288 (1966).
[18] M. Tinkham, *Introduction to Superconductivity* (McGraw-Hill, New York, 1996), 2nd ed.
[19] E. H. Brandt, Phys. Rev. B **37**, 2349 (1988).
[20] H. Suhl *et al.*, Phys. Rev. Lett. **3**, 552 (1959).
[21] T. Xiang and J. M. Wheatley, Phys. Rev. Lett. **76**, 134 (1996).
[22] A. A. Golubov *et al.*, Phys. Rev. B **66**, 054524 (2002).
[23] Y. Nishikayama *et al.*, J. Phys. Soc. Jpn. **76**, 064714 (2007).
[24] F. Bouquet *et al.*, Europhys. Lett. **56**, 856 (2001).
[25] K. Ohishi *et al.*, J. Phys. Soc. Jpn. **72**, 29 (2003).
[26] G. Aeppli *et al.*, Phys. Rev. B **35**, 7129 (1987).
[27] S. Akutagawa *et al.*, Physica (Amsterdam) **460–462C**, 649 (2007).
[28] S. Fujimoto, Phys. Rev. B **76**, 184504 (2007).

Journal of the Physical Society of Japan
Vol. 77, No. 10, October, 2008, 103703

LETTERS

Coexistence of Supercondcutivity and Magnetism in LaFeAs($O_{0.94}F_{0.06}$) Probed by Muon Spin Relaxation

Soshi TAKESHITA[1]*, Ryosuke KADONO[1,2], Masatoshi HIRAISHI[2], Masanori MIYAZAKI[2],
Akihiro KODA[1,2], Yoichi KAMIHARA[3], and Hideo HOSONO[3,4,5]

[1]*Institute of Materials Structure Science, High Energy Accelerator Research Organization (KEK),*
1-1 Oho, Tsukuba, Ibaraki 305-0801
[2]*Department of Materials Structure Science, School of High Energy Accelerator Science,*
The Graduate University for Advanced Studies, 1-1 Oho, Tsukuba, Ibaraki 305-0801
[3]*ERATO-SORST, JST, in Frontier Research Center, Tokyo Institute of Technology,*
4259 Nagatsuta, Midori-ku, Yokohama 226-8503
[4]*Frontier Research Center, Tokyo Institute of Technology, 4259 Nagatsuta, Midori-ku, Yokohama 226-8503*
[5]*Materials and Structures Laboratory, Tokyo Institute of Technology, 4259 Nagatsuta, Midori-ku, Yokohama 226-8503*

(Received July 8, 2008; accepted August 7, 2008; published September 25, 2008)

The presence of macroscopic phase separation into superconducting and spin-glass-like magnetic phases in LaFeAs($O_{1-x}F_x$) is demonstrated by muon spin rotation measurement in a sample near the phase boundary ($x = 0.06$). Both magnetism and superconductivity develop simultaneously below a common critical temperature, $T_m \simeq T_c \simeq 18$ K. This remarkable accordance strongly suggests that the electronic correlations leading to these two competing ground states share a common origin.

KEYWORDS: oxypnictide superconductor, muon spin rotation, electronic correlation, magnetism
DOI: 10.1143/JPSJ.77.103703

The recent discovery of the oxypnictide superconductor $LaFeAsO_{1-x}F_x$ (LFAO-F) with a critical temperature (T_c) of 26 K[1)] and the successful revelation of much increased T_c upon the substitution of La for other rare-earth elements (such as Sm, leading to ~43 K[2)]) and the application of pressure for LFAO-F (~43 K[3)]) have triggered broad interest in the mechanism yielding a relatively high T_c in this new class of compounds. They have a layered structure like high-T_c cuprates, where the dopant and conducting layers are so separated that the doped carriers (electrons introduced by the substitution of O^{2-} with F^- in the La_2O_2 layers) move within the layers consisting of strongly bonded Fe and As atoms. They exhibit another qualitative similarity to cuprates in that superconductivity occurs upon carrier doping of pristine compounds that exhibit magnetism.[4)] Some preliminary results of the muon spin rotation/relaxation (μSR) experiment on a variety of oxypnictide superconductors showed that the superfluid density n_s falls on the empirical line on the n_s vs T_c diagram observed for the *underdoped* cuprates,[5,6)] from which possibility of the common mechanism of superconductivity is argued between oxypnictides and cuprates.

However, in terms of the doping phase diagram, there are certain differences between these two systems, e.g., (i) T_c (> 0 for $0.4 < x < 0.12$) does not vary much with x[1)] as in cuprates known as "bell-shaped" and (ii) the magnetic (spin density wave, SDW) phase shares a boundary with the superconducting phase near $x \simeq 0.04$.[1,7)] The insensitivity of T_c to x is reasonably understood from the conventional BCS theory where condensation energy is predicted to be independent of carrier concentration. The close relationship of magnetism and superconductivity suggests that a detailed investigation of how these two phases coexist (and compete) near the phase boundary will provide important clues to elucidating the paring mechanism. Among various techniques, μSR has a great advantage in that it can be applied in systems consisting of spatially inhomogeneous multiple phases, providing information on respective phases according to their fractional yield. Our μSR measurement in the LFAO-F sample with $x = 0.06$ ($T_c \simeq 18$ K) reveals that these two phases indeed coexist in the form of macroscopic phase separation, and more interestingly, that a spin glass-like magnetic phase develops in conjunction with superconductivity in the paramagnetic phase. This accordance strongly suggests a common origin of the electronic correlation leading to these two competing phases.

Although the oxypnictide with rare-earth (R) substitution RFeAs$O_{1-x}F_x$ exhibits higher T_c than that of LFAO-F, strong random fields from rare-earth ions preclude a detailed study of the ground state using sensitive magnetic probes like μSR. Therefore, we chose the original LFAO-F system for our μSR study. The target concentration of $LaFeAsO_{1-x}F_x$ is set near the phase boundary, $x = 0.06$, for which a polycrystalline sample was synthesized by solid state reaction. The detailed procedure for sample preparation is described in an earlier report.[1)] The sample was confirmed to be mostly of single phase using X-ray diffraction analysis. Of two possible impurity phases, namely, LaOF and FeAs, only the latter exhibits a magnetic (helical) order with $T_N \simeq 77$ K.[8)] As shown in Fig. 1, magnetic susceptibility exhibits no trace of FeAs phase or local magnetic impurities except below ~ 50 K where a small upturn is observed. The susceptibility at a lower field [shown in Fig. 3(a)] provides evidence of bulk superconductivity with $T_c \sim 18$ K from the onset of diamagnetism. Conventional μSR measurement was performed using the LAMPF spectrometer installed on the M15 beamline of TRIUMF, Canada. During the measurement under a zero field (ZF), residual magnetic field at the sample position was reduced below 10^{-6} T with the initial muon spin direction parallel to the muon beam direction [$\boldsymbol{P}_\mu(0) \parallel \hat{z}$]. For longitudinal field (LF) measurement, a magnetic field was applied parallel to $\boldsymbol{P}_\mu(0)$. Time-

---

*E-mail: soshi@post.kek.jp

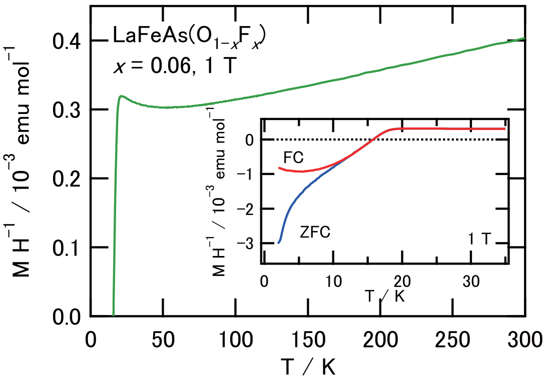

Fig. 1. (Color online) Magnetic susceptibility of LaFeAsO$_{1-x}$F$_x$ with $x = 0.06$ for the sample used for μSR measurement. Inset shows a reduced view of the region below 35 K.

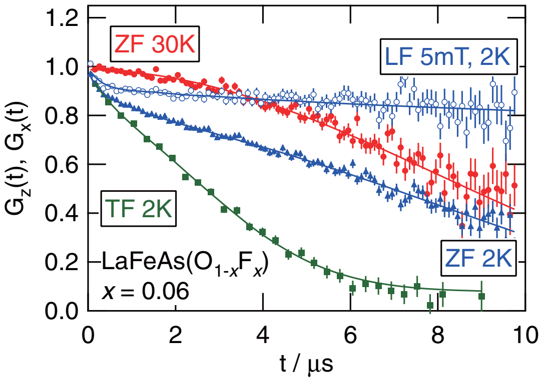

Fig. 2. (Color online) μSR time spectra observed in LaFeAs(O$_{1-x}$F$_x$) with $x = 0.06$ at 2 K under a longitudinal field (LF), a zero field (ZF), and a transverse field (TF), and that under ZF at 30 K. The spectrum under TF is plotted on a rotating reference frame of 6.78 MHz to extract the envelop function.

dependent muon polarization [$G_z(t) = \hat{z} \cdot \boldsymbol{P}_\mu(t)$] was monitored by measuring decay-positron asymmetry along the $\hat{z}$-axis. Transverse field (TF) condition was realized by rotating the initial muon polarization so that $\boldsymbol{P}_\mu(0) \parallel \hat{x}$, where the asymmetry was monitored along the $\hat{x}$-axis to obtain $G_x(t) = \hat{x} \cdot \boldsymbol{P}_\mu(t)$. All the measurements under a magnetic field were made by cooling the sample to the target temperature after the field equilibrated.

ZF-μSR is the most sensitive technique for examining magnetism in any form, where the development of local magnetic moments leads to either the spontaneous oscillation (for long-range order) or exponential damping (inhomogeneous local magnetism) of $G_z(t)$. Figure 2 shows examples of ZF-μSR time spectra collected at 2 and 30 K. The spectrum at 30 K ($>T_c$) exhibits a Gaussian-like relaxation due to weak random local fields from nuclear magnetic moments, indicating that the entire sample is in the paramagnetic state. Meanwhile, the spectrum at 2 K is split into two components, one that exhibits a steep relaxation and the other that remains to show Gaussian-like relaxation. This indicates that there is a finite fraction of implanted muons that sense hyperfine fields from local electronic moments. The absence of oscillatory signal implies that the hyperfine field is highly inhomogeneous, so that the local magnetism is characterized by strong randomness or spin fluctuation. The fractional yield of the component showing steep relaxation is as large as 25% (see below), which is hardly attributed to impurity and therefore implies that the sample exhibits a macroscopic phase separation into two phases.

The magnitude of the hyperfine field and that of spin fluctuation are evaluated by observing the response of the μSR spectrum to a LF. It is shown in Fig. 2 that the relaxation in the paramagnetic component is quenched by applying a weak magnetic field (LF = 5 mT), which is perfectly explained by the suppression of static nuclear dipolar fields ($< 10^0$ mT). Meanwhile, the faster relaxation (seen for $0 < t < 1\,\mu$s) due to the magnetic phase is recovered only gradually over a field range of 10^1–10^2 mT, and there still remains a slow relaxation even at the highest field of 60 mT. This residual depolarization under LF is a clear sign that local spins are slowly fluctuating, leading to the spin-lattice relaxation of $\boldsymbol{P}_\mu(t)$. Such quasi-two-step relaxation is also observed in dilute spin-glass systems,9) which is understood as a distribution of spin correlation time. A detailed analysis is made considering that these two components coming from the magnetic phase (see below).

Under a transverse field, implanted muons experience an inhomogeneity of the field [$B_z(\mathbf{r})$] due to flux line lattice formation below T_c that leads to relaxation, in addition to those observed under a zero field. The TF-μSR time spectrum in Fig. 2 (envelop part of the oscillation) obtained under a field of 50 mT exhibits complete depolarization at 2 K, indicating that the entire volume of the paramagnetic phase falls into the superconducting state. The rapidly relaxing component observed under ZF is also visible (although the coarse binning of the spectra for extracting the envelop part makes it slightly obscure), indicating that the corresponding part of the sample remains magnetic.

Considering the presence of the magnetic phase besides the paramagnetic (=superconducting below T_c) phase, we take special precaution to analyze both TF and ZF/LF μSR spectra in a consistent manner. For the determination of physical parameters describing the behavior of signals from the magnetic phase, we first analyze ZF/LF spectra at 2 K using the χ-square minimization fit with the relaxation function

$$G_z(t) = \left[w_1 + \sum_{i=2}^{3} w_i \exp(-\Lambda_i t) \right] \cdot G_{\mathrm{KT}}(\delta_{\mathrm{N}} : t), \qquad (1)$$

where $G_{\mathrm{KT}}(\delta_{\mathrm{N}} : t)$ is the Kubo–Toyabe relaxation function for describing the Gaussian damping due to random local fields from nuclear moments (with δ_{N} being the linewidth),10) w_1 is the fractional yield for the paramagnetic phase, w_2 and w_3 are those for the magnetic phase ($\sum w_i = 1$) with Λ_2 and Λ_3 being the corresponding relaxation rate described by the Redfield relation

$$\Lambda_i = \frac{2\delta_i^2 \nu_i}{\nu_i^2 + \omega_\mu^2} \qquad (i = 2, 3), \qquad (2)$$

where $\omega_\mu = \gamma_\mu H_{\mathrm{LF}}$, γ_μ is the muon gyromagnetic ratio ($= 2\pi \times 135.53$ MHz/T), H_{LF} is the longitudinal field, δ_2 and δ_3 are the means of the hyperfine fields exerting on muons from local electronic moments, and ν_2 and ν_3 are the fluctuation rates of the hyperfine field. The solid curves in

Fig. 2 show the result of analysis where all the spectra at different fields (only ZF and LF = 5 mT are shown here) are fitted simultaneously using eqs. (1) and (2) with common parameter values (except ω_μ that is fixed to the respective value for each spectrum), which show excellent agreement with all the spectra. The deduced parameters are as follows: $w_1 = 0.754(9)$, $w_2 = 0.165(9)$, $w_3 = 0.081(4)$, $\delta_2 = 0.71(5)\,\mu s^{-1}$, $\delta_3 = 3.9(3)\,\mu s^{-1}$, $\nu_2 = 1.7(2)\,\mu s^{-1}$, and $\nu_3 = 4(1)\,\mu s^{-1}$. Although the depolarization in the magnetic phase is approximately represented by two components with different hyperfine couplings (δ_i), the fluctuation rates (ν_i) are close to each other ($10^7\,s^{-1}$ at 2 K), suggesting that the randomness is primarily due to the distribution in the size of local moments (or in their distances to muons). Since no impurity phase with a fraction as large as 25% is detected by X-ray diffraction analysis, it is concluded that this magnetic phase is intrinsic.

In the analysis of temperature-dependent TF spectra, we used the relaxation function

$$G_x(t) = \exp\left(-\frac{1}{2}\delta_N^2 t^2\right)[w_1 \exp(-\delta_s^2 t^2)\cos(2\pi f_s t + \phi) + (w_2 + w_3)\exp(-\Lambda_m t)\cos(2\pi f_m t + \phi)], \quad (3)$$

where w_i and δ_N are fixed to the values obtained by analyzing ZF/LF-μSR spectra. The first component in the above equation represents the contribution of flux line lattice formation in the superconducting phase, where δ_s corresponds to the linewidth $\sigma_s = \sqrt{2}\delta_s = \gamma_\mu\langle(B(\mathbf{r}) - B_0)^2\rangle^{1/2}$ [with B_0 being the mean $B(\mathbf{r})$], while the second term represents the relaxation in the magnetic phase. Here, the relaxation rate for the latter is represented by a single value Λ_m (instead of $\Lambda_{2,3}$), as it turns out that the two components observed under LF are hardly discernible in TF-μSR spectra. [This does not affect the result of the analysis, because the amplitude is fixed to $w_2 + w_3$ so that Λ_m may represent a mean $\simeq (w_2\Lambda_2 + w_3\Lambda_3)/(w_2 + w_3)$.] The fit analysis using the above form indicates that all the spectra are perfectly reproduced while the partial asymmetry is fixed to the value determined from ZF-μSR spectra. This strengthens the presumption that the paramagnetic phase becomes superconducting below T_c. The result of analysis is summarized in Fig. 3, together with the result of dc magnetization measured in the sample from the same batch as that used for μSR.

It is interesting to note in Fig. 3(b) that, although the central frequency in the superconducting phase (f_s) does not show much change below $T_c \simeq 18$ K probably owing to a large magnetic penetration depth (it is indeed large, see below), that in the magnetic phase (f_m) exhibits a clear shift in the negative direction below $T_m \simeq T_c$. The magnitude of the shift is as large as $\sim 1\%$ and thus is readily identified despite a relatively low external field of 50 mT. As shown in Fig. 3(c), the relaxation rate in the magnetic phase (Λ_m) also develops below T_c in accordance with the frequency shift, demonstrating that a spin-glass-like magnetism sets in below T_c. Here, we note that the development of magnetic phase is already evident in the ZF/LF-μSR spectra, and results are fully consistent with each other. The onset of superconductivity below T_c is also confirmed by an increase in δ_s, as observed in Fig. 3(c). This remarkable accordance of onset temperature between magnetism and superconductivity strongly suggests that there is an intrinsic relationship between the superconducting and magnetic phases that leads to a common characteristic temperature.

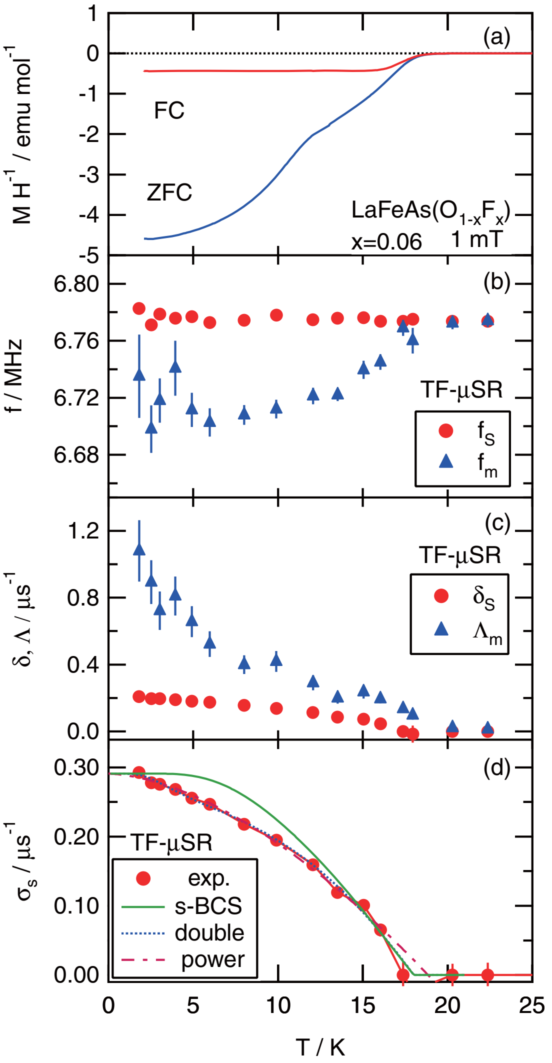

Fig. 3. (Color online) Temperature dependence of dc magnetic susceptibility measured at 1 mT (a), and that of physical parameters deduced by analyzing TF-μSR spectra in superconducting (f_s, δ_s) and magnetic (f_m, Λ_m) phases (b–c), and of σ_s ($= \sqrt{2}\delta_s$) proportional to superfluid density (d). Curves in (d) are fits by models described in the text.

The temperature dependence of σ_s in Fig. 3(d) is compared with theoretical predictions for a variety of models with different order parameters. The weak-coupling BCS model (s-wave, single gap) apparently fails to reproduce the present data, as they exhibit a tendency to vary with temperature over the region $T/T_c < 0.4$. Although a fit using a two-gap model[11)] shown by a dotted line seems to exhibit reasonable agreement with data, the deduced gap parameters ($2\Delta_i/k_B T_c$) are largely inconsistent with the prediction of the weak-coupling BCS model (see Table I). These observations suggest that the superconducting order parameter is not described by a s-wave symmetry with a single gap. When a power law, $\sigma_s = \sigma_0[1 - (T/T_c)^\beta]$, is used in fitting the data, we obtain a curve shown by the broken line in Fig. 3(d) with an exponent $\beta \simeq 2$. This is in good agreement with the case of d-wave symmetry at the dirty limit.

Table I. Parameters for defining the lines in Fig. 3(d).

Two-gap		Power law	
T_c (K)	18.0(5)	T_c (K)	18.9(4)
$\sigma(0)$ (μs^{-1})	0.291(5)	$\sigma(0)$ (μs^{-1})	0.291(4)
w	0.73(6)	β	1.7(1)
$2\Delta_1/k_BT_c$	2.6(3)		
$2\Delta_2/k_BT_c$	1.1(3)		

In the limit of extreme type II superconductors [i.e., $\lambda/\xi \gg 1$, where λ is the effective London penetration depth and $\xi = \sqrt{\Phi_0/(2\pi H_{c2})}$ is the Ginzburg–Landau coherence length, Φ_0 is the flux quantum, and H_{c2} is the upper critical field], σ_s is determined by λ using the relation[12] $\sigma_s/\gamma_\mu = 2.74 \times 10^{-2}(1-h)[1+3.9(1-h)^2]^{1/2}\Phi_0\lambda^{-2}$, where $h = H_{TF}/H_{c2}$ and H_{TF} is the magnitude of external field. From σ_s extrapolated to $T = 0$ and taking $H_{c2} \simeq 50$ T (ref. 13), we obtain $\lambda = 595(3)$ nm. Because of the large anisotropy expected from the layered structure of this compound, λ in the polycrystalline sample would be predominantly determined by in-plane penetration depth (λ_{ab}). Using the formula $\lambda = 1.31\lambda_{ab}$ for such a situation,[14] we obtain $\lambda_{ab} = 454(2)$ nm. This value coincides with that expected from the aforementioned empirical relation between λ_{ab}^{-2} superconductors.[6,15] However, this may not be uniquely attributed to the superfluid density because λ depends not only n_s but also on the effective mass, $\sigma_s \propto \lambda^{-2} = n_s e^2/m^*c^2$.

Finally, we discuss the feature of the spin glass-like phase. Assuming that the local moments are those of off-stoichiometric iron atoms with a moment size close to that in the SDW phase ($\sim 0.36\mu_B$[4]), the mean distance between muon and iron moments in the relevant phase is estimated to be $\sim$0.5 nm from an average of δ_i. Given the unit cell size ($a = 0.404$ nm, $c = 0.874$ nm[1]), this would mean that more than a quarter of iron atoms in the magnetic phase (i.e., $\simeq 7\%$ of the entire sample) should serve as a source of local moments. It is unlikely that such a significant fraction of iron atoms remains as impurities in the present sample.

It might also be noteworthy that there is an anomaly near $T_{m2} \simeq 12$ K in the susceptibility [the onset of ZFC/FC hysteresis in Fig. 1 and a steplike kink in Fig. 3(a)]. This seems to be in accordance with the onset of a steeper increase in Λ_m below T_{m2}, suggesting a change in magnetic correlation.

μSR studies of LFAO-F have been made by a number of groups. According to those preliminary studies, no clear sign of magnetism is observed in the sample over relevant doping concentrations, except for a weak relaxation observed far below T_c for $x = 0.05$ and 0.075 in ZF-μSR spectra and an unidentified additional relaxation observed in TF-μSR spectra for $x = 0.075$.[5–7] This led us to recall the sensitivity to chemical stoichiometry in the emergence of the spin glass-like *A*-phase observed near the boundary between the antiferromagnetic and superconducting phases in CeCu$_2$Si$_2$.[16] In addition to the *A*-phase, the present LFAO-F system exhibits a closer similarity to this classical heavy-fermion superconductor such as the phase diagram against pressure/doping.[17] Further study of the dependence of fractional yield for the magnetic phase with varying x (in small steps near the phase boundary) would provide further insight into the true nature of these phases and the mechanism of superconductivity itself that is working behind the coexistence/competition.

In summary, it has been revealed by our μSR experiment that superconducting and magnetic phases coexist in LaFeAs(O$_{0.94}$F$_{0.06}$). These two phases simultaneously develop just below T_c, strongly suggesting an intimate and intrinsic relationship between these two phases. The result of TF-μSR measurement suggests that the superconductivity of LaFeAs(O$_{0.94}$F$_{0.06}$) cannot be explained by the conventional weak-BCS model (single gap, *s*-wave).

Acknowledgments

We would like to thank the TRIUMF staff for their technical support during the μSR experiment. This work was partially supported by the KEK-MSL Inter-University Program for Oversea Muon Facilities and by a Grant-in-Aid for Creative Scientific Research on Priority Areas from the Ministry of Education, Culture, Sports, Science and Technology, Japan.

1) Y. Kamihara, T. Watanabe, M. Hirano, and H. Hosono: J. Am. Chem. Soc. **130** (2008) 3296.
2) X. H. Chen, T. Wu, G. Wu, R. H. Liu, H. Chen, and D. F. Fang: Nature **453** (2008) 761.
3) H. Takahashi, K. Igawa, K. Arii, Y. Kamihara, M. Hirano, and H. Hosono: Nature **453** (2008) 376.
4) C. de la Cruz, Q. Huang, J. W. Lynn, J. Li, W. Ratcliff II, J. L. Zarestky, H. A. Mook, G. F. Chen, J. L. Luo, N. L. Wang, and P. Dai: Nature **453** (2008) 899.
5) H. Luetkens, H. H. Klauss, R. Khasanov, A. Amato, R. Klingeler, I. Hellmann, N. Leps, A. Kondrat, C. Hess, A. Köhler, G. Behr, J. Werner, and B. Büchner: arXiv:0804.3115.
6) J. P. Carlo, Y. J. Uemura, T. Goko, G. J. MacDougall, J. A. Rodriguez, W. Yu, G. M. Luke, P. Dai, N. Shannon, S. Miyasaka, S. Suzuki, S. Tajima, G. F. Chen, W. Z. Hu, J. L. Luo, and N. L. Wang: arXiv:0805.2186.
7) H. Luetkens, H. H. Klauss, M. Kraken, F. J. Litterst, T. Dellmann, R. Klingeler, C. Hess, R. Khasanov, A. Amato, C. Baines, J. Hamann-Borrero, N. Leps, A. Kondrat, G. Behr, J. Werner, and B. Büchner: arXiv:0806.3533.
8) K. Selte, A. Kjekshus, and A. F. Andresen: Acta Chem. Scand. **26** (1972) 3101.
9) Y. J. Uemura, K. Nishiyama, T. Yamazaki, and R. Nakai: Solid State Commun. **39** (1981) 461.
10) R. S. Hayano, Y. J. Uemura, J. Imazato, N. Nishida, T. Yamazaki, and R. Kubo: Phys. Rev. B **20** (1979) 850.
11) F. Bouquet, Y. Wang, R. A. Fisher, D. G. Hinks, J. D. Jorgensen, A. Junod, and N. E. Phillips: Europhys. Lett. **56** (2001) 856.
12) E. H. Brandt: Phys. Rev. B **37** (1988) 2349.
13) F. Hunte, J. Jaroszynski, A. Gurevich, D. C. Larbalestier, R. Jin, A. S. Sefat, M. A. McGuire, B. C. Sales, D. K. Christen, and D. Mandrus: Nature **453** (2008) 903.
14) V. I. Fesenko, V. N. Gorbunov, and V. P. Smilga: Physica C **176** (1991) 551.
15) Y. J. Uemura, V. J. Emery, A. R. Moodenbaugh, M. Suenaga, D. C. Johnston, A. J. Jacobson, J. T. Lewandowski, J. H. Brewer, R. F. Kiefl, S. R. Kreitzman, G. M. Luke, T. Riseman, C. E. Stronach, W. J. Kossler, J. R. Kempton, X. H. Yu, D. Opie, and H. E. Schone: Phys. Rev. B **38** (1988) 909.
16) R. Feyerherm, A. Amato, C. Geibel, F. N. Gygax, P. Hellmann, R. H. Heffner, D. E. MacLaughlin, R. Müller-Reisener, G. J. Nieuwenhuys, A. Schenck, and F. Steglich: Phys. Rev. B **56** (1997) 699.
17) P. Monthoux, D. Pines, and G. G. Lonzarich: Nature **450** (2007) 1177.

Available online at www.sciencedirect.com
ScienceDirect
Journal of Nuclear Materials 377 (2008) 28–33
journal of nuclear materials
www.elsevier.com/locate/jnucmat

The present status of R&D for the muon target at J-PARC: The development of silver-brazing method for graphite

Shunsuke Makimura [a,*], Hidetsugu Ozaki [b], Hisanori Okamura [b], Masatoshi Futakawa [c], Takashi Naoe [c], Yasuhiro Miyake [a], Naritoshi Kawamura [a], Kusuo Nishiyama [a], Masayoshi Kawai [a]

[a] *Institute of Materials Structural Science, High Energy Accelerator Research Organization, 1-1 Oho, Tsukuba-shi, Ibaraki-ken 305-0801, Japan*
[b] *Kinzoku Giken Co., LTD., 276-21, Motoishikawa, Mito-shi, Ibaraki-ken 310-0843, Japan*
[c] *Japan Atomic Energy Agency, Tokai-mura, Ibaraki-ken 319-1195, Japan*

Abstract

At the J-PARC muon science facility, the muon target was made of an isotropic graphite (IG-43). The energy deposited by the proton beam is estimated to be 3.3 kW on graphite and 600 W on the copper frame. To alleviate the thermal stress, a titanium stress absorber is inserted between the graphite and the copper. Although graphite is known to be difficult to be brazed, the titanium is attached to the graphite through silver-brazing. In this report, we will describe the development of a silver-brazing method for graphite in the fabrication of the J-PARC muon target. A capillary test between the graphite and the titanium was performed to determine the optimal brazing conditions. The test involved bonding graphite and titanium plates while varying the gap between them in order to determine the brazing material and the optimal surface treatment of graphite. Subsequently, a trial muon-production target was fabricated using this optimized brazing method. Specimens were cut from the trial target, and bending test experiments were performed to determine the tensile and shear strength of the interface. As a result, it was confirmed that graphite could be bonded adequately through the silver-brazing.

1. Introduction

At the J-PARC muon science facility, the most intense pulsed muon beam in the world will be produced by a 3 GeV/1 MW/25 Hz proton beam on a target made of 20-mm thick, disc-shaped, isotropic graphite (IG-43). The target frame will be constructed using copper with a stainless steel tube embedded for water cooling. The energy deposited by the proton beam is estimated to be 3.3 kW on the graphite target and 600 W on the copper frame by PHITS [1]. Using the results obtained by PHITS, both the static and the dynamic characteristics of the target such as temperature distributions, thermal stresses, shockwaves, and transient responses were evaluated thorough a finite element method (FEM) simulation. It was found that most of the thermal stress is located at the boundary edge between the graphite and the copper frame because of the difference in thermal coefficients between graphite and copper. To alleviate the thermal stress, a titanium stress absorber is inserted between graphite and copper [2]. Fig. 1 shows the schematic drawing and the picture of the muon target.

Considering that the beta-transition temperature in titanium is 885 °C, the bonding of the muon target must be performed under this temperature. Since the temperature of the interface between graphite and titanium will reach more than 200 °C during the full beam proton operation through the evaluation of an FEM simulation, the brazing material must have a much higher melting point simultaneously. Therefore, the silver-brazing method was selected to bond the two interfaces, which were graphite–titanium and titanium–copper. In general, graphite is known to be difficult to be brazed because the low wetting of graphite

---

[*] Corresponding author.
E-mail address: shunsuke.makimura@kek.jp (S. Makimura).

0022-3115/$ - see front matter © 2008 Elsevier B.V. All rights reserved.
doi:10.1016/j.jnucmat.2008.02.025

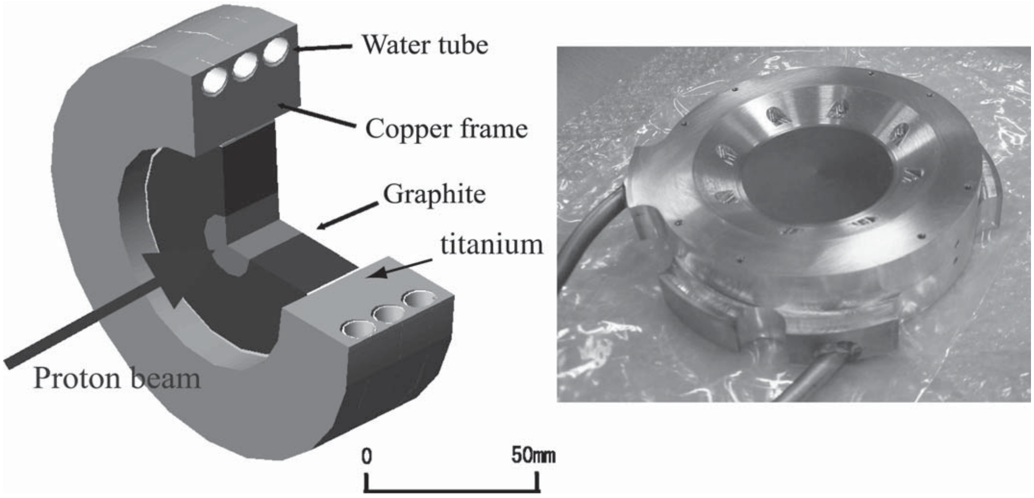

Fig. 1. The schematic drawing and the picture of the muon target. The target itself is made of 20-mm thick, disc-shaped, isotropic graphite (IG-43). The target frame is constructed using copper with a stainless steel tube embedded for water cooling. A titanium stress absorber is inserted between graphite and copper.

disturbs the capillarity, and the brazing material has difficulties to permeate the gap. At first, the commercial silver-brazing Incusil-Aba (59Ag/27.25Cu/12.5In/1.25Ti) was applied to the muon target, since graphite and titanium can be combined to make titanium carbide. But the graphite could not be bonded to the titanium adequately because the silver-brazing did not permeate the whole interface. Later we used a *special* silver-brazing material (76Ag/22Cu/2Ti), which was used to bond C/C composite and the oxygen-free copper in the development of the nuclear diverter [3]. We also considered that the surface treatment might affect the capillarity. Therefore, we performed a capillary test, in which graphite and titanium plates were bonded while varying the gap between them in order to determine the brazing material and the optimal surface treatment of graphite. The capillary test is described in Section 2.

Graphite is known to shrink due to radiation damage [4]. To reduce the tensile stress by the shrinkage, we could expect that the compressive stress, which results as the residual stress from the fabrication process, would compensate the tensile stress. Therefore, the graphite, shaped as a tapered cylinder, and the titanium, shaped as a tapered ring, are inserted into the copper frame at high temperature [5]. Fig. 2 shows the schematic drawing of this configuration used in the silver-brazing method. At room temperature, the copper frame and the titanium layer would shrink more than the graphite target. Then this compressive stress would act on the graphite like a shrink fit. Because the muon target is fabricated by this special configuration, it can be predicted that the properties of the interface are different from that in the capillary test. Subsequently, a trial muon target was fabricated using the optimized brazing method. In Section 3, the interface, which was obtained from the fabricated trial muon target, was observed by using a scanning electron microscope (SEM).

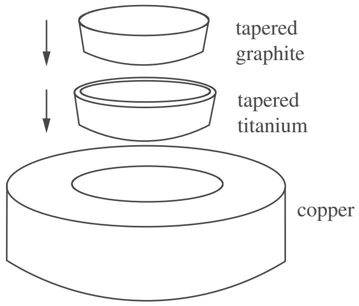

Fig. 2. The schematic drawing of the silver-brazing process for the fabrication of the muon target.

Through an evaluation by FEM, it was found that the compressive stress would take place at almost whole the interface of the graphite and the titanium during the proton beam operation, while the tensile and shear stress would occur simultaneously at the edge of the interface. Hence, specimens were cut from the trial target, and a bending test was performed to measure the tensile and shear strength of the interface. The stress analysis and the bending test experiment are described in Section 4.

A conclusion is given in Section 5.

2. Determination of the silver-brazing method

To determine the optimal silver-brazing method, a capillary test was performed under the following four conditions. (1) The commercial silver-brazing ‘Incusil-Aba’ was applied without any surface treatment to provide a basis of comparison. (2) The *special* silver-brazing material (76Ag/22Cu/2Ti) was applied without any surface treatment to compare with the example of the nuclear diverter. (3) A commercial silver-brazing material BAg-8 was applied after the graphite surface was painted and baked with the special silver-brazing material (76Ag/22Cu/2Ti).

Under this condition, we can expect that the surface of the graphite was wrapped by the metal which is easy to wet, and that the graphite and the titanium in the *special* silver-brazing will combine to make titanium carbide during the baking process. However, the thickness of the wrapped brazing cannot be uniform if the treated surface is vertical against gravity, such as the muon target, where the whole surface of the cylinder cannot stay horizontal at all-time. In fact, the redundant brazing material was removed by machining after baking. (4) The commercial silver-brazing material BAg-8 was applied after the graphite was surface treated using a titanium arc ion plating (AIP) method. We considered that a high ion acceleration voltage is required for the titanium ion to be implanted in the graphite. But too high an acceleration voltage (more than 100 V) will lead to the brittleness of the implanted surface through sputter-etching effect. Therefore, it was decided that the titanium ion should be accelerated to 50 eV in the AIP process. The implantation thickness of the titanium layer was 5 μm.

For each of those four conditions, the graphite and the titanium plates were bonded while varying the gap between them. The gap distance was 0.1 mm, 0.05 mm, and 0.01 mm, since the precision of the machining is better than 0.1 mm for the parts of the muon target. Fig. 3 shows a picture of the capillary test under the second condition with a gap of 0.05 mm. To observe the permeation of the silver-brazing, an ultra-sonic method was utilized. The ultra-sounds were incident to the graphite plate. If there is a gap between the graphite and the titanium, the ultra-sound is reflected on the gap and the echo is detected on the graphite surface faster than if the echo is reflected on the surface of the titanium. Through the capillary test, the following results were obtained. (1) Incusil-Aba could not permeate the gap for each gap distance. (2) The *special* silver-brazing material (76Ag/22Cu/2Ti) could permeate only a gap of 0.1 mm, but could not permeate narrower gaps. The wetting of the brazing material is improved compared with Incusil-Aba. (3) BAg-8 could permeate the gap between the titanium and the graphite with a surface treatment using the *special* silver-brazing material for each gap distance. (4) When using AIP of titanium on graphite, the result was similar to the second case. Thus, we could determine that the graphite and titanium could be bonded by BAg-8 with a surface treatment using the *special* silver-brazing material (76Ag/22Cu/2Ti).

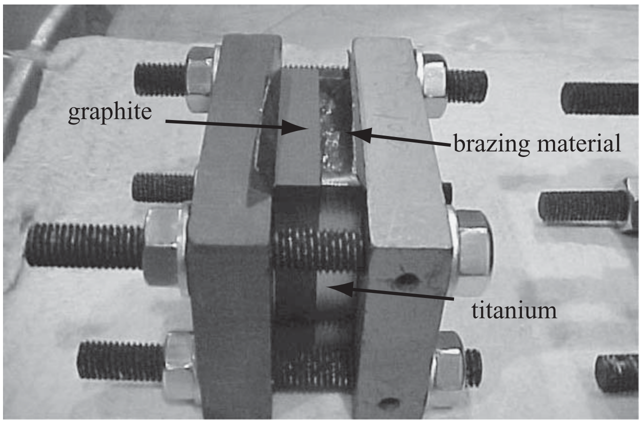

Fig. 3. The picture of the capillary test under the second condition, where the *special* silver-brazing material (76Ag/22Cu/2Ti) was applied without any surface treatment, with a gap of 0.05 mm.

3. Observation of the interfaces on the trial muon target

In the silver-brazing process, the two interfaces, graphite–titanium and titanium–copper, were bonded. Therefore, we must consider the validity of both interfaces. The interfaces, which were obtained from the fabricated trial muon target, were observed by using a scanning electron microscope (SEM). Fig. 4 shows a picture of the interfaces by SEM between the graphite and the titanium on the right-hand side, and between the titanium and the copper on the left-hand side. We could not find any gaps on the whole interfaces through SEM.

4. Stress analysis and bending test experiment

4.1. First stress analysis and FEM simulation

During the proton beam operation, it was found through FEM that 8 MPa of the tensile stress and 6 MPa

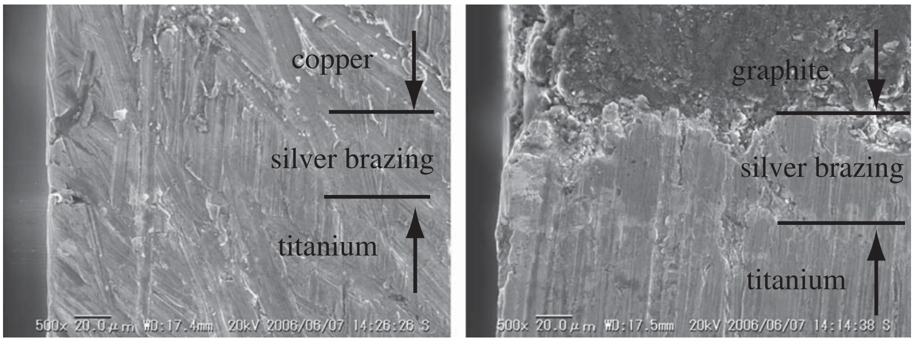

Fig. 4. The picture of the interfaces by SEM between the graphite and the titanium on the right-hand side, and between the titanium and the copper on the left-hand side.

of the shear stress will take place on the interface between the graphite and the titanium [2]. In general, the testing of tensile strength and shear strength is performed by stretching and giving a torque to a specimen, which is chucked at both ends by the testing apparatuses. However in our case, the specimen must be cut from the trial muon target, which is not large enough. Moreover, it is not easy to chuck graphite, since it easily brittles. Therefore, we decided to adopt the bending test of a simple bar, which was cut from the trial muon target with a shape of a parallelepiped. In that way, both the tensile stress and the shear stress on the interface could be evaluated through FEM. If both stresses in the bending test are beyond the design stress values, it can be confirmed that the bonded interface will withstand the proton beam operation. Although the stress-distribution was calculated in detail through FEM, we previously introduced a simple stress analysis to predict the effect of the configuration such as the dimensions of the specimen, the location of the interface, the location of the loading point, and so on. In this analysis, it was assumed that the specimen was made of an uniform material. As shown in Fig. 5, the bar has a distance *l* of the two support points, a width *w*, a height *h*, and a load *F*, which is loaded at the center between the two support points. Then the tensile stress occurs at the lower part of the bar. The maximum tensile stress *T* at a location *x* apart from the loading point is expressed as

$$T = \frac{M}{Z} = \frac{F}{2} \cdot \left(\frac{l}{2} - x\right) \cdot \frac{6}{wh^2} = \frac{3F}{wh^2}\left(\frac{l}{2} - x\right), \tag{1}$$

where M is the bending moment and Z is the section modulus [6].

The shear stress on the vertical plane against the bar axis is expressed as

$$S = \frac{F}{2wh}. \tag{2}$$

When the bending test was actually performed, the existing testing apparatus gave some limitations on the available load and the size of the specimen as well. In our case, the available load was from 1 N to 1000 N, and the specimen dimensions were decided as $l = 30$ mm, $w = 4$ mm, and $h = 6$ mm (variable). When x becomes too large, the properties of the support point and the setting precision of the specimen against the support point cannot be ignored. Therefore, we also applied $x = 5$ mm. In this section, it is assumed that the interface is parallel to the vertical plane against the bar axis. The simple bar model with a tilted interface is discussed in the following section. Although 8 MPa of the tensile stress and 6 MPa of the shear stress on the interface were the criteria, it would be favorable if the interface could be stronger than the graphite itself. Because graphite is known to break under the tensile stress, it is difficult to know the precise shear strength of graphite. Hence, 40 MPa of the tensile strength, that is the tensile strength of graphite, and 6 MPa of the shear strength on the interface were applied as criteria. To let the shear stress S beyond 8 MPa (safety factor of 1.3), F must be beyond 380 N. Then we can obtain $T = 80$ MPa. This means that the graphite will break before the shear stress reaches the criteria of 8 MPa. In the analysis, T was proportional to h^{-2}, and S is to h^{-1}. Hence, if $h = 12$ mm and $F = 760$ N are used, we would obtain $T = 40$ MPa and $S = 8$ MPa. Then the evaluation through a FEM was performed again under these different conditions. Consequently, $T_{\text{fem}} = 57$ MPa and $S_{\text{fem}} = 7$ MPa were obtained. The tensile stress was still larger than that in the stress analysis. We could consider that h was large enough so that the specimen could not be considered as a simple bar anymore. Therefore, it was concluded that the graphite will break under tensile stress before the shear stress can reach the design value, if the interface is on the vertical plane against the bar axis.

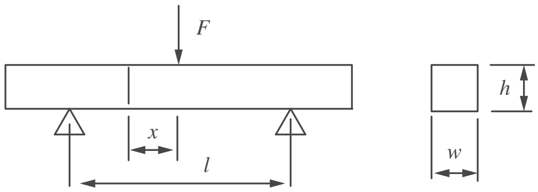

Fig. 5. The schematic drawing of the simple bar for the stress analysis. The bar has a distance *l* of the two support points, a width *w*, a height *h*, and a load *F*, which is loaded at the center between the two support points.

4.2. Second stress analysis and FEM simulation

Before a discussion of the specimen with the tilted interface, the shear stress on the stretched bar will be described. In general, when the tensile load is introduced to the bar, the shear stress occurs on the tilted plane against the load axis. Furthermore, the shear stress is maximized when the tilted angle is 45°. Then the shear stress becomes half of the tensile stress. The bending test in this section was based on this consideration. A tilted angle of 45° against the bar axis was applied to the specimen. Then it was assumed that $l = 30$ mm, $w = 4$ mm, $h = 6$ mm, and $F = 150$ N, which was loaded on the interface between the titanium and the copper. Here the shear stress was defined against the plane, which was parallel to the interface. Fig. 6 shows the shear stress-distribution calculated through FEM, when the bending test was performed. Fig. 7 shows the distribution of the shear stress, the maximum principal stress, and the minimum principal stress, along the interface between the graphite and titanium, where the horizontal axis was defined as the distance from the lower surface to the upper surface. As a result, the maximum stress $T_{\text{fem}} = 41$ MPa and $S_{\text{fem}} = 21$ MPa were obtained on the lower surface. As predicted, the shear stress was approximately half of the tensile stress and it was enough large compared with the criteria of 8 MPa. Finally, we determined that this configuration would be used in the actual bending test. Here, the specimen with the vertical interface was also evaluated through a FEM simulation to confirm that the shear stress

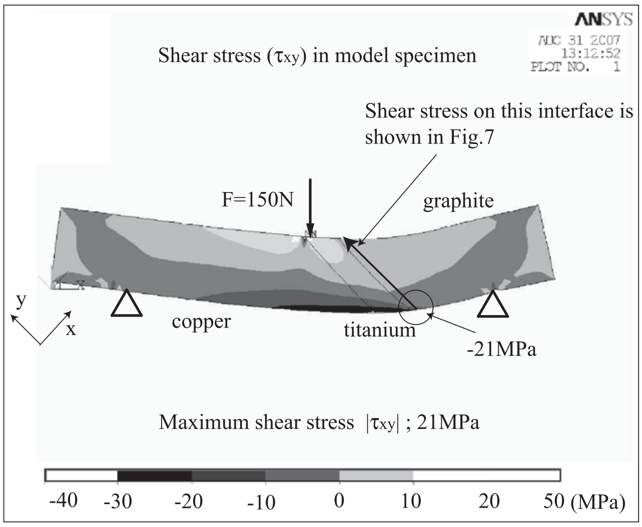

Fig. 6. The shear stress-distribution calculated through FEM, when the bending test with the tilted interface was performed.

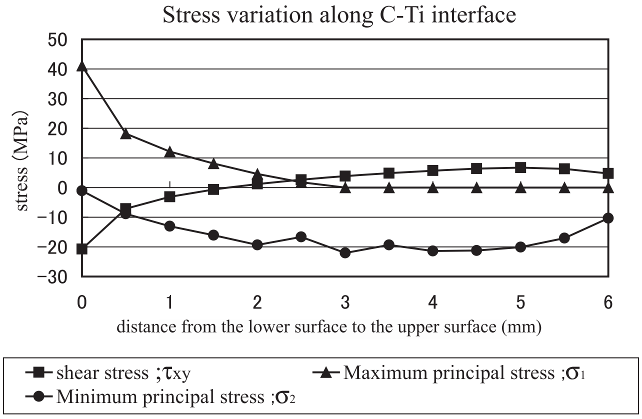

Fig. 7. The distribution of the shear stress, the maximum principal stress, and the minimum principal stress, along the interface between the graphite and titanium, where the horizontal axis was defined as the distance from the lower surface to the upper surface.

increases by tilting the interface. In this model, h, w, and l were the same as for the specimen with the tilted interface. The load was 140 N, and was added on the interface between the titanium and the copper. The difference between the two models is shown in Table 1.

4.3. Experiment

For the bending test, three kinds of the specimens (five samples each) were prepared. First, specimens made of only graphite were tested to make sure the validity of the testing method and the data scatter of the material strength. The specimen would break when the load reaches 130 N. Second, the specimens with the interface vertical to the beam axis were prepared. Although the number of samples was not enough to evaluate the data scatter, it was difficult to obtain more specimens from our trial target. The purpose to test these specimens was to confirm that the interface was stronger than graphite in terms of the tensile stress. Those specimens would break through a FEM simulation when the load reaches 140 N, which is on the interface between the titanium and the copper. Finally, the specimens discussed in the former section were prepared to confirm that the interface could withstand the design shear stress. Those last specimens would break when the load reaches 150 N. Fig. 8 shows a picture of the bending test, in which a specimen with the tilted interface was tested. From the bending test, the following results were obtained: (1) the specimens composed of only graphite were broken when the load reached 160 N, 170 N, 167 N, 160 N, and 160 N, respectively; (2) the specimens with the vertical interface were broken when the load reached a value of 160 N, 180 N, 174 N, 160 N, and 180 N, respectively; and (3) the specimens with the tilted interface were broken when the load reached 170 N, 165 N, 186 N, 192 N, and 164 N, respectively. The calculated loads in the FEM simulation, the measured average loads and their standard deviation are shown in Table 2. The breaking loads in the bending test were beyond the calculated loads in all the specimens. Moreover, it seems that the difference of the standard deviation is caused by the precision of setting the specimens. As shown in Fig. 6, the load was applied on the interface between the titanium and the copper. The brazed interface looked thicker than the actual one, because the brazing material diffused into the titanium and the copper. Considering that the specimens were set by hand, the specimens were positioned with a precision of about 0.7 mm. Since the tensile stress is proportional to $l/2 - x$, and also that the location of breaking is almost

Table 1
The calculated tensile and shear stress by FEM, for the tilted interface model and the vertical interface model

Interface	Load (N)	Tensile stress (MPa)	Shear stress (MPa)
45°-tilted	150	41	21
Vertical	140	44	3.6

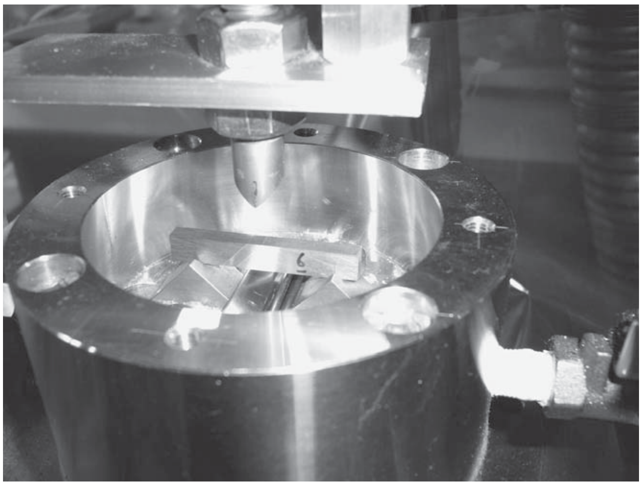

Fig. 8. The picture of the bending test, in which a specimen with the tilted interface was tested.

Table 2
The calculated loads in FEM compared with the measured average loads and their standard deviation

Specimens	Calculation (N)	Average (N)	Standard deviation (N)
Graphite	130	163	4.3
Vertical interface	140	171	9.1
Tilted interface	150	175	11.4

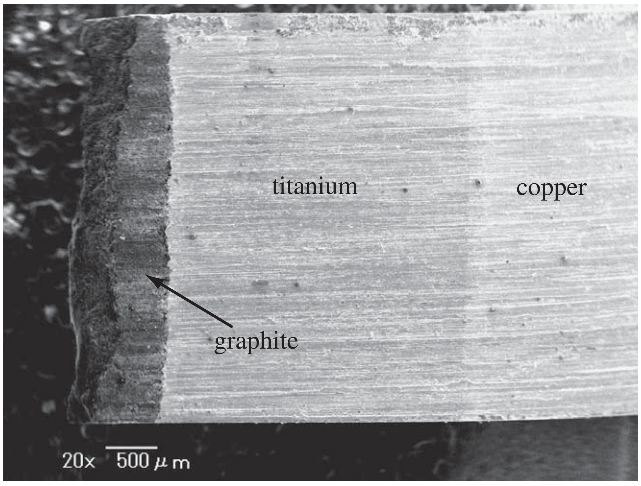

Fig. 9. The picture of a typical broken surface in the bending test observed through SEM.

on the interface ($l/2x = 9$ in the tilted interface), an error of 0.7 mm on x would correspond to an error on the tensile stress in the tilted interface of 14 MPa. Even in the vertical interface, we can obtain an error on the tensile stress of 9 MPa. This seems consistent with the measured values. As a result, it was concluded that the interface could withstand a tensile stress of 41 MPa and a shear stress of 21 MPa.

Additionally, it should be noted that all the specimens broke at the graphite. Fig. 9 shows a picture of a typical broken surface in the bending test observed through SEM. From this experiment, it was concluded that the interface between the graphite and the titanium was bonded adequately during the fabrication process of the muon target.

5. Summary

The silver-brazing method for graphite in fabrication of the muon target has improved. The capillary test was performed to obtain the optimal conditions by observing the interface through an ultra-sonic method. As a result, we could determine that the graphite and the titanium would be bonded by BAg-8 with a surface treatment by the *special* silver-brazing material (76Ag/22Cu/2Ti). Then this method was used to fabricate the trial muon target, and specimens for the bending test were cut. The bending test was performed to confirm that the tensile strength of the interface between the graphite and the titanium was beyond that of graphite (40 MPa), and that the shear strength was beyond the shear stress (8 MPa), which would take place during the proton beam operation. The interface was tilted with an angle of 45° against the bar axis to confirm the shear strength. To extract these strengths from the measurements, a FEM simulation was used. Consequently, it was proved that the tensile strength of the interface was beyond 41 MPa and the shear strength was beyond 21 MPa. Finally, we could determine the optimum silver-brazing method for graphite in the fabrication of the muon target.

References

[1] Hiroshi Iwase, Koji Niita, Takashi Nakamura, J. Nucl. Sci. Technol. 39 (2002) 1142.
[2] Shunsuke Makimura, Yasuhiro Miyake, Kusuo Nishiyama, Kanetada Nagamine, in: Proceedings of the 14th Symposium on Accelerator Science and Technology, Tsukuba, Japan, 2003, p. 22.
[3] Hisanori Okamura, Shouji Kajiura, Masato Akiba, Quart. J. Jpn. Weld. Soc. (1996) 39.
[4] H. Matsuo, Graphite1991 [No. 150], 290.
[5] Shunsuke Makimura, Naritoshi Kawamura, Kusuo Nishiyama, Yasuhiro Miyake, Takashi Anzai, Tomoya Suzuki, Takahiro Sawahata, in: Proceedings of the Second Annual Meeting of Particle Accelerator Society of Japan and the 30th Linear Accelerator Meeting in Japan, Tosu Japan, 2005, p. 173.
[6] S. Timoshenko, D.H. Young, Elements of Strength of Materials, fifth Ed.

Available online at www.sciencedirect.com

Nuclear Instruments and Methods in Physics Research B 266 (2008) 335–346

NIM B
Beam Interactions with Materials & Atoms

www.elsevier.com/locate/nimb

Pulsed source of ultra low energy positive muons for near-surface μSR studies

Pavel Bakule [a,*], Yasuyuki Matsuda [a], Yasuhiro Miyake [b], Kanetada Nagamine [b,1],
Masahiko Iwasaki [a], Yutaka Ikedo [b,2], Koichiro Shimomura [b],
Patrick Strasser [b], Shunshuke Makimura [b]

[a] *Advanced Meson Science Laboratory, RIKEN Nishina Center, RIKEN, Wako, Saitama 351-0198, Japan*
[b] *Muon Science Laboratory, Institute of Materials Structure Science, High Energy Accelerator Research Organization, Tsukuba, Ibaraki 305-0801, Japan*

Received 5 July 2007; received in revised form 8 October 2007
Available online 21 November 2007

Abstract

We have produced a pulsed beam of low energy (ultra slow) polarized positive muons (LE-μ^+) and performed several demonstration muon spin rotation/relaxation (μSR) experiments at ISIS RIKEN-RAL muon facility in UK. The energy of the muons implanted into a sample is tuneable between 0.1 keV and 18 keV. This allows us to use muons as local magnetic microprobes on a nanometre scale. The control over the implantation depth is from several nanometres to hundreds of nanometres depending on the sample density and muon energy. The LE-μ^+ are produced by two-photon resonant laser ionization of thermal muonium atoms. Currently ~15 LE-μ^+/s with 50% spin polarization are transported to the μSR sample position, where they are focused to a small spot with a diameter of only 4 mm. The overall LE-μ^+ generation efficiency of 3×10^{-5} is comparable to that obtained when moderating the muon beam to epithermal energies in simple van der Waals bound solids. In contrast to other methods of LE-μ^+ generation, the implantation of the muons into the sample can be externally triggered with the duration of the LE-μ^+ pulse being only 7.5 ns. This allows us to measure spin rotation frequencies of up to 40 MHz.

PACS: 76.75.+i; 07.77.Ka; 36.10.Dr; 32.80.Rm; 41.75.–i; 42.65.Ky

Keywords: Low energy muons; Ultra slow muons; Muon spin rotation; Muonium generation; Muonium ionization; Vacuum-ultraviolet laser; Lyman-α; Thin film

---

1. Introduction

Spin polarized LE-μ^+ are an important tool in condensed matter research for studying implantation-depth-dependent properties of thin samples, nanomaterials, multilayered thin films, or superconductors. The implantation depth can be easily controlled on a scale ranging from several nanometres to hundreds of nanometres by re-accelerating LE-μ^+ from eV energies to tens of keV in an electrostatic field. Using the technique of μSR (muon spin rotation and relaxation) [1,2] the beam of LE-μ^+ with well-defined initial spin polarization can be used as a depth sensitive microscopic magnetic probe to measure local magnetic fields or spin fluctuations. Alternatively, in samples where it can bind to an electron to form muonium (Mu), the muonium can act as a light hydrogen-like probe that can be studied with the μSR technique.

---

[*] Corresponding author. Tel.: +44 1235445256; fax: +44 1235446881.
E-mail address: p.bakule@rl.ac.uk (P. Bakule).

[1] Present address: (1) Atomic Physics Laboratory, RIKEN, Wako, Saitama 351-0198, Japan. (2) Physics Department, University of California Riverside, Riverside, CA 92521, USA.

[2] Present address: Toyota Central R&D Labs. Inc., 41-1 Yokomichi, Nagakute, Aichi 480-1192, Japan.

0168-583X/$ - see front matter © 2007 Elsevier B.V. All rights reserved.
doi:10.1016/j.nimb.2007.11.009

Over the past 10 years there has been a significant effort to develop an efficient method of LE-μ^+ generation from the surface muon beams with kinetic energies around 4 MeV available at various muon facilities [3–7].

A successful technique for generation of LE-μ^+ has been developed using a continuous muon source at the Paul Scherrer Institute (PSI) in Switzerland. This method, generating LE-μ^+ with epithermal energies down to 15 eV without any loss of spin polarization, is based on the moderation of surface muons in wide band gap insulators. Particularly suitable as moderators are van der Waals bound solids, such as solid argon, neon or nitrogen. Most reliable and efficient so far has been moderation in a thin solid nitrogen layer grown on a microstructured silver substrate with large surface area. With such a target, the efficiency of converting incident muons to LE-μ^+ and transporting them to the sample is as high as 3×10^{-5} [8].

We have been developing an alternative technique at the RIKEN-RAL muon facility [9] located at the Rutherford Appleton Laboratory (UK) using a pulsed surface muon beam with intensity of 1.2×10^6 μ^+/s and pulse repetition rate of 50 Hz. The basis of the technique has been described in detail previously [10,11]. Briefly, the surface muon beam is thermalized in a hot tungsten foil of optimized thickness. The muons that diffuse to the surface can be thermionically emitted to vacuum from the bulk metal as neutral muonium atoms, as the work function for muonium is much lower than that for the charged muon. The thermal muonium is then resonantly ionized through a two-photon 1S→2P→unbound process by a pulsed nanosecond laser to gain "free" muons with mean kinetic energy of only 0.2 eV.

2. Details of the experimental setup

Fig. 1 shows the layout of the experiment as it is set up at the RIKEN-RAL muon facility. The experimental setup for performing μSR measurements with LE-μ^+ consists of a laser system, an ultrahigh vacuum beamline (ion optics) for efficient transport of LE-μ^+ and a well shielded compact μSR spectrometer with all the necessary data acquisition electronics. Most of the laser parameters, as well as the parameters of the ion optics and tungsten target temperature can be remotely controlled and monitored from a dedicated control cabin.

2.1. Laser system

The binding energy of the electron in muonium is 13.6 eV. We believe that the most efficient laser ionization can be achieved through two-photon resonant ionization via the 2P state. This requires using two laser beams of different wavelengths. Firstly, for the strongly allowed electric-dipole transition from the 1S to 2P state, tuneable radiation around 122 nm (Lyman-α, 10.2 eV) is required. The second laser beam, for the ionization from the 2P state,

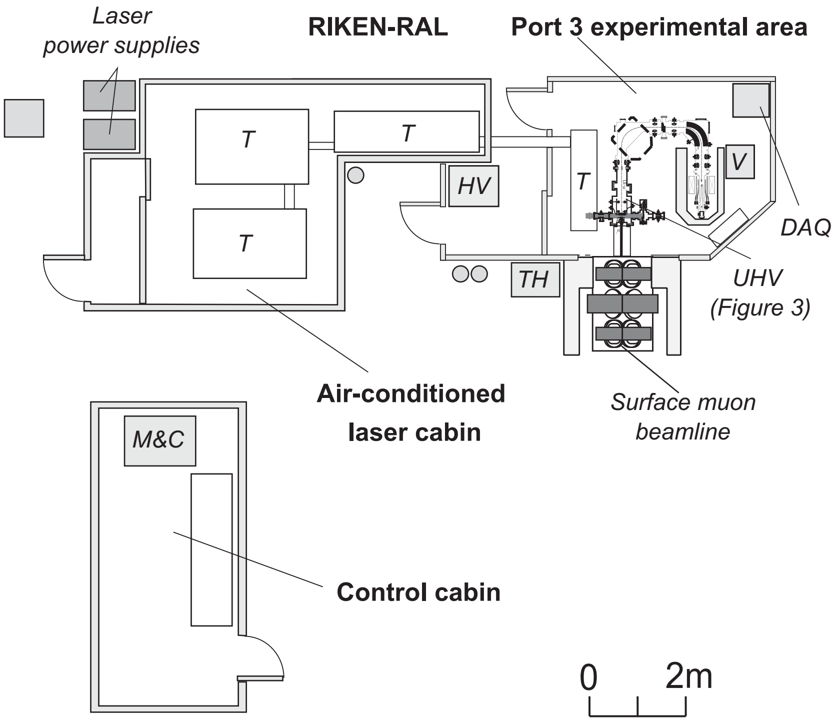

Fig. 1. Layout of the experiment to generate the low energy positive muons at ISIS RIKEN-RAL muon facility. T mark the optical tables with the laser system, UHV is the ultrahigh vacuum apparatus including the LE-μ^+ transport beamline (ion optics) and the μSR spectrometer, HV are the high voltage power supplies for the ion optics, DAQ is the data acquisition electronics for the μSR spectrometer and the computer control of the ion optics, V is the control rack for the ultrahigh vacuum system, TH is the high-current power supply for heating the tungsten foil, and M&C is the monitoring and remote control electronics of the important components of the laser system.

is required to have a wavelength shorter than 366 nm (3.4 eV) and, conveniently, the 355 nm laser beam generated as the third harmonic of a Nd:YAG laser can be used. The laser beam at 122 nm has not only to be tuneable, but also has to have a large bandwidth of about 200 GHz in order to cover the Doppler width of the thermal energy range of the muonium generated from the tungsten foil heated to 2000 K.

The 122 nm radiation is generated through a nonlinear frequency conversion process in a gaseous medium. Although this is inherently rather inefficient, being proportional to the third order nonlinear susceptibility $\chi^{(3)}$ tensor, there is no possibility to use birefringent nonlinear crystals, since none of the known nonlinear crystals is transparent at wavelengths below 190 nm. We are using a two-photon resonant sum-difference frequency mixing scheme in a phase-matched krypton gas [12]. This frequency conversion scheme unfortunately adds to the complexity of the laser system as it requires two laser beams, but it provides a large degree of tuneability and a high conversion efficiency ($\sim 10^{-4}$). The first laser is operating at 212.5 nm and is tuned to a two-photon resonance in Kr, while the second laser operating in the range of 810–850 nm provides the tuneability of the Lyman-α output and is designed to have sufficient bandwidth to cover the Doppler width of muonium. The wide tuneability of the output allows us to ionize under the same conditions not only muonium, but also hydrogen or deuterium. This provides a useful tool for testing the whole apparatus without need for the muon beam.

Fig. 2 shows a simplified schematic diagram of the laser system. The major part of laser system (generating the required beams at 355 nm, 212.5 nm and 810–850 nm respectively) is housed in an air-conditioned cabin connected via a duct with the rest of the apparatus at Port 3 of RIKEN-RAL muon facility (radiation area). The rest of the laser system is attached to the ultrahigh vacuum beamline and consists of beam steering and focusing optics, and a Kr–Ar cell for generating the Lyman-α radiation around 122 nm.

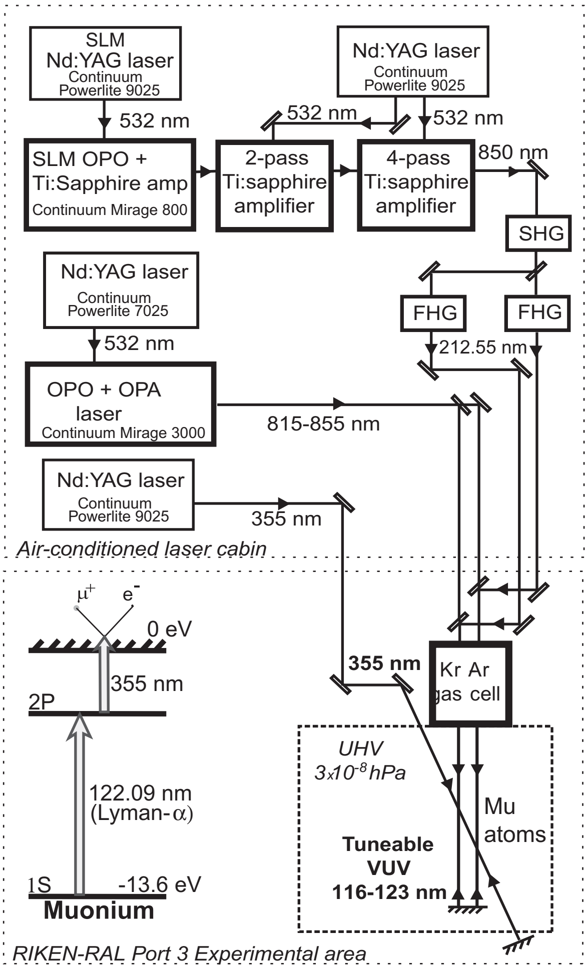

Fig. 2. Schematic diagram of the laser system used for resonant ionization of muonium. The image relay telescopes, beam focusing optics as well as the laser beam diagnostics are not shown in this diagram. SHG is 7 mm long BBO crystal (12 × 12 × 7 mm) for second harmonic conversion to 425 nm; FHG are temperature stabilised, 5 mm long, s-BBO crystals (12 × 12 × 5 mm) for conversion to 212.5 nm; SLM denotes single longitudinal mode operation. An inset shows a simplified energy level diagram of muonium to demonstrate the two-photon resonant ionization scheme used to gain μ^+ with mean energy of just 0.2 eV.

The details of the laser system and its layout have been described previously [13]. The main changes since this publication include a threefold increase of the output at 355 nm to 380 mJ/pulse by replacing the Spectra physics GCR-160 laser with a Continuum Powerlite 9025. At the same time we have also installed an image relay telescope in the path of the 355 nm beam to image the laser output to a distance of ~12 m at the Port 3 experimental area and thus ensure a more uniform intensity profile inside the ultrahigh vacuum beamline. Furthermore, an increase in the output pulse energy at 850 nm has been gained by adding a new 2-pass Ti:sapphire amplification stage at the output of the Continuum Mirage 800 laser and by introducing image relay telescopes in the path of the pump beams of the 4-pass Ti:sapphire amplifier. The resulting increase of the output pulse energy at 850 nm to 250 mJ/pulse and the significant improvement in the beam quality has lead to an increase in the available pulse energy at the generated second harmonic at 425 nm by a factor of two (to 140 mJ/pulse). The 425 nm beam is then split into two beams and converted to 212.5 nm using two 5 mm long s-BBO crystals with conversion efficiency of approximately 15%. Although the s-BBO crystals are superior to BBO crystals at this wavelength, they still exhibit a significant nonlinear absorption at 212.5 nm, resulting in a temperature gradient between the input and exit faces of the crystal. This introduces a phase mismatch for the generated 212.5 nm beam that reduces the conversion efficiency. For this reason we have chosen to generate two separate 212.5 nm beams using two temperature stabilised s-BBO crystals and to cool the centre of the output face of the s-BBO by blowing nitrogen gas from a 1 mm diameter nozzle onto the crystal.

The current output parameters of the laser system are summarized in Table 1. The laser system has excellent long

Table 1
Summary of the laser output parameters

Wavelength	355 nm	212.5 nm	810–850 nm	116–123 nm (Lyman-α)
Pulse duration [FWHM]	10 ns	4 ns	12 ns	~4 ns
Pulse energy	380 mJ	10–12 mJ (×2 beams)	12 mJ (×2 beams)	>0.5 μJ (×2 beams)
Bandwidth	30 GHz	<2 GHz	180 GHz	180 GHz

term reliability. Stable 24 h/day operation can be sustained for up to 20 days, limited primarily by the lifetime of flashlamps used in the Nd:YAG lasers.

It is important to note that the laser system is operating at a repetition rate of only 25 Hz which means that only half of the muon pulses are used for LE-μ^+ generation. This limitation is due to strong thermal effects associated with operating high power solid state laser systems that make it difficult to build 50 Hz system with same pulse energy as achieved with the 25 Hz system.

2.2. LE-μ^+ transport beamline

Fig. 3 shows the layout of the LE-μ^+ beamline with the μSR spectrometer. The pulse of surface muons with momentum of 28 MeV/c enters the apparatus through a

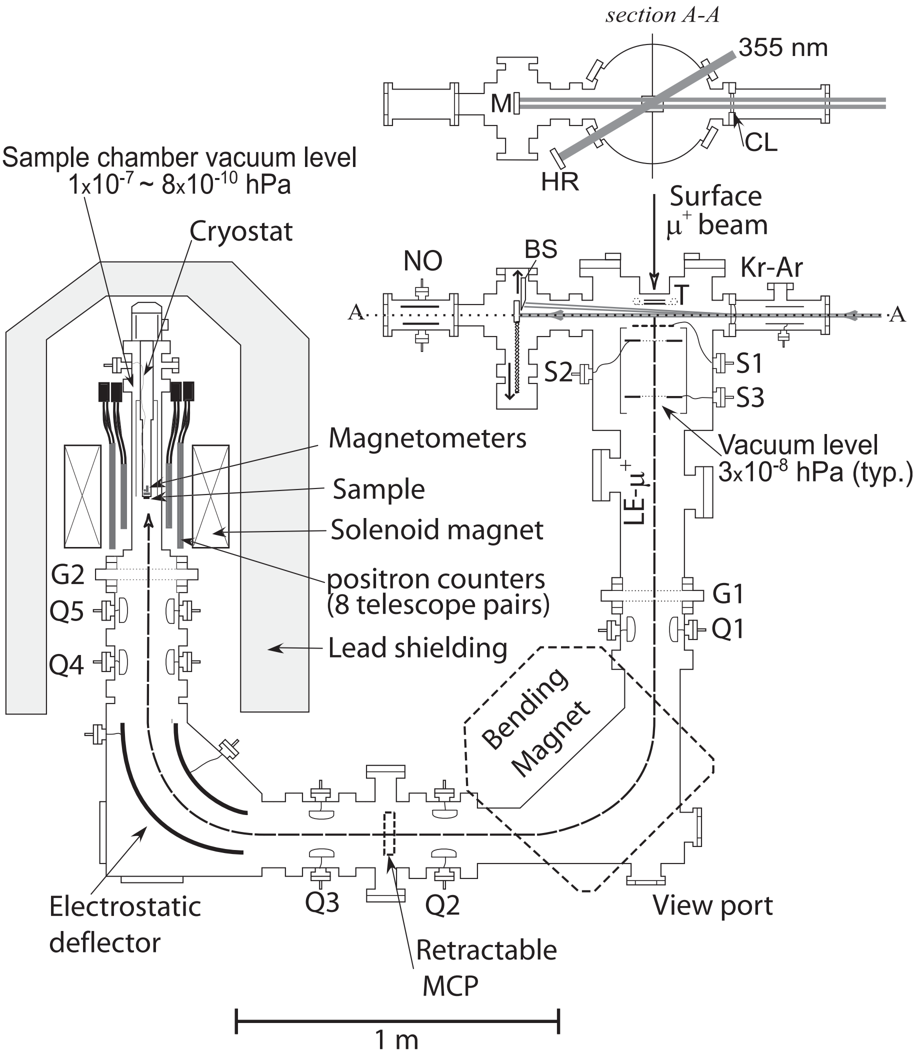

Fig. 3. Layout of the ultrahigh vacuum apparatus used to generate low energy positive muons (LE-μ^+) and to implant them in a sample. The sample is mounted on a cryostat inside a compact μSR spectrometer. Kr–Ar is the gas cell used to generate Lyman-α laser pulse by nonlinear frequency conversion, CL is the cylindrical lens window of the Kr–Ar gas cell, M is a remotely controlled, retractable retro-reflection mirror for the Lyman-α beams, HR is a remotely controlled dielectric retro-reflection mirror for 355 nm beam, BS is a remotely controlled knife-edge beam stop to protect M from 212.5 nm and 820 nm beams, NO is the ionization cell filled with NO gas for monitoring the Lyman-α pulse energy, T is the heated tungsten foil used to generate muonium, G1 and G2 are vacuum gate valves, S1–S3 are electrodes of SOA immersion lens, and Q1–Q5 are electrostatic quadrupole focusing elements. Section A-A shows the overlap of the laser beams in front of the tungsten foil.

50 μm thick stainless steel window and is first moderated by 20 μm thick tungsten foil and then by a 45 μm thick tungsten foil heated by DC current up to 2100 K. The function of the first foil is to shield the stainless steel window from the heat of the 45 μm tungsten target. The area of the tungsten target foil exposed to the muon beam is 40 mm (*W*) × 35 mm (*H*). The foils used were of 6 N purity (99.9999%W), manufactured by PLANSEE. The total thickness of the foils is optimized to stop a significant fraction of the incident beam near the rear surface of the hot foil which results in efficient emission of muonium atoms from the hot tungsten target.

Two sets of laser beams at 212.5 nm and 820 nm are each collinearly focused (with $f = 500$ mm plano-convex spherical lenses) into the cell filled with mixture of krypton and argon gas to generate two Lyman-α beams separated vertically by 10–15 mm. These then enter the ultrahigh vacuum chamber through a thin MgF_2 cylindrical lens (ROC = 78 mm; $f = 120$ mm @ 122 nm). The focusing optics shapes each of the Lyman-α beams to have (in front to the W foil) a width of only 1–2 mm (FWHM) in the horizontal plane and about 5–8 mm in the vertical plane. The two Lyman-α beams pass through a 14 mm wide gap between the tungsten target and the first extraction grid denoted as S1 and overlap the cloud of thermal muonium atoms about 5 mm from the target surface. The 355 nm beam is introduced to the beamline from the top at 30° from the Lyman-α beam and is shaped similarly to have a width of 3 mm by 25 mm. All laser beams are retro-reflected to maximize the ionization yield. Since the retro-reflecting mirrors are placed at the distance of 0.5 m, the width of the ionizing pulse is effectively broadened from 4 ns to 7 ns (FWHM). The overlap of the Lyman-α and 355 nm beams defines an interaction region with a volume of approximately 1 cm^3.

In order to protect the Lyman-α retro-reflecting mirror (Acton Research; Al reflector coated with MgF_2 protection layer; reflectivity @ 122 nm ∼75%) from laser induced damage, the laser beams were aligned slightly off-centre on the cylindrical lens window. This dispersively separates the laser beams, so that the 212.5 nm and 820 nm beams can be blocked by a knife-edge beam stop placed in front of the Lyman-α reflector.

The LE-μ^+ generated by the laser ionization are initially extracted by a low gradient electrical field between the tungsten foil (held at 9.0 kV) and mesh electrode S1 (held at 8.8 kV). S1 is the first of three elements forming an SOA immersion lens [14] which then re-accelerates the LE-μ^+ to 9.0 keV. Such arrangement is necessary in order to minimize the energy variation of the re-accelerated LE-μ^+ beam. The SOA lens also focuses the collected LE-μ^+ to a tight spot of only 2.5 mm (FWHM) which is then imaged to the sample surface with the ion transport optics consisting of five electrostatic quadrupoles (Q1–Q5), a bending magnet and an electrostatic deflector. In this geometry the electrostatic deflector effectively rotates the muon spin polarization, which is originally anti-parallel to the momentum, by 90°. The muons implanted into the studied sample are therefore horizontally polarized with the spin perpendicular to the muon momentum.

The section of the beamline between the bending magnet and the electrostatic deflector houses a retractable position-sensitive microchannel plate detector (ROENTDEK DLD-80). This is used either for checking the yield and profile of the LE-μ^+ beam or for measuring D^+ yield when optimizing the performance of the apparatus by ionizing the residual deuterium dissociated by the hot tungsten target.

The total transmission efficiency of the beamline has not been measured, but it is worth noting that there is a significant loss of muons due to decay. The overall path length from the tungsten target to the focus at the sample chamber is 3.9 m and the time-of-flight for 9.0 keV muons is 1.15 μs, resulting in ∼40% loss of LE-μ^+ due to decay. We are planning to increase the acceleration voltage to 18 keV. This will extend the range of available implantation energies and reduce the loss through decay in flight to about 28%.

2.3. Sample chamber and μSR spectrometer

The sample chamber, which has a diameter of 100 mm and a length of 540 mm, can be isolated from the rest of the ultrahigh vacuum beamline to allow changing of samples. The vacuum level in the apparatus is typically 3×10^{-8} hPa when measured in the vicinity of the heated tungsten foil. The vacuum level in the sample chamber can be as low as 8×10^{-10} hPa several days after a sample change. Experiments with LE-μ^+can be started approximately 6 h after the sample change when the vacuum level reaches about 1×10^{-7} hPa. Samples for the μSR studies can be mounted on a closed circuit two-stage helium cryostat (Iwatani HE-05 with cooling power of 0.5 W at 4 K) capable of cooling samples to about 10 K. Alternatively, the sample chamber can accommodate a position-sensitive microchannel plate detector (ROENTDEK DLD-40) that is used to check the focusing of the LE-μ^+ beam. The energy of the muons implanted into the sample can be continuously varied from zero to 18 keV by applying voltage in the range of +9.0 kV to −9.0 kV directly onto the sample holder, which is isolated from the cryostat finger by 10 mm thick disc of sapphire.

Around this small sample chamber we have built a compact μSR spectrometer designed with the aim of providing a very high signal-to-noise ratio. The sample chamber is surrounded by a close arrangement of eight telescope pairs of plastic scintillation counters covering a solid angle of 80% of 4π sr. These detectors are inserted inside a solenoid type coil with a magnetic length of 260 mm providing magnetic field with strength of up to 60 mT parallel to the muon momentum and perpendicular to the spin. The magnetic field homogeneity at the field value of 8 mT over a distance of 40 mm along the magnet's axis is below 500 ppm. The field homogeneity measured at 3 mT in the transverse direction over a 10 mm radius is below

100 ppm. In-built into the magnet are also coils for compensating external magnetic fields of up to 250 μT (2.5 G) in any direction. The spectrometer can be therefore used for transverse field TF-μSR measurements as well as measurements in zero external magnetic field (ZF-μSR). During the ZF-μSR measurements the zero field compensation can be monitored using three single axis fluxgate magnetometers (Bartington Instruments MAG01-H F-probes). These are mounted on the sample holder immediately behind the sample. The zero field condition can thus be maintained at a level 0.1 μT (1 mG) over a period of several days.

To make meaningful μSR measurements with the relatively low LE-μ^+ rates currently achieved requires a very low background. The combination of the bending magnet and electrostatic deflector provides selection of the transported ions by mass and energy, respectively. This, together with lead shielding with thickness of 100–200 mm around the scintillation detectors and the sample chamber, provides excellent background suppression to less than 0.012 counts over the 15 μs period after each muon pulse. In our case, when the laser is operating at half the repetition rate of the ISIS accelerator, the signal-to-noise ratio can be further increased by subtracting the fixed background of the laser-off spectrum from the laser-on spectrum. This allows us to observe LE-μ^+ decay to at least 6 muon lifetimes after the implantation, see Fig. 4.

3. Experimental results

3.1. Dependence of LE-μ^+ yield on laser pulse energy

The high efficiency of thermal muonium production from the surface muon beam makes this method potentially capable of cooling surface muons to eV energies with efficiency as high as 10^{-2}. However, it is currently limited by the available laser pulse energy, especially at the Lyman-α frequency. The relative measurement of the energy of the Lyman-α pulse is made by passing the Lyman-α beam through an NO gas cell at a pressure of 6.5 hPa and measuring the photoionization current [15]. Fig. 5 shows the observed dependence of the LE-μ^+ yield on the Lyman-α energy. It shows that even though the laser beam overlaps just a small fraction of the muonium cloud (~1 cm^3), the Lyman-α intensity is still not sufficient to saturate the Doppler broadened 1S–2P transition. We do not currently have a detector in our setup to measure the absolute pulse energy of the generated Lyman-α and can only make a rough estimate of ~1 μJ/pulse (total of 2 beams) based on the integrated ionization current of the NO gas cell. Given the beam size in front of the tungsten foil we can estimate the peak intensity to be in the region of several kW/cm^2, still below the expected saturation intensity (for 200 GHz Doppler broadening) of 5 kW/cm^2.

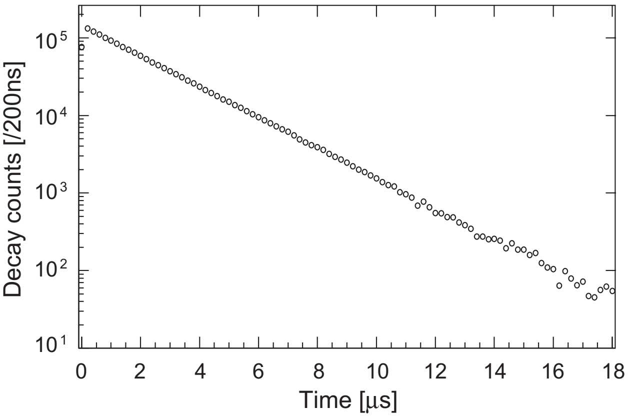

Fig. 4. Histogram of positron counts originating from LE-μ^+ decay in the sample chamber.

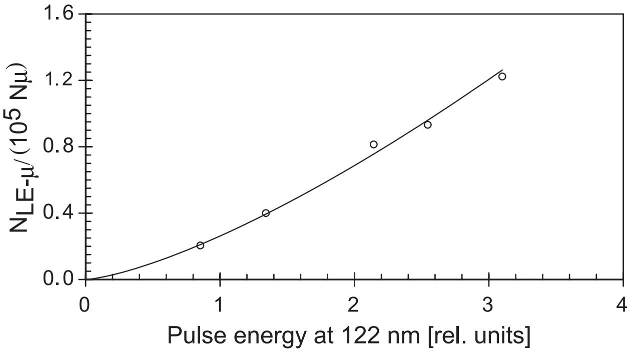

Fig. 5. Dependence of the overall efficiency of LE-μ^+ generation on the pulse energy of the Lyman-α at 122 nm. The efficiency is determined as a ratio of the number of LE-μ^+ delivered at the sample position per laser pulse $N_{\text{LE-}\mu}$ and the number of incident surface muons per pulse N_μ. Relative values of pulse energy at 122 nm are determined from photoionization signal in NO gas. A single 122 nm beam was generated by focusing 212.5 nm beam with energy of 12 mJ and 820 nm beam with pulse energy of 13 mJ into the Kr–Ar cell. In this measurement the 122 nm beam was not retro-reflected and was instead absorbed in the NO gas cell. The energy of the 355 nm pulse measured at the output of the laser was 280 mJ.

Significant improvement (beyond an order of magnitude) of the Lyman-α pulse energy with the existing laser system is not currently envisaged. Our previous investigations have shown that process of Lyman-α generation in krypton gas is saturated [13] and gains achieved by compensating for the phase mismatch in krypton gas with argon gas are not as high as originally anticipated. Our measurements show that for the phase-matched Kr–Ar mixture the conversion efficiency from the UV beam at 212.5 nm is fixed at approximately the 10^{-4} level. For pulse energy E of the 212.5 nm beam in the range of 2–14 mJ the Lyman-α energy is increasing approximately as $E^{0.8}$. Therefore, further increase of Lyman-α energy and consequently a higher LE-μ^+ yield should be possible by increasing the pulse energy of the 212.5 nm beam. Further improvement of the LE-μ^+ yield can be also expected from an increase of the pulse energy of the 355 nm beam judging from the energy dependence of the LE-μ^+ yield shown in Fig. 6.

With the current laser parameters, the overall conversion efficiency including transport losses is 3×10^{-5} and about 15 μ^+/s are observed at the sample chamber – a significant improvement on our first result in 2001 of

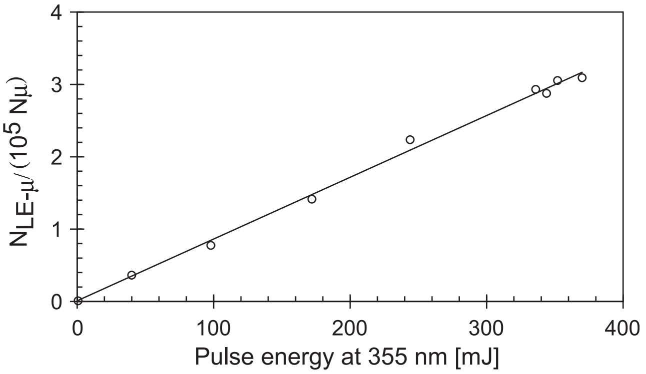

Fig. 6. Dependence of the overall efficiency of LE-μ^+ generation on the laser pulse energy at the wavelength of 355 nm. The laser pulse energy was measured at the output of the laser; the actual pulse energy at 355 nm delivered inside the ultrahigh vacuum system is about 35% lower due to absorption in air and losses on mirrors and optical windows. Estimated intensity of 355 nm beam inside the vacuum system is about 30 MW/cm^2 (at maximum laser output of 380 mJ) Compared to the measurement shown in Fig. 5, the muonium excitation to the 2P state was increased by using two 122 nm beams vertically separated by 15 mm that were retro-reflected by VUV mirror with reflectivity $R = 0.75$. Each of the 122 nm beams was generated from 9.0 mJ at 212.5 nm and 9.5 mJ at 820 nm.

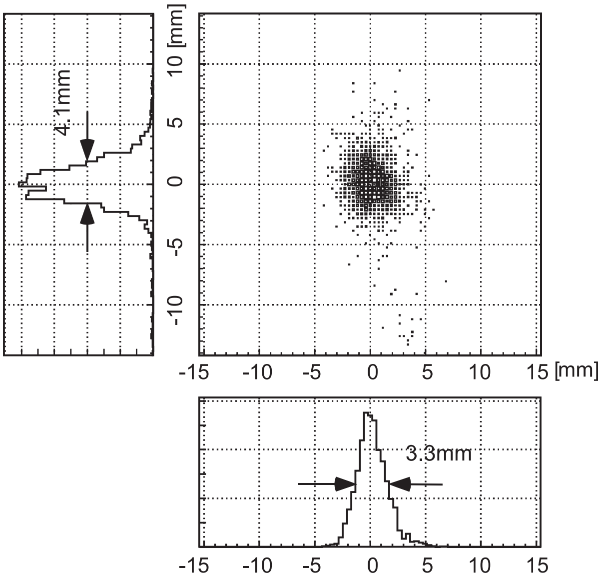

Fig. 7. Plot of the 9 keV LE-μ^+ beam spot at the sample position measured with a position-sensitive microchannel plate detector with a resolution of 0.5 mm.

0.03 μ^+/s [13]. This has allowed us to perform simple μSR experiments and demonstrate the feasibility of this method for pulsed muon sources.

Of as much importance as the LE-μ^+ rate is the capability to focus the muons into a small spot at the sample, since for the μSR investigations with the LE-μ^+ only small samples may be available. While the full-width at half-maximum (FWHM) diameter of the incident surface muon beam is 35 mm, the FWHM diameter of LE-μ^+ beam is about 10 times smaller. The beam spot was measured with a position-sensitive MCP (ROENTDEK DLD-40) placed at the sample position. The spot-size measured at the focus of the LE-μ^+ beam accelerated to 9.0 keV is shown in Fig. 7. Gaussian fitting in the horizontal and vertical directions yields FWHM of 3.3 mm and 4.1 mm, respectively.

3.2. Pulse duration

A particularly important advantage of using the short laser pulse to ionize muonium is the improvement of the muon pulse structure and the capability of having an external control over the triggering of the LE-μ^+. The surface muon beam at RIKEN-RAL has a double-pulse structure consisting of ~80 ns (FWHM) pulses separated by 320 ns. The short laser pulses ionizing muonium atoms are triggered with an optimum delay of about 400 ns relative to the surface muon pulse. This delay allows the muonium – having the mean thermal velocity of 20 mm/μs – to evaporate to a few millimetres away from the tungsten target and reach its maximum density in the laser beam volume. The arrival time of the muons at the sample is determined by the timing of the laser pulse plus a fixed delay corresponding to a time-of-flight (TOF) through the apparatus. As the muonium cloud is expanding relatively slowly, the laser timing and consequently the LE-muon timing can be varied around the optimum value by several hundred nanoseconds at the expense of the LE-μ^+ rate (the rate is approximately halved by delaying the muonium ionization by 400 ns relative to the optimum delay). As the laser itself can be externally triggered with 1 ns accuracy, this feature opens a possibility to perform new μSR measurements requiring precise triggering of the muon implantation and synchronization with pulsed sample excitation. The time of muon implantation relative to an external laser trigger is known to within the pulse width of the LE-μ^+ in the TOF spectrum, which is below 10 ns. This pulse width of the LE-μ^+ is completely independent of the complicated pulse structure of the surface muon beam and is determined primarily by the duration of the laser pulse and partly also by the acceleration voltage. The time-of-flight (TOF) spectrum measured at sample position for 9.0 keV muons is shown in Fig. 8.

3.3. Energy resolution

The generation of LE-μ^+ based on the laser ionization of thermal muonium makes it possible to generate beams with extremely narrow energy resolution, as the LE-μ^+ have kinetic energy of only 0.2 eV after ionization. This is significantly lower than the intrinsic energy resolution of the LE-μ^+ generated by moderation in van der Waals bound solids, where the epithermal muons escape the moderator with rms energy spread of about 15 eV. If the high energy resolution of the order of several eV can be maintained through re-acceleration, transport and deceleration up to the sample, ultra-thin films or surfaces could be studied using the μSR technique with ~1 nm resolution. The depth

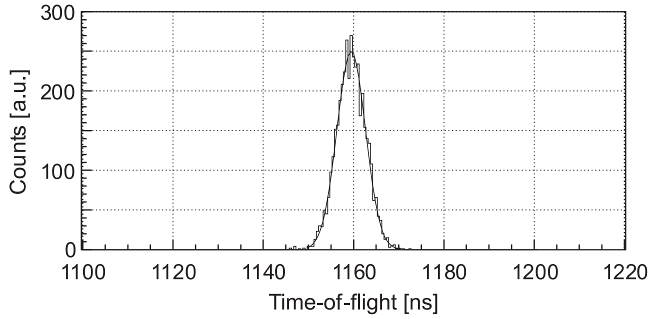

Fig. 8. Time-of-flight histogram of the 9.0 keV LE-μ^+ detected by microchannel plate detector at the sample position. Time zero corresponds to muonium ionization by the laser pulses. Gaussian fit to this histogram yields FWHM pulse duration of 7.5 ns.

resolution in the sample depends mainly on the density of the material and the muons' struggling in it. To give an example, for muons implanted in Al with a mean energy of 20 eV and a standard deviation of 10 eV, the calculation using the Monte Carlo code TRIM.SP [16,17] gives the mean penetration depth to be just 0.7 nm with a spread of 0.7 nm. Reducing the energy resolution below 10 eV, however, does not significantly reduce the width of the muon implantation profile as it is determined by muons' struggling in Al. In this respect the depth resolution of the order of 1 nm should be achievable by either method of LE-μ^+ generation but only using a pulsed muon beam. For continuous muons beams, such as available at PSI, it is necessary to determine the muon implantation time in order to construct the µSR spectrum. This requires inserting a thin foil into the LE-μ^+ beam and thus broadening the energy resolution at the sample to ~400 eV [10].

In our experimental setup achieving the energy resolution of several eV at the sample is possible. The energy variation of the re-accelerated LE-μ^+ depends on the differences in the potential seen by the individual muons at the point of laser ionization relative to the S1 electrode. The difference in electrostatic potential over the 14 mm gap between the tungsten foil and S1 is therefore kept low (at only 200 V). The differences in electrostatic potential seen by the individual muons are mainly arising due to:

(a) the width of the ionization region determined by the overlap of the Lyman-α and 355 nm beams (including the retro-reflected beams), which is of the order of 2 mm (FWHM), thus contributing to the standard deviation of the muon energy with ~13 eV;
(b) the uneven distance between tungsten foil and S1 arising from bending of the heated tungsten foil into the gap – this reduces the gap of 14 mm at the edges of the foil to ~12 mm at its centre – contributing to the standard deviation of the muon energy with ~4 eV;
(c) any differences in aligning the two Lyman-α beams at the same distance from S1 and parallel to S1 – also contributing to the energy variation with ~4 eV.

The effect of the pulse-to-pulse pointing stability of the laser beams is below 1 eV level. These contributions give an estimate of the energy resolution of the extracted LE-μ^+ as $\sigma_E = 14$ eV (33 eV at FWHM). The energy resolution can be improved by reducing the extraction field between the tungsten foil and S1 and possibly also by reducing the width of the interaction region, though this would make alignment of the retro-reflected Lyman-α beams more difficult.

3.4. Test µSR experiments

To demonstrate the feasibility of using the pulsed beam of LE-μ^+ for µSR measurements we have measured some simple muon spin precession spectra in transverse magnetic field. Despite the relatively low rate of 15 μ^+/s implanted into the sample, up to 10^6 positrons originating from the muon decay in sample ($\mu^+ \rightarrow e^+ + \nu_e + \bar{\nu}_\mu$) can be detected per day by the scintillation counters of our µSR spectrometer. The number of detected positrons as a function of time after the muon implantation in each of the detector pairs was recorded in eight histograms $N_i(t)$ ($i = 1,\ldots,8$). Let us assume for simplicity of the explanation that the muons are implanted into a metal, where muonium can not be formed, and subjected to a static magnetic field oriented perpendicular to the initial muon spin direction. The time dependence recorded in these histograms then corresponds to the exponential muon decay with the muon lifetime τ_μ modulated by the free muon spin precession with Larmor precession frequency ω_μ, and by the spin relaxation function $G(t)$ and can be expressed in the form

$$N_i(t) = N_{0i}e^{-t/\tau_\mu}[1 + A_\mu G_\mu(t)\cos(\omega_\mu t + \varphi_i)] + N_i^{BG}(t) \quad (i = 1,\ldots,8), \tag{1}$$

where N_{0i} is normalization constant for each of the detector pairs. The initial phases φ_i are fixed by the geometry to the initial phase φ_1 ($\varphi_i = \varphi_{i-1} + \pi/4$ for $i = 2,\ldots,8$). The background contribution and $N_i^{BG}(t)$ to the signal can in our setup be determined from every second muon pulse when laser is off and the low energy muons are not incident on the sample. The spin relaxation function depends on the distribution of the local magnetic fields seen by the implanted muons. For example, if local fields have a Lorentzian distribution then $G_\mu^L(t) = e^{-\lambda t}$. Simultaneous fitting of all eight histograms then allows determining the parameters ω_μ, λ and the initial amplitude of the precession signal A_μ, the so-called diamagnetic asymmetry. It follows from the angular distribution of the positrons originating from the muon decay that the maximum value of A_μ when integrated over all positron energies is equal to 1/3 if the implanted muons are initially 100% spin polarized. The asymmetry values in the vicinity of 0.2–0.25 are typical for µSR instruments, depending on the setup.

The LE-μ^+ generated by the ionization of muonium, however, are only 50% spin polarized and the asymmetry is therefore expected to be half of the value typical for other µSR instruments. This polarization loss is a result of the interaction with the electron spin in the muonium atom. The muonium bound state is formed with equal probabilities for the muon and electron spins to be either parallel (ortho-muonium) or anti-parallel (para-muonium). In the case of anti-parallel spins, the hyperfine interaction causes rapid depolarization of the initial muon spin [18,19] and hence only half of the low energy muons obtained by the muonium ionization are spin polarized.

In our first experiment we have implanted LE-μ^+ with energy of 9 keV into a 20 mm diameter silver sample at room temperature. The initial diamagnetic asymmetry A_μ determined by fitting the data from the eight detector pairs was $A_\mu^{\rm Ag} = 10.11 \pm 0.23\%$ with no observable spin depolarization ($G(t) = 1$).

In order to visualize the muon spin precession signal we have divided the detectors into two opposing groups of four detectors and added the positron signals in each group into one histogram and subtracted the background signal determined from the “laser off” data. The μSR asymmetry spectrum from these two histograms $N_{G1}(t)$ and $N_{G2}(t)$ is plotted in Fig. 9 simply as

$$a_0(t) = \frac{N_{G1}(t) - N_{G2}(t)}{N_{G1}(t) + N_{G2}(t)}. \qquad (2)$$

The amplitude of the oscillations determined from these two histograms is consistent with multiplying the initial diamagnetic asymmetry A_μ by a geometrical factor of 0.653, reflecting the fact that positron signal is integrated over an angle of π rather than π/4 radians.

In our next test experiment we have used the pulsed LE-μ^+ beam for depth-resolved μSR measurement analogous to the measurements of Morenzoni et al. [17] of a thin metallic film sample coated on an insulator. The purpose of the experiment was to demonstrate the control over the implantation energy and the mean implantation depth. The principle of the experiment is described in detail by Morenzoni et al. [17] and relies on the fact that the stopping site of muons can be determined from the amplitude of the spin precession signal of the “free” diamagnetic muon (diamagnetic asymmetry) in the sample. The muons that penetrate through the metallic layer and thermalize in the insulator substrate will mostly form muonium. For the half of the muons that form para-muonium the polarization will be rapidly lost due to the hyperfine interaction and for the rest that forms ortho-muonium the transitions between muonium triplet states in a weak transverse magnetic field B will yield a single Larmor precession frequency of $\omega_{\rm Mu} = 87.619\ {\rm Mrad/mT} * B$, about 100 times faster than the muon precession of $\omega_\mu = 0.852\ {\rm Mrad/mT} * B$. By choosing the field B sufficiently large, so that $2\pi/\omega_{\rm Mu}$ is much shorter than the binning interval of the positron decay histogram, the muonium spin precession signal can be averaged out. The muons that formed muonium will then show in the measured signal as a loss of the diamagnetic asymmetry, which will be reduced proportionally to reflect the remaining number of diamagnetic muons in the sample.

Our sample, placed at the focus of the LE-μ^+ beam (~4 mm FWHM), was an optically flat SiO_2 substrate, 20 mm in diameter, coated by sputtering with a pure Al layer with a nominal thickness of 40 nm. The experiment was performed at the room temperature under UHV conditions at a pressure of $\approx 10^{-9}$ hPa in a 4 mT (40 G) external magnetic field transverse to the muon spin.

The implantation profile for muons – taking into account the muon energy, the incidence angle and the sample density – can be accurately calculated using the Monte Carlo code TRIM.SP. Fig. 10 shows the calculated implantation profiles in the sample for several implantation energies.

Fig. 11 shows the measured initial amplitude of the diamagnetic muon precession (diamagnetic asymmetry) as a function of the muon implantation energy. This measured dependence is in a good agreement with the calculated fraction of diamagnetic muons using the TRIM.SP program. The measured asymmetry is a sum of contributions from diamagnetic muons that have thermalized in the Al layer and from the small fraction of muons in the SiO_2 substrate that did not form muonium; there is also a small background contribution from muons that thermalized in any metal parts outside the sample, e.g. in the metal ring holding the edges of the sample. For muons that penetrate the

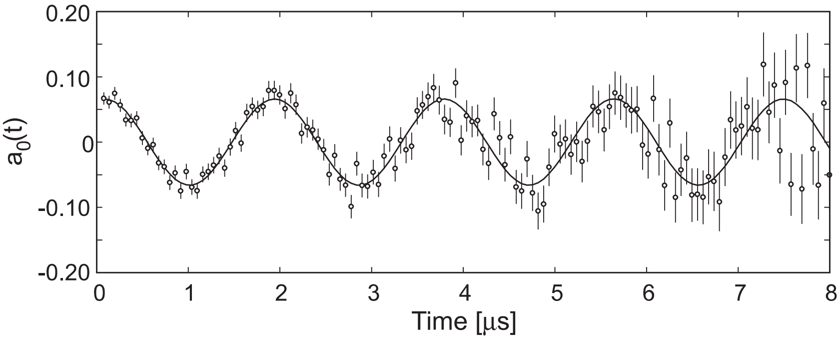

Fig. 9. Muon spin precession signal measured in pure Ag sample with 9 keV LE-μ^+. The signal represents asymmetry in the positron decay spectrum observed between two opposing groups of four detectors. Since the signals from four detectors in each group were added into one histogram the amplitude of the oscillations reflecting the spin precession of μ^+ is effectively reduced. The diamagnetic asymmetry A_μ as defined in Eq. (1) for eight individual detectors can be obtained by dividing the amplitude of the spin precession signal shown here by a factor of 0.653.

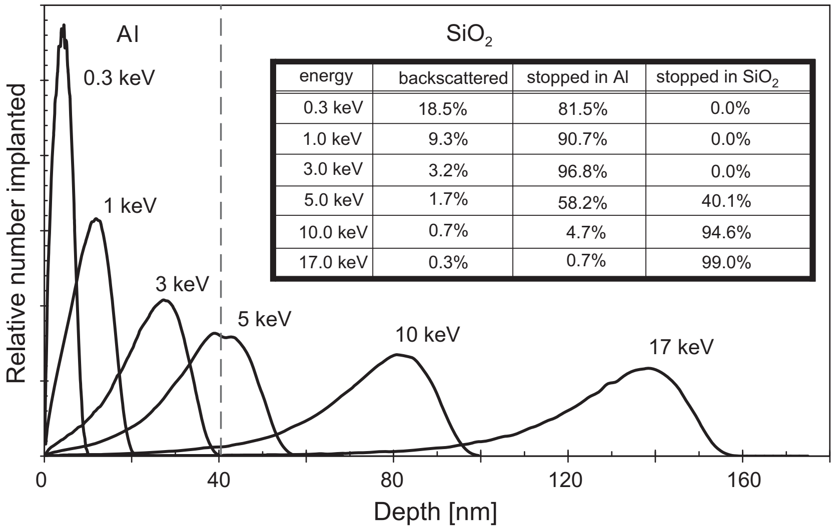

energy	backscattered	stopped in Al	stopped in SiO$_2$
0.3 keV	18.5%	81.5%	0.0%
1.0 keV	9.3%	90.7%	0.0%
3.0 keV	3.2%	96.8%	0.0%
5.0 keV	1.7%	58.2%	40.1%
10.0 keV	0.7%	4.7%	94.6%
17.0 keV	0.3%	0.7%	99.0%

Fig. 10. The implantation profiles for LE-μ^+ in 40 nm thick Al layer on SiO$_2$ substrate calculated for different implantation energies using TRIM.SP code. Calculation assumes narrow Gaussian energy distribution of the incident muons with a standard deviation of $\sigma_E = 14$ eV and the incidence angle being perpendicular to the sample surface with $\sigma_\alpha = 5$.

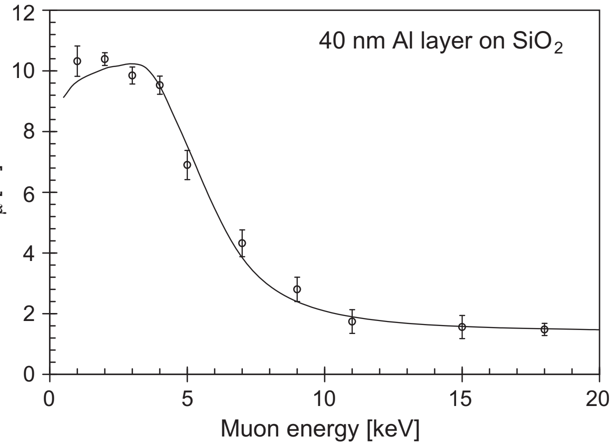

Fig. 11. Energy dependence of the asymmetry of the diamagnetic muon A_μ measured in SiO$_2$ sample coated with 40 nm thick Al layer. For muon implantation energies below 4 keV the muons are mostly stopped in Al layer and remain as free muons and consequently the measured asymmetry approaches the maximum observable asymmetry $A_{\max}$ of the μSR spectrometer. With increasing implantation energy, the muons penetrate into SiO$_2$ substrate (see Fig. 10) where most of the stopped muons form muonium. This results in proportional loss of the measured diamagnetic asymmetry A_μ. The solid line is the expected energy dependence of A_μ derived from the muon stopping profiles calculated using the TRIM.SP code.

SiO$_2$ with residual energy below 5 keV there remains a relatively large fraction that does not form muonium and the diamagnetic asymmetry contribution from the SiO$_2$ substrate is therefore energy dependent. We have used this energy dependence $A_{\mathrm{SiO_2}}(E)$ measured in [[17] (Fig. 8)] to determine the contribution from free diamagnetic muons in the SiO$_2$ substrate to the measured asymmetry. The mean residual energies of muons after passing through the 40 nm Al layer as well as the numbers of muons implanted to SiO$_2$ and Al layer were calculated using the TRIM.SP code for 10^5 incident LE-μ^+. In the calculation we have assumed standard deviation of the incident muon energy to be $\sigma_E = 14$ eV and the standard deviation of the incidence angle from the normal incidence to be $\sigma_\alpha = 5°$. We have included in the calculation small thickness variation of the Al layer with a standard deviation of 2 nm. We have not considered any Al$_2$O$_3$ oxide layer that might have formed on the surface of the sample as we have seen no reduction of the measured asymmetry for low implantation energies. The TRIM.SP calculation predicts reflection of a fraction of muons at low incident energies (about 9% of the total at 1 keV and as much as 30% at 0.1 keV). Upon reflection there is a high probability that the muon captures an electron and forms muonium and this should result in a corresponding reduction of the measured diamagnetic asymmetry. We have not, however, seen this reduction for muons implanted at energy of 1 keV, given the low statistics we have accumulated for this data point.

The background contribution to the asymmetry from the muons stopping in metal parts outside the sample was determined from the diamagnetic asymmetry of $1.5 \pm 0.2\%$ measured at 18 keV. At this energy all of the incident muons are implanted in SiO$_2$, where about 0.09 ± 0.01 of them will remain as diamagnetic muons [17] contributing to the asymmetry with $1.0 \pm 0.1\%$. The background contribution to the measured asymmetry is then estimated to be $0.5 \pm 0.2\%$, corresponding to about 0.045 of the incident muons stopping outside of the 20 mm diameter of the sample.

It should be noted that at room temperature the muons implanted in the Al layer will rapidly diffuse throughout the metal layer, but not necessarily into the SiO$_2$ substrate. For the muon energies in the range of 1–4 keV, when most of the muons are implanted into the Al layer, we have observed a small spin relaxation rate $\lambda = 0.10\ \mu s^{-1}$

independent of the implantation energy (within our experimental error). It was found by measurements in bulk Al that pure Al gives rise to no depolarization in the temperature range of 0.1–300 K [20]. Our own measurements with 18 keV muons implanted into a 500 nm thick pure Al sample at room temperature also show minimal relaxation rate $\lambda = 0.03 \pm 0.02\ \mu s^{-1}$. The small relaxation observed in our 40 nm thick Al layer is therefore most likely related to a small fraction of muons diffusing across the Al/SiO$_2$ interface. The structural disorder and imperfections at the layer interface in samples prepared by sputtering significantly hinder the diffusion across the interface, as was observed for the Cr/Au interface prepared by sputtering [21].

The short pulse duration of the LE-μ^+ generated by the laser ionization of muonium allows us to measure very high precession frequencies and extend the dynamic range for pulsed µSR to measure processes on a timescale ranging from nearly 10 ns to more than 10 µs. For a Gaussian pulse shape with FWHM width of τ_p the amplitude A of the harmonic component at frequency f will reduce by a factor

$$\frac{A(f)}{A(0)} = \exp(-\frac{\pi^2\tau_p^2 f^2}{4\ln 2}). \tag{3}$$

We have measured this frequency response using the orthomuonium spin precession signal in a transverse field of up to 3 mT (30 G). LE-μ^+ with energy of 15 keV were implanted into the Al (40 nm) coated SiO$_2$ sample. If the positron decay time histograms are binned in intervals shorter than $2\pi/\omega_{Mu}$ the fitting function (Eq. (1)) has to include an additional term describing the muonium spin precession

$$\begin{aligned} N_i(t) = {} & N_{0i}e^{-t/\tau_\mu}[1 + A_\mu G_\mu(t)\cos(\omega_\mu t + \varphi_i) \\ & + \frac{A_{Mu}}{2} G_{Mu}(t)\cos(\varpi_{Mu} t + \varphi_i^{Mu})] \\ & + N_i^{BG}(t) \quad (i = 1, \ldots, 8), \end{aligned} \tag{4}$$

where the amplitude of the muonium precession signal is written in the usual convention as one half of the initial muonium asymmetry A_{Mu}, since the other half of the muonium asymmetry is not observed due to fast depolarization. On implantation, the sum of A_μ and A_{Mu} must equal the maximal experimentally observable asymmetry A_{max} which we have determined from our measurement of diamagnetic asymmetry in pure metal sample ($A_{max} = A_\mu^{Ag} = 10.11 \pm 0.23\%$). As we have determined in the measurements shown in Fig. 11, the diamagnetic asymmetry from the free diamagnetic muons at 15 keV is $1.56 \pm 0.38\%$, the expected muonium asymmetry A_{Mu} is then $8.55 \pm 0.44\%$. The ratio of the observed muonium asymmetry and the expected muonium asymmetry is then plotted against the muonium precession frequency in Fig. 12. As expected from the short duration of the LE-μ^+ pulse, fast spin precession frequencies and fast relaxation rates can be observed; although this is admittedly limited by the relatively low count rate. With about 10^6 muon decay events detected, the muonium spin precession at 28 MHz could be clearly observed with muonium asymmetry reduced by 25% compared to the asymmetry measured at low frequency. By fitting the measured data points with frequency dependence according to Eq. (3) the pulse width τ_p can be determined as $\tau_p = 12.7 \pm 2.0$ ns. This value is somewhat higher than the LE-μ^+ pulse duration determined from the time-of-flight spectrum (Fig. 8) as it also includes various optical and electronics delays involved in detecting the positrons from the muon decay in the µSR spectrometer.

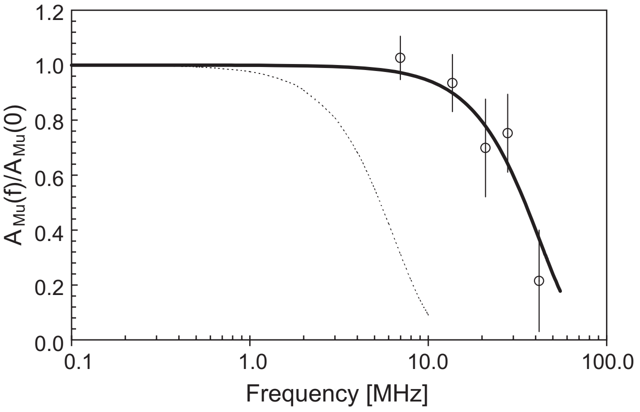

Fig. 12. Frequency response plot of the LE-μ^+ µSR apparatus as measured using muonium spin precession signal in SiO$_2$ sample. The data points show the ratio of the measured muonium asymmetry to the expected muonium asymmetry obtained for several precession frequencies from 7 MHz up to 42 MHz. The solid line represents fit to the data points with frequency dependence according to Eq. (3) yielding $\tau_p = 12.7 \pm 2.0$ ns. For comparison, the dotted line shows the frequency response for $\tau_p = 82$ ns, equivalent to FWHM duration of the ISIS surface muon pulse.

4. Conclusions

An experimental setup has been constructed at RIKEN-RAL muon facility to perform depth-resolved µSR measurements on nanometre scale with pulsed ultra low energy muons. Several µSR experiments have been carried out to demonstrate the characteristics of the apparatus. The parameters of the pulsed low energy muon beam are summarised in Table 2. The efficiency of the surface muon beam cooling to eV level is comparable to the method using the cryogenic moderator (of $\sim 3 \times 10^{-5}$). The efficiency of thermal muonium production is, however, of the order of 10^{-2}. As Figs. 5 and 6 demonstrate, the laser pulse energy is not yet sufficient to ionize all muonium atoms, even though the laser beams overlap only a small fraction of the generated thermal muonium cloud. Therefore, there is a clear prospect that with development of a new and more intense VUV laser source, the efficiency of LE-μ^+ production could be increased by up to two orders of magnitude. The muonium ionization method of LE-μ^+ generation has distinct advantages for pulsed operation. The LE-μ^+ implantation in the sample can be externally triggered with nanosecond accuracy that makes it possible to perform µSR experiments where the muon implantation is synchronised with a sample

Table 2
Present characteristics of the pulsed LE-μ^+ beam and of the μSR spectrometer

Low energy muon beam parameters	
Intensity at sample	15 μ^+/s
Beam spot diameter at sample	4 mm (FWHM)
Energy at W target region	0.2 eV
Energy after reacceleration	0.1–18 keV
Energy uncertainty after reacceleration	$\sigma_E \approx 14$ eV
Pulse repetition rate	25 Hz
Pulse duration in TOF spectrum at 9.0 keV	7.5 ns (FWHM)
μ^+ spin polarization	≈50%
μSR spectrometer parameters	
Solid angle covered by detectors	80% of 4π sr
Maximum instrumental asymmetry of μSR spectrometer	10.1%
Maximum measurable spin precession frequency	≈40 MHz
Sample cryostat temperature range	10–300 K
Transverse magnetic field range	0–60 mT
Zero field compensation	≈0.1 μT

excitation. The LE-μ^+ pulse duration is reduced to only 7.5 ns (measured at FWHM), which is in fact as short as the time resolution for the LE-μ^+ implantation at continuous muon source [22]. This short pulse duration is independent of the initial pulse structure of the incident surface muon beam, which would be of particular advantage if this method of LE-μ^+ generation was used at the new J-PARC Muon Science Facility where each muon pulse will consist of two bunches each of 100 ns duration and separated by as much as 600 ns [23].

Acknowledgements

The authors would like to thank F. Pratt for his advice on analysing the data from μSR measurements and his keen interest in our experiments. We are also very grateful to E. Morenzoni and W. Eckstein for kindly providing us with the TRIM.SP code. We are also indebted to R. Scheuermann for his contribution to the construction of the ion beamline. The construction of this low energy muon facility was possible due to large financial support of KEK-MSL and UT-MSL (for purchasing the high power lasers and ion optics), and of RIKEN (for construction and operational costs). This research was partially supported by the Grant-in-Aid for Scientific Research (A)16206005, (B)11559019, (C)11650052 and Grant-in-aid for Exploratory Research 16656295 by the Ministry of Education, Culture, Sports, Science and Technology of Japan.

References

[1] S.J. Blundell, Spin-polarized muons in condensed matter physics, Contemp. Phys. 40 (1999) 175.

[2] Special issue on μSR: muon spin rotation, relaxation or resonance, in: R.H. Heffner, K. Nagamine, (Eds.), J. Phys.: Condens. Matter, 16 (2004).

[3] K. Nagamine, Y. Miyake, K. Shimomura, P. Birrer, J.P. Marangos, M. Iwasaki, P. Strasser, T. Kuga, Ultraslow positive-muon generation by laser ionization of thermal muonium from hot tungsten at primary proton beam, Phys. Rev. Lett. 74 (1995) 4811.

[4] D.R. Harshman, A.P. Mills Jr., J.L. Beveridge, K.R. Kendall, G.D. Morris, M. Senba, J.B. Warren, A.S. Rupaal, J.H. Turner, Generation of slow positive muons from solid rare-gas moderators, Phys. Rev. B 36 (1987) 8850.

[5] E. Morenzoni, F. Kottmann, D. Maden, B. Matthias, M. Meyberg, Th. Prokscha, Th. Wutzke, U. Zimmermann, Generation of very slow polarized positive muons, Phys. Rev. Lett. 72 (1994) 2793.

[6] K. Träger et al., Production of pulsed ultra slow muons and first μSR experiments on thin metallic and magnetic films, Physica B 289–290 (2000) 662.

[7] E. Morenzoni, T. Prokscha, A. Suter, Applied muon science: novel perspectives in nano-science, Nucl. Phys. B (Proc. Suppl.) 149 (2005) 73.

[8] T. Prokscha, E. Morenzoni, C. David, A. Hofer, H. Glückler, L. Scandella, Moderator gratings for the generation of epithermal positive muons, Appl. Surf. Sci. 172 (2001) 235.

[9] T. Matsuzaki, K. Ishida, K. Nagamine, I. Watanabe, G.H. Eaton, W.G. Williams, The RIKEN-RAL pulsed muon facility, Nucl. Instr. and Meth. A 465 (2001) 365.

[10] P. Bakule, E. Morenzoni, Generation and applications of slow polarized muons, Contemp. Phys. 45 (2004) 203.

[11] Y. Miyake, K. Shimomura, S. Makimura, Y. Matsuda, P. Bakule, K. Nagamine, Ultra-sensitive detection of hydrogen isotopes by Lyman-α RIS, J. Nucl. Sci. Technol. 39 (2002) 287.

[12] J.P. Marangos, N. Shen, H. Ma, M.H.R. Hutchinson, J.P. Connerade, Broadly tuneable vacuum-ultraviolet radiation source employing resonant enhanced sum-difference frequency mixing in krypton, J. Opt. Soc. Am. B 7 (1990) 1254.

[13] P. Bakule, Y. Matsuda, Y. Miyake, P. Strasser, K. Shimomura, S. Makimura, K. Nagamine, Slow muon experiment by laser resonant ionization method at RIKEN-RAL muon facility, Spectrochim. Acta B 58 (2003) 1019.

[14] K.F. Canter, P.H. Lippel, W.S. Crane, A.P. Mills Jr., in: A.P. MillsJr., W.S. Crane, K.F. Canter (Eds.), Positron Studies of Solids, Surfaces, and Atoms, World Scientific, Singapore, 1984, p. 199.

[15] J.A.R. Samson, D.L. Ederer, Vacuum ultraviolet spectroscopy, Experimental Methods in the Physical Sciences, Academic Press, London, 2000.

[16] W. Eckstein, Computer Simulation of Ion–Solid Interaction, Springer, Berlin, 1991.

[17] E. Morenzoni, H. Glückler, T. Prokscha, R. Khasanov, H. Luetkens, M. Birke, E.M. Forgan, Ch. Niedermayer, M. Pleines, Implantation studies of keV positive muons in thin metalic layers, Nucl. Instr. and Meth. B 192 (2002) 254.

[18] V.W. Hughes, D.W. McColm, K. Ziock, R. Prepost, Muonium. I. Muonium formation and larmor precession, Phys. Rev. A 1 (1970) 595.

[19] M. Senba, Spin dynamics of positive muons during cyclic charge exchange and muon slowing down time, J. Phys. B 23 (1990) 1545.

[20] K.W. Kehr, D. Richter, J.-M. Welter, O. Hartmann, E. Karlsson, L.O. Norlin, T.O. Niinikoski, A. Yaouanc, Muon diffusion and trapping in aluminum and dilute aluminum alloys: Experiments and comparison with small-polaron theory, Phys. Rev. B 26 (1982) 567.

[21] H. Luetkens, J. Korecki, E. Morenzoni, T. Prokscha, N. Garif'yanov, H. Glückler, R. Khasanov, F.J. Litterst, T. Slezak, A. Suter, Diffusion of muons in metallic multilayers, Physica B 326 (2003) 545.

[22] T.K. Paraïso, E. Morenzoni, T. Prokscha, A. Suter, Geant4 simulation of low energy μSR experiments at PSI, Physica B 374–375 (2006) 498.

[23] Y. Miyake et al., J-PARC Muon Science facility with use of 3 GeV proton beam, Nucl. Phys. B (Proc. Suppl.) 149 (2005) 393.

PHYSICAL REVIEW SPECIAL TOPICS - ACCELERATORS AND BEAMS **11**, 064201 (2008)

Particle tracking study of the injection process with field interferences in a rapid cycling synchrotron

M. J. Shirakata, H. Fujimori, and Y. Irie
KEK, Oho 1-1 Tsukuba, Ibaraki 305-0801, Japan

T. Takayanagi
Japan Atomic Energy Agency, Tokai-mura, Naka-gun, Ibaraki 319-1195, Japan

(Received 2 October 2006; revised manuscript received 1 July 2007; published 4 June 2008)

The large-bore magnets in the injection system of a high-intensity proton synchrotron are placed close to each other as compared to their bore sizes. In such cases, the magnetic cores interfere with the fringe fields of adjacent magnets. Moreover, the incoming beam passes through several kinds of time-varying fields along the injection line and the nonlinear field region of the ring quadrupole magnet. The beam behavior under these conditions is analyzed by using the Runge-Kutta method. Although the interference of the magnetic fields does not result in emittance growth, it produces a closed-orbit distortion. Field fluctuations of the time-varying field cause an emittance growth and the nonlinear field deforms the beam profile in phase space of the incoming beam. These effects lead to the modification of the injection scheme. This study focuses on the particle tracking with magnetic field interferences during the early stage of beam commissioning, when the space charge force is not important.

DOI: 10.1103/PhysRevSTAB.11.064201 PACS numbers: 41.85.Ar, 41.75.−i, 29.27.−a

I. INTRODUCTION

The rapid cycling synchrotron (RCS) of the Japan Proton Accelerator Research Complex (J-PARC) [1] is designed to have a very large transverse acceptance of 324π mm mrad in order to achieve beam power in the order of megawatts. The main parameters of the RCS are listed in Table I. The drift spaces between the magnets are short as compared to the bore radius of quadrupoles and the gap height of dipoles. The magnetic fringe fields interfere with each other especially at the beam-injection area where the magnetic components are installed at short distances. Moreover, the injected beam passes through the regions where the linearity of the magnetic field is not preserved. These contributions to the painting beam injection of the J-PARC RCS were investigated.

The beam-injection line in the J-PARC RCS is shown in Fig. 1. The Cartesian right-hand coordinate system (x, y, z) is adopted in the orbit tracking, and its z axis is defined as the central orbit of the ring in this area. The beam from the LINAC is injected into the ring by using the charge exchange and phase-space painting methods in order to accumulate the high-intensity protons. Two orbit-bump systems are prepared [2,3]. One is the shift-bump system to form an orbit offset of $x = 90$ mm at the carbon-stripping foil, and the other is the paint-bump system for the beam painting. The shift-bump system produces a flat-top field during the entire injection period. On the other hand, the paint-bump system has a time dependence for painting the RCS beam in the phase space of 216π mm mrad with an injected beam of 6π mm mrad. The injection process continues for approximately 320 turns. Each bump system has four bump magnets, which are called SB1, SB2, SB3, and SB4 in the shift-bump system, and PB1, PB2, PB3, and PB4 in the paint-bump system. A carbon-stripping foil is placed between SB2 and SB3. The foil position is defined as the injection point. A similar injection system has been designed in the Spallation Neutron Source (SNS) project in Oak Ridge National Laboratory (ORNL) [4,5].

The field-data preparation is described in Sec. II. The particle-tracking procedure is introduced in Sec. III. Results and discussions are presented in Sec. IV. Finally, the conclusion is given in Sec. V.

II. FIELD INTERFERENCE

A. Magnetic fields of the injection area

The magnetic fields of bump magnets and quadrupoles interfere with the neighboring magnetic materials because the distance between the magnets is not sufficiently long as compared to their apertures. In such a case, two or more

TABLE I. Main parameters of J-PARC RCS.

Parameter	Value	Unit
Circumference	348.333	[m]
Average radius	55.44	[m]
Injection energy	0.181/0.4	[GeV]
Ejection energy	3.0	[GeV]
Tune	$(\nu_x, \nu_y) = (6.680, 6.270)$	
Physical aperture	$>486\pi$	[mm mrad]
Collimation	324π	[mm mrad]
Painting area	216π	[mm mrad]
Injected beam	(unnormalized full) 6π	[mm mrad]

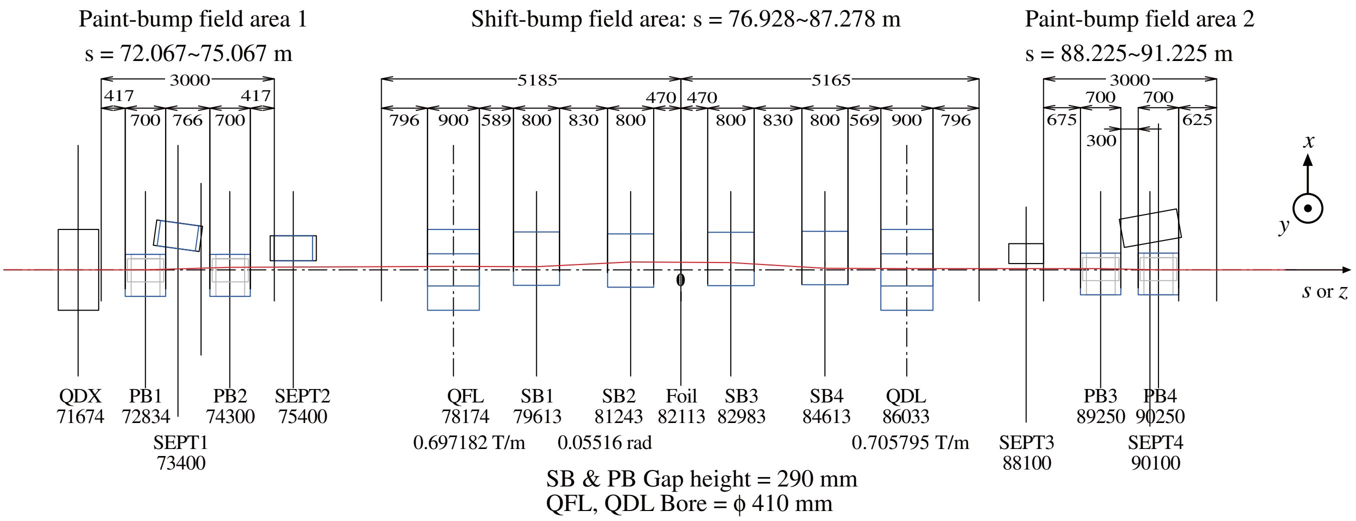

FIG. 1. (Color) Layout of the beam-injection line in the J-PARC RCS. The element positions and lengths are presented in [mm]. The s axis is along the designed beam orbit. In a straight section of the ring, the s and z axes are identical.

magnets are treated as a whole system. The magnetic field is calculated by using the magnet design code OPERA-3D [6]. The field calculations are performed at a time for the shift-bump field area, where the area is defined from $s = 76.928$ to $s = 87.278$ m; the area includes four dipole magnets and two quadrupole ones as shown in Fig. 1. The analysis procedure requires the division of the target object into small pieces. Figure 2 shows the broad mesh design of the magnets for the complex dipole and quadrupole system. First, all the vertices of the magnets must coincide with the mesh points. Then, the sizes of the mesh should be small enough as compared to the field variation. It is possible to satisfy these conditions by defining a sufficiently small mesh size. On the other hand, the number of elements that can be treated at a time is limited by the memory size and time required for calculation. This is the main difficulty with the magnetic field calculation. In order to reduce the number of elements required for the calculation, the mesh size along the z (or s) axis should be set larger than the sizes in the x and y directions. The maximum mesh sizes were determined to be 10 mm for the x and y directions and 100 mm for the z direction. The reliability of the calculated field was confirmed with a more precise analysis, which uses meshes with a maximum size of 25 mm for the z direction.

OPERA-3D produces a lattice-structured field-data file. The lattice lengths of the field data also have to be short as compared with the shape of the magnetic field. The field data were sampled in steps of 10 mm for the x and y directions and in step of 25 mm for the z direction.

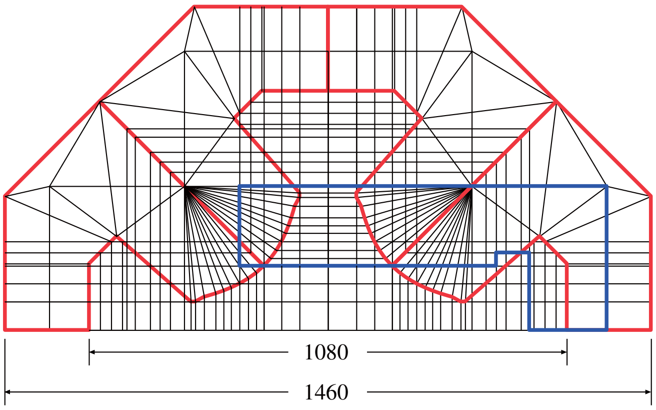

FIG. 2. (Color) Cross-sectional view of the magnet mesh design for the complex dipole and quadrupole system. The yoke shape of the dipole and quadrupole magnets are shown by blue and red lines, respectively. Black lines show the broad blocks of analysis. Moreover, these blocks are divided into smaller pieces when the field calculation is performed (units in mm).

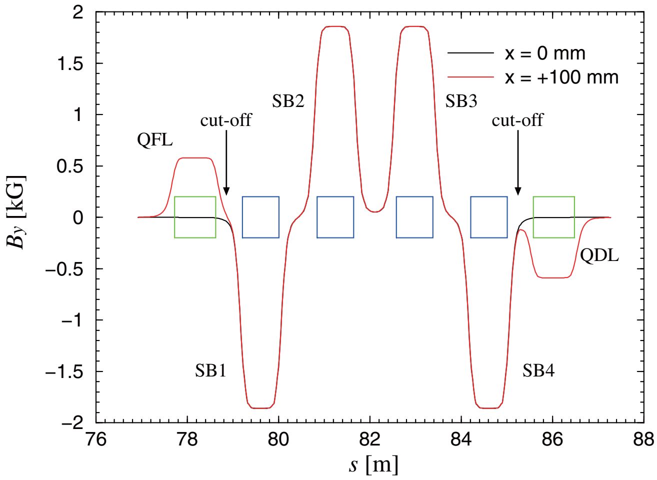

FIG. 3. (Color) B_y distribution in the shift-bump field area at $x = 0$ and $+100$ mm with $y = 0$. The cutoffs are introduced in order to distinguish the dipole field from the quadrupole field.

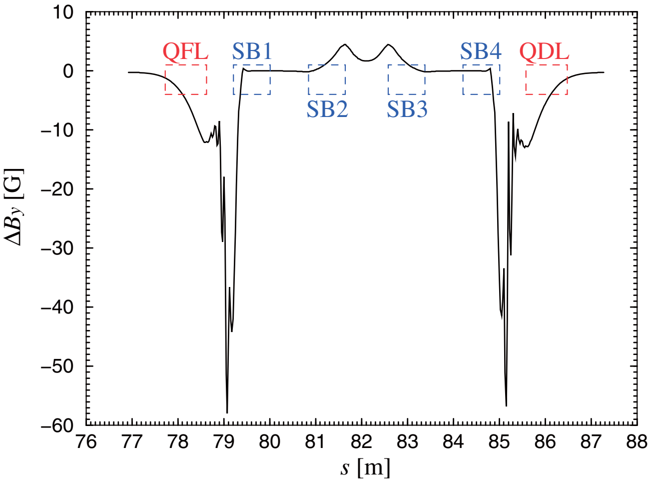

FIG. 4. (Color) Magnetic field difference between the two methods of field calculations at $x = y = 0$. The whole-system calculation result was subtracted from the sum of the individual calculations of an isolated system.

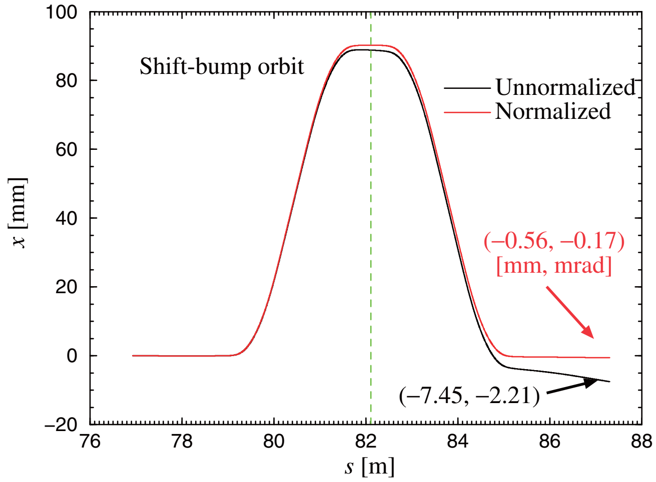

FIG. 5. (Color) Central orbit trajectory in the shift-bump area, which began from $x = y = 0$. The black line shows the orbit of a test particle with the unnormalized field data, the red line shows the case after the Bl normalization, and the green dashed line indicates the stripping foil position ($s = 82.113$ m).

Figure 3 shows the magnetic field component B_y given by OPERA-3D using the whole-system calculation method. Because every bump field is time dependent, they should contain the sextupole and other higher-order multipole components which are induced by eddy currents. However, the horizontal aperture of bump magnets is large, and the effects on beam by the sextupole or higher-order multipole components are negligible. The bump field was then calculated as a static field for simplicity. The black line of $x = y = 0$ mm shows only the shift-bump field, where there is no contribution from the quadrupole field. The field interference between the shift-bump magnets can be observed. The magnetic field between SB1 and SB2 and that between SB3 and SB4 falls sharply to zero. On the other hand, the magnetic field between SB2 and SB3 does not decrease to zero because there are two fringe fields overlapping in the same direction. The red line of $x = 100$ mm shows the quadrupole-field contribution. As shown in Fig. 4, the superposition of the individual fields of each magnet does not reproduce the result of the whole-system calculation, even if the mesh sizes used in the field calculation by OPERA-3D are the same for both methods. The dipole field is diverted into the quadrupole magnet core particularly near the quadrupole magnets, thereby resulting in a big difference. Preliminary simulation studies by particle tracking using interfered fields were presented in some reports [7–9] and such a field interference is also investigated for the SNS design [10].

TABLE II. Bl values of the shift-bump magnets at the central position: $x = y = 0$. Designed value = 0.175 59 Tm.

Name	Bl [Tm]
SB1	0.173 73
SB2	0.175 48
SB3	0.175 51
SB4	0.173 65

B. Normalization of the magnetic fields

The shift-bump magnets SB1 to SB4 have the same design and are connected in series so as to form a local bump orbit. The field integral Bl along the z axis of each magnet should ideally have the same value; however, due to the field interferences discussed above, it is necessary to modify the bump fields in order to obtain the required kick angles. The interval for the field integration is defined as the region between the zero cross point and local minimum for SB2 and SB3, and the region between the zero cross point and the tail end for SB1 and SB4. The Bl values thus obtained at $x = y = 0$ are listed in Table II. The Bl's for SB1 and SB4 are 1% smaller than those for SB2 and SB3 due to the field interference. Particle tracking with imbalanced fields was performed, and the imbalance of the Bl values causes an orbit distortion, as shown in Fig. 5. While the test particle with $x = x' = 0$ and $y = y' = 0$ starts at the entrance of the shift-bump area, it does not return to its original coordinates at the exit due to the imbalance. Such

TABLE III. Central orbit trajectory with the shift-bump system before and after the Bl normalization at the foil position ($s = 82.113$ m) and at the exit of the shift-bump field area ($s = 87.278$ m). Test particle starts from $x = x' = 0$ and $y = y' = 0$.

	x (foil) [mm]	x' (foil) [mrad]	x (exit) [mm]	x' (exit) [mrad]
Unnormalized	88.83	−0.60	−7.45	−2.21
Normalized	90.26	−0.05	−0.56	−0.17

TABLE IV. Bump-orbit summaries at the injection point ($s = 82.113$ m) with the shift-bump and paint-bump fields.

	x (design) [mm]	x' (design) [mrad]
Shift-bump	90.26 (90.00)	-0.05 (0.00)
Paint-bump	41.09 (41.00)	-5.51 ($-$ 5.50)
Both	131.44 (131.00)	-5.51 ($-$ 5.50)

an imbalance can be corrected by increasing the gap height of SB2 and SB3 by inserting a thin insulating sheet into the vertically splitting plane of the return yoke. In the calculation, however, the field strength of each region was scaled to give the design Bl value for simplicity. The result with this normalization is also shown in Fig. 5 and in Table III where the residuals of closed-orbit distortion (COD) are negligibly small. In order to distinguish the dipole field of SB1 and SB4 from the quadrupole field, the tail-end field facing the quadrupole magnet is discarded by introducing a "cutoff." The position of the cutoff is defined as a zero cross point of B_y with the quadrupole field at $x = +100$ mm for the QFL and $x = -100$ mm for the QDL. Although these cutoffs discard the tails of the shift-bump field from SB1 and SB4, the effect on the central orbit trajectory is negligible. The orbit deviations are less than 0.1 mm both at the top of the bump orbit and at the returning point, in comparison with 90.26 and -0.56 mm, respectively. With the shift-bump and paint-bump magnets in operation, Table IV summarizes the calculated bump orbit in comparison with the designed value. The paint-bump magnet fields were also normalized similarly.

In actual operations, a small amount of orbit distortion may remain even after the gap height adjustment. The decay time of the shift-bump orbit is too short for the ordinary orbit correctors to make up for the residual COD. The paint-bump magnets can be used for such a fast orbit correction if necessary, because they are driven by independent power supplies with a sufficient power capacity.

Similarly to the dipole fields, the Gl value is defined as the integral of the field gradient along the z axis from the field edge to the cutoff. The QFL field is defined in the area from the entrance of the shift-bump field area to the cutoff position. The QDL field is also defined in the area from the cutoff position to the exit of the shift-bump field area. The deviation of the Gl values due to the field interference was approximately 0.15% here; the cutoff contribution was negligible.

III. PARTICLE-TRACKING METHOD

The particle-tracking code "TRACY-II" [11], which was originally developed for simulating the KEK Proton Synchrotron slow-extraction process [12,13], was used in this study. It has been applied to the J-PARC project. Since TRACY-II assumes that the target particles exist in the accelerator and/or beam-transport line, the tracking procedure is carried out using the transfer-matrix method. In order to take into account the realistic fringe field and field interference, a more general particle tracking code, "GENERICSOLVER," was developed as an additional feature of TRACY-II. GENERICSOLVER is a subprocedure communicating with the particle data file. Although beam tracking simulators that can consider the magnetic fringe fields have already been developed, for example, COSY [14], SAD [15], MAD [16] etc., they are not designed for field interference.

GENERICSOLVER traces the particle motion in an arbitrary three-dimensional magnetic field, which is given by field analysis codes such as OPERA-3D. Since the field data required here has a text-based data format, it can also be prepared by using any other magnet design tools. GENERICSOLVER is a 4th order Runge-Kutta integrator of Lorentz equation with a time-independent magnetic field. Although this numerical integration module does not ensure symplecticity, it is confirmed that the system energy is conserved in the present calculations. The magnetic field is given by the distributed field vectors on the lattice structure that forms a rectangular box in the Cartesian coordinate system. The magnetic field at the particle position is interpolated from eight vectors at the corner of a box to which the particle belongs. It is important to choose a proper structure size because the field-data file easily becomes large leading to wastage of computer resources. The magnetic field is divided into the lattice structure of $10 \times 10 \times 25$ mm. In the particle-tracking process, the time step of the integration along the particle trajectory was surveyed. It was determined in order to perform more than ten integrations per box of the magnetic field, which corresponds to approximately 1 mm. More than one interpolation methods [17] are available in GENERICSOLVER. The "cloud-in-cell" method is the default method, and it uses eight data points. The "triangular-shaped-cloud" method uses 27 data points for the second-order interpolations. The accuracy of the interpolated field depends on the algorithm and the intervals of the distributed data points. When the intervals are short enough in comparison with the variations in the magnetic field, the dependence on interpolation methods is not very important. The difference on tracking results among these interpolation methods was negligible. For example, the difference in the bump height obtained by the shift-bump system was less than the order of 10^{-4}.

IV. TRACKING RESULTS

A. Injected H^- beam

As a first step, single particle tracking of 300 turns is performed with the shift-bump magnets in operation. Figure 6 shows the footprints in the phase space of test particles with three emittances at the stripping foil position. The distributed field data is applied only for the shift-

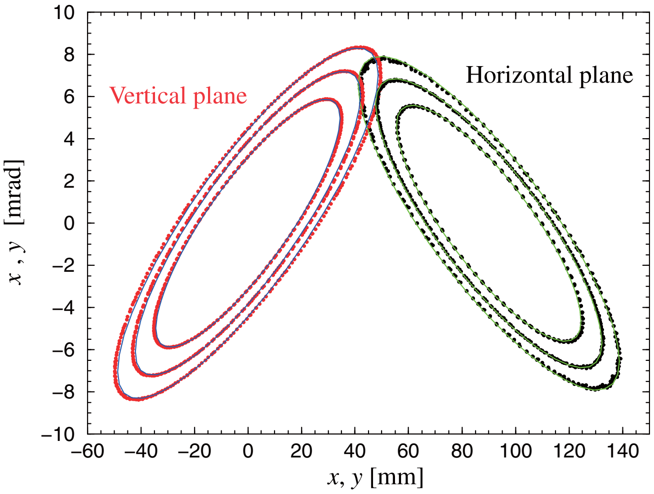

FIG. 6. (Color) Poincaré map at the stripping foil between SB2 and SB3 ($s = 82.113$ m) during 300 turns with shift-bump magnets in operation. Lines correspond to the bare ring parameters without any bump system.

TABLE V. Twiss parameters for the test particle generation at the foil ($s = 82.113$ m), as calculated by transfer matrices.

Optics	β_x [m]	α_x	β_y [m]	α_y
RCS (shift-bump off)	11.02	1.481	10.95	−1.584
RCS (shift-bump on)	11.01	1.480	10.85	−1.603
L3BT line	11.66	−1.788	12.86	0.174

bump field area and a linear lattice is assumed for the other magnets. Test particles were generated at 10.0895 m upstream of the stripping foil, $s = 72.0235$ m; three emittance ellipses of 216, 162, and 108π mm mrad were used, where the emittance of 216π mm mrad corresponds to the painting size of an injected beam for both phase-space planes. Table V shows the Twiss parameter sets with or without the shift-bump orbit. In the vertical plane, the Twiss parameters are changed due to the effect of edge focusing. On the other hand, in the horizontal plane, the effect of edge focusing is small but there is y dependence of integrated B_y, which can be seen as a small diffusion of the plot. In GENERICSOLVER, the momentum component p_z, which is conserved in the transfer-matrix method, changes slightly; however, the total energy is well conserved. As shown in Fig. 6, no emittance growth was observed for all the cases.

Next, the painting injection process was simulated. The injection parameters are as follows: (i) 400 MeV H$^-$ ion $\Delta p/p = \pm 0.3\%$; (ii) $\epsilon_x = \epsilon_y = 6$ and $\epsilon_x = 11.3$, $\epsilon_y = 8.9\pi$ mm mrad. (unnormalized full beam); (iii) injection point is $(x, x', y, y') = (131, -5.5, 0, -3.7)$ [mm, mrad] at the stripping foil position; (iv) painted transverse area is 216π mm mrad; (v) collimator acceptance is 324π mm mrad. The carbon-stripping foil is placed at $(x, y) = (131, 0)$ mm and $s = 82.113$ m in the ring. A beam size on the foil is estimated to be 6.829 mm wide and 7.171 mm high. The stripping foil size is determined with a margin of 10 mm. Thus, (i) $x \geq 131 - 6.829 - 10$ mm and (ii) $y = \pm(7.171 + 10)$ mm. The linac beam is collimated to 4π mm mrad by a collimator at the L3BT

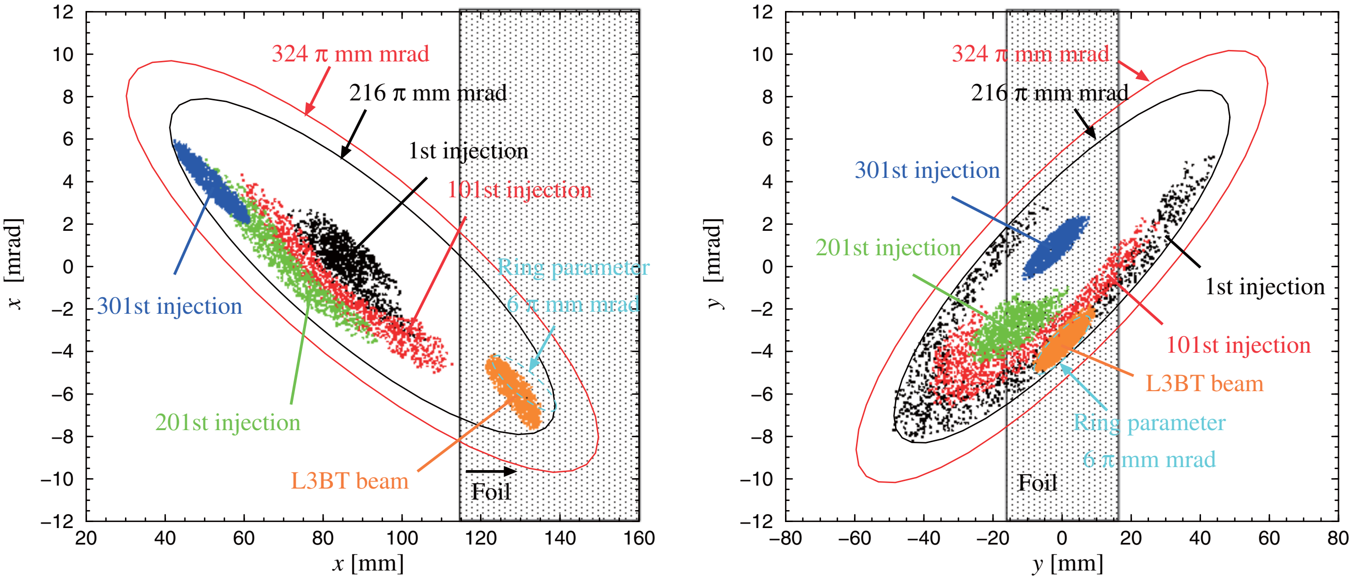

FIG. 7. (Color) Phase-space distribution of the ring optics beam of 6π mm mrad at the injection point ($s = 82.113$ m) during 308 turns with the painting process. The 1st (black), 101st (red), 201st (green), and 301st (blue) injected bunches are traced. Ring optics of 6π mm mrad is shown by a broken line at the outermost position of the painting area, which corresponds to the last bunch for the horizontal plane and the first bunch for the vertical one. Beam ellipses with 216 and 324π mm mrad are drawn by original ring parameters without any bump orbits (bump off in Table V).

(LINAC—3 GeV RCS beam transport) line. However, a typical beam emittance at the primary foil is estimated to be 6π mm mrad due to the emittance growth by the space charge force while passing from the collimator to the foil. Test particles were generated with the designed Twiss parameters of the RCS ring with the shift-bump magnets at the foil position and traced back to the entrance of the shift-bump field area with the linear lattice matrices. The particle tracking begins from the entrance of the shift-bump field area.

The results of the painting injection with a 6π mm mrad beam are shown in Fig. 7. When all the bump magnets are fully excited, the injection point corresponds to the central orbit where the carbon-stripping foil is located. The paint-bump system adds a horizontal displacement of 41 mm to the shift-bump orbit at the beginning of the beam injection. The paint-bump decreases to zero according to the painting function: $1 - \sqrt{t/\tau}$, where τ is an injection period. In the horizontal plane, the first bunch is injected into the center of the phase space, and the last bunch is injected into the outermost one. In the vertical plane, the injection angle of -3.7 mrad decreases according to the function: $\sqrt{1 - t/\tau}$. The last bunch is injected into the center of the phase space. This painting scheme causes a flat distribution on the circulating beam and is called "anticorrelated painting." The L3BT beam indicates the beam projections at the foil position after QFL, SB1, and SB2, which correspond to the last bunch for the horizontal plane and the first bunch for the vertical one. When the injected beam emittance is less than 6π mm mrad, the injected beam in the synchrotron ring can be contained within the design emittance of 216π mm mrad with the designed bump-orbit parameters. Here, the 1st, 101st, 201st, and 301st injected bunches are traced. The first injected bunch has 308 turns in the ring. On the other hand, the 301st injected bunch has only 8 turns.

In the actual J-PARC L3BT line, the line optics does not match the ring optics. The H^- beam passes through the defocusing quadrupole magnet (QFL), which acts as a focusing magnet to the circulating proton beam, as shown in Fig. 1. The horizontal beam parameter (α_x) for the circulating beam is positive at the foil, but that for the incoming beam is negative. It is possible in principle to obtain a matched beam. However, a very large β_x is generated upstream of the foil, resulting in a large modulation of the beta function along the L3BT line. Such a modulation of the beta function enhances the emittance growth by the space charge force in addition to the aperture problem. The beam parameters along the L3BT line are chosen to ensure that the emittance growth is as small as possible. The Twiss parameters at the injection point ($s = 82.113$ m) thus obtained are listed in Table V with a comparison of those in the ring.

At the beam-injection line, the beam passes through several kinds of time-varying fields until it reaches the primary stripping foil. The stability/precision of these fields results in the emittance growth. Vertical painting magnets are located in the L3BT line, and this is assumed to cause the ±5% fluctuations in the vertical coordinate and its divergence. Pulsed horizontal bending magnets are utilized for changing the painting areas depending upon the beams for neutron users and the injection into the 50 GeV ring, the stability of which is ±0.5%. An incoming beam also passes through the ring quadrupole magnet (QFL) and the shift-bump magnets, the stabilities of which are ±0.2% and ±1.0%, respectively. All these fluctuations give the effective emittances $(\epsilon_x, \epsilon_y) = (11.3, 8.9)\pi$ mm mrad, while the nominal one is 6π mm mrad. Further, the incoming beam passes through the QFL magnet with $x > 250$ mm where the quadrupole field is not linear any more, as shown in Fig. 8. When the initial beam emittance was large, the beam profile is deformed because it passes outside the good field region of the QFL magnet, as shown in Fig. 9.

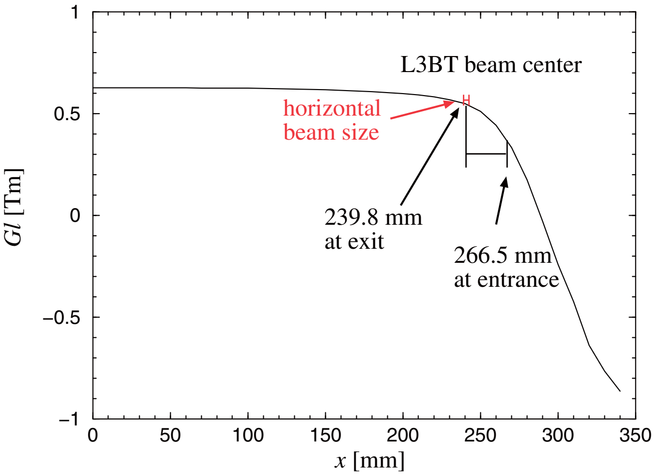

FIG. 8. (Color) Gl distribution of QFL at $y = 0$. The incoming beam center passes at $x = 266.5$ mm for the entrance and at $x = 239.8$ mm for the exit of QFL.

Under these conditions, the heights of the shift-bump orbit and the paint-bump orbit, and also the covered area of the carbon-stripping foil should be readjusted in order to accommodate the painted beam within 216π mm mrad. Since the injection point should be fixed to $(x, y) = (131, 0)$ mm, the shift-bump height increases from 90 to 102 mm. On the other hand, the paint-bump height decreases from 41 to 29 mm. For the vertical plane, the injection angle is changed from 3.7 to 2.5 mrad. With such a limited painting range, the beam core of the circulating beam remains within the designed emittance, as shown in Fig. 10. However, the number of foil hits by the H^- and circulating protons increases from 26 to 64 on an average, which may in turn shorten the life of the stripping foil and produce greater beam loss due to nuclear and multiple scatterings. Since an optics mismatch is a control-

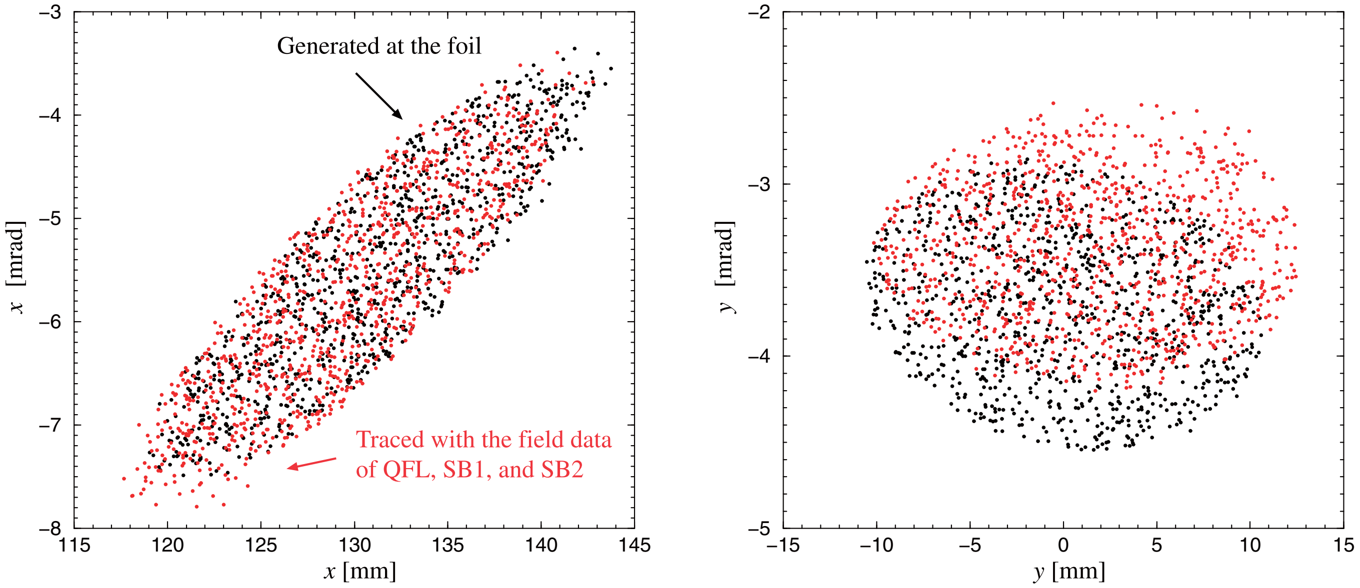

FIG. 9. (Color) Beam profile deformations on the incoming beam of $(11.3, 8.9)\pi$ mm mrad. The beam is located outside the good field region of QFL. Test particles were originally generated at the foil position ($s = 82.113$ m) and traced back to the entrance of the shift-bump field area by transfer matrices assuming an ideal QFL. Particle tracking was carried out with the distributed field data.

lable parameter, the foil-hitting rate and emittance growth of the incoming beam can be optimized.

B. Stripped electrons

The stripped electrons from the injected beam have a power of 145 W. In this case, the electron catcher plays a very important role for the H^- injection [18]. When the stripped electrons have the same speed as the injected proton, the corresponding electron momentum becomes $519 \sim 521$ keV/c ($217 \sim 219$ keV). In this energy range, electrons lose their energy by ionization. The energy loss by the carbon-stripping foil is given by $dE/dx = -2.41$ eV/(μg/cm^2) at an energy of 218 keV. Test particles are generated at the entrance of the foil of 300 μg/cm^2. The nuclear multiple scattering angle of electrons in the foil is estimated to be $\sigma_{\rm rms} \approx 3.1$ degrees [19]. Figure 11 shows the electron track downstream of the stripping foil without taking into account large angle scat-

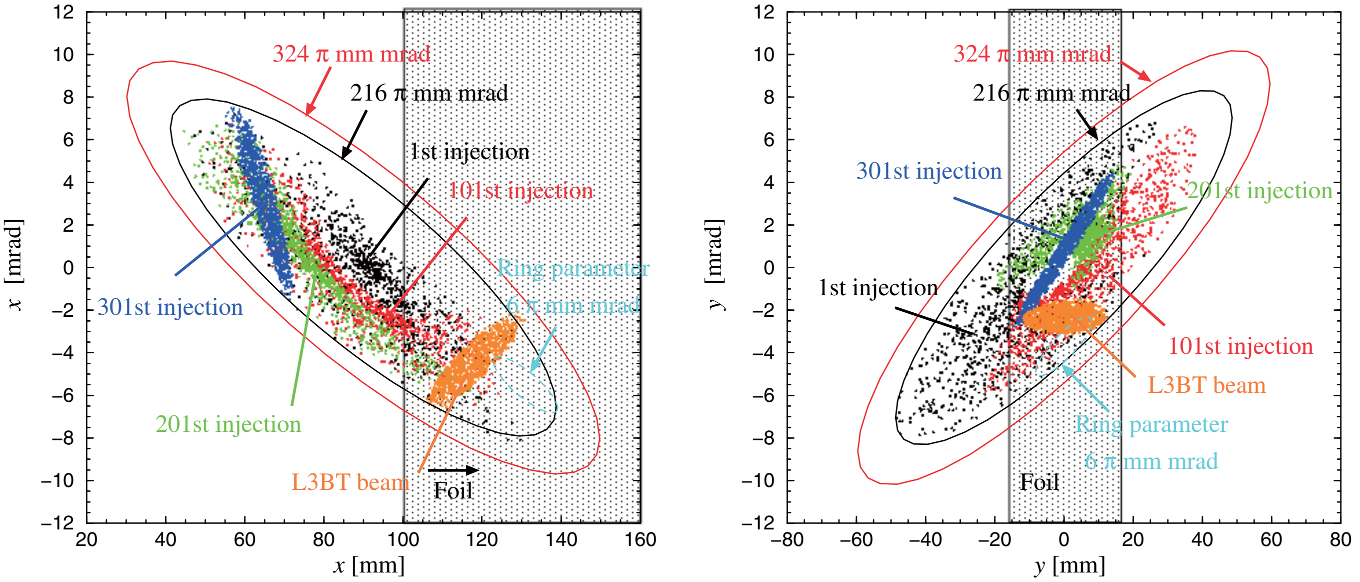

FIG. 10. (Color) Phase-space distribution with a limited painting area of the mismatched and deformed beam with the L3BT optics of $(11.3, 8.9)\pi$ mm mrad at the injection point ($s = 82.113$ m) during 308 turns with the painting process. The 1st (black), 101st (red), 201st (green), and 301st (blue) injected bunches are traced.

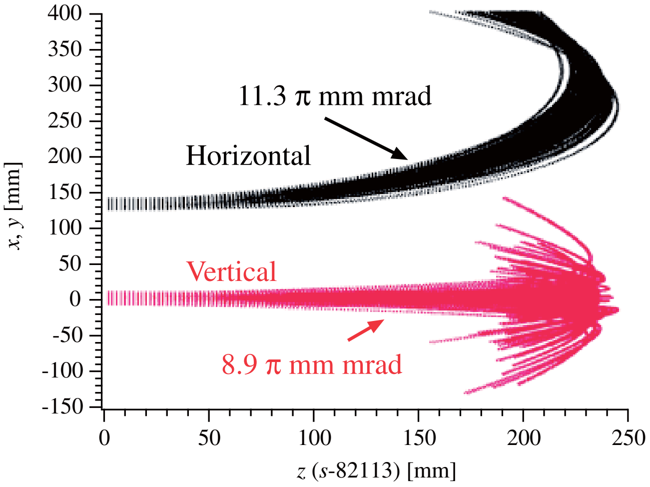

FIG. 11. (Color) Stripped electron trajectory. The stripping foil is placed at $z = 0$. The black line is for the horizontal plane, and the red line is for the vertical plane (200 particles).

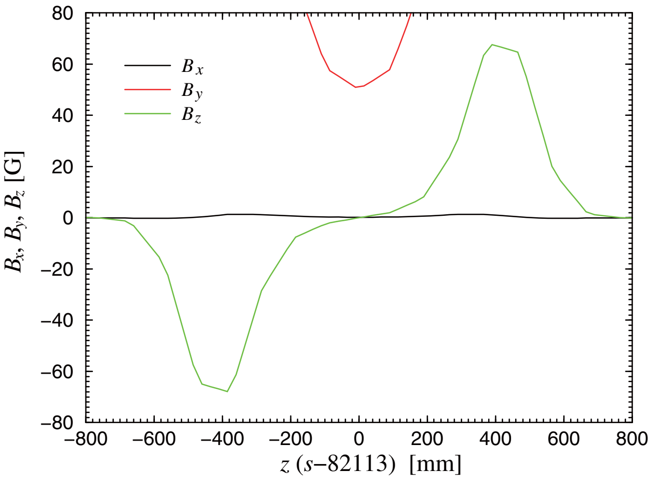

FIG. 13. (Color) B_x, B_y, B_z distribution in the shift-bump area at $(x, y) = (131, 10)$ [mm]. The stripping foil is placed at $z = 0$ ($s = 82.113$ m).

terings. As the trajectory diffuses in the vertical plane, an electron catcher should be placed at $x = +320$ mm in this case. A cross-sectional view at $x = +320$ mm is shown in Fig. 12.

The x, y trajectories of the stripped electrons can be understood from the fringe field between SB2 and SB3. Figure 13 shows B_x, B_y, B_z at $(x, y) = (131, 10)$ [mm], corresponding to 10 mm above the injection point. In order to observe the B_z components, the y location is set to a nonzero value. The x dependence of the B_z amplitude is small in the range of $x = 0$ to 131 mm, and B_x is almost zero around the region of the carbon-stripping foil. B_z is dominant for the diffusion in the vertical direction. Downstream of the carbon-stripping foil, B_z is positive for the $+y$ region and negative for the $-y$ region. Electrons move toward the $+x$ direction due to B_y, which increases with z. Consequently, the stripped electrons diverge vertically.

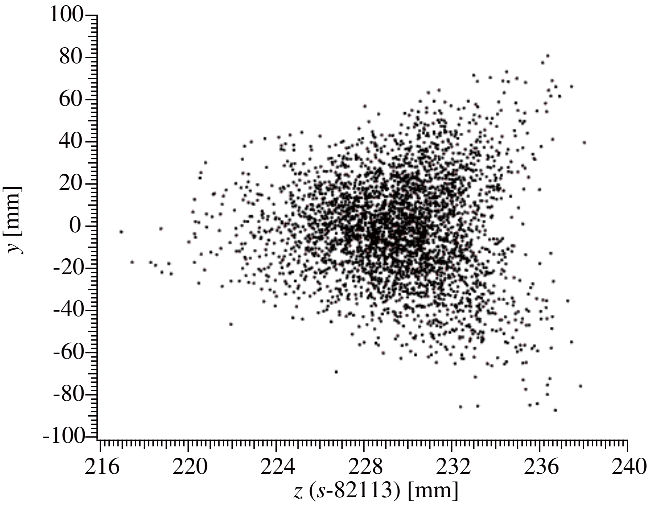

FIG. 12. Stripped electron distribution in the y-z plane at $x = +320$ mm (4000 particles).

A rough estimate of the space charge fields exerted upon electrons by the circulating proton beam is given by

$$E_r = \frac{e\lambda}{2\pi\epsilon_0}\frac{1}{r} = 2.5 \times 10^4 \text{ V/m} \tag{1}$$

$$\nu B_\phi = \nu\frac{\mu_0 I_b}{2\pi}\frac{1}{r} = 1.3 \times 10^4 \text{ V/m}, \tag{2}$$

where λ is the line density, I_b is the beam current of the circulating beam, ν is the velocity of the stripped electrons, and r is a proton beam size at the foil (5 cm). As seen in Fig. 13, the fringe field at the stripping foil is ~60 Gauss at the minimum for the B_y-component, resulting in $\nu B_y = 1.3 \times 10^6$ V/m. Comparing the space charge forces at the edge of the beam with the one by the fringe field, the latter is more than 30 times stronger than the sum of the space charge forces. The space charge effect from the circulating protons can be omitted.

V. CONCLUSION

A beam-injection process with field interferences was simulated by a three-dimensional particle tracker without taking into account the space charge force. This simulation study was applied to the design of the injection-straight section of the J-PARC RCS, where the magnetic fields were calculated by OPERA-3D. Magnetic field interference causes the Bl imbalance, resulting in a closed-orbit distortion. However, such an imbalance can be compensated by adjusting the gap height of the relevant dipole magnets and the paint-bump magnets can also be used for the orbit correction if necessary.

Additional features of the RCS injection are the fluctuations of the time-varying fields along the injection line, and the fact that an injected beam passes through the far side of the ring quadrupole magnet. Field fluctuations cause an emittance growth of the incoming beam. The nonlinear field of the quadrupole magnet deforms the beam profile. Hence, a modification of the originally planned painting scheme is required and the hitting rate of the carbon-stripping foil by the circulating beam is increased. The orbit of the stripped electrons was also investigated for efficient electron collection.

These results will be used in the early stage of the RCS commissioning. The space charge effect will be included in forthcoming simulations of the subsequent beam commissioning at higher intensity.

[1] Accelerator Group JAERI/KEK Joint Project Team, KEK Report No. 2002-13, 2003.

[2] Y. Irie *et al.*, *Proceedings of the European Particle Accelerator Conference, Stockholm, 1998*, p. 2103, http://accelconf.web.cern.ch/AccelConf/.

[3] I. Sakai *et al.*, *Proceedings of the 8th European Particle Accelerator Conference, Paris, 2002* (EPS-IGA and CERN, Geneva, 2002), p. 1040.

[4] J. Wei *et al.*, Phys. Rev. ST Accel. Beams **3**, 080101 (2000).

[5] J. G. Wang, *Proceedings of the Particle Accelerator Conference, Albuquerque, New Mexico, 2007*, p. 3660, http://accelconf.web.cern.ch/AccelConf/.

[6] Vector Fields Ltd; 24 Bankside Kidlington Oxford OX5 1JE, UK.

[7] M. Shirakata *et al.*, *Proceedings of the 8th European Particle Accelerator Conference, Paris, 2002*, Ref. [3], p. 1670.

[8] M. J. Shirakata *et al.*, *Proceedings of the European Particle Accelerator Conference, Lucerne, 2004* (EPS-AG, Lucerne, 2004), p. 2658.

[9] M. J. Shirakata *et al.*, *Proceedings of ICFA HB2006, 2006*, p. 253, http://accelconf.web.cern.ch/AccelConf/.

[10] Y. Papaphilippou *et al.*, *Proceedings of the Particle Accelerator Conference, Chicago, IL, 2001* (IEEE, New York, 2001), p. 1667.

[11] M. J. Shirakata, see TRACY-II http://www-accps.kek.jp/staff/shir/TRACY/ (1997). The TRACY-II described in this paper is different from the TRACY-2 written by J. Bengtsson *et al.*

[12] M. J. Shirakata *et al.*, *Proceedings of the Particle Accelerator Conference, Vancouver, B.C., 1997*, p. 267, http://accelconf.web.cern.ch/AccelConf/.

[13] M. Shirakata, ICFA Mini-workshop on slow extraction, BNL 2002.

[14] M. Berz and K. Makino, COSY INFINITY, Michigan State University (2001), p. 1.

[15] K. Oide, see SAD/Tkinter, KEK http://acc-physics.kek.jp/SAD/sad.html (1997).

[16] See CERN-MAD http://mad.home.cern.ch/mad/.

[17] Roger W. Hockney and J. W. Eastwood, *Computer Simulation Using Particles* (IOP, London, 1988).

[18] Y. Lee *et al.*, *Proceedings of the Particle Accelerator Conference, Knoxville, Tennessee, 2005*, p. 2384, http://accelconf.web.cern.ch/AccelConf/.

[19] W. M. Yao *et al.*, J. Phys. G **33**, 1 (2006).

REVIEW OF SCIENTIFIC INSTRUMENTS **79**, 053502 (2008)

Preparation of ortho-para ratio controlled D_2 gas for muon-catalyzed fusion

H. Imao,[1,a)] K. Ishida,[2] N. Kawamura,[3] T. Matsuzaki,[2] Y. Matsuda,[2] A. Toyoda,[4]
P. Strasser,[3] M. Iwasaki,[2] and K. Nagamine[1,3,5]
[1]*Atomic Physics Laboratory, Discovery Research Institute, RIKEN, Wako, Saitama 351-0198, Japan*
[2]*Advanced Meson Science Laboratory, RIKEN Nishina Center, RIKEN, Wako, Saitama 351-0198, Japan*
[3]*Muon Science Laboratory, Institute of Materials Structure Science, High Energy Accelerator Research Organization, Tsukuba, Ibaraki 305-0801, Japan*
[4]*Institute of Particle and Nuclear Studies, High Energy Accelerator Research Organization, Tsukuba, Ibaraki 305-0801, Japan*
[5]*Physics Department, University of California Riverside, Riverside, California 92521, USA*

(Received 22 December 2007; accepted 9 April 2008; published online 9 May 2008)

A negative muon in hydrogen targets, e.g., D_2 or D–T mixture, can catalyze nuclear fusions following a series of atomic processes involving muonic hydrogen molecular formation (muon-catalyzed fusion, μCF). The ortho-para state of D_2 is a crucial parameter not only for enhancing the fusion rate but also to precisely investigate various muonic atom processes. We have developed a system for controlling and measuring the ortho-para ratio of D_2 gas for μCF experiments. We successfully collected para-enriched D_2 without using liquid-hydrogen coolant. Ortho-enriched D_2 was also obtained by using a catalytic conversion method with a mixture of chromium oxide and alumina. The ortho-para ratio of D_2 gas was measured with a compact Raman spectroscopy system. We produced large volume (5–30 l at STP), high-purity (less than ppm high-Z contaminant) D_2 targets with a wide range of ortho-para ratios (ortho 20%–99%). By using the ortho-para controlled D_2 in μCF experiments, we observed the dependence of μCF phenomena on the ortho-para ratio. © *2008 American Institute of Physics.* [DOI: 10.1063/1.2918538]

I. INTRODUCTION

Negative muons stopped in hydrogen isotopes induce a variety of atomic and molecular processes and nuclear fusion reactions, i.e., muon-catalyzed fusion (μCF).[1–3] In μCF reactions, resonant muonic molecular formation[4] is an essential process because it determines how many fusions occur within the muon lifetime of 2.2 μs. In order to enhance the fusion rate and, ultimately, to realize "energy break-even" and energy production by μCF, the resonant molecular formation rate must be increased by changing the target conditions. For this purpose, the ortho-para ratio of D_2 is an important parameter because the resonance condition of the muonic molecular formation in D_2 strongly depends on the ortho-para ratio. A large enhancement of the $dt\mu$ molecular formation rate for para-D_2 in μCF with a deuterium-tritium mixture (d-t μCF) has been theoretically predicted.[5,6] In addition, for the understanding of the resonant molecular formation mechanism and the relevant muonic atom processes, the observation of the ortho-para ratio dependence is significant. Such observations are crucial for several unsolved problems related to the condensed-matter effect in μCF, e.g., unexpectedly high rates of resonant $dd\mu$ formation observed in several studies.[7–9]

Resonant muonic molecular formation mechanism in pure D_2 was first explained by Vesman.[4] Because of the shallow bound state ($\epsilon_{11} \sim -1.96$ eV) in the $dd\mu$ molecule with the rotational/vibrational state $(J,\nu)=(1,1)$, a $dd\mu$ molecule is formed resonantly from a $d\mu$ atom:

$$(d\mu)_F + (D_2)_{K_i,\nu_i} \rightarrow [(dd\mu)dee]^*_{K_f,\nu_f}, \tag{1}$$

where F denotes a hyperfine state, K_i and ν_i are the initial rotational and vibrational quantum numbers, and K_f and ν_f are the final quantum numbers. The collision energy of the incident particles and the $dd\mu$ binding energy are transmitted to the final rotational and vibrational energy of the muonic molecular complex of $[(dd\mu)dee]$. Resonant $dt\mu$ formation for the collision between $t\mu$ atoms and D_2 or DT in d-t μCF takes place in the same scheme.

The energy matching for resonant $dd\mu$ formation is described by the parameter ϵ_τ[3]

$$\epsilon_\tau = \epsilon_{11} + \delta\epsilon_{dd\mu}(S) + E_C(K_f,\nu_f) - \epsilon_{d\mu} - \delta\epsilon_{d\mu}(F) - E_{D_2}(K_i,\nu_i), \tag{2}$$

where E_C and E_{D_2} are the rotational energies of $[(dd\mu)dee]$ and D_2 relative to the D+D dissociation energy. The spin splitting energies $\delta\epsilon_{d\mu}(F)$ for $d\mu$ and $\delta\epsilon_{dd\mu}(S)$ for $dd\mu$ and the collision energy $\epsilon_{d\mu}$ are also essential for energy matching. When energy matching occurs ($\epsilon_\tau=0$), a $dd\mu$ molecule is resonantly formed. Figure 1 shows a simplified scheme of the $dd\mu$ molecular formation mechanism for isolated D_2 molecules.

The resonance energy ϵ_{if} is an important parameter for resonant molecular formation. It is defined as the energy difference between the initial state (atomic and molecular rotational/vibrational/spin state) and the final state except the collision energy.[10] As described in Eq. (2), the resonance energy is compensated by the collision energy $\epsilon_{d\mu}$. Reso-

---

[a)] Electronic mail: imao@riken.jp.

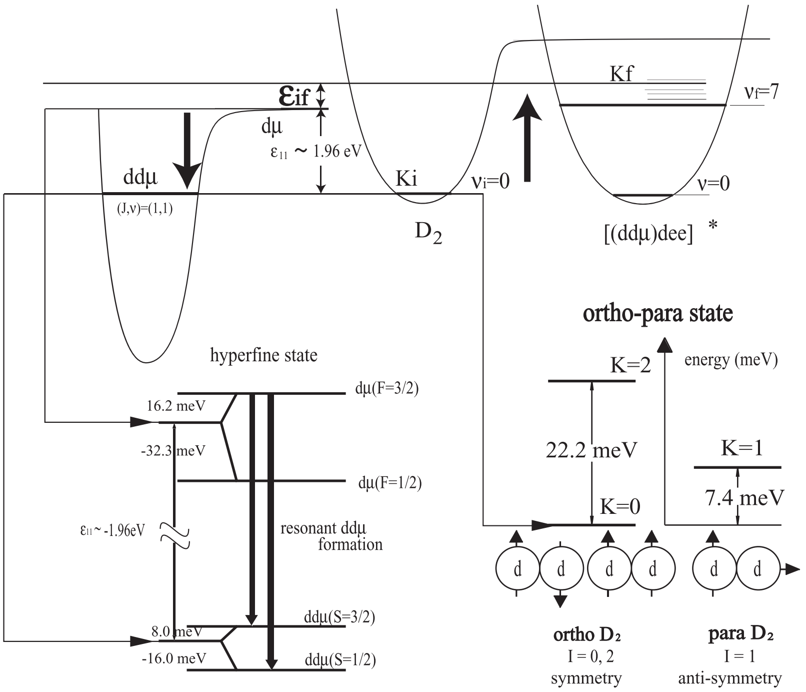

FIG. 1. Scheme of the resonant $dd\mu$ molecular formation mechanism for isolated D_2 molecules. The loose binding energy of $\sim$1.96 eV for $dd\mu$ $(J=1,\nu=1)$ formation can be absorbed into the vibrational excitation energy $(\nu_f=7)$ of the muonic molecular complex $[(dd\mu)dee]^*$. The resonance energy ϵ_{if} depends on the initial atomic and molecular states, i.e., the $d\mu$ hyperfine state and the rotational state of D_2, and the final states, i.e., the spin state of $dd\mu$ and the rotational and vibrational state of $[(dd\mu)dee]^*$. The parity of the initial rotational state of D_2 is determined by the parity of the ortho-para state. The energy splitting between the ground state $(K_i=0)$ and the first excited state $(K_i=1)$ is 7.4 meV, which is comparable to the resonance energy.

nance energies on the order of meV for $d\mu$ atoms with the hyperfine state $F=2/3$ are realized in *d*-*d* μCF.

Resonant molecular formation is sensitive to the ortho-para states, which was first considered by Leon and Cohen.[5] Because of the symmetric property of D_2 for the permutation of the indistinguishable boson *d*, we can artificially control the distribution of the initial rotational state K_i of D_2 by controlling the ortho-para ratio. The splitting energy (7.4 meV for isolated D_2 molecules) between the rotational states of the ground state $(K=0)$ and the first excited state $(K=1)$ is comparable to the resonance energy. We note that the splitting energy should be slightly distorted (sub-meV broadening) due to anisotropic electric quadrupole-quadrupole interaction by the $K=1$ molecules in the solid phase.[11] The small energy splitting of the nuclear spin states, the ortho-para states, causes a large effect on the nuclear fusion on the order of MeV energy in μCF.

Our group has investigated the resonant $dd\mu$ formation mechanism while controlling the ortho-para ratio of deuterium.[12–15] Producing high-purity and large-amount D_2 gas for μCF experiments under a controlled ortho-para ratio was indispensable step and required special care. This paper reports the developed system for controlling and measuring the ortho-para ratio of the D_2 targets applied in μCF experiments. In Sec. II, we describe the gas handling system for making ortho-para controlled μCF targets. The practical method and apparatus for controlling the ortho-para ratio of D_2 is described in Sec. III and the system for measuring the ortho-para ratio is described in Sec. IV. We discuss the performance of our system with some typical results obtained by gas analysis in Sec. V. In Sec. VI, applications to μCF experiments are discussed.

II. D_2 GAS HANDLING SYSTEM

We used deuterium or hydrogen targets in various phases (solid, liquid, and gas) in our μCF experiments. Each target was enclosed in an oxygen-free high-conductivity (OFHC) copper target cell, which was fixed to a cryogenic system with a helium-flow cryostat (Oxford Instruments). The target cell was connected to a gas handling system through gas transfer lines.

The gas handling system was designed and constructed to make high-purity D_2 gas with a controlled ortho-para ratio under safe operating conditions. Figure 2 shows a schematic diagram of the gas handling system. It consists of a deuterium bottle, gas storage buffers, vacuum gauges, metal valves (SS-4H-V51, Swagelok Inc.), tubing, a palladium filter, a para-to-ortho converting system (ortho converter), a para-D_2 collecting system (para converter), gas sample cells for Raman spectroscopy and the target cell. Most of the tubing was made of 1/4 in. stainless steel. Cajon VCR-seal couplings were used for the connections.

μCF experiments require highly purified deuterium to avoid muon loss due to muon transfer to heavier impurities in the target.[16] Assuming nitrogen as an impurity, the transfer rate is expressed as $1.45\times10^5\phi_N\ \mu s^{-1}$, where ϕ_N is the concentration of N_2. Even a 5 ppm contamination of N_2 causes muon loss comparable to the muon-decay rate. The whole system was baked and a vacuum-leak check was performed before the gas handling operation. The palladium filter (LS-09, Japan Pionics Inc.) was used to remove impurities from the hydrogen isotopes. The palladium filter ensures that D_2 gas is produced with impurity levels less than 1 ppb. This equipment was also important for preparing ortho-66% D_2 gas (normal equilibrium D_2). The deuterium is physically adsorbed on the surface of the palladium, where the molecular deuterium becomes nuclear deuterium. Deuterons and electrons are dissociated and penetrate the lattice of the palladium. The difference in pressure causes the nuclear deuterium to diffuse throughout the palladium texture. On the opposite side of the membrane, the deuterons and electrons again couple, becoming a gas. The palladium filter was

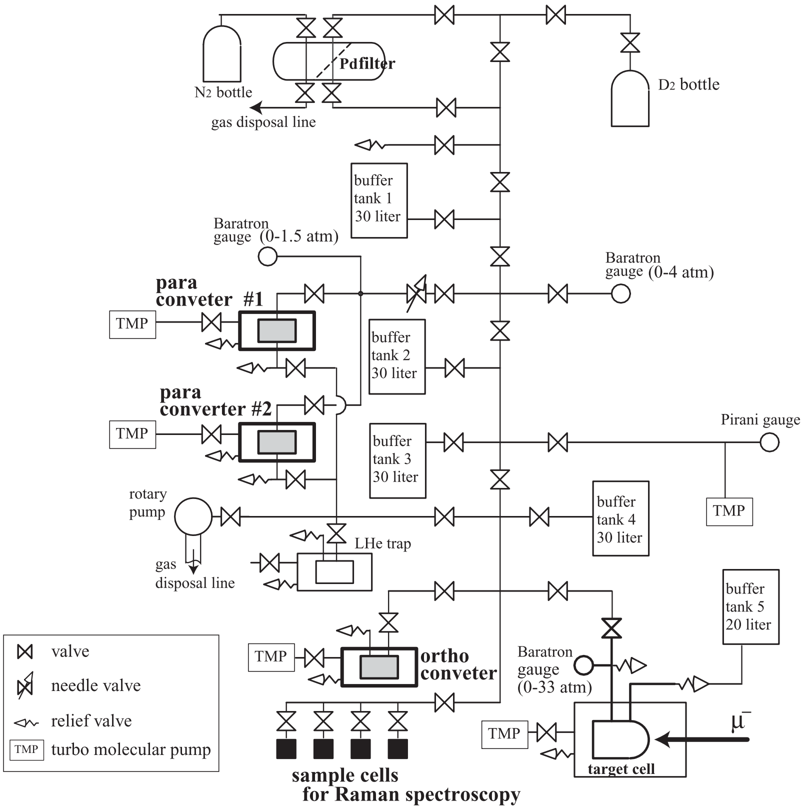

FIG. 2. Schematic diagram of the gas handling system to make ortho- and para-enriched D_2 targets. The D_2 gas is purified through a palladium filter and is converted to ortho-or para-enriched gas in the respective converters.

heated to 420 °C for increased deuterium permeability. Once it has passed through the palladium filter, the D_2 gas is in completely normal equilibrium (66% ortho). Because of this property, we used the palladium filter only before the ortho-para conversion.

III. ORTHO-PARA CONVERSION

The ortho-para conversion rate due to intermolecular interactions is only 1%/year in gaseous D_2 because of the small magnetic dipole moment.[17,18] There is a chance of ortho-para conversion for D_2 in various phases due to the metallic wall of the container and impurity contamination like for O_2, if the ratio is not in equilibrium (we monitored the ortho-para ratio every experimental run, as discussed in Sec. VI) Such natural conversion rate is generally so slow that we cannot produce highly enriched ortho- and para-D_2 gas by just waiting during μCF experiments over a period of about two weeks. In the present study, it was required that a large volume (5–30 l at STP) of ortho-or para-D_2 enriched gas is prepared several times in the limited beamtime. We developed special devices and techniques to enrich ortho- and para-D_2 to achieve this requirement.

A. Ortho-D_2 enrichment

Enrichment of the lowest energy state of hydrogen with $K=0$ (ortho-D_2 and para-H_2 are the molecular rotation even state because of the parity of the nuclear spin) has important applications in many fields of science, e.g., hydrogen storage,[19] studies of surface interactions,[20,21] and ultracold neutron production targets.[22,23] Enrichment can be realized by cooling and allowing the deuterium to reach equilibrium through ortho-para conversion, e.g., the equilibrium concentration of ortho-D_2 at 10 K becomes 0.999. Because the spontaneous conversion rate is quite low, a paramagnetic catalyst is commonly used to promote ortho-para conversion toward equilibration.

The basic theory of catalytic conversion for hydrogen isotopes was proposed by Wigner in 1933.[24] Because ground state hydrogen has no electron spin, the magnetic conversion is due to a hyperfine dipolar interaction between an external catalyst spin and the two nuclear spins. An inhomogeneous magnetic field, created by the magnetic moment of the magnetic catalyst, provides a differential torque on the proton's spins, and a relative dephasing occurs in the precession of the two nuclear spins. As a result, a singlet-triplet nuclear transition occurs, together with a rotational transition.

The best catalysts are those that contain impurities with large magnetic moments and substrates that can adsorb large quantities of D_2. The conversion reactions dynamically occur at 2–3 Å from the surface in the ortho-para frequency range ($\sim 10^{12}$ s^{-1}). Surface cleanliness by pretreatment is important to ensure a route for the molecules to approach to the magnetic impurities. Combinations of paramagnetic catalysts and suitable adsorbents are effective as catalysts. Historically, many catalysts consisting of magnetic materials have been used, e.g., chrome-nickel, $Mn(OH)_4$, CrO_3, Cr_2O_3, $Fe(OH)_3$ and MnO_2.[17,25] Common adsorbents for increasing the surface are charcoal, rutile, alumina, and hydroxide gels. $Cr_2O_3-Al_2O_3$ is one of the best combinations.[26,27] In the present experiments, a mixture of Al_2O_3 and Cr_2O_3 was used ($Al_2O_3:Cr_2O_3=2:1$ in volume).

The para-to-ortho conversion cell (made of OFHC copper), enclosed by a 80 K copper thermal-radiation shield, was placed in a thermal insulating vacuum chamber (Fig. 3).

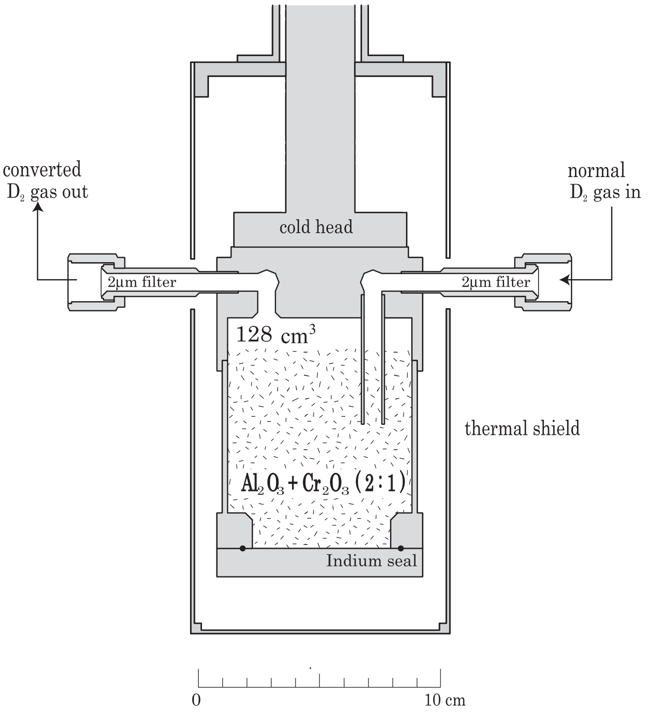

FIG. 3. Cross-sectional view of the para-to-ortho conversion cell. The cell was filled with a mixture of Al_2O_3 and Cr_2O_3 powders. D_2 gas was introduced and condensed in the cell at 10–20 K. The condensed D_2 was held in the cell for an appropriate time for the desired ortho concentration.

A helium-flow cryostat was used to cool the cell. A heater equipped with a cryostat was used to control the temperature of the cell, monitored by thermometers attached to the cell and the cold head of the cryostat. The 128 cm^3 inner volume of the cell was filled with a mixture of Al_2O_3 (4 μm mean diameter; Furuuchi Chem.) and Cr_2O_3 (15 μm mean diameter; Furuuchi Chem.) powders. The cell was carefully baked to 100 °C (below the melting temperature of the indium seal) for a day, outgassing to a low pressure ($<10^{-6}$ torr) before experiments.

In order to make ortho-enriched D_2, purified normal D_2 gas was first introduced and condensed in the cell at 10–20 K. We then controlled the ortho-para ratio by controlling the holding time of the condensed D_2 (solid or liquid) in the conversion cell. Typical holding time for producing 30 l at STP of fully ortho D_2 gas ($\geqslant 98\%$) was about 24 h. After the conversion, the converted D_2 gas was extracted to a gas buffer tank by heating the cell to 40 K. Because the temperature rise of the cell was a possible cause of back conversion (para-to ortho-D_2), the extraction was done as quickly as possible. The extraction time was typically within 15 min for 30 l at STP of gas in our operation. We did not observe significant back conversion in this extraction procedure.

B. Para-D_2 enrichment

It is impossible to produce concentrations of para-D_2 higher than 33% by the catalytic "conversion" method used for ortho-D_2 enrichment. In 1954, Sandler first pointed out that the ortho-para ratio of H_2 adsorbed on TiO_2 was greater than that of the equilibrium ratio.[28] Because the rotational energy levels of the adsorbed molecules are distorted from those in the gas phase,[17,29,30] preferential adsorption of para-D_2 occurs on various porous substrates. This "preferential absorption" method for preparing para-enriched D_2 (or ortho-enriched H_2) has been reported in several old papers. Cunningham *et al.* studied this method with γ alumina to produce para-enriched D_2 in 1958.[31] Depatie and Mills further developed the technique with activated alumina (8–14 mesh) in 1968.[32] Because the collecting efficiency increases near the liquidification temperature of adsorbed H_2 or D_2,[17,30] the apparatuses developed in the previous studies used large amounts of liquid hydrogen as a cryogen and the para-D_2 collecting cell filled with suitable adsorbent was immersed in a bath of liquid hydrogen. The device developed by Silvera and Nielsen could produce ~5 l at STP of 98%–99% para-enriched D_2 by withdrawing the adsorption cell immersed into liquid-hydrogen Dewar.[17] Although liquid hydrogen (or deuterium) is an ideal coolant for achieving the liquidification temperature of D_2 with high cooling power, it is quite problematic in the point of view of the difficulty of the treatment and the safety issues (e.g., explosion hazard). For producing para-enriched D_2 in muon-accelerator facilities, it was essential to use the liquid-hydrogen-free system and technique. We have newly developed para-D_2 collecting system without using liquid hydrogen coolant.

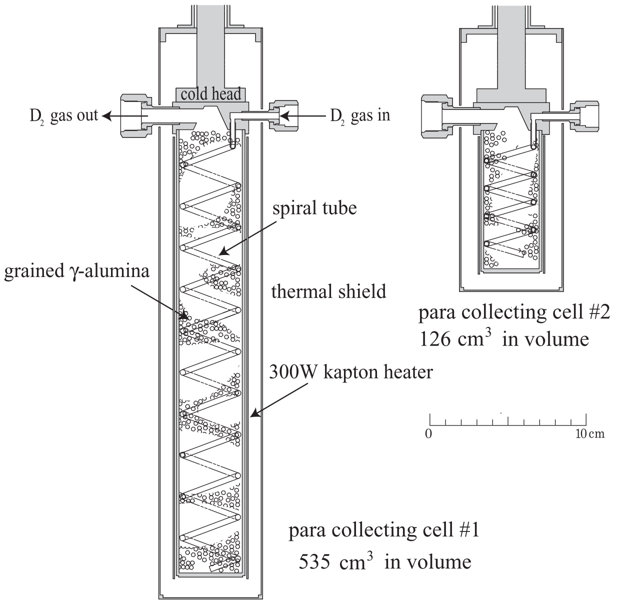

FIG. 4. Cross-sectional views of the para-D_2 collecting cells. The cells cooled at 25–35 K are filled with grained γ-alumina pellets. The cooled adsorbent preferentially filters para-D_2 from the flow gas introduced through the coiled inlet tube. The flow gas is continuously evacuated through the gas exit by a rotary pump. Adsorbed para-enriched D_2 gas is then rapidly extracted with the Kapton heater.

Figure 4 shows the para collecting cells developed in the present study. The OFHC copper cell placed in a vacuum chamber is cooled to 25–35 K by a helium-flow cryostat (Oxford Instruments). The temperatures at the end of cold head and the bottom of the cell were monitored by using two resistance thermometers. We used two cells depending on the desired amount and concentration of para-D_2. Collecting cell No. 1 (535 cm^3 inner volume) can produce a large amount (~20 l at STP) of para-enriched D_2 in one operation. Col-

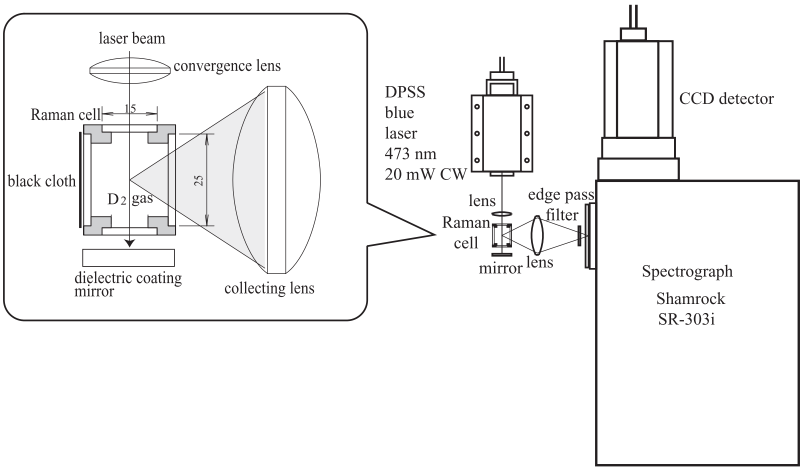

FIG. 5. Schematic view of the Raman laser system and a magnification around the Raman cell. The whole system was placed near the experimental area of the muon beamline for instant measurements.

lecting cell No. 2 ($126\ \text{cm}^3$ inner volume) provides ~6 l at STP of para-enriched D_2 in one operation and is suitable when an amount of para-enriched D_2 gas is required quickly. The para enrichment must be performed quickly to reduce the catalytic conversion on the alumina surface [$\sim 3 \times 10^{-7}$ mol/s/g (Ref. 31)]. Typical times for one operation are 3.5 h for cell No. 1 and 1.5 h for cell No. 2. We used grained γ-alumina pellets (10−20 mesh, Soegawa Chemical) as an adsorbent (440 g for cell No. 1 and 110 g for cell No. 2), baked (~200 °C) before use. The gas inlet tube was coiled inside the cell to increase the heat conductance to the pellets. The cell was wound with a high-power Kapton heater (300 W for cell No. 1 and 100 W for cell No. 2; Yagami), used for baking to reactivate the absorbent and also for rapid extraction of adsorbed D_2 gas.

The procedure to concentrate para-D_2 is as follows. First, the collecting cell and absorbent were precooled for ~12 h. Next, the purified gas (approximately 30 l at STP for collecting cell No. 1 and 9 l at STP for cell No. 2) was adsorbed on the γ-alumina pellets with the temperature of the para collecting cell maintained at 25–30 K monitored at the end of the cold head. An absorption equilibrium pressure of 50–60 torr was realized; the first adsorbed molecular layer forms under this pressures.[31] Because the lower cooling power of the helium-flow cryostat compared to liquid-hydrogen coolant, the initial gas was gradually introduced keeping the temperature of the cell constant to within $\pm 5.0°$. Maintaining the temperature and pressure, further normal-D_2 gas was slowly passed through the adsorbent by evacuating the exit with a rotary pump. After the gas flow process, the cell was evacuated for 1 min. The "preferentially adsorbed" para-enriched D_2 was then extracted by rapidly heating the cell with the Kapton heater. Because ortho-D_2 is more easily desorbed than para-D_2 in the extraction procedure, the para-D_2 concentration of the initially desorbed D_2 gas was decreased. Therefore, the initially desorbed gas (less than half of the amount of the initially absorbed gas) was separately extracted as a disposal gas. The achieved para-D_2 concentration was dependent on the para-D_2 concentration of the flow gas. Further para concentration was realized by repeating the above procedure with para-enriched gas used as a flow gas.

IV. MEASUREMENT OF ORTHO-PARA RATIO

It was essential to check the ortho-para ratio of the D_2 gas during the beamtime, requiring a reliable and instant system to confirm the ortho-para ratio. Raman spectroscopy[33] is a good way to measure the ortho-para ratio because it can determine the absolute value of the ortho-para ratio. For measuring the ortho-para ratio of D_2 in μCF experiments, we used Raman spectroscopy method with a compact and portable laser system. The populations of the molecular rotational states are obtained by analyzing the intensity of the rotational Raman transitions in the Raman spectrum. As a complementary method to know the ortho-para ratio, we also used a thermal conductivity method.

A. Raman laser system

In order to instantly analyze the gas sampled from a target during the beamtime at muon-accelerator facilities, a compact Raman laser system was developed and placed beside the experimental area. Measurement of the sampled D_2 gas was carried out immediately after the gas operations. A schematic diagram of the laser system is illustrated in Fig. 5. The Raman laser system consists of a diode pumped solid state (DPSS) laser, an optical system to induce the laser light and to collect the scattered light, a sample cell and a spectrometer connected to a photon-detection system.

The compact DPSS blue laser (New Lambda Corp.) had a 20 mW cw output and a single 473 nm TEM_{00} line. The whole laser path was packed in a shade box for safety. The laser light was focused by a biconvex lens into the center of a cubic sample cell (Raman cell). A spherical biconvex lens of BK7 (SLB-25B-25PM; Sigma Koki Inc.) was used to collect the laser beam.

The Raman cell was used to expose the sampled D_2 gas to laser irradiation. The aluminum housing was mat black to reduce stray light. The cell had four flat parallel BK7 windows ($2\times$WBMA-25C02-550 and $2\times$WBMA-15C02-10-550; Sigma Koki) with broadband antireflection coatings on both faces for high transmittance more than 99%. The cell was connected to the gas handling system when the gas sampling was performed. In order to

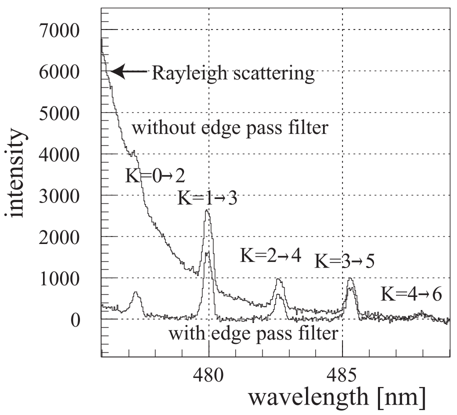

FIG. 6. Typical Raman spectrum with and without the edge pass filter. The five peaks in each spectrum show the $K_i=0\rightarrow K_f=2$, $K_i=1\rightarrow K_f=3$, $K_i=2\rightarrow K_f=4$, $K_i=3\rightarrow K_f=5$, and $K_i=4\rightarrow K_f=6$ transitions. The Rayleigh peak was strongly suppressed by the edge pass filter. The spectrum is for para enriched D_2.

increase the signal of the Raman scattered light, the D_2 gas sampled in the cell was pressurized to 3 atm.

The laser beam exiting from the Raman cell was reflected by a dielectric mirror (10D10DM.6, New Port Inc.) back through the cell for a second pass. This second reflected beam increased the Raman scattering signals by 20%. The Raman scattered light was collected by a large biconvex lens ($\phi=50.8$, fl=38.1) of BK7 (KBX139, New Port Inc.) with a solid angle of 5% of 4π. The window opposite the light-collecting side was covered by a mat-black cloth to block stray light.

A Czerny–Turner spectrograph (Shamrock SR-303i, Andor Tech.) with a charge coupled device (CCD) detector (DV420A-OE, Andor Tech.) was used for photon detection. The spectrograph was equipped with a 1800 lines/mm grating of holographic blaze. The spectra of the Raman scattered light were measured by the CCD detector, which had a 1024×255 array of 26 μm pixels. We can perform a simultaneous measurement for different wavelengths with the CCD detector. The obtained spectra are nearly unaffected by the small power fluctuations ($<1\%$) and the wavelength drift and shift (<0.01 nm) of our laser. The CCD was cooled to around −60 °C with a built-in Peltier cooler to suppress dark current.

Optical filters were critical in the Raman spectroscopy system to prevent undesired light from reaching the spectrometer and swamping the relatively weak Raman signal ($\sim 10^{-6}$). To eliminate the Rayleigh (elastic) scattering from the surrounding material, a 473 nm edge pass filter (LP01-473RU-25, Semrock), which blocks with an optical density exceeding 12 from 385 to 471 nm, was inserted between the sample cell and the slit of the spectrograph in the present system. This filter greatly improved the system performance (Fig. 6). The data acquisition for obtaining the Raman spectra was executed with the equipped software of the SR-303i. The cosmic-ray background was removed by the software.

B. Thermal conductivity

As a complimentary method to the Raman spectroscopy, we also measured the thermal conductivity of the sampled gas. The ortho-para ratio can be determined from the difference between the thermal conductivity of ortho- and para-D_2 because the thermal conductivity is linearly dependent on the ortho concentration. The thermal conductivity analyzer shown in Fig. 7 was used for the measurement. Both 300 cm^3 chambers of the analyzer were immersed in liquid nitrogen at 77 K, because the difference in the thermal conductivity is higher around that temperature.[34] Two Pirani gauges (WPB-10-34, Ulvac Technologies) were used to measure the difference of the thermal conductivity of the two kinds of gas. In a Pirani gauge, the thermal conductivity is detected by the change in the heat divergence of the Pt resistance of the filament. When the same current is supplied to both resistances, the difference of the resistance temperature ($\propto$ the difference of the resistance values) depends on the thermal conductivity difference. We detected the difference of the resistances by using a bridge circuit, as shown in Fig. 7. The procedure is summarized as follows. First, both chambers were filled with normal D_2 gas at the same pressure of 300 hPa with accuracy of 0.1 hPa. After the stabilization of the temperature at 77 K, the bridge circuit was balanced. The normal-D_2 gas in one of the chambers was replaced by the sampled gas, whose ortho-para ratio was unknown, at the same pressure. The unbalanced current due to the difference in the thermal conductivity between the reference normal-D_2 gas and the sampled gas was detected.

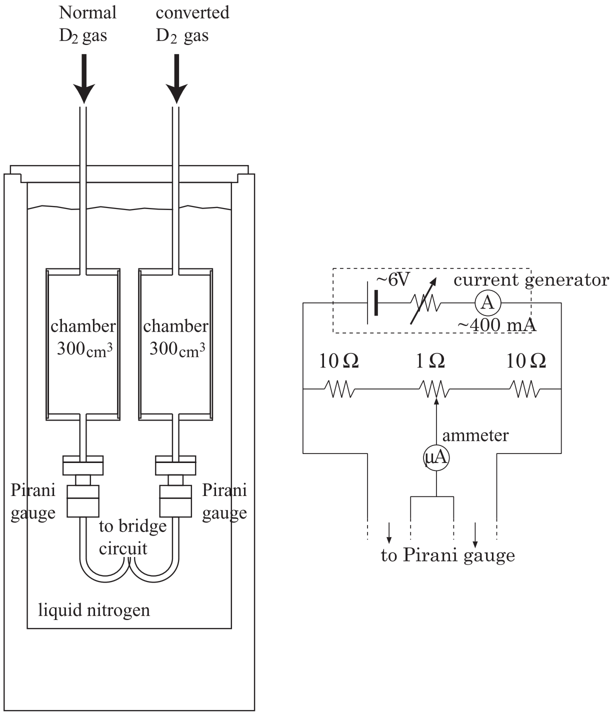

FIG. 7. Schematic drawing of the thermal conductivity analyzer and the bridge circuit to detect the difference between the resistances of the Pirani gauges.

V. RESULTS AND DISCUSSION

By using the apparatus and techniques presented in Sec. II, we produced ortho-para controlled D_2 gas. The ortho-para ratio was measured and analyzed with the Raman laser sys-

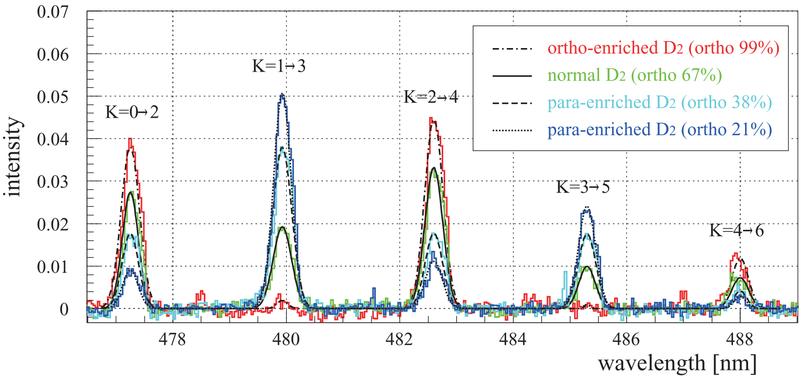

FIG. 8. (Color online) Typical fitting results of Raman spectra for normal and concentrated D_2, showing the $K_i=0 \rightarrow K_f=2$, $K_i=1 \rightarrow K_f=3$, $K_i=2 \rightarrow K_f=4$, $K_i=3 \rightarrow K_f=5$, and $K_i=4 \rightarrow K_f=6$ transitions. The ortho-D_2 concentration for each gas was determined as shown in the figure.

tem and the thermal conductivity analyzer discussed in Sec. III. In this section, we describe the results and the performance of our system.

A. Raman spectra

The five obtained Stokes lines of the Raman scattering for the various ortho-concentrations of D_2 gas are shown in Fig. 8. The peak at the lowest Raman shift corresponds to the transitions from $K_i=0$ to $K_f=2$. The second to fifth peaks correspond to the transition from $K_i=1$ to $K_f=3$, $K_i=2$ to $K_f=4$, $K_i=3$ to $K_f=5$ and from $K_i=4$ to $K_f=6$, respectively. The analysis method to obtain the ortho-para ratio was based on a comparison between the unknown spectra of ortho-or para-enriched D_2 gas to the well-known spectra of normal-D_2 gas. The spectra were fitted to five Gaussian functions with appropriate background functions. The yield of the Raman scattering for K_i, $Y(K_i)$, is given by

$$Y(K_i) = \frac{I}{\lambda_I^4} \epsilon(K_i) B_{K_i,K_f} f(K_i), \tag{3}$$

where I is the incident laser flux, λ_I is the wavelength (=473 nm), $\epsilon(K_i)$ is the total efficiency for a K_i-th Raman scattered photon, B_{K_i,K_f} is the Placzeck–Teller coefficient and $f(K_i)$ is the fraction of the state K_i. In our system, $\epsilon(K_i)$ is given by

$$\epsilon(K_i) = \Omega \epsilon_{\mathrm{rf}}(K_i) \epsilon_{\mathrm{SP}}(K_i) \epsilon_{\mathrm{CCD}}(K_i), \tag{4}$$

where Ω is the solid angle for the light collection including the efficiency of the optics, $\epsilon_{\mathrm{rf}}(K_i)$ is the transmission efficiency of the edge pass filter, $\epsilon_{\mathrm{SP}}(K_i)$ is the transmission efficiency of the spectrograph, and $\epsilon_{\mathrm{CCD}}(K_i)$ is the sensitivity of the CCD detector. B_{K_i,K_f} is theoretically given as follows:[18]

$$B_{K_i,K_f=K_i+2} = \frac{3(K_i+1)(K_i+2)}{2(2K_i+1)(2K_i+2)}, \tag{5}$$

where E_{K_i} is the rotational energy for state K_i and k_B is Boltzmann's constant. Assuming a sharp linewidth, the yield ratio between ortho (K_i=even) and para (K_i=odd) components is proportional to the fraction ratio:

$$\frac{\Sigma_{K_i=\mathrm{odd}} Y(K_i)}{\Sigma_{K_i=\mathrm{even}} Y(K_i)} \cong \alpha \frac{\Sigma_{K_i=\mathrm{odd}} f(K_i)}{\Sigma_{K_i=\mathrm{even}} f(K_i)}, \tag{6}$$

where the proportionality coefficient α was determined from the data for normal D_2 (fraction ratio=0.5). In the present analysis, the ortho concentration c_o was determined by five Stokes lines $K_i=0-4$:

$$c_o \cong \frac{1}{1 + [\Sigma_{K_i=1,3} Y(K_i)] / [\alpha \Sigma_{K_i=0,2,4} Y(K_i)]}. \tag{7}$$

Typical fitting results are also shown in Fig. 8. The uncertainty, including systematic uncertainty, in the ortho-para ratio of ~2% was estimated in the analysis.

B. Dependence of conversion time in catalysis method

The ortho-D_2 concentration achieved by the catalytic conversion depends on the conversion time. In order to investigate the conversion time dependence, D_2 gas (30 l at STP) was held in the para-to-ortho converter at 19 K and then intermittently sampled after the conversion times of 3, 9, 20, and 30 h. Figure 9 shows the time dependence of the ortho concentration. The ortho-para ratio of the sampled D_2 gas for each conversion time was determined by Raman spectroscopy. After about 1 day of conversion, the ortho-para ratio stabilized at the equilibrium ratio. The time dependence is fitted with a function

$$c_{\mathrm{ortho}} = 1 - 0.333 e^{-k_1 t}, \tag{8}$$

where c_{ortho} is the ortho concentration of the sampled gas and k_1 is the time constant of the conversion (fit parameter). The obtained time constant was $k_1=0.13(1)\ \mathrm{h}^{-1}$ (Fig. 9). We performed similar measurements by using the thermal conduc-

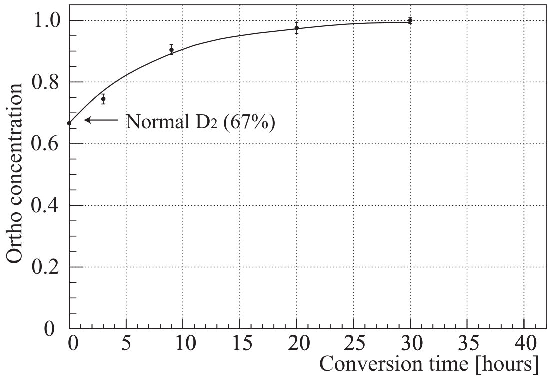

FIG. 9. Dependence of the ortho-para ratio on the conversion time measured by Raman spectroscopy. A fitting line is also shown. The operating temperature of the converter was 19 K. Conversion is almost complete after 1 day.

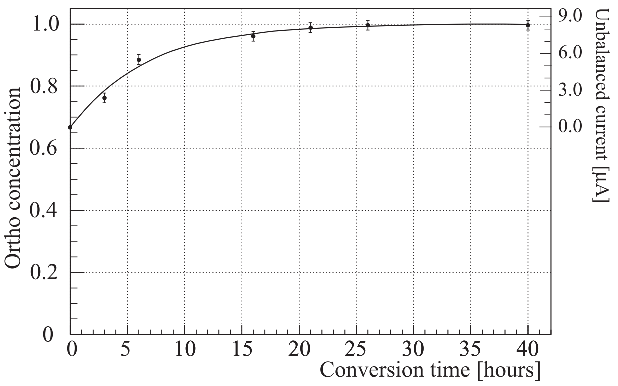

FIG. 10. Dependence of the ortho-para ratio on the conversion time measured by the thermal conductivity method. Scales for measured unbalanced current (right) and calibrated ortho concentration (left) are shown. The solid line indicates a fitting result. The time for saturation is consistent with the Raman spectroscopy results (Fig. 9).

tivity method (Fig. 10). The time dependence of the measured unbalanced current i_u is fitted with

$$i_u = k_2(c_{\mathrm{ortho}} - 0.667), \tag{9}$$

where k_2 is a proportionality coefficient (fit parameter) and c_{ortho} is defined as Eq. (8). We obtained k_1=0.15(2) h^{-1} and k_2=25.2(8) μA from the thermal conductivity method. The obtained time constant k_1 was consistent with that using Raman spectroscopy.

C. Para-enriched D_2

We studied the dependence of the concentration of para-enriched D_2 on the experimental procedure and condition in the present system without using liquid hydrogen coolant. The obtained para-D_2 concentration under various conditions (initial adsorbed amount, ortho-para ratio of the flow gas, amount of flow gas, equilibrium condition, disposal gas amount, finally extracted yield, and ortho concentration) are listed in Table I. Slowly flowing a sufficient amount of normal-D_2 gas (approximately twice the volume of the adsorbed gas) was important to produce para-enriched D_2 from normal-D_2 gas. Typically, about 20 l at STP of 50% ortho-D_2 gas was produced from normal gas (ortho 66%) flow of ~60 l at STP with para converter No. 1 (first operation). By using the para-enriched D_2 gas as a flow gas, we obtained 45% ortho D_2 with para converter No. 2 (second operation). Furthermore, we obtained 38% ortho-D_2 by using the 45% ortho D_2 gas obtained in the second operation as flow gas in the third operation. The total gas consumption to make 5.2 l of 21% ortho-D_2 obtained in the fourth operation was about 500 l at STP. The separation coefficient is defined as

$$S = (c^a_{\mathrm{para}}/c^a_{\mathrm{ortho}})/(c^g_{\mathrm{para}}/c^g_{\mathrm{ortho}}), \tag{10}$$

where $c^a_{\mathrm{para}}/c^a_{\mathrm{ortho}}$ is the ratio of the adsorbed mole fraction of para- and ortho-D_2 and $c^g_{\mathrm{para}}/c^g_{\mathrm{ortho}}$ is that in the gas phase. The separation coefficient $S \sim 2.0$ for our system was obtained assuming that the conversion of gaseous and adsorbed molecules is negligible. The value is similar to that in the earlier measurements by using multistaging conversion cell ($S \lesssim 3$),[31] and is smaller than that for the withdrawing method with liquid hydrogen Dewar ($S \sim 5$).[17,32] By using the double stage method similar to ours, Cunningham *et al.* produced ~3 l at STP of ~25% ortho-D_2.[31] Our system yields comparatively large amount of para-enriched D_2 under the safe operating condition without using liquid hydrogen coolant. We did not observe significant dependence of the achieved para-D_2 concentration on the equilibrium temperature, 25–32 K, in the present study.

VI. APPLICATION TO μCF

We have performed *d-d* μCF experiments under a controlled ortho-para ratio of D_2 at TRIUMF laboratory in Canada. By applying the apparatus and techniques developed in the present study, we made D_2 targets with a wide range of ortho-para ratios (ortho 20%–99%) in solid, liquid and gaseous phases. These targets enclosed by copper target cells were irradiated by muon beams (Fig. 2). The gas analysis with Raman spectroscopy method to determine the ortho-para ratio was carried out before each experimental run to confirm that the expected ortho-para ratio was achieved. The

TABLE I. Summary of typical conditions for para-D_2 enrichment. The ortho-para ratio of the extracted D_2 gas strongly depends on the flow gas condition, i.e., the amount and ortho-para ratio of the flow gas, as well as on the equilibrium temperature and pressure. The temperature was monitored at the end of the cold head. Some of the initially desorbed gas was separately extracted as a disposal gas.

Initial condition			Flow gas condition			Extraction		
Converter	initial charge (STP ℓ)	Ortho (%)	Flow (STP ℓ)	Temperature (K)	Pressure (hPa)	Disposal (STP ℓ)	Yield (STP ℓ)	Ortho (%)
1	35.0	66	62.1	29.0	55	14.8	22.0	55
1	32.0	66	64.0	32.0	50	12.6	20.4	60
1	35.0	66	35.0	30.0	100	14.8	23.2	65
2	8.0	66	26.8	27.0	50	2.2	5.3	52
2	9.2	66	20.6	27.0	50	1.8	6.0	45
		60	9.9	27.0	50			
2	9.2	66	33.8	25.5	50	1.4	6.5	38
		45	11.2	27.0	50			
2	9.2	66	31.6	25.5	50	1.3	5.2	21
		38	10.8	27.0	50			

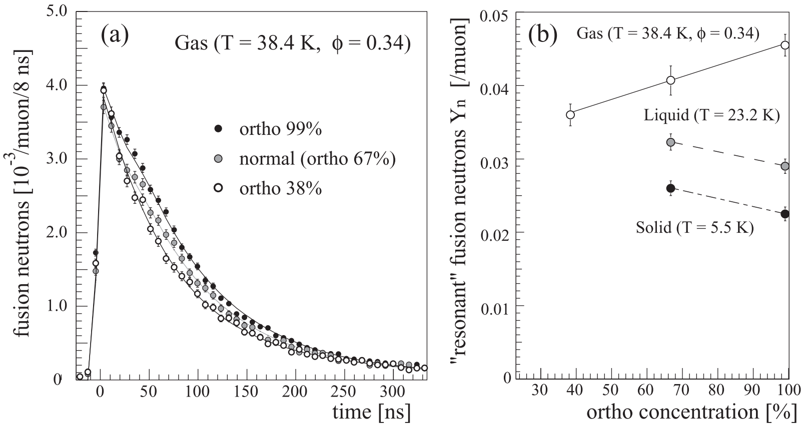

FIG. 11. Fusion neutron time spectra for gaseous ortho-, normal-, and para-enriched D_2 (a) and the dependence of the emission number of resonant fusion neutrons on the ortho concentration in solid (5.5 K), liquid (23.2 K) (Ref. 14), and gaseous (38.4 K) deuterium (b). A fitting straight line is also drawn. The target density of gaseous deuterium is 0.34 liquid-hydrogen density.

analysis was also carried out after each run to check that the ortho-para ratio had not changed during the experiment. We did not observe significant changes of the ortho-para ratio in gaseous, liquid, and solid D_2 targets during the experimental run within our uncertainty of 2%.

The main observable in the experiments was 2.5 MeV *d*-*d* fusion neutrons. These neutrons were detected by using liquid scintillators NE213.[14,15] The fusion neutron spectrum, $N(t)$, is given by

$$N(t) = \widetilde{n}_{\mu}\{N_{F=3/2}(t) + N_{F=1/2}(t)\}, \tag{11}$$

where $N_{F=3/2}(t)$ and $N_{F=1/2}(t)$ are the emission-time distribution of fusion neutrons from two $d\mu$ hyperfine states. The number of "resonant" fusion neutrons after resonant $dd\mu$ formation per muon, $Y_{\rm res}=\int N_{F=3/2}{\rm d}t$, strongly reflects the ortho-para dependence of the resonant molecular formation process. The resonant fusion neutrons yield $Y_{\rm res}$ is the most important parameter from the point of view of energy production. We extracted $Y_{\rm res}$ from the observed fusion neutron time spectra with a kinetics model in $d-d\mu$CF.[3] On the other hand, "nonresonant" fusion neutrons $N_{F=1/2}(t)$, i.e., those emitted following Auger-stabilized $dd\mu$ formation from $d\mu$ atoms with $F=1/2$, show no dependence on the ortho-para ratio. The disappearance rate of $N_{F=1/2}(t)$ ($\propto$ muon transfer rate to impurity nuclei) observed in the experiments indicated that nonhydrogen impurities were less than 1 ppm.

First, the dependence of the fusion neutron time spectra on the ortho-para ratio in solid and liquid deuterium was observed in the temperature range from 5.5 to 23.2 K.[14] We found that $Y_{\rm res}$ was significantly decreased in ortho-D_2, e.g., approximately 8% lower than that for normal-D_2. This dependence in solid and liquid phases are opposite to theoretical predictions for an isolated D_2 molecule,[5,6] where the fusion neutron yield is enhanced approximately 6% in ortho-D_2.

We also have observed the dependence of *d*-*d* fusion neutron time spectra on the ortho-para ratio in the gas phase.[15] Typical neutron time spectra for ortho-, normal-, and para-enriched gaseous $D_2(T=38.4\text{ K})$ and $\phi=0.34$, where ϕ is the deuterium density in units liquid-hydrogen (density $=4.25\times10^{22}$ atoms/mℓ) are shown in Fig. 11(a). The number of resonant fusion neutrons $Y_{\rm res}$ for ortho-D_2 was $12\pm3\%$ higher than that for normal in the gas phase, which was consistent with theoretical predictions for an isolated D_2. We also found that $Y_{\rm res}$ for para-enriched D_2 (ortho 38%) was consistently decreased from those for normal- and ortho-D_2 [Fig. 11(a)].

The data for gaseous D_2 were fitted with a linear function, $Y_{\rm res}(\xi)=p_1\xi+p_2$, where p_1 and p_2 were fitting parameters. The weights for the χ^2 fit were determined as

$$\text{weight} = [(\delta Y_{\rm res})^2 + (p_1\delta\xi)^2]^{-1}. \tag{12}$$

The parameters of $p_1=1.6(4)\times10^{-2}$ and $p_2=Y_{\rm res}(0)=0.030(3)$ were obtained. The dependence of $Y_{\rm res}$ on the ortho-para ratio in the gas phase differed drastically from that in the solid and liquid phases [Fig. 11(b)]. This fact indicates that the resonance condition on the $dd\mu$ formation is changed by a high-density effect in *d*-*d* μCF reactions.

The existence of the clear ortho-para effect in *d*-*d* μCF would warrant the importance of this effect in *d*-*t* μCF, where the large effect, e.g., $dt\mu$ formation rate for para-D_2 is approximately three times higher than that for normal-D_2 around $T=30$ K, was theoretically predicted.[5,6] The present apparatus and techniques have been applied in *d*-*t* μCF experiments with a pulsed muon beam at Rutherford Appleton Laboratory in the UK (Ref. 35) and the first results have been reported recently.[36] The efforts to enhance the *d*-*t* fusion rate toward "energy break-even" are continuing.

VII. CONCLUSION

We have developed and established experimental apparatus and techniques for controlling the ortho-para ratio of D_2. Large volume of para-enriched D_2 was collected without using a liquid-hydrogen coolant for the first time. We successfully produced D_2 gasses of large volume (5–30 l at STP) and high-purity (less than ppm) with a wide range of ortho-para ratio (ortho 20%–99%) for μCF targets in solid, liquid, and gaseous phases. By actually applying the developed system, we performed μCF experiments under a controlled ortho-para ratio of D_2. The ortho-para dependence of the fusion neutron time spectra were clearly observed in the solid, liquid, and gaseous phases. Such studies offered new insights concerning the resonant muonic $dd\mu$ molecular formation. Further applications of the controlled ortho-para D_2 gasses in *d*-*t* μCF experiments has been started.

ACKNOWLEDGMENTS

We would like to thank Professor G.M. Marshall and Professor J.-M. Poutissou for arranging the experiments. We are indebted to Professor T. Okano, Professor K. Fukutani, Dr. K. Mishima and Ms. K. Niki for their useful comments. We are grateful to Professor K. Nishiyama, Professor S.N. Nakamura, and Professor Y. Yamazaki, and Dr. T. Koike and Dr. W. Higemoto for fruitful discussions. H. Imao is grateful to Dr. Y. Ikedo, Dr. D. Tomono, Dr. H. Tanaka, and Dr. H. Miyadera for their encouragement. This research was partially supported by a Grant-in-Aid for Young Scientists (B) (16740154, 2004) from the Japanese Ministry of Education, Culture, Sports, Science and Technology, by the Core-to-Core Program of the Japan Society for the Promotion of Science (JSPS) (15005, 2004) and by a Grant-in-Aid for a JSPS fellowship.

[1] F. C. Frank, Nature (London) **160**, 525 (1947).
[2] W. H. Breunlich, P. Kammel, J. S. Cohen, and M. Leon, Annu. Rev. Nucl. Part. Sci. **39**, 311 (1989).
[3] A. Scrinzi, P. Kammel, J. Zmeskal, W. H. Breunlich, J. Marton, M. P. Faifman, L. I. Ponomarev, and T. A. Strizh, Phys. Rev. A **47**, 4691 (1993).
[4] E. A. Vesman, Zh. Eksp. Teor. Fiz. **5**, 50 (1967) [JETP Lett. **5**, 91 (1967)].
[5] M. Leon and J. S. Cohen, Phys. Rev. A **31**, 2680 (1985).
[6] M. P. Faifman, personal communication (2005).
[7] A. Adamczak and M. P. Faifman, Phys. Rev. A **A64**, 052705 (2001).
[8] D. L. Demin, V. P. Dzhelepov, V. V. Filchenkov, V. G. Grebinnik, A. D. Konin, D. V. Migachev, M. E. Ravodin, A. I. Rudenko, V. T. Sidorov, Yu G. Zhestov, and V. G. Zinov, Hyperfine Interact. **101/102**, 13 (1996).
[9] P. E. Knowles, G. A. Beer, G. R. Mason, T. A. Porcelli, A. Adamczak, J. M. Bailey, J. L. Beveridge, G. M. Marshall, A. Olin, M. C. Fujiwara, T. M. Huber, R. Jacot-Guillarmod, F. Mulhauser, P. Kammel, J. Zmeskal, S. K. Kim, A. R. Kunselman, C. J. Martoff, and C. Petitjean, Phys. Rev. A **56**, 1970 (1997).
[10] M. P. Faifman, L. I. Men'shikov, and T. A. Strizh, Muon Catal. Fusion **4**, 1 (1989).
[11] J. Van Kranendonk, *Solid Hydrogen* (Plenum, New York, 1983).
[12] A. Toyoda, K. Ishida, K. Shimomura, Y. Matsuda, W. Higemoto, S. N. Nakamura, T. Matsuzaki, and K. Nagamine, Phys. Lett. B **509**, 30 (2001).
[13] A. Toyoda, K. Ishida, K. Shimomura, S. N. Nakamura, Y. Matsuda, W. Higemoto, T. Matsuzaki, and K. Nagamine, Phys. Rev. Lett. **90**, 243401 (2003).
[14] H. Imao, N. Kawamura, K. Ishida, T. Matsuzaki, Y. Matsuda, A. Toyoda, and K. Nagamine, Phys. Lett. B **632**, 192 (2006).
[15] H. Imao, K. Ishida, N. Kawamura, T. Matsuzaki, Y. Matsuda, A. Toyoda, P. Strasser, M. Iwasaki, and K. Nagamine, Phys. Lett. B **658**, 120 (2008).
[16] S. S. Gershtein, Zh. Eksp. Teor. Fiz. **43**, 706 (1962); [Z. Tech. Phys. (Leipzig) **53**, 872 (1981)].
[17] I. F. Silvera, Rev. Mod. Phys. **52**, 393 (1980).
[18] P. C. Souers, *Hydrogen Properties for Fusion Energy* (University of California Press, Berkeley, CA, 1986).
[19] S. A. Sherif and N. Sullivan, Hydrogen Storage, Transportation and Handling, NASA Project Report (2002).
[20] E. Ilisca and S. Sugano, Phys. Rev. Lett. **57**, 2590 (1986).
[21] K. Fukutani, Y. Yoshida, M. Wilde, W. A. Diño, M. Matsumoto, and T. Okano, Phys. Rev. Lett. **90**, 096103 (2003).
[22] K. Mishima, Ph.D. thesis, Osaka University, (2004).
[23] C.-Y. Liu, Nucl. Instrum. Methods Phys. Res. A **A508**, 257 (2003).
[24] E. P. Wigner, Z. Phys. Chem. Abt. B **B23**, 28 (1933).
[25] R. A. Buyanov, Kinet. Katal. **1**, 2 (1960) .
[26] P. W. Selwood, J. Am. Chem. Soc. **88**, 2676 (1966).
[27] M. Misono and P. W. Selwood, J. Am. Chem. Soc. **91**, 1300 (1968).
[28] Y. L. Sandler, J. Phys. Chem. **53**, 58 (1954).
[29] D. White and E. N. Lassettre, J. Chem. Phys. **32**, 72 (1960).
[30] R. A. Trasca, M. K. Kostov, and M. W. Cole, Phys. Rev. B **67**, 035410 (2003).
[31] M. Cunningham, D. S. Chapin, and H. L. John-ston, J. Am. Chem. Soc. **80**, 2283 (1958).
[32] D. A. Depatie and R. L. Mills, Rev. Sci. Instrum. **39**, 105 (1968).
[33] A. Compaan and A. Wagoner, Am. J. Phys. **62**, 639 (1994).
[34] A. Farkas, *Orthohydrogen, Parahydrogen and Heavy Hydrogen* (Cambridge University, Cambridge, England, 1935).
[35] T. Matsuzaki, K. Ishida, K. Nagamine, I. Watanabe, G. H. Eaton, and W. G. Williams, Nucl. Instrum. Methods Phys. Res. A **465**, 365 (2001).
[36] K. Ishida *et al.*, Proceedings of the International Conference on Muon Catalyzed Fusion and Related Topics, 2007 (in press).

Available online at www.sciencedirect.com
ScienceDirect
ELSEVIER
Physics Letters B 658 (2008) 120–124
PHYSICS LETTERS B
www.elsevier.com/locate/physletb

Density effect in *d–d* muon-catalyzed fusion with ortho- and para-enriched D_2

H. Imao [a,*], K. Ishida [b], N. Kawamura [c], T. Matsuzaki [b], Y. Matsuda [b], A. Toyoda [d], P. Strasser [c], M. Iwasaki [b], K. Nagamine [a,c,e]

[a] *Atomic Physics Laboratory, Discovery Research Institute, RIKEN, Wako, Saitama 351-0198, Japan*
[b] *Advanced Meson Science Laboratory, RIKEN Nishina Center, RIKEN, Wako, Saitama 351-0198, Japan*
[c] *Muon Science Laboratory, Institute of Materials Structure Science, High Energy Accelerator Research Organization, Tsukuba, Ibaraki 305-0801, Japan*
[d] *Beam Channel Group, Institute of Particle and Nuclear Studies, High Energy Accelerator Research Organization, Tsukuba, Ibaraki 305-0801, Japan*
[e] *Physics Department, University of California Riverside, Riverside, CA 92521, USA*

Received 14 August 2007; received in revised form 16 October 2007; accepted 17 October 2007

Editor: D.F. Geesaman

Abstract

The ortho–para dependence of *d–d* fusion neutrons time spectra was investigated in wide range of the target densities at similar temperatures [$\phi = 0.86$ liquid-hydrogen density (LHD), $T = 35$ K for liquid and $\phi = 0.03$–0.17 LHD, $T = 36$ K for gas]. The result showed significant density dependence. For the first time, a delayed transient structure in the spectra that depends on the ortho ratio, presumably due to the slow $d\mu$ thermalization, was found in gaseous D_2, whereas no significant structure was observed in liquid. The resonant $dd\mu$ formation rates in the gas phase were extracted considering the structure.

Keywords: Muon catalyzed fusion; Density effect; Ortho deuterium; Para deuterium

1. Introduction

Among a variety of muon-catalyzed fusion (μCF) reactions in hydrogen isotopes, the resonant muonic molecular formation plays an essential role because it primarily determines how many fusion reactions take place within a muon lifetime of 2.2 µs. The resonant $dd\mu$ formation in pure deuterium [1] occurs in a similar way to the $dt\mu$ formation in deuterium–tritium mixture. A $dd\mu$ molecule is formed resonantly from a $d\mu$ atom because of a shallow bound state (~ -2 eV) in the $dd\mu$ molecule with the rotational and vibrational state $(J, \nu) = (1, 1)$:

$$(d\mu)_F + (D_2)_{K_i,\nu_i} \to \left[(dd\mu)dee\right]^*_{K_f,\nu_f} \tag{1}$$

(F denotes hyperfine state, K_i and ν_i are initial rotational and vibrational quantum numbers and K_f and ν_f are the final ones), where the collision energy of incident particles and the $dd\mu$ binding energy are transmitted to the final rotational and vibrational energy of the muonic molecular complex of $[(dd\mu)dee]$. As a competing process, the hyperfine transition from $F = 3/2$ to $F = 1/2$ and the thermalization of $d\mu$ energy takes place. At our observed temperatures ($\leqslant 36.2$ K), $d\mu$ with $F = 3/2$ resonantly forms $dd\mu$ at the rate of approximately two orders of magnitude higher than that of the non-resonant $dd\mu$ formation rate from $d\mu$ with $F = 1/2$, $\tilde{\lambda}_{\frac{1}{2}}$.

The resonant $dd\mu$ formation rate $\tilde{\lambda}_{\frac{3}{2}}$ is sensitive to the $d\mu$ kinetic energy and the thermal motion of D_2 because they are of the same order as the resonance energy, which is required to match the resonant condition. The resonance energy is defined as the energy difference between the initial atomic and molecular states, i.e., the $d\mu$ hyperfine state and the rotational state of D_2, and the final states, i.e., the spin state of $dd\mu$ and the rotational and vibrational state of $[(dd\mu)dee]$. The resonance energies on various initial and final states were deter-

---

[*] Corresponding author.
E-mail address: imao@riken.jp (H. Imao).

0370-2693/$ – see front matter © 2007 Elsevier B.V. All rights reserved.
doi:10.1016/j.physletb.2007.10.068

mined by a theoretical fitting to the temperature dependence of $\tilde{\lambda}_{\frac{3}{2}}$ extracted from PSI data only with normal-D_2 gas, i.e., 67% ortho-D_2 (K_i = even) and 33% para-D_2 (K_i = odd), assuming the rapid $d\mu$ thermalization [2–5]. Whereas the theory with the resonance energies predicts a rapidly decreasing formation rate as the temperature drops, high formation rates in the solid phase were reported by several groups [6–9]. The dependence of the rates on the ortho–para ratio observed in the solid and liquid phases ($\phi \sim 1.2$ LHD) [10] did not agree with the theory, which predicted a higher rate in ortho-D_2 [11,12]. The recent theories taking into account the $d\mu$ slow thermalization mechanism and the shift and broadening of the resonant condition due to correlations between D_2 molecules in the solid phase [13,14] have not yet succeeded in completely explaining the ortho–para dependence.

The systematic study of the dependence of the resonant $dd\mu$ formation on the target density at fixed temperature (density effect) is necessary to resolve the discrepancies. Such study has not been realized in the previous experiments with normal-D_2. By performing the ortho–para controlled μCF experiment in wide range of target densities at similar temperatures, we can directly investigate the density dependence of resonant condition both for ortho- and para-D_2. Such an experiment is not only a sensitive test of the existing μCF theories but also a novel approach to investigate the density effect for extending the theory to high densities.

2. Experiment

We measured the emission-time distribution of *d–d* fusion neutrons from ortho–para controlled deuterium both in liquid ($\phi = 0.86$ LHD, $T = 35.0$ K) and gas ($\phi = 0.17$ LHD, $T = 36.2$ K) phases. The measurement was performed at the TRIUMF M9B muon channel. We changed the μ^- beam momentum in the range of 48–52 MeV/*c* for different target densities. A cross-sectional view of the experimental setup is shown in Fig. 1. The coincidence signal of two muon beamline counters (B1, B2) opens a 14-μs gate for data taking. Four NE-213 liquid scintillators (diameter 5″ and length 2″, N1–N4) for detecting 2.5-MeV *d–d* fusion neutrons covered a large solid angle ($\sim 40\%$ of 4π) around the deuterium target. The high detection efficiency was especially required for low-density targets. Muon-decay electrons were detected by using four pairs of plastic scintillation counters (E1–E8). We used two types of bullet–shaped target cells made of oxygen-free high-conductivity (OFHC) copper for the gas (50 mm in diameter and 120 mm in length) and the high-temperature liquid (30 mm in diameter and 55 mm in length) targets, respectively. These cells were designed to sustain a maximum operating pressure of 12.2 bars (e.g., vapor pressure of normal-D_2 at 35 K is 10.5 bars [16]).

We used deuterium with wide-ranging ortho–para ratios, i.e., 50%, 55%, 66% (normal) and 99% ortho-D_2. Para-enriched D_2 target was required not only to enhance the ortho–para dependence of observable but also to ensure the consistency of the difference in ortho and normal targets. Gaseous para-D_2 was collected by using the preferentially adsorption method [17]. As an adsorbent, we used grained γ-alumina powder (10–20 mesh), which was filled in an OFHC copper cell at a temperature of 30 K. By keeping normal-D_2 gas flowing through the adsorbent, 55% ortho-D_2 gas (typically 20 STP-liter in one operation) was collected. For further para concentration (e.g., ortho 50%) the 55% ortho-D_2 was used as the original gas. We used the paramagnetic conversion method [17] to produce ortho-rich D_2. In order to measure the ortho–para ratio, the Raman spectroscopy method was employed. The gas analysis was performed before and after each experimental run to check that the ortho–para ratio was not changed during the run.

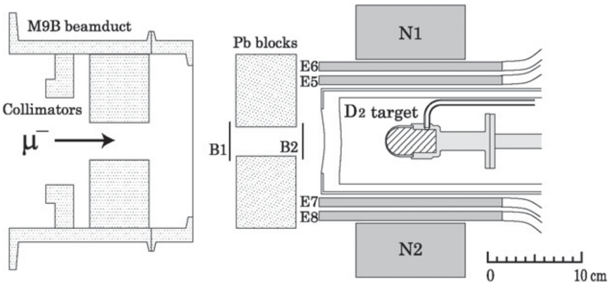

Fig. 1. Schematic view of the experimental setup. The 30-cc cell for high-temperature liquid target is placed in the vacuum chamber.

In the analysis to obtain *d–d* fusion neutrons time spectra, the delayed-electron condition [15] was essential. The background neutrons due to the muon nuclear capture reactions were strongly suppressed by requiring the muon-decay electron to be detected between 0.3 and 5 μs after the neutron signal. The remaining background under the delayed-electron condition mainly came from ambient neutrons with no correlation to muon arrival. The time distribution of background neutrons was determined by using the observed distribution with the hydrogen target.

3. Results and discussion

3.1. Density effect and delayed structure

Fig. 2 shows observed emission time spectra of *d–d* fusion neutrons from ortho- and para-enriched D_2 target in the liquid (a) and gas (b) phases, respectively. The numbers of fusion neutrons are normalized by both the number of muons stopped in the target and the density ϕ. Because the collision reaction rates between $d\mu$ and D_2 are linearly proportional to the target density, the obvious density dependence is removed. The ortho–para dependence of the spectra with 35-K liquid D_2 and that with 36.2-K gas D_2 are clearly different even they are at similar temperatures, i.e., density effect.

The ortho–para dependence for 35-K liquid D_2 emerges in the prompt time region of the spectra. The neutrons yield in the prompt region in ortho-rich D_2 is lower than that in normal-D_2, which is opposite to the theory but is similar to that observed in 3.5–18-K solid and 19–23-K liquid [10]. The resonant $dd\mu$ formation rate, $\tilde{\lambda}_{\frac{3}{2}}$, and the hyperfine transition rate, $\tilde{\lambda}_{\frac{3}{2}\frac{1}{2}}$ in 35-K liquid D_2 were extracted by fittings with a theoretical time dis-

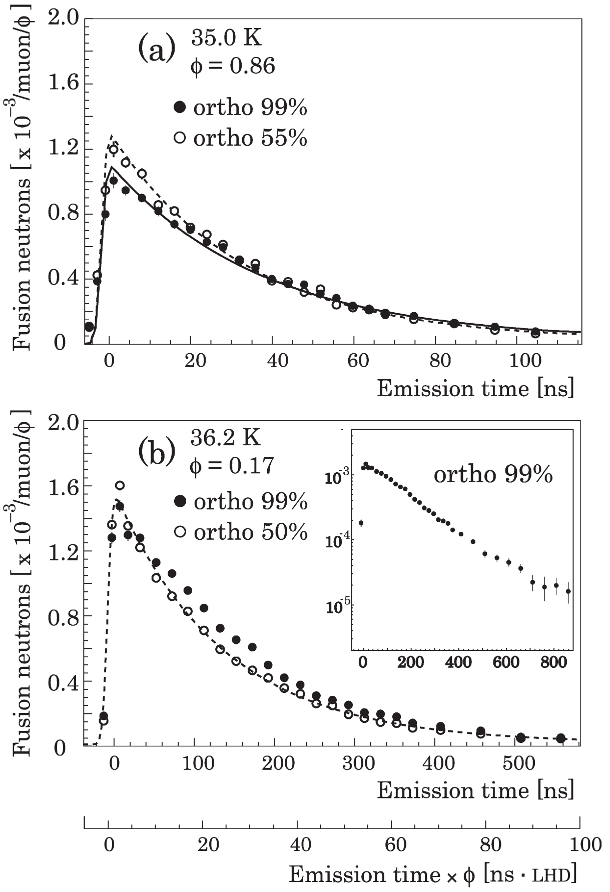

Fig. 2. Fusion neutrons emission time spectra for ortho- and para-enriched D_2 in 35.0-K liquid (a) and 36.2-K gas (b). The emission time after muon injection normalized by the target density is also shown. The solid and dotted lines are fitting results for ortho- and para-enriched D_2 with exponential functions derived from a static kinetics model in *d–d* μCF [4], respectively. The upper-right inset of (b) shows the spectrum for ortho-D_2 on a logarithmic scale. The fast component cannot be described by an exponential time spectrum.

Table 1
The resonant $dd\mu$ formation rate $\tilde{\lambda}_{\frac{3}{2}}$ and the hyperfine transition rate $\tilde{\lambda}_{\frac{3}{2}\frac{1}{2}}$ for 35-K liquid D_2 with different ortho–para concentrations

Temp. [K]	ϕ [LHD]	Ortho [%]	$\tilde{\lambda}_{\frac{3}{2}}$ [μs^{-1}]	$\tilde{\lambda}_{\frac{3}{2}\frac{1}{2}}$ [μs^{-1}]
35.0	0.86	55(1)	3.53(9)	33.2(5)
		66(1)	3.40(9)	32.1(6)
		99(1)	2.99(5)	29.2(5)

tribution function derived from a static kinetics model for *d–d* μCF [4] (Table 1).

In the gas phase, we found that the neutron time spectrum for 36.2-K gas D_2 had a delayed structure that depends on the ortho concentration with overlapping exponential spectrum. This delayed structure was prominent in the spectrum for ortho-D_2 gas. Such structure did not clearly appear in the spectra for 35-K liquid D_2. We note that it is difficult to notice this delayed structure only by analyzing the neutron time spectra with normal-D_2. A similar delayed structure was also clearly observed in the spectra at the lower target densities (e.g., $\phi = 0.03$ and 0.07 LHD). The fusion neutron yield in the prompt time region (e.g., 0–500 ns) for 36.2-K gas D_2 decreases with decrease in the ortho concentration. This tendency is consistent with the theory for isolated D_2 [11]. From the spectra for 36.2-K gas at $\phi = 0.17$ LHD, we also extracted the rates $\tilde{\lambda}_{\frac{3}{2}} = 4.1(1)\ \mu s^{-1}$ and $\tilde{\lambda}_{\frac{3}{2}\frac{1}{2}} = 37.2(5)\ \mu s^{-1}$ for normal-D_2 and the rates $\tilde{\lambda}_{\frac{3}{2}} = 4.2(3)\ \mu s^{-1}$ and $\tilde{\lambda}_{\frac{3}{2}\frac{1}{2}} = 38.5(5)\ \mu s^{-1}$ for para-enriched D_2 (50% ortho) by using the static model. The rates in normal-D_2 are consistent with the PSI data, $\tilde{\lambda}_{\frac{3}{2}} = 3.96(6)\ \mu s^{-1}$ and $\tilde{\lambda}_{\frac{3}{2}\frac{1}{2}} = 36.6(7)\ \mu s^{-1}$ observed at $\phi = 0.0514$ LHD [5]. However, the spectra for ortho-D_2 gas strongly deviate from exponential functions in the time region around ~150 ns. The delayed structure cannot be explained by the conventional theory assuming the rapid $d\mu$ thermalization, which predicts an exponential time spectrum for the resonant *d–d* fusion neutrons. Our result indicates the slow $d\mu$ thermalization taking more than at least 150 ns in gas D_2.

The transient $dd\mu$ formation from $d\mu$ atoms in the thermalizing stage, which was ignored in the static kinetics model of *d–d* μCF, possibly causes the observed delayed structure. In *d–t* μCF, a significant contribution to the transient $dt\mu$ formation of epithermal $t\mu$ in low density targets was reported [18]. This is caused by strong resonance at $t\mu$ kinetic energy of several hundred meV and $t\mu$ acceleration mechanism due to muon transfer and spin-flip process. In our case, the energy region of $d\mu$ participating the transient process should be much lower. The delayed structure depends on the two ortho–para states. The difference between the $d\mu$ deceleration process in ortho- and para-D_2 is negligible in the gas phase due to large D_2 thermal motion [19]. Therefore, the resonant conditions with the lowest resonance energies for ortho- and para-D_2 at several meV dominantly contribute to the transient $dd\mu$ formation.

The origin of the structure would be understood as followings. The theoretical deceleration rate of $d\mu(F = 3/2)$ atoms at energy higher than ~0.1 eV is quite rapid ($\sim 10^9\phi\ s^{-1}$) [19]. In this initial rapid cooling stage of ground-state $d\mu$ (> 0.1 eV), the $d\mu$ energy distribution at 36.2 K is very broad because of the large energy loss. These $d\mu$ atoms cause fusion-neutron emissions independently of the ortho–para ratio in the prompt time region. In the further $d\mu$ deceleration stage (slow thermalization stage), the population of $d\mu(F = 3/2)$ atoms satisfy the lowest resonance conditions for ortho- and para-D_2, which causes the ortho–para dependence of the delayed transient structure.

3.2. Time dependent $dd\mu$ formation rate

In order to extract meaningful parameters from the spectra with the transient structure, time dependent analysis methods are required. We analyzed the time spectra for gas D_2 taking account of the time evolution of the resonant $dd\mu$ formation, $\tilde{\lambda}_{\frac{3}{2}}(t)$, in the early time region. The contribution of $\tilde{\lambda}_{\frac{3}{2}}(t)$ to $\tilde{\lambda}_{\frac{3}{2}\frac{1}{2}}$ through the back decay process of the molecular complex is included as [4]

$$\tilde{\lambda}_{\frac{3}{2}\frac{1}{2}}(t) = \tilde{\lambda}^{\mathrm{scat}}_{\frac{3}{2}\frac{1}{2}} + \frac{\Gamma_{\frac{1}{2}\frac{1}{2}}}{\tilde{\lambda}_f}\left(\tilde{\lambda}_{\frac{3}{2}}(t) - \lambda_{nr}\right), \tag{2}$$

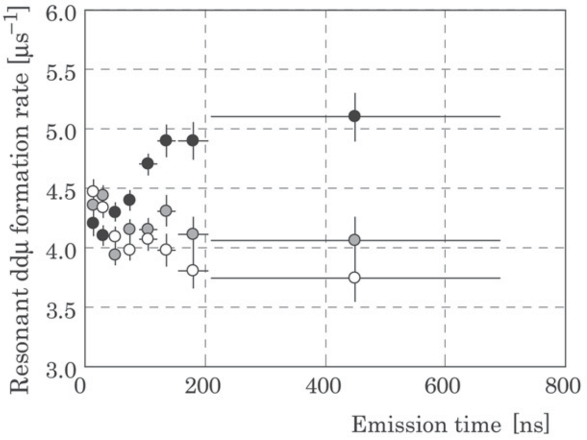

Fig. 3. Time-dependent resonant $dd\mu$ formation rates extracted from fusion neutrons spectra in 36.2-K gas D_2 at $\phi = 0.17$ LHD. The ortho concentrations are 99% (black), 66% (gray) and 50% (white), respectively.

where $\tilde{\lambda}^{\text{scat}}_{\frac{3}{2}\frac{1}{2}}$ is the hyperfine transition rate via scattering, $\Gamma_{\frac{1}{2}\frac{1}{2}}$ is the back-decay rate from the $dd\mu$ with the spin state $S = 1/2$ to the $d\mu$ with $F = 1/2$ and $\tilde{\lambda}_f$ is the d–d fusion rate in the $dd\mu$ molecule. In this analysis, $\Gamma_{\frac{1}{2}\frac{1}{2}}/\tilde{\lambda}_f$ was fixed to a theoretical value 2.6 [20] and $\tilde{\lambda}^{\text{scat}}_{\frac{3}{2}\frac{1}{2}}$ was a fitting parameter. The effective number of muons stopped in the target, $\tilde{n}_\mu = n_\mu \epsilon_n$ (n_μ is number of muons stopped in the target, ϵ_n is total detection efficiency for fusion neutrons) were determined by the analysis in the steady-state region of spectra (e.g., after 1000 ns for $\phi = 0.17$ LHD) with a fixed non-resonant $dd\mu$ formation rate $\tilde{\lambda}_{\frac{3}{2}} = 0.049\ \mu\text{s}^{-1}$. The observed fusion neutron spectrum $N(t)$ is given by [4]

$$N(t) \simeq \tilde{n}_\mu \sum_F \beta_F \phi \tilde{\lambda}_F N_{d\mu F}(t), \tag{3}$$

where β_F is the branching ratio for fusion neutron from $d\mu$ with F, ϕ is the target density in LHD and $N_{d\mu F}$ and $\tilde{\lambda}_F$ are the population and the $dd\mu$ formation rate of $d\mu$ with F, respectively.

The rate of $\lambda_{\frac{3}{2}}(t)$ was determined by a stepwise approach starting with $t = 0$. From the comparison between $N(t)$ and $N_{d\mu F}(t)$ at the time $t = t_0$, we determined $\lambda_{\frac{3}{2}}(t_0)$. The time derivative of $N_{d\mu F}$ at t_0 was calculated by using $\lambda_{\frac{3}{2}}(t_0)$ and Eq. (2), and then the time evolution after $\mathrm{d}t$, $N_{d\mu F}(t_0 + dt)$, was determined. After $t = 200$ ns, a constant value of $\tilde{\lambda}_{\frac{3}{2}}$ was assumed as a steady-state formation rate at 36.2 K. The extracted $\lambda_{\frac{3}{2}}(t)$ for each ortho concentration is shown in Fig. 3. The rate $\tilde{\lambda}^{\text{scat}}_{\frac{3}{2}\frac{1}{2}} = 25(2)\ \mu\text{s}^{-1}$ was also obtained in the fitting. The steady-state resonant rate for normal D_2 extracted in the time-dependent analysis method approximately coincides with that obtained in the conventional analysis with the exponential function due to the small deviation from the exponential function.

The steady-state rate for 99% ortho-D_2 is 24(5)% larger than that for normal-D_2, which is a similar tendency to the theory ($\sim 6\%$) [11].

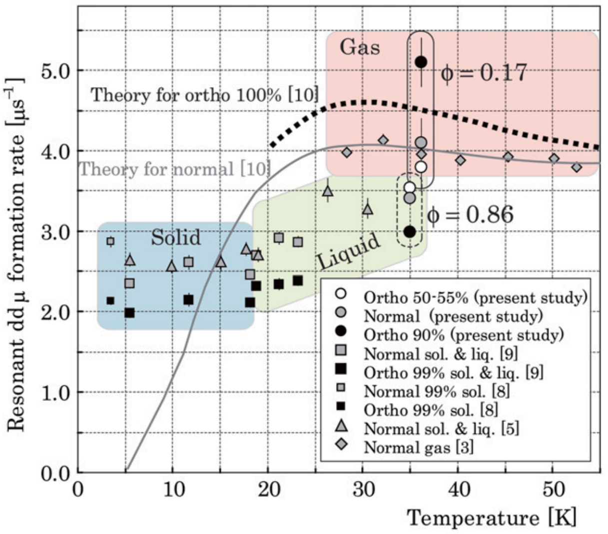

Fig. 4. Temperature dependence of the resonant $dd\mu$ formation rate. We note that the rates at $\phi = 0.17$ LHD were extracted in the time-dependent analysis. The rates at $\phi = 0.86$ LHD and all other rates in previous experiments were extracted with the conventional static model.

Obtained rates of $\tilde{\lambda}_{\frac{3}{2}}$ as a function of temperature are plotted in Fig. 4 with those in other experiments. A large density dependence of the resonant $dd\mu$ formation, especially for ortho-D_2, can be clearly seen. The resonant $dd\mu$ formation rate in ortho-D_2 at $\phi = 0.17$ LHD is 71(10)% higher than that at $\phi = 0.85$ LHD. The dependence is opposite to that in resonant $dt\mu$ formation, where the rate increases with increasing density most likely due to the three-body effect caused by the sub-threshold resonance [21,22].

4. Conclusion

In conclusion, we found the density dependence of the fusion neutrons spectra for various D_2 with different ortho–para concentrations. In the emission-time spectra with ortho-rich gas D_2, the delayed structures have been observed for the first time. Because of the ortho–para dependence, the delayed structure is interpreted as the effect of the transient $dd\mu$ formation of non-thermalized $d\mu$ atoms. The steady-state resonant $dd\mu$ molecular formation rates for ortho–para controlled D_2 were determined taking the transient $dd\mu$ formation into account. The ortho–para dependence of the neutron yield and the extracted rates in the gas phase was opposite to that observed in the liquid phase, which was the experimental evidence of high-density effects in resonant $dd\mu$ formation, especially in ortho-D_2. Further theoretical investigation of high-density effects in $dd\mu$ formation (e.g., rotational and vibrational levels of $[(dd\mu)dee]^*$ at a high density, the contribution of the sub-threshold resonance caused by the three-body effect) and in $d\mu$ thermalization (e.g., competition with $dd\mu$ formation in gas D_2) is required.

Acknowledgements

The authors thank Profs. G.M. Marshall and J.M. Poutissou for their helpful support with the experiment. We thank

Profs. A. Adamczak, L.I. Ponomarev and M.P. Faifman for their useful comments. H. Imao is grateful to Profs. K. Nishiyama and Y. Yamazaki and Drs. Y. Ikedo, D. Tomono, H. Tanaka and H. Miyadera for their encouragement. Part of this study was supported by a Grant-in-Aid for Young Scientists (B)(16740154) from the Japanese Ministry of Education, Science, Sports and Culture, and by the Core-to-Core Program of JSPS (15005) and by a Grant-in-Aid for a JSPS fellowship.

References

[1] E. Vesman, Zh. Eksp. Teor. Fiz. Pis'ma 5 (1967) 50, Sov. Phys. JETP Lett. 5 (1967) 91.
[2] M. Faifman, L. Men'shikov, T. Strizh, Muon Cat. Fus. 4 (1989) 1.
[3] J. Zmeskal, et al., Phys. Rev. A 42 (1990) 1165.
[4] A. Scrinzi, et al., Phys. Rev. A 47 (1993) 4691.
[5] N. Voropaev, et al., Hyperfine Interact. 138 (2001) 191.
[6] D. Demin, et al., Hyperfine Interact. 101/102 (1996) 13.
[7] P. Knowles, et al., Phys. Rev. A 56 (1997) 1970.
[8] A. Toyoda, et al., Phys. Lett. B 509 (2001) 30.
[9] A. Toyoda, et al., Phys. Rev. Lett. 90 (2003) 243401.
[10] H. Imao, et al., Phys. Lett. B 632 (2006) 192.
[11] M. Faifman, private communication, 2005.
[12] M. Leon, J.S. Cohen, Phys. Rev. A 31 (1985) 2680.
[13] A. Adamczak, M.P. Faifman, Phys. Rev. A 64 (2001) 052705.
[14] A. Adamczak, Habilitation thesis, Henryk Niewodniczański Institute of Nuclear Physics, 2003.
[15] V.M. Bystritsky, Phys. Lett. B 94 (1980) 476.
[16] P.C. Souers, Hydrogen Properties for Fusion Energy, University of California Press, Berkeley and Los Angeles, USA, 1986.
[17] I. Silvera, Rev. Mod. Phys. 52 (1980) 393.
[18] M. Jeitler, et al., Phys. Rev. A 51 (1995) 2881.
[19] A. Adamczak, et al., At. Data Nucl. Data Tables 65 (1996) 255;
A. Adamczak, et al., At. Data Nucl. Data Tables 65 (1996) 315;
A. Adamczak, et al., At. Data Nucl. Data Tables 65 (1996) 329.
[20] Y. Petrov, et al., Phys. Rev. A 57 (1998) 1636.
[21] S. Jones, et al., Phys. Rev. Lett. 51 (1983) 1757.
[22] J.S. Cohen, M. Leon, Phys. Rev. A 39 (1989) 946.

DOI: 10.1007/s10967-008-1610-x *Journal of Radioanalytical and Nuclear Chemistry, Vol. 278, No.3 (2008) 777–781*

Non-destructive elemental depth-profiling with muonic X-rays

M. K. Kubo,[1]* H. Moriyama,[1] Y. Tsuruoka,[1] S. Sakamoto,[2] E. Koseto,[3] T. Saito,[3] K. Nishiyama[4]

[1] *International Christian University, Mitaka, Tokyo 181-8585, Japan*
[2] *Japan Atomic Energy Agency, Ibaraki 319-1195, Japan*
[3] *National Museum of Japanese History, Sakura, Chiba-285-8502, Japan*
[4] *High Energy Accelerator Research Organization, Tsukuba, Ibaraki 305-0805, Japan*

(Received July 10, 2008)

An elemental analysis method using muonic X-rays has been developed. Applying the unique features of the negative muon, this method enables elemental distribution in an object to be obtained three dimensionally and non-destructively. Especially, by choosing the incident muon beam energy, depth-profiling as deep as several cm from the surface can be achieved by detecting the high energy muonic X-rays carrying the information of the atom which captured the muon. We obtained some preliminary results and showed the applicability of the technique in future analytical facilities.

Introduction

The elemental composition of archaeological relics, antiquities and artifacts is useful information to understand the history of technology and the propagation of culture. Especially, the composition of materials inside bulk samples gives important information. The destruction of precious samples should be avoided, and so there is an increasing need for non-destructive elemental analysis methods. Requirements for the analysis of historical and archaeological samples are summarized as follows: (1) simultaneous and multi-element; (2) non-destructive, without residual activity; and (3) regioselective analysis bulk samples analysis of inside material: elemental analysis as well as two dimensional scan, since the surface has usually deteriorated and is contaminated. There are a variety of elemental analysis methods, but few satisfy these three criteria. Optical emission spectroscopic methods like ICP require chemical decomposition and cause damage to the sample. Activation analysis is suitable for simultaneous and multi-element purposes, but achieving site specificity without sample destruction is not easy. Charged particle or photon excitation X-ray fluorescence analysis is limited in depth due to the self-absorption of the low energy of electronic X-rays.

The negative muon (μ^-) is a lepton and one of the elementary particles with a lifetime of 2.0 μs, decaying into an electron and two neutrinos.[1] The negative muon μ^- has a mass of 105.7 $\text{MeV}\cdot c^{-2}$, nine times lighter than the proton, but two hundred times heavier than the electron. So, a μ^- with an atomic nucleus can form a muonic atom in which μ^- orbits around the nucleus with a binding energy corresponding to an orbital with an average radius two hundred times smaller than the electronic one. Since the atomic energy levels are approximately proportional to the mass of the orbiting negative particle, the μ^- is two hundred times more strongly bound to the nucleus compared with the electrons.

Negative muons entering materials lose kinetic energy and are eventually captured by atoms to form muonic atoms.[2] After atomic capture, the negative muon experiences a cascade transition from higher orbitals to lower ones with emission of muonic X-rays. The energy of a muonic X-ray is again two hundred times greater than the corresponding electronic X-rays (Table 1).[3] The probability of muon capture by an atom is known to be approximately proportional to the atomic number (*Z*) of the capturing atom, which is known as the FERMI-TELLER law.[4] The yield of muonic X-rays from the material is proportional to the atomic density of the element in the material as a first approximation. It is known that there is some deviation from the Fermi-Teller law depending on the chemical state of the capturing atom,[5,6] but a suitable material chemically similar to the target will work as a standard for qualitative analysis. Every atom in the target has a muonic X-ray emission probability which depends on their abundance. Detection of all elements is possible using proper semiconductor detectors effective over the required photon energy range. All elements present in sufficient amounts are detected.

Table 1. Typical muonic X-ray energy in keV

Element	Kα	Kβ	Lα	Lβ
C	75.8	89.2	13.9	18.8
O	134	158	24.8	33.5
Al	347	422	65.8	88.8
Fe	1256	1704	264	357
Cu	1513	2126	307	444

---

* E-mail:kkubo@icu.ac.jp

0236–5731/USD 20.00

Akadémiai Kiadó, Budapest
Springer, Dordrecht

Table 1 shows some typical muonic X-ray energies. The energy extends up to several MeV depending on *Z*. Muonic X-rays emitted inside the target can be measured easily by gamma-ray detection devices. Normally, particle accelerators used for muon beam production provide muon beams with muon kinetic energies in the range of sub MeV to over a hundred MeV. Muons in this energy region have a stopping range in the orders of mm to cm in bulk materials. By varying the incident energy of the muon beam, it is possible to control the muon penetration depth and obtain elemental depth-profiles by measuring the muonic X-rays emitted from the sample. Since muonic X-ray can penetrate the bulk sample, elemental analysis without destroying the sample is possible. By changing the target position to the beam, two-dimensional element mapping can be carried out. Additional three-dimensional elemental mapping eliminates the possibility of improper sampling caused by inhomogeneity of the sample. An additional advantage of this method is that the measurement can be carried out under atmospheric conditions because muonic X-rays have high energy while PIXE requires samples to be placed in vacuum. Since the timescale of the atomic capture of a negative muon and its cascade down with emission of muonic X-rays is less than ns and much shorter than the lifetime of the muon (which depends on the nucleus capturing the muon, because a negative muon in a 1s state is captured by the nucleus similarly with the EC decay), every muon stops in the target yields more than one muonic X-ray photon. The fluorescence yield is high.

In summary, muonic X-ray measurement is a unique elemental analysis method satisfying the three conditions mentioned above. While the principle of elemental analysis by muonic X-ray has been known for a long time, only a few attempts were made to apply it. We now wish to report our development of a muonic X-ray measurement system and our preliminary results.

Experimental

The muon beam utilized was provided at the Meson Science Laboratory (MSL) at the High Energy Physics Accelerator Organization (KEK) in Tsukuba, Japan. The muon beam was prepared by irradiating a beryllium target with a 500 MeV proton beam to produce pions. The pion decays into a muon and two neutrinos with a lifetime of 26 ns. At the μ-port of MSL, muon beams with particle momenta of 40 to 70 $\text{MeV}\cdot\text{c}^{-1}$ were used. In this energy range the facility had maximum beam intensity of about 10^3 stopping negative muons per pulse in the 20 Hz pulse mode beam operation. Muons were obtained as the decay product of the pion. The beam size was 3 cm in diameter in FWHM and was collimated when a sharp beam was needed. Four CZT (cadmium zinc telluride) detectors (AmpTec), covering the energy range of up to several hundred keV, and two HPGe detectors (Eurisys and Princeton Gamma Tech.), for 100 keV to 2 MeV photons, were arrayed around the target.

Several pure elemental materials were chosen for the first feasibility study. The target materials were placed in the beam as a self-supported target or put on a thin styrofoam target holder. For a check of applicability to archeological artifacts, a bronze mirror made in the first century BC in China was analyzed and also a model Tang San Cai horse was examined. Preliminary depth-profiling capability was studied using three aluminum plates with different thicknesses and a copper plate. Since changing the beam energy by adjusting the current in many beam line magnets is consuming, a copper target was initially positioned in the beam, and then aluminum plates of different thicknesses were placed with the copper plate on the upstream beam side, and the yield of copper and aluminum muonic X-ray yields were measured. Typical measurement runs took 10 to 20 hours for accumulating a statistically sufficient amount of data.

Results and discussion

A typical muonic X-ray energy spectrum for Cu observed with a CZT detector is shown in Fig. 1. Photon energies and corresponding X-ray types are given. The energy of muonic CuKα is 1512 keV. Other L and M series lines were also clearly detected. An annihilation photon and electronic Pb X-rays from the shield were observed. No other significant peaks were observed.

The ancient Chinese bronze mirror gave the muonic X-ray energy spectrum detected by an HPGe detector shown in Fig. 2. Peak area evaluation yielded an atomic ratio of Cu : Sn = 85 : 15 with 10% uncertainty. The number of counts was rather low due to limitations in beam intensity and the peak area estimation error was large. Chemical analysis of the sample showed Cu : Sn = 74 : 26. An increased number of counts would be expected to yield an elemental composition value close to the chemical analysis.

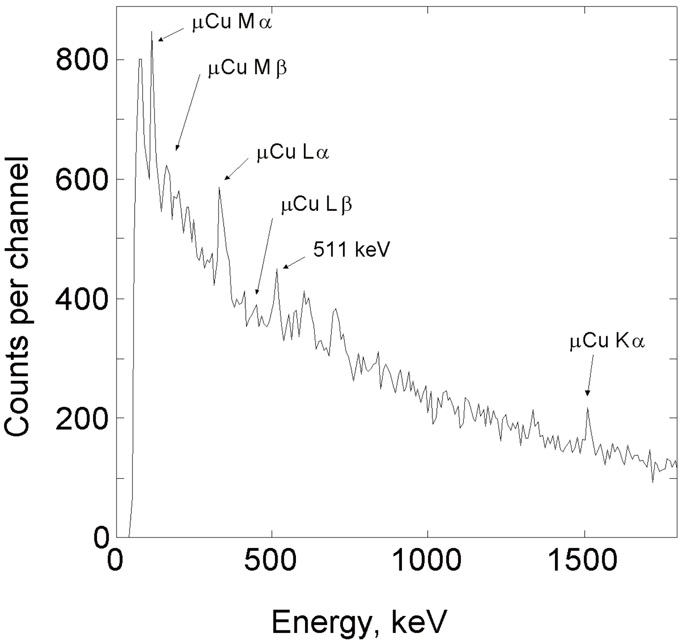

Fig. 1. Muonic X-ray spectrum of copper

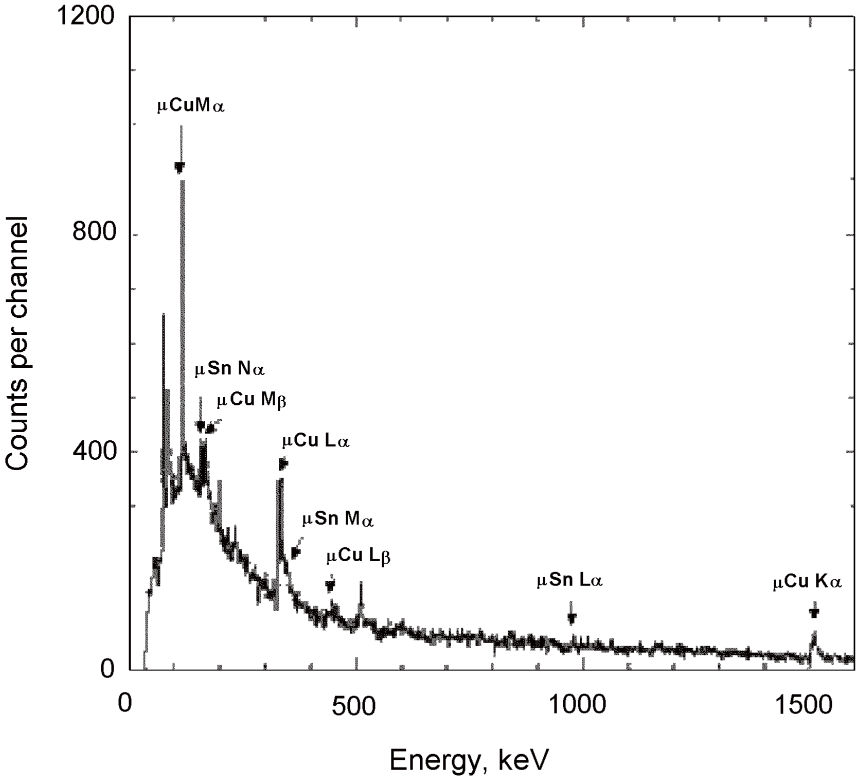

Fig. 2. Muonic X-ray spectrum of an ancient Chinese bronze mirror

A depth-profiling test result with Al and Cu plates is shown in Fig. 3. The base sample was a 2 mm thick copper plate. Three Al plates of the same shape with different thicknesses were placed upstream in the muon beam. As the thickness of the Al plate increased, the muonic X-ray yield increased for Al but decreased for Cu. An approximate depth-profiling of elements was achieved. If the muon stopping range had been sharp and the momentum byte (energy distribution) of the beam had been very narrow, all the muons should have stopped at the same depth from the surface. But in the real situation, the stopping range was broadened by the finite energy distribution of the beam and the longitudinal straggling of the beam particles.

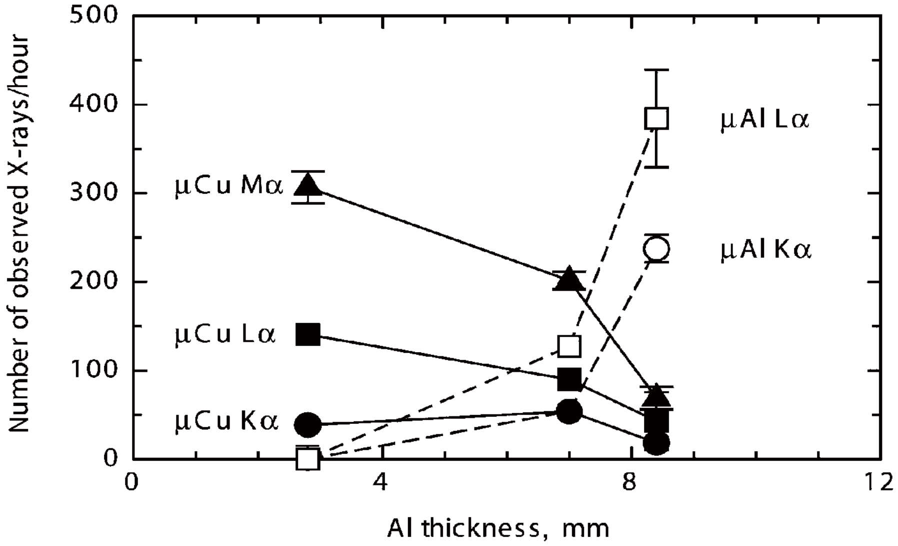

Fig. 3. Depth-profiling experiment result. Three Al plate with 3 mm, 7 mm, 8.4 mm were placed upstream of a Cu plate. Al and Cu muonic X-ray yields were plotted

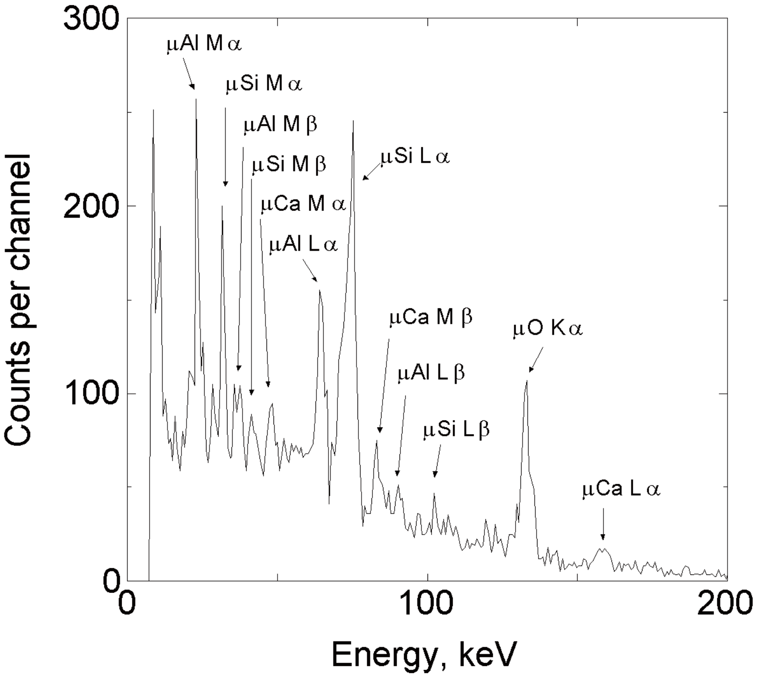

Fig. 4. Muonic X-ray spectrum recorded using a CZT detector of a model Tang San Cai horse

Figure 4 shows a muonic X-ray spectrum recorded with a CZT detector for the model Tang San Cai horse. The sample dimension was about 20 cm long and 12 cm high. Various muonic X-rays from Mg, Al, Si, Ca etc. were observed. The sample was simply placed in the muon beam and the spectrum manifested the elemental composition of the model.

Conclusions

We developed a muonic X-ray elemental analysis system. A feasibility study of the non-destructivity, multi-elementality and depth-selectivity of the method was undertaken. Though the beam intensity limited the statistics, the key advantages of the negative muon approach were demonstrated. Unfortunately the KEK-MSL facility was shut down in 2006. A new high intensity muon beam facility is now under construction in Tokai-mura in Japan. On completion, the facility is to provide a muon beam with an intensity 10^3 times higher than that used in this study. Muonic X-ray analysis will become a useful technique at that site in the near future.

References

1. W.-M. YAO et al., J. Phys., G 33 (2006) 1.
2. K. NAGAMINE, Introductory Muon Physics, Cambridge, 2003.
3. R. ENGFER, H. SCHNEWLY, J. L. VUILLEUMIER, H. K. WALTER, A. ZEHNDER, Atom. Data and Nucl. Data Tables, 14 (1974) 509.
4. E. FERMI, E. TELLER, Phys. Rev., 23 (1947) 39.
5. Y. SAKAI, T. TOMINAGA, K. ISHIDA, K. NAGAMINE, Radiochim. Acta, 36 (1984) 173.
6. M. K. KUBO, Y. SAKAI, T. TOMINAGA, K. NAGAMINE, Radiochim. Acta, 47 (1989) 77.

Journal of the Physical Society of Japan
Vol. 78, No. 2, February, 2009, 023710

Full Gap Superconductivity in $Ba_{0.6}K_{0.4}Fe_2As_2$ Probed by Muon Spin Rotation

Masatoshi HIRAISHI[1], Ryosuke KADONO[1,2]*, Soshi TAKESHITA[2], Masanori MIYAZAKI[1],
Akihiro KODA[1,2], Hirotaka OKABE[3], and Jun AKIMITSU[3]

[1]*Department of Materials Structure Science, School of High Energy Accelerator Science,*
The Graduate University for Advanced Studies, 1-1 Oho, Tsukuba, Ibaraki 305-0801
[2]*Muon Science Laboratory, Institute of Materials Structure Science,*
High Energy Accelerator Research Organization (KEK), 1-1 Oho, Tsukuba, Ibaraki 305-0801
[3]*Department of Physics and Mathematics, Aoyama Gakuin University,*
Fuchinobe, Sagamihara, Kanagawa 229-8558

(Received December 11, 2008; accepted December 24, 2008; published February 10, 2009)

Superfluid density (n_s) in the mixed state of an iron pnictide superconductor $Ba_{1-x}K_xFe_2As_2$ is determined by muon spin rotation for a sample with optimal doping ($x = 0.4$). The temperature dependence of n_s is perfectly reproduced using the conventional BCS model for *s*-wave paring, where the order parameter can be either a single-gap structure with $\Delta = 8.35(6)$ meV [$2\Delta/k_BT_c = 5.09(4)$] or double-gap structure with $\Delta_1 = 12$ meV (fixed) [$2\Delta_1/k_BT_c = 7.3$] and $\Delta_2 = 6.8(3)$ meV [$2\Delta_2/k_BT_c = 4.1(2)$]. The latter is consistent with the recent result obtained by the angle-resolved photoemission spectroscopy. The large gap parameters ($2\Delta/k_BT_c$) indicate the extremely strong coupling of carriers to bosons that mediate the Cooper pairing.

KEYWORDS: oxypnictide superconductor, order parameter, muon spin rotation
DOI: 10.1143/JPSJ.78.023710

The recent discovery of high-T_c superconductivity in $LaFeAsO_{1-x}F_x$ (LFAO-F, $T_c \simeq 26$ K) and of related compounds[1–14] has attracted broad attention regarding the mechanism of superconductivity on Fe_2As_2 layers that show some apparent similarities with CuO_2 layers. They have a common feature, that is, the superconductivity occurs upon carrier doping to the transition metal oxide/pnictide layers that exhibit instability towards magnetic order at low temperatures. In the case of LFAO-F and its family compounds, *electrons* are introduced by the substitution of O^{2-} with F^- in the La_2O_2 layers.[1–4] Moreover, very recent developments demonstrate increasing variety in the methods of electron doping such as oxygen depletion[5,6] or Co substitution for Fe.[7–10] In contrast, *hole* doping is attained in AFe_2As_2 ($A =$ Ba, Sr, Ca) by the substitution of divalent cations (A^{2+}) with alkali metals (B^+).[11–14] This situation provides an excellent opportunity to examine the "electron-hole symmetry" regarding the superconducting properties of iron pnictides, which is also one of the major issues in cuprates.

Microscopic evidence shows that the parent compound $BaFe_2As_2$ exhibits magnetic order (SDW) below 140 K, which is accompanied by a structural phase transition.[15,16] The situation is common to $Sr_{1-x}K_xFe_2As_2$,[17] and it is suggested that the electronic ground state of Fe_2As_2 layers in the parent compound is quite similar to that in LaFeAsO. However, the doping phase diagram is markedly different from LFAO-F, because it exhibits superconductivity over a wide range of hole content $p = x/2$ (per FeAs chemical formula) from 0.05 to 0.5 that far exceeds LFAO-F (i.e., $0.06 \le x \le 0.2$).[12] The phase diagram is also characterized by a bell-shaped variation of T_c against x, where the maximal $T_c \simeq 38$ K is attained near $x \sim 0.4$ ($p \sim 0.2$). Considering the manifold nature of electronic band structure of Fe_2As_2 layers suggested by theories,[18–20] this difference may be attributed to that of the bands relevant to the doped carriers. Here, we report the result of our μSR study on $Ba_{1-x}K_xFe_2As_2$ (BKFA) for samples with $x = 0.1$ ($T_c < 2$ K) and 0.4 ($T_c \simeq 38$ K). The result indicates that, while the magnetic ground state for $x = 0.1$ is mostly identical with that of other pristine iron pnictides, the superconducting property in the optimally doped sample is characterized by gap parameters that are much greater than those of LFAO-F[21–23] and $CaFe_{1-x}Co_xAsF$ (CFCAF, another subclass of electron-doped iron pnictide superconductor).[24]

Polycrystalline samples of $Ba_{1-x}K_xFe_2As_2$ with nominal compositions of $x = 0.1$ and 0.4 were prepared by a solid-state reaction using Ba (99%, Furuya Metal), K (99%, Kojundo-Kagaku), Fe (99.9%, Kojundo-Kagaku), and As (99.9999%, Furuchi Chemical) as starting materials; the details of the preparation process are described in an earlier report.[14] Concerning the K-doped samples, the reproducibility of synthesis was improved with the use of barium and potassium arsenides as precursors. The purity of as-grown samples (sintered slabs with a dimension of $\sim 10 \times 12$ to 15×1 mm^3, net weight of ~ 0.3 g) was examined by powder X-ray diffraction using a diffractometer with a graphite monochromator (MultiFlex, Rigaku). All the observed diffraction peaks in the sample with $x = 0.4$ were perfectly reproduced with those of the single-phase compound,[11] while a minor unknown impurity phase ($\sim$2%) was observed for $x = 0.1$. Conventional μSR measurements were performed using the LAMPF spectrometer installed on the M20 beamline of TRIUMF, Canada. During the measurement under a zero field (ZF), the residual magnetic field at the sample position was reduced below 10^{-6} T with the initial muon spin direction parallel to the muon beam direction [$\boldsymbol{P}_\mu(0) \parallel \hat{z}$]. Time-dependent muon polarization [$G_z(t) = \hat{z} \cdot \boldsymbol{P}_\mu(t)$] was monitored by measuring the decay-positron asymmetry along the $\hat{z}$-axis. Transverse field (TF) condition was realized by rotating the initial muon polarization so that $\boldsymbol{P}_\mu(0) \parallel \hat{x}$, where the asymmetry was monitored along the $\hat{x}$-axis to obtain $G_x(t) = \hat{x} \cdot \boldsymbol{P}_\mu(t)$. All the measurements under

---

*E-mail: ryosuke.kadono@kek.jp

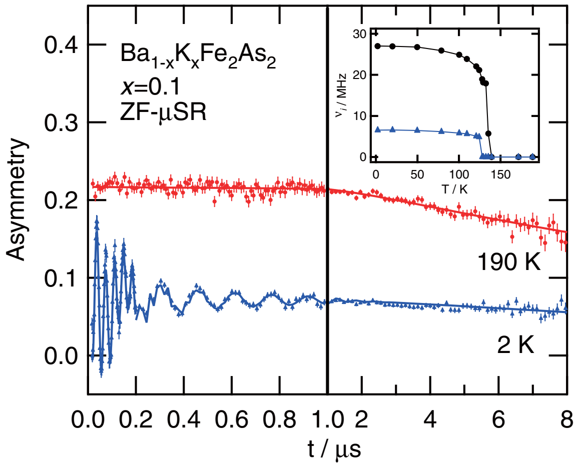

Fig. 1. (Color online) ZF-μSR time spectra observed at 190 and 2 K in $Ba_{1-x}K_xFe_2As_2$ sample with $x = 0.1$ ($T_c < 2$ K), where a spontaneous muon precession signal (mainly consisting of two frequencies) is clearly seen. Inset shows the temperature dependence of the precession frequency.

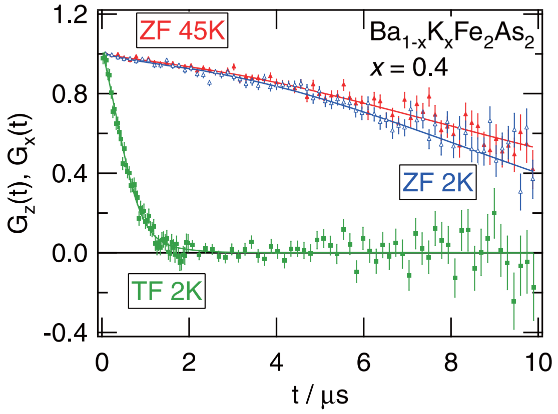

Fig. 2. (Color online) ZF-μSR time spectra observed at 45 and 2 K in $Ba_{1-x}K_xFe_2As_2$ sample with $x = 0.4$ ($T_c \simeq 38$ K). No trace of magnetic phase is observed. The spectra under a transverse field (TF) at 2 K is displayed on a rotating reference frame to extract the envelop function. Solid curves are fits using a Gaussian relaxation function described in the text.

a magnetic field were made by cooling the sample to the target temperature after the field equilibrated.

Figure 1 shows the μSR spectra obtained upon muon implantation to the sample with $x = 0.1$ under zero external field, where one can readily identify an oscillatory signal with multiple-frequency components in the spectrum at 2 K. The Fourier transform of the spectrum indicates that there are actually two components, one approaching to $\nu_1 = 27.0(1)$ MHz and another to $\nu_2 = 6.53(2)$ MHz [at 2 K, corresponding to internal fields of 0.20(1) and 0.0482(1) T, respectively]. This is consistent with an earlier result of a μSR study in $Ba_{1-x}K_xFe_2As_2$, where signals were observed at 28.8 and 7 MHz in a parent compound ($x = 0$).[16] While the quality of their K-doped sample ($x = 0.45$) seems to have some problem regarding homogeneity (see below), its magnetic phase exhibits a tendency that ν_1 is slightly reduced (~26 to 27 MHz). This is quite in line with the slight reduction of ν_1 observed for our sample with $x = 0.1$, and naturally understood as a result of enhanced itinerant character for *d* electrons in K-doped compounds. The magnitude of the internal field probed by μSR is close to that observed in LFAO (~23 and 3 MHz),[21,25] and thus, it is suggested that the high-frequency component corresponds to the signal from muons situated on the Fe_2As_2 layers (while the low-frequency component coming from those located near the cation sites). The onset temperature for the high frequency component is close to 140 K, which is also consistent with earlier reports.[15,16]

On the other hand, it is inferred from ZF-μSR spectra in Fig. 2 that no trace of magnetism is found in the sample with $x = 0.4$. This is in marked contrast with the earlier report on μSR measurements in a sample with $x = 0.45$ where a magnetic phase seems to dominate over a large volume fraction (~80%).[16] Concerning the bulk superconducting property, the quality of our specimen can be assessed by looking into magnetization data, which is shown in Fig. 3(a). The sharp onset as well as a large Meissener fraction ($\geq 4\pi$ for ZFC) confirms the excellent quality of the present specimen.

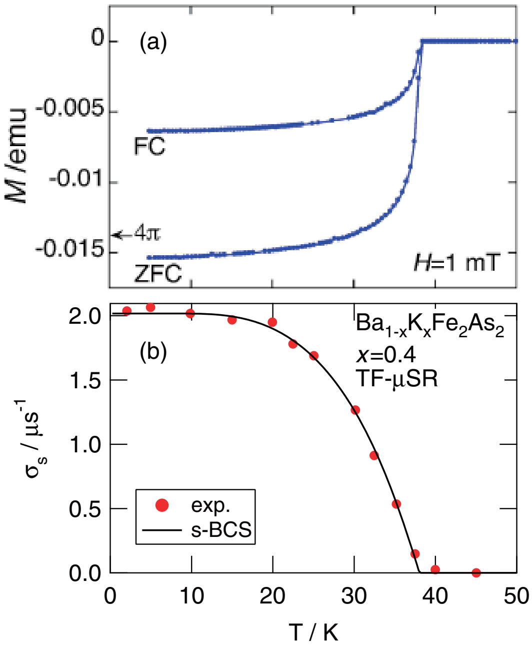

Fig. 3. (Color online) (a) Magnetization of $Ba_{1-x}K_xFe_2As_2$ measured on the μSR sample with $x = 0.4$, where data were obtained after cooling under an external field (FC) or zero field (ZFC). The total weight of the sample is 0.1 g, and the magnetization corresponding to 4π is obtained using the structural parameters reported in ref. 11. (b) Temperature dependence of Gaussian linewidth $\sigma_s = \sqrt{2}\delta_s$ determined by TF-μSR measurement with $H = 0.1$ T. Solid curve is a fit using weak-coupling BCS model (see text for detail).

The μSR time spectra under a transverse field ($\mu_0 H = 0.1$ T) is shown in Fig. 2, where the envelop of the damping oscillation is extracted (by displaying on a rotating reference frame). It exhibits depolarization towards zero, indicating that the entire sample falls into the flux line lattice state to exert strongly inhomogeneous internal field [$B(\mathbf{r})$] to implanted muons. The lineshape is well represented by a Gaussian damping, and the analysis is made by curve fit using the following model function,

$$G_x(t) = \exp\left[-\frac{1}{2}(\delta_N^2 + \sigma_s^2)t^2\right]\cos(2\pi f_s t + \phi), \qquad (1)$$

where $\sigma_s = \gamma_\mu \langle (B(\mathbf{r}) - B_0)^2 \rangle^{1/2}$ with $B_0 \simeq \mu_0 H$ being the mean value of the local field $B(\mathbf{r})$,[26] $2\pi f_s \simeq \gamma_\mu B_0$ (with $\gamma_\mu = 2\pi \times 135.53\,\mathrm{MHz/T}$), and δ_N is the depolarization due to random local fields from nuclear magnetic moments. For the extraction of σ_s, δ_N is determined by curve fits above T_c and then subtracted from the total linewidth obtained for the spectra below T_c.

The deduced linewidth, σ_s, is plotted against temperature in Fig. 3(b), where σ_s is the quantity proportional to the superfluid density n_s,

$$\sigma_s \propto \frac{1}{\lambda^2} = \frac{n_s e^2}{m^* c^2}, \qquad (2)$$

where λ is the effective London penetration depth and m^* is the effective mass of the superconducting carriers. Compared with the results of μSR studies in LFAO-F[21–23] and that recently obtained for CFCAF,[24] it is clear that σ_s rises relatively sharply just below T_c, and becomes mostly independent of temperature below 15 K ($\simeq 0.4T_c$). A curve fit using the power law, $\sigma_s = \sigma_0[1 - (T/T_c)^\beta]$, yields $\beta = 4.08(5)$, which is perfectly in line with the prediction using the conventional BCS model for *s*-wave pairing. The gap parameter is obtained with a fit using the weak-coupling BCS model to yield $\Delta = 8.35(6)\,\mathrm{meV}$ and corresponding ratio $2\Delta/k_B T_c = 5.09(4)$. While these values are consistent with the superconducting order parameter of the isotropic *s*-wave pairing, the gap parameter far exceeds the prediction using the weak-coupling BCS theory ($2\Delta/k_B T_c = 3.53$), and thereby suggesting a very strong coupling of superconducting carriers to some bosonic excitations.

It is inferred from a recent angle-resolved photoemission spectroscopy (ARPES) study on BKFA with the same potassium content that the magnitude of the superconducting gap depends on the Fermi surfaces.[27] It is reported that $\Delta_1 \sim 12\,\mathrm{meV}$ on small Fermi surfaces and $\Delta_2 \sim 6\,\mathrm{meV}$ on the large one. We examined the consistency of our data with the ARPES result by employing a phenomenological double-gap model with *s*-wave symmetry,[28,29]

$$\sigma_s(T) = \sigma(0) - w \cdot \delta\sigma(\Delta_1, T) - (1 - w) \cdot \delta\sigma(\Delta_2, T),$$

$$\delta\sigma(\Delta, T) = \frac{2\sigma(0)}{k_B T}\int_0^\infty f(\varepsilon, T)\cdot[1 - f(\varepsilon, T)]\,d\varepsilon,$$

$$f(\varepsilon, T) = \left(1 + e^{\sqrt{\varepsilon^2 + \Delta(T)^2}/k_B T}\right)^{-1},$$

where Δ_i ($i = 1$ and 2) is the energy gap at $T = 0$, w is the relative weight for $i = 1$, k_B is the Boltzmann constant, $f(\varepsilon, T)$ is the Fermi distribution function, and $\Delta(T)$ is the standard BCS gap energy. The curve fit assuming a common $T_c = 38\,\mathrm{K}$ and a large gap fixed to 12 meV ($2\Delta_1/k_B T_c = 7.3$) perfectly reproduces the data in Fig. 3(b) with $\Delta_2 = 6.8(3)\,\mathrm{meV}$ [$2\Delta_2/k_B T_c = 4.1(2)$] and the relative weight $w = 0.30(3)$, where the obtained curve is virtually identical with that for the single gap on Fig. 3(b). This, while endorsing the credibility of our data in terms of temperature dependence of σ_s, indicates that the quasiparticle excitation spectrum associated with multiple-gap superconductivity tends to be merged into that of the single gap when the small gap has a large value for $2\Delta/k_B T_c$.

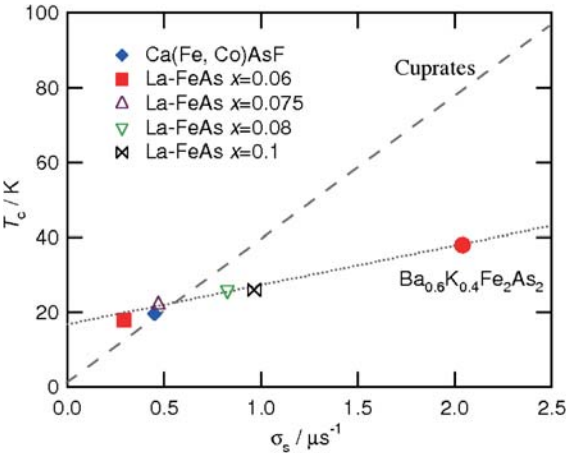

Fig. 4. (Color online) A plot of superconducting transition temperature vs muon spin relaxation rate $\sigma_s(T \to 0)$, where a solid circle indicates the present data. Other points are quoted selectively for relevant iron pnictides (LFAO-F,[21–23] CFCAF[24]). The empirical relation is indicated by a dashed line,[30] and the dotted line connecting points for iron pnictides is only meant as a guide for the eye.

It has been shown in our previous μSR studies on LFAO-F[23] and CFCAF[24] that the temperature dependence of σ_s in these compounds (with a doping range near the boundary between magnetic and superconducting phases) can be reproduced using the above-mentioned double-gap model, where the gap parameters are considerably smaller than those in BKFA [e.g., $2\Delta_1/k_B T_c = 4.2(3)$, $2\Delta_2/k_B T_c = 1.1(3)$ in LFAO-F with $x = 0.06$, and $2\Delta_1/k_B T_c = 3.8(8)$, $2\Delta_2/k_B T_c = 1.1(7)$ in CFCAF with $x = 0.075$]. The double-gap feature revealed by ARPES supports a view that superconductivity occurs on complex Fermi surfaces consisting of many bands (at least five Fe *d* bands) that would give rise to certain intricacy.[18–20] Apart from the validity of applying the double-gap model to electron-doped iron pnictides, these figures suggest that the hole doping may occur in the bands different from those for electron doping, where the characteristic energy of the Cooper pairing may differ among those bands.

Finally, we point out that the superfluid density in the optimally doped $Ba_{1-x}K_xFe_2As_2$ does not satisfy the empirical linear relation with T_c observed for underdoped cuprates.[30] As shown in Fig. 4, the corresponding muon spin relaxation rate [$\sigma_s(0) = 2.02(1)\,\mu\mathrm{s}^{-1}$, which yields the magnetic penetration depth $\lambda = 230(1)\,\mathrm{nm}$] is more than twice as large as what is expected for compounds with $T_c = 38\,\mathrm{K}$ from the empirical line indicated by a dashed line. The data for other iron pnictides are also plotted for comparison, in which we omitted those for the compounds containing rare-earth elements (Ce, Nd, Sm,...) because of the general ambiguity anticipated for extracting σ_s under strong additional depolarization due to the magnetism of rare-earth ions. They show a tendency that σ_s (and accordingly n_s) is independent of T_c. This is qualitatively different from underdoped cuprates, and rather close to the behavior predicted on the basis of the conventional BCS theory where the condensation energy does not depend on n_s.

In summary, we have shown in a hole-doped iron pnictide, $Ba_{1-x}K_xFe_2As_2$, that the superconducting order parameter is characterized by a strong coupling to paring bosons, as inferred from large gap parameters ($2\Delta_i/k_{\rm B}T_{\rm c} \gg 3.53$). The temperature dependence of the superfluid density, $n_{\rm s}(T)$, determined by μSR is perfectly in line with that predicted using the conventional BCS model with fully gapped s-wave pairing. A detailed analysis with phenomenological double-gap model indicates that $n_{\rm s}(T)$ is also consistent with the presence of a double gap, although the large gap parameters make it difficult to determine the multitude of the energy gap solely from $n_{\rm s}(T)$.

Acknowledgments

We would like to thank the TRIUMF staff for their technical support during the μSR experiment. This work was partially supported by the KEK-MSL Inter-University Program for Oversea Muon Facilities and by a Grant-in-Aid for Creative Scientific Research on Priority Areas from the Ministry of Education, Culture, Sports, Science and Technology, Japan.

1) Y. Kamihara, T. Watanabe, M. Hirano, and H. Hosono: J. Am. Chem. Soc. **130** (2008) 3296.
2) X. H. Chen, T. Wu, R. H. Liu, H. Chen, and D. F. Fang: Nature **453** (2008) 761.
3) Z. A. Ren, W. Lu, J. Yang, W. Yi, X. L. Shen, Z. C. Li, G. C. Che, X. L. Dong, L. L. Sun, F. Zhou, and Z. X. Zhao: Chin. Phys. Lett. **25** (2008) 2215.
4) G. F. Chen, Z. Li, D. Wu, G. Li, W. Z. Hu, J. Dong, P. Zheng, J. L. Luo, and N. L. Wang: Phys. Rev. Lett. **100** (2008) 247002.
5) H. Kito, H. Eisaki, and A. Iyo: J. Phys. Soc. Jpn. **77** (2008) 063707.
6) Z. A. Ren, G.-C. Che, X.-L. Dong, J. Yang, W. Lu, W. Yi, X. L. Shen, Z. C. Li, L.-L. Sun, F. Zhou, and Z.-X. Zhao: Europhys. Lett. **83** (2008) 17002.
7) A. S. Sefat, A. Huq, M. A. McGuire, R. Jin, B. C. Sales, D. Mandrus, L. M. D. Cranswick, P. W. Stephens, and K. H. Stone: Phys. Rev. B **78** (2008) 104505.
8) A. S. Sefat, R. Jin, M. A. McGuire, B. C. Sales, D. J. Singh, and D. Mandrus: Phys. Rev. Lett. **101** (2008) 117004.
9) Y. Qi, Z. Gao, L. Wang, D. Wang, X. Zhang, and Y. Ma: Supercond. Sci. Technol. **21** (2008) 115016.
10) S. Matsuishi, Y. Inoue, T. Nomura, H. Yanagi, M. Hirano, and H. Hosono: J. Am. Chem. Soc. **130** (2008) 14428.
11) M. Rotter, M. Tegel, and D. Johrendt: Phys. Rev. Lett. **101** (2008) 107006.
12) K. Sasmal, B. Lv, B. Lorenz, A. M. Guloy, F. Chen, Y. Y. Xue, and C. W. Chu: Phys. Rev. Lett. **101** (2008) 107007.
13) G. F. Chen, Z. Li, G. Li, W. Z. Hu, J. Dong, J. Zhou, X. D. Zhang, P. Zheng, N. L. Wang, and J. L. Luo: Chin. Phys. Lett. **25** (2008) 3403.
14) G. Wu, H. Chen, T. Wu, Y. L. Xie, Y. J. Yan, R. H. Liu, X. F. Wang, J. J. Ying, and X. H. Chen: J. Phys.: Condens. Matter **20** (2008) 422201.
15) M. Rotter, M. Tegel, D. Johrendt, I. Schellenberg, W. Hermes, and R. Pöttgen: Phys. Rev. B **78** (2008) 020503.
16) A. A. Aczel, E. Baggio-Saitovitch, S. L. Budko, P. C. Canfield, J. P. Carlo, G. F. Chen, P. Dai, T. Goko, W. Z. Hu, G. M. Luke, J. L. Luo, N. Ni, D. R. Sanchez-Candela, F. F. Tafti, N. L. Wang, T. J. Williams, W. Yu, and Y. J. Uemura: Phys. Rev. B **78** (2008) 214503.
17) J. Zhao, D. X. Yao, S. Li, T. Hong, Y. Chen, S. Chang, W. Ratcliff II, J. W. Lyn, H. A. Mook, G. F. Chen, J. L. Luo, N. L. Wang, E. W. Carlson, J. Hu, and P. Dai: Phys. Rev. Lett. **101** (2008) 167203.
18) I. I. Mazin, D. J. Singh, M. D. Johannes, and M. H. Du: Phys. Rev. Lett. **101** (2008) 057003.
19) K. Kuroki, S. Onari, R. Arita, H. Usui, Y. Tanaka, H. Kontani, and H. Aoki: Phys. Rev. Lett. **101** (2008) 057004.
20) Y. Nagai, N. Hayashi, N. Nakai, H. Nakamura, M. Okumura, and M. Machida: New J. Phys. **10** (2008) 103026.
21) J. P. Carlo, Y. J. Uemura, T. Goko, G. J. MacDougall, J. A. Rodriguez, W. Yu, G. M. Luke, P. Dai, N. Shannon, S. Miyasaka, S. Suzuki, S. Tajima, G. F. Chen, W. Z. Hu, J. L. Luo, and N. L. Wang: arXiv:0805.2186.
22) H. Luetkens, H. H. Klauss, R. Khasanov, A. Amato, R. Klingeler, I. Hellmann, N. Leps, A. Kondrat, C. Hess, A. Köhler, G. Behr, J. Werner, and B. Büchner: Phys. Rev. Lett. **101** (2008) 097009.
23) S. Takeshita, R. Kadono, M. Hiraishi, M. Miyazaki, A. Koda, Y. Kamihara, and H. Hosono: J. Phys. Soc. Jpn. **77** (2008) 103703.
24) S. Takeshita, R. Kadono, M. Hiraishi, M. Miyazaki, A. Koda, S. Matsuishi, and H. Hosono: arXiv:0812.1670.
25) H.-H. Klauss, H. Luetkens, R. Klingeler, C. Hess, F. J. Litterst, M. Kraken, M. M. Korshunov, I. Eremin, S.-L. Drechsler, R. Khasanov, A. Amato, J. Hamann-Borrero, N. Leps, A. Kondrat, G. Behr, J. Werner, and B. Büchner: Phys. Rev. Lett. **101** (2008) 077005.
26) E. H. Brandt: Phys. Rev. B **37** (1988) 2349.
27) H. Ding, P. Richard, K. Nakayama, K. Sugawara, T. Arakane, Y. Sekiba, A. Takayama, S. Souma, T. Sato, T. Takahashi, Z. Wang, X. Dai, Z. Fang, G. F. Chen, J. L. Luo, and N. L. Wang: Europhys. Lett. **83** (2008) 47001.
28) F. Bouquet, Y. Wang, R. A. Fisher, D. G. Hinks, J. D. Jorgensen, A. Junod, and N. E. Phillips: Europhys. Lett. **56** (2001) 856.
29) K. Ohishi, T. Muranaka, J. Akimitsu, A. Koda, W. Higemoto, and R. Kadono: J. Phys. Soc. Jpn. **72** (2003) 29.
30) Y. J. Uemura: J. Phys.: Condens. Matter **16** (2004) S4515.

Insular Superconductivity in a Co-Doped Iron Pnictide $CaFe_{1-x}Co_xAsF$

S. Takeshita,[1] R. Kadono,[1,2] M. Hiraishi,[2] M. Miyazaki,[2] A. Koda,[1,2] S. Matsuishi,[3] and H. Hosono[3,4]

[1]*Institute of Materials Structure Science, High Energy Accelerator Research Organization, Tsukuba, Ibaraki 305-0801, Japan*
[2]*Department of Materials Structure Science, The Graduate University for Advanced Studies, Tsukuba, Ibaraki 305-0801, Japan*
[3]*Frontier Research Center, Tokyo Institute of Technology, Yokohama, Kanagawa 226-8503, Japan*
[4]*Materials and Structures Laboratory, Tokyo Institute of Technology, Yokohama, Kanagawa 226-8503, Japan*

(Received 9 December 2008; published 8 July 2009)

The presence of a macroscopic phase separation between the superconducting and magnetic phases in $CaFe_{1-x}Co_xAsF$ is demonstrated by muon spin rotation measurements conducted across their phase boundaries ($x = 0.05$–0.15). The magnetic phase tends to retain the high transition temperature ($T_m > T_c$), while Co doping induces strong randomness. The volumetric fraction of the superconducting phase is nearly proportional to the Co content x with a constant superfluid density. These observations suggest the formation of superconducting "islands" (or domains) associated with Co ions in the Fe_2As_2 layers, indicating a very short coherence length.

DOI: 10.1103/PhysRevLett.103.027002 PACS numbers: 74.70.Ad, 74.25.Jb, 76.75.+i

The oxypnictide superconductor $LaFeAsO_{1-x}F_x$ (LFAO-F) with a critical temperature (T_c) of 26 K [1] was recently discovered. The successful revelation about the considerable increase in T_c on substitution of La with other rare-earth elements (Ce, Pr, Nd, Sm, etc., leading to a maximum T_c of 55 K [2–5]) and application of pressure for LFAO-F (~43 K [6]) has triggered wide interest in mechanisms that yield a relatively high T_c for this new class of compounds. These compounds have a layered structure like that exhibited by high-T_c cuprates, where the conducting Fe_2As_2 layers are isolated from the charge reservoir layers so that the doped carriers (*electrons* in this case) introduced by the substitution of O^{2-} with F^- in the La_2O_2 layers can move within the layers of strongly bonded Fe and As atoms. LFAO-F exhibit another qualitative similarity to cuprates: they exhibit superconductivity upon carrier doping of pristine compounds that exhibit magnetism [7–14]. The results of the recent muon spin rotation or relaxation (μSR) experiment conducted on a variety of iron-pnictide superconductors showed that the superfluid density n_s falls on the empirical line on the n_s vs T_c diagram of the *underdoped* cuprates [10,15]; on the basis of this result, the possibility of the oxypnictides and cuprates having the same mechanism of superconductivity is discussed.

The iron pnictides exhibit another interesting similarity with cuprates: the variation of their T_c with doping concentration (x) is "bell-shaped" in hole-doped compounds ($A_{1-x}K_xFe_2As_2$, $A =$ Ba, Sr) [16,17], while T_c does not vary significantly with x in electron-doped compunds [1,18]. Recent investigations on electron-doped (n-type) cuprates strongly suggest that such electron-hole "asymmetry" is a consequence of the difference in the fundamental properties of underlying electronic states between the hole-doped and electron-doped compounds; the n-type cuprates are more like normal Fermi liquids rather than doped Mott insulators [19]. This result is strongly supported by the fact that given that all the doped carriers participate in the Cooper pairs (as suggested experimentally), the insensitivity of T_c to the variation of n_s ($\propto x$) cannot be reconciled with the above mentioned empirical linear relation (n_s vs T_c); the result is also reasonably understood on the basis of the conventional BCS theory, in which condensation energy is predicted to be independent of carrier concentration. More interestingly, the very recent revelation about superconductivity induced by substitution of Fe with Co in LFAO and other iron pnictides (the Co atoms serve as electron donors) brings out the sheer contrast between the oxypnictides and cuprates in terms of tolerance to distortions in the conducting layers [20–23].

Considering the close relationship between magnetism and superconductivity, it is suggested that a detailed investigation of how these two phases coexist (and compete) near the phase boundary will provide important clues for the elucidation of the pairing mechanism. Among the various techniques available for this, (μSR) has an important advantage in that it can be applied to systems consisting of spatially inhomogeneous multiple phases to provide information on each phase, depending on their fractional yield. We conducted μSR measurements on $CaFe_{1-x}Co_xAsF$ (CFCAF, a variation of LFAO with trivalent cation and oxygen replaced with divalent alkali metal and fluorine, respectively, with the carrier doping achieved by substituting Co for Fe) and found a unique character of the Fe_2As_2 layers; it was found that the superconducting state exists over the vicinity of Co atoms, as inferred from the observation that the superconducting volume fraction is nearly proportional to the Co concentration, while n_s remains unchanged. The rest of the CFCAF specimen exhibits magnetism (strongly modulated spin density wave), indicating that superconductivity coexists with magnetism in the form of a phase separation.

Unlike other oxypnictides with rare-earth metals, CFCAF has a major advantage because it is possible to identify the origin of magnetism, if at all detected by μSR, in the Fe_2As_2 layers without ambiguity. With the target concentration set around the phase boundary, polycrystalline samples with $x = 0$, 0.05, 0.075, 0.10, and 0.15 have been synthesized by solid state reaction. The detailed procedure of sample preparation is the same as that described in an earlier report [23], except that the sintering was carried out at 900 °C for 20 h. The samples were confirmed to be mostly of single phase by the x-ray diffraction method; CaF_2 (2.6, 3.3, and 6.2 wt % for $x = 0$, 0.075, and 0.15, respectively) and FeAs (3.3 wt % for only $x = 0.15$) were identified as the major impurities. It is known that the muons in fluorite exhibit a spin precession under zero field, which is characteristic of the F-μ-F complex ($\simeq$0.5 MHz) [24]; the absence of such a signal indicates that the contribution of muons in fluorite is negligible. As shown in Fig. 1, the pristine compound exhibits an anomaly in resistivity around 120 K, while the others (except for $x = 0.05$) exist in the superconducting state below $T_c \simeq 18$–21 K (defined as the midpoint of the fall in the resistivity). The homogeneity of the samples is supported by two findings: (i) the gradient of normalized resistivity above ~150 K increases monotonically with increasing Co content x (Fig. 1), and (ii) the lattice parameter decreases linearly with increasing x (Fig. 1, inset).

The conventional μSR measurement was performed using the LAMPF spectrometer installed on the sample with $x = 0$, 0.075, and 0.15 at the $M20$ beam line at TRIUMF, Canada. Additional data were obtained for the samples with $x = 0.05$ and 0.10 using a new apparatus installed at the $D1$ beam line at the J-PARC MUSE Facility, Japan. In the measurements under zero field (ZF), the residual magnetic field at the sample position was reduced to below 10^{-6} T with the initial muon spin direction parallel to the muon beam direction [$\vec{P}_\mu(0) \parallel \hat{z}$]. For the longitudinal field (LF) measurements, a magnetic field was applied parallel to $\vec{P}_\mu(0)$. The time-dependent muon polarization [$G_z(t) = \hat{z} \cdot \vec{P}_\mu(t)$] was monitored by measuring the decay-positron asymmetry along the $\hat{z}$ axis. The transverse field (TF) condition was achieved by rotating the initial muon polarization such that $\vec{P}_\mu(0) \parallel \hat{x}$, where the asymmetry was monitored along the $\hat{x}$ axis to obtain $G_x(t) = \hat{x} \cdot \vec{P}_\mu(t)$. All measurements under magnetic field were performed by cooling the sample to the target temperature, after the field was equilibrated.

From the ZF-μSR measurement of the pristine compound ($x = 0$), it was inferred that the anomaly around 120 K corresponds to the occurrence of magnetic phase transition. As shown in Fig. 2, the μSR spectra below $T_m \simeq$ 120 K exhibit a spontaneous oscillation with a well-defined frequency, which approaches $\nu \simeq 25$ MHz with decreasing temperature. This indicates that the implanted muons sense a unique internal magnetic field of $B_m = 2\pi\nu/\gamma_\mu \simeq 0.18$ T. The magnitude of B_m is in good agreement with those reported in earlier μSR measurements of RFeAsO [9,10,14], where it was suggested that a commensurate spin density wave (SDW) with a reduced moment of $\sim 0.25\mu_B$ exists at the iron sites [9]. In addition, from the LF-μSR spectra, it was inferred that the internal field is static within the time scale of μSR ($<10^{-5}$ s).

It has been reported that Co doping effectively suppresses the anomaly in the resistivity at T_m; the anomaly virtually disappears at $x \simeq 0.1$, where the superconductivity seems to be close to its optimum, as suggested from the maximal $T_c \simeq 22$ K [23]. However, the ZF-μSR measurements of the samples with $x > 0.05$ indicate that the superconductivity does not uniformly develop over the specimen. As shown in Fig. 3, the time spectra exhibit a character similar to that observed in the case of LFAO-F ($x = 0.06$) [25]; that is, they consist of two components, one showing rapid depolarization and the other showing slow Gaussian damping, with the relative yield of the latter

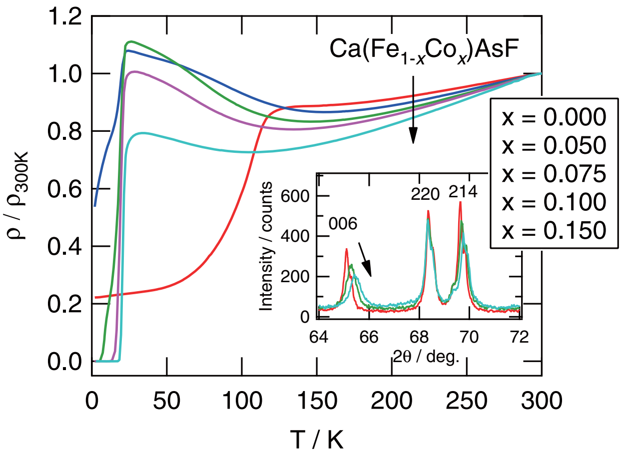

FIG. 1 (color online). Temperature dependence of electrical resistivity in $CaFe_{1-x}Co_xAsF$ with $x = 0$, 0.05, 0.075, 0.10, and 0.15 normalized by the value at 300 K. (Inset) X-ray diffraction pattern around 006 peak for $x = 0$, 0.075, and 0.15 (order of arrow direction).

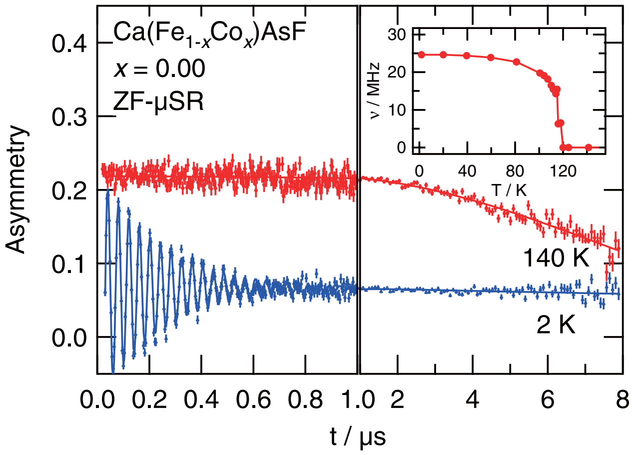

FIG. 2 (color online). ZF-μSR time spectra of CaFeAsF (undoped) at 140 and 2 K. (Inset) Frequency of spontaneous oscillation against temperature.

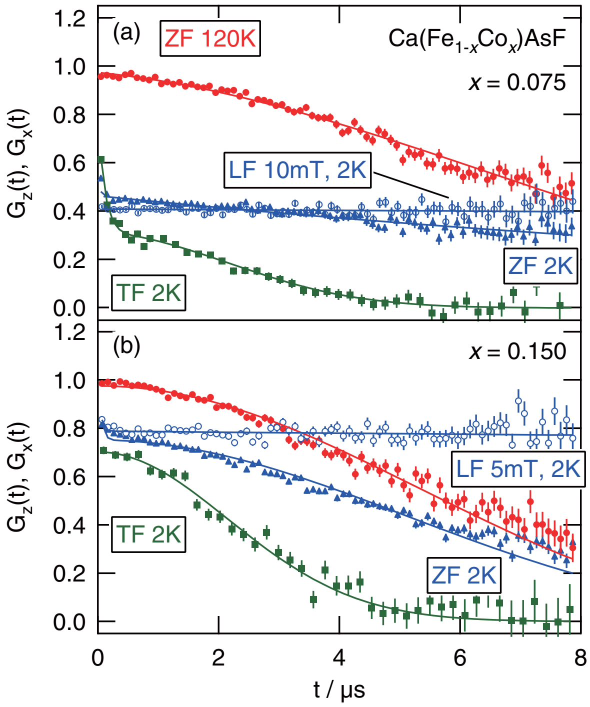

FIG. 3 (color online). μSR time spectra observed in $\mathrm{CaFe}_{1-x}\mathrm{Co}_x\mathrm{AsF}$ [$x = 0.075$ (a) and 0.15 (b)] at 2 K under a longitudinal field (LF, open circles), a zero field (ZF, triangles), and a transverse field (TF, squares), and that under ZF above T_m (triangles). The spectrum under TF is plotted on a rotating reference frame to extract the envelop function.

increasing progressively with x. A closer look at the initial time range of the spectra of the sample with $x = 0.075$ shows that the rapid depolarization corresponds to a strongly damped oscillation with a frequency roughly equal to ν. This oscillation, together with the consistent onset temperature for magnetism ($T_m \simeq 120$ K), confirms that the signal arises from the SDW phase with a strong modulation caused by Co doping. The very recent neutron diffraction experiment showed a similar result for $x = 0.06$; however, only a volume-averaged signal was observed [26]. As observed in the TF-μSR measurements (see below), the rest of the samples exhibit superconductivity below T_c. Considering these results, the ZF-μSR spectra are analyzed by the χ-square minimization fit using a model function

$$G_z(t) = [w_1 + w_2 G_m(t)] G_{\mathrm{KT}}(\delta_N{:}t) \qquad (1)$$

$$G_m(t) = \tfrac{1}{3} + \tfrac{2}{3} e^{-\Lambda_m t}\cos(2\pi\nu t + \phi), \qquad (2)$$

where $G_{\mathrm{KT}}(\delta_N{:}t)$ is the Kubo-Toyabe relaxation function that describes the Gaussian damping due to random local fields generated by nuclear moments (with δ_N being the depolaization rate) [27], w_1 is the fractional yield for the nonmagnetic phase, w_2 is that for the SDW phase ($\sum w_i = 1$), Λ_m is the depolarization rate for the spontaneous oscillation, and ϕ is the initial phase of rotation ($\simeq$0). The first term in Eq. (2) represents the spatial average of $\cos\theta$, where θ is the angle between $\vec{P}_\mu(0)$ and $\vec{B}_m$ at the muon site, which is equal to $1/3$ in a polycrystalline specimen under zero external field. (This term would also be subject to depolarization under a fluctuating local field). The fractional yields of the respective components are shown in Fig. 4. Depending on the magnitude of the internal field in the magnetically ordered phase of FeAs impurity, w_2 in the sample with $x = 0.15$ might have a small uncertainty ($\simeq$3.3%) below $T_N \simeq 77$ K.

To analyze the temperature-dependent TF spectra, we used a model function

$$G_x(t) = [w_1 e^{-\delta_s^2 t^2}\cos(2\pi f_s t + \phi) + w_2 G_m(t)] e^{-(1/2)\delta_N^2 t^2}, \qquad (3)$$

where w_i and δ_N are fixed as the values obtained by analyzing ZF- and LF-μSR spectra. The first component in the above equation denotes the contribution of the flux line lattice formation in the superconducting phase, where $2\pi f_s \simeq \gamma_\mu H$ under an external field H, δ_s corresponds to the linewidth $\sigma_s = \sqrt{2}\delta_s = \gamma_\mu \langle (B(\mathbf{r}) - B_0)^2\rangle^{1/2}$, and $B_0 \simeq H$ is the mean value of the local field $B(\mathbf{r})$ [28]. The second term represents the relaxation in the magnetic phase. The fit analysis using the above model indicates that all the spectra are perfectly reproduced when the fractional yield is fixed as the value determined from the ZF-μSR spectra. This supports the assumption that the paramagnetic phase becomes superconducting below T_c. The obtained values of σ_s are shown in Fig. 5(a).

The magnetic phase develops at temperatures much higher than the superconducting transition temperature ($T_m > T_c$), and in the case of $x \le 0.075$, T_m almost remains unchanged [see Fig. 5(b)]. Meanwhile, the oscillation observed in Fig. 2 disappears in the spectra of all the Co-doped samples (Fig. 3, ZF, 2 K), indicating that the SDW state is strongly modulated. This observation, together with the absence of the μSR signal expected for

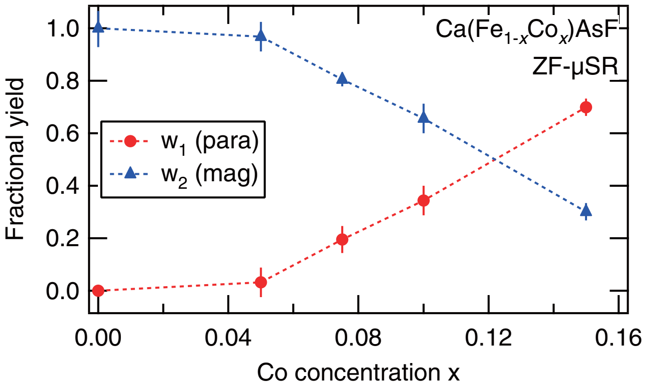

FIG. 4 (color online). Relative yield of volumetric fraction of superconducting (w_1) and magnetic (w_2) components in $\mathrm{CaFe}_{1-x}\mathrm{Co}_x\mathrm{AsF}$ as a function of Co concentration (x).

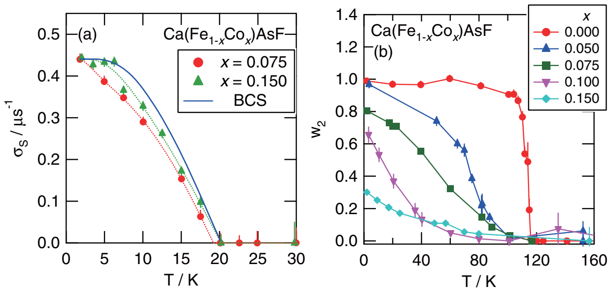

FIG. 5 (color online). Temperature dependence of (a) superfluid density ($\sigma_s = \sqrt{2}\delta_s$) and (b) fractional yield of magnetic phases for each sample. The solid curve in (a) (labeled as BCS) represents the profile predicted using a weak-coupling BCS model with s-wave pairing and single gap.

ferromagnetic cobalt (4–5 MHz [29]) in the spectra serves as evidence that the phase separation is not merely due to the aggregation of cobalt atoms during sample preparation.

As observed from its temperature dependence curves, shown in Fig. 5(a), σ_s ($\propto n_s$) is almost independent of x. Considering that the volume fraction of the superconducting phase (w_1) is nearly proportional to x, the insensitivity of n_s to x indicates that the superfluid (and corresponding carrier density in the normal state) is confined to certain domains (“islands”) centered around Co ions. A crude estimation showed that the domain size may be given as $d_s \sim [(abc/2)(0.8/0.15)]^{1/3} \simeq 0.9$ nm in diameter (where a, b, and c are the unit cell sizes). In other words, the superfluid behaves as an incompressible fluid in CFCAF.

The temperature dependence of σ_s shown in Fig. 5(a) is compared to the weak-coupling BCS model (s-wave, single gap). The model fails to reproduce the present data for the cases of both $x = 0.075$ and 0.15, as they exhibit a tendency of σ_s to vary with temperature over the region of $T/T_c < 0.4$. A very similar result is reported in the case of LFAO-F near the phase boundary ($x = 0.06$) [25]. This suggests that provided the influence of flux pinning is negligible, the superconducting order parameter in CFCAF may not be explained by the simple weak-coupling BCS model with s-wave pairing and single-gap parameter.

The volumetric expansion of superconducting domains on electron doping to the Fe_2As_2 layers by substituting Fe with Co is a remarkable feature with no counterpart in high-T_c cuprates. Nonetheless, this feature, to some extent, is reminiscent of the parallelism observed in cuprates on the substitution of Cu with Zn; it appears that superconductivity is suppressed over a certain domain around the Zn atoms like a “Swiss cheese” [30]. Although the effect discussed in the case of cuprates is completely opposite to that in the case of iron pnictides, the observed “local” character of doping in CFCAF, which appears to originate from a short coherence length ξ_0 (that probably determines the domain size, so that $\xi_0 \sim d_s/2 \simeq 0.45$ nm), may provide a hint for the microscopic understanding of superconductivity on the Fe_2As_2 layers, particularly in n-type doping.

Moreover, the superconducting character of p-type iron pnictides seems to be considerably different from that of the n-type ones, as suggested by the behavior of superfluid density of $Ba_{1-x}K_xFe_2As_2$ observed by μSR [31]. The double-gap feature revealed by the angle-resolved photoemission spectroscopy supports the view that superconductivity occurs on complex Fermi surfaces consisting of many bands (at least five of them) which can give rise to certain intricacies [32,33]. The peculiar feature of Co doping in CFCAF might also be understood in this context.

We would like to thank the staff of TRIUMF and J-PARC MUSE for their technical support in the μSR experiment. This study was partially supported by the KEK-MSL Inter-University Program for Overseas Muon Facilities and by a Grant-in-Aid for Creative Scientific Research on Priority Areas from the Ministry of Education, Culture, Sports, Science and Technology, Japan.

[1] Y. Kamihara *et al.*, J. Am. Chem. Soc. **130**, 3296 (2008).
[2] X. H. Chen *et al.*, Nature (London) **453**, 761 (2008).
[3] Z. A. Ren *et al.*, Chin. Phys. Lett. **25**, 2215 (2008).
[4] Z. A. Ren *et al.*, Europhys. Lett. **83**, 17 002 (2008).
[5] G. F. Chen *et al.*, Phys. Rev. Lett. **100**, 247002 (2008).
[6] H. Takahashi *et al.*, Nature (London) **453**, 376 (2008).
[7] C. de la Cruz *et al.*, Nature (London) **453**, 899 (2008).
[8] Y. Nakai *et al.*, J. Phys. Soc. Jpn. **77**, 073701 (2008).
[9] H.-H. Klauss *et al.*, Phys. Rev. Lett. **101**, 077005 (2008).
[10] J. P. Carlo *et al.*, Phys. Rev. Lett. **102**, 087001 (2009).
[11] M. A. McGuire *et al.*, Phys. Rev. B **78**, 094517 (2008).
[12] S. Kitao *et al.*, J. Phys. Soc. Jpn. **77**, 103706 (2008).
[13] J. Zhao *et al.*, Phys. Rev. Lett. **101**, 167203 (2008).
[14] A. A. Aczel *et al.*, Phys. Rev. B **78**, 214503 (2008).
[15] H. Luetkens *et al.*, Phys. Rev. Lett. **101**, 097009 (2008).
[16] M. Rotter, M. Tegel, and D. Johrendt, Phys. Rev. Lett. **101**, 107006 (2008).
[17] K. Sasmal *et al.*, Phys. Rev. Lett. **101**, 107007 (2008).
[18] H. Luetkens *et al.*, arXiv:0806.3533.
[19] See, for example, K. H. Satoh *et al.*, Phys. Rev. B **77**, 224503 (2008).
[20] A. S. Sefat *et al.*, Phys. Rev. B **78**, 104505 (2008).
[21] A. S. Sefat *et al.*, Phys. Rev. Lett. **101**, 117004 (2008).
[22] Y. Qi *et al.*, Supercond. Sci. Technol. **21**, 115016 (2008).
[23] S. Matsuishi *et al.*, J. Am. Chem. Soc. **130**, 14 428 (2008).
[24] J. H. Brewer *et al.*, Phys. Rev. B **33**, 7813 (1986).
[25] S. Takeshita *et al.*, J. Phys. Soc. Jpn. **77**, 103703 (2008).
[26] Y. Xiao *et al.*, Phys. Rev. B **79**, 060504 (2009).
[27] R. S. Hayano *et al.*, Phys. Rev. B **20**, 850 (1979).
[28] E. H. Brandt, Phys. Rev. B **37**, 2349 (1988).
[29] N. Nishida *et al.*, J. Phys. Soc. Jpn. **44**, 1131 (1978).
[30] Y. J. Uemura, Solid State Commun. **126**, 23 (2003).
[31] M. Hiraishi *et al.*, J. Phys. Soc. Jpn. **78**, 023710 (2009).
[32] I. I. Mazin *et al.*, Phys. Rev. Lett. **101**, 057003 (2008).
[33] K. Kuroki *et al.*, Phys. Rev. Lett. **101**, 087004 (2008).

Nuclear Instruments and Methods in Physics Research A 600 (2009) 316–318

Contents lists available at ScienceDirect

Nuclear Instruments and Methods in Physics Research A

journal homepage: www.elsevier.com/locate/nima

Study of hydrogen diffusion in superprotonic ionic conductors, $MHXO_4$, by μ^+SR and QENS

Yutaka Ikedo [a], Hiroshi Nozaki [a], Masashi Harada [a], Jun Sugiyama [a,*], Taku J. Sato [b], Yasumitsu Matsuo [c], Kusuo Nishiyama [d], James S. Lord [e], Yiming Qiu [f,g], John R.D. Copley [f]

[a] Toyota Central Research & Development Labs. Inc., Nagakute-machi, Aichi-gun, Aichi 480.1192, Japan
[b] Institute of Solid State Physics, University of Tokyo, Kashiwa-shi, Chiba 277.8581, Japan
[c] Faculty of Engineering, Setsunan University, Neyagawa-shi, Osaka 572.8508, Japan
[d] Institute of Materials and Structure Science, Tsukuba-shi, Ibaraki 305.0801, Japan
[e] ISIS Facility, Rutherford–Appleton Laboratory, Chilton, Didcot, Oxon OX11 0QX, UK
[f] NIST Center for Neutron Research, Gaithersburg, MD 20899-6102, USA
[g] Department of Materials Science and Engineering, University of Maryland, College Park, MD 20742, USA

ARTICLE INFO

Available online 27 November 2008

Keywords:
Proton diffusion
Superprotonic conductors
Muon spin rotation/relaxation
Quasi-elastic neutron scattering

ABSTRACT

In order to clarify the mechanism of high proton conductivity (σ_{H+}) for superprotonic ionic conductors, $MHXO_4$, where M=Cs and Rb, X=S and Se, muon-spin rotation and relaxation (μ^+SR) and quasi-elastic neutron scattering (QENS) measurements have been performed at temperatures mainly in the vicinity of T_c, at which $MHXO_4$ undergoes a structural phase transition from a low-T orthorhombic phase (Phase II) to a high-T tetragonal phase (Phase I). The μ^+SR experiment shows the presence of muonium (Mu) state even in Phase I only for $CsHSO_4$ (CHS), while no Mu state was found in Phase I of $CsHSeO_4$ (CHSe). Considering the fact that the σ_{H+} in Phase I of CHS is more than 10 times larger that of CHSe, this implies a relationship between the presence of the atomic hydrogen (Mu) state and high σ_{H+} in Phase I of CHS. According to the QENS measurements using a single crystal of CHSe, line shapes of the energy spectra along three crystallographic directions are found to be slightly anisotropic in Phase I, in contrast to the isotropic conductivity reported by AC conductivity measurements.

1. Introduction

Cesium hydrogen sulfate, $CsHSO_4$ (CHS), and related materials, $MHXO_4$, where M=Rb, K and X=S, Se, are considered to be promising candidates for the solid electrolyte of fuel cells operated in intermediate region of temperature from 300 to 600 K [1]. This is because $MHXO_4$ exhibits extraordinarily high proton conductivity (σ_{H+}) at temperatures above its first order structural phase transition from a low-T monoclinic phase (Phase II) to a high-T tetragonal phase (Phase I) (T_c=414 K for CHS). It is known that σ_{H+} leaps by four orders of magnitude at T_c with increasing T [2]. Phase I is therefore called the "superprotonic" conducting (SPC) phase.

Several experiments, such as ^{1}H-NMR measurement [3], powder neutron diffraction for $CsDSO_4$ [4] and quasi-elastic neutron scattering (QENS) for CHS using powder samples [5] have been carried out, and also computations of proton diffusion (PD) processes using density functional theory [6] were made in order to investigate the mechanism of the high σ_{H+} in Phase I of CHS. It has been reported that there are two PD paths in CHS; one is the PD via hydrogen bond between the first nearest neighbor (FNN) sulfate tetrahedra, SO_4^{2-}, and the other is a direct diffusion between the second nearest neighbor (SNN) SO_4^{2-}s [5,6]. In order to realize the practical use of CHS as the electrolyte for the fuel cell, it is essential to improve performance of CHS as a solid electrolyte. In particular, it is necessary to increase σ_{H+} and to decrease T_c. For this purpose we need detailed information on the PD in CHS, such as which path is the dominant process for the proton motion, and what is the key process for σ_{H+} in Phase I of CHS.

In order to clarify the detailed mechanism responsible for the high σ_{H+} of $MHXO_4$, positive muon-spin rotation and relaxation (μ^+SR) and QENS experiments have been performed at temperatures mainly in the vicinity of T_c. Both techniques provide us complimentary information on proton diffusive properties, because their time scales for detectable diffusive motion are 10^{-5} to 10^{-9} s for μ^+SR and 10^{-9} to 10^{-13} s for QENS, respectively. Particularly, in order to elucidate the existence/absence of anisotropic σ_{H+}, we have prepared single crystal samples of $MHXO_4$. In this paper, we focus on the results of μ^+SR measurements for CHS and $CsHSeO_4$ (CHSe), and QENS experiments on CHSe.

---

*Corresponding author. Tel.: +81 561 71 8029; fax: +81 561 63 6137.
E-mail address: e0589@mosk.tytlabs.co.jp (J. Sugiyama).

0168-9002/$ - see front matter © 2008 Elsevier B.V. All rights reserved.
doi:10.1016/j.nima.2008.11.052

2. Experimental

Single crystal samples of $MHXO_4$ were grown by a slow evaporation method at ambient T from an aqueous solution [7]. The μ^+SR experiments were performed on the πA spectrometer at KEK and on EMU at the ISIS Pulsed Muon Facility at the Rutherford Appleton Laboratory using pulsed surface muon beam. Experimental setup and techniques were described elsewhere [8]. The QENS experiment on single crystal CHSe was carried out using the Disk Chopper time-of-flight Spectrometer (DCS) at the NIST Center for Neutron Research (NCNR) [9] with a wavelength of 9 Å and energy resolution of ~10 μeV half width at half maximum (HWHM). The single crystal sample of CHSe was wrapped in aluminum foil, and then inserted into a Pb-sealed aluminum-cell under ambient He gas environment. The sample was measured in the temperature range between 410 K and 470 K. To detect anisotropic PD, time-of-flight spectra along [1 0 0], [0 0 1], and [1 1 0] directions were measured. The measured data were converted to energy spectra as a function of Q using the DAVE software of NCNR [10].

3. Results and discussion

Zero-field (ZF) and longitudinal-field (LF) μ^+SR measurements for CHS were performed as a function of temperature in the temperature range from 250 to 450 K to explore the dynamics of muons in CHS as a radioactive tracer of H$^+$. ZF time spectra exhibit slow Gaussian type relaxation. The relaxation behavior is almost decoupled by applying LF less than 10^{-2} T. This indicates that the muons feel nuclear dipole field caused by randomly distributed Cs and H$^+$. Both ZF and LF μ^+SR spectra were well fitted by a dynamic Kubo–Toyabe (KT) function using common parameters, the muon hopping rate (ν_μ) and field distribution width (Δ_{KT}) at each T [8]. Fig. 1 shows the dependences of KT parameters, ν_μ and Δ_{KT} on inverse T. The T dependence of ν_μ is found to be two orders of magnitude larger than that of Δ_{KT} in the whole T range measured. As T increases from ambient T, the $\nu_\mu(T)$ curve exhibits an abrupt increase at T_c, corresponding to the T dependence of σ_{H+}. Assuming the Arrhenius relation, the activation energies of ν_μ in Phase I, $E_{a,I}$ and Phase II, $E_{a,II}$, are estimated as $E_{a,I}$=0.01 eV and $E_{a,II}$=0.1 eV, respectively. This is qualitatively in good agreement with values from the calculation and σ_{H+} measurements, although these values are rather small for those evaluated from conductivity measurements of H$^+$. The difference could be explained by the mass effect between the H$^+$ and the μ^+.

Fig. 2 shows normalized initial asymmetries (A_{TF}) of the weak transverse-field (wTF) μ^+SR spectra for CHS and CHSe as a function of T. For both samples, as T increases from ambient T, the A_{TF} gradually increases up to T_c, and then A_{TF} exhibits a sudden increase at T_c, and finally levels off to a constant value with further increasing T. It should be noted that the A_{TF} of CHS does not reach its full value (=1) even in Phase I, while A_{TF} for CHSe is 1.0 above T_c. In most cases for non-magnetic insulators, the missing fraction of A_{TF} means that some of the embedded μ^+ couple with electrons, forming muonium (Mu) [8]. The $A_{TF}(T)$ behavior therefore shows that Mu fraction in Phase I is found only in CHS, while Mu is not formed in Phase I of CHSe. In addition, high LF measurements up to 0.45 T for CHS show a clear decoupling curve due to the presence of the triplet Mu state and a fast relaxation remains even in 0.45 T. This means that Mu is found to be diffusing very rapidly and also that Mu is thought to be converted to μ^+ quickly [11]. Considering these results, this implies that Mu's, i.e., atomic hydrogens, are likely to exist even in the SPC phase of CHS. One would deduce a relationship between the presence of atomic hydrogen state and high σ_{H+} of CHS.

By QENS measurements for CHSe, it is found that each spectrum consists of two Lorentzian components, one "narrow" and the other one "wide". The HWHM of the narrow component is of the order of μeV and that of the wide component is ~100 μeV. A typical reduced energy spectrum for CHSe at 425 K, and the two Lorentzian components, are shown in Fig. 3. The spectrum was well fitted using a combination of the two Lorentzian function convoluted with the instrument resolution function. The Q dependences of the HWHMs of both components at 410 K are shown in Fig. 4. The HWHM curves for both components show clear anisotropic behavior in the three directions, [1 1 0], [1 0 0], and [0 0 1]. The HWHMs of the narrow components for the all directions exhibit monotonic increases with increasing Q up to 0.7 Å^{-1}. The slope of the HWHM along the [1 1 0] direction seems to be larger than those along the other two directions, indicating anisotropic PD in Phase I of CHSe. Since, in the small Q region, the slope of HWHM as a function of Q^2 in a given directions is directly proportional to the diffusion constant along that direction [12],

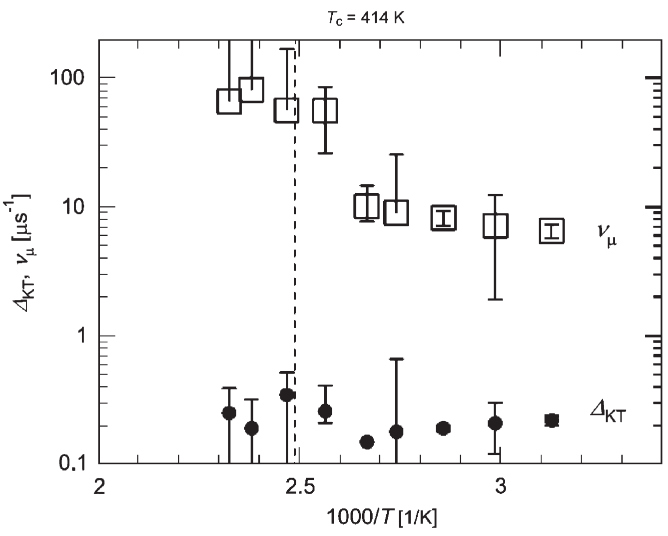

Fig. 1. The fitting results of ZF and LF μ^+SR spectra for CHS using dynamic KT function. In this and subsequent figures, error bars represent ± one standard deviation.

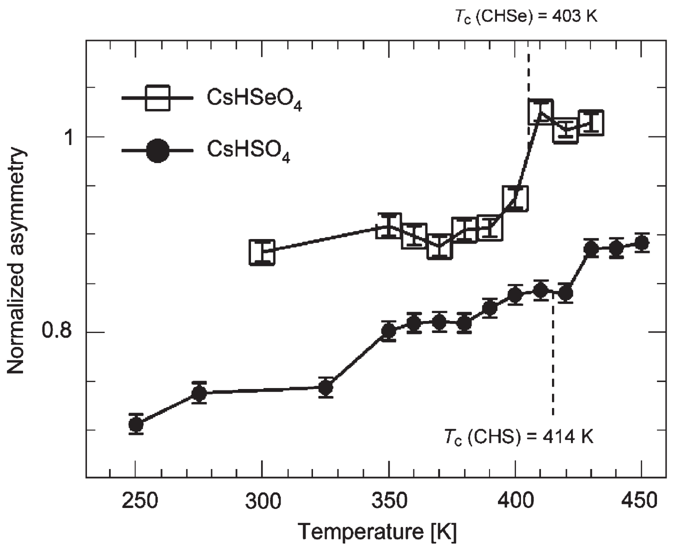

Fig. 2. Temperature dependence of normalized asymmetry of wTF μ^+SR spectra for CHS and CHSe.

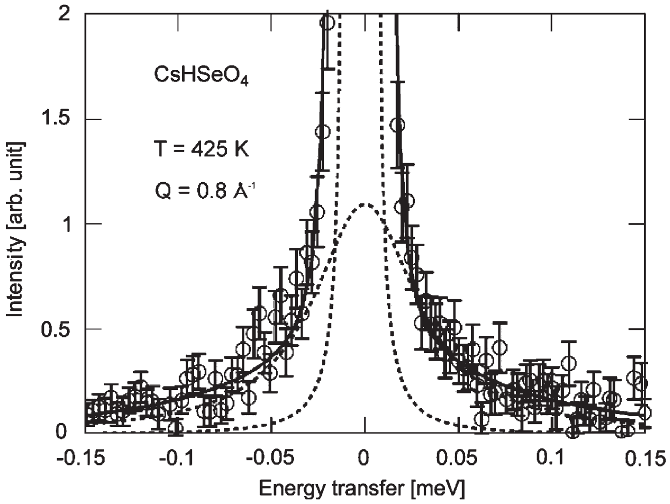

Fig. 3. A typical QENS spectrum for CHSe at 425 K. Dotted lines show the fitting results of the two Lorentzian components.

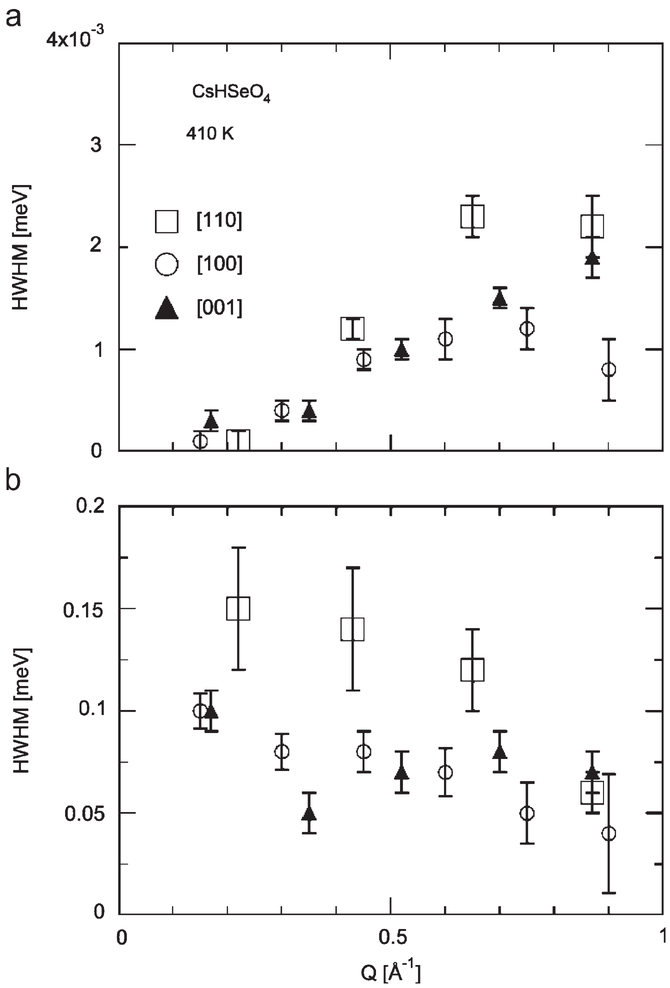

Fig. 4. *Q* dependences of HWHM of the two Lorentzian components of the QENS spectra in three crystallographic directions of CHSe. (a) Narrow component and (b) wide component.

the diffusion constant along the [110] direction appears to be larger than the diffusion constant for the other two directions. Unfortunately, the energy resolution of the instrument of the present study would not be enough to quantitatively discuss the HWHM of the narrow component. We need to perform additional QENS experiments for CHS using higher energy resolution instrument, such as back-scattering spectrometer.

Finally, we should mention the relationship between μ^+SR and QENS results. The HWHMs, which are obtained from QENS measurements, should correspond to the jump rates of the proton hopping, of the order of 100 MHz for the narrow component and 10 GHz for the wide component, respectively. Since the muon hopping rate observed in Phase I of CHS is ~100 MHz, the muon hopping would be assigned to the proton hopping represented by the narrow component in the QENS spectrum. But the fast proton motion observed by QENS measurement is too fast to detect by μ^+SR. Although the narrow component of the QENS spectra was assigned to the hopping between SNN sulfate by the powder QENS measurements [4], our preliminary calculations for the QENS spectrum of single crystal CHSe sample using extended Chudley–Elliott model [12] suggest that the narrow component represents the hopping between FNN sulfate [11]. However, in order to discuss the detailed proton motion, we need to calculate using a refined model of the proton motion. The Mu site and its dynamics, and the relationship to QENS results are also issues that remain to be solved by further study of Phase I of CHS.

Acknowledgment

This work utilized facilities supported in part by the National Science Foundation under Agreement no. DMR-0454672.

References

[1] S.M. Haile, D.A. Boysen, C.R.L. Chishohm, R.B. Merle, Nature 410 (2001) 910.
[2] A.I. Baranov, L.A. Shuvalov, N.M. Shchagina, JETP Lett. 36 (1982) 459.
[3] S. Hayashi, M. Mizuno, Solid State Ionics 171 (2004) 289.
[4] A.V. Belushkin, W.I.F. David, R.M. Ibberson, L.A. Shuvalov, Acta Cryst. B 47 (1991) 161.
[5] A.V. Belushkin, C.J. Carlile, L.A. Shuvalov, J. Phys. Condens. Matter 4 (1992) 389.
[6] X. Ke, I. Tanaka, Phys. Rev. B 69 (2004) 165114.
[7] Y. Yoshida, Y. Matsuo, S. Ikehata, J. Phys. Soc. Jpn. 72 (2003) 1590.
[8] G.M. Kalvius, D.R. Noakes, O. Hartmann, in: K.A. Gschneider Jr., et al., Handbook on the Physics and Chemistry of Rare Earths, North-Holland, Amsterdam, 2001.
[9] J.R.D. Copley, J.C. Cook, Chem. Phys. 292 (2003) 477.
[10] 〈http://www.ncnr.nist.gov/dave/〉.
[11] Y. Ikedo, in preparation.
[12] R. Hempelmann, Quasielastic Neutron Scattering and Solid State Diffusion, Oxford Science Publications, England, 2000.

Physica B 404 (2009) 713–716

Contents lists available at ScienceDirect

Physica B

journal homepage: www.elsevier.com/locate/physb

Effect of Zn substitution for Cu on $Ca_{2-x}Na_xCuO_2Cl_2$ near the hole concentration of $\frac{1}{8}$ per Cu

Kohki H. Satoh [a,*], Masatoshi Hiraishi [a], Masanori Miyazaki [a], Soshi Takeshita [b], Akihiro Koda [a,b], Ryosuke Kadono [a,b], Ikuya Yamada [c], Kengo Oka [c], Masaki Azuma [c], Yuichi Shimakawa [c], Mikio Takano [c]

[a] *Department of Materials Structure Science, The Graduate University for Advanced Studies (Sokendai), Tsukuba, Ibaraki 305-0801, Japan*
[b] *Institute of Materials Structure Science, High Energy Accelerator Research Organization (KEK), Tsukuba, Ibaraki 305-0801, Japan*
[c] *Institute for Chemical Research, Kyoto University, Uji, Kyoto 611-0011, Japan*

ARTICLE INFO

Keywords:
High-T_c cuprates
$\frac{1}{8}$ anomaly
Stripe correlation
μSR

ABSTRACT

A weakening of superconductivity upon substitution of Cu by Zn (0.5–1%) is observed in a high-T_c cuprate, $Ca_{2-x}Na_xCuO_2Cl_2$, near the hole concentration of $\frac{1}{8}$ per Cu. The superconducting transition temperature and its volume fraction, estimated by magnetic susceptibility, exhibit a sizable anomaly for $x = 0.12-0.14$, where the slowing down of Cu spin fluctuations below 5 K is demonstrated by muon spin relaxation experiments. These observations are in close resemblance to other typical cuprates including $YBa_2Cu_3O_{7-\delta}$, and $Bi_2Sr_2Ca_{1-x}Y_xCu_2O_{8+\delta}$, providing further evidence that Zn-induced "stripe" correlation is a universal feature of high-T_c cuprate superconductors common to that of $La_{2-x}A_xCuO_4$ (A = Ba, Sr).

1. Introduction

It is established that the superconducting transition temperature (T_c) is suppressed near the hole concentration $p \sim \frac{1}{8}$ in $La_{2-x}Ba_xCuO_4$ (LBCO) and $La_{2-x-y}Nd_ySr_xCuO_4$ (LNSCO), where a charge- and spin-stripe order develops in place of superconductivity [1,2]. A similar tendency has been reported for $La_{2-x}Sr_xCuO_4$ (LSCO) with a slight shift of x for the strongest strip correlation [3]. This so-called "$\frac{1}{8}$ anomaly" has drawn considerable attention in view of a potential link to the mechanism of high-T_c superconductivity in cuprates [4]. It has been shown that substitution of Cu by small amounts of Zn stabilize this stripe correlations, as it leads to the "$\frac{1}{8}$ anomaly" in a variety of cuprates including LSCO [5], $YBa_2Cu_3O_{7-\delta}$ (YBCO) [6], and $Bi_2Sr_2Ca_{1-x}Y_xCu_2O_{8+\delta}$ (BSCCO) [7]. However, it is still controversial whether this anomaly is a common feature in cuprates or that unique to the La214 system.

Here, we report on the $\frac{1}{8}$ anomaly in $Ca_{2-x}Na_x$-CuO_2Cl_2 (Na-CCOC) studied by magnetic susceptibility and muon spin relaxation (μSR). While Na-CCOC has a similar structure to $La_{2-x}Sr_xCuO_4$, it is characterized by flat CuO_2 planes even at low temperatures owing to substitution of apical oxygen with chlorine in the CuO_6 octahedra. This is in marked contrast to the case of LSCO or LBCO that have a periodic distortion of the CuO_2 planes at low temperatures. The excellent cleavability of Na-CCOC crystals makes it feasible to investigate the electronic properties using surface-sensitive measurements such as angle resolved photoemission spectroscopy (ARPES) and scanning tunneling microscopy and spectroscopy (STM/STS). The latter reports the occurrence of a checkerborad-like electronic modulation and the coexistence of charge order and superconductivity [8], which exhibits a good correspondence with the inhomogeneous (spin glass-like) magnetic ground state revealed by μSR [9]. Meanwhile, the previous search for the $\frac{1}{8}$ anomaly in Na-CCOC came to a negative result [10].

Considering that Zn substitution enhances stripe correlations in other cuprates, we prepared Zn-free and Zn substituted Na-CCOC samples near the hole concentration of $\frac{1}{8}$ per Cu, and searched for the $\frac{1}{8}$ anomaly in this compound by means of magnetization and muon spin relaxation (μSR) measurements.

2. Experimental details

Polycrystalline samples of Na-CCOC were prepared by high-pressure synthesis techniques. $Ca_2CuO_2Cl_2$ and $Ca_2Cu_{0.9925}Zn_{0.0075}O_2Cl_2$, prepared by solid state reaction of Ca_2CuO_3, CuO, ZnO, $CaCl_2$ in N_2 flow with several grindings under ambient pressure, were mixed with $NaClO_4$ and CuO, and then sealed in a cylindrical capsule made out of gold. High-pressure synthesis was performed using a cubic anvil-type high pressure apparatus operated under 6 GPa at a maximum temperature of 1000 °C. Due to the extreme high hygroscopicity of Na-CCOC, all manipulations of the samples

---

[*] Corresponding author. Tel.: +81 29 879 6028; fax: +81 29 864 5623.
E-mail address: ksatoh@post.kek.jp (K.H. Satoh).

0921-4526/$ - see front matter © 2008 Elsevier B.V. All rights reserved.
doi:10.1016/j.physb.2008.11.191

were carried out in glove-boxes filled with Ar. All samples (with varying x) were confirmed to be of single phase by means of X-ray diffraction measurements. Their structure is I4/mmm space group at room temperature, where the lattice parameters change continuously as x varies. More specifically, the a-axis shrinks as the Na concentration increases, indicating that hole carriers are introduced into the CuO_2 plane while the c-axis expands. The magnetic susceptibility was measured using a superconducting quantum interference device (MPMS, Quantum Design Co.), where the measurements were made while the temperature was scanned upwards after field cooling of 20 Oe. Conventional μSR measurements were performed on the M15 beamline of TRIUMF (Vancouver, Canada).

3. Result and discussion

Fig. 1(a) shows the Na doping dependence of T_c, where T_c is defined as the temperature at which the temperature gradient of the magnetic susceptibility, $d\chi/dT$, is at its maxima. The error bars in Fig. 1(a) are evaluated from the spread of χ around T_c and that of T_c itself among several samples with the same x. For Zn-free samples, T_c exhibits a monotonous increase with Na doping between $x = 0.11$ and 0.15. In contrast, an overall reduction of T_c is observed for Zn substituted samples ($y = 0.005$) as compared with Zn-free ones. Moreover, T_c shows a clear trend of leveling off around 13 K for $0.12 \leqslant x \leqslant 0.135$, which is followed by a jump to ~18 K at $x = 0.14$. This step-like behavior is similar to the one observed in Zn substituted $YBa_2Cu_3O_{7-\delta}$ [6]. Fig. 1(b) shows the Na doping dependence of the superconducting volume fraction estimated from the diamagnetic susceptibility at 5 K. The fraction in Zn-substituted samples is also reduced as compared with that in Zn-free samples. Furthermore, a step-like change is also observed near $\frac{1}{8}$ hole concentration in line with the case of T_c. Thus, the $\frac{1}{8}$ anomaly is clearly observed as anomalies of both T_c and the superconducting volume fraction in Na-CCOC upon Zn-substitution for Cu.

We have performed μSR experiments to investigate the microscopic details of this anomaly. As has been demonstrated in earlier reports [5–7], μSR serves as a sensitive local magnetic probe that covers a unique time window of observation (10^{-9}–10^{-5} s) complementary to other magnetic probes like neutron diffraction and nuclear magnetic resonance. It does not rely on the long-range coherence of any magnetic order, and therefore is useful to examine the random local magnetism, e.g., a spin-glass state.

Fig. 2 shows μSR spectra measured under zero external field conditions (ZF) in $Ca_{2-x}Na_xCu_{1-y}Zn_yO_2Cl_2$ for (a) Zn-free samples ($x = 0.14$, $y = 0.00$) and (b) 0.5% of Zn substitution for Cu ($x = 0.125$, $y = 0.005$). We observe a Gaussian depolarization due to random local fields from nuclear moments in the Zn-free samples over the entire temperature range down to 2 K. Meanwhile, in the latter case, an exponential damping is observed in the compound with Zn-substitution at 2 K. The spectra suggest a slowing down of Cu spin fluctuations with decreasing temperature below ~5 K. A similar phenomenon associated with Zn substitution was also reported for the case of the La214 systems, YBCO, and BSCCO, and it suggests that the Zn impurity effect is a common feature of High-T_c cuprate superconductors [5–7]. However, it must be noted that the Cu spins are not completely static nor in any long-range ordered state at 2 K, as inferred from the absence of a spontaneous oscillatory signal in the μSR time spectrum. This might be because the temperature is still too high to freeze out the Cu spins.

The μSR time spectra (= asymmetry) are analyzed by fits using the following form:

$$AP(t) = [A_1 + A_2 \exp(-\lambda t)]G_{\rm DKT}(\Delta, \nu, t), \qquad (1)$$

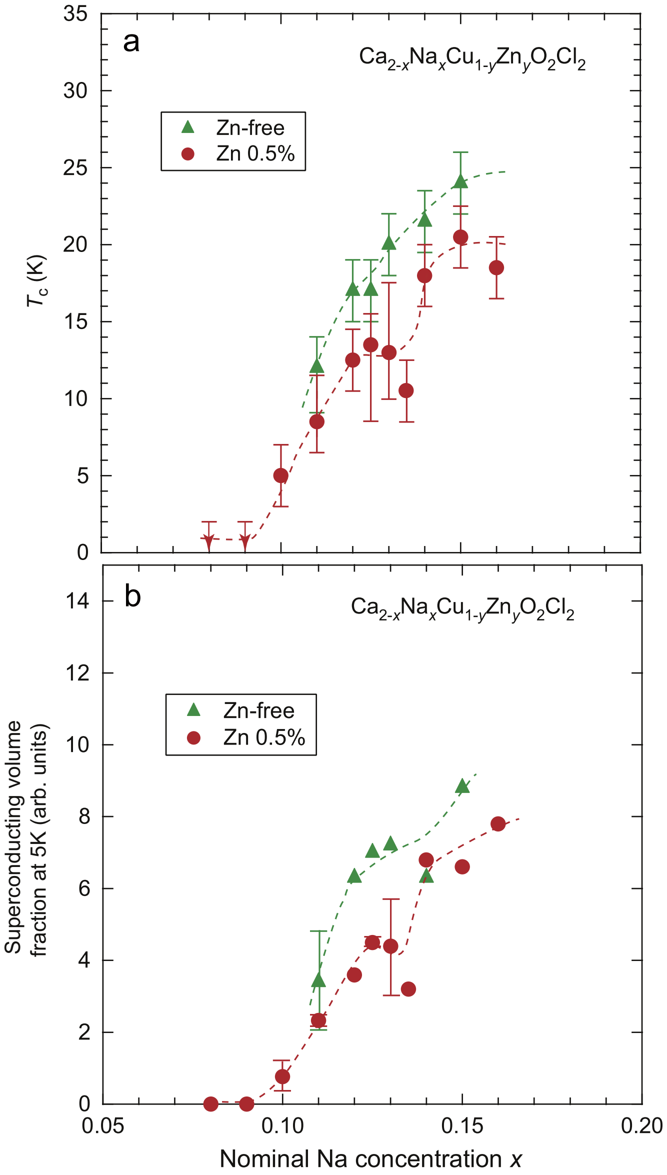

Fig. 1. (Color online) (a) Superconducting transition temperature (T_c) versus nominal Na concentration (x) in $Ca_{2-x}Na_xCu_{1-y}Zn_yO_2Cl_2$. Triangles and circles are T_c in Zn-free samples and in Zn 0.5% ($y = 0.005$) substituted samples, respectively. (b) Superconducting volume fraction estimated by the magnetic susceptibility at 5 K. Dashed lines are giudes to eyes.

where the first term represents a signal from muons stopping in a non-magnetic region. The second term represents that of magnetic regions in which the muon senses Cu spin fluctuations, A_i are the partial asymmetries which are proportional to the respective volume fractions, λ is the depolarization rate, and $G_{\rm DKT}(\Delta, \nu, t)$ is the Kubo–Toyabe function that represents the Gaussian damping due to nuclear random local fields (with Δ being the linewidth and ν the fluctuation rate of the nuclear random local fields).

As shown in Fig. 3, λ is almost zero in Zn-free samples [$x = 0.14$, $y = 0.00$ (T_c~22 K), $x = 0.0125$, $y = 0.00$ (T_c~17 K)] and in the sample with $x \neq \frac{1}{8}$ [$x = 0.15$, $y = 0.01$ (T_c~10 K)], where the non-magnetic region dominates over the entire sample volume. On the other hand, it increases below 5 K in Zn-substituted samples near $x \sim \frac{1}{8}$ [$x = 0.0125$, $y = 0.005$ (T_c~13 K) and $x = 0.0125$, $y = 0.01$ (not superconducting)] Thus, it is inferred from ZF-μSR experiments that the $\frac{1}{8}$ anomaly observed in bulk

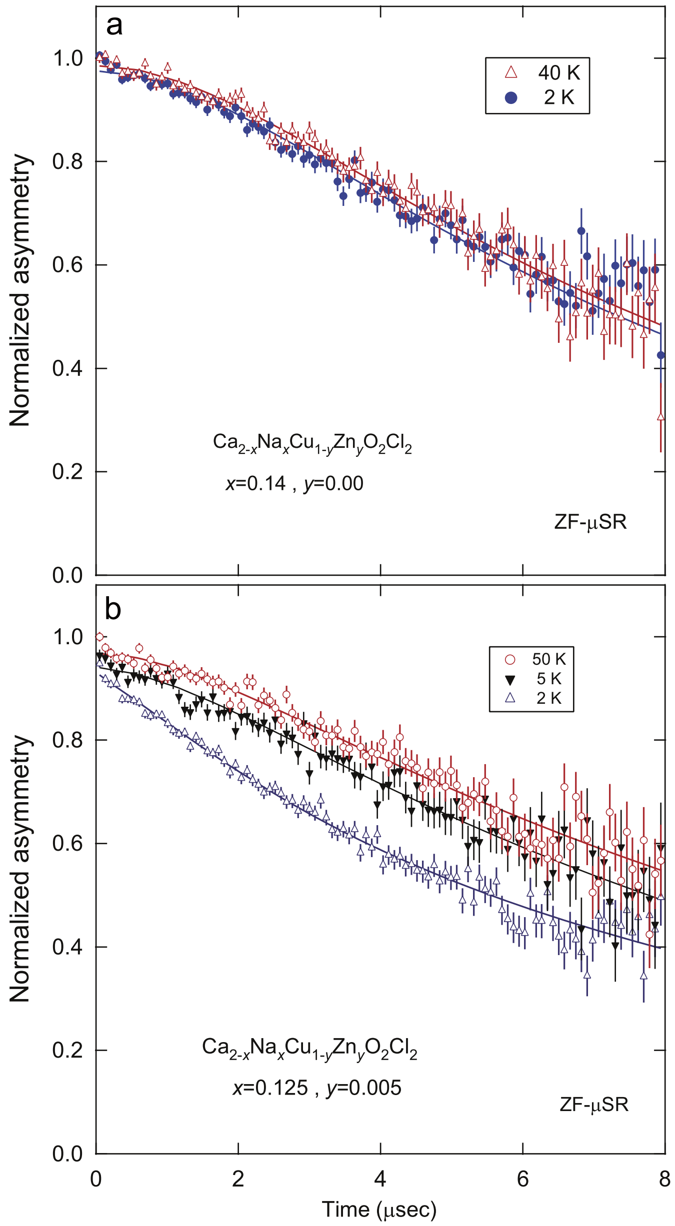

Fig. 2. (Color online) ZF-μSR spectra in $Ca_{2-x}Na_xCu_{1-y}Zn_yO_2Cl_2$ with (a) $x = 0.14$, $y = 0.00$ and (b) $x = 0.125$, $y = 0.005$. Solid curves represent fits to the data using Eq. (1).

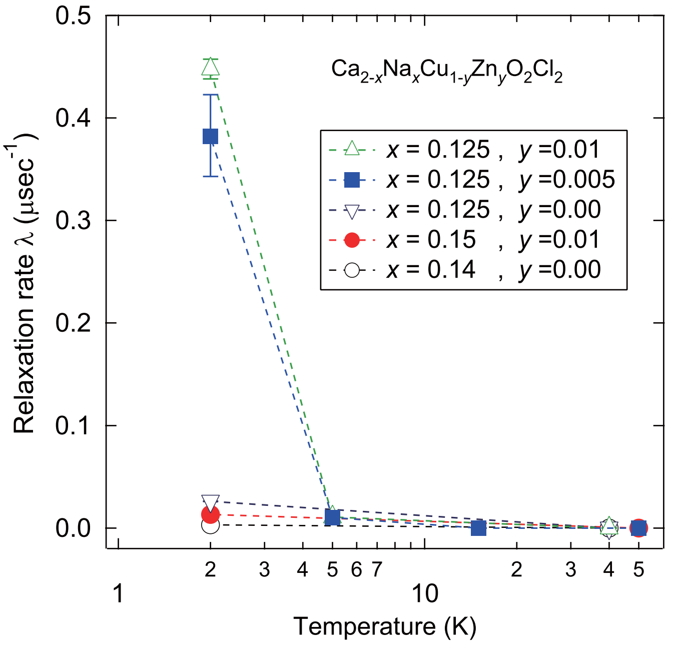

Fig. 3. (Color online) Temperature dependence of the muon spin depolarization rate (λ) in $Ca_{2-x}Na_xCu_{1-y}Zn_yO_2Cl_2$ with a variety of Na (x) and Zn (y) concentrations.

properties is associated with the slowing down of Cu spin fluctuations in Na-CCOC.

In LBCO and LNSCO near $x \simeq \frac{1}{8}$, the appearance of an incommensurate spin density wave (SDW) phase and an associated suppression of superconductivity has been reported within the present range of temperature [1,11]. The absence of (or the reduction of the characteristic temperature for) such a static SDW phase in Na-CCOC may be attributed to that of the structural phase transition which is known to occur in La214 system [12]. In LBCO at $x = \frac{1}{8}$, the lattice structure exhibits a successive change with decreasing temperature from a high-temperature tetragonal (HTT) phase at room temperature to a low-temperature orthorhombic (LTO) phase, and then to a low-temperature tetragonal (LTT) phase. Each phase is different in symmetry with respect to the distortion along the CuO_2 planes, and the SDW phase occurs in accordance with the LTT phase in LBCO. Meanwhile, in the case of LSCO that does not exhibit the LTT phase, the suppression of superconductivity is relatively weak. Since Na-CCOC remains in the HTT phase over the entire temperature range of observation (>2 K), the absence of the static SDW phase near $x = \frac{1}{8}$ may suggest a common trend that the LTT phase stabilizes the SDW phase (by "pinning the dynamical stripe"). However, it is repoted that Zn substitution for Cu enhances the SDW state in LSCO [5], and that the SDW phase survives in spite of the suppression of the LTT phase by applying hydrostatic pressure [13]. These observations might in turn point to the reversed role of cause and effect between the instability towards the SDW phase and the occurrence of LTT phase. The present result would make a strong case for the SDW instability as an intrinsic feature of the CuO_2 planes irrespective of the LTT phase.

It might be speculated that the electronic state of the Cu ions are sensitive to the *local* lattice distortion (but not to the long-range lattice morphology) so that the local impurities like Zn have relatively strong influence on the SDW instability. In this regard, another factor would be the degree of A-site disorder that is known to be different between LBCO and LSCO. Eisaki et al. reported that the A-site disorder has a certain influence on T_c [14], suggesting that the CuO_2 planes are strongly affected by the A-site ions.

In conclusion, we demonstrated the presence of the $\frac{1}{8}$ anomaly in $Ca_{2-x}Na_xCuO_2Cl_2$ with a small fraction of Cu substituted by Zn. Such an anomaly is also observed in many families of cuprates near the hole doping concentration of $\frac{1}{8}$, and it suggests that the SDW instability against local distortion of the CuO_2 planes is a common feature of high-T_c cuprate superconductors.

Acknowledgments

We would like to thank the staff of TRIUMF for their technical support during the μSR experiment. This work was supported by the KEK-MSL Inter-University Program for Oversea Muon Facilities and a Grant-in-Aid for Scientific Research on Priority Areas by Ministry of Education, Culture, Sports, Science and Technology, Japan.

References

[1] J.M. Tranquada, et al., Nature 375 (1995) 561.
[2] B. Nachumi, et al., Phys. Rev. B 58 (1998) 8760.
[3] I. Watanabe, et al., Hyperfine Interact. 86 (1994) 603.
[4] S.A. Kivelson, et al., Rev. Modern Phys. 75 (2003) 1201.
[5] I. Watanabe, et al., J. Phys. Chem. Solids 63 (2002) 1093.
[6] M. Akoshima, et al., Phys. Rev. B 62 (2000) 6761.
[7] I. Watanabe, et al., Phys. Rev. B 62 (2000) 14524.
[8] T. Hanaguri, et al., Nature 430 (2004) 1001.
[9] K. Ohishi, et al., J. Phys. Soc. Japan 74 (2005) 2408.
[10] D. Hirai, et al., Physica C 463–465 (2007) 56.
[11] J.M. Tranquada, et al., Phys. Rev. B 54 (1996) 7489.
[12] S. Katano, et al., Phys. Rev. B 48 (1993) 6569.
[13] K.H. Satoh, et al., Physica B 374–375 (2006) 40.
[14] H. Eisaki, et al., Phys. Rev. B 69 (2004) 064512.

Physica B 404 (2009) 737–739

Contents lists available at ScienceDirect

Physica B

journal homepage: www.elsevier.com/locate/physb

Magnetic response of noncentrosymmetric superconductor La_2C_3: Effect of double-gap and spin–orbit interaction

R. Kadono [a,b,*], M. Hiraishi [b], M. Miyazaki [b], K.H. Satoh [b], S. Takeshita [a], S. Kuroiwa [c], S. Saura [c], J. Akimitsu [c]

[a] Muon Science Laboratory, Institute for Materials Structure Science, High Energy Accelerator Research Organization (KEK), Tsukuba, Ibaraki 305-0801, Japan
[b] Department of Materials Structure Science, The Graduate University for Advanced Studies, Tsukuba, Ibaraki 305-0801, Japan
[c] Department of Physics, Aoyama Gakuin University, Sagamihara, Kanagawa 229-8558, Japan

ARTICLE INFO

Keywords:
Superconductivity
Spin–orbit interaction
Quasiparticle excitation

ABSTRACT

The presence of spin–orbit (SO) interaction in a noncentrosymmetric superconductor, La_2C_3 ($T_c \simeq 11$ K) is demonstrated by muon spin rotation (μSR) in its *normal state*, where μSR spectra exhibit field-induced weak depolarization due to van Vleck-like local susceptibility. In the mixed state, muon spin relaxation due to inhomogeneity of internal field (σ_v) exhibits a field dependence that is characterized by a kink, where σ_v (and hence the superfluid density) is more strongly reduced at lower fields. This is perfectly in line with the presence of a secondary energy gap previously inferred from the temperature dependence of σ_v, and also consistent with the possible influence of asymmetric deformation of the Fermi surface due to the SO interaction.

Multigap superconductivity is interesting in its own right as a manifestation of anisotropic superconductivity. Even within the framework of the BCS mechanism, anisotropy in crystal structure may lead to multi-band structure and associated complex superconducting order parameter because of the possible coupling of electrons to different phonon modes upon formation of the Cooper pairs in the respective energy bands. The discovery of high-T_c superconductivity in magnesium diboride (MgB_2) [1] and subsequent struggle for proper understanding of its double-gap nature associated with σ- and π-bands brought the multigap superconductivity to the forefront of considerable attention in this field.

Recently, we have shown in a pair of sesquicarbide superconductors Ln_2C_3 (Ln = La, Y) that the multigap structure would take great variety in its appearance, where despite a common double-gap structure in the order parameter, the temperature dependence of superfluid density exhibits a remarkable difference between La_2C_3 and Y_2C_3 that is understood as resulting from the alteration of interband coupling upon substitution of La for Y [2].

Meanwhile, sesquicarbides are drawing further attention as a possible stage for exotic superconductivity caused by their noncentrosymmetric crystal structure [3]. The absence of inversion symmetry leads to mixing of parity in the Cooper pairs, making it irrelevant to classify the states in terms of spin-multiplet. It also gives rise to the spin–orbit (SO) interaction that may affect superconductivity as well as the electronic property of normal (paramagnetic) state. In particular, Ln_2C_3 may be in a unique situation that the SO interaction is of comparable magnitude to that of superconducting gap, so that pair correlation between subbands (split by the SO interaction) induced by external field might lead to a drastic change in the low energy properties of superconductivity. More specifically, considering the Dresselhaus-type interaction appropriate for the crystal symmetry of $I\bar{4}3d$, the energy gap along the Fermi momentum $\mathbf{k}_F \parallel (0\,0\,1)$, $(1\,1\,1)$, and $(1\,0\,0)$, for example, is $\sqrt{(\mu_B H_z)^2 + \Delta^2} - \mu_B H_z$, so that it may be reduced to zero when $\mu_B H_z \gg \Delta$ (where Δ is the gap energy at zero field, H_z is the external field applied along $(0\,0\,1)$ axis) [4]. This means the occurrence of field-induced point nodes that would lead to enhanced quasiparticle excitation. It must be noted, however, that the presence of double-gap in Ln_2C_3 may require a more careful examination for this effect, since the suppression of smaller gap (having a smaller upper critical field H_{c2}) by external field would show up in a similar way. Here, we report on the result of field-induced effect in La_2C_3 studied by muon spin rotation (μSR) experiment.

A conventional μSR experiment was carried out for a La_2C_3 sample ($T_c = 10.9$ K) on the M15 beamline of TRIUMF, Canada, where details on the experiment are described in the previous report [2]. The sample was common to the previous experiment, which turned out to be a typical double-gap superconductor ($\Delta_1(0) = 2.7(1)$ meV, $\Delta_2(0) = 0.6(1)$ meV). For the

---

[*] Corresponding author at: Muon Science Laboratory, Institute for Materials Structure Science, High Energy Accelerator Research Organization (KEK), Tsukuba, Ibaraki 305-0801, Japan. Tel.: +81 29 864 5625; fax: +81 29 864 5623.
E-mail address: ryosuke.kadono@kek.jp (R. Kadono).

0921-4526/$ - see front matter © 2008 Elsevier B.V. All rights reserved.
doi:10.1016/j.physb.2008.11.186

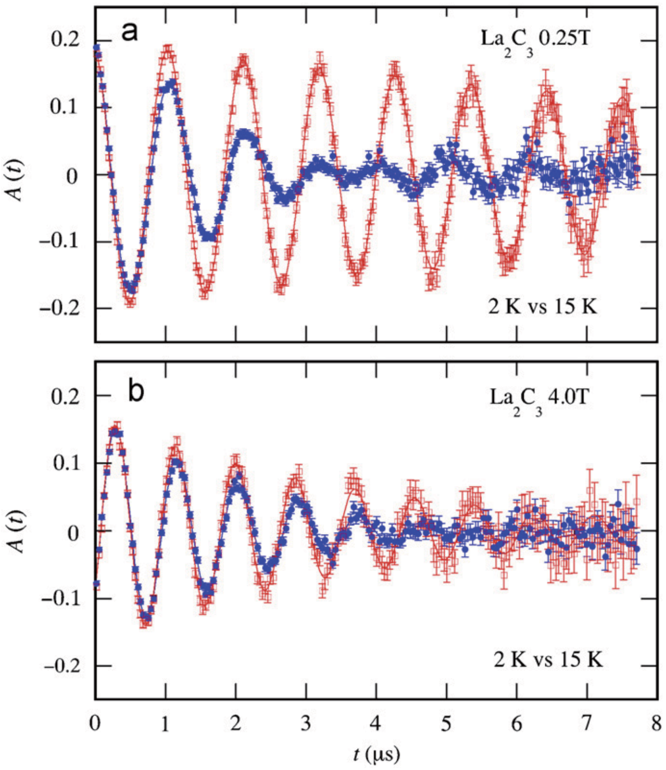

Fig. 1. Examples of TF-μSR time spectra displayed in the rotating reference frame of (a) 33 MHz and (b) 541 MHz, respectively. In the paramagnetic state (15 K, shown by open symbols), the spectrum of 4.0 T exhibits faster relaxation than that of 0.25 T, indicating occurrence of field-induced magnetism. Additional relaxation due to the formation of flux line lattice at 2 K (spectra shown in filled symbols) is seen in both cases. Solid curves are fits by a Gaussian relaxation.

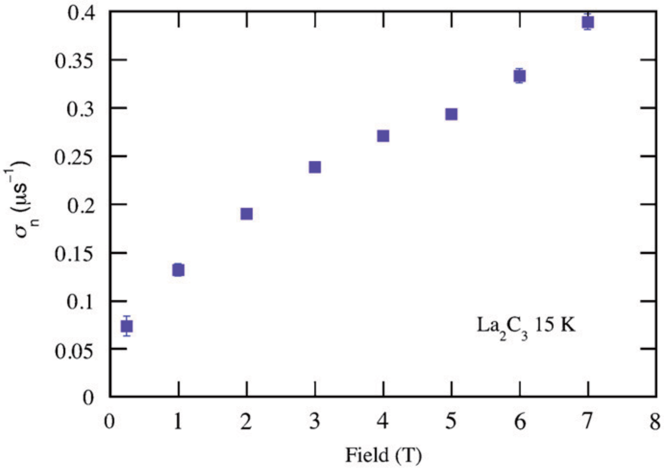

Fig. 2. Muon spin relaxation rate versus transverse field observed in the normal state of La_2C_3 (at 15 K).

field-scan measurements at 2 K (where both gaps are present), the sample was cooled down to the target temperature after the external magnetic field was stabilized at a temperature above T_c in order to minimize the effect of flux pinning. Fig. 1 shows some examples of μSR time spectra obtained under a field of 0.25 and 4.0 T, where open symbols show the data in the normal state. While the enhancement of spin relaxation upon cooling down to 2 K is observed for both cases (filled symbols), it is also noticeable that the relaxation *in the normal state* is enhanced by increasing external field. Considering that La_2C_3 has a cubic structure (bcc, $I\bar{4}3d$) and that it is free from any local *d* or *f* electrons, we can attribute this field-induced magnetization uniquely to the van Vleck-like paramagnetism due to the SO interaction.

The spin relaxation rate in the normal state is deduced from fits using a Gaussian damping

$$A(t) = A_0 \exp(-\sigma_n^2 t^2)\cos(\gamma_\mu B t + \phi), \qquad (1)$$

where A_0 is the initial asymmetry, γ_μ is the muon gyromagnetic ratio (= 135.53 MHz/T), B is the local field felt by muons ($\simeq \mu_0 H$, with H being the external field), and ϕ is the initial phase of rotation. Although the fit with Eq. (1) does not reproduce data at higher fields (particularly above 3 T) where the spectra exhibit a tendency toward an exponential damping, we resort to this simple form for the convenience of evaluating qualitative trend for σ_n versus field. As shown in Fig. 2, σ_n exhibits a quasi-linear dependence on the external field. This is understood by considering the field-induced van Vleck-like susceptibility (χ^{vv}) whose magnitude depends on the direction of the primary axis for the SO interaction, so that it may lead to an inhomogeneity of effective field in polycrystalline sample,

$$\sigma_n^2 \simeq \gamma_\mu^2 H^2 \langle (\chi^{vv})^2 \rangle + \sigma_0^2, \qquad (2)$$

where σ_0 is the contribution of random local fields from ^{139}La nuclear magnetic moments. (More specifically, χ^{vv} also includes the Pauli paramagnetic term from the SO subbands.) The slight change of σ_n observed around 3–4 T might be an artifact due to the deteriorated quality of fit with Gaussian damping. We also note that σ_n is mostly independent of temperature between 11 and ~150 K under a field of 0.25 T.

Considering the contribution of field inhomogeneity due to the van Vleck-like paramagnetism, we deduce the spin relaxation rate in the mixed state by fits of μSR time spectra using a form,

$$A(t) = A_0 G^n(t;B)\exp[-\tfrac{1}{2}\sigma_v^2 t^2]\cos(\gamma_\mu B t + \phi), \qquad (3)$$

where, instead of Eq. (1), $G^n(t;B)$ is chosen to best reproduce the spectra at 15 K ($>T_c$) at each field. ($G^n(t;B)$ consists of a sum of two exponential damping signals, where the parameters describing $G^n(t;B)$ is determined by the spectra at 15 K at each field and then fixed to these values for the fit of spectra at 2 K to extract σ_v reliably.) In this definition, σ_v corresponds to the second moment for the field distribution ($B(\mathbf{r})$) in the mixed state [5]

$$\sigma_v^2 = \gamma_\mu^2 \langle (B(\mathbf{r}) - \mu_0 H)^2 \rangle. \qquad (4)$$

Fig. 3 shows the deduced value of σ_v at respective fields, where one can clearly observe a trend of steeper reduction with increasing field at lower fields (below ~3 T).

In the limit of extreme type II superconductors (i.e., $\lambda/\xi \gg 1$, where λ is the effective London penetration depth and $\xi = \sqrt{\Phi_0/(2\pi H_{c2})}$ is the Ginzburg–Landau coherence length, Φ_0 is the flux quantum, and H_{c2} is the upper critical field), σ_v is determined by λ using a relation [5]

$$\sigma_v(h) = 0.0274\frac{\gamma_\mu \Phi_0}{\lambda^2}(1-h)\sqrt{1+3.9(1-h)^2}, \qquad (5)$$

where h is the field normalized by the upper critical field ($h = H/H_{c2}$). Although Eq. (5) exhibits a tendency of concave curve, it does not reproduce the field dependence of σ_v observed in Fig. 3. This is particularly true when the known value of H_{c2} ($\simeq$ 13 T at 2 K) is considered; the situation is illustrated by a dashed curve in Fig. 3.

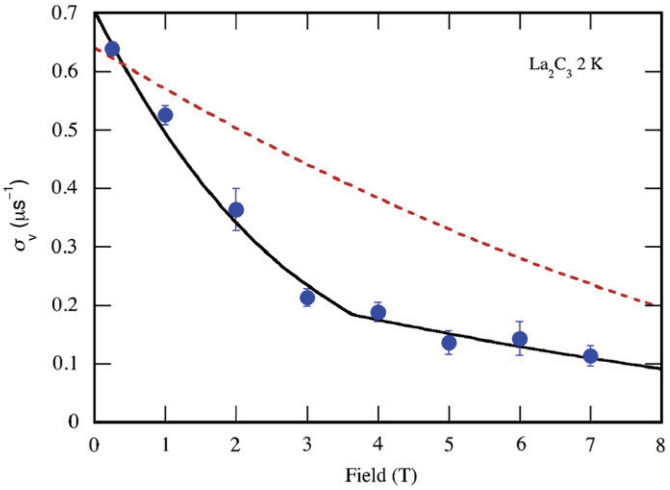

Fig. 3. Muon spin relaxation rate versus transverse field observed in the mixed state of La_2C_3 (at 2 K). Dashed curve shows σ_v expected for the case of single-gap (*s*-wave), whereas solid curve is a fit using the double-gap model (see text).

Since La_2C_3 is known to have a double-gap structure in the order parameter, it is natural to expand Eq. (5) into the following form:

$$\sigma_v(h) = w\sigma_v(h_1) + (1-w)\sigma_v(h_2), \tag{6}$$

where $h_i = H/H_{c2}^{(i)}$, and $H_{c2}^{(i)}$ is the upper critical field corresponding to the respective energy gap ($\sigma_v(h_i)$ must be set to zero for $h_i > 1$). The linear combination of two components is appropriate, as σ_v is proportional to the superfluid density (i.e., $\sigma_v \propto n_s$). The solid curve in Fig. 3 is the best fit with Eq. (6), which yields $\lambda = 390(3)$ nm, $H_{c2}^{(1)} = 16(4)$ T, $H_{c2}^{(2)} = 3.6(4)$ T, and $w = 0.41(9)$.

It is interesting to note that the ratio of the upper critical field ($H_{c2}^{(1)}/H_{c2}^{(2)} = 4.4 \pm 1.4$) is comparable with that of the two energy gaps ($\Delta_1(0)/\Delta_2(0) = 4.5(1)$), and that the relative weight w also agrees with that deduced from the temperature dependence of σ_v (where $w = 0.38(2)$) [2]. Provided that the physical parameters obtained at 2 K is not far from those at $T = 0$, it might be allowed to discuss the relation between the BCS coherence length and energy gap based on the equation,

$$\xi_0 = \frac{\hbar v_F}{\pi \Delta(0)} \simeq \xi \quad (T \to 0), \tag{7}$$

where v_F is the Fermi velocity. Since the upper critical field is proportional to the inverse squared of ξ ($H_{c2} = \Phi_0/(2\pi\xi^2)$), one may expect $H_{c2} \propto \Delta^2(0)/v_F^2$. Thus, the observed coincidence between the ratios of H_{c2} and of $\Delta(0)$ may imply that the Fermi velocity also varies between bands nearly by a factor of two.

Another possible reason for the steeper reduction of superfluid density is the field-induced nodes in the energy gap and associated quasiparticle excitation (QP) specific to noncentrosymmetric superconductors [3]. The characteristic field, H_{so}, may be provided in relation to the gap,

$$H_{so}^{(i)} \simeq \frac{\Delta_i(0)}{\mu_B}, \tag{8}$$

which yields $H_{so}^{(1)} = 47(2)$ T and $H_{so}^{(2)} = 10(2)$ T. It is predicted in the calculation of electronic specific heat that the QP excitation is strongly enhanced to reduce the superfluid density towards a field 0.55–0.7H_{so} (depending on the magnitude of the coherence length). Both of two corresponding fields, however, seem to be too high to explain the characteristic field of kink observed in Fig. 3 ($\simeq$ 3 T). On the other hand, it is also predicted for the case of small SO interaction (compared with $\Delta(0)$) that the QP excitation might be enhanced below $\sim 0.1 H_{so}$, primarily due to the asymmetric deformation of the Fermi surface. In this case, both of the characteristic fields ($\simeq$ 4.7 and 1.0 T) are not far from that observed in Fig. 3, and the weighted average ($\simeq$ 2.5 T) turns out to be in good accord with the kink of σ_v.

It is presumable as an actual situation that the field dependence of σ_v reflects the effect of double-gap as well as that of the SO interaction, and they are not discernible within the present resolution of data along the magnetic field.

In conclusion, we demonstrated the presence of SO interaction by showing the occurrence of field-induced enhancement of muon spin relaxation in the normal state of a noncentrosymmetric superconductor, La_2C_3. In the mixed state of La_2C_3, we also showed that the field dependence has a clear kink around 3 T, and that this feature may be well explained by considering the effect of (i) double-gap structure in the order parameter previously established by the temperature dependence of σ_v and (ii) that of the SO interaction leading to the field-induced deformation of the Fermi surface.

We would like to thank the staff of TRIUMF for their technical support during the μSR experiment. We also thank S. Fujimoto for helpful discussion on the effect of noncentrosymmetry on the electronic property of sesquicarbides. This work was supported by the KEK-MSL Inter-University Program for Oversea Muon Facilities and a Grant-in-Aid for Scientific Research on Priority Areas by Ministry of Education, Culture, Sports, Science and Technology, Japan.

References

[1] J. Nagamatsu, N. Nakagawa, T. Muranaka, Y. Zenitani, J. Akimitsu, Nature 410 (2001) 63.
[2] S. Kuroiwa, Y. Saura, J. Akimitsu, M. Hiraishi, M. Miyazaki, K.H. Satoh, S. Takeshita, R. Kadono, Phys. Rev. Lett. 100 (2008) 097002.
[3] For a recent review, see, for example, S. Fujimoto, J. Phys. Soc. Japan 76 (2007) 051008.
[4] S. Fujimoto, Phys. Rev. B 76 (2007) 184504.
[5] E.H. Brandt, Phys. Rev. B 37 (1988) 2349.

Physica B 404 (2009) 740–742

Contents lists available at ScienceDirect

Physica B

journal homepage: www.elsevier.com/locate/physb

Coexistence of superconductivity and magnetism in the Tm-based superconductor probed by muon spin relaxation

Naoki Kase[a,*], Jun Akimitsu[a], Yasuyuki Ishii[b], Takao Suzuki[b], Isao Watanabe[b], Masanori Miyazaki[c], Masatoshi Hiraishi[c], Soshi Takeshita[d], Ryosuke Kadono[c,d]

[a] Department of Physics and Mathematics, Aoyama Gakuin University, Sagamihara, Kanagawa 229-8558, Japan
[b] Advanced Meson Science Laboratory, RIKEN Nishina Center, Wako, Saitama 351-0198, Japan
[c] Department of Materials Structure Science, The Graduate University for Advanced Studies, Tsukuba, Ibaraki 305-0801, Japan
[d] Institute of Materials Structure Science, High Energy Accelerator Research Organization, Tsukuba, Ibaraki 305-0801, Japan

ARTICLE INFO

Keywords:
$(Sn_{1-x}Tm_x)Tm_4Rh_6Sn_{18}$
Superconductivity
Magnetism
μSR

ABSTRACT

The magnetic property of a thulium-based superconductor, $Tm_5Rh_6Sn_{18}$ (superconducting transition temperature $T_c = 2.2$ K), is investigated by muon spin relaxation (μSR). Below around 6 K, the development of a quasi-static local magnetic field is clearly inferred from the observation of spontaneous oscillation signal in the μSR spectra under zero external field, where the magnetism persists even below T_c. The internal magnetic field at the muon site, H_μ, is estimated to be approximately 175 Oe. The fractional volume of the magnetic component is estimated to be 100%, strongly suggesting that the magnetism coexists with superconductivity.

1. Introduction

$(Sn_{1-x}R_x)R_4T_6Sn_{18}$ T = transition metal) compounds belong to a large stannide series [1]. These stannides crystalize in a tetragonal structure with a space group $I4_1/acd$, and exhibit magnetic and/or superconducting transitions [2]. The reentrant superconductor $(Sn_{1-x}Er_x)Er_4Rh_6Sn_{18}$ has attracted much interest for the magnetic and superconducting state, because the physical properties dramatically change due to the difference of the composition of x; $x\sim0$ is superconducting below $T \simeq 1.3$ K down to 50 mK; $x\sim0.3$ is a reentrant superconducting with $T_c \simeq 1.05$ K and $T_M \simeq 0.5$ K; $x\sim0.75$ has a magnetic order at 0.65 K and is not superconductor [2,3].

On the other hand, $(Sn_{1-x}Tm_x)Tm_4Rh_6Sn_{18}$ becomes superconductor at 2.2 K and exhibits a reentrant superconducting behavior demonstrated by the temperature dependence of the resistivity at fields higher than 1.4 kOe (above 0.4 K). In addition, because the composition of x is a constant value of about 0.8, $(Sn_{1-x}Tm_x)Tm_4Rh_6Sn_{18}$ can be nearly described as a chemical formula of $Tm_5Rh_6Sn_{18}$ ($x \simeq 0.8$) [4].

However, compared to the other reentrant superconductors, $Tm_5Rh_6Sn_{18}$ still has far less information on the magnetic ordering or superconducting properties from the previous literature. This motivated us to investigate the superconducting state and the relationship between magnetism and superconductivity more preciously from the view point of microscopic measurements.

We investigated at the microscopic level the coexistence between magnetism and superconducting state by means of the muon spin relaxation (μSR) method. The μSR measurement shows the development of a quasi-static local magnetic field is clearly inferred from the observation of a spontaneous oscillation signal in the μSR spectra under zero external field, where the magnetism persists even below T_c. Our result establishes the coexistence of superconductivity and magnetic ordering in the Tm-based superconductor.

2. Experimental detail

Single crystals of $Tm_5Rh_6Sn_{18}$ were grown by the Sn flux method. The starting materials were 99.9%-Tm powder, 99.9%-Rh powder and 99.999%-Sn shot. These materials were sealed in an evacuated quartz tube, with off-stoichiometric composition of Tm:Rh:Sn = 1: 1.2: 10. The quartz tube was heated up to 1050, maintained at this temperature for about 3 h, and cooled down to 200 at the rate of 5/h, taking 7 days in total. The excess flux was removed from the crystals by spinning the ampoule in the centrifuge.

The single-crystalline nature has been verified by using backscattering X-ray technique. The powder X-ray diffraction patterns could be indexed as the $Tm_5Rh_6Sn_{18}$ with the space group $I4_1/acd$. The electrical resistivity was measured by the conventional DC four-probe method in the temperature range

---

[*] Corresponding author.
E-mail address: n-kase@phys.aoyama.ac.jp (N. Kase).

0921-4526/$ - see front matter © 2008 Elsevier B.V. All rights reserved.
doi:10.1016/j.physb.2008.11.185

from 0.4 to 300 K under various (including zero) applied magnetic fields with a PPMS system (Quantum Design Co., Ltd.).

The μSR measurements were carried out at the RIKEN-RAL Muon Facility in the Rutherford Appleton Laboratory, which provided a pulsed beam of nearly 100% spin-polarized muons. The polycrystalline samples obtained from single crystals crushed into a fine powder were pressed into pellets, and sintered at 900 for 24 h under a high vacuum condition of 4.0×10^{-3} Pa. The sample was glued onto a high purity silver (99.998%) holder to avoid a depolarizing background μSR signal, and mounted into a ^{3}He cryostat. During the measurement under zero field (ZF), residual magnetic field at the sample position was reduced below 10^{-5} kOe.

3. Experimental results and discussion

3.1. Electrical resistivity

Superconductivity can be inferred from electrical resistivity measurements, as shown in Fig. 1. The onset temperature of the superconducting transition and the temperature of zero resistivity are observed to be 2.30 and 2.20 K. The transition width ΔT is considered as the temperature interval between 10% and 90% of the transition and is observed to be approximately 0.07 K. The electrical resistivity in the normal state increases with a decrease in the temperature, indicating abnormal metallic behavior. This anomaly can be described as $-\ln T$ behavior, which strongly indicates that Kondo effect is significant in this material.

Fig. 2(a) shows the temperature dependence of the electrical resistivity under several magnetic fields. $Tm_5Rh_6Sn_{18}$ become superconducting at 2.2 K and does not return to the normal state down to 0.4 K under zero magnetic field. At fields higher than 1.3 kOe, the superconducting state is broken due to the occurrence of the magnetic ordering. In fields exceeding 1.70 kOe the superconducting state is no longer fully established. Fig. 2(b) shows the superconducting phase diagram of $Tm_5Rh_6Sn_{18}$. The T_M and T_c are determined by the mid-point temperature of T^{zero} and T^{onset}, and T^* is the moderate drop of the resistivity. What is the origin of T^* is not understood, but the fact that T^* depends on magnetic fields indicates low probability of the impurity effect of Sn (Sn; $H_c(0) = 305$ Oe) or magnetic ordering.

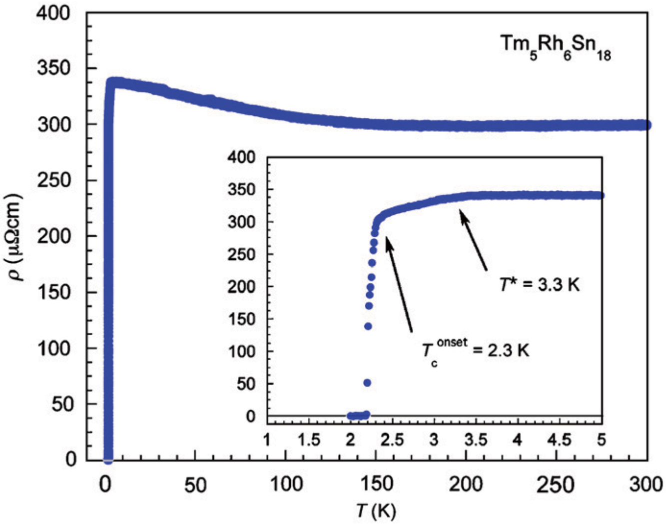

Fig. 1. Temperature dependence of the electrical resistivity of $Tm_5Rh_6Sn_{18}$. The inset shows the expansion at low temperature region.

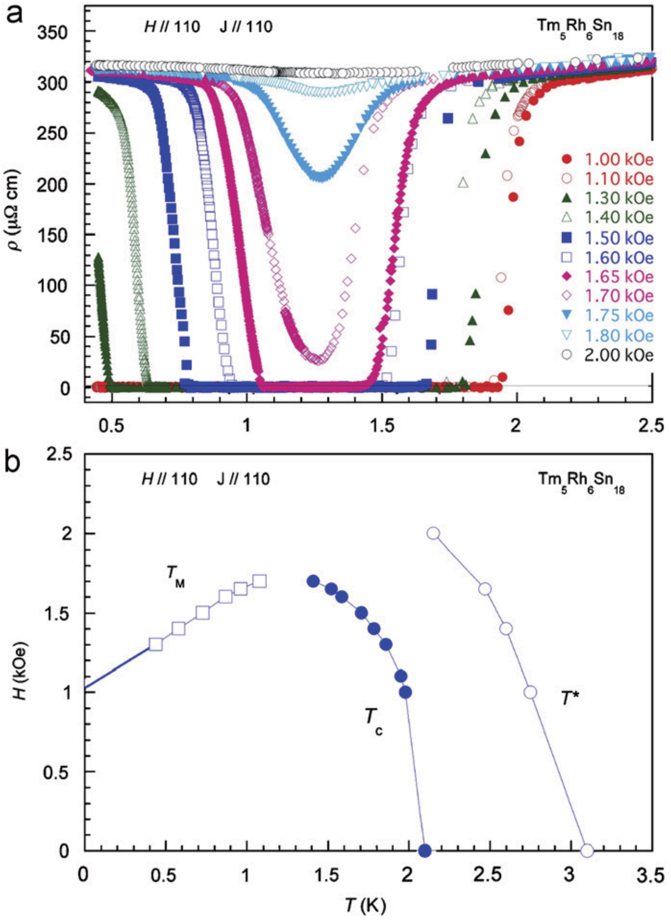

Fig. 2. (a) Temperature dependence of the electrical resistivity of $Tm_5Rh_6Sn_{18}$ under several magnetic fields. (b) Phase diagram of $Tm_5Rh_6Sn_{18}$. The closed symbol shows superconducting transition, the square symbol shows breaking superconducting transition, and the open symbol shows a moderate drop of the resistivity.

3.2. μSR measurement

ZF-μSR is the most sensitive technique to examine magnetism in any form, where the development of local magnetic moment leads to either spontaneous oscillation or exponential damping of $A(t)$. Fig. 3 shows the time-dependent muon–positron decay asymmetry under zero external field at several temperatures in $Tm_5Rh_6Sn_{18}$. Below around 6 K, development of a quasi-static local magnetic field is clearly inferred from the observation of a spontaneous oscillation signal in the μSR spectra. Surprisingly, the spontaneous oscillation signal was observed even below the superconducting transition temperature $T_c = 2.2$ K.

The ZF-μSR time spectra below $T_m = 6$ K are analyzed by using the following formula for powder specimen, $P(t) = A_1\exp(-\lambda_1 t)\cos(2\pi ft+\phi) + A_2\exp(-\lambda_2 t) + A_B$, where A_i refers to the asymmetry of muons stopped in the sample, A_B is a background, λ_i is the relaxation rate, and f $(=\gamma_\mu H_\mu/2\pi$, where γ_μ is the muon gyromagnetic ratio of $2\pi\times13.553$ MHz/kOe) is the precession frequency with H_μ being the spontaneous local field. The solid curves are the best fits of the data in the time domain, as shown Fig. 3. The model yields good fits to data as indicated by reasonably small values of reduced chi square: χ^2/N_f is mostly less than 1.3, with N_f being the number of degrees of freedom.

As expected for a polycrystalline sample, the $\frac{1}{3}$ term of each component represents the fraction of the muons possessing an initial polarization along the same direction of the internal field.

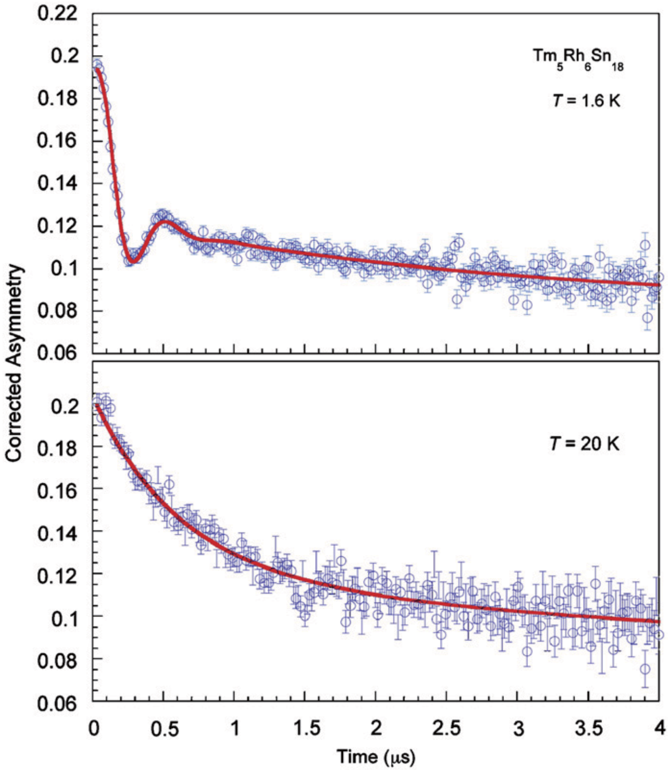

Fig. 3. ZF-μSR time spectra in $Tm_5Rh_6Sn_{18}$ at 1.6 and 20 K. Solids curves represent those obtained by fitting with equation $P(t)$.

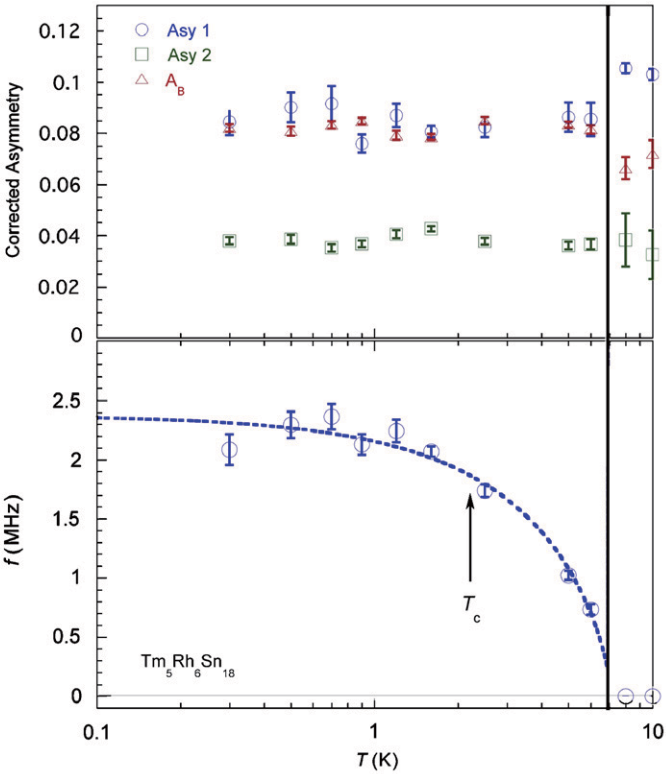

Fig. 4. The temperature dependence of muon spin precession frequency f, and corrected asymmetry. The dashed curve is the fitting result of $f(T) = f(0)(1 - T/T_m)^{\beta}$.

The fractional volume of the magnetic component $[= A_1/(A_1 + A_2)]$ is estimated to be 0.67, strongly suggesting that the magnetism occurs in the whole volume of the sample and therefore coexisting with superconductivity.

The muon spin precession frequency f is displayed as a function of temperature in Fig. 4. The dashed curve for f in the down panel of Fig. 4 is the fitting result with a form $f(t) = f(0)(1 - T/T_m)^{\beta}$, which yields $T_m = 7.1\,\mathrm{K}$, $f(0) = 2.38\,\mathrm{MHz}$. The obtained T_m is almost consistent with the temperature at which the oscillation signals appear. The internal magnetic field at the muon site, H_{μ}, is estimated to be approximately 175 Oe from the relationship between $f(0)$ and H_{μ}, $f(0) = \gamma_{\mu} H_{\mu}/2\pi$. It is noticeable that these spectra also exhibit an exponential damping without oscillation, which is described as a tail in equation $P(t)$ (see Fig. 3). This longitudinal spin relaxation might be due to dynamical fluctuation of internal fields. This strong spin fluctuation indicates that the magnetic order is not represented by a simple static antiferromagnetism.

4. Conclusions

In summary, we studied the magnetic properties of the Tm-based superconductor, $Tm_5Rh_6Sn_{18}$, by means of the ZF-μSR technique. The observation of clear muon spin precession signals below 6 K reveals a magnetic order invisible in bulk measurements. From the temperature dependence of f and corrected asymmetry, we confirmed the growth of a magnetic ordered state below 6 K. In the ordered state, the magnetic volume fraction is calculated to be nearly 100%. We conclude that reentrant superconductor $Tm_5Rh_6Sn_{18}$ exhibits the coexistence of superconductivity and magnetism at the microscopic level.

Acknowledgments

This work was partially supported by “High-Tech Research Center Project” for Private Universities and Grant-in-Aid for Scientific Research from the Ministry of Education, Culture, Sports, Science and Technology, Japan. One of the authors (N. Kase) acknowledges the support of the Iwanami Fujukai Foundation.

References

[1] J.P. Remeika, et al., Solid State Comm. 34 (1980) 923.
[2] S. Miraglia, et al., Acta Cryst. B 43 (1987) 76.
[3] H.R. Ott, et al., in: Proceedings of the International Conference on Ternary Superconductors, Lake Geneva, WI, USA, 1980, p. 251.
[4] A. Rojek, et al., Phys. C 223 (1994) 111.

Physica B 404 (2009) 743–745

Contents lists available at ScienceDirect

Physica B

journal homepage: www.elsevier.com/locate/physb

μSR study of magnetic ground state in Mo_3Sb_7

H. Okabe [a], J. Akimitsu [a,*], S. Takeshita [b], M. Miyazaki [c], M. Hiraishi [c], R. Kadono [b,c]

[a] *Department of Physics and Mathematics, Aoyama Gakuin University, Fuchinobe 5-10-1, Kanagawa 229-8558, Japan*
[b] *Institute of Materials Structure Science, High Energy Accelerator Research Organization (KEK), Tsukuba, Ibaraki 305-0801, Japan*
[c] *School of High Energy Accelerator Science, The Graduate University for Advanced Studies, Tsukuba, Ibaraki 305-0801, Japan*

A R T I C L E I N F O

Keywords:
Superconductivity
Spin-gap
μSR

A B S T R A C T

μSR study on the anomalous magnetic behavior of an intermetallic superconductor Mo_3Sb_7 is reported. Muon depolarization rate due to dynamically fluctuating electronic spins is reduced with decreasing temperature, which is in line with the development of a spin-liquid state. Meanwhile, the detailed analysis of structural deformation below 50 K suggests that the presumed spin-gap is not fully opened, and that the magnetic state just above T_c might be understood as an itinerant paramagnetic state with localized spin-singlets.

1. Introduction

A binary intermetallic superconductor Mo_3Sb_7 ($T_c = 2.3$ K [1]), which crystallizes in a cubic Ir_3Ge_7 type structure, may belong to a novel class of metals in which the conventional s-wave superconductivity coexists with paramagnetic spin fluctuation [2]. The temperature dependence of magnetic susceptibility above T_c exhibits a broad peak similar to that observed in low-dimensional spin systems. It is argued that the origin of such anomalous magnetic behavior is attributed to the opening of a gap in spin excitation spectrum, as suggested by an anomaly observed at 50 K in specific heat associated with a slight drop of susceptibility [3]. According to the analysis based on the isolated-dimer model, the coupling within Mo–Mo pairs leads to a tendency of forming a spin-singlet state. On the other hand, it is pointed out that Mo_3Sb_7 is a geometrically frustrated system in three-dimension which might lead to a long-range order of spin-singlet dimers, as suggested by NQR, zero-field (ZF-) μSR and structural studies [4]. This also points to the possibility of another spin-gap state in Mo_3Sb_7 of different origin.

However, since the muon spin depolarization in Mo_3Sb_7 is dominated by random local fields from nuclear magnetic moments, it is important to know the density distribution of fluctuation over certain range of frequency to assess the electronic spin contribution to the local fields. We therefore performed μSR measurements under a longitudinal field in Mo_3Sb_7 to investigate the Mo 4d electronic spin state and clarify microscopic magnetic properties around the phase transitions.

2. Experimental

The polycrystalline sample was synthesized by a solid-state reaction of high purity Mo (99.99%) and Sb (99.999%) powders (obtained from Kojundo-Kagaku Co. Ltd.). The stoichiometric mixtures were pressed into pellets and sintered at 1023 K for 2 weeks in an evacuated quartz tube with several intermediate grindings. The obtained samples were confirmed to be in a single phase by the powder X-ray diffraction. The magnetic susceptibility was measured using a SQUID magnetometer (MPMSR2, Quantum Design Co.), and the specific heat was measured by a standard thermal relaxation method (PPMS, Quantum Design Co.). μSR experiment was performed at TRIUMF, Vancouver, Canada. Nearly 100% spin-polarized positive muons with a momentum of 28 MeV/*c* were implanted into the polycrystalline sample and the time-dependent muon spin polarization was measured using positron detectors.

3. Result and discussion

As shown in Fig. 1, magnetic susceptibility in Mo_3Sb_7 exhibits a broad maximum approximately at 170 K, resembling a feature characteristic to low-dimensional spin systems, and it drops at 50 K accompanying a specific heat anomaly, reproducing the earlier result [3]. The anomaly at 50 K is closely associated with the structural transition that leads to a reduced crystal symmetry [4]. Previously, we reported detailed structural analysis of Mo_3Sb_7 below 50 K, where we showed that the nearest neighboring Mo–Mo couples along *z*-axis tends to form dimers [5]. If this structural deformation is associated with the occurrence of spin-singlet state, muon depolarization due to the fluctuating electronic dipolar fields is predicted to disappear.

---

[*] Corresponding author. Tel./fax: +81 42 759 6287.
E-mail address: jun@phys.aoyama.ac.jp (J. Akimitsu).

0921-4526/$ - see front matter © 2008 Elsevier B.V. All rights reserved.
doi:10.1016/j.physb.2008.11.184

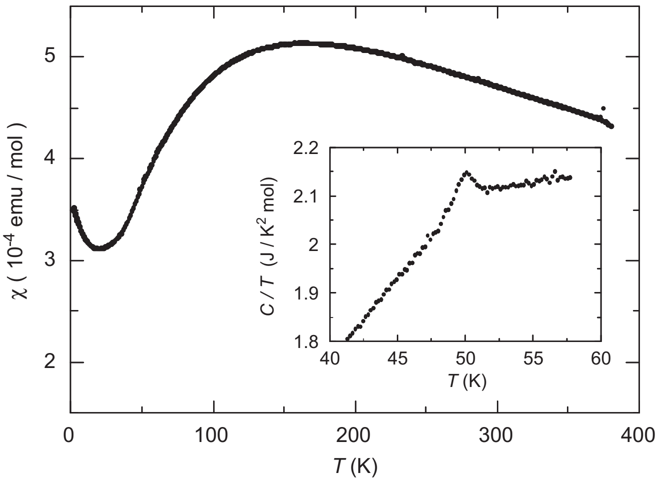

Fig. 1. Temperature dependence of magnetic susceptibility χ and specific heat C/T (inset) of Mo_3Sb_7.

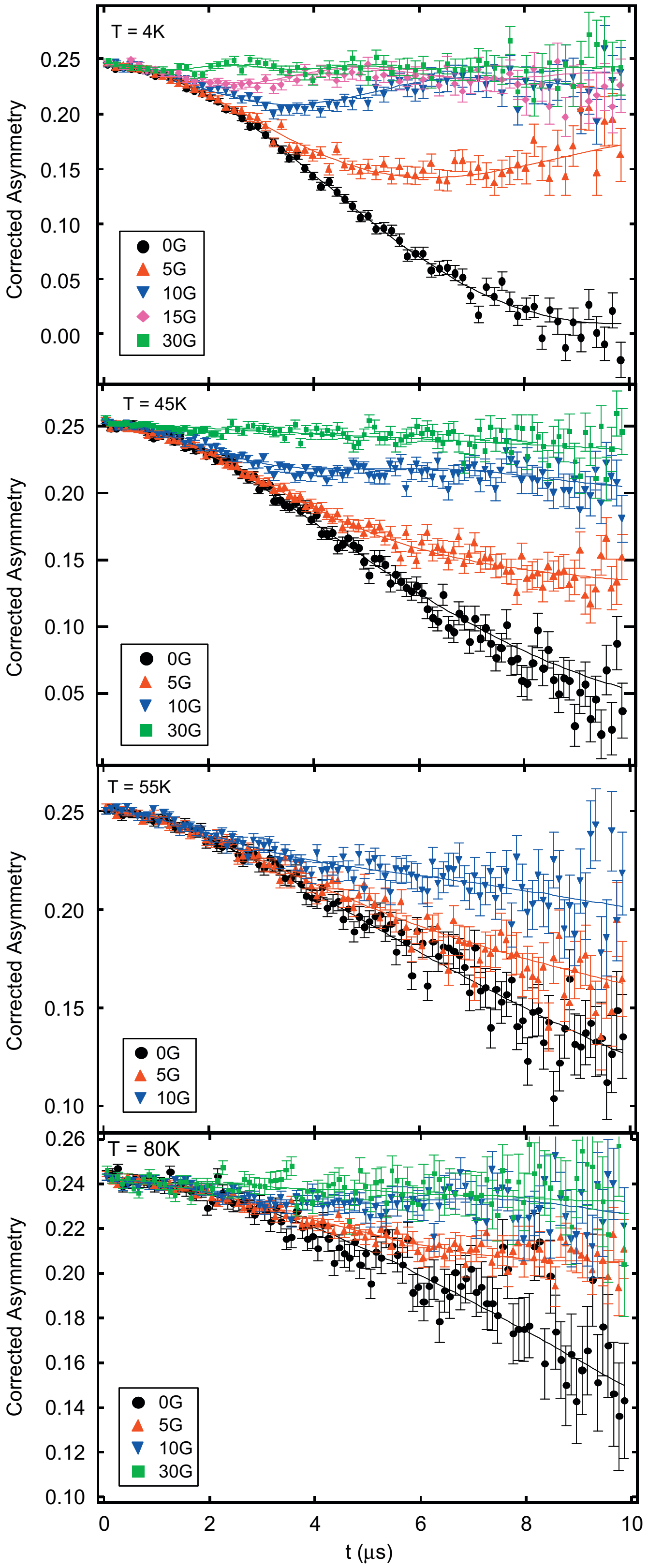

Fig. 2. ZF- and LF-μSR time spectra in Mo_3Sb_7 at various temperatures. Solid curves are results of curve fitting by the theoretical functions described in the text.

Fig. 2 shows μSR spectra ZF or LF measured at several different temperatures around 50 K. There is no sign of spontaneous precession under ZF, indicating that Mo_3Sb_7 has a non-magnetic ground state.

It is inferred from the Gaussian-like time dependence of ZF-μSR spectra that they are described by the Kubo–Toyabe (KT) relaxation for the random local fields from nuclear magnetic moments [6]. LF-μSR spectra show that muon depolarization is mostly quenched by an applied longitudinal field of 30 G, indicating that the local field is quasi-static. However, it turns out that the quenching is not complete, especially above 45 K, implying the presence of dynamically fluctuating electronic spins. We therefore analyzed these spectra using the following form:

$$A_0G_Z(t) = A_0G_{KT}^{nuc}(\sigma, t)\exp(-\lambda t), \tag{1}$$

$$\lambda(\omega_\mu) = \frac{2\delta^2 \nu}{\omega_\mu^2 + \nu^2}, \tag{2}$$

where A_0 is the initial asymmetry, G_{KT}^{nuc} is the dynamical Kubo–Toyabe relaxation function [7] arising from quasi-static nuclear moments with σ being the linewidth, and λ is the damping rate due to the fluctuating electronic spins. The field dependence (= densitydistribution) of λ is described by the Redfield's model shown in Eq. (2), where δ is the hyperfine coupling between muon and electron spins, ν is their fluctuation rate, and $\omega_\mu = \gamma_\mu H_{LF}$ (with H_{LF} being the longitudinal field, $\gamma_\mu = 2\pi \times 135.54$ MHz/T being the muon gyromagnetic ratio) [Eq. (2) is valid for $\lambda < \delta$]. In the case of Mo_3Sb_7, small values of λ ($\sim\frac{1}{10}$ of σ) make it difficult to deduce δ and ν separately from curve fitting, and thereby we deduced λ as a single parameter.

Displayed in Fig. 3(a) is the temperature dependence of the relaxation rate σ. It exhibits a gradual increase near 50 K and levels off at lower temperatures. This increase is hardly explained by the variation of distances between muons and nuclei associated with the structural deformation (of the order of 0.01 Å), strongly suggesting that muons occupy a site different from that above 50 K [8]. Interestingly, λ shown in Fig. 3(b) exhibits a tendency of increase with increasing temperature with a slight peak anomaly at 50 K. This feature might be attributed to localized Mo 4d electrons, where the small value of λ suggests a small moment size and associated very weak hyperfine coupling constant. Furthermore, the decrease of λ below 50 K recalls a spin-liquid ground state in which the hyperfine coupling is reduced upon the formation of short-ranged spin-singlet correlations (local spin-singlet pairs) as observed in geometrically frustrated spin system [9].

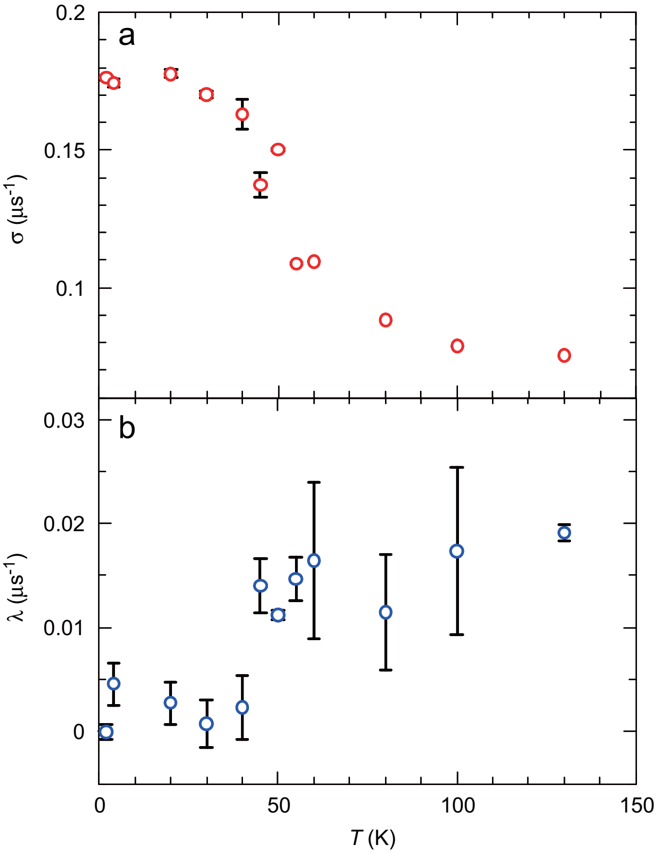

Fig. 3. Fitted data for Mo_3Sb_7 using Eq. (1). (a) Relaxation rate σ and (b) damping rate λ for various temperatures above and below the transition temperature.

As mentioned above, since Mo–Mo pairs form dimers only along z direction, the two thirds of Mo ions may remain relatively independent of the spin-singlet correlation and might be delocalized over the entire crystal [5]. Thus, the magnetic ground state of Mo_3Sb_7 just above T_c might be understood as a coexistent state of local spin-singlets and itinerant paramagnetism.

In summary, we investigated the nature of anomalous magnetic behavior in Mo_3Sb_7 using ZF/LF-μSR technique. Our μSR result suggests that the electronic spin fluctuation decreases sharply below 50 K, which might be interpreted as a sign for the occurrence of spin-singlet state. Taking into account the structural deformation at 50 K, we argue that the ground state just above T_c is a mixture of localized spin-singlets and itinerant electrons.

Acknowledgments

We would like to thank TRIUMF staff for technical support during our experiment. This work was financially supported by a Grant-in-Aid for Scientific Research in Priority Area “Invention of Anomalous Quantum Materials” (no. 16076212) and the “High-Tech Research Center” project for private universities from the Ministry of Education, Culture, Sports, Science and Technology of Japan.

References

[1] Z. Bukowski, D. Badurski, J. Stepien-Damm, R. Troc, Solid State Commun. 123 (2002) 283.
[2] C. Candolfi, B. Lenoir, A. Dauscher, C. Bellouard, J. Hejtmánek, E. Śantavá, J. Tobola, Phys. Rev. Lett. 99 (2007) 037006;
C. Candolfi, B. Lenoir, A. Dauscher, C. Bellouard, J. Hejtmánek, E. Śantavá, J. Tobola, Phys. Rev. B 77 (2008) 092509.
[3] V.H. Tran, W. Miiller, Z. Bukowski, Phys. Rev. Lett. 100 (2008) 137004.
[4] T. Koyama, H. Yamashita, Y. Takahashi, T. Kohara, I. Watanabe, Y. Tabata, H. Nakamura, arXiv:0805.3892v1.
[5] H. Okabe, S. Yano, T. Muranaka, J. Akimitsu, in: The Proceedings of the International Conference on Low Temperature Physics LT25, Journal of Physics: Conference Series, 2008, to be published.
[6] R.S. Hayano, Y.J. Uemura, J. Imazato, N. Nishida, T. Yamazaki, R. Kubo, Phys. Rev. B 20 (1979) 850.
[7] Y.J. Uemura, T. Yamazaki, D.R. Harshman, M. Senba, E.J. Ansaldo, Phys. Rev. B 31 (1985) 546.
[8] H. Okabe, et al., in preparation.
[9] H. Sakai, M. Kato, K. Yoshimura, K. Kosuge, J. Phys. Soc. Japan 71 (2002) 422.

Physica B 404 (2009) 781–784

Contents lists available at ScienceDirect

Physica B

journal homepage: www.elsevier.com/locate/physb

Microscopic investigation of antiferromagnetic order in A-site-ordered perovskite manganite $YBaMn_2O_6$

Y. Kawasaki [a,*], T. Minami [a,1], Y. Kishimoto [a], T. Ohno [a], A. Koda [b], K.H. Satoh [b], R. Kadono [b], J.L. Gavilano [c], H. Luetkens [d], T. Nakajima [e], Y. Ueda [f]

[a] *Institute of Technology, University of Tokushima, Tokushima 770-8506, Japan*
[b] *Institute of Material Structure Science, High Energy Accelerator Research Organization, Tsukuba 305-0801, Japan*
[c] *Laboratory for Neutron Scattering, PSI and ETHZ, Villigen CH-5232, Switzerland*
[d] *Laboratory for Muon-Spin Spectroscopy, Paul Scherrer Institut, Villigen CH-5232, Switzerland*
[e] *AMRI, National Institute of Advanced Industrial Science and Technology, Tsukuba 305-8565, Japan*
[f] *Institute for Solid State Physics, University of Tokyo, Kashiwa 277-8581, Japan*

ARTICLE INFO

Keywords:
A-site-ordered perovskite manganite
Magnetic structure
Charge order
NMR
μSR

ABSTRACT

The electromagnetic properties of the A-site-ordered perovskite manganite $YBaMn_2O_6$ have been investigated by ^{55}Mn-NMR and μSR measurements. ^{55}Mn-NMR spectrum of $YBaMn_2O_6$ at the ground state is consistent with a charge-ordered antiferromagnetic state, where e_g-electrons of Mn^{3+} ions are well localized. In the antiferromagnetic state, three components of muon spin oscillation are observed in the μSR time spectra. The observed muon spin oscillating frequencies are consistently explained by the checker-board-type charge order and the antiferromagnetic spin order proposed by the previous neutron diffraction study. The most probable candidate for the muon site is near O(7) in the BaO plane of $YBaMn_2O_6$.

For the last several decades, the perovskite manganites $R_{1-x}A_xMnO_3$ (R = rare earth element, A = Ca, Ba, Sr) have been intensively investigated, because they show a rich variety of fascinating electromagnetic properties, such as a colossal magnetoresistance (CMR), charge and orbital ordering (COO) and metal–insulator transition. Recently, A-site-ordered perovskite manganites $RBaMn_2O_6$ have been synthesized for $x = 0.5$ and attracting great interest [1–5]. As schematically shown in the inset of Fig. 2 (R = Y in the drawing), $RBaMn_2O_6$ has a layer-type ordering of R and Ba ions at the A site of perovskite structure along the *c*-axis, resulting in the two-dimensional structure with the stacking sequence of $–RO–MnO_2–BaO–MnO_2–$ planes. One of the peculiar features to the A-site-ordered $RBaMn_2O_6$ is their much higher COO and magnetic ordering temperatures compared with A-site disordered $R_{0.5}Ba_{0.5}MnO_3$. These high ordering temperatures in $RBaMn_2O_6$ are considered to originate mainly from the ordering of R and Ba in the structure, which results in the absence of electrostatic potential disorder. This point of $RBaMn_2O_6$ is considered to be a key feature for the development of new materials that exhibit CMR at room temperature [6].

Among the series of $RBaMn_2O_6$, $YBaMn_2O_6$ has the highest ordering temperatures; orbital at 520 K, charge at $T_{co} = 480$ K, and antiferromagnetic orders at $T_N = 195$ K [7]. In the AFI(CE) phase below T_N, transmission electron spectroscopy experiments suggest a checker-board type COO in the MnO_2 plane. The neutron diffraction experiments suggest that the spin-ordering pattern in the MnO_2 plane below T_N is the same as that observed in $R_{0.5}A_{0.5}MnO_3$ [8], but it has a fourfold periodicity along the *c*-axis. It is considered that the Y/Ba order along the *c*-axis in $YBaMn_2O_6$ makes the interlayer magnetic interactions alternated between ferro- and antiferromagnetic arrangements, resulting in this spin structure. Since these ordering patterns may be closely related to the peculiar structure to the A-site-ordered perovskites, $YBaMn_2O_6$ is suitable for investigation into the characteristic of the A-site-ordered manganites. We have performed nuclear-magnetic-resonance (NMR) and muon-spin-relaxation (μSR) measurements to get further information on the magnetic properties of $YBaMn_2O_6$.

A polycrystalline sample of $YBaMn_2O_6$ was prepared by a solid-state reaction and subsequent sintering process in pure Ar gas, followed by annealing in flowing O_2 gas. The details of the preparation method are described in the literature [2]. The crystal structure and magnetic properties of this sample are confirmed to be consistent with the conclusions based on the previous data [2,7,9]. ^{55}Mn-NMR spectra have been measured in both zero and elevated magnetic fields with a phase-coherent spectrometer by

---

[*] Corresponding author. Tel./fax: +81 88 656 9878.
E-mail address: yu@pm.tokushima-u.ac.jp (Y. Kawasaki).
[1] Present address: Seiryo Engineering Co., Ltd.

0921-4526/$ - see front matter © 2008 Elsevier B.V. All rights reserved.
doi:10.1016/j.physb.2008.11.174

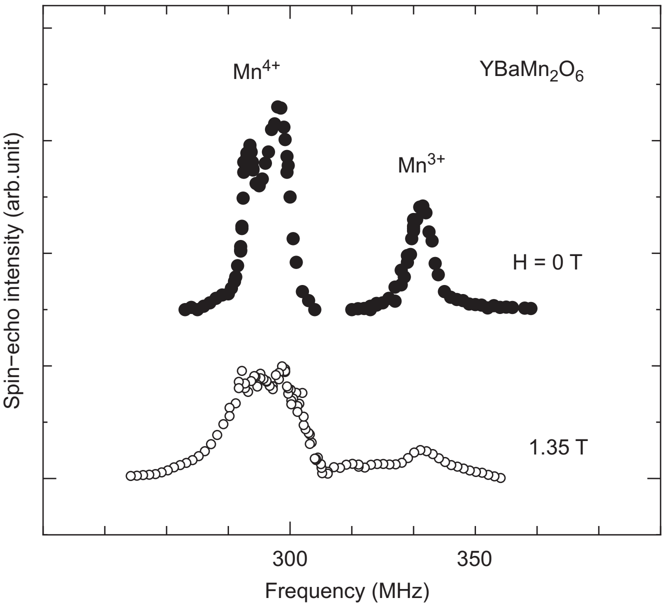

Fig. 1. ^{55}Mn-NMR spectra of YBaMn$_2$O$_6$ at 4.2 K under 0 T (filled circles) and 1.35 T (open circles).

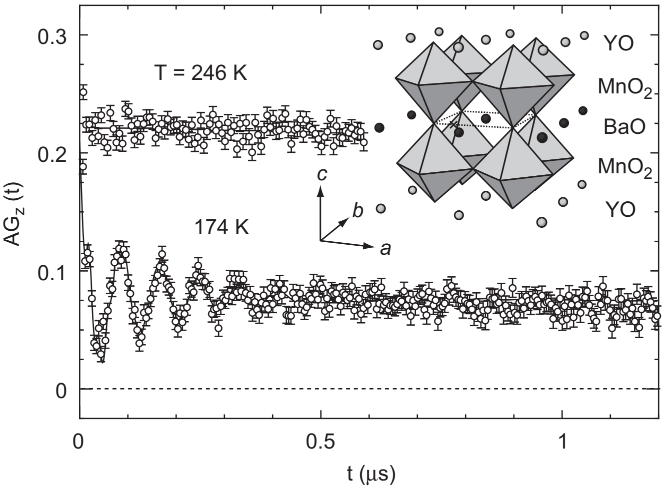

Fig. 2. ZF-μSR time spectra at 246 and 174 K. Inset: crystal structure of YBaMn$_2$O$_6$. Cross represents the most probable candidate for the muon site.

using a spin-echo technique. The μSR data have been taken by using surface muon at TRIUMF (Vancouver, Canada), KEK (Tsukuba, Japan) and PSI (Villigen, Switzerland). All the μSR data have been measured in zero field (ZF).

In Fig. 1, we show the ^{55}Mn-NMR spectra of YBaMn$_2$O$_6$ at 4.2 K under 0 T (filled circles) and 1.35 T (open circles). ZF antiferromagnetic resonances are observed at around 297 and 322 MHz, where the signal around 297 MHz consists of slightly separated two lines. The NMR signals around 297 and 322 MHz are considered to originate from nuclei of Mn^{4+} and Mn^{3+} ions, respectively. The observation of both signals from Mn^{4+} and Mn^{3+} indicates localization of holes, in agreement with the charge ordering. The antiferromagnetic state is assured by the fact that these peaks are unshifted with small broadenings by an external magnetic field of 1.35 T. The small splitting of signal for Mn^{4+} in ZF suggests two inequivalent Mn^{4+} ions, where either hyperfine coupling strength or size of Mn magnetic moment is slightly different.

One can estimate the sizes of Mn magnetic moments from the resonance frequency using a hyperfine coupling constant. The ^{55}Mn-NMR signals are observed at 264 MHz for Mn^{4+} in CaMnO$_3$ [10] and 350 MHz for Mn^{3+} in LaMnO$_3$ [11]. Because the size of magnetic moment is reported to be 2.65μ_B for CaMnO$_3$ and 3.89μ_B for LaMnO$_3$ from neutron diffraction experiments [12], hyperfine coupling constants A_{hf}'s for Mn^{4+} and Mn^{3+} are estimated to be 99.6 and 90.4 MHz/μ_B, respectively. Using these A_{hf}'s, we estimate the size of magnetic moment in YBaMn$_2$O$_6$ to be $\mu^{4+}_{\rm ord} = 2.98\mu_B$ for Mn^{4+} and $\mu^{3+}_{\rm ord} = 3.56\mu_B$ for Mn^{3+} from the NMR frequencies. The value of $\mu^{4+}_{\rm ord}$ is very close to the ordered moment expected for $S = \frac{3}{2}$. $\mu^{3+}_{\rm ord} = 3.56\mu_B$ is about 11% reduced from the expected ordered moment of 4μ_B for the case of $S = 2$. These results suggest weak hybridization between Mn-3d of Mn^{3+} and O-2p orbital in YBaMn$_2$O$_6$, in agreement with the picture that YBaMn$_2$O$_6$ has the smallest e$_g$-electron transfer interaction due to the large distortion of MnO$_6$ octahedra among RBaMn$_2$O$_6$ [2].

Next, we turn to the μSR results in ZF. Two examples of the ZF-μSR time spectra above and below $T_N = 195$ K are shown in Fig. 2. A spontaneous Larmor precession is observed in the data below T_N, which is characteristic for a static magnetic-ordered phase. The time spectra data above T_N have been fitted using $G_z(t) = A\exp(-\lambda t)$, where A and λ are the initial total asymmetry and the relaxation rate, respectively. Below T_N, the functional form of the ZF-μSR time spectra includes an oscillating term

$$G_z(t) = A_1\exp(-\lambda_1 t) + \sum_{i=1}^{4} A_{2,i}\exp(-\lambda_{2,i}t)\cos(2\pi\nu_i t + \phi)$$

describing the effect of the static internal fields. $A_{2,i}$ ($\sum_i A_{2,i} = A - A_1$) and ν_i are the i-th oscillating components of amplitude and frequency, respectively. ϕ is an initial phase. The relaxation rate for each component is λ_1 and $\lambda_{2,i}$. The solid lines in Fig. 2 represent the best fits to the data by using the above equations for $G_z(t)$. The initial phase of $\phi \simeq -0.17^\circ$ is almost independent of temperature.

The parameters (a) A and A_1, (b) λ and λ_1 as well as (c) ν_i obtained for various temperatures are summarized in Fig. 3, where A and λ (A_1 and λ_1) are those for $T > T_N$ ($T < T_N$). A slight but clear hysteretic behavior in these parameters, shown by the difference between the data measured on cooling (filled symbols) and on heating (open symbols) in the figure, indicates the first-order nature of the antiferromagnetic phase transition. The first-order nature may be related to a possible structural transition. Actually, the antiferromagnetic order is accompanied by the reformation of the COO superstructure that may induce a structural change [7].

The initial total asymmetry $A \simeq 0.22$ has a very weak temperature dependence above T_N. Below T_N, A_1 represents the signal from muons polarized along the direction of the internal field. The ratio $A_1/A \simeq \frac{1}{3}$ is expected if all implanted muons are exposed to a static local field in a polycrystalline sample. A_1/A is, however, slightly larger than $\frac{1}{3}$ below T_N and reaches $\frac{1}{3}$ below 50 K. This result suggests that a minor part of sample, most probably an impurity phase, orders magnetically below 50 K. Therefore, the muon spin oscillation with $\nu_4 = 101.1$ MHz (see Fig. 3(c)), that appears only below 50 K, is considered to be extrinsic. We recall that there is an anomaly in $\chi(T)$ at the same temperature [9]. The broad peak in the relaxation rate around 175 K may be due to a critical slowing down of Mn magnetic moments accompanied by the antiferromagnetic order. The temperature-independent component of $\lambda, \lambda_1 \sim 0.04\,\mu s^{-1}$ may originate from a nuclear contribution.

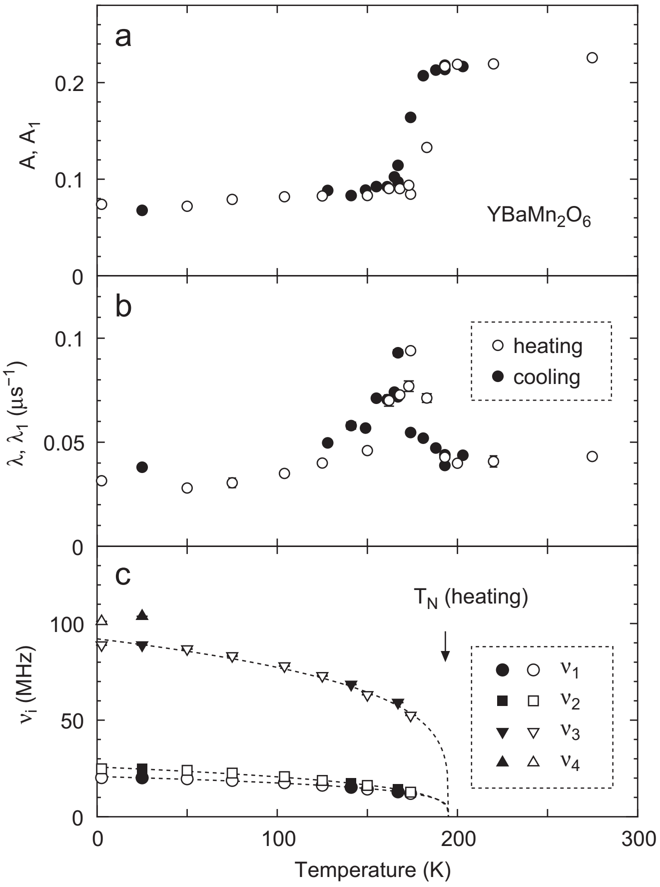

Fig. 3. (a) A and A_1, (b) λ and λ_1 and (c) ν_i in $YBaMn_2O_6$.

Below T_N, one detects the muon oscillation frequency, given by $(\gamma_\mu/2\pi)B$, where $\gamma_\mu = 2\pi \times 135.5\,MHz/T$ is the muon gyromagnetic ratio and B is a local static magnetic field at muon site. The frequencies $\nu_1 = 20.2$, $\nu_2 = 24.8$ and $\nu_3 = 88.9\,MHz$ indicate the local fields of 1.5 kOe, 1.8 kOe and 6.6 kG at 2.5 K. The temperature dependence of ν_i is well described by the power function, $\nu_i(T) = \nu_0(1 - T/T_N)^\beta$, as indicated by dotted lines in Fig. 3(c). Here, ν_0 is the muon frequency at zero temperature and the exponent $\beta \sim 0.31$ for $YBaMn_2O_6$. The obtained value of β is consistent with the value observed also in $LaMnO_3$ near T_N [13]. To summarize, the static magnetic properties of $YBaMn_2O_6$ indicated by the NMR and μSR results agree with the expectations for a normal charge-ordered antiferromagnet.

Finally, we argue possible muon sites in $YBaMn_2O_6$ on the basis of the previous works in the perovskite manganite $LaMnO_3$ [13,14]. De Renzi et al. concluded that the muons lie at 1.05 Å from an apical O ion on the line connecting the O ion and the midpoint between two adjacent La ions in the LaO plane. In addition, Heffner et al. have considered a second muon site, about 1 Å apart from a planer O ion in the MnO_2 plane. We recall that $YBaMn_2O_6$ has two Mn sites, Mn(1) and Mn(2), and eight oxygen sites, O(1)−O(8), below T_{co}, where crystallographically inequivalent two MnO_6 octahedra show distinct volume difference due to the charge ordering [9]. The positions near apical oxygens, O(1), O(2) in the YO plane and O(7), O(8) in the BaO plane of $YBaMn_2O_6$, may be closely related to the first muon site in $LaMnO_3$. The positions near planer oxygens, O(3)−O(6) in the MnO_2 plane, may be closely related to the second muon site.

Considering that dipolar field dominates a local field at muon site in many perovskite manganites [13,14], we have calculated the strength of the dipolar fields at eight muon site candidates.

Table 1
Calculated values of the local dipolar field at several muon site candidates, positions 1 Å away from eight inequivalent oxygen sites.

Position	Nearest oxygen	Dipolar field (kG)
(0.128, 0.111, 0)	O(1)	$B_1 = 4.1, 11.1$
(0.628, 0.703, 0)	O(2)	$B_2 = 6.1, 10.5$
(0.460, 0.268, 0.195)	O(3)	$B_3 = 14.0, 19.2$
(0.946, 0.271, 0.212)	O(4)	$B_4 = 9.8, 13.8$
(0.428, 0.771, 0.237)	O(5)	$B_5 = 19.2, 26.7$
(0.890, 0.798, 0.247)	O(6)	$B_6 = 7.8, 12.2$
(0.128, 0.179, 0.5)	O(7)	$B_7 = 1.6, 6.2$
(0.628, 0.622, 0.5)	O(8)	$B_8 = 3.8, 6.0$
Experiments		$B = 1.5, 1.8, 6.6$

The estimated values from the experiments is given for comparison.

These are classified into three groups: (a) B_i $(i = 1, 2)$ at the position 1 Å apart from O(i) on the line connecting O(i) and the midpoint between two adjacent Y ions in the YO plane, (b) B_i $(i = 3, 4, 5, 6)$ at the positions 1 Å apart from O(i) in almost the same direction proposed by the previous works as the second muon site in the MnO_2 plane, (c) B_i $(i = 7, 8)$ at the position 1 Å apart from O(i) on the line connecting O(i) and the midpoint between two adjacent Ba ions in the BaO plane. Here, we use the structural parameters at 350 K listed in Table 1 of Ref. [9], the magnetic structure proposed by the neutron diffraction measurements [7], and the size of magnetic moment $3.56\mu_B$ for Mn^{3+} and $2.98\mu_B$ for Mn^{4+} estimated from NMR. The calculations are summarized in Table 1, where each muon site candidate has more than two magnetically inequivalent sites due to the zig-zag type magnetic structure in the MnO_2 plane.

Clearly, B_i $(i = 3, 4, 5, 6)$ cannot explain the estimated values from the experiments, which rules out these muon site candidates in the MnO_2 plane. One of B_2, two of B_7 and one of B_8 are comparable to the experimental values. From these results, we propose that muon stops at position 1 Å apart from O(7) in the BaO plane. The proposed muon site is indicated by cross in the inset of Fig. 2. A similar conclusion on the muon site has been reported for layered cobaltites $RBaCo_2O_{5.5}$ [15]. It seems reasonable that positive muons stop in the BaO plane by two reasons: (i) Ba^{2+} has smaller positive charge than Y^{3+}, (ii) the average distance between BaO and MnO_2 planes is larger by 25% than that between YO and MnO_2 planes due to the distortion of MnO_6 octahedra. Furthermore, positive muons may favor rather position near O(7) than position near O(8) in the BaO plane, because the nearest Mn ion to O(7) is Mn^{3+} while that to O(8) is Mn^{4+}. The observation of three local fields may be related to the existence of two inequivalent Mn^{4+} ions as indicated by the ^{55}Mn-NMR spectrum.

In conclusion, the magnetic properties extracted from the ^{55}Mn-NMR and μSR results agree with the expectations for a simple charge-ordered antiferromagnet. The observed muon spin oscillating frequencies below T_N are consistent with the checkerboard-type charge order and the antiferromagnetic spin order proposed by the neutron diffraction study. The most probable candidate for the muon site is the position near O(7) in the BaO plane.

References

[1] F. Millange, et al., Chem. Mater. 10 (1998) 1974.
[2] Y. Ueda, T. Nakajima, J. Phys. Condens. Matter 16 (2004) S573.
[3] D. Akahoshi, et al., Phys. Rev. Lett. 90 (2003) 177203.
[4] S.V. Trukhanov, et al., Phys. Rev. B 66 (2002) 184424.
[5] Y. Kawasaki, et al., Phys. Rev. Lett. 96 (2006) 037202.

[6] T. Nakajima, et al., J. Appl. Phys. 98 (2005) 046108.
[7] H. Kageyama, et al., J. Phys. Soc. Japan 72 (2003) 241.
[8] Z. Jirák, et al., Phys. Rev. B 61 (2000) 1181.
[9] T. Nakajima, et al., J. Phys. Soc. Japan 73 (2004) 2283.
[10] K. Shimizu, et al., Phys. Rev. B 73 (2006) 174420.
[11] G. Allodi, et al., J. Magn. Magn. Mater. 242–245 (2002) 635.
[12] E.O. Wollan, W.C. Koehler, Phys. Rev. 100 (1955) 545.
[13] R.H. Heffner, et al., Phys. Rev. B 63 (2001) 094408.
[14] R. De Renzi, et al., Physica B 289–290 (2000) 52.
[15] H. Luetkens, et al., Phys. Rev. Lett. 101 (2008) 017601.

Physica B 404 (2009) 801–803

Contents lists available at ScienceDirect

Physica B

journal homepage: www.elsevier.com/locate/physb

Muon spin relaxation in hydrogen tungsten bronze

M. Mihara [a,*], K. Shimomura [b], I. Watanabe [c], Y. Ishii [c], T. Suzuki [c], T. Kawamata [c], J. Komurasaki [a], D. Nishimura [a], K. Nishiyama [b], R. Kadono [c], S. Takai [d], T. Nakano [a]

[a] *Department of Physics, Osaka University, Toyonaka, Osaka 560-0043, Japan*
[b] *Muon Science Laboratory, High Energy Accelerator Research Organization (KEK), Tsukuba, Ibaraki 305-0801, Japan*
[c] *Advanced Meson Science Laboratory, RIKEN, Wako, Saitama 351-0198, Japan*
[d] *Department of Materials Scinence, Tottori University, Tottori 680-8552, Japan*

ARTICLE INFO

Keywords:
Muon spin relaxation
Diffusion
Hydrogen tungsten bronze

ABSTRACT

The zero-field muon spin relaxation in hydrogen tungsten bronze H_xWO_3 was observed at temperatures between 5 K and 440 K in order to study the diffusion property of muons. The result shows that the relaxation curves are nearly identical at temperatures lower than 100 K and at above 100 K the relaxation rate becomes slower with increasing temperature. The local field and its fluctuation at a muon site in H_xWO_3 were estimated from the present data.

1. Introduction

The insertion of hydrogen into WO_3 forms a nonstoichiometric compound H_xWO_3, called hydrogen tungsten bronze, which causes the dark blue coloration. In a WO_3 thin film the colored and bleached states are reversibly controlled by applying a voltage to take H^+ ions into and out of the WO_3 layer (electrochromic effect). The electrochromic device based on WO_3 has been developed to apply in passive display, smart windows and so on [1]. One of the key issues for practical use is quick response to which the proton mobility in WO_3 under an electric field is closely related. In this situation, it is important to understand the basic diffusion property of hydrogen in the lattice of H_xWO_3 for the development of the WO_3 electrochromic device.

The positive muon spin relaxation (μ^+SR) is a potentially useful technique to investigate dynamical properties of hydrogen, since positive muons with $\frac{1}{9}$ the proton mass are considered as a light isotope of proton. In the present study, we have performed the zero-field (ZF) and longitudinal field (LF) μSR measurements and demonstrated that the μSR method is useful to obtain information on the basic proton diffusion process in H_xWO_3 from the study of dynamical properties of muons.

2. Experimental

We used two powder samples of pure WO_3 and H_xWO_3 for the μSR measurements. The method for the preparation of hydrogen tungsten bronze H_xWO_3 was similar to that described in Ref. [2]. A commercial powder sample of WO_3 was reduced with zinc turnings and boiling 1 N HCl solution over a period of about 3 h. Excess zinc was dissolved by prolonged boiling with additional HCl solution. The sample was washed by replacing supernatant solution with water a few times and subsequently was dried in a vacuum desiccator. H_xWO_3 is unstable towards oxidation [2] so that the hydrogen content gradually decreases in the presence of oxygen. Therefore, the samples were sealed within 30-μm-thick silver foils by glue in He atmosphere. Although hydrogen concentration x was not determined, $0.15<x<0.50$ is expected from an X-ray diffraction pattern measured for the present sample, which was in good agreement with that for the tetragonal phase shown in this composition range [3].

Polarized positive muon beams with a momentum of 28 MeV/c were implanted into the samples. For pure WO_3, the ZF-μSR measurements were performed at temperatures between 10 K and 300 K using the ARGUS spectrometer at the RIKEN–RAL muon facility. For H_xWO_3 the ZF- and LF-μSR were done at temperatures between 5 K and 440 K with the general purpose surface-muon (GPS) instrument at Paul Scherrer Institut (PSI) with a muon-on-request (MORE) mode to observe slow relaxation phenomena.

3. Results and discussions

Figs. 1(a) and (b) show typical ZF-μSR spectra in WO_3 and H_xWO_3, respectively. The baseline for these spectra was determined by doing measurements on the transverse field muon spin rotation for each sample. The exponential like relaxing component with the fraction of ~20% was observed in addition to the non-relaxing component for the pure WO_3 sample at low temperatures, and the relaxation rate decreases with increasing

---

[*] Corresponding author. Tel.: +81 6 6850 5520; fax: +81 6 6850 5535.
E-mail address: mihara@vg.phys.sci.osaka-u.ac.jp (M. Mihara).

0921-4526/$ - see front matter © 2008 Elsevier B.V. All rights reserved.
doi:10.1016/j.physb.2008.11.169

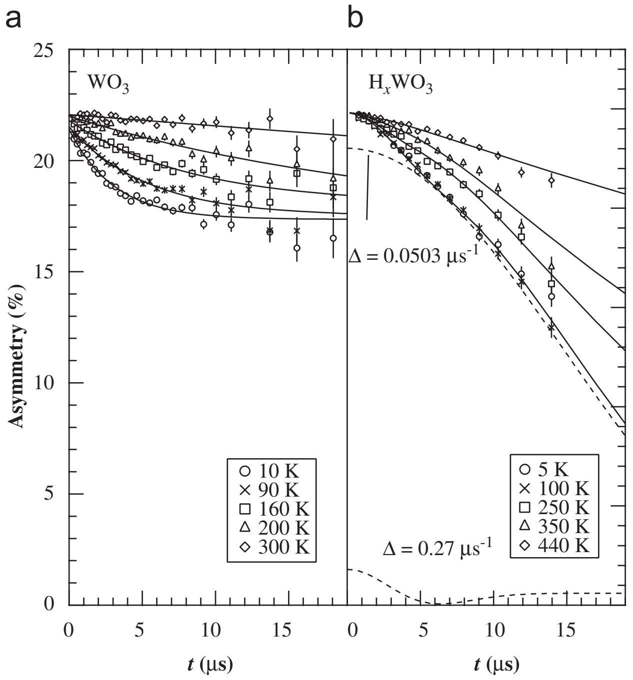

Fig. 1. Typical ZF-μSR spectra in pure WO_3 (a) and hydrogen tungsten bronze H_xWO_3 (b). The solid curves in (a) are exponential plus constant fitted to the data for WO_3, and in (b) two-component Kubo–Toyabe (KT) functions with ($T > 100$ K) and without ($T \leqslant 100$ K) fluctuation of internal field fitted to the data for H_xWO_3. The dotted curves are each component for KT functions deduced from the sum of the data at $T = 5-100$ K.

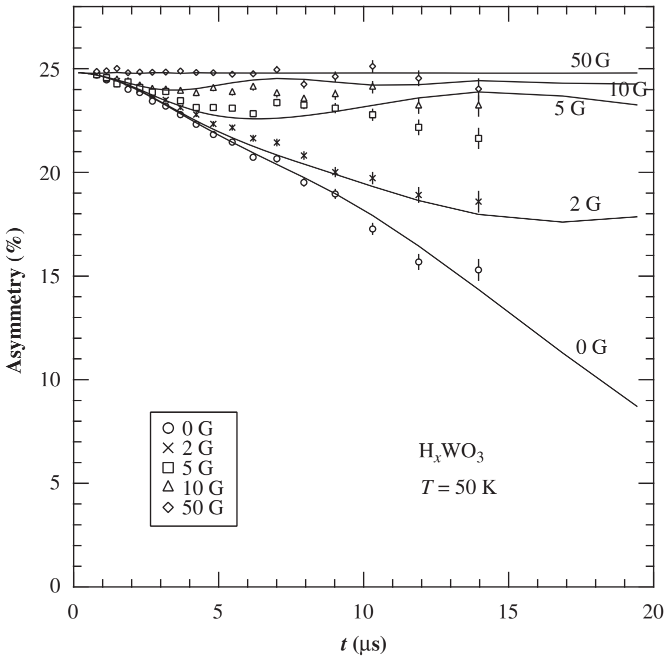

Fig. 2. Typical LF-μSR spectra in hydrogen tungsten bronze H_xWO_3. The solid curves are two-component Kubo–Toyabe functions under longitudinal fields in which parameters deduced from the ZF-μSR data at 5–100 K were used.

temperature. Because the contribution of the nuclear dipolar field from W and O nuclei is negligibly small, this relaxation might be attributed to paramagnetic defects or impurities, or the local electronic structure at a muon site in WO_3 originated from the characteristics of an isolated hydrogen impurity in semiconductors such as the formation of shallow donor states as was suggested in Ref. [4]. The muon motion might also contribute these temperature dependent relaxation curves. However, it is hard to extract this effect from the data for the pure WO_3 sample.

On the other hand, the spectra for hydrogen tungsten bronze H_xWO_3 is characterized by a Gaussian damping. The relaxation curves at temperatures lower than 100 K remain unchanged and gradually the relaxation rate becomes slower with increasing temperature. Because the tungsten bronze shows metallic properties [5], contributions of paramagnetic states to the muon spin relaxation observed for pure WO_3 have disappeared. Therefore, nuclear dipolar fields from host nuclei, mainly protons in the present case, are expected to be the main contribution to cause the muon spin relaxation for H_xWO_3. The reduction of a relaxation rate at temperatures higher than 100 K is considered to be due to the dynamical behavior such as muon diffusion. Because the spectra at temperatures between 5 and 100 K were almost identical, the sum of the data were used to the analysis in this temperature range. The data were well accounted for by a two-component Kubo–Toyabe (KT) function with a reduced $\chi^2 = 1.4$ which is also shown in Fig. 1(b). The fraction of the main component is about 93% giving a Gaussian distribution width of the local field at the muon site, $\Delta = (0.0503 \pm 0.006)\,\mu s^{-1}$, and the other component gives $\Delta = (0.27 \pm 0.01)\,\mu s^{-1}$.

The decoupling properties of muon spins from the local field were examined by measuring the LF-μSR spectra at 50 K which are shown in Fig. 2. The data were roughly explained but not reproduced very well by calculated two-component KT functions in case that a LF is applied, using the above values of Δ and amplitudes deduced from the ZF-μSR data at $T = 5-100$ K.

The present value of $\Delta = 0.0503\,\mu s^{-1}$ for the main component is not in agreement with the previous result on the line width of 0.13 mT for the proton NMR in $H_{0.39}WO_3$ [6], which gives $\Delta = 0.17\,\mu s^{-1}$. The disagreement cannot be explained even if the ambiguity of the hydrogen content x is considered since $\Delta \propto x^{1/2}$. Therefore, the lattice location of muons or the local atomic configuration at muon sites should be considered, which will directly affect the value of Δ. Even though this is still an open problem, the present ZF- and LF-μSR spectra for H_xWO_3 at low temperatures are basically understood by the existence of static local fields at the muon site due to the dipole-dipole interaction between protons and muons.

In order to extract the dynamical properties of muons in H_xWO_3, the ZF-μSR data at higher temperatures were analyzed based on the data at low temperatures ($T = 5-100$ K). In the analysis, a two-component KT function was also assumed. As deduced from the ZF data at low temperatures, it consists of a KT function under a fluctuating field with Δ fixed at $0.0503\,\mu s^{-1}$ as the main component and another without fluctuation. The fluctuation rate ν for the main component, Δ for another one and a fractional ratio of these two components were deduced by the χ^2-fitting procedure under the fixed total asymmetry. The data were well reproduced by this trial function over the temperature range between 250 K and 440 K. The fraction of the minor component decreased from 7% at below 100 K to 3% at 250 K and almost vanishes at about 400 K. The values of Δ for this component were nearly identical at $T = 250-350$ K and similar to $\Delta = 0.27\,\mu s^{-1}$ deduced at $T = 5-100$ K. Therefore, this component is considered that the local field might be static at below 350 K.

As the result, the fluctuation rate ν was deduced, which is shown as a function of inverse temperature in Fig. 3. The values of ν seem to follow an Arrhenius equation together with constant contribution $\nu = \nu_0 \exp(-E_a/kT) + \text{const}$. Using this equation, the

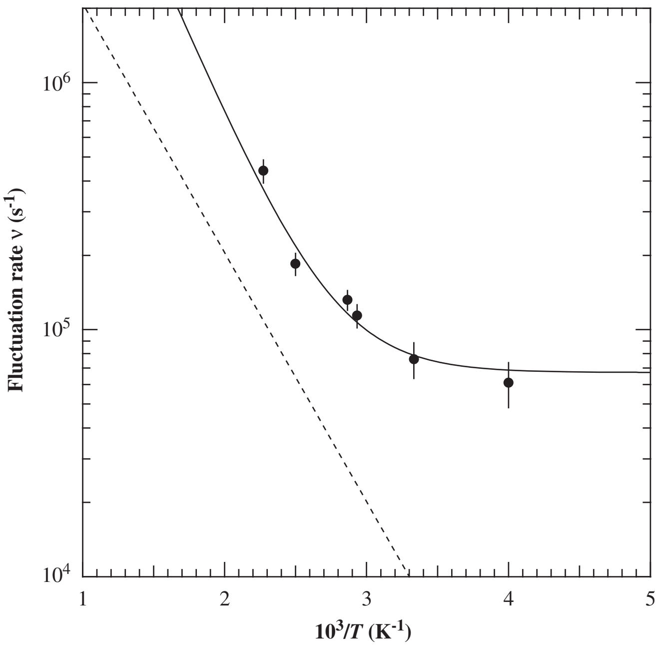

Fig. 3. Fluctuation rate for muon in H_xWO_3 plotted as a function of inverse temperature deduced from the ZF-μSR spectra. The solid curve shows an Arrhenius equation with a constant component fitted to the data. The dotted line is derived from the result of the proton NMR line widths [6].

activation energy $E_a = (0.26 \pm 0.06)$ eV was estimated. This is near to the value deduced from the proton NMR line widths in $H_{0.39}WO_3$ showing a motional narrowing, which gave Arrhenius parameters as $1/\nu_0 = (47 \pm 14)$ ns and $E_a = (0.200 \pm 0.011)$ eV [6] (see Fig. 3). The fluctuation rates for muons, considered as the hop rates, are more than twice those for protons, which is qualitatively reasonable for light mass of muons. Hereafter, it is interesting and important to examine whether the muons in H_xWO_3 feel the same diffusion barrier as protons and the origin of a large difference in the value of Δ between muons and protons, in order to simulate the proton diffusion properties in H_xWO_3 by muons as a light hydrogen isotope. For this purpose, further μSR studies are being planned to deduce the local field distribution width Δ and fluctuation rate ν to obtain more precise value of E_a as a function of a hydrogen content x.

Acknowledgments

We would like to thank the staff of the RIKEN-RAL Muon Facility and PSI for their technical support. This work was supported by a Grants-in-Aid for Scientific Research Program of Japan Society for the Promotion of Science and the KEK-MSL Inter-University Program for Oversea Muon Facilities.

References

[1] H. Yoshimura, N. Koshida, Japan J. Appl. Phys. 45 (2006) 3479.
[2] P.G. Dickens, J.H. Moore, D.J. Neild, J. Solid State Chem. 7 (1973) 241.
[3] E. Cazzanelli, et al., Solid State Ionics 123 (1999) 67.
[4] S.F.J. Cox, et al., in: Proceedings of International Conference Physics of Semiconductors, 2005, p. 193.
[5] P.G. Dickens, R.J. Hurditch, in: L. Eyring, M. O'Keefe (Eds.), The Chemistry of Extended Defects in Nonmetallic Solids, North-Holland, Amsterdam, 1970, p. 555.
[6] P.G. Dickens, D.J. Murphy, T.K. Halstead, J. Solid State Chem. 6 (1973) 370.

Hyperfine Interact (2009) 194:213–217
DOI 10.1007/s10751-009-0074-x

Muon science in J-PARC

Naritoshi Kawamura · Shunsuke Makimura · Koichiro Shimomura · Patrick Strasser · Akihiro Koda · Hiroshi Fujimori · Kazutaka Nakahara · Mineo Kato · Soshi Takeshita · Ryosuke Kadono · Wataru Higemoto · Kusuo Nishiyama · Kanetada Nagamine · Yasuhiro Miyake

Abstract The intensity of proton accelerator has attained to the order to mega-watt, and several MW-class proton accelerators start to operate in the world. J-PARC is a complex of three accelerators, and generates a variety of secondary beams, i.e. muon beam, neutron beam, meson beam and neutrino beam. The muon facility is established in order to provide a pulsed muon beam for various experimental programs. The first muon beam is transported to the experimental area in September 2008. Although the accelerator is still under commissioning, and the beam power doesn't reach the design value of 1 MW yet, the world strongest pulsed muon beam will be provided shortly. In this paper, we review the muon beam line in J-PARC, and discuss evolved scientific programs.

Keywords Muon · Secondary beam · Muon facility

PACS 01.52.+r · 52.59.-f · 29.20.-c

N. Kawamura · S. Makimura · K. Shimomura · P. Strasser · A. Koda · H. Fujimori ·
K. Nakahara · M. Kato · S. Takeshita · R. Kadono · W. Higemoto · K. Nishiyama · Y. Miyake
Muon Science Section, Materials and Life Science Division, J-PARC Center, Tokai, Naka,
Ibaraki 319-1195, Japan

N. Kawamura (✉) · S. Makimura · K. Shimomura · P. Strasser · A. Koda · H. Fujimori ·
K. Nakahara · M. Kato · S. Takeshita · R. Kadono · K. Nishiyama · Y. Miyake
Muon Science Laboratory, High Energy Accelerator Research Organization (KEK),
Tsukuba, Ibaraki 305-0801, Japan
e-mail: nari.kawamura@kek.jp

W. Higemoto
Advanced Science Research Center, Japan Atomic Energy Agency (JAEA),
Tokai, Naka, Ibaraki 319-1195, Japan

K. Nagamine
University of California, Riverside, CA 92521, USA

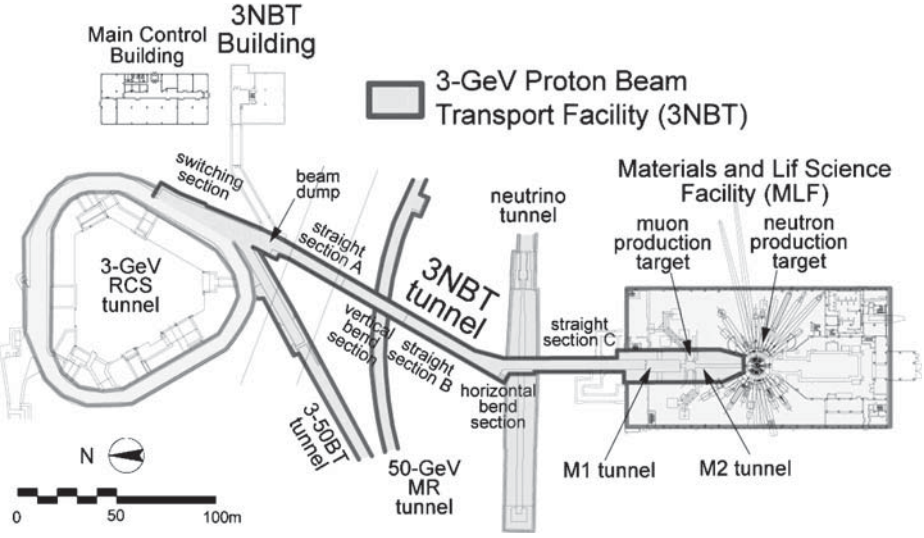

Fig. 1 A schematic drawing from 3-GeV rapid cycling synchrotron (RCS) to MLF

1 Introduction

A high intensity proton accelerator (Japan Proton Accelerator Research Complex, J-PARC) project was proposed jointly by Japan Atomic Energy Agency (JAEA) and High Energy Accelerator Research Organization (KEK) [1]. The new facility consists of a 400-MeV linac, 3-GeV and 50-GeV synchrotron rings, which provide an intense proton beam to pursue particle physics, nuclear physics, material science, life science and nuclear technology. A 1-MW proton beam is transported from the 3-GeV synchrotron ring to Material and Life Science Facility (MLF) which consists of the muon and the spallation neutron facilities. As shown in Fig. 1, the proton-beam-line tunnel runs through the center of MLF building from the north to the south. The east and the west wings are experimental halls where the neutron and muon beam lines are constructed. In order to avoid the diffusion of radioactive contamination, and to make the structure of radiation shield simple, the proton-beam transport tunnel is isolated from the experimental hall. Namely, the beam transport tunnel divides the MLF building into east and west wing.

The muon-production target is inserted 30-m upstream of the neutron target in the proton beam line. The concept of the cascade-type muon-target is similar to ISIS muon facility, UK, which is 0.24-MW (800-MeV, 300 μA) proton accelerator. From the muon target, we decided to extract four muon beam lines. Each of them provides the world-strongest pulsed muon beam with an individual design concept to be utilized for the variety of muon science, such as muon catalyzed fusion study, μSR spectroscopy and so on. Two of the secondary beam lines are extracted at the angle of 60 degrees to the proton beam line (forward), and the others are at 135 degrees (backward). At the exterior of proton-beam transport tunnel, four opening exist, and

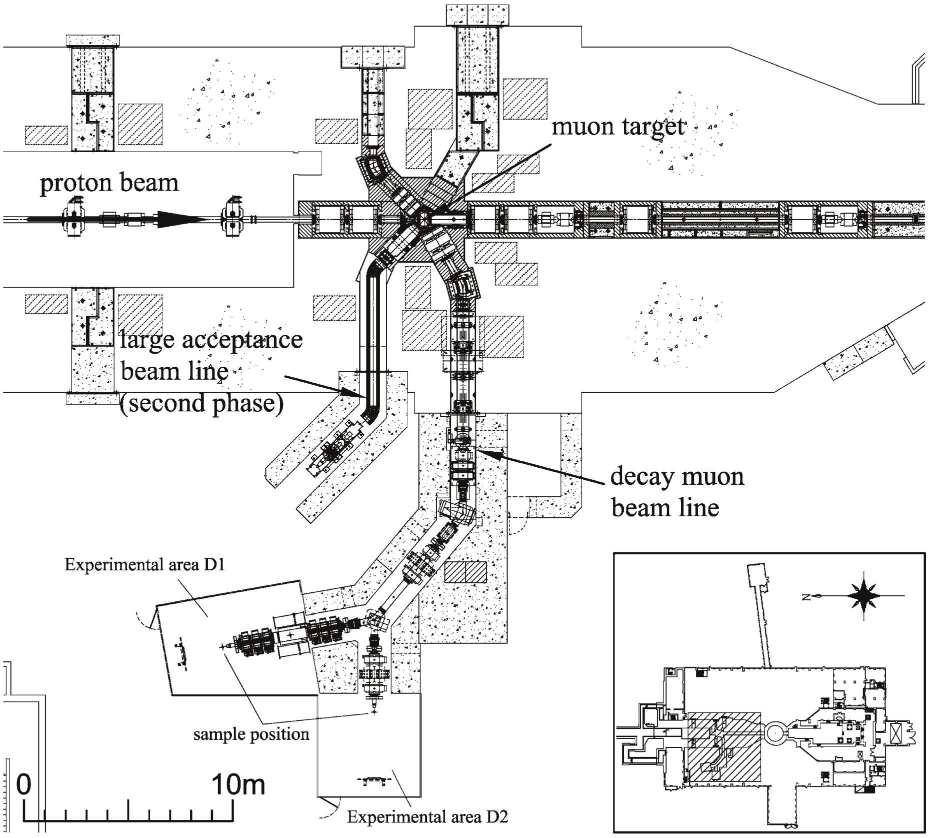

Fig. 2 A schematic drawing of muon facility in east-side experimental hall of MLF

correspond to each muon beam line. At the primary phase, we don't construct all the muon beam lines to leave the future open (Fig. 2).

2 Decay-muon beam line

The decay-muon beam line uses a super conducting solenoid magnet to capture muons from in-flight-decay pions. The design principle of decay-muon beam line was established in Muon Science Laboratory, a utilization facility of 500-MeV booster synchrotron, KEK. Based on this design concept, M9 beam line, TRIUMF and the RIKEN-RAL Muon Facility [2] were constructed. In J-PARC, the decay-muon beam line extracts both negative and positive decay muons up to their momenta of 120 MeV/c, as well as 30-MeV/c surface and cloud muons. This high momentum-tune-ability meets the demands of most user programs, and thus we gave priority to the decay-muon beam line in the construction scheme. At the primary phase, double-pulse beam, which is due to the proton-beam bunch structure, is transported to either experimental area, exclusively. After the upgrade by installing the kicker device, single-pulse beam is able to be utilized at both experimental areas, simultaneously.

3 Large acceptance beam line

A large acceptance beam line (Super Omega) extends at 135 degree into backward angles to transport surface muons (30-MeV/c μ^+) and cloud muons (30-MeV/c μ^-) to the east-side experimental hall [3]. The beam line consists of normal-conducting capture solenoids, superconducting transport solenoids, and a Dai Omega-type axial focusing magnet [4]. At present, the construction of the capture solenoid magnet, with an acceptance of about 400 mstr, is near completion. The design of the transport solenoid magnet is underway, and 80% transmission efficiency is achieved in the simulation. Test solenoid coils are fabricated and examined. The axial focusing magnet, used to focus the muon beam on the experimental sample, is under consideration with particular emphasis on its compatibility with the transport solenoid magnet. This new-concept beam line aims at an order of magnitude higher beam intensity in comparison with the conventional decay-muon beam line.

The most attractive utilization of this high-intensity beam is the source for the world's most intense pulsed ultra-slow muon beam. The ultra-slow muons, which are created by laser-resonant ionization method [5] will have low penetration depths, high energy-and-temporal resolutions, and tunable energies, which can be used to probe surface phenomenon using muon. The negative cloud muons will be used for experiments such as muon catalyzed fusion, muonic nuclei study [6], etc.

4 Muon science in muon facility, J-PARC

At present, Muon Facility is shifting from the construction and system-commissioning phase to the experimental utilization phase. The first user program starts in 2008FY. Although the beam power does not reach 1 MW yet, the step-by-step upgrade schedule is kept, and 0.25-MW proton beam will be obtained in 2009.

The world's most intense pulsed muon is a powerful tool not only for materials and life science but also high precision studies requiring high statistics, such as muon life time measurement, muon $g-2$ measurement, rare decay search and so forth.

Acknowledgements We acknowledge fruitful discussion by Drs. Y. Ikeda, T. Kato, M. Futakawa and other Neutron Source Section, MLF. We express our sincere gratitude to Drs. M. Iwasaki, T. Matsuzaki, K. Ishida and other staff of the RIKEN-RAL Muon Facility.

References

1. The Joint Project for High-Intensity Proton Accelerators. KEK Report 99-4; JAERI-Tech 99-056; JHF-99-3 (1999)
2. Nagamine, K., et al.: Construction of RIKEN-RAL Muon Facility at ISIS and advanced μSR. Hyperfine Interact. **87**, 1091 (1994)
3. Shimomura, K., et al.: Super Omega—new concepts of super intense surface muon beam. In: AIP Conference Proceedings, p. 721; Neutrino Factories and Superbeams, p. 346 (2004)

4. Miyadera, H., et al.: Design, construction and performance of Dai Omega, a large solid-angle axial-focusing superconducting surface-muon channel. Nucl. Instrum. Methods A **569**, 713 (2006)
5. Bakule, P., et al.: Slow muon experiment by laser resonant ionization method at RIKEN-RAL muon facility. Spectrochim. Acta Part B **58**, 1019 (2003)
6. Strasser, P., et al.: In: These proceedings

Nuclear Instruments and Methods in Physics Research A 600 (2009) 22–24

Contents lists available at ScienceDirect

Nuclear Instruments and Methods in
Physics Research A

journal homepage: www.elsevier.com/locate/nima

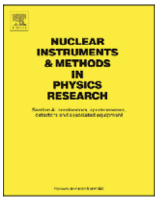

J-PARC muon source, MUSE

Y. Miyake [a,b,*], K. Nishiyama [a,b], N. Kawamura [a,b], P. Strasser [a,b], S. Makimura [a,b], A. Koda [a,b], K. Shimomura [a,b], H. Fujimori [a,b], K. Nakahara [a,b], R. Kadono [a,b], M. Kato [a,b], S. Takeshita [a,b], W. Higemoto [c], K. Ishida [d], T. Matsuzaki [d], Y. Matsuda [d], K. Nagamine [a,d]

[a] *Muon Science Laboratory, High Energy Accelerator Research Organization (KEK), 1-1 Oho, Tsukuba, Ibaraki, 305-0801, Japan*
[b] *Muon section, Materials and Life Science Division, J-PARC Center, 2-4 Shirane Shirakata, Tokai-mura, Naka-gun, Ibaraki 319-1195, Japan*
[c] *Advanced Science Research Center, Japan Atomic Energy Agency, Tokai, Ibaraki 319-1195, Japan*
[d] *Advanced Meson Science Laboratory, RIKEN Nishina Center, Wako, Saitama 351-0198, Japan*

ARTICLE INFO

Available online 25 November 2008

Keywords:
Muon
J-PARC
MLF
Slow muons
Spin polarized muons
Pulsed muon sources
Muon spin rotation
Muonium
Laser ionization
Lyman-α
Thin films
Multilayers
Magnetic probe

ABSTRACT

The muon science facility (MUSE), together with the neutron, hadron, and neutrino facilities, is one of the experimental areas of the J-PARC project, which was approved for construction in a period from 2001 to 2008. The MUSE facility is located in the Materials and Life Science Facility (MLF) built for both neutron and muon sciences. Construction of the MLF building began in the beginning of 2004, and was completed in the end of the 2006 fiscal year. We have been working on the installation of the decay/surface muon beam line, expecting first muon beam in the Autumn of 2008.

1. Introduction

The accelerator complex of the Japan Proton Accelerator Research Complex (J-PARC) has been constructed in the south part of the Tokai-JAEA site, and consists of a 181 MeV LINAC (400 MeV in future), and 3 and 50 GeV proton synchrotron rings. About 90% of the 3 GeV, 333 μA (1.0 MW) beam is sent to the Materials and Life Science Facility (MLF) for the production of the intense pulsed neutron and muon beams, while the remaining 10% would be sent to the 50 GeV ring for further acceleration to produce a 15 μA, 50 GeV proton beam for the kaon or neutrino physics programs. The 3 GeV proton beam is transported through the beam transport line (so called 3NBT line) over a distance of about 300 m and focused onto the 24 mm diameter muon target with a spot size that is as small as possible.

The parameters of the 3 GeV proton beam are:

(1) The number of protons will be 8.3×10^{13}/ pulse.
(2) The average beam power will be 0.6 MW since the LINAC energy will start with 181 MeV in phase 1, although it will go up to 1 MW in the future when the LINAC energy will be increased to 400 MeV.
(3) The repetition rate is 25 Hz, so each pulse is separated by 40 ms. One proton pulse consists of two bunches which are separated by 600 ns with a full width of 100–130 ns for a LINAC energy of 400 MeV.
(4) The transverse emittance (ε) will be 81 π mm mrad (beam core) and 324 π mm mrad (maximum halo).

2. The muon science facility with tandem-type production graphite target

The MLF consists of the neutron and the muon science facilities which utilizes the 3 GeV, 1 MW, 25 Hz proton beam. In order to reduce the total cost of the project through common use of the utilities, getting rid of the severe beam dump construction associated with high-level tritium water handling, and by sharing the beam with the neutron facility, we decided to have a tandem-target muon facility, rather than construct a separate building with our own proton (1 MW) beam dump, as was the case in KEK–MSL. Through discussion with the neutron science group, we reached an agreement that the total beam loss induced by placing

---

[*] Corresponding author at: Muon Science Laboratory, High Energy Accelerator Research Organization (KEK), 1-1 Oho, Tsukuba, Ibaraki 305-0801, Japan.
Tel.: +81 29 284 4624; fax: +81 284 4878.
E-mail address: yasuhiro.miyake@kek.jp (Y. Miyake).

0168-9002/$ - see front matter © 2008 Elsevier B.V. All rights reserved.
doi:10.1016/j.nima.2008.11.016

the muon production targets should be no more than 10%, which allows us to install 10 and 20 mm thick graphite targets on the beamline upstream of the neutron target, corresponding to a beam loss of 3.5% and 6.5%, respectively [1]. Detailed calculations on heat, radiation and duct-streaming in the vicinity of the muon target were performed by NMTC/JAM and MCNP Monte-Carlo codes [2]. In the case of the 20 mm thick graphite target, heat loss as much as 3.5 kW is deposited into a 25 mm diameter region through irradiation of the 3 GeV, 1 MW proton beam.

One possible candidate for the muon production target is a rotating carbon target, which has been developed at PSI and has been working well for more than 10 years [3]. In the end, we adopted an edge- cooled non-rotating graphite target, because of its ease of the handling and maintenance. In this target, graphite is indirectly cooled by the copper frame, which surrounds the graphite. For the graphite material, we are adopting an isotropic graphite IG-43 which has a thermal conductivity of 139 W/mK, 1.82 g/cm^2 density at 300 K, thermal expansion of 4.8 ppm/K, Young's modulus of 10.8 GPa, and Poisson's ratio of 0.28. In the copper frame, three turns cooling pipe, a SUS tube with O.D. 12.7 mm and I.D. 10.7 mm, are embedded through HIP (hot isostatic press). In order to reduce stress, a titanium buffer layer of 2 mm is placed as interface between the graphite disk and the copper frame. The copper frame, the 20 mm thick graphite, and the titanium buffer layer are bonded by silver brazing in vacuum. Calculations of the heat and stress induced by the heat deposit of the 3.5 kW beam through ANSYS demonstrate that the edge-cooled graphite target can be used safely as the 1 MW muon production target. Detailed calculations of the neutron irradiation effect on the thermal conductivity and the thermal stress induced by the proton beam will be reported elsewhere [4].

3. Building structure and maintenance

The MLF consists of the proton beam line tunnel (M1 and M2 tunnel), and two wings for experimental halls Nos. 1 and 2. The tunnel structure is intended for the purpose of keeping radioactive materials inside of the tunnel, in order to provide for safe areas operation during the maintenance works of either the neutron or the muon target. The height of the building is 28 m for the tunnel and 22 m for the wings of the experimental halls, respectively. The tunnel is 14.5 m wide, 24.5 m wide in the east wing, and 32 m wide in the west wing. The proton beam height is 1.6 m from the floor level. Since a certain fraction of the primary 3 GeV proton beam is scattered preferentially downstream towards the neutron target, two sets of scrapers are installed to prevent damage on the beam line components such as quadrupole magnets, beam ducts, etc. Learning from the experience PSI has had in dealing with 1 MW class proton beams [3], all maintenance work, including power and water connections, is done from the maintenance region located 4 m above floor level.

Construction of the MLF building began in the beginning of 2004, and was completed in the end of the 2006 fiscal year. Furthermore, fabrication and installation of various beam line components such as magnets, muon target, scrapers, shields, monitors, and vacuum components were completed in 2007, as scheduled. Fig. 1 shows a schematic drawing of the J-PARC Muon Facility, MUSE.

4. Secondary line

Muons (μ^+/μ^-), together with neutrinos, is a decay product of pions (π^+/π^-). Through the pp or pn nuclear reactions between the 3 GeV proton beam and the 20 mm thick graphite target, π^+ and π^- are generated. Experimentally, two kinds of muon beams are produced and delivered to experiments; one is the decay muon beam, and the other is the surface muon beam. Decay muons are obtained from π^+/π^- decaying in-flight in a long superconducting solenoid magnet. Its energy is rather higher to be up to ~165 MeV (250 MeV/c). On the other hand, surface muons are obtained when π^+ decay after stopping at the surface of the production target. Therefore it has a lower kinetic energy of around 4 MeV (30 MeV/c), and only positive muons are available.

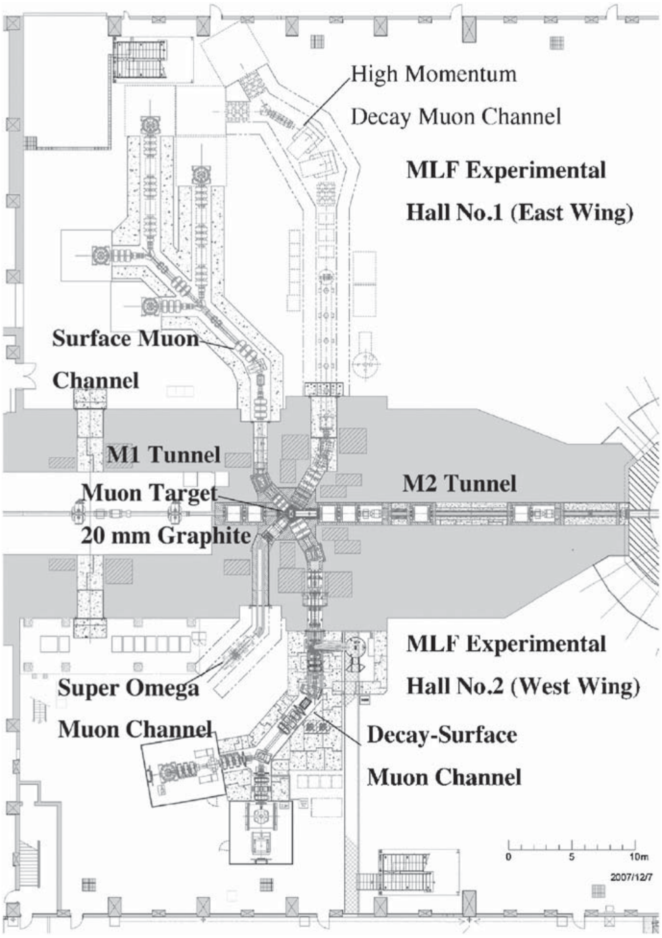

Fig. 1. Schematic drawing of the J-PARC Muon Facility, MUSE.

For Phase 1, one graphite target is installed, from which four sets of the secondary lines are extracted and extended into two experimental halls (toward the west wing, one decay-surface muon channel and the super omega channel, and towards the east wing one surface muon channel and possibly one high momentum muon channel). In this fiscal year, we are planning to install one superconducting decay/surface channel with a modest-acceptance (about 40 mSr) pion injector. It will provide an estimated surface muon rate of 3×10^7 /s with a beam size of 25 mm in diameter, and 10^6/s decay muons (μ^+/μ^-) at 60 MeV/c (and up to 10^7/s at 120 MeV/c) with a beam size of 50 mm in diameter. These intensities are about 30 times higher than those available at the RIKEN/RAL Muon facility [5].

In addition to Phase 1, we are planning to install one surface muon channel with a modest-acceptance (about 50 mSr), and one super omega muon channel for the study of thin film magnetism or negative muon physics. In the case of the surface muon channel, we can expect a total of 1.6×10^7 /s surface muons with a 1 MW proton beam. By installing a kicker and beam slicer, we are planning to place four experimental ports. In the case of the super

Table 1
Muon beams available at J-PARC Muon Facility, MUSE.

	Surface muon (μ^+)	Decay muon($\mu^\pm$)
Decay surface muon channel (Phase 1)		
Muon energy	4.1 MeV	2–54 MeV
Range	~0.2 mm	1 mm–~ cm
Energy width	~10%	~15%
Temporal width	~100–130 ns	~100–130 ns
Beam size	30 nm × 40 nm	70 nm × 70 nm
Intensity	3×10^7 /s	10^6–10^7 /s
Port number	2	2
	Surface muon (μ^+)	
Surface muon channel (Phase 2)		
Muon energy	4.1 MeV	
Range	~0.2 mm	
Energy width	~10%	
Temporal width	~100–130ns	
Beam size	30 nm × 40 nm	
Intensity	10^6–10^7 /s	
Port number	4	
	Slow muon (μ^+)	Cloud muon (μ^-)
Super omega muon channel (Phase 2)		
Muon energy	0–30 KeV	2–15 MeV
Range	1–200 nm	~ mm
Energy width	$\leqslant$1%	~5–10%
Temporal width	8.3 ns(now) → sub ns	~100–130ns
Beam size	3 × 4 mm(now) → 1 ϕ	ϕ 50
Intensity	10^4–10^6 /s	10^6–10^7 /s
Port number	2	2

omega beam channel, we are going to install a large acceptance solenoid made of mineral insulation cables (MIC) and a superconducting curved transport solenoid. We can collect either surface or cloud muons with a large acceptance of 400 mSr. Finally, we are expecting 4×10^8 /s surface muons and 10^7 /s negative cloud muons in the experimental hall [6]. Although many of these studies can be performed using either surface or decay muons, at the super omega channel we are aiming to create a new type of muon source; the intense ultra-slow muon source. Slow muons are generated through resonant ionization of muonium (Mu). Mu is formed by stopping intense surface muon on the rear surface of a hot W foil.

At the RIKEN/RAL muon facility, 20 slow μ^+/s are obtained out of 1.2×10^6 /s surface muons [7]. Taking into account the repetition rate of the pulsed laser system and the proton beam, as well as the surface muon yield between RIKEN-RAL and J-PARC MUSE, we can expect 1.3×10^4 /s of slow μ^+/s without any additional laser development. A rate of 1.3×10^6 /s slow μ^+/s can be achieved with sufficient laser development such as the tripling of 366 nm photons with pico second pulse width to match the Doppler broadening of the Mu at 2000 K. Table 1 shows parameters of the individual muon channels at the J-PARC muon facility (MUSE).

When the production of intense ultra-slow muon beams is realized, the use of its short-range penetration depth [8] will allow muon science to be expanded towards a variety of new scientific fields such as,

(1) Surface/boundary magnetism utilizing its spin polarization and unique time-window.
(2) Surface chemistry, utilizing a feature of a light isotope of hydrogen; such as catalysis reactions.
(3) Precise atomic physics such as QED.
(4) Ion sources and towards $\mu^+ \mu^-$ collider experiments in high-energy physics.

5. Conclusion

Construction of the MLF building began in the beginning of 2004, and was completed in the end of the 2006 fiscal year. Also fabrication and installation of various beam line components such as magnets, muon target, scrapers, shields, monitors, and vacuum components were completed in 2007, as scheduled. We are expecting first muon beam in the decay/surface muon channel in the Autumn of 2008.

References

[1] Y. Miyake, K. Nishiyama, N. Kawamura, S. Makimura, P. Strasser, K. Shimomura, J.L. Beveridge, R. Kadono, K. Fukuchi, N. Sato, K. Ueno, W. Higemoto, K. Ishida, T. Matsuzaki, I. Watanabe, Y. Matsuda, M. Iwasaki, S.N. Nakamura, J. Doornbos, K. Nagamine, Physica B 374–375 (2006) 484.
[2] N. Kawamura, et al., 2008, this issue.
[3] G. Heidenreich, P. Baumann, A. Geissler, A. Strinning, W. Wagner, PSI Scientific Report VI (1998) 16.
[4] S. Makimiura et al., 2008, this issue.
[5] K. Nagamine, T. Matsuzaki, K. Ishida, I. Watanabe, S.N. Nakamura, R. Kadono, N. Kawamura, S. Sakamoto, M. Iwasaki, M. Tanase, M. Kato, K. Kurosawa, G.H. Eaton, H.J. Jones, G. Thomas, W.G. Williams, Hyperfine Interact. 101–102 (1996) 521.
[6] K. Nakahara et al., 2008, this issue.
[7] P. Bakule, Y. Matsuda, Y. Miyake, K. Nagamine, M. Iwasaki, Y. Ikedo, K. Shimomura, P. Strasser, S. Makimura, Nucl. Instr. and Meth. B 266 (2008) 355.
[8] E. Morenzoni, T. Prokscha, A. Suter, H. Luetkens, R. Khasanov, J. Phys. Condens. Matter 16 (2004) S4583.

Nuclear Instruments and Methods in Physics Research A 600 (2009) 35–37

Contents lists available at ScienceDirect

Nuclear Instruments and Methods in
Physics Research A

journal homepage: www.elsevier.com/locate/nima

Prospects for ultra-low-energy muon beam at J-PARC

Pavel Bakule [a,*], Yasuyuki Matsuda [a], Yasuhiro Miyake [b], Kanetada Nagamine [b], Koichiro Shimomura [b], Patrick Strasser [b], Shunshuke Makimura [b], Masahiko Iwasaki [a]

[a] *Advanced Meson Science Laboratory, RIKEN Nishina Center, RIKEN, Wako, Saitama 351-0198, Japan*
[b] *Muon Science Laboratory, Institute of Materials Structure Science, High Energy Accelerator Research Organization, Tsukuba, Ibaraki 305-0801, Japan*

A R T I C L E I N F O

Available online 27 November 2008

Keywords:
Low-energy muons
Spin-polarized muons
Pulsed muon sources
Muon spin rotation
Muonium
Laser ionization
Lyman-α
Thin films
Multi-layers
Magnetic probe

A B S T R A C T

Spin-polarized ultra-low-energy muons (LE-μ^+) with energies in eV–keV range provide a sensitive magnetic microprobe for studying near-surface regions, thin-film samples, multi-layered materials, etc. with depth resolution on a nanometer scale. Yet, worldwide there is currently only one (continuous) source of low-energy muons that is routinely used for such measurements. A pulsed source with many unique parameters (such as low-energy resolution of ~14 eV, time resolution of 7 ns, low background and spot size of just 4 mm) has been demonstrated at RIKEN-RAL muon facility at ISIS, but its use is limited by a rate of only 15 μ^+/s. The method of low-energy muon generation is based on a resonant laser ionization of thermal energy muonium and is ideally suited for a pulsed muon source such as J-PARC MUSE, since the pulse structure of the generated LE-μ^+ is then determined by the laser pulse duration. The double pulse structure of the surface muon beam can, therefore, be converted to a single LE-μ^+ pulse with a pulse duration that can be as short as 1 ns and can also be externally triggered. J-PARC is designed to deliver surface muon beam with rates up to 4×10^8 μ^+/s and direct transfer of the same laser technology from RIKEN-RAL to J-PARC would provide a LE-μ^+ beam with rates comparable to the existing continuous LE-μ^+ beam at PSI (~10^4 LE-μ^+/s). An improvement in the laser pulse energy could lead to a higher efficiency and higher rates up to 10^6 LE-μ^+/s may be possible. Construction of an intense LE-μ^+ beamline at J-PARC MUSE would open up the possibility to do routine depth-dependent μSR measurements with thin film samples, with the muon implantation depth as low as 1 nm. In addition, the unique capability to synchronize the muon implantation with the sample excitation (e.g. by another laser or rf pulse) would allow to carry out pump-probe-type experiments.

1. Introduction

The technique of μSR (muon spin rotation, relaxation and resonance) spectroscopy is established as the major application for spin-polarized positive muon beams. By using muons as microscopic magnetic microprobes that act in the material like a light proton, a wealth of information can be gained about magnetism, superconductivity, hydrogen behaviour, charge transport and even molecular dynamics or conduction electron polarization in a wide range of samples. Bulk properties are routinely studied with ~4 MeV surface muon beams having a typical stopping range (in solids) of 0.1–1 mm with the struggling of about 20% of the mean value. With new and rapidly advancing fields of nanotechnology and spintronics, there is an increasing need for control over the muon implantation depth on the nanometer scale that allows to carry out depth-dependent μSR measurements of near-surface regions, thin film samples, multi-layered materials etc. Such applications require a beam of low-energy muons (LE-μ^+) with energies of eV–keV range. Apart from the nanometer-scale depth resolution, the LE muons can also be focused to a small spot of just a few mm in diameter, thus allowing to measure small samples with a very good signal-to-noise resolution.

Currently, there are only two sources of low-energy muons available (see Table 1), both based on rapid cooling of the surface muon beam in matter:

1. Continuous LE muon beam at PSI (Switzerland) [1] based on cryogenic moderator using a ~100-μm-thick silver foil coated with solid Ar, Ne or N_2.
2. Pulsed (25 Hz) LE muon beam at RIKEN-RAL muon facility at ISIS (UK) based on laser ionization of thermal energy muonium generated by thermionic re-emission of muons stopped in heated W foil [2].

Any method of muon cooling to eV level is inherently very inefficient and both these methods reach approximately the same

---

*Corresponding author. Tel.: +44 1235 445256 ; fax: +44 1235 446881.
E-mail address: p.bakule@rl.ac.uk (P. Bakule).

0168-9002/$ - see front matter © 2008 Published by Elsevier B.V.
doi:10.1016/j.nima.2008.11.075

Table 1
Parameters of available LE muon beams.

	PSI (continuous)	RIKEN-RAL (50 Hz pulsed)
Surface muon beam intensity	$2.0\times10^8\,\mu^+/s$	$1.2\times10^6\,\mu^+/s$
Repetition rate	Continuous	25 Hz
Time resolution	~5 ns	~7 ns
Energy resolution	σ_E=400 eV	σ_E=14 eV
Spin polarization	92%	≈50%
Spot size at sample [FWHM]	10 mm	4 mm
S/N ratio	~50	~4000
LE muon beam intensity at sample	$8000\,\mu^+/s$	$15\,\mu^+/s$
Cooling efficiency	4×10^{-5}	3×10^{-5}

conversion efficiency of only $\sim3\times10^{-5}$ from the incident-surface muon beam to the LE muon beam on the sample. However, only the PSI continuous LE muon beam is available to μSR users since the rate between 3000 and 5000 LE-μ^+/s (92% spin polarized) at the sample allows one to perform a whole range of μSR experiments. The pulsed LE muon beam is currently delivered at a rate of only 15 LE-μ^+/s (50% spin polarized) at the sample and can therefore, only be used for a limited number of experiments. This situation would significantly change if such a beamline for pulsed ultra-low energy muons was to be built at the J-PARC Muon Science facility (MUSE). This is projected to deliver almost 700 times larger number of surface muons per pulse compared to RIKEN-RAL. The rate of pulsed LE muon beam would then be at least 10^4 LE-μ^+/s. This would open up a routine use of pulsed LE muon beam with many of its unique parameters in terms of timing and energy resolution.

2. Pulsed LE muon beam parameters

The method of LE-μ^+ generation, based on the pulsed laser ionization of thermal energy muonium, is ideally suited to be used at the pulsed muon source, since it overcomes the limitation of the long pulse duration that significantly restricts the time resolution of the μSR spectra. Compared to the ISIS RIKEN-RAL facility, this limitation is even more severe at J-PARC MUSE where each double pulse at a repetition rate of 25 Hz is expected with the two pulses with 100 ns pulse duration (FWHM) separated by 600 ns (determined by the synchrotron geometry). The thermal energy muonium generated from the W foil heated to 2000 K has a mean velocity of only 20 mm/μs. Therefore, once the surface muon beam is converted to the thermal muonium, the cloud of these muonium atoms spreads relatively slowly. The muonium from the surface muon double pulse can then be effectively accumulated in front of the W foil and then ionized with a short laser pulse at an optimum time when the density of the generated muonium reaches the maximum. The resulting LE muon beam pulse duration is then dependent only on the duration of the laser pulse and on the ion transport optics time-of-flight limitations. For example, the laser pulse at the RIKEN-RAL with effective pulse duration of 7 ns generates a pulse of LE-μ^+ with just 7.5 ns (FWHM) pulse duration. By using a shorter ionization laser pulse, the LE-μ^+ pulse duration can be, in principle, further reduced to 1 ns level, thus obtaining a beam with a better time resolution than achievable from a continuous source.

The pulsed LE-μ^+ beam thus offers a much larger dynamic range than a continuous source. The measurements can be potentially performed in a time window from ~1 ns to ~20 μs. The long measurements over several muon lifetimes are possible due to the inherently low background of the pulsed LE-μ^+ beam generated by the laser ionization of muonium.

Another direct consequence of determining timing by only the laser pulse is that the muon pulse can be externally triggered with ~1 ns resolution. This opens up a possibility for pump-probe type of μSR experiments, where the muon implantation can be synchronized with sample excitation (e.g. by a laser pulse, electric or rf pulse etc.).

Because the muon implantation is controlled by an external trigger, there is no need to detect each LE muon implanted into the sample as is the case with the continuous muon source. The ultra-thin trigger detector used at PSI [3] unfortunately causes a broadening of the energy spectrum with $\sigma_E\approx400$ eV and also limits the time resolution to 5 ns due to the energy loss and scattering at the trigger. The broadening of the energy spectrum is not a problem if the required implantation depth is more than 10 nm, since the straggling in the sample will anyway lead to a broadening of the stopping profile. For near-surface studies, however, muon implantation energies below 1 keV are necessary. These low energies need to be generated by a pulsed muon source offering a high-energy resolution.

3. Implantation on a nanometer scale

The implantation profiles of LE muons in matter can be calculated using the TRIM.SP Monte Carlo code [4]. The calculations show that the resolution of the order of 1 nm can be only achieved near the sample surface and only with an ultra-low energy muon beam (below 100 eV). Previous experimental tests verifying the stopping profile and back-reflected fraction of muons calculated by TRIM.SP using continuous LE-μ^+ beam [5] have shown a very good agreement down to energies of 2 keV in various metals. At lower energies, the measured diamagnetic asymmetry (corresponding to the fraction of μ^+ stopped in the metal) was lower than expected based on the TRIM.SP calculations, especially for gold samples. Since the energy resolution of the pulsed LE-μ^+ beam is higher than in the case of the continuous beam, we have repeated the measurement of muon implantation in a 500-nm-thick Au layer in the range of energies between 0.3 and 9 keV. With the decreasing muon implantation energy, an increasingly larger fraction of muons is backscattered and reflected back from the sample. The reflected fraction forms neutral muonium with a probability exceeding 90%, which results in an apparent reduction of the measured asymmetry corresponding to the diamagnetic muon. The part of μ^+ that may reflect without forming neutral muonium also will not contribute to the measured asymmetry, since it will either fly out of the acceptance angle of the detectors or thermalize off-axis in the wall of the chamber with the resulting signal being averaged out. The change in the ratio between the measured asymmetry and the maximum instrumental asymmetry (corresponding to all muons implanted in the bulk metal) can, therefore, be interpreted as the measurement of the fraction of the muon beam implanted in the sample. The measurement is shown in Fig. 1 together with the calculated implanted fraction using the TRIM.SP code. Compared to the continuous beam with the broadened energy spectrum, there is a larger fraction of muons stopped in the sample at very low energies (<2 keV) in agreement with the fraction predicted by the TRIM.SP calculation. This demonstrates the fine depth resolution that can be achieved with the pulsed LE-μ^+ beam when probing in the near-surface region. In this measurement, the implantation energy was controlled by applying a potential of up to +8.7 kV directly on the sample to decelerate muons transported at 9 keV through the low-energy muon beamline. The minimum implantation energy of 0.3 keV in this measurement was limited by the muon beam defocusing when the sample is held at high potential. With more optimized deceleration electrodes, it should

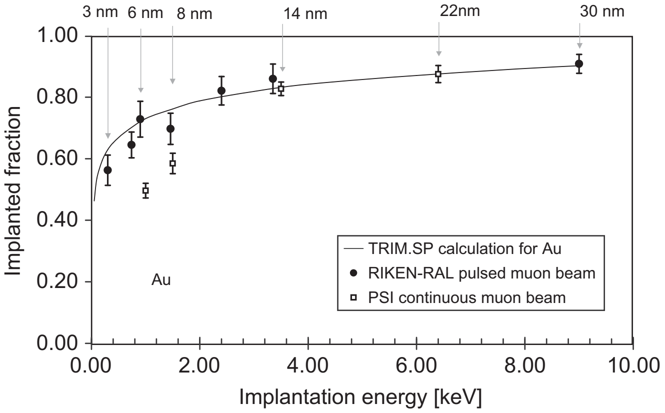

Fig. 1. Measurement of the implanted muon fraction in gold at ultra-low implantation energies. The datapoints obtained using the pulsed beam with a high-energy resolution shows a good agreement with the TRIM.SP calculation. The mean implantation depth for the lowest energy point of 300 eV corresponds to just 3 nm.

be possible to reduce the implantation energy to 0.1 keV level corresponding to the mean implantation depth in gold of just 1.5 nm.

4. Conclusion

Current construction of the intense surface muon beamline, the so-called Super Omega Muon Channel, at J-PARC MUSE [6] projected to deliver up to 4×10^8 μ^+/s offers an exciting prospect of subsequent construction of ultra-low-energy muon beamline delivering an intense LE-μ^+ beam with high energy and time resolution, low background and a unique possibility to externally trigger the muon implantation. The unique parameters of the pulsed LE-μ^+ beam have been demonstrated at RIKEN-RAL but only the intensity increase offered by J-PARC MUSE will allow routine μSR measurements with up to 1 nm depth resolution. Direct transfer of the same laser technology from RIKEN-RAL to J-PARC would provide the LE-μ^+ beam with rates comparable to the existing continuous beam at PSI ($\sim 10^4$ LE-μ^+/s). However, there is still a large scope for improvement of the laser ionization efficiency. Cooling efficiency from the surface muon beam to the LE muon beam can be potentially improved to a $\sim 10^{-3}$ level through a significant increase in the laser pulse energy at the Lyman-α wavelength for muonium (122 nm). Lyman-α pulse energy of the order of 0.1 mJ would be required for such an improvement. It is conceivable that this may be achieved through a third harmonic generation of a high-energy picosecond laser with output at 366 nm. This would be a worthwhile development, which could lead to rates approaching 10^6 LE-μ^+/s, i.e., comparable even with the pulsed surface muon beam at ISIS.

References

[1] E. Morenzoni, T. Prokscha, A. Suter, H. Luetkens, R. Khasanov, J. Phys.: Condens. Matter 16 (2004) S4583.
[2] P. Bakule, Y. Matsuda, Y. Miyake, K. Nagamine, M. Iwasaki, Y. Ikedo, K. Shimomura, P. Strasser, S. Makimura, Nucl. Instr. and Meth. B 266 (2008) 355.
[3] E. Morenzoni, in: S. Lee, S Kilcoyne, R. Cywinski (Eds.), Muon Science, Institute of Physics Publishing, 1999.
[4] W. Eckstein, Computer Simulation of Ion–Solid Interaction, Springer, Berlin, 1991.
[5] E. Morenzoni, H. Glückler, T. Prokscha, R. Khasanov, H. Luetkens, M. Birke, E.M. Forgan, Ch. Niedermayer, M. Pleines, Nucl. Instr. and Meth. B 192 (2002) 254.
[6] Y. Miyake, et al., JPARC muon source—MUSE, Nucl. Instr. and Meth. B this issue, 2008.

Nuclear Instruments and Methods in Physics Research A 600 (2009) 87–90

Contents lists available at ScienceDirect

Nuclear Instruments and Methods in Physics Research A

journal homepage: www.elsevier.com/locate/nima

Settlement of Materials and Life Science Experimental Facility at J-PARC

M. Harada [a,*], S. Meigo [a], M. Ito [a], E. Dantsuji [a], K. Takagiwa [a], H. Takada [a], F. Maekawa [a], M. Futakawa [a], M. Nakamura [a], Y. Miyake [b], Y. Ikeda [a]

[a] *Materials and Life Science Division, J-PARC Center, Japan Atomic Energy Agency, Tokai-mura, Naka-gun, Ibaraki-ken 319-1195, Japan*
[b] *Muon Science Laboratory, High Energy Accelerator Research Organization, 1-1 Oho, Tsukuba-Shi, Ibaraki-ken 305-0801, Japan*

ARTICLE INFO

Available online 27 November 2008

Keywords:
Settlement
Level measurement
Settlement expectation
J-PARC
MLF

ABSTRACT

A lot of even and uneven settlement is expected to occur due to the heavy weight of the buildings and shields located at the Materials and Life Science Experimental Facility (MLF) and in the proton beam line (3NBT) that runs from the 3 GeV Rapid-Cycling Synchrotron (RCS) to the neutron target at the Japan Proton Accelerator Research Complex (J-PARC). Because of this, and in order to achieve the necessary alignment of less than 1 mm in precision, the settlement that has occurred with the MLF building and the 3NBT tunnel has been periodically surveyed (level measurement) since June 2004 until now when the MLF building has been completed. The survey results were used in determining the levels at which the beam line components were installed. The survey results indicated that the values of the settlement that had taken place were almost proportional to the located weight and could be used in estimating the settlement that would take place in the future. These results were reflected in the alignment of the proton and beam line components.

1. Introduction

A lot of even and uneven settlement of the MLF building at the Materials and Life Science Experimental Facility (MLF) of the Japan Proton Accelerator Complex (J-PARC) is expected as the building and shields weigh as much as 130,000 and 80,000 ton, respectively. Even and uneven settlement is also expected along the proton beam line from the 3 GeV Rapid-Cycling Synchrotron (RCS) to the neutron target (3NBT) due to the several constructions around the 3NBT tunnel and its long length of about 300 m. Installation of the neutron beam lines, which is being constructed in the MLF buildings, and the proton beam line in the 3NBT tunnel require the very precise alignment of less than 1 mm to minimize any beam loss.

The ground beneath the J-PARC facilities, which is located near the sea, is sandy. And therefore to help suppress the expected large amounts of settlement, many piles were put in place beneath the buildings and tunnels. For example, the MLF building has tens of piles of about 100 m in length beneath it and a concrete foundation of about 10 m in thickness.

Construction of the MLF building began in July of 2004 and was completed at the end of 2005. Heavy neutron source components such as shielding blocks were then installed from October 2004 through to April 2007. The 3NBT tunnel was constructed from August 2004 through to October 2006. Installation of the beam line components in the 3NBT tunnel began at the end of 2005 and was precisely aligned in July 2007. Various neutron beam line components such as guide tubes began to be installed in April 2007, which is still in progress.

To achieve precision alignment in the situation where a lot of settlement is expected to take place, periodic measurements of the settlement at the MLF building and the 3NBT tunnel were taken, and the results taken into consideration in determining the level at which the beam line components were installed [1].

In this paper we describe the settlement survey and estimations for how the MLF and the 3NBT have settled.

2. Measurement

The settlement began to be surveyed in July 2004 and has continued till the present time (March 2008). The method used was to periodically measure the differences between a datum level and a measuring level. For the survey several tens of measuring points were prepared in the MLF building and the 3NBT tunnel. The levelling survey devices included the DNA03 (Leica) and the PL1 (Sokkia) and were used with Invar staffs. The datum point was located outside the MLF building where it is not affected by any settlement. In order to obtain very precise data each of the measurements was round levelled. The error with each measurement was within ±0.5 mm for a 1 km round levelling,

---

[*] Corresponding author. Tel.: +81 29 282 6217; fax: +81 29 282 6496.
E-mail address: harada.masahide@jaea.go.jp (M. Harada).

0168-9002/$ - see front matter © 2008 Elsevier B.V. All rights reserved.
doi:10.1016/j.nima.2008.11.058

which satisfies the class 1 defined for levelling measurement precision (within ±2.5 mm with 1 km round levelling).

3. Results and discussion

3.1. Settlement at MLF building

Fig. 1 gives the positions of the major level points that were used in measurements in the MLF building. Two of the points were located near the neutron target while another two were located near the muon target. These points were directly fixed to piles beneath the MLF building to avoid any effect of the concrete flooring that was put in place during the early stages of construction.

Fig. 2 gives the variations in level differences for the major level points as a function of time. Settlement of the building rapidly took place as construction went on and reached the value of 40 mm after the completion. The settled value increased to an average of 48 mm with the installation of the heavy neutron source components. It should be noted that the maximum difference of 4 mm between the neutron target and the muon target was caused by uneven settlement due to the weight difference of the components between those sources. In October 2007 the average settled value was 50 mm and the difference 4 mm.

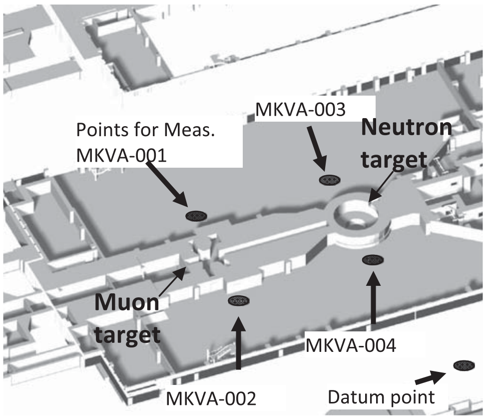

Fig. 1. Major level points measured at the MLF.

3.2. Extrapolated settlement at the MLF building

Using the results of the measurements mentioned in the previous subsection the relationship between the settled value and total weight was plotted and is given in Fig. 3.

Generally speaking, settlement is more related to the weight per unit of area than total weight. However, in this case the settled value can be presumed to have been more sensitive to the total weight than the weight per unit of area as the total weight is uniformly spread over the basement of the MLF building, which is as thick as 10 m and supported by piles. Which is why, then, it was selected for the horizontal axis in Fig. 3. Judging by the relationship revealed in Fig. 3 settlement seems to have been elastic. By assuming that the settled value is proportional to the added weight, the relationship can be expressed with

$$LD = E \cdot W + C \tag{1}$$

where LD is the difference in level (mm), E the proportional factor (mm/ton), W the weight (ton) and C a constant (mm). The values E and C can be obtained by best fitting in the relationship between the primary settlement result and the weight up till then. Future settled values can be extrapolated for plans to add more weight.

The fitted result obtained using Eq. (1) is also given in Fig. 3. The fitted line is in good agreement with the measured values. It also indicates that the relationship between the settled value and the weight has almost proportionality with the factor E of about 0.3 mm/1000 ton.

According to the fitted results, the settled value will be about 54 mm when the first proton beam is injected at the neutron target (seven neutron beam lines are installed) in May 2008. It will be about 72 mm when all the neutron beam line components are completed.

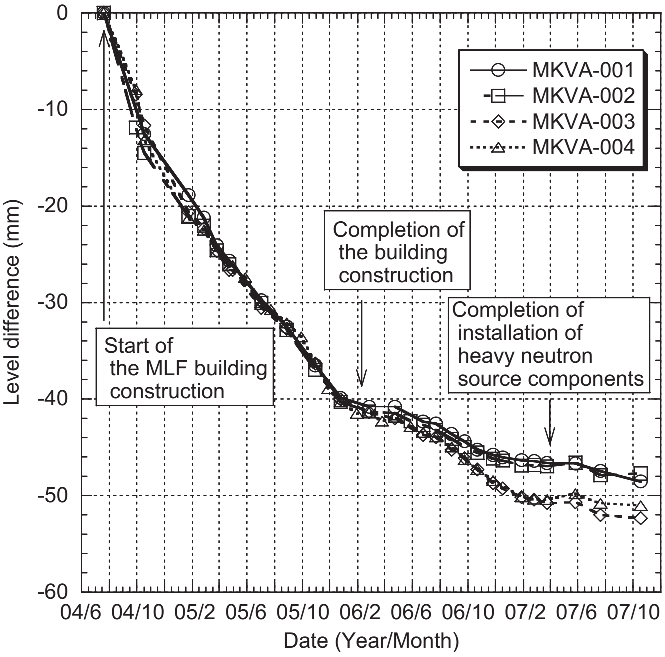

Fig. 2. Level differences of major level points at MLF. The value is normalized to zero at start of the MLF building construction.

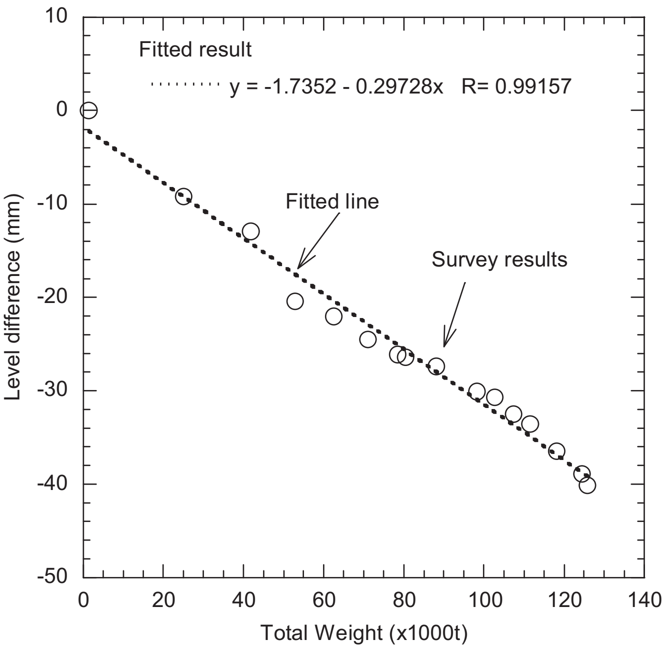

Fig. 3. Relationship between differences in level and weight for the settlement that has taken place at MLF.

3.3. Settlement at the MN tunnel

The MN tunnel is for a proton beam line between the muon target and the neutron target and is given in Fig. 1. Maintenance of the beam line components in the MN tunnel must be carried out remotely as a lot of beam loss occurs due to large proton-beam scattering at the muon target. To align the beam line components in the MN tunnel it was decided that the base plates should be precisely located and aligned before installing them, and that the other beam line components such as magnets be located on the plates without precise adjustments. However, parts of the concrete side walls in the MN tunnel were positioned after installation of aforementioned base plates. And therefore the settled value at completion of the side wall had to be estimated using the value measured before the wall was constructed.

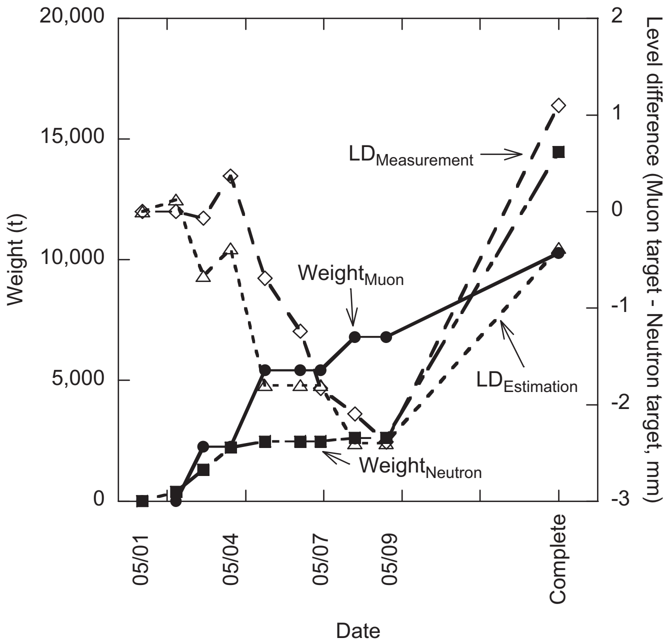

Fig. 4. Settled value in the MN tunnel.

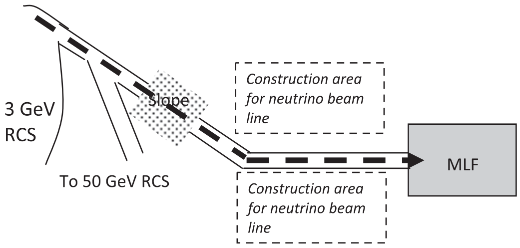

Fig. 5. Schematic diagram of the 3NBT tunnel.

Based on the relationship of the difference in levels between the muon target and the neutron target to these weights from January 2005 to September 2005, the level differences at completion of construction were extrapolated to be about 1 mm, as given in Fig. 4. Use of this extrapolated data was used in deciding the beam height of the proton beam line in the MN tunnel. The measured level difference was −0.2 mm at completion, which was in good agreement with the extrapolated value.

3.4. Settlement at 3NBT tunnel

Fig. 5 gives a schematic diagram of the 3NBT tunnel. Settlement at the 3NBT tunnel was measured along the proton beam line from an extracted point from the 3 GeV RCS to the MLF building. The results of the survey are given in Fig. 6. From November 2006 to May 2007 the 3NBT tunnel rose a maximum of about 2 mm, particularly downstream. Conversely from May 2007 to September 2007 the 3NBT tunnel settled a maximum of about 3 mm, once again particularly downstream. The floating and settling that has occurred at the 3NBT tunnel are due to the construction of the neutrino beam facility, one of the J-PARC facilities, near the downstream of the 3NBT tunnel. And although the 3NBT beam line components were precisely aligned in July 2007, alignment will need to take place again as construction of the neutrino facility is still ongoing.

4. Summary

Surveying the settlement began in July 2004 and continued after completion of building. Settlement of the MLF building increased as construction proceeded but after completion then slowly increased. From the results obtained it was discovered that the settled value of the MLF was proportional to the weight that had been installed. After assuming that the relationship between the settled value and the added weight was fairly elastic and good, the estimated value proved to be in good agreement with the

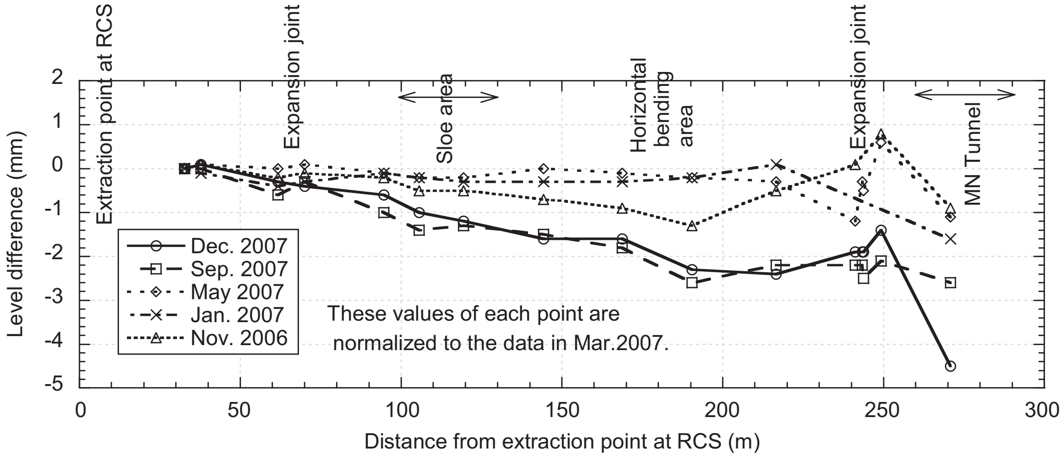

Fig. 6. Settlement in the 3NBT tunnel.

survey results. Settlement had also occurred with the 3NBT, in the downstream area in particular, due to construction of a J-PARC facility near the tunnel.

Surveying the settlement at the MLF and the 3NBT will continue until the settlement has ceased.

Acknowledgments

The authors would like to thank the staff of the "High-Intensity Proton Accelerator Facility Construction Section" of the Japan Atomic Energy Agency for having provided valuable data. And the authors would also like to thank Dr. Mishima in Pasco Corporation for providing instruction on a level measurement technique.

Reference

[1] H. Takada, et al., in: Proceedings of the 17th Meeting of the International Collaboration on Advanced Neutron Sources (ICANS-XVII), LA-UR-06-3904, Santa Fe, New Mexico, April 25–29, 2005, (2006), pp. 346–354.

Nuclear Instruments and Methods in Physics Research A 600 (2009) 114–116

Contents lists available at ScienceDirect

Nuclear Instruments and Methods in Physics Research A

journal homepage: www.elsevier.com/locate/nima

Design strategy for devices under high radiation field in J-PARC muon facility

Naritoshi Kawamura *, Shunsuke Makimura, Patrick Strasser, Akihiro Koda, Hiroshi Fujimori, Kusuo Nishiyama, Yasuhiro Miyake, M.L.F Muon section

Muon Science Section, Materials and Life Science Division, J-PARC, Toukai-mura, Naka-gun, Ibaraki 319-1195, Japan

ARTICLE INFO

Available online 27 November 2008

Keywords:
Muon production target
Radiation evaluation
Radiation shield
Monte-Carlo simulation

ABSTRACT

The intensity of proton accelerator has attained the order of mega-watt, and several MW-class proton accelerators have started operating in the world. In comparison with the other MW-class accelerators, Japan Proton Accelerator Research Complex (J-PARC) is unique due to the muon facility. Materials and Life Science Facility, J-PARC, has not only the mercury target but also the graphite target to provide spallation neutrons and muons, respectively. The muon target is inserted upstream of the neutron target in the proton beam line. Full use of several mutually linking Monte-Carlo codes enables the design work of devices in the muon facility, which has to be operated under high radiation field from the muon target.

1. Introduction

A high-intensity proton accelerator (Japan Proton Accelerator Research Complex, J-PARC) project was proposed jointly by Japan Atomic Energy Agency (JAEA) and High Energy Accelerator Research Organization (KEK). The new facility consists of 400-MeV linac, 3- and 50-GeV synchrotron rings, which provide an intense proton beam to pursue particle physics, nuclear physics, materials science, life science and nuclear technology. A 1-MW proton beam is transported from the 3-GeV synchrotron ring to Material and Life Science Facility (MLF), which consists of the muon and the spallation neutron facilities. As shown in Fig. 1, the proton-beam-line tunnel runs through the center of the MLF building from the north to the south. The east and west wings are the experimental hall where the neutron and muon beam lines are constructed. In order to avoid the diffusion of radioactive contamination, proton-beam transport tunnel is isolated from the experimental hall. Namely, the beam transport tunnel divides the MLF building into the east and the west wings.

The muon-production target is inserted 30-m upstream of the neutron target in the proton beam line. The concept of the cascade-type muon-target is similar to the ISIS muon facility, UK, which is a 0.24 MW (800 MeV, 300 μA) proton accelerator. From the muon target, we decided to extract four muon beam lines. Each of them provides world's strongest pulsed muon beam with an individual design concept to be utilized for the variety of muon science, such as μSR spectroscopy, muon catalyzed fusion experiment, and so on. Two of the secondary beam lines are extracted at the angle of 60° to the proton beam line (forward) and the others are at 135° (backward). At the exterior of the proton-beam transport tunnel (M2 tunnel), four openings exist, and correspond to each muon beam line. At the first stage, we do not construct every muon beam lines to leave the future option.

Although the design layout with four beam-lines from a target has the advantage to perform various experiments simultaneously, not only the radiation shield but also the devices around the muon target become complicated. Thus, we developed the design strategy for the devices around the muon target using several Monte-Carlo codes.

2. Devices under high radiation field

The design work of the devices around the proton beam-line from the muon target to the neutron target (M2 tunnel) has to take into account the effect of high radiation field. In addition to the fundamental design work, material selection requires taking into account the effect of radiation damage, that is the accumulated dose. Especially, some non-metallic material has to be swapped with the field-resistant one or metal. For instance, PTFE used in a coolant-water gasket and so forth was swapped with the grafoil one. In addition to the radiation damage, heat deposit by scattered protons, secondary neutrons and gamma-rays is important information for the devices close to the muon target, such as the muon target itself, beam collimator and so forth, in order to design the coolant system and to check the effect of thermal expansion. The simulated result was fed back to the device design and the revised one was simulated again. The feedback procedure was repeated until a design satisfying all

---

*Corresponding author.
E-mail address: nari.kawamura@kek.jp (N. Kawamura).

0168-9002/$ - see front matter © 2008 Elsevier B.V. All rights reserved.
doi:10.1016/j.nima.2008.11.073

requirements was obtained. Both the accumulated dose and heat generation are evaluated by a Monte-Carlo code, PHITS [1].

In the simulation, protons are created just upstream of the muon target with a practical emittance, and then protons and secondary particles originating from nuclear reactions are transported. In order to select the material, a detailed structure of an intended device has to be realized, as shown in Fig. 2. In addition to the simulated result of accumulated dose, change in the material properties against the accumulated dose [2] was taken into account for material selection. For some candidates with no radiation data, an irradiation test was performed at ^{60}Co irradiation facility, Takasaki, JAEA. In this way, devices in the M2 tunnel, such as the muon target and its chamber [3], beam-transport magnets [4] and inflatable-metal vacuum seal, that is pillow seal, were designed.

DPA in the material is also evaluated by PHITS. DPA is used as an index of radiation damage in graphite. Because it is difficult to monitor the radiation damage in the graphite muon target in the beam line, we defined the lifetime of the target to be 1 DPA irradiation. Thus, the number of protons to be injected is evaluated, and the lifetime of the target is determined as a half year under 1-MW beam.

Using the evaluated residual activity by PHITS and DCHAIN-SP [5], which evaluates the high-energy-particle-induced radio-activity and its decay chain, gamma-ray dose from the irradiated material is evaluated by MCNP [6] with additional cross-section data [7]. MLF is designed to be operated for forty years under 1-MW beam. Thus, taking into account the effect of gamma-ray dose during the maintenance, any device is designed and its maintenance scenario is constructed. For instance, a consumed target is replaced with a new one in a remote-handling room of MLF. In order to transport the irradiated target from the muon-target chamber to the remote-handling room, a cask device is designed [3]. Time limit to stay beside the cask is evaluated, and this gives some restriction to the target exchange work.

For accelerator operation, evaluation of radio-activity production in coolant water and air is important. The amount and concentration of radio-activity are also evaluated in the same manner mentioned above and checked against the disposal limit. The initial design of cooling water for the muon target and the collimator system was expected to be heavily activated and thus the pipe route was changed. In addition, we have to pay attention to tritium, which is generated in the target and evaporates to the beam-line vacuum due to the high temperature of the target.

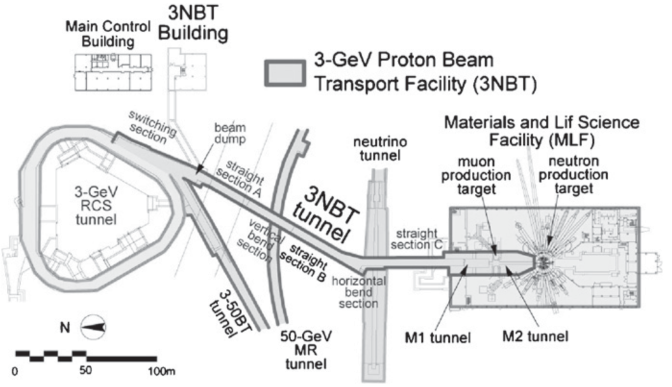

Fig. 1. Schematic drawing from the 3-GeV synchrotron to the MLF.

3. Radiation shield

As already mentioned in the introduction, the muon facility is a complicated structure due to four secondary beam-lines, and thus we developed a technique to use Monte-Carlo simulation.

The first step of muon facility design was the determination of maximum beam loss due to the muon target. At the standpoint of neutron and muon utilization, this was optimized to be 10%. The 2-cm graphite target was adopted. This causes about 5% beam loss and remains as future options.

The parameter of the magnet from the muon target to the neutron target is determined by a calculation of the TRANSPORT code [8], and rough evaluation of beam loss is obtained by DECAY-TURTLE [9]. In the detailed design work, we made full use of the Monte-Carlo simulation. For safety, we multiplied the simulated result by the margin factor of two, and the radiation dose was required to be below the design limit at the boundary between the controlled area and the public area, which is introduced in the J-PARC site.

We optimized the amount, the arrangement and the material of radiation shield, not only to a movable one but also to a fixed wall.

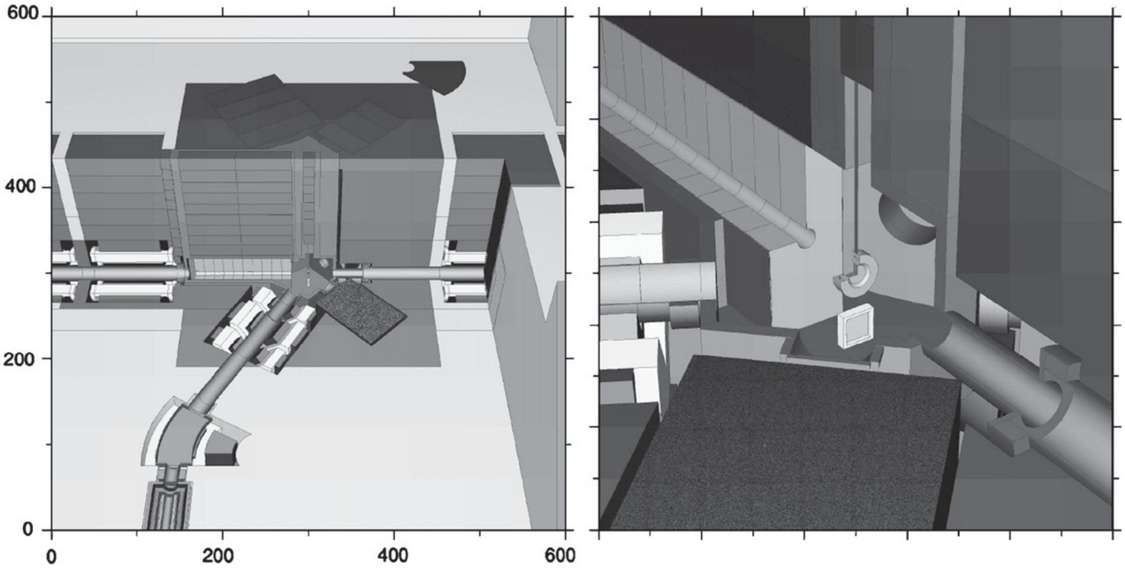

Fig. 2. A typical model for PHITS simulation: a cut-away view from east side to the muon target (left) and around the target (right).

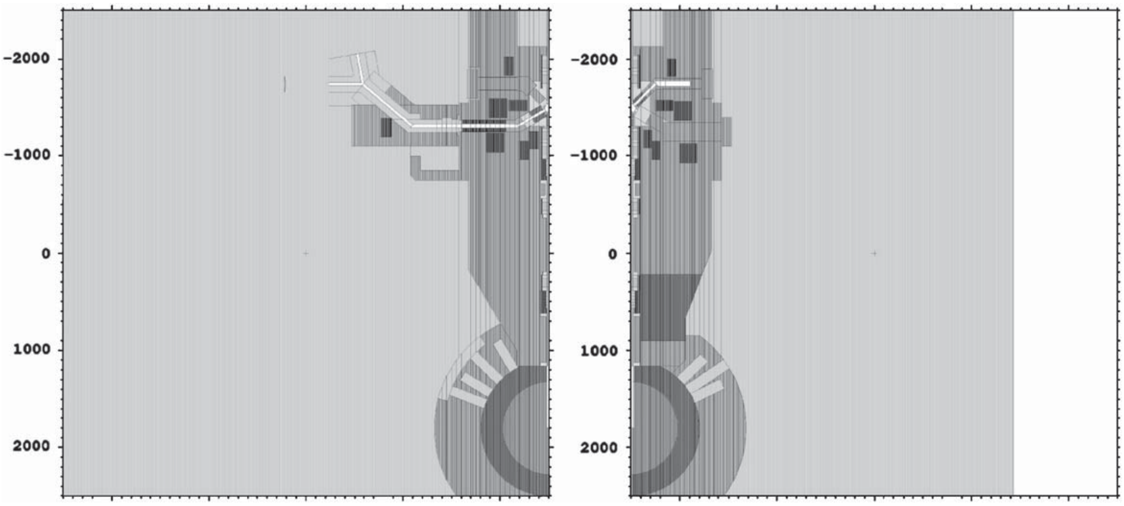

Fig. 3. A typical model for radiation dose evaluation. East side (left) and west side (right) is divided to reduce the computing time.

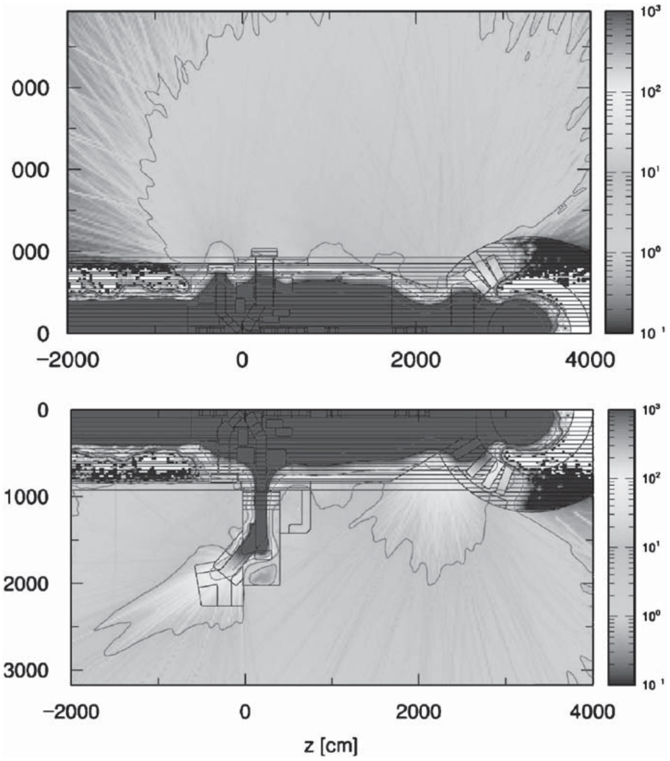

Fig. 4. The result of radiation dose for the model shown in Fig. 3.

For this purpose, using Monte-Carlo simulation is suitable because of the flexibility of modeling. We adopted the PHITS code, and Fig. 3 shows a typical simulated model. In comparison with the above-mentioned evaluation for the device design, the created model is simple, and a non-effective structure is omitted to reduce the computing time. Fig. 4 shows a contour plot of a radiation-dose map in the simulated result. The radiation dose from downstream of the M2 tunnel is separately evaluated with a safety margin in the beam loss, and then added to the evaluated result originating from the muon target. This safety margin supposes the miss-alignment of beam-line magnets and the subsidence of the MLF building, that is the quadrupole magnet plays a role of a bending magnet. Recent progress in PHITS code enabled us to evaluate the effect of magnet miss-alignment and the subsidence, and we confirmed that this safety margin was high enough, and that we were able to reduce this margin.

4. Summary

We developed the design strategy using several Monte-Carlo codes. Although the cross-check was performed by MARS and MCNPX codes partially, reliability of code and modeling procedure should be checked by a low-intensity beam.

The muon facility, MLF, J-PARC, is the most intense pulsed muon facility in the world and provides muons from the 1-MW proton beam. The MW-class accelerator is the world trend, and thus this design strategy is applicable to other facilities.

Acknowledgements

We acknowledge fruitful discussion by Drs. F. Maekawa, S. Meigo, Y. Kasugai, M. Harada, T. Kai, M. Ohi and other staff of Neutron Source Section. We are deeply grateful to Prof. G. Heidenreich and other PSI muon facility staff for helpful discussion. We express our sincere gratitude to Prof. K.H. Tanaka and Hadron Group, J-PARC for their inspired advice. We also thank Dr. J. Kusano and other related people as concerned about an irradiation test at the ^{60}Co irradiation facility, Takasaki, JAEA.

References

[1] H. Iwase, K. Niita, T. Nakamura, J. Nucl. Sci. Technol. 39 (2002) 1142;
K. Niita, T. Sato, H. Iwase, H. Nose, H. Nakashima, L. Sihver, Radiat. Meas. 41 (2006) 1080.
[2] J. Kusano, Y. Uno (Ed.), JAERI-DATA/Code 2003-015.
[3] S. Makimura, et al., Nucl. Instr. and Meth. A, doi:10.1016/j.nima.2008.11.110.
[4] H. Fujimori, et al., Nucl. Instr. and Meth. A, doi:10.1016/j.nima.2008.11.025.
[5] T. Kai, et al., JAERI-Data/Code 2001-016.
[6] J.F. Briesmeister (Ed.), MCNP–a general Monte Carlo N-particle transport code, LA-12625-M, Los Alamos Narional Laboratory, 1993.
[7] T. Nakagawa, et al., J. Nucl. Sci. Technol. 32 (1995) 1259.
[8] K.L. Brown, D.C. Carey, Ch. Iselin, F. Rothacker, CERN 73-16 (1973) and CERN 80-04 (1980).
[9] K.L. Brown, Ch. Iselin, D.C. Carey, CERN 74-2, 1974.

Nuclear Instruments and Methods in Physics Research A 600 (2009) 132–134

Contents lists available at ScienceDirect

Nuclear Instruments and Methods in
Physics Research A

journal homepage: www.elsevier.com/locate/nima

The super omega muon beamline at J-PARC

K. Nakahara [a,*], Y. Miyake [a], K. Shimomura [a], P. Strasser [a], K. Nishiyama [a], N. Kawamura [a], H. Fujimori [a], S. Makimura [a], A. Koda [a], K. Nagamine [a], T. Ogitsu [b], A. Yamamoto [b], T. Adachi [b], K. Sasaki [b], K. Tanaka [b], N. Kimura [b], Y. Makida [c], Y. Ajima [d], K. Ishida [e], Y. Matsuda [e]

[a] Muon Science Laboratory, High Energy Accelerator Research Organization, Oho, Tsukuba, Ibaraki 305-0801, Japan
[b] Cryogenic Science Center, High Energy Accelerator Research Organization, Oho, Tsukuba, Ibaraki 305-0801, Japan
[c] Institute of Particle and Nuclear Studies, High Energy Accelerator Research Organization, Oho, Tsukuba, Ibaraki 305-0801, Japan
[d] Mechanical Engineering Center, High Energy Accelerator Research Organization, Oho, Tsukuba, Ibaraki 305-0801, Japan
[e] Advanced Meson Science Laboratory, RIKEN Nishina Center, RIKEN, Hirosawa-2-1, Wako, Saitama 351-0198, Japan

ARTICLE INFO

Available online 3 December 2008

Keywords:
Muon
Beam transport
Ultra-slow muons

ABSTRACT

The Materials and Life Science Facility (MLF) is currently under construction at J-PARC in Tokai, Japan. The facility houses both muon (graphite) and neutron (mercury) production targets, and is located at the end of the 3 GeV proton beamline. The Super Omega muon beamline (one of four secondary muon beamlines) extends at 45° into backward angles to transport the surface μ^+ and cloud μ^- to experimental hall 2. Once completed, it will produce the highest intensity pulsed muon beam in the world, with $4\times10^8\,\mu^+$/s and $10^7\,\mu^-$/s, which will be used for a variety of purposes such as experiments in muon-catalyzed fusion and the production of ultra-slow muons. The beamline consists of normal-conducting capture solenoids, superconducting transport solenoids, and a Dai Omega-type axial focusing magnet. Currently, the construction of the capture solenoids is nearing completion. The design of the transport solenoids is under way, and tests solenoids will be fabricated and tested during the summer of 2008. The axial focusing magnet, used to focus the muon beam on the experimental target, is under consideration with particular emphasis on its compatibility with the transport solenoids.

1. Introduction

The J-PARC Materials and Life Science Facility (MLF) accepts a 3 GeV/1 MW/333 μA proton beam from the Rapid Cycling Synchrotron (RCS) to produce secondary muon and neutron beams. The primary beam first passes through the graphite muon production target, losing about 10% of its luminosity, after which it is incident on the mercury neutron production target.

Four secondary beamlines extend from the muon target. Surface muons are produced when pions stop at the surface of the production target and decay, while cloud muons originate from pions decaying in flight outside the target. The Super Omega muon beamline [1] (Fig. 1) is designed to simultaneously capture/transport both surface and cloud muons of various momentums into experimental hall 2.

The captured surface muons will be used for the production of the world's most intense pulsed ultra-slow muon beam with intensities of order 10^5/s. These ultra-slow muons, which will be created through laser-resonant ionization [2,3] to have low penetration depths, high energy and termporal resolutions, and tuneable energies, can be used to probe surface phenomenon using μSR techniques [4].

The negative cloud muons will be used for experiments such as muon-catalyzed fusion. The increased beam intensity will provide improved signal-to-noise in the μCF X-ray spectra.

This contribution will describe the design of various components of the beamline as well as the expected rates.

2. Capture solenoids

The capture solenoids (Fig. 2) consist of four normal-conducting solenoids designed to capture the secondary muons with a solid angle acceptance of 400 msr.

The solenoids are located between 60 and 150 cm from the production target. Although the proximity of the solenoids to the target results in a large solid angle acceptance, due to the high level of exposure to radiation, the solenoids are wound with radiation-resistant mineral insulation cables (MIC). The cables are water-cooled with a total cross-section of 20 × 20 mm, and are rated up to 2000 A. Due to constraints in power and water availability, the first three solenoids will be connected in series with an operating current of 1000 A for a muon momentum of 30 MeV/*c*, while the last solenoid will operate at approximately 500 A at the same momentum. The trajectories as well as the rates

---

[*] Corresponding author. Tel.: +81 029 864 4623.
E-mail address: nakahara@post.kek.jp (K. Nakahara).

0168-9002/$ - see front matter © 2008 Elsevier B.V. All rights reserved.
doi:10.1016/j.nima.2008.11.106

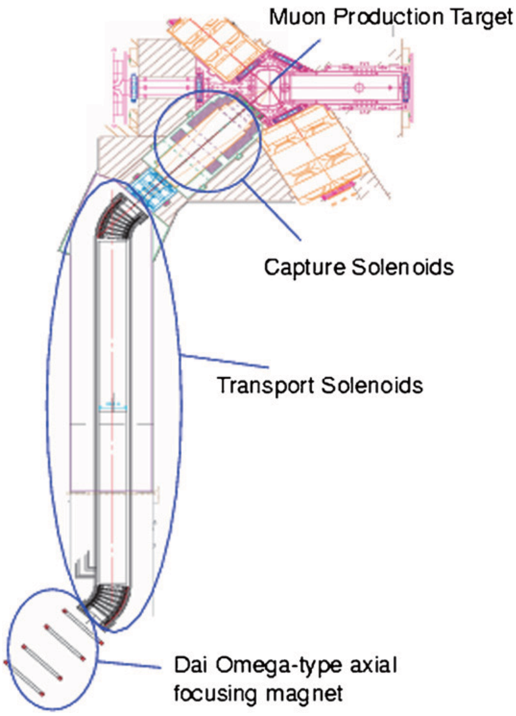

Fig. 1. Schematic drawing of the Super Omega muon beamline.

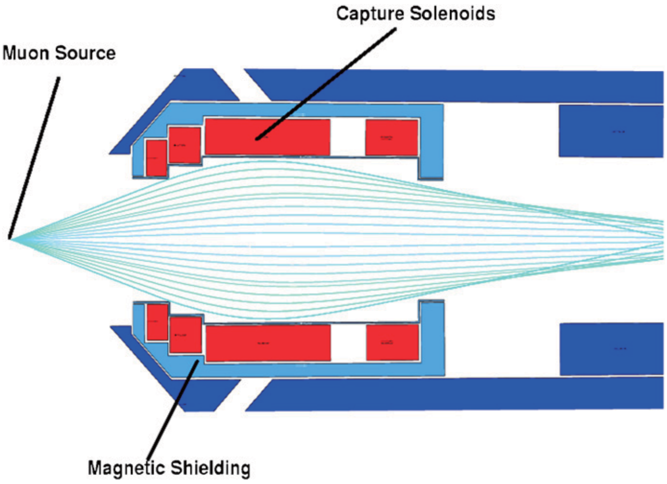

Fig. 2. Schematic drawing of the capture solenoids with simulated trajectories.

of the captured muons are simulated using GEANT4, while the field distribution within the solenoids is calculated through TOSCA. Although the solenoids will be placed at beam level 1.6 m above the ground (FL1.6), there will be 2.4 m of radiation shielding placed above the coils such that maintenance can be performed at the 4 m level (FL4). For similar reasons, the water and power connectors for the solenoids will all be placed on top of the radiation shielding.

The capture solenoids have been constructed/tested by NEC/TOKIN. The magnetic field distributions have been measured and were seen to be in agreement with simulation.

3. Superconducting transport solenoids

The superconducting transport solenoids (Fig. 3), consisting of two 45° 6-segmented curved sections and one 6-m-long straight section, are designed to transport the captured muons into experimental hall 2.

The vacuum connection between the capture and transport solenoids is made with a gate-valve pillowseal. The pillowseals attach to the vacuum ducts of both solenoids with a 2 t force to seal the vacuum. The gate valve is in place such that the transport solenoids can be extracted from the beamline for maintenance without spoiling the vacuum upstream. Most of the beamloss is seen to take place at the gate-valve pillowseal (6%) and the curved sections (12%).

A series of Gifford–McMahon (GM) [5] refrigerators will be used to cool down the superconducting coils. The total heat load on the solenoids is expected to be 5–10 W. The contribution from radiation heating is calculated through GEANT4 and PHITS to be between 1 and 2 W, with structural heat load contributing the rest. Two layers of cryogenic shielding, 10 and 50 K, will be placed around the solenoids to minimize the heat load. Most of the structural heat load originate from the fiber-reinforced plastic support posts on which the solenoids are placed, and the power leads to a connection between the normal-conducting and superconducting transition cables. Two segments of the curved section will be constructed and tested to determine the feasibility of the curved design during the fiscal year 2008.

4. Axial focusing

The muons transported through the beamline are focused onto the experimental target. When producing ultra-slow muons, the surface muons must be focused within the width of the laser (10 mm), in order to maintain the beam intensity as high as possible. The design of the axial focusing magnet is based on the Dai-Omega magnet [6] used at the KEK muon port. Although the Dai-Omega magnet at KEK was placed immediately downstream of the muon production target to capture the muons and provide point-to-point focusing, the design for the Super Omega muon

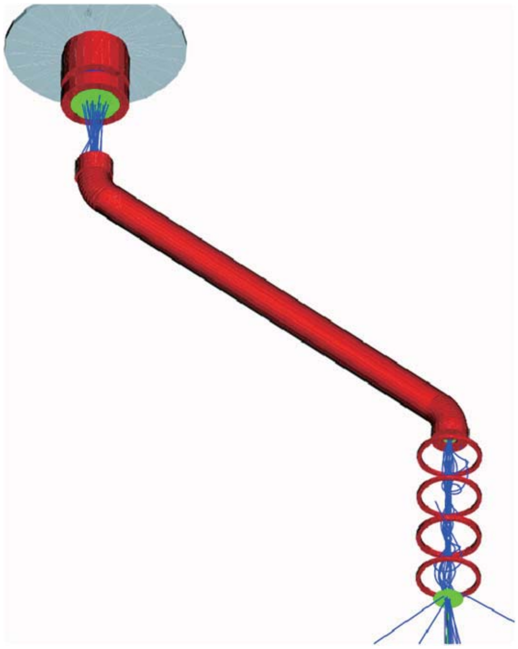

Fig. 3. GEANT4 simulation of the Super Omega muon beamline. The 6-m-long straight section together with the two 45° curved sections are the superconducting transport solenoids.

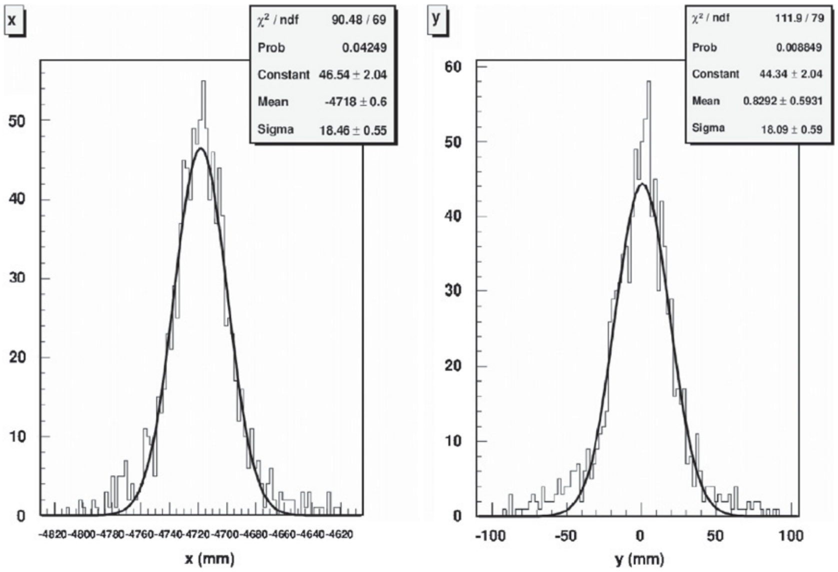

Fig. 4. The transverse distribution of surface muons at the focus of the axial focusing magnet.

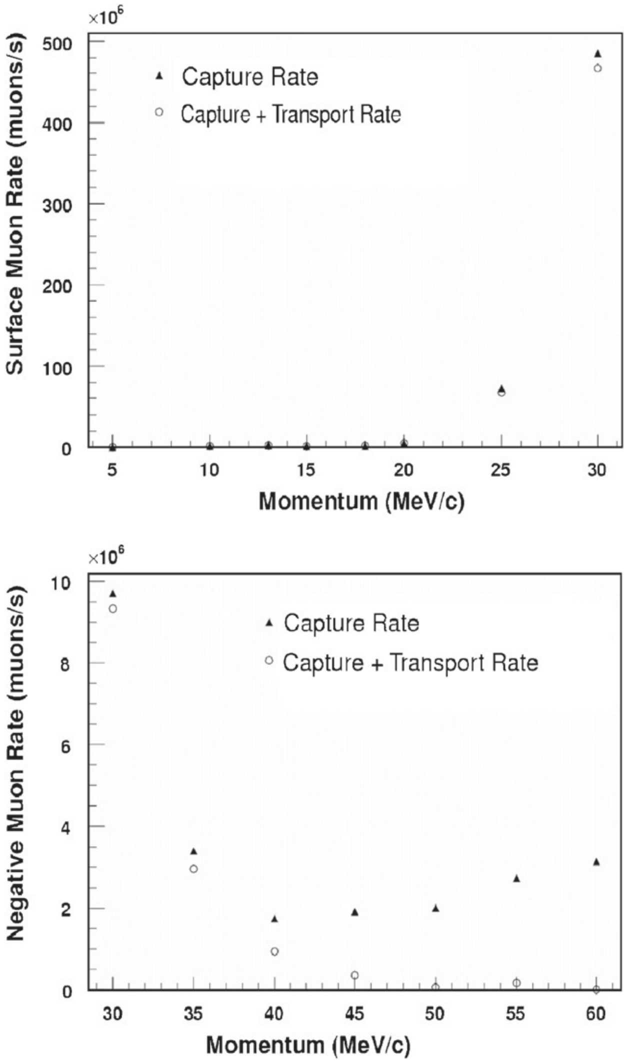

Fig. 5. Simulated capture and transport rates for surface and cloud muons with the beamline optimized for 30 MeV/*c*.

beamline must be altered such that it is compatible with the capture and transport solenoids.

Currently, the size of the focus is approximately 40 mm FWHM (Fig. 4). Modifications are being considered to focus the beam to within the width of the laser pulse.

5. Muon rates

The muon rates are calculated using a GEANT4-based simulation package called G4Beamline [7]. The pion production cross-section used for the simulation is from Pirone and Smith [8], while the pion to surface muon conversion rate and their target distributions are calculated by Ishida [9]. Total beam loss is approximately 18% for 30 MeV/*c* muons. The beamline will be used for a variety of experiments with differing muon momentum. Surface muons have a maximum momentum of 30 MeV/*c*, while μCF experiments require muons with a momentum up to 60 MeV/*c*. (Fig. 5).

For the production of ultra-slow muons, the capture efficiency is optimized for 30 MeV/*c*. At this momentum, the rates are $4–5\times10^8\,\mu^+/\mathrm{s}$ and $1\times10^7\,\mu^-/\mathrm{s}$. Above 30 MeV/*c*, although the muon production cross-section increases with momentum, the capture and transport efficiencies drop off rapidly. The resulting rates at 60 MeV/*c* are well below $10^7\,\mu^-/\mathrm{s}$ and the beamline will need to be re-tuned to accommodate the higher momentum muons.

References

[1] K. Shimomura, et al., AIP Conference and Proceedings of the 721 Neutrino Factories and Superbeams, 2004 pp. 346–349.
[2] K. Shimomura, et al., Nucl. Phys. B 155 (2006) 343.
[3] P. Bakule, et al., Spectrochim. Acta B 58 (2003) 1019.
[4] E. Morenzoni, et al., Physica B 289–290 (2000) 653.
[5] Sumitomo Heavy Industries, Type CG310SC GMJT refrigerator.
[6] H. Miyadera, et al., Nucl. Instr. and Meth. A 569 (2006) 713.
[7] Muons, Inc. 552 N. Batavia Avenue, Batavia, IL, USA.
[8] P.A. Pirone, A.J.S. Smith, Phys. Rev. 148 (1966) 1315.
[9] K. Ishida, Internal Report.

Nuclear Instruments and Methods in Physics Research A 600 (2009) 139–142

Contents lists available at ScienceDirect

Nuclear Instruments and Methods in Physics Research A

journal homepage: www.elsevier.com/locate/nima

Development of positron detector for μSR based on multi-pixel photon counter

Soshi Takeshita [a,*], Masatoshi Hiraishi [b], Masanori Miyazaki [b], Akihiro Koda [a,b], Ryosuke Kadono [a,b], Soh Y. Suzuki [a], Yoshiji Yasu [a], Manobu Tanaka [a,b], Yasuyuki Matsuda [c], Katsuhiko Ishida [c], Teiichiro Matsuzaki [c]

[a] *High Energy Accelerator Research Organization, Oho 1-1, Tsukuba-shi, Ibaraki 305-0801, Japan*
[b] *The Graduate University for Advanced Studies, Shonan Village, Hayama-cho, Miura-gun, Kanagawa 240-0193, Japan*
[c] *RIKEN, Hirosawa 2-1, Wako-shi, Saitama 351-0198, Japan*

ARTICLE INFO

Available online 3 December 2008

Keywords:
Photodetector
Multi-pixel photon counter

ABSTRACT

In the pulsed muon facility (MUSE) being built as a part of J-PARC, muon beams with unprecedented intensity ($\sim 10^6\,\mu^+$/pulse) will be delivered at its full operation. Because of the extreme instantaneous μ–e decay positron rates ($\sim 10^4$–$10^5\,e^+$/pulse), development of a highly segmented positron detection system is crucial for practical application of μSR. To this end, we have designed a new positron detector based on a multi-pixel photon counter (MPPC). The advantages of MPPC over conventional phototubes are its small size, low operation voltage, functionality under a high magnetic field, and low cost. The result of test experiment for the detector using a pulsed muon beam is reported.

1. Introduction

In the pulsed muon facility at J-PARC (Muon Science Establishment, MUSE), it is expected that three orders of magnitude more intense muon beam than that of KEK-MSL will be delivered at its full operation, where 10^4–10^5 positron events must be recorded at every muon pulse within the time range of mean lifetime for μ^+ ($\sim 10^{-5}$ s). Any existing μSR spectrometer for pulsed muon beam would not be able to handle such a high positron event rate, because of the limited segmentation numbers for the positron detectors that would lead to pile-up of events and associated distortion of spectrum. This is because the time interval of these positron events becomes shorter than the double pulse resolution of the detector at each segment. In order to eliminate this pile-up effect, it is necessary to reduce the size of segmented scintillators while increasing their number to keep a sufficient total solid angle. To this end, small and economical positron detectors are necessary. In addition, tolerance to high magnetic field is strongly desired, because μSR measurements are routinely performed under a magnetic field.

Up to now, a photomultiplier tube (PMT) has been employed as optical sensor for positron detectors in μSR spectrometers. Unfortunately, the use of PMT will not be feasible for highly segmented detectors, as it is expensive, bulky, and its gain is strongly reduced by magnetic field. As an alternative, we focused on a multi-pixel photon counter (MPPC) that would satisfy the above-mentioned requirements as optical sensor. We designed a telescope counter based on MPPC for high-energy positron detection, and examined the performance using a pulsed muon beam under zero and high magnetic field at RIKEN-RAL muon facility.

2. Detector

2.1. Multi-pixel photon counter

MPPC is made up of multiple avalanche photodiode (APD) pixels operated in the Geiger mode where a bias is applied over the breakdown voltage. It is characterized by a high gain ($\sim 10^6$) comparable to PMT in spite of low operation voltage ($\sim$70 V). Since it is based on semiconductor technology, MPPC is economical, small ($5\times6\times1.5\,\mathrm{mm}^3$), and functional under a high magnetic field. One of the few drawbacks for MPPC would be relatively large dark current noise.

2.2. Detector design

The design of a positron detector is schematically illustrated in Fig. 1. It mainly consists of two solid scintillation counters [forward, S1 (CH1), and backward, S2 (CH2), made of BC408, with $10\times12\times10\,\mathrm{mm}^3$ thickness], two wavelength shifter fibers

---

[*] Corresponding author. Tel.: +81 29 879 6028; fax: +81 29 864 5623.
E-mail address: soshi@post.kek.jp (S. Takeshita).

0168-9002/$ - see front matter © 2008 Elsevier B.V. All rights reserved.
doi:10.1016/j.nima.2008.11.108

(WLS1 and WLS2, made of Y11), and two MPPCs (MPPC1 and MPPC2, 40S10362-11-050C). Each WLS fiber is tightly attached to the MPPC and absorbs light from the counter, where the light is converted to a longer wavelength suitable for MPPC. All the optical components are coated with reflector paint (BC620) to avoid crosstalk. Cabling for bias voltage and signal output is made through a 4-pin LEMO connector. The two counters form a telescope so that the coincidence of these two signals from MPPCs can define the decay positron while noise event from each MPPC is eliminated.

2.3. Electronics and data acquisition

The MPPC signal, after passing through a filter circuit, is amplified and discriminated to generate a timing pulse. Then it is guided to a newly developed time-to-digital converter (TDC) built in fully programmable gated allay (FPGA) for the COPPER system (developed by KEK-Electronics group). The details of this TDC system are reported elsewhere [1].

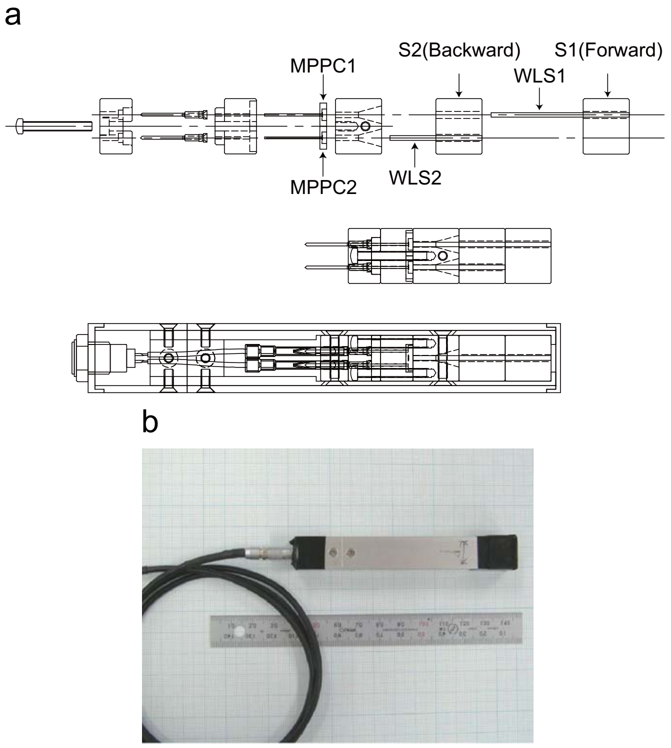

Fig. 1. Schematic drawing of the design for a positron detector (a) and a picture of actual product (b).

3. Experiment

We have performed test experiments using (1) a checking source (0.99MBq of ^{90}Sr, which emits β^--ray with a maximal energy of 546 keV) and decay positrons from a pulsed muon beam under (2) zero magnetic field (ZF), and (3) a high magnetic field (HF). The ZF and HF measurements were performed at Port-1 of RIKEN-RAL muon facility; a schematic view of the experimental setup is shown in Fig. 2. A trigger signal for beam kicker magnet is used to define the time origin of TDC. A superconducting Helmholtz coil (SHC) was used to apply a high magnetic field of 3.6 T. In the muon experiment, arrangement of channels is as follows: CH1 and CH2 are connected to the MPPC1 (S1, WLS1) and MPPC2 (S2, WLS2), respectively, CH3 is the coincidence signal of CH1 and CH2, CH4 and CH5 are connected to the PMT1 and PMT2, respectively, CH6 is the coincidence signal of CH4 and CH5, and CH7 is the coincidence signal of CH1 and CH6.

3.1. Test by checking source

First, we investigated the noise level due to the dark counts of MPPC caused by thermal excitation and tunneling effect. Fig. 3(a) shows the dark count rate as a function of threshold voltage (V_{th}) for discrimination (corrected to that before amplification). It clearly exhibits activation-type dependence with the slope determined by the bias voltage (V_{b}). This allows us to readily control the noise level by changing the threshold voltage. Fig. 3(b) shows the count rate with and without the checking source under the fixed V_{b}(=71.3 V). In this condition, the dark counts are suppressed at $V_{\text{th}}\sim-25$ mV, while the β^- event remains even at $V_{\text{th}}=-40$ mV. Thus, we can easily suppress the noise event and extract the e$^+$ event by tuning V_{b} and V_{th}.

3.2. Test under zero magnetic field

The positron detector was exposed to decay positrons from a pulsed muon beam with V_{b}=69.7 V and $V_{\text{th}}=-3$ mV, where the dark counts are virtually absent. Fig. 4(a) shows a time spectrum of μ^+–e$^+$ decay events obtained through CH1. The average event rate of this particular run was 0.7 events/pulse. The typical pulse height and width were approximately 5–10 mV and 20 ns, respectively. Prompt peaks observed at the beginning of the spectrum (0–1 μs) are attributed to the in-beam positrons derived from μ^+–e$^+$ decay in the muon production target or in the process

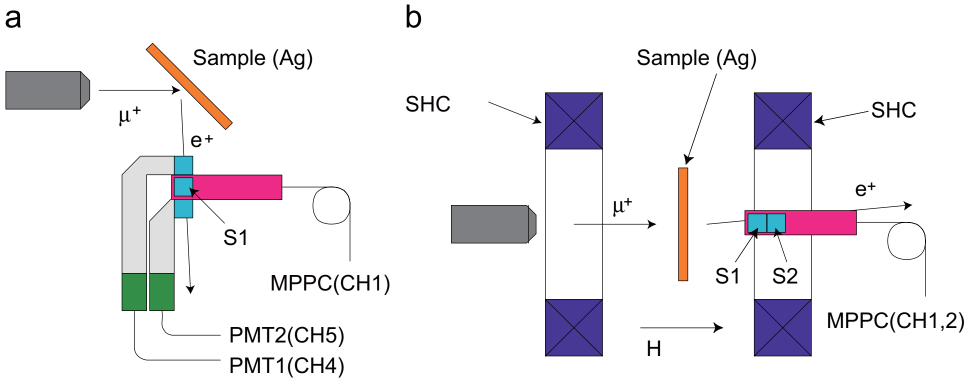

Fig. 2. Schematic drawing of the experimental setup for (a) ZF and (b) HF.

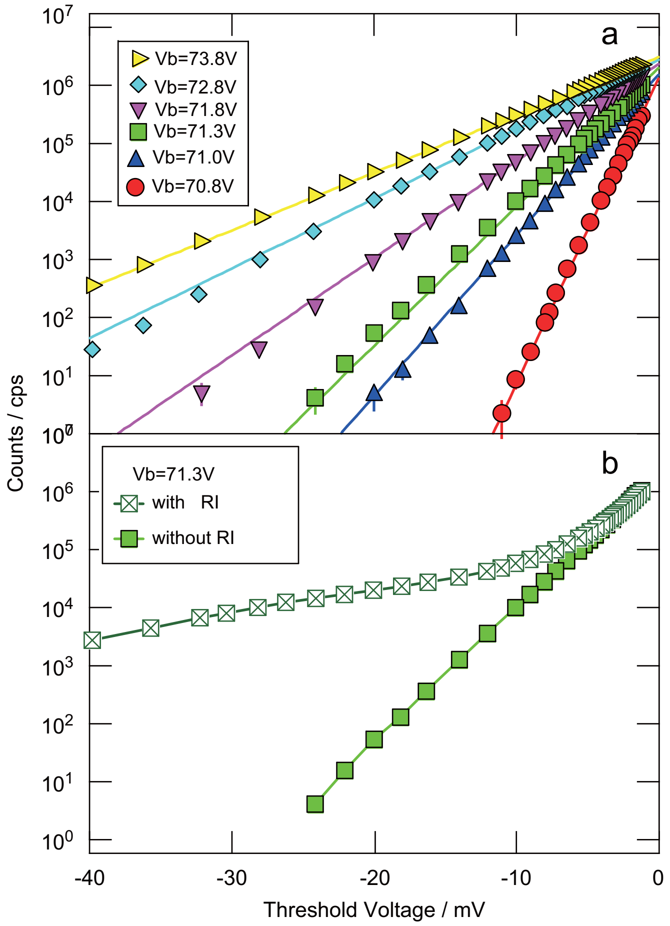

Fig. 3. Threshold voltage dependence of count rate under various bias voltages without (a) and with (b) a checking source (^{90}Sr).

of beam transport. The muon lifetime (τ_μ) deduced by a fit of the spectrum over a time range between 1 and 17 μs is 2.198(4) μs. This is in perfect agreement with the well-established value [2], and thereby demonstrates that the detection system (including TDC) has no appreciable time-dependent distortion.

We also measured the detection efficiency of the positron detector relative to that based on PMT using a geometrical configuration shown in Fig. 2(a). We define the event at PMT1, PMT2, and MPPC1 as $\mathrm{Ev}_{\mathrm{PMT1}}$, $\mathrm{Ev}_{\mathrm{PMT2}}$, and $\mathrm{Ev}_{\mathrm{MPPC1}}$, respectively. The total number of good PMT event N_{good} is defined as $N(\mathrm{Ev}_{\mathrm{PMT1}}$ & $\mathrm{Ev}_{\mathrm{PMT2}})$, where "&" means a logical "AND" (coincidence). This event defines a positron passing through the S1. The total number of good MPPC event N_{MPPC} is described as $N(\mathrm{Ev}_{\mathrm{PMT1}}$ & $\mathrm{Ev}_{\mathrm{PMT2}}$ & $\mathrm{Ev}_{\mathrm{MPPC1}})$. Therefore, the detection efficiency P is described as $P = N_{\mathrm{MPPC}}/N_{\mathrm{good}}$. In this measurement, P turned out to be approximately 57%. This low efficiency might be partly due to the high threshold voltage and associated deterioration of double pulse resolution; enhanced rate of crosstalk and secondary pulses caused by high V_b might have led to the wider signal pulse width, because the output signal is a convolution of these secondary pulses and the original pulse.

3.3. *Test in a high magnetic field*

Fig. 4(b) shows the time spectra of decay positron events obtained at CH1, CH2, and CH3, where the data were collected under a high magnetic field of 3.6 T. The average event rate is 17.6 events/pulse. The typical pulse height and width were approximately 10 mV and 30 ns, respectively. Difference between CH3 and CH1 indicates that positrons coming from the uncorrelated direction are excluded by the telescope configuration of S1 and S2. Some prompt peaks observed at the earlier time region (0–1 μs) may be attributed to the in-beam noise and direct muon hit (as the detector was placed near the beam axis to detect the positrons whose orbits are axially confined by the magnetic field). As inferred from the residual errors shown at the top of Fig. 4(b), a strong deviation from the fitting curve is observed over the early time range of the spectrum (0–5 μs). This distortion may be partially attributed to the high positron event rate and/or the direct hit of muons on the counter, where the latter generates a huge number of photo-electrons and thereby temporally reduces the efficiency of the counter. Smaller scintillation counters to reduce the solid angle and consideration of geometric configuration to avoid direct muon hit are needed to eliminate such distortion.

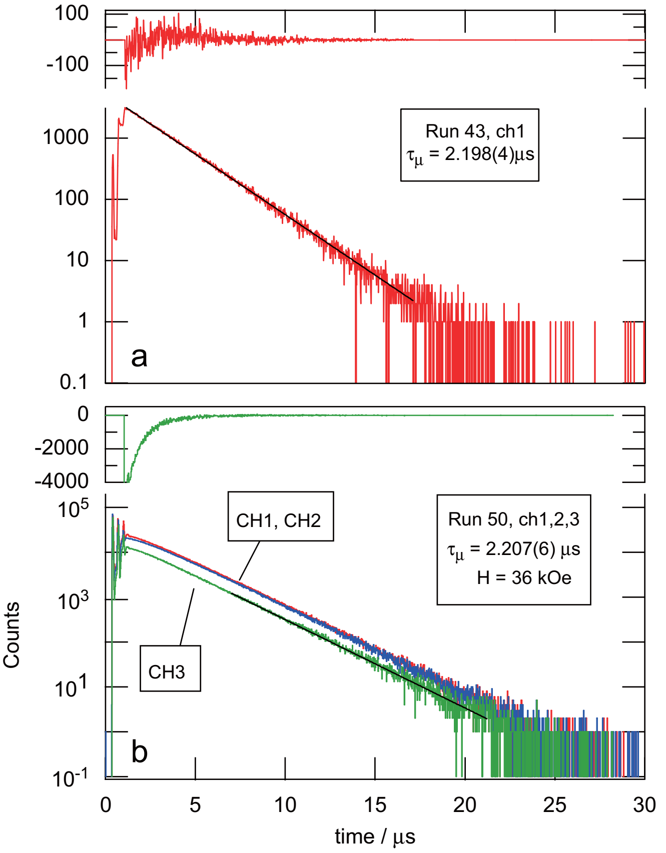

Fig. 4. Time spectra of the decay positron events under (a) ZF and (b) HF. Curves displayed at the top of each graph are residual errors between raw data and fitting curve.

4. Summary

We have designed a positron detector for pulsed μSR based on MPPC and tested it under exposure to β^- ray and μ^+–e^+ decay positrons. In ZF, a nearly undistorted μ^+–e^+ decay time spectrum is observed. The estimated τ_μ is in excellent agreement with the established value. The detection efficiency is estimated to be 57%, which is attributed to enhanced crosstalk and secondary pulse rate with high V_b. While the normal operation of the detector under a high magnetic field of 3.6 T was also confirmed by observations of μ^+–e^+ decay spectra, the spectrum is distorted by high event rate and/or direct muon hit. The present result would be useful for further optimization of MPPC-based positron detectors.

Acknowledgement

The authors would like to thank T. Nakadaira and J. Haba of KEK and D. Tomono of RIKEN for fruitful discussion.

References

[1] S.Y. Suzuki, et al., New pipelined data acquisition system for μSR experiments At J-PARC, Proceedings of IPS08, Nucl. Instr. and Math. A, this issue.
[2] D. Tomono, et al., Nucl. Phys. B 149 (2005) 341.

Nuclear Instruments and Methods in Physics Research A 600 (2009) 146–149

Contents lists available at ScienceDirect

Nuclear Instruments and Methods in
Physics Research A

journal homepage: www.elsevier.com/locate/nima

Present status of construction for the muon target in J-PARC

S. Makimura [a,*], Y. Miyake [a], N. Kawamura [a], P. Strasser [a], A. Koda [a], K. Shimomura [a], H. Fujimori [a], K. Nishiyama [a], M. Kato [a], K. Nakahara [a], R. Kadono [a], Y. Kobayashi [a], J. Sagawa [b], T. Nakamura [c], M. Kaneko [c], H. Ozaki [d], H. Okamura [d], T. Suzuki [d], K. Fujimoto [e], K. Kira [e]

[a] *High Energy Accelerator Research Organization (KEK), 1-1, Oho, Tsukuba, Ibaraki 319-0801, Japan*
[b] *Hitachi Engineering and Services Co., Ltd., 3-2-1, Saiwai-cho, Hitachi, Ibaraki 317-0073, Japan*
[c] *Mirapro Co., Ltd., 1100, Anahira, Sudama, Kitamori-shi, Yamanashi 408-0111, Japan*
[d] *Kinzoku Giken Co., Ltd., 276-21, Motoishikawa, Mito-shi, Ibaraki-ken 310-0843, Japan*
[e] *Hitachi Zosen Co., Ltd., 2-2-11, Funa-machi, Taisho-ku, Osaka 551-0022, Japan*

ARTICLE INFO

Available online 3 December 2008

Keywords:
Muon target
Graphite target
Vacuum chamber
High radiation
Remote control maintenance
High-power target

ABSTRACT

At the J-PARC muon science facility, the most intense pulsed muon beam in the world will be produced by a 3 GeV/1 MW/25 Hz proton beam on a target made of 20-mm-thick, disc-shaped, isotropic graphite (IG-43). The energy deposited by the proton beam is estimated to be 4 kW on the muon target. While the muon target is located in vacuum, the maintenance of the target must be performed from the maintenance area, which is located 4 m above floor level. In addition, a plug shield is required between the primary proton beam and the maintenance area for radiation shielding. Therefore, a huge vacuum chamber was fabricated so that the muon target and two scrapers, which are positioned downstream of the muon target for proton collimation, could be included. As the muon target and the scrapers will be highly irradiated, the replacement of these components must be performed in a remote handling room. The irradiated components will be transported to the remote handling room inserted into a shielding vessel, called the Muon Transfer Cask, which has a remote controlled gripper. In this paper, the present status of the construction for the muon target station, namely the muon target, the muon target chamber, and the muon transfer cask, will be described.

1. Introduction

At the J-PARC muon science facility, the most intense pulsed muon beam in the world will be produced by a 3 GeV/1 MW/25 Hz proton beam on a target made of 20-mm-thick, disc-shaped, isotropic graphite (IG-43). The energy deposited by the proton beam is estimated to be 4 kW on the muon target by PHITS [1]. Using the results obtained by PHITS, temperature distribution and the thermal stress are evaluated. Graphite will experience a dimensional change due to proton irradiation. Consequently, the lifetime of the muon target will be determined by the radiation damage of graphite. Fig. 1 shows a picture of the muon target. In Section 2, the simulation of the muon target and the actual fabrication will be described.

The muon target is located in a vacuum chamber. As a plug shield of about 2-m high is required between the primary proton beam and the maintenance area for radiation shielding, the chamber must be huge. Therefore, the positioning method of the muon target must be carefully conceived. Furthermore, the pressure of the chamber and the maintenance of the target by remote handling had to be considered. In Section 3, the design of the muon target chamber will be introduced.

In the primary proton beamline, some of the components will be so highly irradiated that hand-on maintenance cannot be performed. Therefore, the irradiated component will be inserted into a shielding vessel, called the "Muon Transfer Cask". In Section 4, the muon transfer cask will be described.

2. Muon target

2.1. Simulation of thermal stress and radiation damage by FEM

As the target is located in a vacuum chamber, almost all of the heat must be removed by the cooling water through the stainless steel tube embedded in the copper frame. Considering the thermal conductivity of graphite under neutron irradiation [2], the maximum temperature of graphite (at the target centre) reaches up to 1500 °C according to an analysis by the finite element method (FEM). Then, the thermal stress was evaluated. If the copper frame is just placed around the graphite target, the stress on graphite is very close to the strength of graphite itself.

---

[*] Corresponding author. Tel.: +81 29 284 4723 ; fax: +81 29 284 4878.
E-mail address: shunsuke.makimura@kek.jp (S. Makimura).

0168-9002/$ - see front matter © 2008 Elsevier B.V. All rights reserved.
doi:10.1016/j.nima.2008.11.110

Therefore, in order to absorb the thermal stress, a titanium layer is adopted as an intermediate material between the graphite target and the copper frame. Titanium has a thermal expansion coefficient just in between graphite and copper. Table 1 shows the calculated stress on the graphite target without and with a 2-mm titanium layer as a stress absorber. In case the thickness of the titanium layer is 2 mm, the maximum compressive stress is 42 MPa (compared with a strength of 90 MPa), and the tensile stress is 8 MPa (compared with a strength 37 MPa). Fig. 2 shows the distribution of the maximum principal stress (S1) and the minimum principal stress (S3) in case the thickness of the titanium layer is 2 mm [3].

Then, the issue from the dimensional change of graphite by radiation damage is described. The dimension of graphite will be dramatically reduced under neutron irradiation [4]. It will shrink by 1% per dpa. As the graphite will shrink almost proportionally with the radiation dose, the graphite on the beam spot will shrink much more than the rest of the graphite. Therefore, a large stress will take place in the vicinity of the beam spot. Through a FEM, 39 MPa of tensile stress, which is beyond the tensile strength of 37 MPa, will occur after half a year at 1 MW beam operation.

Fig. 1. A picture of the fabricated muon target.

Table 1
The stress on graphite without and with a 2-mm titanium layer.

	Strength	No Ti	Ti 2 mm
Temperature (°C)		1460	1490
Tensile stress (MPa)	37	35	8
Compressive stress (MPa)	90	40	42

As a reference, the strengths of graphite are also shown.

2.2. Fabrication of the muon target

At first, the target frame will be fabricated using copper parts with a stainless steel tube embedded for water cooling by a Hot Isostatic Press (HIP) method, which gives high temperature and high pressure simultaneously. It was experimentally confirmed that stainless steel and copper can easily be bonded; however, it was difficult to bond copper together. Therefore copper parts with nickel coating are utilized for the fabrication of the copper frame. Then the copper frame, the titanium ring, and the graphite disc are bonded by silver brazing. In general, graphite is known to be difficult to be brazed because the low wetting of graphite disturbs the capillarity, and the brazing material cannot easily permeate the gap. Hence we used a special silver brazing material (76Ag/22Cu/2Ti) for the metallization of graphite. The bonded interface was confirmed by bending tests.

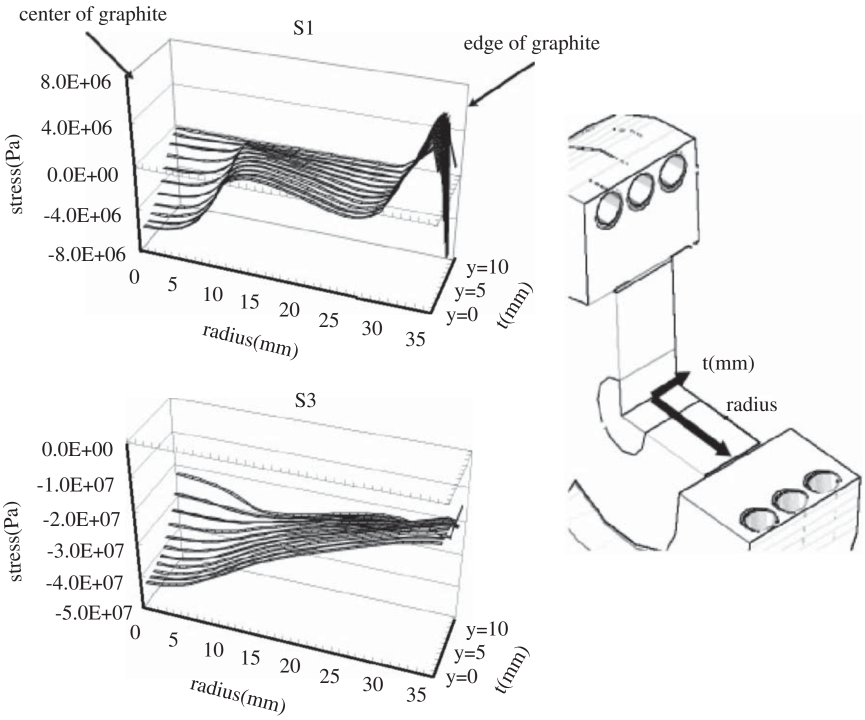

Fig. 2. The distribution of the maximum principal stress (S1) and the minimum principal stress (S3). The thickness of the titanium layer is 2 mm.

3. Muon target chamber

In the M2 tunnel, the maintenance of the components must be performed from the maintenance area, which is located 4 m above the floor level. Therefore, the boundary of the vacuum, the feedthrough for the signal cables, the thermo-couples, the motion drive, and so on must be positioned at the maintenance area. In addition, a plug shield is required between the primary proton beam and the maintenance area for radiation shielding. Fig. 3 shows a picture of the muon target chamber. Downstream of the muon target, two pairs of scrapers will collimate the scattered proton beam. The plug shields of the muon target and the scrapers have adjustable female guides, while the chamber has male guides. The muon target and the scrapers can be positioned with 0.5-mm precision against the beam axis.

As the muon target, which has to be replaced twice a year at full beam operation, will be highly irradiated, the target assembly is disassembled into a plug shield and a target rod in the remote handling room. The vacuum connections of the muon target chamber in the M2 tunnel are performed by pillowseals, which are remotely controlled by compressed air. The leak rate of the pillowseal of the muon target chamber was $10^{-9}\,\mathrm{Pa\,m^3/s}$. The outgassing rate of the chamber itself was measured to be $10^{-7}\,\mathrm{Pa\,m^3/s/m^2}$. An overall pressure of $10^{-5}\,\mathrm{Pa}$ was achieved in the beamline.

4. Muon transfer cask

In the M2 tunnel, the irradiated component will be inserted into a shielding vessel, called the “Muon Transfer Cask”. The muon target, the monitor, the scraper, and the pillowseal can be transported by the muon transfer cask. The maximum weight of the handled component is 6 tons for the scraper. When the muon transfer cask is installed on the beamline, the cask base will be set at a floor level of 6 m on the steps that are used for the M2 tunnel ceiling shield blocks. The gripper can catch a component and hang it into the muon transfer cask. After temporary storage in the storage pod, it will be transported to the remote handling room, and handled by the remote handling devices. Fig. 4 shows the muon transfer cask installed on the beamline over the muon target.

The up–down motion and the catch–release motion are performed just by two chains. The two chains are hung by two gear wheels, which can be independently moved in the vertical direction. When a component is lifted or lowered, both chains are wound or unwound, respectively. On the other hand, when a component is gripped or released, the two gear wheels are vertically moved in opposite directions, so as to open or close the hook. Fig. 5 shows the schematic view of the gripper. The weight of the component is measured by two load cells, which are fixed under the two gear wheels. The position of the component is

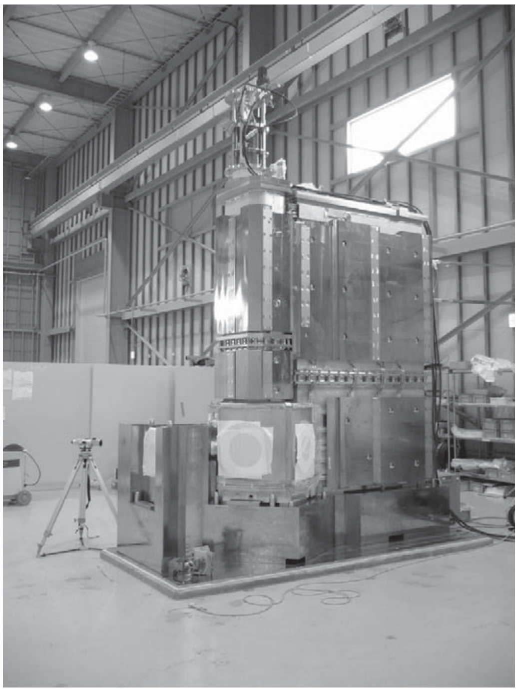

Fig. 3. Muon target chamber.

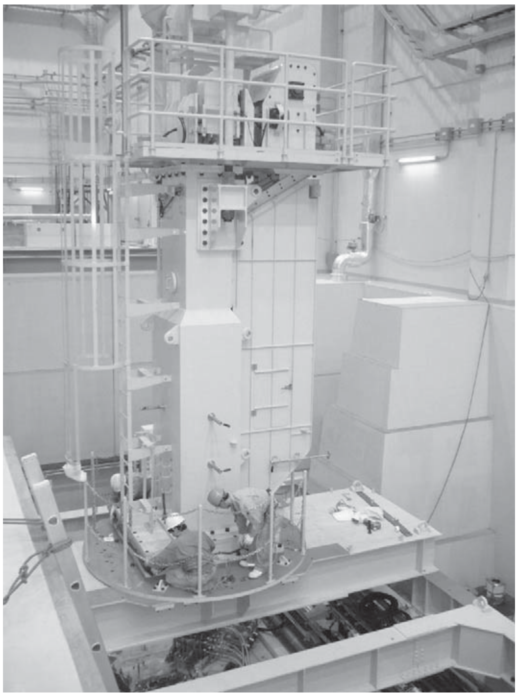

Fig. 4. The Muon Transfer Cask on the beamline over the muon target.

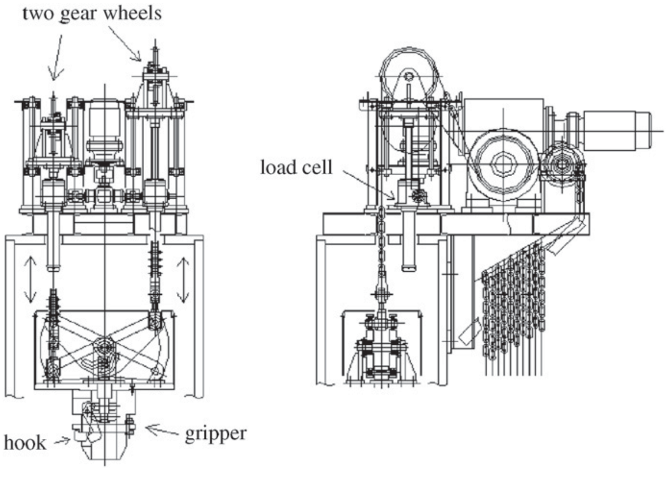

Fig. 5. Schematic view of the gripper.

measured by the encoder of the up–down motor. The gripper can catch or release only when there is no weight measured by the load cells and the component is in the appropriate position. During the up–down motion, any error from an overload, an underload, and an unbalanced load are carefully monitored.

The hanging test of all the components by the muon transfer cask was successfully performed in the MLF building.

References

[1] H. Iwase, K. Niita, T. Nakamura, J. Nucl. Sci. Technol. 39 (2002) 1142.

[2] T. Maruyama, M. Harayama, J. Nucl. Mater. 195 (1992) 44.

[3] S. Makimura, Y. Miyake, K. Nishiyama, K. Nagamine, Design of Muon Target at J-PARC, in: Proceedings of the 14th Symposium on Accelerator Science and Technology, Tsukuba, Japan, 2003, pp. 22–24.

[4] H. Matsuo, graphite1991 [no. 150], pp. 290–302.

Nuclear Instruments and Methods in Physics Research A 600 (2009) 154–156

Contents lists available at ScienceDirect

Nuclear Instruments and Methods in
Physics Research A

journal homepage: www.elsevier.com/locate/nima

Alignment and shields in the M2 primary proton beamline at J-PARC

P. Strasser [a,b,]*, Y. Miyake [a,b], N. Kawamura [a,b], S. Makimura [a,b], K. Nishiyama [a,b]

[a] Muon Science Laboratory, High Energy Accelerator Research Organization (KEK), 1-1 Oho, Tsukuba, Ibaraki 305-0801, Japan
[b] Muon Section, Material and Life Science Division, J-PARC Center, 2-4 Shirane Shirakata, Tokai-mura, Naka-gun, Ibaraki 319-1195, Japan

ARTICLE INFO

Available online 3 December 2008

Keywords:
Alignment
Radiation shield

ABSTRACT

In the J-PARC project, the 3-GeV 333-μA proton beam will be transported from the 3-GeV ring to the neutron source located in the Materials and Life Science Facility. In the M2 tunnel, where the muon target is situated, the radiation level is expected to reach up to 20 MGy/y. Therefore, beamline components will need to be installed and aligned remotely from the maintenance area, which is located 4 m above the floor level. We have adopted alignment plates with pivots to position each component precisely in the beamline. Then, by using the surrounding iron shields as guides, a beamline component can be smoothly inserted and precisely aligned onto its alignment plate. In this paper, the alignment strategy used in the M2 tunnel is described.

1. Introduction

In the J-PARC (Japan Proton Accelerator Research Complex) project, the 3-GeV 333-μA proton beam will be transported from the 3-GeV ring to the neutron source situated in the Materials and Life Science Facility (MLF). There, in the M2 primary proton beamline (M2 tunnel) just 33 m upstream of the neutron source, the muon target is located, which is the core of the J-PARC Muon Science Facility (MUSE) [1]. In the M2 tunnel, the radiation level is expected to reach up to 20 MGy/y at 1 MW beam operation. Therefore, beamline components, such as magnets, beam profile monitors, pillowseals, vacuum beam ducts, and so forth, will need to be installed and aligned remotely from the maintenance area, which is located 4 m above the floor level. We have adopted alignment plates with pivots located 990 mm below the beam level to position each component precisely. Then, by using the surrounding iron shields as guides, a beamline component can be smoothly inserted and precisely aligned onto its alignment plate. The required accuracy for the installation of the magnets was typically ±0.5 mm at the beam center and along the beam axis, which is determined by the beam transport. Other beamline components might require a lower accuracy.

2. Alignment plates

Fig. 1 shows the layout of the alignment plates in the M2 tunnel. They are made of 45-mm-thick iron plates (SS400). The thickness of each alignment plate was determined after measuring the level of the base plates that were installed in the M2 tunnel one and a half years earlier. A level difference of 2 mm was observed along the proton beamline due to ground settlement during the early phase of the building construction. In March 2006, a total of 40 alignment plates were installed (see Figs. 2 and 3). The level of each plate was adjusted using shims with a precision of ±0.1 mm, and positioned using a laser tracker with an accuracy of better than ±0.2 mm. The horizontal (*X*/*Y*) position of the alignment plates is not expected to change significantly with time, since they are firmly fixed onto 70-mm-thick iron base plates. However, due to the ground settlement in the MLF building, the level of the alignment plates might change. For that reason, the height of each beamline component can be later adjusted by ±10 mm using shims fixed at the bottom of the component with 0.5 mm steps. The pivots of the alignment plates are made of nickel-plated S45C steel 50 mm in diameter. The counterpart holes at the bottom of the component are made of a circular hole and an elongated hole, respectively, preventing pivots from getting stuck. The first hole precisely defines the *X*/*Y* position of the component and the second hole its direction.

3. Guide shields

In the M2 tunnel, the amount, the arrangement and the material of the radiation shield has been carefully evaluated and optimized [2]. The radiation shield around the muon target and in

---

*Corresponding author at: Muon Science Laboratory, High Energy Accelerator Research Organization (KEK), 1-1 Oho, Tsukuba, Ibaraki 305-0801, Japan.
Tel.: +8129 864 5603; fax: +8129 864 5623.
E-mail address: patrick.strasser@kek.jp (P. Strasser).

0168-9002/$ - see front matter © 2008 Elsevier B.V. All rights reserved.
doi:10.1016/j.nima.2008.11.112

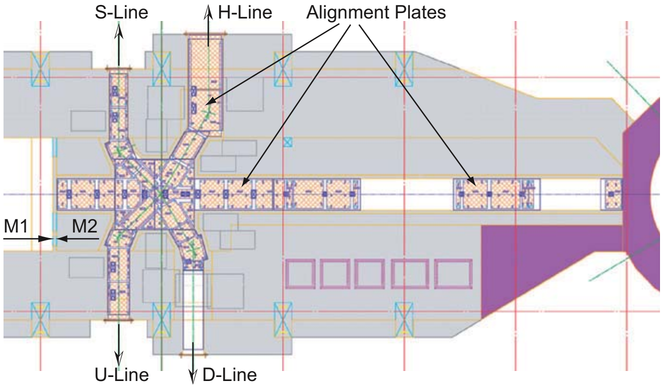

Fig. 1. Layout of the alignment plates in the M2 tunnel.

Fig. 2. Alignment plate with pivots used to position and align beamline components.

Fig. 3. View of the alignment plates installed in the M2 tunnel around the muon target area.

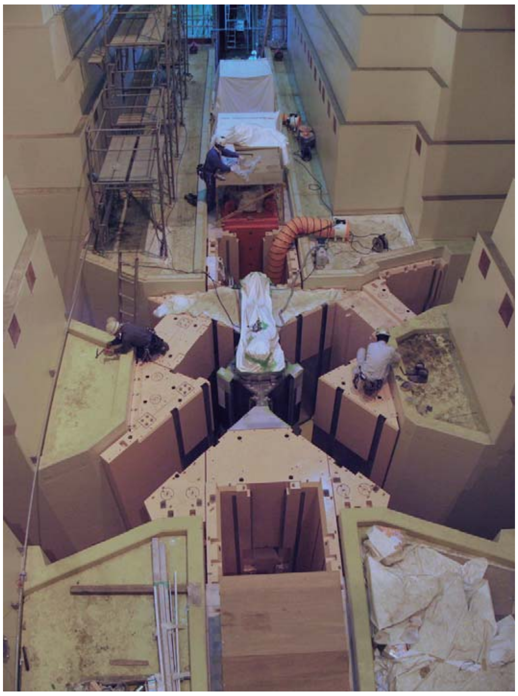

Fig. 4. Guide shields installation around the muon target area in the MLF building.

the primary proton beamline is mainly made of iron. Each iron shield in the M2 tunnel was also positioned using alignment plates, and then fixed to the tunnel wall using embedded tapped holes. Very large iron shields were fabricated by casting, while thinner ones were manufactured directly from iron slabs (SS400). The gap between each iron shield is about 10 mm. Then, a beamline component can be smoothly inserted using the surrounding iron shields as guides (i.e., guide shields) and precisely aligned onto the alignment plate by the pivots. Fig. 4 shows the guide shields installed around the muon target area. The magnets for the primary proton beamline and the secondary muon channels are just waiting to be installed. The iron shields are coated with epoxy painting. However, the triangular guide shields, which are located downstream of the muon target, were covered with stainless-steel (SUS) lining at a height of ±1 m from the beam level to avoid paint deterioration due to the high radiation field around the muon target. The vertical stripes on the shields around the muon target in Fig. 4 are SUS female guide used to insert magnets. The counterpart male guides with bearings are attached on each magnet. After the installation of a component, iron lids, 190-mm-thick around the target area and 100-mm-thick elsewhere, cover the remaining gaps between the iron shields and the different components.

4. Beam duct assembly

There are three vacuum beam duct sections in the M2 primary proton beamline connecting magnets. All the vacuum connections in the M2 tunnel are performed using pillowseals, which are remotely controlled by compressed air [3]. The pillowseals and the beam ducts were also installed and positioned using pivots. The required accuracy is not as severe as with other beamline components, such as magnets. Indeed, the KEK-MSL model pillow seal is able to seal two flanges even if they are misaligned by ±5 mm with respect to the beam center, ±5 mm along the beam axis, and if the two flange surfaces have an angle up to 10 mrad. The beam duct is attached using SUS supports to the bottom of a 250 mm iron slab connected to a 2-m-high concrete block. The beam duct height can be adjusted by ±10 mm using shims fixed between the duct support and the iron slab with 0.5 mm steps.

Fig. 5. Beam duct assembly for the M2 primary proton beamline.

This particular design provides an easy access to the beam duct for later height adjustment, or replacement if the flanges of the beam duct become damaged. Fig. 5 shows a beam duct assembly being installed on the primary proton beamline. Two kinds of pivot are used to position precisely the beam duct assembly in the beamline. At first, a large SUS pivot, 100 mm in diameter, is used to guide the assembly onto a normal pivot that will perform the final positioning.

5. Secondary muon channels

There are four secondary muon channels that are originating from the muon target in the M2 tunnel, namely the decay muon channel (D-line), the surface muon channel (S-line), the ultra-slow muon channel (U-line), and the high-momentum muon channel (H-line). At present, only the decay muon channel is under construction [4,5]. The other three secondary muon channels that will not be operational on day one were temporarily closed with iron shields and concrete blocks. In the M2 tunnel, iron shields were installed around the muon target in the U-line and the H-line. The iron shield that is directly facing the muon target chamber has a blank flange attached to it to close the vacuum of the primary beamline. In addition, the first two iron shields in the H-line are also water-cooled, since they are located downstream of the muon target and that the energy deposited by the scattered proton beam is expected to be large. Only in the S-line, the actual front magnets could be manufactured and are already installed. Then concrete blocks with crank shapes were used to close the exit of the remaining empty secondary muon channels inside the M2 tunnel. At the tunnel exit of the secondary muon channel, where there is no crane access, the concrete blocks were installed using a forklift from the experimental hall. Fig. 6 shows the concrete blocks being installed in the exit of the H-line. The two secondary muon channels in the M1 tunnel, which are located about 16 m upstream of the muon target in the M2 tunnel, were also temporarily closed with concrete blocks. The M1 tunnel is the location for a second muon target station for future development.

Fig. 6. Installation of the temporary concrete blocks in the exit of the secondary muon channel (H-line) that will not be operational on day one: with a crane inside the M2 tunnel (above) and with a forklift from the experimental hall (below).

The exit of the M1-West secondary muon channel was closed similarly to the H-line. Only at the exit of the M1-East secondary muon channel, a large concrete block was installed using rollers (Tirtank) because of the limited space available under the power supply yard.

6. Concluding remarks

The result of error of alignment is difficult to quantify, since once the beamline components are installed, there is not enough space to perform an accurate measurement. The few measurements that were performed are however consistent with the required accuracy of ± 0.5 mm. The achieved vacuum of 3×10^{-5} Pa in the beamline mainly results from outgassing of the surface of the beam ducts and the target chamber. The effects due to the pillow seal leak rate of $1\times10^{-8}\,\mathrm{Pam^3/s}$ and the alignment accuracy of the beam duct are negligible.

References

[1] Y. Miyake, et al., Nucl. Instr. and Meth. A, these proceedings.
[2] N. Kawamura, et al., Nucl. Instr. and Meth. A, these proceedings.
[3] N. Satou, et al., Fabrication of KEK-MSL Model Pillowseal, in: Proceedings of the 4th Annual Meeting of Particle Accelerator Society of Japan and the 32nd Linear Accelerator Meeting in Japan, 1–3 August 2007, Wako, Japan, pp. 838–840.
[4] K. Shimomura, et al., in: AIP Conf. Proc. 981 (2008) 381.
[5] K. Shimomura, et al., Nucl. Instr. and Meth. A, these proceedings.

Nuclear Instruments and Methods in Physics Research A 600 (2009) 170–172

Contents lists available at ScienceDirect

Nuclear Instruments and Methods in Physics Research A

journal homepage: www.elsevier.com/locate/nima

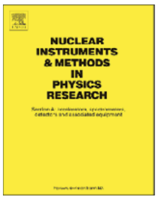

Radiation resistant magnets for the J-PARC muon facility

Hiroshi Fujimori [a,*], Naritoshi Kawamura [a], Shin-Ichiro Meigo [b], Patrick Strasser [a], Kazutaka Nakahara [a], Yasuhiro Miyake [a]

[a] *J-PARC Center KEK, Tsukuba, Ibaraki 305-0801, Japan*
[b] *J-PARC Center Japan Atomic Energy Agency, Tokai, Ibaraki 319-1195, Japan*

ARTICLE INFO

Available online 27 November 2008

Keywords:
Magnet
Muon
M2 line
Radiation resistance
MIC
OPERA-3D simulation

ABSTRACT

At J-PARC, the M2 line will become a high radiation area with a large amount of radiation originating from the muon production target. Therefore, for the magnets near the muon target, radiation resistance conductor, that is, mineral insulation cable (MIC), was used. Above the saturated magnet yoke, iron radiation shields are installed. Therefore, a careful study of the effects of shielding on the magnetic fields is performed through a non-linear 3D simulation (OPERA-3D).

1. Introduction

At the Japan Proton Accelerator Research Complex (J-PARC), a 3-GeV proton beam is extracted from the Rapid-Cycling Synchrotron (RCS) and transported through the 3-GeV to Neutron Beam Transport (3NBT) line [1] to the Materials and Life Science Facility (MLF). The beamline in MLF is divided into two sections. One is the M1 line where a second muon production target can be installed in the future, and the other is the M2 line, which extends from the existing muon production target to the neutron source. The magnets in the M2 line are divided into two categories as shown in Fig. 1; the magnets along the primary line guiding the proton beam to the neutron source, and those installed around the muon production target to extract the secondary muons to the experimental halls. The M2 line will become a high radiation area with a large amount of radiation originating from the muon production target. Therefore, for the magnets near the muon target, we adopted either hollow conductor MIC or solid conductor MIC. The utilities (electrical power and cooling water) for the magnets are connected at the maintenance area, 4 m above floor level (FL+4 m), i.e., 2.4 m above the beamline level (FL+1.6 m), with no existing joints or connectors below this area. In the case of magnet replacement due to a failure, replacement work can be performed remotely. Above the magnet yoke, iron radiation shields (plug shields) are installed, and thus access to the maintenance area becomes possible during shutdown periods. These plug shields inevitably affect the magnetic field distribution. Therefore, a careful study of the effects of shielding on the magnetic fields is performed through a non-linear 3D OPERA simulation.

2. Material of magnet-coils and maintenance

Due to the large beam loss of approximately 60 kW expected near the muon production target on the M2 line, the magnets were designed to withstand high levels of radiation. The coils, therefore, were wound with direct water-cooled MIC (hollow MIC—Hitachi Co.) for QN1-3 and XY22 in the primary line and indirect water-cooled MIC (solid MIC—Hitachi Co.) for SQ1-3 in the surface muon line as shown in Fig. 2. On the other hand, direct water-cooled mineral insulation cables (made in Russia) were used for DQ1-3 in the decay muon line. The specification of a direct water-cooled MIC (hollow MIC—Hitachi Co.) is presented in Table 1.

Although each pole of the quadrupole magnet (Q2690MIC), installed on the primary beamline, requires 188 m of MIC cables, the maximum length of these MIC cables is 60 m, as can be seen in the above table. Therefore, each pole is constructed by connecting four individual pancakes. The beamline level (FL+1.6 m) will be a high radiation area, so radiation shielding is placed on top of the magnet such that maintenance can be performed on the FL+4 m area during shutdown periods. Therefore, all electrical and water connections are made on the FL+4 m area, with no connections below this area. While the electrical connections of the four pancakes are in series, the water connections are made to be parallel. A total of 16 parallel water paths (Fig. 3) are used for each magnet to keep the temperature rise to below 25 °C. Furthermore, the pressure gauges as well as the temperature switches are

---

*Corresponding author. Tel.: +81 29 284 4506; fax: +81 29 284 4878.
E-mail address: fujimori@post.kek.jp (H. Fujimori).

0168-9002/$ - see front matter © 2008 Elsevier B.V. All rights reserved.
doi:10.1016/j.nima.2008.11.025

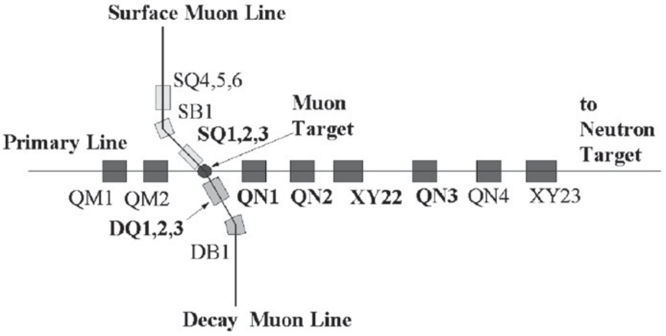

Fig. 1. Outline of the M2 line.

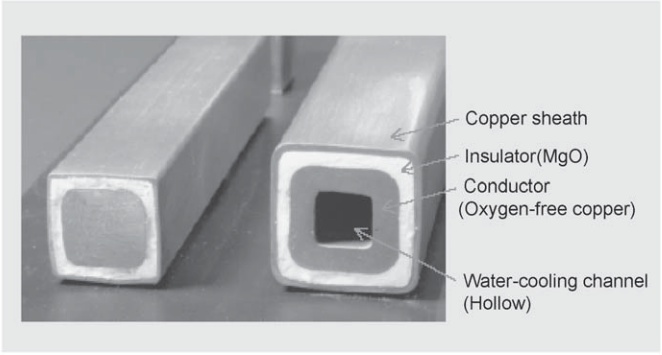

Fig. 2. Solid MIC—Hitachi Co. (left) and hollow MIC—Hitachi Co. (right).

Table 1
Specification of hollow MIC (MIHC-2000A-H).

Copper sheath	Size	19.8 mm
	Thickness	0.9 mm
Insulator	Size	18.0 mm
	Thickness	1.75 mm
Copper conductor	Size	14.5 mm
	Thickness	3.6 mm
Conductor cross section		149.0 mm^2
Hollow area		53.1 mm^2
Unit weight		2.201 kg/m
Available length		60 m

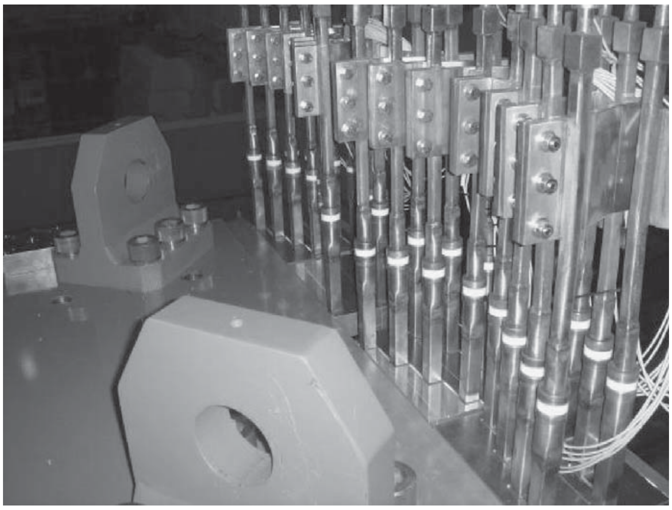

Fig. 3. Connectors: electrical cables are connected in series, while the water coolants are separated into 16 parallel lines (FL+4 m).

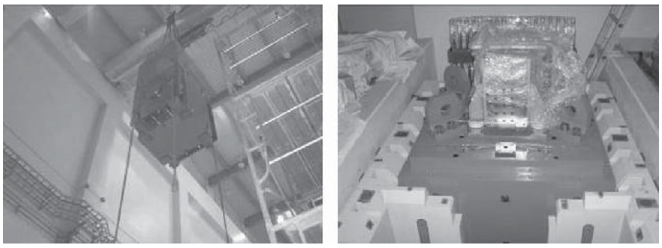

Fig. 4. Lifting (left) and placing (right) the QM1 magnet on the primary line.

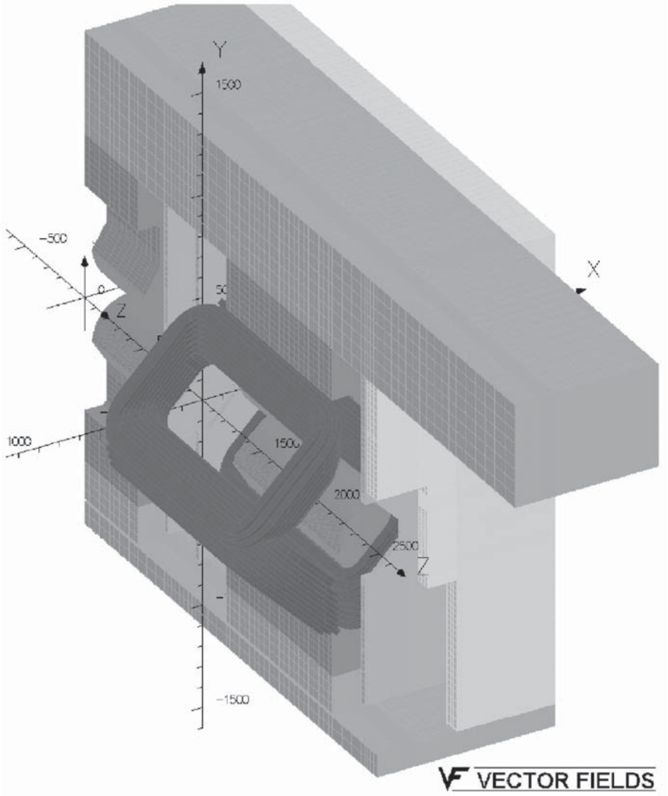

Fig. 5. The simulated model used to analyze the quadrupole magnets on the primary line.

placed on FL+4 m, allowing for maintenance/replacement in the event of malfunctions.

The magnets placed on the M2 line are all compartmentalized such that in the event of malfunctions, the electrical cables and the coolant joints can be disconnected so that the magnet, together with the plug shields, can be lifted out of the beamline and replaced. The efficiency and feasibility of the replacement process has been tested (as seen in Fig. 4) through the use of the floor pivots and the guide-rails place on the beamline walls. By lifting the magnet (together with the plug shields) with a crane and lowering it by sliding it along the guide-rails, it can be placed on top of the floor pivots, allowing for an alignment tolerance of less than 0.5 mm. The vacuum duct inserted within the magnet can be sealed with a remotely detachable Pillowseal [2].

3. Field analysis and field quality

The field distributions of the quadrupoles on the primary line are heavily affected by the saturation of the poles as well as the plug shields. Furthermore, due to the large aperture

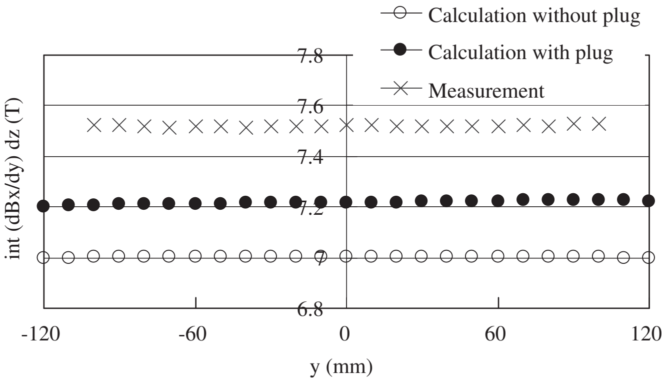

Fig. 6. Comparisons between the calculated and measured values (GL-integrated values of the Bx component).

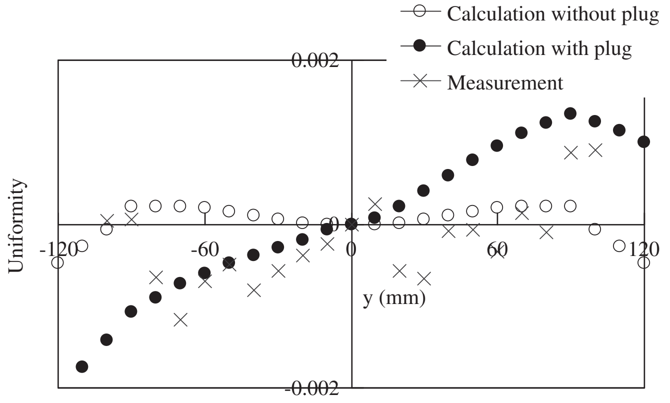

Fig. 7. Comparison between calculated and measured values (uniformity of GL-integrated values).

Table 2
Specifications of the magnets placed on the primary beamline.

Coil	Unit	QN1-3 MIC	QM1-2 QN4 Polyimide	XY22 MIC	XY23 Polyimide
Field or gradient	T, T/m	7.93	7.93	0.096	0.13
Bore	mm	260	260	260	260
Pole length	mm	900	900	400	300
Pole width	mm	262	262	270	270
Field uniformity[a]		$<3\times10^{-3}$	$<3\times10^{-3}$	$<3\times10^{-2}$	$<3\times10^{-2}$
Winding turn/pole	Turn	49	95	12	36
Flow	L/min	130	63	6.2	3.7
Current	A	1098	566	520	200
Voltage	V	105	125	4.4	7
Weight	Ton	37.4	37.1	56.9	56.1
Number		3	3	2	2

The weight of the XY22 and the XY23 are the combined weights of the X and Y correctors.

[a] In the region of ±120 mm.

(260 mm diameter), the effect of fringe fields due to nearby magnets was expected [3]. Therefore it is necessary to use a realistic model to calculate the field distribution. The model can be seen in Fig. 5.

In order to maintain as much symmetry in the fields as possible, magnetic shielding was placed below the magnet in order to balance out the effects of the plug shields. Additional shielding was installed to reduce the effects of adjacent magnets. Iron was used in locations where magnetic flux tends to concentrate, while SS400 is used for other locations to reduce cost. Field distributions were optimized through the use of shims.

At TOKIN Machinery, a hall probe was used to compare the measured and calculated values (GL integration of the Bx component and uniformity of GL-integration), as can be seen in Figs. 6 and 7. The effects of the plug shields can be also seen in them. The measured GL-integrated value [4] is larger due to the fact that the calculated values have the effects of adjacent magnets included. The fringe fields along the beamline are causing the difference between the measured and calculated values.

Although the insertion of the plug shields reduces field saturation, strengthening the fields, the Bx component becomes asymmetric. However, the no asymmetry in the By component can be seen.

While the measured fields have some spread, the measured field uniformity was seen to be better than what was calculated as seen in Fig. 7. The beam optics requirements have been met.

Meanwhile, the corrector magnets are created as a doublet (X,Y) which uses a common set of plug shields and beam duct. Currently, of the 18 magnets placed in the M2 line, 10 along the primary beamline have been tested at their respective nominal operating currents. The specifications of the magnets on the primary beamline can be seen in Table 2.

4. Summary

- On the muon beamline, magnets placed in high radiation areas will use MIC cables, and will be capable of remote-replacement. Furthermore, gauges and connectors that maybe susceptible to radiation damage will be placed on the FL+4 m level where maintenance is possible.
- In designing the magnets, simulated models were created to optimize the asymmetry in the field distribution. In addition to satisfying the optical requirements, comparisons with the measured values showed satisfactory results.
- All the magnets on the M2 line (primary line: six quadrupole magnets, two sets of XY corrector magnets; secondary line: two sets of quadrupole triplets, two bending magnets) were constructed and placed on the beamline by NEC/TOKIN (TOKIN Machinery).

References

[1] H. Fujimori, M. Harada, T. Kai, N. Kaneko, Y. Kasugai, C. Konno, S.-I. Meigo, S. Muto, S. Sakamoto, Accelerator Technical Design Report for J-PARC (3.2.5 Beam Transport Components to Neutron and Muon Production Targets), KEK Report 2002-13, JAERI-Tech 2003-044, J-PARC 03-01, March 2003, pp. 463–484.

[2] N. Satou, S. Makimura, P. Strasser, A. Koda, Y. Miyake, N. Kawamura, K. Ueno, H. Fujimori, K. Shimomura, K. Nishiyama, Fabrication of KEK-MSL Model Pillowseal, in: Proceedings of the Fourth Annual Meeting of Particle Accelerator Society of Japan and the 32nd Linear Accelerator Meeting in Japan, Wako, Japan, 2007.

[3] M.J. Shirakata, H. Fujimori, Y. Irie, Beam Tracking in the 3D distributed magnetic Fields, in: Proceedings of SAST 2003, November 2003, pp. 389–391.

[4] H. Fujimori, et al., Optimization of the field uniformity for large aperture magnets at the J-PARC 3 GeV Beam Transport-line (3NBT), in: Proceedings of the Third Annual Meeting of Particle Accelerator Society of Japan and the 31st Linear Accelerator Meeting in Japan, 2–4 August 2006, Sendai, Japan.

Nuclear Instruments and Methods in Physics Research A 600 (2009) 179–181

Contents lists available at ScienceDirect

Nuclear Instruments and Methods in Physics Research A

journal homepage: www.elsevier.com/locate/nima

J-PARC muon control system

W. Higemoto [a,*], K. Shimomura [b], Y. Kobayashi [b], S. Makimura [b], Y. Miyake [b], T. Kai [a], K. Sakai [a]

[a] *Japan Atomic Energy Agency, Ibaraki 319-1195, Japan*
[b] *High Energy Accelerator Research Organization, Ibaraki 305-0801, Japan*

ARTICLE INFO

Available online 27 November 2008

Keywords:
Muon science
Control system
Interlock

ABSTRACT

At the J-PARC MLF muon science facility (MUSE), muon experimental instruments are operated by means of a Muon Control System. The following are subject to the Muon Control System: (1) Muon production target and the beam scrapers, (2) M1/M2 line air-conditioning system, (3) Cryogenic system for the superconducting solenoid magnet, (4) Muon secondary line vacuum system, (5) Muon secondary line magnets, and (6) Muon beam blockers and related safety instruments. Details of the muon control system are described below.

1. Introduction

At the J-PARC materials and life science facility (MLF) muon science facility (MUSE), muons are utilized in various fields of science. At MUSE, a pion is generated at the graphite target after being struck by a 1 MW 3 GeV proton beam, and the pion immediately decays to become a muon. The muons are collected and an intense, pulsed muon beam is delivered to the muon experimental ports. When operations at MUSE first started, only one decay/surface muon line and two experimental ports were constructed at MLF Experimental Hall No. 2.

To ensure the safe operation of MLF-MUSE, a number of safety systems have been incorporated into the system. For example, to prevent users from being exposed to excess dosage of radiation, entry to experimental ports is strictly controlled. In addition, proper and safe operation of the machines is also necessary. To ensure this, all muon experimental instruments are controlled by means of the Muon Control System. The purpose of the Muon Control System is to control and monitor the safe operation of all muon instruments.

2. The muon control system and the MLF general control system

The muon control system manages: (1) muon target and scrapers, (2) the air-conditioning system for the M1 and M2 beam line, (3) cryogenic operation system for the superconducting solenoid magnet at the decay/surface muon line, (4) muon secondary line vacuum system (5) muon secondary line beam magnets and (6) muon blockers and entry system for the experimental ports. Most of the subsystems are constructed as local control systems. At the same time, operating information is automatically recorded and stored by the MLF General Control System (MLF-GCS). The MLF-GCS consists of three layers: the PLC link layer, the server layer, and the network layer. The PLC link layer controls the subsystems in MLF; the server layer acquires, stores and distributes data, mediating the PLC link layer. The network layer exchanges information with the central control room (CCR), other facilities and users. The muon control system is linked to the PLC link layer as "Local Instruments." At the PLC link layer, "MELSEC-NET" is used as a PLC link network. Thus, most of the muon control system is connected to the MLF-GCS via MELSEC-NET. Event information is recorded and stored on the MLF database by means of SCADA software.

3. Interlock systems

MLF interlocks consist of several categories: PPS (personal protection system), MPS (machine protection system), TPS (mercury target protection systems), and other interlock systems. The PPS is in place to prevent personnel from being exposed to high levels of radiation, and is the highest priority interlock system at J-PARC. The MPS is used to prevent machines from unusual beam irradiation. When these interlock systems are tripped, the Linac is stopped immediately in the most reliable way—namely ion source termination (PPS) or RF termination (MPS). Some muon instruments are also categorized as PPS or MPS. For example, the emergent beam termination button (panic button) in the experimental port is directly connected to the PPS system. The "air damper" of the M1/M2 line air-conditioning system is also connected to the PPS system to avoid anomalous contamination of the air in the experimental halls by radioactive products that appear in the M1/M2 line. Their beam-stop signals

---

[*] Corresponding author. Tel.: +81 29 284 3873; fax: +81 29 282 5927.
E-mail address: higemoto.wataru@jaea.go.jp (W. Higemoto).

0168-9002/$ - see front matter © 2008 Elsevier B.V. All rights reserved.
doi:10.1016/j.nima.2008.11.026

are transferred to the CCR through a dedicated route. In particular, the PPS consists of independent instruments such as PPS management devices and PPS local instruments.

Information on the status of several key elements of the muon production target and the beam scrapers is directly relayed to the MPS. For example, if the temperature of the muon target were to rise to an unexpected value, serious problems could occur. Therefore, information on the temperature, status of the cooling water, and the position of the muon production target is sent to the MPS via a hardwired feed.

4. Muon instruments control system

This section describes in detail each subsystem.

4.1. Muon production target and muon beam scrapers

Both the muon production target and muon beam scrapers are located at the primary proton beam line. There are two roles for the control system that manages the muon target and scrapers. One is monitoring the position of the muon target. The other is monitoring the statuses of the muon target and the muon scraper, as shown in Figs. 1 and 2. The position of the muon target is controlled in the MLF control room by a MLF operator. The operator moves the target to the "Monitor," "Target," "Clear," and "OT" positions. If the position of the muon target is incorrect, the MPS will be tripped. The temperature and water flow of the muon target and the muon scrapers are monitored. If these values are out of setting range 1, a warning signal is displayed by the MLF Control System. If these values exceed setting range 2, the MPS is tripped. These values are continuously monitored and stored on both the local system, and the MLF-GCS.

4.2. M1/M2 line air-conditioning system

This subsystem is for controlling the condition of the air around the M1/M2 line. The statuses and conditions of the valves and the temperature of the air around the M1/M2 line are monitored both locally and at MLF. To prevent radioactive contamination of the air, several damper valves are controlled by the PPS.

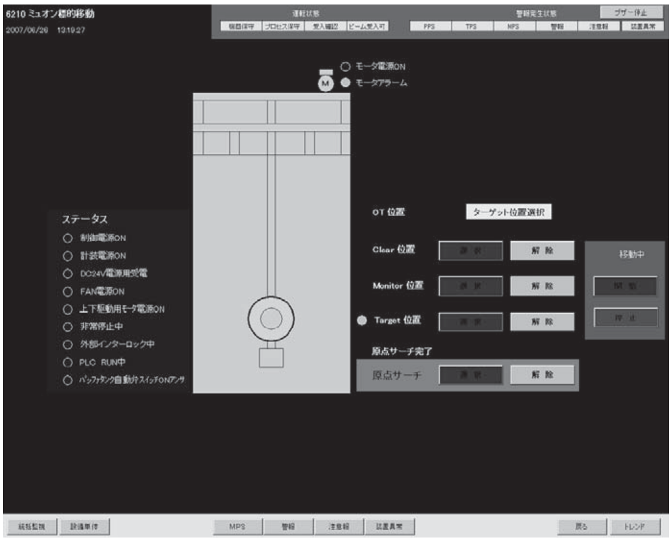

○ モータ電源ON
● モータアラーム

ステータス
○ 制御電源ON
○ 計装電源ON
○ DC24V電源用受電
○ FAN電源ON
○ 上下駆動用モータ電源ON
○ 非常停止中
○ 外部インターロック中
○ PLC RUN中
○ バッファタンク自動弁スイッチONアンサ

Fig. 1. Image of a subsystem window for target position.

4.3. Cryogenics for superconducting solenoid magnet

This subsystem is for on-line helium refrigerator system for the superconducting magnet of the decay/surface muon line. This is a local control system and the operation itself is a local operation. Most of the information is stored on the MLF database.

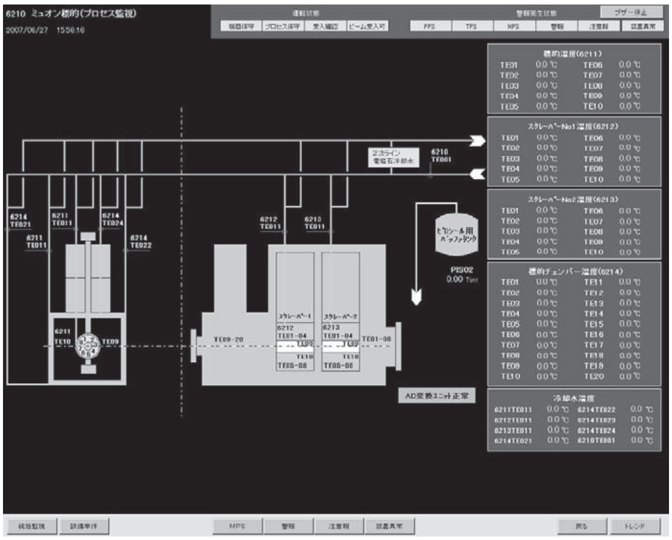

PIS02
0.00 Torr

標的温度(6211)
TE01 0.0 ℃ TE06 0.0 ℃
TE02 0.0 ℃ TE07 0.0 ℃
TE03 0.0 ℃ TE08 0.0 ℃
TE04 0.0 ℃ TE09 0.0 ℃
TE05 0.0 ℃ TE10 0.0 ℃

スクレーパーNo1温度(6212)
TE01 0.0 ℃ TE06 0.0 ℃
TE02 0.0 ℃ TE07 0.0 ℃
TE03 0.0 ℃ TE08 0.0 ℃
TE04 0.0 ℃ TE09 0.0 ℃
TE05 0.0 ℃ TE10 0.0 ℃

スクレーパーNo2温度(6213)
TE01 0.0 ℃ TE06 0.0 ℃
TE02 0.0 ℃ TE07 0.0 ℃
TE03 0.0 ℃ TE08 0.0 ℃
TE04 0.0 ℃ TE09 0.0 ℃
TE05 0.0 ℃ TE10 0.0 ℃

標的チェンバー温度(6214)
TE01 0.0 ℃ TE11 0.0 ℃
TE02 0.0 ℃ TE12 0.0 ℃
TE03 0.0 ℃ TE13 0.0 ℃
TE04 0.0 ℃ TE14 0.0 ℃
TE05 0.0 ℃ TE15 0.0 ℃
TE06 0.0 ℃ TE16 0.0 ℃
TE07 0.0 ℃ TE17 0.0 ℃
TE08 0.0 ℃ TE18 0.0 ℃
TE09 0.0 ℃ TE19 0.0 ℃
TE10 0.0 ℃ TE20 0.0 ℃

冷却水温度
6211TE011 0.0 ℃ 6214TE022 0.0 ℃
6212TE011 0.0 ℃ 6214TE023 0.0 ℃
6213TE011 0.0 ℃ 6214TE024 0.0 ℃
6214TE021 0.0 ℃ 6210TE001 0.0 ℃

Fig. 2. Image of a subsystem window for target processing.

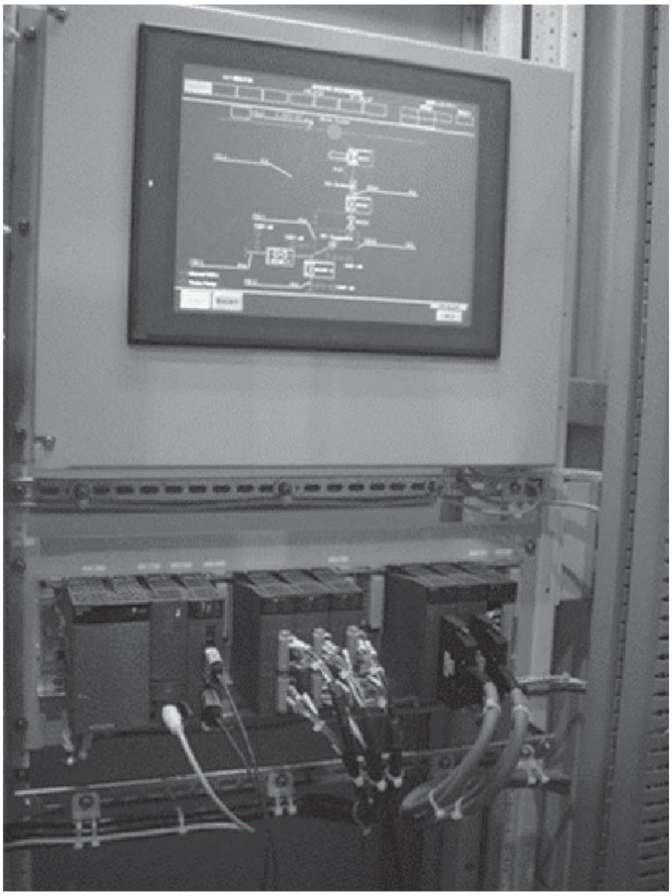

Fig. 3. Photograph of a subsystem for vacuum control. The touch panel window and the PLC's are seen.

4.4. Vacuum system

The vacuum system of the muon secondary line is operated as a local control system. The statuses of the valves and vacuum level are monitored. Fig. 3 shows the photograph of vacuum system controller.

4.5. Secondary line magnets

The statuses of several states of the muon secondary beam line magnets are monitored. For example, polarity, current value, and error signals for the magnet power supplies are monitored by both local systems and by MLF. MLF only monitors the status of the magnets, the setting of the current value is done locally. Likewise, current tuning of the magnet is also done by the local control system by using EPICS, which is under construction.

4.6. Muon blockers and experimental port [1]

Knowing the statuses of beam blockers is important to ensure the safety of personnel. The status of the muon and the pion blockers is interlocked with the entry system of the muon experimental port. Fig. 4 shows a diagram of the muon blockers and experimental port. The door and the locks of the experimental port are connected to the PPS controller. The statuses of the blockers, door, and locks are monitored by MLF control. This system is common with the neutron shutter control system. Details of the system are described elsewhere [1].

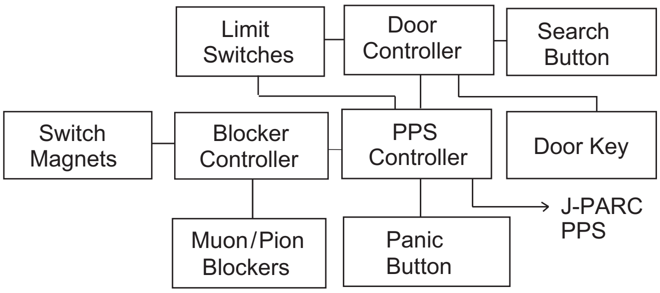

Fig. 4. Diagram of muon and pion blockers and muon experimental port.

5. Summary

At J-PARC MLF MUSE, muon instruments are controlled by the Muon Control System. This system ensures the safe operation of the muon instruments. Construction is going on.

Reference

[1] See also T. Kai et al., Nucl. Instr. and Math. A (2008), doi:10.1016/j.nima.2008.11.091.

Nuclear Instruments and Methods in Physics Research A 600 (2009) 182–184

Contents lists available at ScienceDirect

Nuclear Instruments and Methods in Physics Research A

journal homepage: www.elsevier.com/locate/nima

JAEA-ASRC μSR project at J-PARC MUSE

W. Higemoto [a,*], R.H. Heffner [a,c], K. Shimomura [b], K. Nishiyama [b], Y. Miyake [b]

[a] *Advanced Science Research Center, Japan Atomic Energy Agency, Ibaraki 319-1195, Japan*
[b] *Muon Science Laboratory, High Energy Accelerator Research Organization, Ibaraki 305-0801, Japan*
[c] *Los Alamos National Laboratory, Los Alamos, NM 87545, USA*

ARTICLE INFO

Available online 27 November 2008

Keywords:
μSR
Spectrometer
f-Electron physics

ABSTRACT

The Japan Atomic Energy Agency (JAEA)-Advanced Science Research Center (ASRC) is advancing a "μSR project" at the J-PARC MLF muon science facility (MUSE). This project entails extracting part of the muon beam into a muon spectrometer constructed downstream from the Decay/Surface muon beam line. One of the main subjects of study at the ASRC μSR project will be an examination of strongly correlated electron systems, especially f-electron systems. The intense muon beams available at MUSE will yield new insights for f-electron physics.

1. Introduction

The muon science facility (MUSE) at the J-PARC Materials and Life Sciences Facility (MLF) will be utilized for various fields of science, including nuclear and condensed matter physics and chemistry. Muons are created at MUSE from pions which are generated in a graphite target impacted by a 1 MW, 3 GeV proton beam; the pions decay into muons within a half-life of 26 ns. These muons are collected by magnets and an intense pulsed muon beam is delivered to the muon experimental ports.

The JAEA-Advanced Science Research Center (ASRC) is building a "μSR project" at the J-PARC-MLF-MUSE facility. In this paper, we present the details of this ASRC μSR project.

2. ASRC μSR project

The ASRC μSR project was started FY2005. The main purpose of the project is the study of f-electron materials using the μSR technique as a microscopic magnetic probe. In some f-electron systems, a tiny and fluctuating magnetic field plays the dominant role in determining their characteristics, and μSR has great sensitivity to detect these fields. The intense muon beams at J-PARC will allow us to understand important details of a specific magnetic state, and thus J-PARC has great merit in the study of f-electron systems.

In this project, the muon beam extraction and muon spectrometer will be installed downstream of the Decay/Surface muon beam line of MUSE, as a branch of the main beam line. A surface muon beam (29 MeV/c) will be primarily used for our experiments. The beam line will have a "beam slicer" to obtain higher time resolution, as discussed below. Fig. 1 shows a layout of the beamline of the ASRC muon instruments. The main components are two triplet quadrupole magnets and the beam slicer. This beamline is connected to the septum magnet of the Decay/Surface muon line. We note that at the beginning operation of the Decay/Surface muon line, the septum magnet will not be used, but a conventional bending magnet will be installed.

3. Beamline magnets

Fig. 2 shows a photograph of the triplet quadrupole magnets (NEC-TOKIN). Conventional triplet quadrupole magnets are used. The maximum magnetic field gradient is 1.675 T/m at 375 A, which was determined based on calculations of the beam optics. The bore radius of the magnet is 300 mm. Star-shape vacuum ducts are installed into each magnet. These magnets are connected to power supplies (IDX Corporation) which are controlled from the Experimental Physics and Industrial Control System (EPICS).

4. Beam slicer

For pulsed-beam μSR experiments, the observable muon spin precession frequency is restricted by the width of the muon pulse. Since the time structure of the muon pulse is about the same as that of the proton pulse, the width of the muon pulse is longer than 100 ns. In addition, the proton beam has two bunch structures, and this fact also suppresses the observable muon

---

[*] Corresponding author. Tel.: +81 29 284 3873; fax: +81 29 282 5927.
E-mail address: higemoto.wataru@jaea.go.jp (W. Higemoto).

0168-9002/$ - see front matter © 2008 Elsevier B.V. All rights reserved.
doi:10.1016/j.nima.2008.11.027

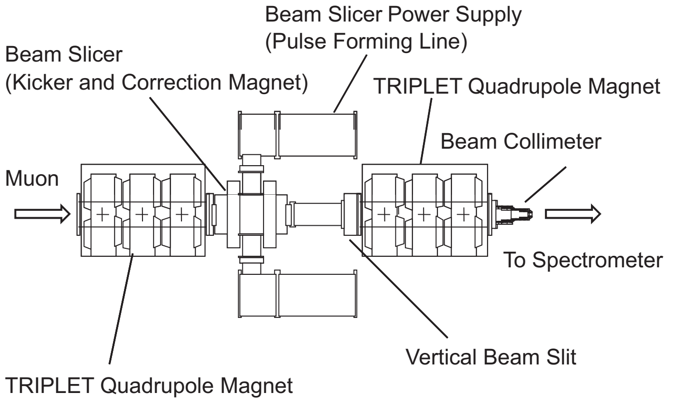

Fig. 1. Layout of the ASRC beamline (top view). This beamline will be connected to the septum magnet of the Decay/Surface muon line.

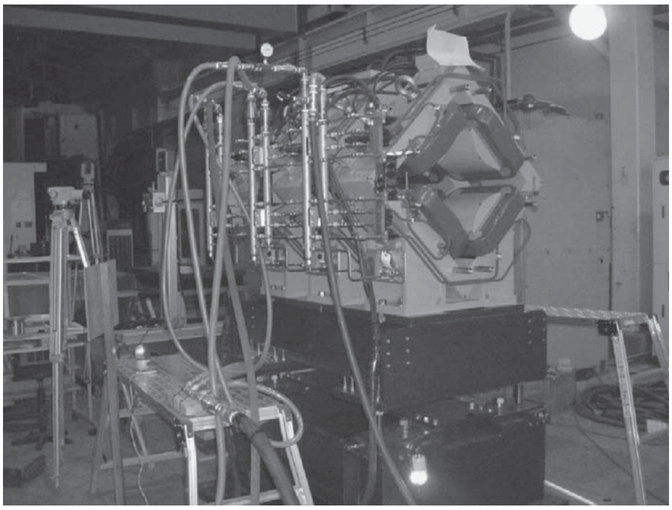

Fig. 2. Photograph of the triplet quadrupole magnet.

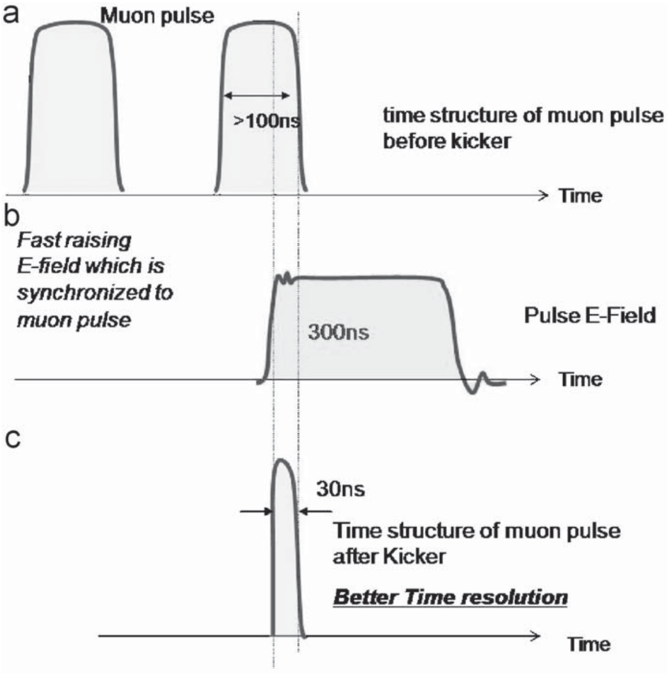

Fig. 3. Schematic of the operating mode of the muon slicer. (a) Original structure of muon pulse. (b) Electric field which is applied to the muon pulse. (c) Obtained muon pulse (width: less than 30 ns).

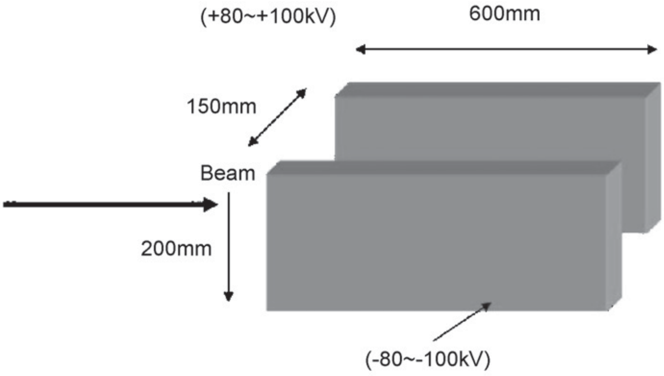

Fig. 4. Schematic of the electric kicker. Two electric pads are located in the vacuum chamber.

spin precession frequency. To overcome the limited time resolution which comes from the time structure of the proton beam, a muon beam slicer is installed. The beam slicer consists of an electric kicker, a pulsed electric power supply which has a fast rise time, and a correction magnet. Fig. 3 schematically illustrates the operating mode of the beam slicer. By applying a pulsed electric field (±(80–100)kV) which is synchronized to the muon pulse, the muon pulse is sliced to a narrower time width. As shown in Fig. 1, the power supply of the electric kicker (Nichicon Corp.) is directly connected to the kicker without cables to reduce the kicker's capacitance. A rise time for the electric field less than 20 ns (10–90%) and a pulse width of about 300 ns can be achieved. This will allow a chopped muon pulse width of less than 30 ns. By using such a short pulse, we can observe a muon spin rotation frequency of more than 10 MHz. We note that the muon pulse width can be controlled by tuning the timing of the electric field. Fig. 4 shows a schematic of the kicker, designed with the help of the company KT Science. The kicker consists of 200 mm × 600 mm electric pads (Suzuno Giken) located in the vacuum chamber. The distance between the electric pads is 150 mm. By using this configuration, a muon beam with momentum 29 MeV/*c* can be deflected nearly 100 mm at a position of 1000 mm from the edge of the pads.

The muon pulse is then selected by using a horizontal beam slit located downstream of the kicker. The direction of the beam is corrected by using a small bending magnet ("correction magnet").

5. Spectrometer

The μSR spectrometer will consist of a transverse field magnet, a longitudinal field magnet, zero-field correction magnets and positron counters. The design of the spectrometer is in progress. We are planning to have 2 kG longitudinal field and 100 G transverse field by using normal conducting magnets. We are also planning to use positron counters with more than 1000 segments to prevent counting losses from the high instantaneous positron event rate. To reduce background which comes from muons stopping in the sample holder, walls and windows, a "fly-pass technique" will be employed [1]. This method was developed at ISIS. By putting the sample in a long vacuum chamber, muons which do not hit the sample fly far away from the sample and their decays are not detected.

6. Scientific topics

One of the main subjects of the ASRC μSR project is the study of strongly correlated electron systems, especially f-electron systems. Examples of topics are as follows:

- Heavy fermions.
- Anisotropic superconductivity.
- Multipole ordering.
- Physics in the vicinity of a quantum critical point (QCP).
- Unconventional magnetism (tiny moments, etc.).

The studies of these topics are quite suitable for μSR experiments. For example, a small and fluctuating magnetic field is often seen near a QCP, and the high sensitivity of the muon probe is a good tool for such an investigation. The world's highest sensitivity will be obtained by using the intense muon beams of J-PARC, allowing us to obtain new insights into f-electron systems.

7. Conclusion

The JAEA-ASRC μSR project will add new capabilities to MUSE, highly enhancing our knowledge of f-electron physics. Construction is in progress, with the operational goal being the first muon beam delivery period in the fall of 2008.

Reference

[1] M.C. Lynch, et al., Physica B 326 (2003) 270.

Nuclear Instruments and Methods in Physics Research A 600 (2009) 192–194

Contents lists available at ScienceDirect

Nuclear Instruments and Methods in Physics Research A

journal homepage: www.elsevier.com/locate/nima

Superconducting muon channel at J-PARC

K. Shimomura [a,b,*], A. Koda [a,b], P. Strasser [a,b], N. Kawamura [a,b], H. Fujimori [a,b], S. Makimura [a,b], W. Higemoto [b,c], K. Nakahara [a,b], K. Ishida [d], K. Nishiyama [a,b], K. Nagamine [a], Y. Miyake [a,b]

[a] *Meson Science Laboratory, High Energy Accelerator Research Organization, Oho, Tsukuba, Ibaraki 305-0801, Japan*
[b] *Muon Section, Materials and Life Science Division, J-PARC Center, 2-4 Shirane Shirakata, Tokai-mura, Naka-gun, Ibaraki 319-1195, Japan*
[c] *Advanced Science Research Center, Japan Atomic Energy Agency, Ibaraki 319-1195, Japan*
[d] *Advanced Meson Science Laboratory, RIKEN Nishina Center, RIKEN, Hirosawa-2-1, Wako, Saitama 351-0198, Japan*

ARTICLE INFO

Available online 27 November 2008

Keywords:
Muon
Beam
Secondary beam line

ABSTRACT

The Muon Science Laboratory at the Materials and Life Science Facility is now under construction in Japan Proton Accelerator Research Complex (J-PARC), where four types of muon channels are planned to be installed. A conventional superconducting muon channel will be installed at the first stage, which can extract surface (positive) muons and decay positive/negative muons up to 120 MeV/*c*, and the expected muon yield is a few 10^6/s at 60 MeV/*c* (for both positive and negative). This channel will be used for various kinds of experiments like muon catalyzed fusion, μSR and nondestructive elements analysis. The present status of the superconducting muon channel is briefly reported.

1. Introduction

The Japan Proton Accelerator Research Complex (J-PARC) is now under construction at the Tokai Campus of JAEA (Japan Atomic Energy Agency) in Tokai, Ibaraki, Japan, with the collaboration of KEK and JAEA. The Muon Science Laboratory is located at the Materials and Life Science Facility (MLF) in J-PARC, where 1 MW (3 GeV, 333 μA) pulsed proton beam (25 Hz, 2 bunches) from the 3 GeV rapid synchrotron will be available and, at first, one graphite target of 2 cm thick is planned to be installed for the production of intense pulsed pion and muon beams [1]. To achieve the best performance of this facility, four dedicated muon channels are planned to be installed. The experimental area is divided into two parts, east and west. In this condition, we arranged the superconducting muon channel and the large acceptance surface muon channel (Super Omega) at the west area [2], and the surface muon channel and the high-momentum muon channel at the east area.

In this paper, we will report briefly on the present status of the superconducting muon channel construction. In the fiscal year (FY) 2008, we will obtain first muon beam.

2. Layout and construction schedule

As shown in Fig. 1, a conventional superconducting muon channel will be installed at the southwest part, which can extract surface (positive) muon and decay positive/negative muon up to 120 MeV/*c*. It consists of three parts: (1) a pion injector, (2) a decay solenoid, and (3) a muon extraction. Two experimental ports are planned for simultaneous use.

1. A quadrupole triplet is placed at a position of 65 cm from the graphite target [3], which can accept pions in a solid angle of 65 msr. The following bending magnet transports pions to the solenoid up to 250 MeV/*c* at maximum.
2. The decay solenoid consists of 12 pieces of superconducting coils with 6 cm in bore radius and 50 cm in length. The applied magnetic field is 5 T. The pions and muons are confined within a radius of 5 cm and therefore transported without any significant loss. The solenoid that was currently used at KEK-MSL will be modified for this purpose. This superconducting solenoid is cooled by an on-line He refrigerator (TCF 50).
3. The extraction can transport muons up to 120 MeV/*c*. A magnetic kicker will be installed for single-pulse experiments. The major components of the old decay muon channel at KEK-MSL, such as the bending magnets, the quadrupole magnets, and the DC separator will be used.

The overall transport efficiency is estimated by TURTLE. The expected muon yield is a few 10^6/s at 60 MeV/*c* (for both positive and negative). This channel will be used for various kinds of

---

[*] Corresponding author at: Meson Science Laboratory, High Energy Accelerator Research Organization, Oho, Tsukuba, Ibaraki 305-0801, Japan.
Tel.: +81 298 64 5624; fax: +81 298 64 5623.
E-mail address: koichiro.shimomura@kek.jp (K. Shimomura).

0168-9002/$ - see front matter © 2008 Published by Elsevier B.V.
doi:10.1016/j.nima.2008.11.029

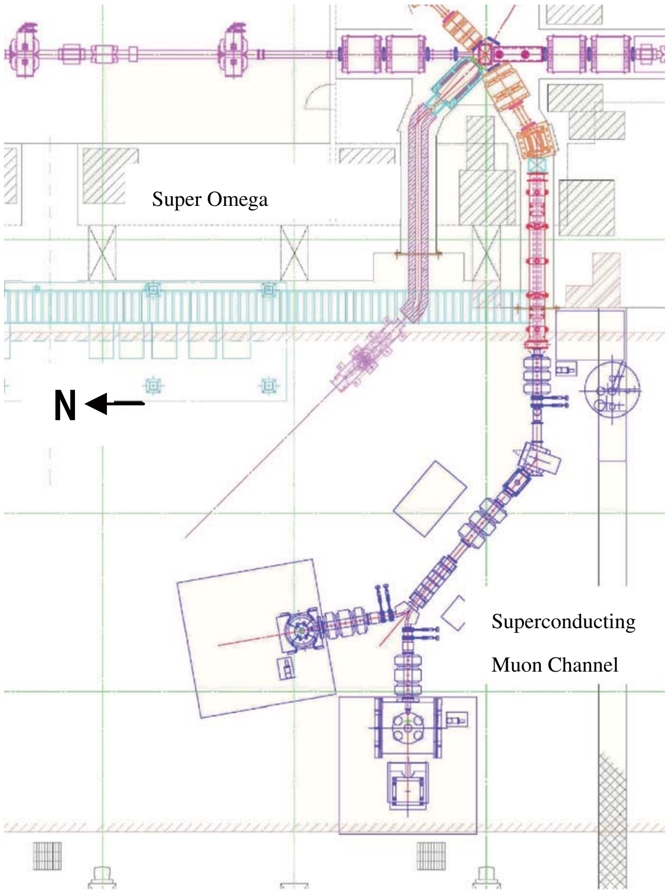

Fig. 1. Layout of the superconducting muon channel at MLF in J-PARC. Super Omega is also shown in the figure.

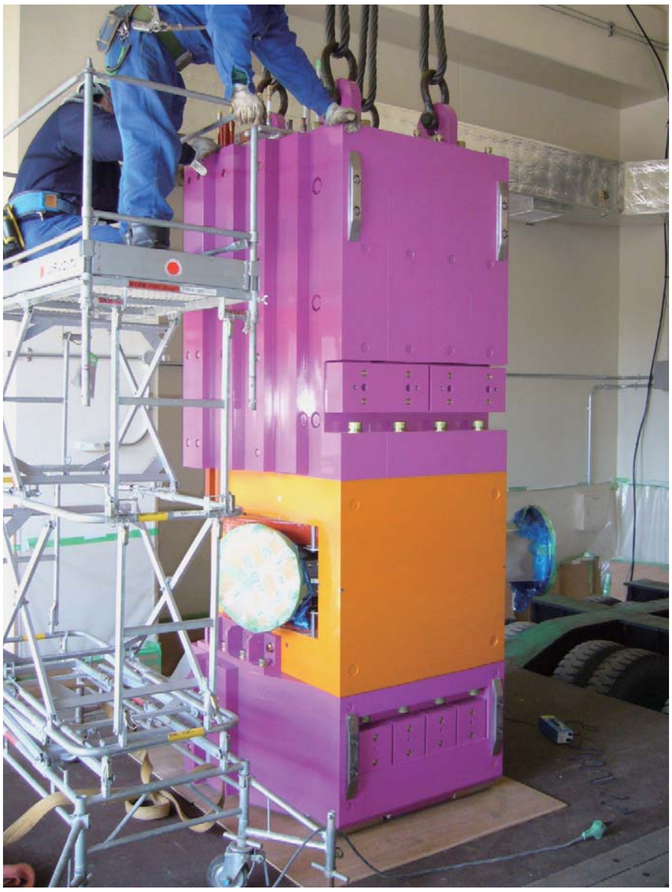

Fig. 2. Bending magnet at the injection part.

Fig. 3. Photograph of the solenoid insertion device.

experiments like muon catalyzed fusion, μSR and nondestructive elements analysis.

In the FY 2006, a quadrupole triplet and a bending magnet for the injection part were successfully installed, whose coils are made by MIC for the hard radiation environment, as shown in Fig. 2. We also developed an insertion device for the superconducting solenoid, because it will be set between the M2 tunnel and the experimental hall, as shown in Fig. 3. Six iron blocks, with a total weight of about 50 ton, are also set on the insertion device for the radiation protection from the M2 line. Therefore, we adopted two sets of linear guide for the horizontal transport motion to keep good reproducibility.

To obtain single-bunch pulsed muon beam, we are now developing an electric kicker system, which is useful for relatively low energy muon beam up to 45 MeV/*c*. In the FY 2007, we installed the superconducting solenoid, and the on-line He refrigerator concrete shield. In the early stage of the FY 2008, the magnets for extraction will be installed and all the work for cabling and interlock system will be finished.

3. Solenoid and on-line refrigeration system

To obtain a high-intensity decay muon beam, a superconducting solenoid magnet is employed for the pion to muon decay section. The basic design is similar to those used in the muon beam lines at KEK-MSL, TRIUMF, and RIKEN-RAL. The superconducting solenoid magnet consists of 12 unit coils of 0.5 m in length. The magnet coil is forced-indirectly cooled by a supercritical helium gas (4.8 K at 1.0 MPa) supplied from an on-line helium refrigeration system. To achieve the muon extraction at low momentum, this cold bore magnet is directly connected to the muon beam line using only thin thermal insulating aluminum foils of 12.5 μm thick at the entrance and exit of the superconducting solenoid magnet, respectively.

The 80 K copper thermal shield is positioned between the 6 K shield tube and the warm iron cryostat vessel. The 6 and 80 K thermal shields are supported by insulation rods extending from the cryostat wall. The 80 K shield is cooled by the helium gas taken from the intermediate heat exchanger in the cold box.

For the long-term stable operation, an on-line helium refrigeration system is employed. The helium refrigeration system consists principally of the followings:

(1) He buffer tank (20 m^3, 0.95 MPa(G)).
(2) Cooling tower and water cooling pump.
(3) Helium gas screw compressor (Kaeser).
(4) After cooler.
(5) Oil separator.
(6) Load, unload, and bypass valve.
(7) Cold box.
(8) VME based digital control device.
(9) PC system for control and data logging.
(10) Cryopanel for safety interlock control.

The screw compressor supplies high-pressure helium gas (0.85 MPa) to the cold box. The cold box is designed to supply various types of helium requested to the superconducting solenoid. Before the cooling down procedure from the room temperature is commenced, the oxygen concentration of the circulating helium gas is reduced to be less than 50 ppm by the operating He gas purifier.

The cooling power is 35 W at 4.5 K and 200W at 80 K, and it can produce 8 l/h of liquid helium. The whole system is monitored and controlled by a VME controller combined with a personal computer with dedicated software based on LabVIEW System, and cools down automatically. The typical cooling period from the room temperature to the operation temperature (~6 K) is about 4 days. The long-term (3 months) operation will be established under quite stable condition.

To protect any serious damage to the superconducting coils and the He refrigeration system, a VME based interlock system is installed. The system can detect any anomaly in the voltage of superconducting solenoid, the power lead temperature and the trip signal from the He refrigeration system. Once any emergency status is detected, the electric power supply immediately stops the current supply and the refrigeration system changes to self-operation mode. This part can also record the temperatures and pressures of the superconducting coils, the cryostat and the power leads.

References

[1] Y. Miyake, et al., Nucl. Instr. and Meth. A, this issue.
[2] K. Nakahara, et al., Nucl. Instr. and Meth. A, this issue.
[3] S. Makimura, et al., Nucl. Instr. and Meth. A, this issue.

Physica B 404 (2009) 957–961

Contents lists available at ScienceDirect

Physica B

journal homepage: www.elsevier.com/locate/physb

Birth of an intense pulsed muon source, J-PARC MUSE

Yasuhiro Miyake [a,b,*], Koichiro Shimomura [a,b], Naritoshi Kawamura [a,b], Patrick Strasser [a,b], Shunsuke Makimura [a,b], Akihiro Koda [a,b], Hiroshi Fujimori [a,b], Kazutaka Nakahara [a,b], Ryosuke Kadono [a,b], Mineo Kato [a,b], Soshi Takeshita [a,b], Kusuo Nishiyama [a,b], Wataru Higemoto [c,b], Katsuhiko Ishida [e], Teiichiro Matsuzaki [e], Yasuyuki Matsuda [d], Kanetada Nagamine [a,e]

[a] *Muon Science Laboratory, High Energy Accelerator Research Organization, Tsukuba, Ibaraki 305-0801, Japan*
[b] *Muon Section, Materials and Life Science Division, J-PARC Center, 2-4 Shirane Shirakata, Tokai-mura, Naka-gun, Ibaraki 319-1195, Japan*
[c] *Advanced Science Research Center, Japan Atomic Energy Agency, Tokai, Ibaraki 319-1195, Japan*
[d] *Graduate School of ARTS and Sciences, University of Tokyo, Meguro, Komaba 3-8-1 153-8902, Japan*
[e] *Advanced Meson Science Laboratory, The Institute of Physical and Chemical Research (RIKEN), Wako, Saitama 351-0198, Japan*

ARTICLE INFO

Keywords:
Muon
J-PARC
MUSE
Pulsed muon
MLF
Remote handling
Slow muon

ABSTRACT

The muon science facility (MUSE), along with neutron, hadron, and neutrino facilities, is one of the experimental areas of the J-PARC (Japan Proton Accelerator Research Complex) project, which was approved for construction between 2001 and 2008. The MUSE facility is located in the Materials and Life Science Facility (MLF), which is a building integrated to include both neutron and muon science programs. Construction of the MLF building was started at the beginning of 2004, and was recently completed at the end of the 2006 fiscal year. We have been working on the installation of the beamline components, expecting the first muon beam in the autumn of 2008. For Phase 1, we are planning to install one superconducting decay/surface channel with a modest-acceptance (about 40 mSr) pion injector, with an estimated surface muon (μ^+) rate of 3×10^7/s and a beam size of 25 mm diameter, and a corresponding decay muon (μ^+/μ^-) rate of 10^6/s for 60 MeV/*c* (up to 10^7/s for 120 MeV/*c*) with a beam size of 50 mm diameter. These intensities correspond to more than 10-times what is available at the RIKEN/RAL muon facility, which currently possess the most intense pulsed muon beams in the world. In addition to Phase 1, we are planning to install, a surface muon channel with a modest-acceptance (about 50 mSr), mainly for experiments related to material sciences, and a super-omega muon channel with a large acceptance of 400 mSr. In the case of the super-omega muon channel, the goal is to extract 4×10^8 surface muons/s for the generation of ultra-slow muons and 1×10^7 negative cloud muons/s with a momentum of 30–60 MeV/*c*. One of the important goals for this beamline is to generate intense ultra-slow muons at MUSE, utilizing an intense pulsed VUV laser system. $10^4 - 10^6$ ultra-slow muons/s are expected, which will allow for an extension of μSR into the area of thin film and surface science.

At this symposium, the current status of J-PARC MUSE will be reported.

1. The 3 GeV proton beam at J-PARC

J-PARC (Japan Proton Accelerator Research Complex) will be constructed in the south part of the Tokai-JAEA (Japan Atomic Energy Agency) site, will consist of a 181 MeV LINAC (400 MeV in future), as well as 3 and 50 GeV proton synchrotron rings. About 90% of the 3 GeV, 333 μA (1.0 MW) beam will be sent to the Materials and Life Science Facility (MLF) for the production of intense pulsed neutron and muon beams, while the remaining 10% will be sent to the 50 GeV ring for further acceleration for the kaon and neutrino physics programs [1]. The parameters of the 3 GeV proton beam are:

(i) The number of protons will be 8.3×10^{13}/pulse.
(ii) The average beam power will be 0.6 MW, since the LINAC energy will start with 181 MeV in Phase 1, and will reach 1 MW in the future when the LINAC energy is increased up to 400 MeV.
(iii) The repetition rate is 25 Hz, so each pulse is separated by 40 ms. One proton pulse consists of two bunches, each with a bunchwidth of $\sim 100-140$ ns, and separated by 600 ns.
(iv) The transverse emittance (ε) will be 81π mm mrad (beam core) and 324π mm mrad (maximum halo).

---

* Corresponding author at: Muon Science Laboratory, High Energy Accelerator Research Organization, Tsukuba, Ibaraki 305-0801, Japan. Tel.: +81 29 284 4624; fax: +81 29 284 4878.
E-mail address: yasuhiro.miyake@kek.jp (Y. Miyake).

0921-4526/$ - see front matter © 2008 Elsevier B.V. All rights reserved.
doi:10.1016/j.physb.2008.11.227

2. Design of the MLF building and the NM tunnel

The MLF consists of a proton beamline tunnel (the so-called NM tunnel), and two experimental halls (east wing, experimental hall No. 1; west wing, experimental hall No. 2). The tunnel structure is designed to keep radioactive materials inside the tunnel in order to ensure safe operations during maintenance work on the neutron or muon targets. The height of the building is 31 m inside the tunnel and 21 m in the experimental halls. The width of the tunnel is 13.5 m, and the east and west wings are 24.5 and 32 m wide, respectively. The proton beam height is 1.6 m from the floor level. The muon-science facility is 30 m long along the proton beamline, and is located upstream of the neutron facility. Fig. 1 (top) shows a schematic drawing of the first floor of the MLF building. The proton beamline in the MLF building consists of the M1 and the M2 line regions. The M1 line is located upstream of the muon target, where no significant beam loss occurs. On the other hand, the M2 line is in the vicinity of the muon target, where severe beam loss occurs due to the surrounding beamline components. Fig. 1 (bottom) shows a cutaway view along the primary beamline, showing a schematic of the NM tunnel structure of the MLF building. Since a fraction of the primary 3 GeV proton beam is scattered preferentially downstream towards the neutron target, two sets of scrapers were installed to mitigate damage to the beamline components, such as the quadrupole magnets and the beam ducts. Although some of the scattered beam is deposited on the scrapers, the various beamline components, such as the quadrupole magnets, target chamber, scraper chamber, pillow-seal, and vacuum ducts located along both the primary and secondary beamlines, will suffer not only from tremendously high radiation, but also from corrosion induced by NO_x in irradiated air [2]. Therefore, following what PSI has done in dealing with their 1 MW-class proton beam [3], all of the maintenance work along the M2 beamline involving power and water connections is intended to be performed remotely from the top of the maintenance area, located 4 m above floor level. Construction of the MLF building was started at the beginning of 2004, and was completed at the end of the 2006 fiscal year.

3. Installation of the M2 line beamline components

In the M2 beamline, all of the beamline components must be installed via remote handling from a maintenance area above (FL 4 m). For that purpose, we installed baseplates with a precision of $XY \pm 0.5$ mm on the floor of 0.5 m FL, and then we placed alignment plates matching to the individual beamline components with a precision of $XY \pm 0.1$ mm, $Z \pm 0.1$ mm. Iron guide shields equipped with a guiding rail structure were aligned by placing knock pins on the alignment plates. The target chamber, the various beamline magnets (M2 primary line; six quadrupole magnets QM1, QM2, QN1, QN2, QN3, QN4 and four steering magnets, X22, Y22, X23, and Y23 and secondary line; DQ-1–3 , SQ 1–3 triplet magnets, DB1 and SB1 bending magnets), two sets of profile monitor assemblies, 20 sets of pillow-seal assemblies, a gate valve assembly and seven sets of duct assemblies were also installed on alignment plates equipped with knock pins, which allow precise positioning, guided by the guide shields. The power

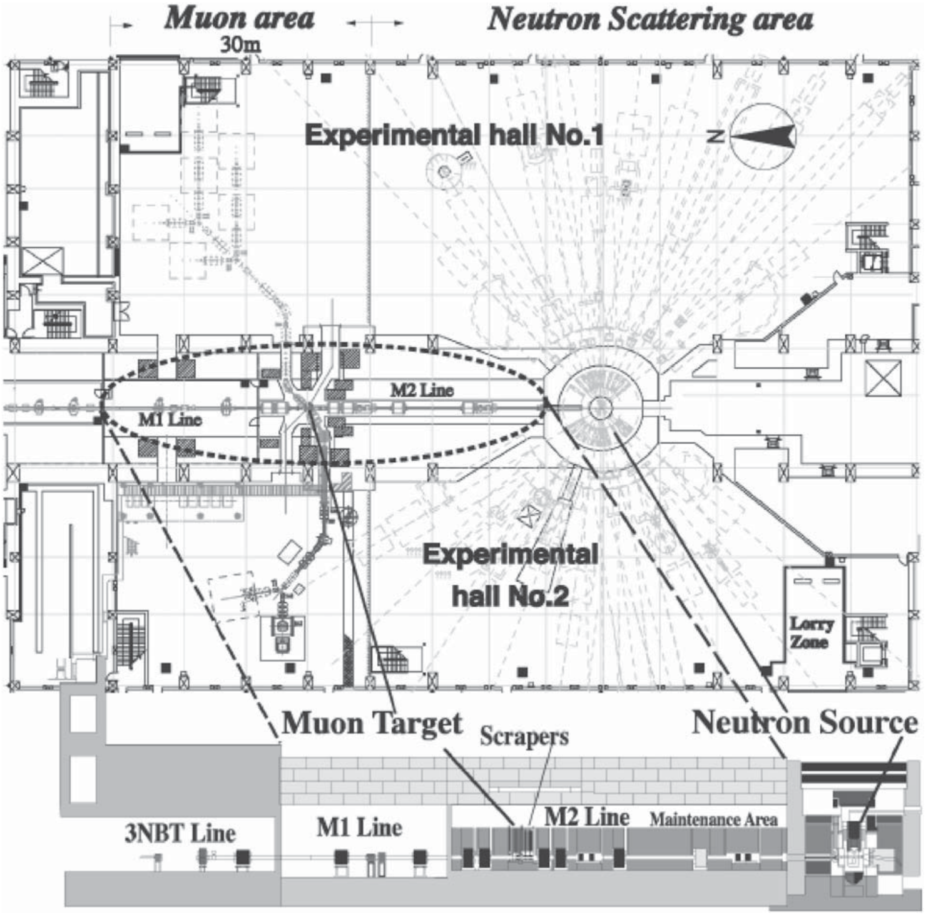

Fig. 1. The top figure shows a schematic drawing of the first floor of the MLF building. The bottom figure shows a cutaway view along the primary beamline, showing a schematic of the NM tunnel structure of the MLF building.

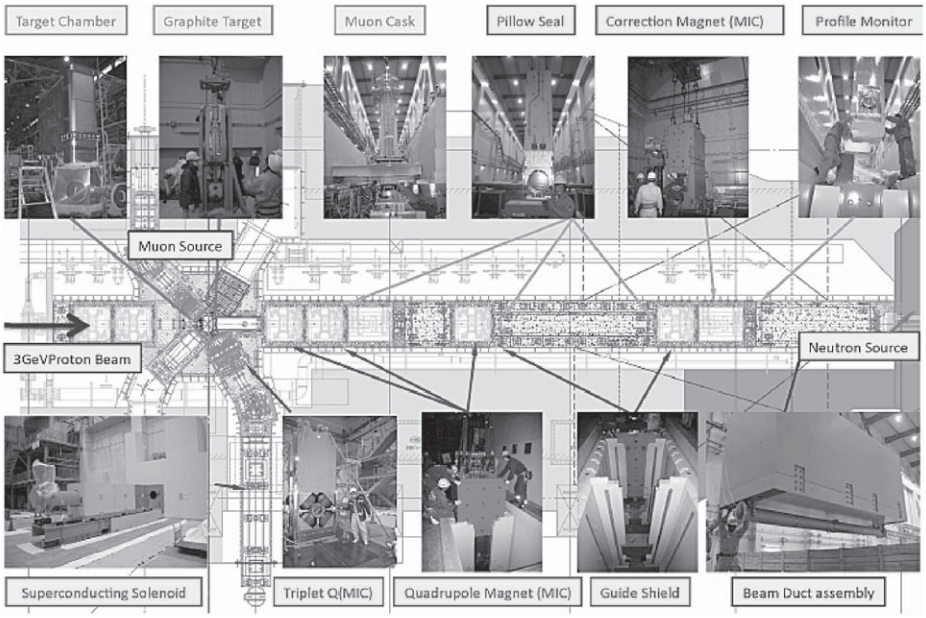

Fig. 2. Schematic view of the M2 line in the vicinity of the muon target, and pictures of the beamline components.

and control cables were then connected between the magnets on the M2 line and the corresponding power supplies.

Finally, a successful test was performed on the magnets on the M2 line by running them continuously for 12 hours. In addition, after completing of the vacuum connection, the ultimate vacuum achieved was as low as 3×10^{-5} Pa. Fig. 2 shows a schematic view and the latest pictures of the MLF M2 tunnel in the vicinity of the muon target.

All of the beamline components in the M2 tunnel were successfully demonstrated to function properly, delivering a 3 GeV proton beam from the muon target to the neutron source as expected during the period from the first proton beam injected into MLF on May 30th, 2008, to the following commissioning period.

4. Tandem-type graphite muon production target

The MLF consists of neutron and muon science facilities that utilize the 3 GeV, 1 MW, 25 Hz proton beam. In order to reduce the total cost of the project through common use of the utilities, getting rid of the severe beam-dump construction associated with high-level tritium water handling, and by sharing the beam with the neutron facility, we decided to have a tandem-target muon facility, rather than construct a separate building with our own proton (1 MW) beam dump, as was the case in KEK-MSL. Through discussions with the neutron science group, we reached an agreement that the total beam loss induced by placing the muon production targets should be no more than 10%, which allows us to install 10 and 20 mm thick graphite targets on the beamline upstream of the neutron target, corresponding to a beam loss of 3.5% and 6.5%, respectively. Detailed calculations on heat, radiation and duct-streaming in the vicinity of the muon target were performed by NMTC/JAM and MCNP Monte-Carlo codes [4]. In the case of a 20 mm thick graphite target, as much as 3.5 kW is deposited into a 25 mm diameter region of the target through irradiation of the 3 GeV, 1 MW proton beam. One possible candidate for the muon production target is a rotating carbon target, which has been developed at PSI, and has been working well for more than 10 years [3]. In the end, we adopted an edge-cooled non-rotating graphite target, because of its ease of handling during maintenance. In this target, graphite is indirectly cooled by a copper frame, which surrounds the graphite. For the graphite material, we chose isotropic graphite, IG-43, which has a thermal conductivity of 139 W/mK, $1.82\,\mathrm{g/cm^2}$ density at 300 K, a thermal expansion of 4.8 ppm/K, Young's modulus of 10.8 GPa, and Poisson's ratio of 0.28. In the copper frame, three turns of cooling pipe, an SUS tube with OD 12.7 mm and ID 10.7 mm, are embedded through HIP (hot isostatic press). In order to reduce stress, a titanium buffer layer of 2 mm is placed between the graphite disk and the copper frame. The copper frame, the 20 mm thick graphite, and the titanium buffer layer are bonded by silver brazing in a vacuum. Calculations of the heat and stress induced by the heat deposit of the 3.5 kW beam through ANSYS demonstrate that an edge-cooled graphite target can be used safely as the 1 MW muon production target. Detailed calculations of the neutron irradiation effect on the thermal conductivity and the thermal stress induced by the proton beam will be reported elsewhere [5].

The designs of the two sets of scrapers and the muon production target are such that they are both placed in one large vacuum chamber in order to make remote handling simple during maintenance work. All of the water and cable connections will be done at the top of the maintenance area. Particular care was given to the means of mounting the target, moving and inserting the target with the required precision, as well as cooling, monitoring, and changing the target in the hot cell. The design was complete by September 2004, and the installation was finished in May 2006. In 2007 we made a dedicated muon cask, together with a stand to position it on top of the target chamber with good precision, for the maintenance of the muon target assembly, the scraper assembly, and the profile monitor assembly. The damaged target or profile monitor assembly can be lifted into the cask, and transferred to a storage pit located in the M2 tunnel at a level of 10 m. A new target assembly will then be installed in the chamber as soon as possible. During long shutdown periods, damaged targets will be lifted into the cask, and transferred to the hot cell. In the hot cell, a target assembly consisting of the graphite target, water pipes, and a target slide table are exchanged through remote handling. Since the beginning of April 2008, we have been performing maintenance tests of the remote handling system by utilizing a power manipulator or special devices in the hot cell. Fig. 3 shows a picture of the target assembly transported down to the storage basement, and one picture of the maintenance test of the target slide table in the hot cell.

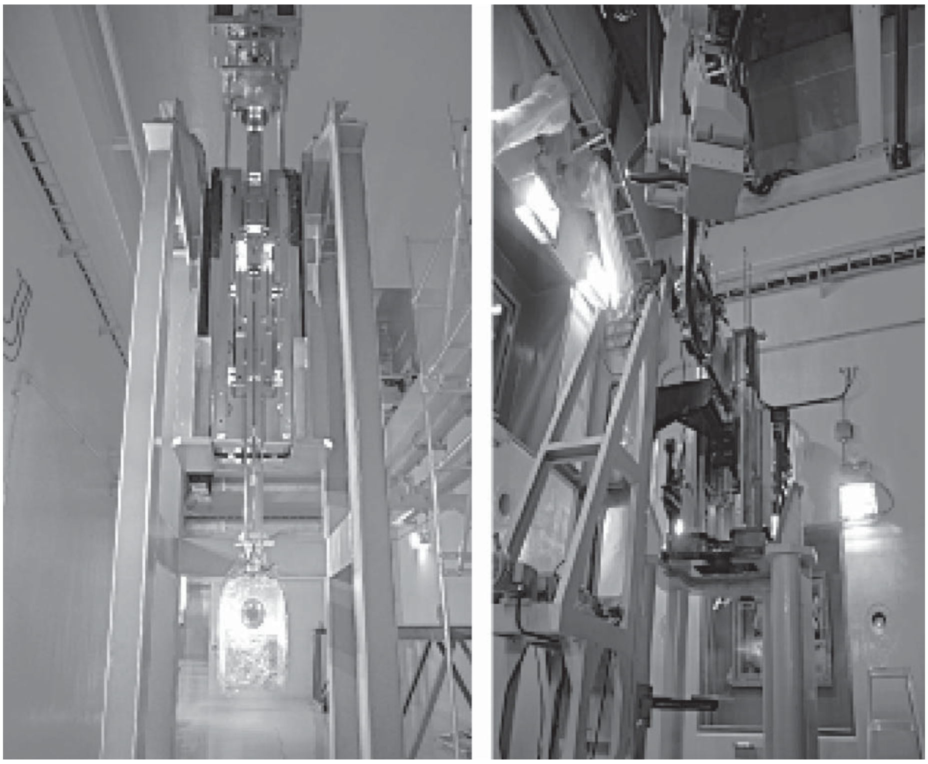

Fig. 3. Left: a picture of the target assembly transported down to the storage basement. Right: a picture of the maintenance commissioning of the target slide table in the hot cell.

Fig. 4. A picture of the decay surface muon channel under construction.

Table 1
Muon beams available at J-PARC muon facility, MUSE.

	Surface muon (μ^+)	Decay muon ($\mu^\pm$)
Decay surface muon channel (*Phase* 1)		
Muon energy	4.1 MeV (30 MeV/*c*)	up to 54 MeV (120 MeV/*c*)
Range	~0.2 mm	1 mm to ~cm
Energy width	~10%	~15%
Temporal width	~100–140 ns	~100–140 ns
Beam size	30 mm × 40 mm	70 mm × 70 mm
Intensity	3×10^7/s	10^6/s–10^7/s
Port number	1	1
	Surface muon (μ^+)	
Surface muon channel (*Phase* 2)		
Muon energy	4.1 MeV (30 MeV/*c*)	
Range	~0.2 mm	
Energy width	~10%	
Temporal width	~100–140 ns	
Beam size	30 mm × 40 mm	
Intensity	10^6/s–10^7/s	
Port number	4	
	Slow muon (μ^+)	Cloud muon (μ^-)
Super-omega muon channel (*Phase* 2)		
Muon energy	0–30 keV	up to 15 MeV (60 MeV/*c*)
Range	1 nm–200 nm	~mm
Energy width	<1%	~5–10%
Temporal width	8.3 ns (now) → sub-ns	~100–140 ns
Beam size	3 × 4 mm (now) → ϕ 1	ϕ 50
Intensity	10^4/s–10^6/s (surface muon 4×10^8/s)	10^6/s–10^7/s
Port number	2	2

5. Secondary muon channels

For Phase 1, the installation of the decay surface muon secondary channel in the MLF No. 2 experimental hall has started. To begin with, on December 25, 2007, we defined a restricted area near the decay surface muon line to be a radiation controlled area. These are areas where we may bring in radioactive components, such as superconducting coils, which have been used on the KEK beamline for more than 30 years. These superconducting coils were then assembled into the solenoid vacuum chamber in January 2008. In February 2008, installation of the on-line refrigeration system started with full operation expected by August 2008. In parallel, the secondary beamline components, such as triplet quadrupole magnets, bending magnets, slits, blockers, gate valves, separator, beam ducts, and shielding blocks, were fabricated, and their installation will be completed by the summer of 2008. Fig. 4 shows a picture of the decay surface beamline under construction.

In addition to Phase 1, we are planning to install one surface muon channel with a modest-acceptance (about 50 mSr), and one super-omega muon channel with a large acceptance of 400 mSr. In the case of the surface muon channel, we can expect a total of 1.6×10^7/s surface muons with a 1 MW proton beam. By installing a kicker and beam slicer, we are planning to place four experimental ports in experimental hall No. 1. In the case of the super-omega beam channel, we are going to install a large acceptance solenoid made of mineral insulation cables (MIC) and a superconducting curved transport solenoid. We can collect either surface or cloud muons up to 60 MeV/*c* very efficiently. Finally, we are expecting 4×10^8/s surface muons and 10^7 negative cloud muons in the experimental hall No. 2 [6]. Although many of these studies can be performed using either surface or decay muons, at the super-omega channel we are aiming to create a new type of muon source, the intense ultra-slow muon source. Ultra-slow muons are generated through resonant ionization of muonium (Mu). Mu is formed by stopping intense surface muons on the rear surface of a hot W foil. At the RIKEN/RAL muon facility [7], 20 slow μ^+/s are obtained out of 1.2×10^6/s surface muons [8]. Taking into account the repetition rate of the pulsed laser system and the proton beam, as well as the surface muon yield between RIKEN-RAL and J-PARC MUSE, we can expect 1.3×10^4/s of slow μ^+/s without any additional laser development. A rate of 1.3×10^6/s slow μ^+ can be achieved with sufficient laser development, such as a tripling of 366 nm photons with a picosecond pulse width to match the Doppler broadening of the Mu at 2000 K.

When the production of intense ultra-slow muon beams is realized, the use of its short-range penetration depth and smaller beam size will allow muon science to be expanded towards a variety of new scientific fields, such as: (1) surface/boundary magnetism utilizing its spin polarization and unique time-window; (2) surface chemistry, utilizing the feature of a light isotope of hydrogen, such as catalysis reactions; (3) precise atomic physics, such as QED; (4) ion sources and towards $\mu^+\mu^-$ collider experiments in high-energy physics.

Table 1 shows the parameters of the individual muon channels at the J-PARC muon facility (MUSE).

6. Summary

Construction of the MLF building as well as the fabrication and installation of various beamline components, such as magnets, the muon target, scrapers, shields, monitors, and vacuum components, were completed in 2007, as scheduled. We are expecting the first muon beam from the decay/surface muon channel in the autumn of 2008.

References

[1] S. Nagamiya, T. Nagae, Y. Ooyama, Y. Miyake, H. Takano, J.R. Helliwell, J.C. Peng, Energy Rev. 19 (12) (1999) 4.

[2] Y. Miyake, K. Nishiyama, K. Fukuchi, N. Kawamura, S. Makimura, K. Shimomura, R. Kadono, W. Higemoto, J.L. Beveridge, K. Ishida, T. Matsuzaki, I. Watanabe, Y. Matsuda, K. Nagamine, Physica B 326 (2003) 255.

[3] G.Heidenreich, P. Baumann, A. Geissler, A. Strinning, W. Wagner, PSI Scientific Report VI, 1998, p. 16.

[4] N. Kawamura, et al., in: IPS08 Proceedings, 2008, to be published.

[5] S. Makimura, et al., in: IPS08 Proceedings, 2008, to be published.

[6] K. Nakahara, Y. Miyake, K. Shimomura, AIP Conference Proceedings 981 (2007) 312.

[7] K. Nagamine, T. Matsuzaki, K. Ishida, I. Watanabe, S.N. Nakamura, R. Kadono, N. Kawamura, S. Sakamoto, M. Iwasaki, M. Tanase, M. Kato, K. Kurosawa, G.H. Eaton, H.J. Jones, G. Thomas, W.G. Williams, Hyperfine Interactions 101/102 (1996) 521.

[8] P. Bakule, Y. Matsuda, Y. Miyake, K. Nagamine, M. Iwasaki, Y. Ikedo, K. Shimomura, P. Strasser, S. Makimura, Nuclear Instr. Methods B 266 (2008) 355.

Physica B 404 (2009) 996–998

Contents lists available at ScienceDirect

Physica B

journal homepage: www.elsevier.com/locate/physb

High transverse field μSR with $\pi/2$-RF pulse spin control technique

R. Kadono [a,b,*], K.H. Satoh [b], A. Koda [a,b], K. Nishiyama [a], M. Mihara [c]

[a] *Muon Science Laboratory, Institute for Materials Structure Science, High Energy Accelerator Research Organization (KEK), Tsukuba, Ibaraki 305-0801, Japan*
[b] *Department of Materials Structure Science, The Graduate University for Advanced Studies, Tsukuba, Ibaraki 305-0801, Japan*
[c] *Department of Physics, Osaka University, Toyonaka, Osaka 560-0043, Japan*

ARTICLE INFO

Keywords:
μSR
Spin echo
Pulsed muon beam

ABSTRACT

We report on the time-differential μSR measurement at 200 MHz (under a transverse field of 1.475 T) using a pulsed muon beam at KEK ($\delta \simeq 50$ ns). The initial muon spin direction is flipped by 90° using a radio-frequency (RF) pulse immediately after muon implantation, which allows observation of μSR time spectra without limitation of beam pulse width δ. A prospect for the routine use of this $\pi/2$-RF pulse technique at the J-PARC MUSE is discussed.

Pulsed muon beam (generated by proton synchrotron) has many advantages over a continuous muon beam (generated by cyclotron), such as high muon intensity and low positron background that allows both wider time window of measurements ($>20\,\mu$s) and high data rate, readiness for combination with transient extreme conditions, and so on. Meanwhile, it has an inherent problem that the time resolution for the conventional μSR measurements is limited by the beam pulse width ($=\delta$); because of the ambiguity of arrival time for the individual muons in a beam bunch, the highest frequency tractable for transverse field (TF) μSR is limited by the Nyquist frequency $f_N{\sim}1/(2\delta)$. Considering the importance of TF-μSR that provides precious information such as the muon Knight shift or the magnetic field profile in the mixed state of type II superconductors, it is highly desirable to establish a routine technique to overcome the limit of beam pulse width. This is particularly true for experiments at the J-PARC Muon Science Facility (MUSE) where f_N would be as low as 4–6 MHz according to the machine parameters of the accelerator ($\delta \simeq 80$–120 ns).

It has been demonstrated that the use of radio-frequency (RF) technique is a key for this purpose [1,2]. The basic idea is to rotate the initial muon spin polarization ($\vec{P}_\mu$) from the direction $\vec{P}_\mu \parallel H_0$ to $\vec{P}_\mu \perp H_0$ by applying a short RF pulse that satisfies the condition $\gamma_\mu H_1 \Delta t = \pi/2$, where H_1 ($\perp H_0$) is the RF field, Δt is the RF duration, and H_0 is the holding field [3]. Then, because the time relative to the RF pulse is well-defined irrespective of the muon arrival time, P_μ exhibits coherent Larmor precession around H_0. Thus, as long as there is no fast depolarization (or spin rotation) within f_N^{-1} and/or Δt originating from samples, the $(\pi/2)$-RF pulse allows us to observe TF-μSR without limitation from f_N (Fig. 1).

In an earlier report, we showed the preliminary result of a test experiment for the $\pi/2$-RF pulse technique at 36.65 MHz [4]. Since then, we installed a series of high power RF amplifiers (peak power ~18 kW) at several frequency bands (50, 75, 125, 200, 300, 400, and 475 MHz) to develop the technique in the more systematic manner. Here, we report our result for the test experiment at 200 MHz (corresponding to 1.475 T), the highest precession frequency to our knowledge ever observed using pulsed muon beam. As shown in Fig. 2, a single-turn split-ring resonator fitting to a He gas-flow cryostat was fabricated [5], and the sample space ($\simeq 3 \times 3 \times 1\,\text{cm}^3$) in the resonator was filled with MgB_2 powder (a type II superconductor with $T_c \simeq 39$ K). A pulsed muon beam with a momentum of ~60 MeV/c was irradiated through a beam window of the cryostat. Under the optimal condition, an RF field of nearly 40 G ($=H_1$) was attained at the sample position with the rise time $\simeq 0.15\,\mu$s and decay time $\simeq 0.1\,\mu$s. It turned out that the probability of RF discharge at the gap of the split-ring was reduced by using a shorter RF pulse. This is understood by considering the fact that it takes typically a few μs for the discharge to develop in gas under a pressure realized in usual operation conditions. The time origin of time-to-digital converters (TDCs) for measuring the positron event timing was defined by a trigger pulse made as a logical product of two pulses, one defining the incoming muon beam timing and the other that is generated by discriminating a signal from RF synthesizer, where the timing is controlled by the latter. The duration of RF pulse $[\Delta t = \pi/(2\gamma_\mu H_1) \simeq 0.46\,\mu\text{s}]$ was optimized by monitoring the backward/forward asymmetry $A_z(t)$ so that $A_z(\Delta t) \simeq 0$.

Examples of the μSR spectrum after the fast Fourier transform (FFT, 50 K) and time-differential spectra at two temperatures above and below T_c are shown in Figs. 3 and 4, where one can see a coherent precession signal with a frequency of 200 MHz.

---

[*] Corresponding author at: Muon Science Laboratory, Institute for Materials Structure Science, High Energy Accelerator Research Organization (KEK), Tsukuba, Ibaraki 305-0801, Japan. Tel.: +81 29 864 5625; fax: +81 29 864 5623.
E-mail address: ryosuke.kadono@kek.jp (R. Kadono).

0921-4526/$ - see front matter © 2008 Elsevier B.V. All rights reserved.
doi:10.1016/j.physb.2008.11.208

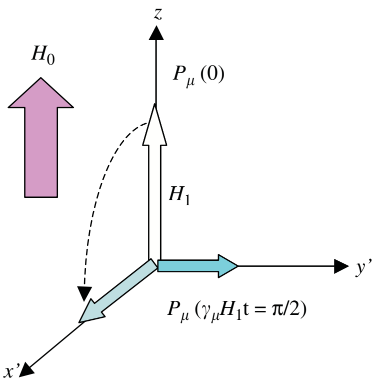

Fig. 1. Schematic illustration of muon spin control by $\pi/2$-RF pulse. The cartesian coordinates are taken on a rotating reference frame of the RF, so that the RF field ($=\mu_0 H_1$) may appear as a static field (where the RF is equal to $\gamma_\mu H_0/2\pi$, with H_0 being the holding field).

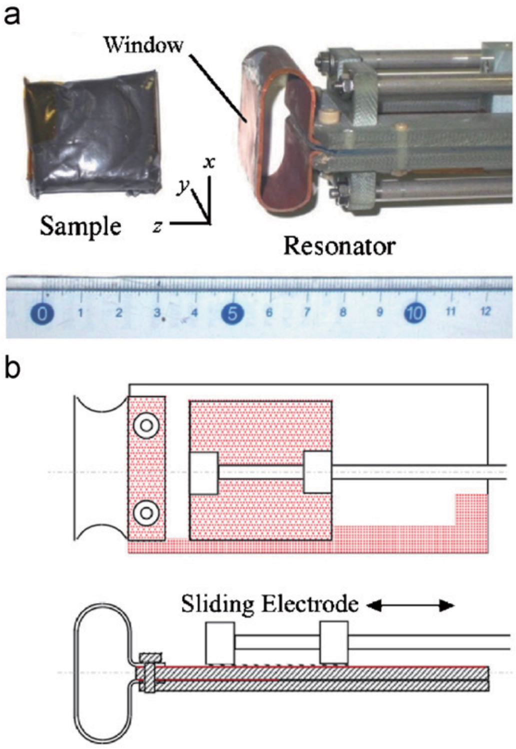

Fig. 2. (a) 200 MHz RF-resonator consisting of a single-turn split-ring (right). The ring is furnished with a beam window made out of thin copper foil. The definition of axes shown by solid lines correspond to those in Fig. 1. A bag made of Kapton film (left) is used to seal MgB_2 powder sample, and placed inside the ring resonator. The whole piece is inserted to a He gas-flow cryostat. (b) A schematic illustration of the split-ring resonator, where the tuning is made by sliding an electrode to change the capacitance.

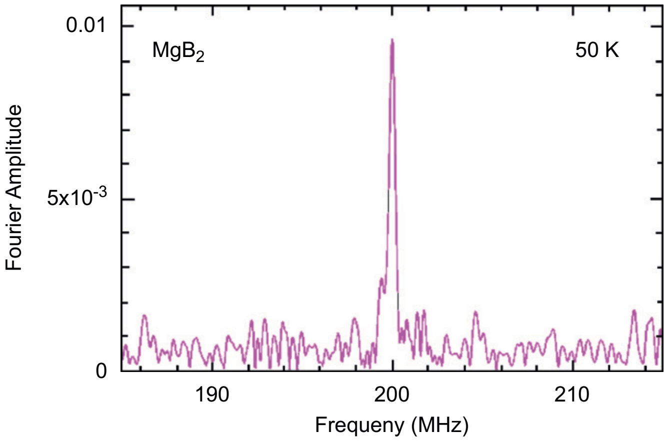

Fig. 3. Fast Fourier transform of μSR spectrum over a time region from 1.5 to 6 μs (where the RF noise is negligible) obtained from a time spectrum.

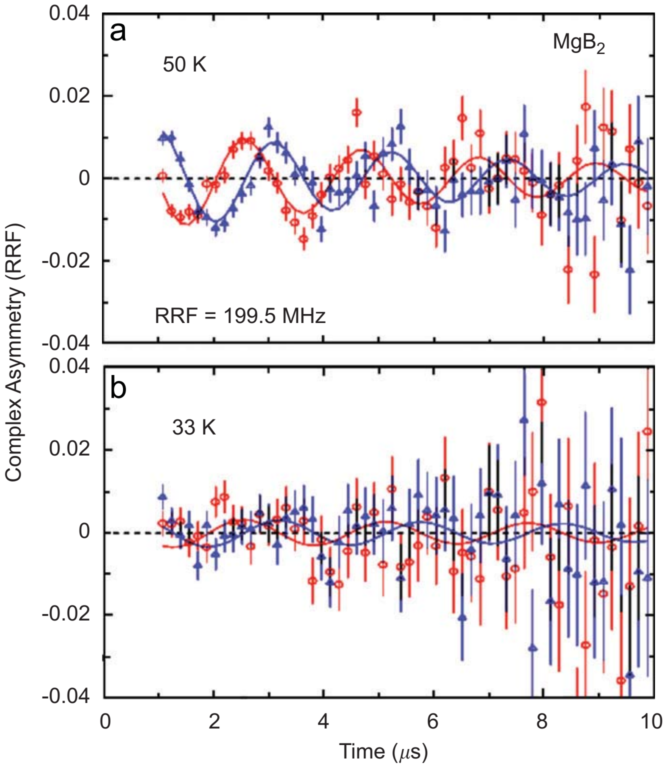

Fig. 4. Time-differential μSR spectra obtained by splitting detectors into four groups (90° each) and combining them to form a complex asymmetry $A_x(t) + iA_y(t)$. They are displayed on a rotating reference frame (RRF) of 199.5 MHz for clarity.

(Note that the Nyquist frequency for the KEK-MSL muon beam is about 10 MHz.) The signal is considerably reduced upon cooling down below T_c, indicating that the sample falls into superconducting state and muons might be depolarized by strong inhomogeneity of internal field due to flux line lattice formation. It is not possible at this stage, however, to evaluate the depolarization rate reliably in the superconducting state because the spectrum lacks the initial part ($0 \leqslant t \leqslant 1$ μs): the depolarization rate expected for the conditions in Fig. 4b is 1–2 μs^{-1} according to some earlier reports, suggesting that the asymmetry remaining at $t \simeq 1$ μs may be too small to identify. The small initial asymmetry makes it further difficult to deduce the depolarization rate from the present data. In this sense, we cannot rule out the possibility that the measurement might have been done with off-resonance condition below T_c due to the diamagnetism. (We note that the resonator and RF were left unchanged while temperature was reduced from 50 to 33 K.)

The small initial asymmetry results mainly from the condition that the positron detectors have never been optimized for this type of measurement. In particular, the time resolution (δt) of the positron detectors is 3–4 ns at best, probably due to a long (~1 m) light guide between scintillator and photomultiplier, so that f_N for the detector system [$1/(2\delta t)\simeq 130$–170 MHz] is lower than expected. [The resolution of TDC (model 3377, LeCroy Co. Ltd.) is 0.5 ns, and therefore it is not a limiting factor for the net resolution.] This actually leads to a drastic reduction of the asymmetry by a factor as large as 5–10 (assuming a Gaussian distribution for the timing fluctuation with a standard deviation equal to δt). Thus, further improvement for the positron detection system is necessary for practical applications. Moreover, the inhomogeneity of H_1 (which is not known, particularly for the short pulse) would lead to the reduction of the initial muon spin polarization within the xy plane. These factors may account for the net reduction of asymmetry by 10–20, as is observed in Fig. 4. The uniformity of H_1 might be more important for the measurements with large samples, which will be monitored by the magnitude of the initial asymmetry.

In addition to the problem mentioned above, we found that each positron detector has an offset of delay time (~a few ns) that varies from one detector to the other (probably due to the subtle difference among individual phototubes). Such random offsets, when a sum is taken over signals from several detectors, would also lead to the serious reduction of asymmetry due to the lack of phase coherence among detectors. This raises an issue of synchronizing many positron detectors with a precision better than that of the inverse Nyquist frequency required for the target frequency of observation. As a matter of fact in deducing the spectra shown in Fig. 4, we corrected the offset of 32 detectors relative to the RF signal that was observed as a noise overlapped with the positron signals over the earlier time range of the spectra ($0\leqslant t<\sim 1\,\mu$s). Since this is effective only when the RF noise is picked up directly at the photon sensors, a more appropriate method for adjusting the timing offset should be developed for practical application.

For the improvement of time resolution of the positron detectors, it is required that the distance between scintillators and optical sensors is minimized to reduce the time jitter of photons reaching the sensor. In this regard, recently developed "multi-pixel photon counter" (MPPC) is a promising optical sensor for its tolerance to high magnetic field, together with its small size, fast timing character, and relatively high gain. We are currently developing a compact positron detector based on MPPC for use under a strong magnetic field (placed near the center of spectrometer magnet). The detector consists of a pair of small scintillators (about 1 cm^3) to which MPPC (with a sensitive area of $1\times 1\,\text{mm}^2$) is connected through a plastic fiber that penetrates the each scintillator [6]. (The fiber is cut at the edge of scintillator where MPPC is placed. It also serves as a light-collecting device for MPPC). The pair is used as a "telescope" to reduce the dark current noise from each MPPC by taking logical "coincidence" condition. With this new positron detector, we are planning to install a μSR spectrometer capable of measurements under a transverse field up to 6 T.

We would like to thank the staff of KEK-MSL for their technical support during the μSR experiment. This work was supported by a Grant-in-Aid for Scientific Research on Priority Areas by Ministry of Education, Culture, Sports, Science and Technology of Japan.

References

[1] S.P. Cottrell, C.A. Scott, B. Hitti, Hyperfine Interact. 106 (1997) 251.
[2] A.D. Hiller, S.P. Cottrell, P.J.C. King, G.H. Eaton, M.A. Clarke-Gayther, Phys. B 326 (2003) 275.
[3] A. Carne, S.F.J. Cox, G.H. Eaton, R. De Renzi, C.A. Scott, G.C. Stirling, Hyperfine Interact. 17–19 (1984) 945.
[4] R. Kadono, K. Nishiyama, K. Shimomura, W. Higemoto, A. Koda, K. Ohishi, KEK-MSL Report, 2003, p. 11.
[5] W.N. Hardy, L.A. Whitehead, Rev. Sci. Instrum. 52 (1981) 213.
[6] S. Takeshita, M. Hiraishi, M. Miyazaki, A. Koda, R. Kadono, S. Suzuki, Y. Yasu, M. Tanaka, Y. Matsuda, K. Ishida, T. Matsuzaki, Nucl. Instr. and Meth. A., to be published.

Physica B 404 (2009) 1002–1006

Contents lists available at ScienceDirect

Physica B

journal homepage: www.elsevier.com/locate/physb

Development of a pipelined data acquisition system for μSR experiments at J-PARC

Soh Yamagata Suzuki [a,*], Manobu Tanaka [a,b], Kazuya Tauchi [a], Yoshiji Yasu [a], Soshi Takeshita [a], Akihiro Koda [a,b], Masatoshi Hiraishi [b], Masanori Miyazaki [a,b], Kohki Satoh [b], Ryosuke Kadono [a,b], Katsuhiko Ishida [c], Dai Tomono [c], Teiichiro Matsuzaki [c]

[a] *High Energy Accelerator Research Organization, Tsukuba, Ibaraki 305-0801, Japan*
[b] *The Graduate University for Advanced Studies (Sokendai), Shonan Village, Hayama, Kanagawa 240-193, Japan*
[c] *Advanced Meson Science Laboratory, The Institute of Physical and Chemical Research (RIKEN), Wako, Saitama 351-0198, Japan*

ARTICLE INFO

Keywords:
μSR method
DAQ

ABSTRACT

We have developed a pipelined data acquisition (DAQ) system for μSR experiments at the Japan-Proton Accelerator Research Complex (J-PARC). From September 2008, the J-PARC accelerator will begin the beam delivery to the muon source and the first μSR experiment will be in operation. When fully operable, the muon beam intensity at the Muon Experiment Facility will be two to three orders of magnitude greater than that of the Muon Science Laboratory (KEK-MSL). This will force us to replace the detector and the DAQ system. The new DAQ system must fit the framework for the run automation at J-PARC. We have developed a new DAQ system for this purpose, which will be used in the first experiment and will be ready for new μSR detectors for the full operation of the accelerator.

1. Introduction

The High Energy Accelerator Research Organization (KEK) and the Japan Atomic Energy Agency (JAEA) have collaborated in a joint project to develop the Japan Proton Accelerator Research Complex (J-PARC). J-PARC will be used for research in the fields of particle physics, nuclear physics, material science, life science, and nuclear technology. The accelerator has already begun delivering a proton beam to a neutron source and will start delivery to a muon source in fall 2008 [1]. The expected intensity of the muon beam is two to three orders of magnitude greater than that of KEK Muon Science Laboratory (KEK-MSL). This intensive beam will bring high hit multiplicity of the detector and μSR experiments in J-PARC may encounter new problems that were not seen at KEK-MSL.

2. μSR experiments at J-PARC

From fall 2008, J-PARC will begin beam delivery to the MUon Science Establishment (MUSE). When the accelerator provides a proton beam in full operation, the intensity of the muon beam at MUSE will be two to three orders of magnitude higher than that of KEK-MSL. This high intensity results in extremely high multiplicity in the detector and it is necessary to replace both the detector and the data acquisition (DAQ) system.

The spectrometer in μSR experiments consists of segmented scintillators to detect positrons from the μ^+ decay. Using a pulsed muon beam, the spectrometer must observe many μ^+ decays from one pulse. The DAQ system uses a time-to-digital converter (TDC) to measure the time spectrum of the decay events, and this TDC must be equipped with multi-hit functionality. The segmentation number of the spectrometer in the KEK-MSL is 64 and the DAQ system used CAMAC-TDC, LeCroy 3377 which has a hit buffer of up to 16 hits per channel. The geometrical acceptance is about 10% and the multiplicity is about 5 hits per pulse. The double pulse resolution of the DAQ system is about 20 ns which is limited by the CAMAC discriminator.

Precise measurement of the time spectrum requires fine double pulse resolution and a deep buffer to hold multiple hits in the TDC. If either is insufficient, several hits will be missed and the observed time spectrum will be distorted. A more intensive beam will cause a higher multiplicity and make it harder to prevent distortion.

If we rebuild the spectrometer with finer segmentation, the multiplicity becomes lower and the distortion problem will be solved. However, if we solve the distortion only by the finer segmentation, the segmentation number will be 64 000 and almost impossible. On the other hand, if we solve the problem only by DAQ system replacement, it must be equipped with a buffer for 5000 hits per channel and 20 ps double pulse resolution. This is also impossible.

---

[*] Corresponding author. Tel.: +81 29 864 5481.
E-mail address: soh.suzuki@kek.jp (S.Y. Suzuki).

0921-4526/$ - see front matter © 2009 Elsevier B.V. All rights reserved.
doi:10.1016/j.physb.2008.11.220

Therefore our upgrade plan for the spectrometer is to increase the segmentation number to 2000, the double pulse resolution and the time resolution are better than 1 ns, and to achieve a sufficient buffer depth in the TDC. We will arrange these scintillators like a honeycomb sphere because of space limitations. Therefore, the geometrical acceptance will be larger than that of the KEK-MSL. If we keep the solid-angle of each scintillator the same in the KEK-MSL, the expected multiplicity of the planned spectrometer will be about 160 hits per channel.

3. COPPER system

As there is no commercially available TDC that has a buffer suitable for such multiplicity, we decided to supersede the CAMAC system using the "COmmon Platform for Pipelined Electronics Readout (COPPER)," which was designed by KEK [2]. Fig. 1 shows the components of the COPPER system. A COPPER board consists of a 9U size base board, four digitizer mezzanine cards, a trigger receiver and one processor module that is standardized as a PrPMC (IEEE P1368 VITA32). This processor module runs the Linux operating system: it reads data from the digitizer cards and sends them via a network to another computer. The form factor of the base board is a 9U VME, but data transmission uses the network rather than the VME bus. The base board is equipped with Fast Ethernet for data transmission. The deadtime of the COPPER system is defined as the data transmission time from pipeline on the digitizer card to the buffer on the base board, which is 23 ns per words.

The first COPPER system was installed in the DAQ system of the Belle experiment at KEK and the existing COPPER-TDC is available for μSR experiments. However, the buffer depth of the TDC module is 256 hits and this hit buffer is shared by 24 channels. This depth maybe insufficient for our requirement and we

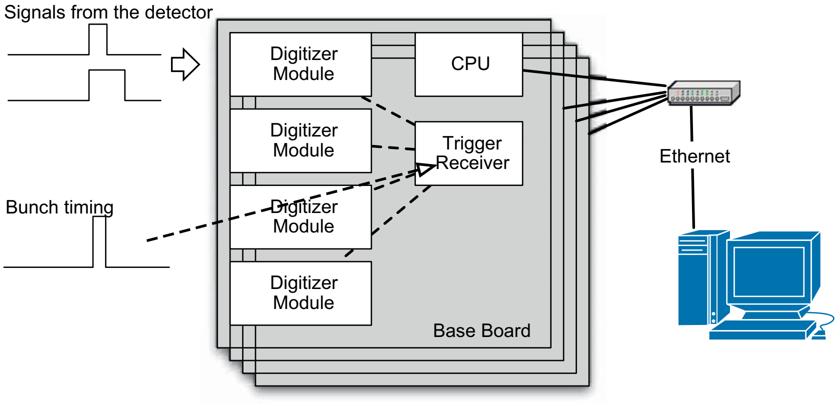

Fig. 1. Copper components.

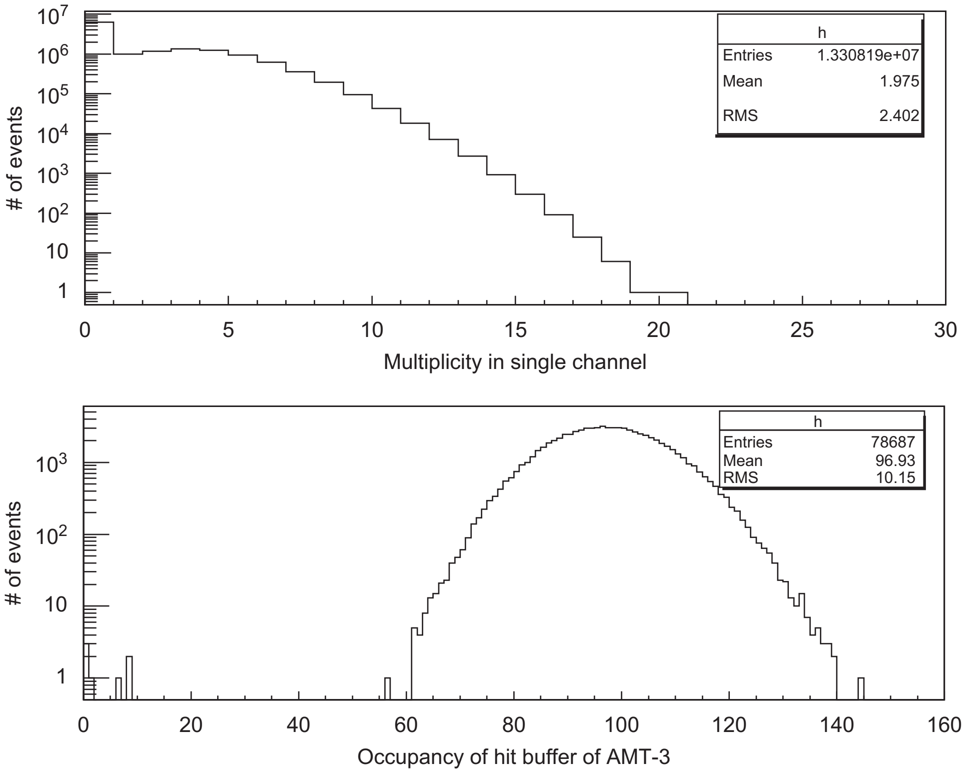

Fig. 2. The multiplicity in a single channel and the occupancy of the hit buffer shared by 24 input channels. The depth of the hit buffer was 256 and no hits were lost in this test experiment.

developed a new TDC mezzanine card with a sufficient buffer depth.

A new discriminator is also necessary to achieve the 1 ns double pulse resolution, so we are developing an application-specific integrated circuit (ASIC) for the discrimination. The prototypes are ready to use and the detail of the ASIC will be described in a future report.

4. Experiment

4.1. COPPER applicability

In the first step, we tested the applicability of the COPPER system to the μSR experiment.

In winter 2006, we installed the COPPER system with existing TDC modules in the readout system of the detector Advanced Riken General purpose mUsr Spectrometer (ARGUS) [4] at the RIKEN-RAL Muon Facility [5] of the Rutherford Appleton Laboratory in the UK. At present, this facility provides the strongest pulsed μ beam in the world. The DAQ system for ARGUS and KEK-MSL are similar.

The existing TDC module was originally developed for the Belle experiment. The LSB is 780 ps, the time resolution is 0.54 LSB and the buffer depth is 256 hits for 24 channels [3].

Using this COPPER system, we measured the time spectrum and the multiplicity of μ−e decay with a silver plate target under a magnetic field of 500 G. In this test, the collimator was fully opened to obtain the maximum multiplicity. The maximum occupancy of the hit buffer was about 150 hits per bunch (Fig. 2).

4.2. New TDC module development

The muon beam rate at the RIKEN-RAL Muon Facility is 50 times smaller than that of the fully operational J-PARC facility, and the buffer depth of the existing TDC is almost insufficient for our requirement. In the case of other commercial TDCs, such as the VME V1290 by CAEN, which uses the HPTDC chip developed by CERN, the hit buffer is shared by 16−32 channels with a depth of 256 or 512 hits. This is insufficient for our requirements.

Therefore we have developed a new TDC module that has a sufficient buffer size, at least 160 hits per channel. Our new TDC module is equipped with one Xilinx SPARTAN XC35400, which contains the TDC logic and the interface logic to the COPPER base board. The specifications of this TDC are as follows: 16 input channels per module, LSB of 1 ns, time resolution of 0.65 ns and the depth of the hit buffer is 1024 hits per channel. When all channels receive 160 hits, this TDC will issue about 60 μs deadtime. This is negligibly short in the case of μSR experiments in the J-PARC. The linearity of this TDC is shown in Fig. 3.

4.3. New TDC applicability

We tested this new COPPER-TDC with ARGUS in 2007 and 2008. Fig. 4 is the observed time spectrum from the Ag plate in 500 G magnetic field.

In this test, the beam intensity was three times higher than that of the 2006 run and the maximum multiplicity reached 34

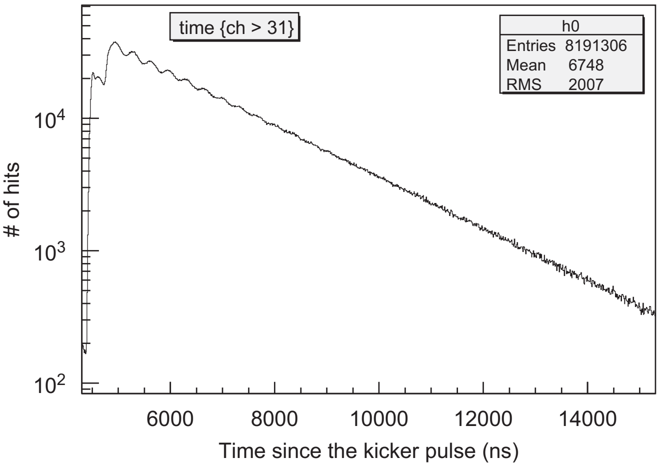

Fig. 4. Observed time spectrum using the new TDC with the ARGUS. The collimator is fully open, but there is no distortion. The left side structure comes from the double bunch of the ISIS accelerator.

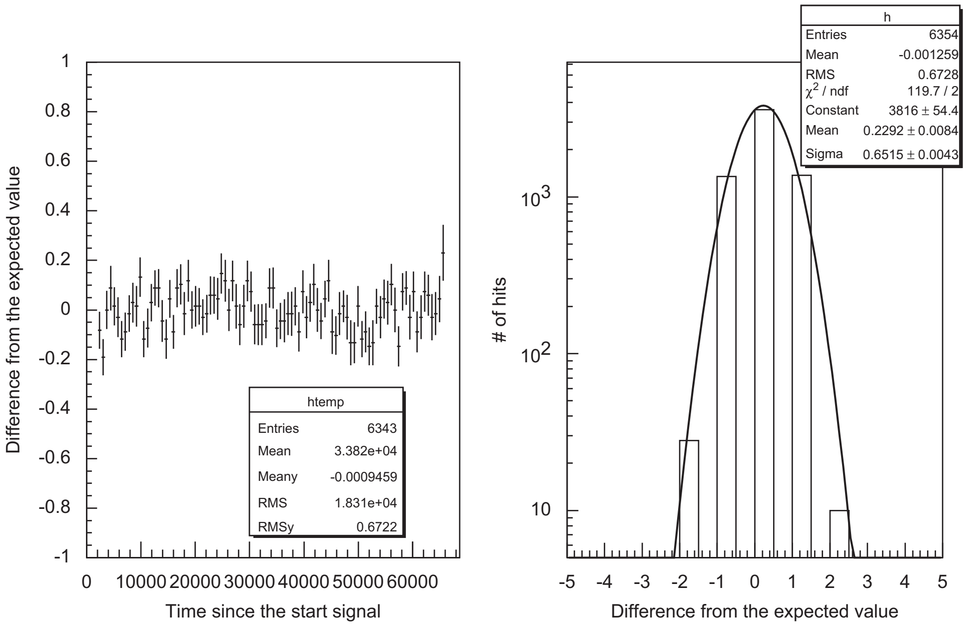

Fig. 3. Linearity of the new COPPER-TDC. The left graph shows the difference between the time measured by the TDC and the actual signal time from a TDC tester. No significant tendency was observed. The right histogram shows the error distribution in the overall range of the TDC. The RMS was 0.65 ns.

hits per channel. The buffer depth of the new TDC, 1024 hits per channel, is sufficient for these conditions.

5. Integration with the slow control system

5.1. DAQ middleware

Experiments in the J-PARC MLF must be controlled from the “Working Desktop” [6] which is the user interface framework to control the DAQ system, the analyzer system and the environment, such as the temperature, the pressure, and the beam collimator. The Working Desktop can be controlled using the Python language, and the run automation must be implemented as a Python script. Most of the components have already been implemented and used in the neutron experiments in the J-PARC.

The DAQ middleware [7] is used for the whole operation of the DAQ system. An unit of this middleware consists of Gatherer, Dispatcher, Logger, and Monitor. The Working Desktop can handle multiple middleware units of these middleware via DAQ operators connected to each unit.

The performance of the DAQ middleware was confirmed to up to 20 MB/s per unit. If the spectrometer requires higher throughput, multiple units are necessary (Fig. 5).

5.2. Modification for μSR experiments

The DAQ middleware was originally developed for neutron experiments in the J-PARC and lacks an essential function for μSR, which is a way to monitor the correlations of different frontends.

μSR experiments must measure the asymmetry of time spectrums from μ−e decays. To minimize the distortion of the time spectrum, all events containing missing hits must be excluded. When N_A and N_B are the total numbers of hits from channels grouped in A and B, respectively, the amplitude of the asymmetry is defined as

$$Asym = \frac{N_A - N_B}{N_A + N_B}$$

If N_A is larger than N_B but N_A misses some hits, the *Asym* is smaller than expected. To prevent this problem, it is necessary to exclude events that contain missing hits. To eliminate such events, the event data must contain all hits from all channels. However, the original DAQ middleware works as follows: collect data that contains multiple events from the first frontend, send it to the Dispatcher, collect data from the second frontend, send it to the Dispatcher, and so on. The number of events in the single data transmission is not constant. They must be rewritten to collect and process the data in an event-by-event.

The asymmetry histogram is calculated from two group histograms. The direction of the magnetic field in μSR experiments in J-PARC is varied and the monitor must be able to change the grouping dynamically. We prepared a channel selector using the ROOT toolkit (Fig. 6). When the Monitor receives the data from the Dispatcher, it updates histograms for every channel after excluding events that miss several hits. The channel selector continuously displays the sum of histograms of chosen channels. The displayed histogram is always updated continuously.

6. Summary

MUSE will be in operation from September 2008, and we have developed a pipelined DAQ system for μSR experiments. At the beginning of MUSE, the beam intensity will not be so high and we will reuse the spectrometer that was used in the KEK-MSL. Our first spectrometer consists of 256 scintillators and the first DAQ system for this spectrometer uses two COPPER-TDCs and one DAQ middleware unit.

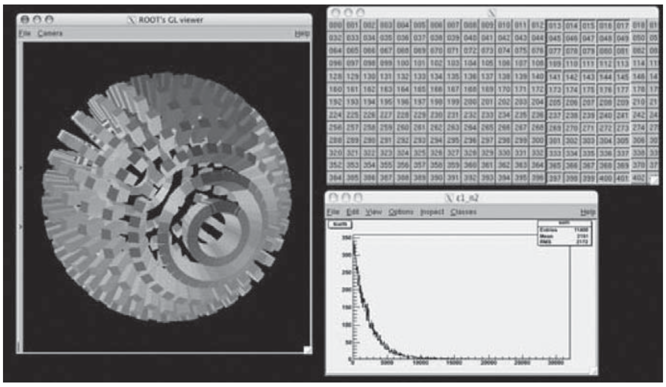

Fig. 6. Screenshot of the dynamic channel selector. The user can choose channels to be treated as a group. The summed histogram of the channel group is always displayed continuously during the run.

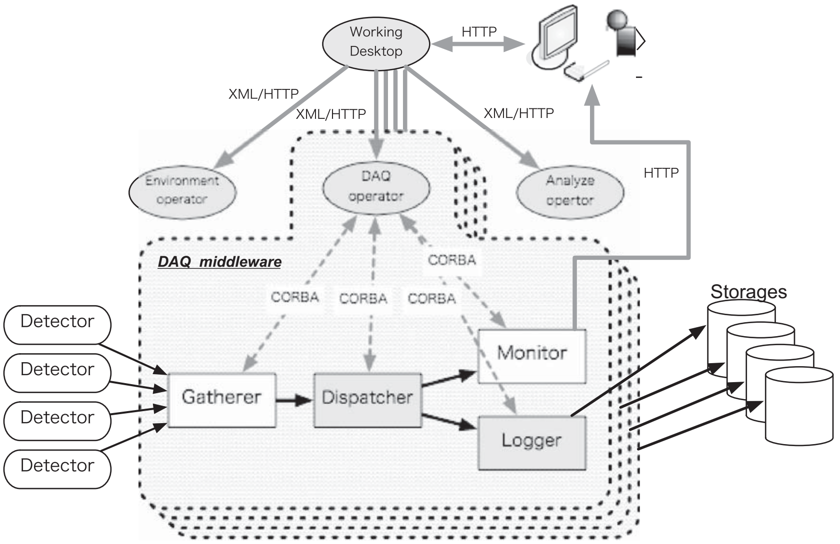

Fig. 5. Components related to the DAQ system. A unit of the DAQ middleware collects data from multiple inputs and sends it to the storage. The user controls the run via the working desktop and confirms the status of the run from the output of the monitor. The working desktop can manage multiple units of the DAQ middleware.

References

[1] K. Shimomura, et al., Nucl. Phys. Proc. Suppl. 155 (2006) 343.

[2] T. Higuchi, et al., IEEE Trans. Nucl. Sci. 52 (2005) 1912.

[3] S.Y. Suzuki, et al., in: Performance of the AMT-3 based TDC system at Belle in Nuclear Science Symposium, Conference Record, vol. 1, 2006, pp. 128–131.

[4] R. Kadono, et al., RIKEN Accelerator Progress Report, vol. 29, 1996, p. 196; R. Kadono, et al., RIKEN-RAL Muon Facility Report, vol. 1, 1997, p. 27.

[5] T. Matsuzaki, et al., Nucl. Instrum. Meth. A 465 (2001) 365.

[6] T. Nakatani, et al., Day-1 status of the software framework for experimental instruments in J-PARC/LF, Presented at International Symposium on Pulsed Neutron and Muon Sciences (IPS08), March 2008, Mito, Japan.

[7] Y. Yasu, et al., A Data Acquisition Middleware, Conference Record/15th IEEE NPSS RealTime Conference, Fermilab, Batavia IL, 60510, April 29–May 4, 2007.

Hyperfine Interact (2009) 193:121–127
DOI 10.1007/s10751-009-0055-0

Muon spectroscopy with trace alkaline-earth and rare-earth isotopes implanted in solid D_2

P. Strasser · A. Taniguchi · T. Matsuzaki · K. Ishida ·
Y. Matsuda · S. Ohya · M. Iwasaki · K. Nagamine

Abstract New intense muon beams with flux several orders of magnitude higher than at present muon facilities would allow many novel experimental studies that were until now statistically not feasible. The investigation of the nuclear properties of short-lived nuclei using muonic atom spectroscopy would become possible. A feasibility study at RIKEN-RAL muon facility using the cold hydrogen film method to produce radioactive muonic atoms is in progress. A new surface ionization type ion source was recently installed to expand the variety of available ions. Encouraging experimental results were obtained with stable alkaline-earth and rare-earth isotope ions implanted in solid deuterium films. The latest results are reported in this paper.

Keywords Muonic X-ray spectroscopy · Muonic atom · Solid hydrogen film · Ion implantation

---

P. Strasser (✉)
Muon Science Laboratory, Institute of Materials Structure Science, High Energy Accelerator Research Organization (KEK), Tsukuba, Ibaraki 305-0801, Japan
e-mail: patrick.strasser@kek.jp

A. Taniguchi
Research Reactor Institute, Kyoto University, Kumatori, Osaka 590-0494, Japan

T. Matsuzaki · K. Ishida · M. Iwasaki
Advanced Meson Science Laboratory, RIKEN Nishina Center,
RIKEN, Wako, Saitama 351-0198, Japan

Y. Matsuda
Department of Basic Science, Graduate School of Arts and Science,
University of Tokyo, Komaba, Meguro-ku, Tokyo 153-8902, Japan

S. Ohya
Department of Physics, Faculty of Science, Niigata University, Niigata 950-2181, Japan

K. Nagamine
Physics Department, University of California Riverside, Riverside, CA 92521, USA

PACS 36.10.Dr • 36.10.k • 29.30.Kv

1 Introduction

Muonic atom X-ray spectroscopy has been successfully used for many years to determine the nuclear charge distribution [1–3]. The most precise charge radii of nuclei have been obtained by use of the muonic atom spectroscopy method. They have been determined for almost all elements, but only for stable isotopes. The most recent and precise results have been reviewed by Fricke et al. [4]. With the recent strong interest in unstable nuclei, the charge radius of such nuclei is an important research topic. New intense muon beams, with fluxes several orders of magnitude higher than at present muon facilities, would allow many novel experimental studies that were statistically not feasible until now. The investigation of the nuclear properties of unstable nuclei using muonic atom spectroscopy would become possible. This would be a unique tool to increase our knowledge of the nuclear structure far from stability where new effects may be expected, in particular, the nuclear charge distribution and the deformation properties of nuclei. It would usefully complement the knowledge obtained from electron scattering and laser spectroscopy, since in the past calibration data were used from muonic atom measurements with stable nuclei. Also, measurements of the quadrupole hyperfine splittings of muonic X-rays could provide precise and reliable absolute values of nuclear quadrupole moments, which are sensitive to the deviation of the shape of a nuclear charge distribution from spherical symmetry.

We proposed the cold hydrogen film method [5, 6] to expand muonic atom spectroscopy by utilizing nuclear beams, including, in the future, radioactive isotope (RI) beams, to produce radioactive muonic atoms. This method will enable studies of the nuclear properties and nuclear sizes of unstable nuclei by means of the muonic X-ray method at facilities in which both intense negative muon (μ^-) and RI beams will be available. The basic concept is to stop both μ^- and nuclear beams simultaneously in a solid deuterium film, followed by the application of the direct muon transfer reaction to higher Z nuclei to form radioactive muonic atoms. Although most of the muons first produce μd atoms, the fast muon transfer reaction occurs from deuteron to implanted Z nuclei to form μZ atoms with a rate of $\lambda_Z \approx$ Z $C_Z \times 10^{10}$ s^{-1}, where Z is the atomic number of the nucleus and C_Z is its atomic concentration in deuterium. At low concentration, most of the muon transfer occurs delayed, and the S/N ratio can be greatly improved by selecting only delayed events.

An experimental program to perform muonic atom spectroscopy with stable ions implanted in a solid hydrogen (H_2 and/or D_2) film is in progress at the RIKEN-RAL muon facility port 4 to experimentally demonstrate the feasibility of this method. Studies were carried out to establish the most efficient way of forming muonic atoms via the muon transfer mechanism by using stable argon beam. Already very promising results were obtained in pure solid D_2 films with argon ions implanted non-uniformly, to study the muon transfer reaction and the diffusion process of dμ atoms [7]. Clear muonic X-ray peaks were observed from implanted argon ions even at a concentration of 0.5 ppm. A summary of the experimental results were reported in [8].

2 Recent progress

A new surface ionization type ion source has been constructed and installed on the existing μA* apparatus at port 4 to expand the variety of available ions and with the aim of using in the future radioactive isotopes. This type of ion source is capable of producing ions from alkali and alkaline-earth metals with high efficiency. At the moment, only stable beams will be produced to optimize the new surface ion source and tune the beam transport optics. Barium and strontium ions were successfully generated from barium oxide and strontium oxide, and accelerated up to 30 keV with a new ion extraction unit. Beam intensities of 1–2 μA were obtained. The ion beam optics was tuned to transport the beam to the solid hydrogen target and optimize the beam spot to efficiently use the large muon beam size at the target position ($\sim$ 40 mm in diameter). All barium and strontium isotopes could be separated on the focal plane after the bending magnet, allowing the implantation of only one specific isotope on the target.

The first transfer experiment was performed by measuring different targets with isotopically separated strontium ions. As shown by Monte Carlo simulations performed with SRIM, the range of 30-keV Sr ions in solid D_2 is only about 200 nm, with a range straggling of about 60 nm (FWHM). Therefore, it is very difficult to perform a uniform implantation in a thick D_2 film. Consequently, the same procedure as that used previously to implant argon ions was utilized [7]. Each Sr implantation was separated from the next by depositing a fixed amount of D_2 to yield a total D_2 film thickness of 1 mm. Each implantation region was identical, and a total of 20 implantations separated by 50 μm were performed for each target, corresponding to an average Sr concentration of about 1 ppm throughout the D_2 film. Figure 1 shows the delayed energy spectra measured by the Ge detector with 1-mm pure D_2 and about 1 ppm Sr ions implanted non-uniformly; (a) ^{88}Sr (solid line) and ^{86}Sr (dotted line), and (b) ^{87}Sr (solid line) with the fitted curves obtained for μ^{88}Sr (dotted line) and μ^{86}Sr (dashed line), respectively. Clear peaks from the 2p→1s muonic transitions were observed from implanted strontium ions, showing a distinct isotope shift for ^{88}Sr and ^{86}Sr. The isotope shift for ^{88}Sr and ^{87}Sr is almost negligible. A preliminary analysis shows that the measured isotope shifts are consistent with that observed in previous experiments performed using enriched strontium isotopes in very large quantities. These experiments were performed using natural strontium oxide (SrO) in the ion source, and only about 7×10^{16} ions of ^{88}Sr, 5×10^{16} ions of ^{86}Sr and 4×10^{16} ions of ^{87}Sr in the target, respectively. The data are now being analyzed, and the detailed analysis will be reported in later publication.

Measurements with barium isotopes were also performed. The experiments were realized with isotopically separated ^{138}Ba and ^{137}Ba ions implanted into 1-mm D_2 film in a way similar to that used with strontium isotopes. Transfer X-rays were successfully observed at around 4 MeV. The energies of muonic barium X-rays are relatively high resulting in low detection efficiency. Our measurements are consistent with previous experiments performed using enriched Ba isotopes. The energy calibration was determined from muonic lead X-rays at around 6 MeV in a separate measurement.

The new surface ion source is also capable of producing ions from rare-earth elements with high efficiency. They seem ideal candidates for an experiment to study very high Z nuclei with deformation properties. For instance, samarium isotopes

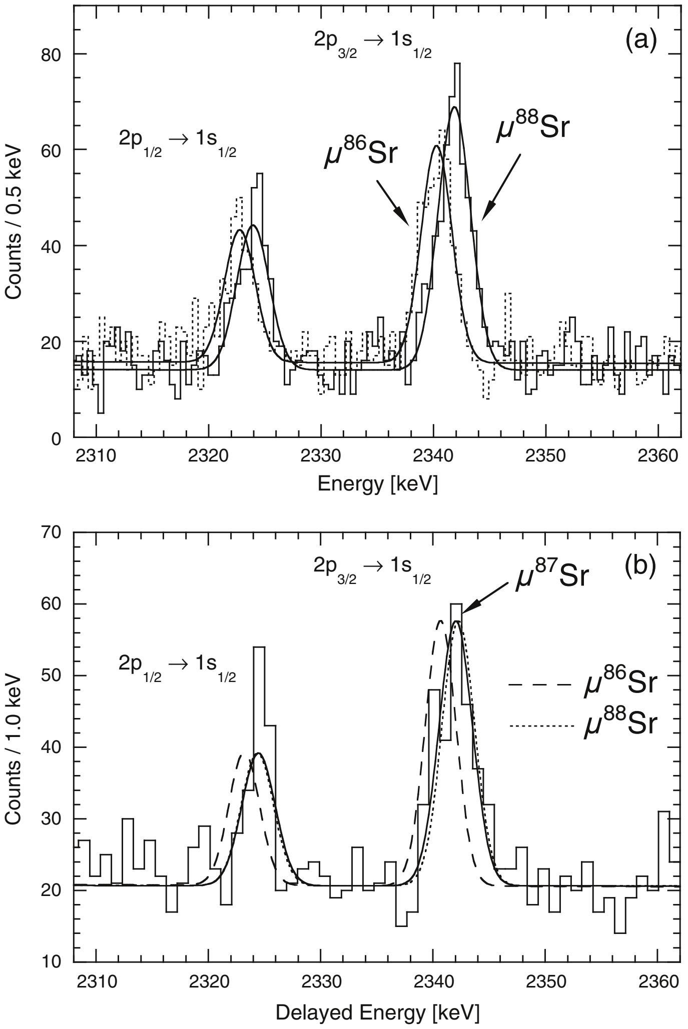

Fig. 1 Muonic strontium delayed energy spectra with 1-mm pure D_2 and about 1 ppm of Sr ions implanted non-uniformly: **a** 2p→1s muonic transitions in ^{88}Sr (*solid line*) and ^{86}Sr (*dotted line*); **b** 2p→1s muonic transitions in ^{87}Sr (*solid line*) showing the *fitted curves* for μ^{88}Sr (*dotted line*) and μ^{86}Sr (*dashed line*), respectively

show very abrupt changes in their nuclear characteristics from spherical to highly deformed nuclei. ^{144}Sm is magic in neutrons ($N = 82$) and display the characteristics of a stiff spherical nucleus which is very hard to excite, whereas ^{152}Sm and ^{154}Sm reveal low energy levels characteristic of highly deformed nuclei whose muonic X-ray spectra show a 2p hyperfine structure (h.f.s.). The latest measurements were performed with isotopically separated samarium ions. Figure 2 shows the delayed energy spectra measured by the Ge detector with 1-mm pure D_2 and about 1 ppm of ^{148}Sm and ^{152}Sm ions implanted non-uniformly, respectively. Here too, the measured isotope shifts are consistent with that observed in previous experiments performed

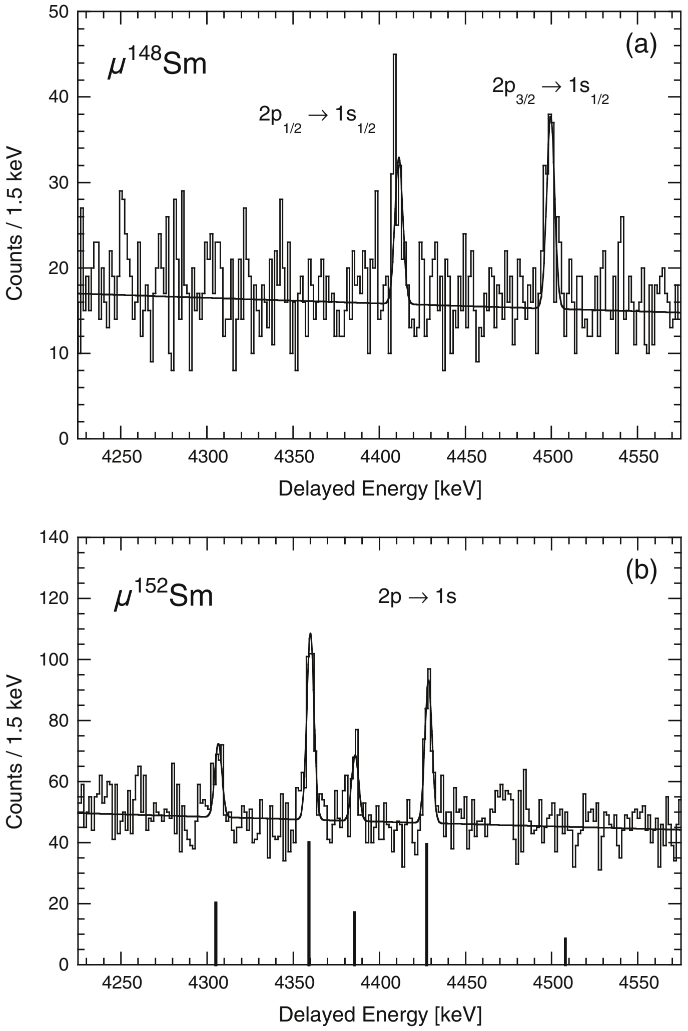

Fig. 2 Delayed energy spectrum of the 2p→1s muonic transitions in Samarium measured with 1-mm pure D_2 and about 1 ppm of Sm ions implanted non-uniformly: **a** ^{148}Sm and **b** ^{152}Sm, respectively. Theoretical prediction shown underneath for ^{152}Sm [14, 15]

using enriched samarium isotopes. ^{148}Sm has still a spherical nucleus, while ^{152}Sm is clearly showing a 2p h.f.s. characteristic of a highly deformed nucleus. The detailed analysis will be presented elsewhere.

In all the present measurements, the experimental precision is limited essentially for statistical reasons. Indeed, it is very difficult to compete with other measurements that use enriched stable isotopes in very large quantities. However, one advantage of this ion implantation method is that the isotope separation can be done during the implantation, and that high purity isotopes can be measured. The measurement is also free form the chemical substance of the element if it can be completely ionized.

3 Future plans

As an intermediate step towards muonic spectroscopy with unstable nuclei, an experiment using long-lived isotopes is now under study. For elements heavier than bismuth, there are no stable isotopes for good measurements of nuclear parameters like the nuclear charge radius. In particular, radium isotopes are of strong interest since these parameters would be urgently needed to exploit the full potential of the radium atom for atomic parity non-conservation studies [9]. To that extend, the new surface ion source could be used to produce long-lived RI beams. Improvements to the existing apparatus are currently under consideration to handle long-lived RI safely.

At present, these experiments are still performed with a relatively large number of implanted ions, because of the relatively low μ^- beam intensity at a momentum of 27 MeV/c. Future intense muon beams with higher muon flux would require fewer implanted ions. For instance, the new muon experimental facility that is now under construction at the Materials and Life Science Facility (MLF) in the J-PARC project [10] is also very attractive to realize the proposed study. A proposal exists to built there the world highest intensity surface muon channel called "Super Omega" [11, 12]. This advanced muon channel consists of a double normal conducting solenoid lens to accept muons in a solid angle of nearly 400 msr, a curved superconducting solenoid for transportation, and a set of superconducting coils to focus the beam at the exit of the solenoid. According to Monte Carlo simulations, a surface muon intensity of 2–5 10^8/sec is expected. Since this muon beam channel uses only solenoids and coils, cloud μ^- can also be extracted simultaneously. By placing a magnetic bend right at the end of this channel, both negative and positive muon beams with the same momentum can be produced. The cloud μ^- intensity at 27 MeV/c is roughly 1–2% of the surface muon intensity, and a μ^- beam of 10^{6-7}/sec could be obtained. This is more than 2–3 orders of magnitude higher than presently available at RIKEN-RAL, and very attractive to perform the proposed study. This advanced muon channel "Super Omega" is now being carefully designed [13], but unfortunately it has not been completely funded yet.

Acknowledgements We acknowledge Profs. S. Ichikawa, H. Miyatake and T. Shinozuka for their helpful collaboration in designing the new surface ionization ion source. Gratitude is also extended to Mr. H. Mochizuki for his collaboration in participating in the strontium experiment and the data analysis. This research was partially supported by the Japanese Ministry of Education, Science, Sports and Culture, Grant-in-Aid for Scientific Research (B) 15340091 (2003) and 20340062 (2008).

References

1. Hüfner, J., Scheck, F., Wu, C.S.: Muon Physics, vol. 1, pp. 201–307. Academic, New York (1975)
2. Engfer, R., et al.: At. Data Nucl. Data Tables **14**, 509 (1974)
3. Schaller, L.: Z. Phys., C **56**, S48 (1992)
4. Fricke, G., Bernhardt, C., Heilig, K., Schaller, L.A., Schellenberg, L., Shera, E.B., de Jager, C.W.: At. Data Nucl. Data Tables **60**, 177 (1995)
5. Strasser, P., Matsuzaki, T., Nagamine, K.: Hyperfine Interact. **119**, 317 (1999)
6. Strasser, P., Matsuzaki, T., Nagamine, K.: Nucl. Instrum. Methods, A **460**, 451 (2001)
7. Strasser, P., Nagamine, K., Matsuzaki, T., Ishida, K., Matsuda, Y., Iwasaki, M.: Nucl. Phys., B Proc. Suppl. **149**, 390 (2005)

8. Strasser, P., Nagamine, K., Matsuzaki, T., Ishida, K., Matsuda, Y., Iwasaki, M.: AIP Conf. Proc. **793**, 242 (2005)
9. Jungmann, K.P.: Hyperfine Interact. **138**, 463 (2001)
10. Kawamura, N., Makimura, S., Shimomura, K., Strasser, P., Koda, A., Fujimori, H., Nakahara, K., Kato, M., Takeshita, S., Kadono, R., Higemoto, W., Nishiyama, K., Nagamine, K., Miyake, Y.: Hyperfine Interact. (2009). doi:10.1007/s10751-009-0074-x
11. Shimomura, K., Ishida, K., Miyadera, H., Nagamine, K.: AIP Conf. Proc. **721**, 346 (2004)
12. Shimomura, K., Ishida, K., Doornbos, J., Strasser, P., Kawamura, N., Miyake, Y., Nishiyama, K., Makimura, S., Miyadera, H., Nagamine, K.: Nucl. Phys., B Proc. Suppl. **155**, 343 (2006)
13. Nakahara, K., Miyake, Y., Shimomura, K., Strasser, P., Nishiyama, K., Kawamura, N., Fujimori, H., Makimura, S., Koda, A., Nagamine, K., Ogitsu, T., Yamamoto, A., Adachi, T., Sasaki, K., Tanaka, K., Kimura, N., Makida, Y., Ajima, Y., Ishida, K., Matsuda, Y.: AIP Conf. Proc. **981**, 312 (2008)
14. Hitlin, D., Bernow, S., Devons, S., Duerdoth, I., Kast, J.W., Macagno, E.R., Rainwater, J., Wu, C.S.: Phys. Rev., C **1**, 1184 (1970)
15. Powers, R.J., Barreau, P., Bihoreau, B., Miller, J., Morgenstern, J., Picard, J., Roussel, L.: Nucl. Phys., A **316**, 295 (1979)

Hyperfine Interact (2009) 193:159–163
DOI 10.1007/s10751-009-9994-8

Density effect in *d*-*d* catalyzed fusion with ortho- and para-enriched deuterium

H. Imao · K. Ishida · N. Kawamura · T. Matsuzaki · Y. Matsuda · A. Toyoda · P. Strasser · M. Iwasaki · K. Nagamine

Abstract The ortho-para dependence of *d*-*d* fusion neutrons time spectra has been investigated using different target densities at similar temperatures. Even at the similar temperatures, the ortho-para effect on the fusion neutron yields in the liquid phase showed the opposite tendency from that in the gas phase. The result evidenced significant density dependence on resonant $dd\mu$ formation.

Keywords Muon catalyzed fusion · Ortho deuterium · Para deuterium

1 Introduction

The resonant muonic molecular formation [1] is an essential process in muon-catalyzed fusion (μCF) because it is one of the rate limiting processes:

$$(d\mu)_F + (\mathrm{D}_2)_{K_i,\nu_i} \rightarrow \left[(dd\mu)_{J=1,\nu=1}dee\right]^*_{K_f,\nu_f}. \tag{1}$$

H. Imao (✉)
Atomic Physics Laboratory, RIKEN, Wako, Saitama 351-0198, Japan
e-mail: imao@riken.jp

K. Ishida · T. Matsuzaki · Y. Matsuda · M. Iwasaki
Advanced Meson Science Laboratory, RIKEN, Wako, Saitama 351-0198, Japan

N. Kawamura · P. Strasser
Muon Science Laboratory, Institute of Materials Structure Science, High Energy Accelerator Research Organization, Tsukuba, Ibaraki 305-0801, Japan

A. Toyoda
Institute of Particle and Nuclear Studies, High Energy Accelerator Research Organization, Tsukuba, Ibaraki 305-0801, Japan

K. Nagamine
Physics Department, University of California Riverside, Riverside, CA 92521, USA

The collision energy of incident particles and the binding energy of $dd\mu$ are transmitted to the final rotational and vibrational energy of the muonic molecular complex of $[(dd\mu)dee]$, where small resonance energies of the order of meV are realized. This process is owing to the existence of $dd\mu_{J=1,\nu=1}$ state with the small binding energy (~ -1.96 eV) lower than both the electric ionization energy (~ 15 eV) and the dissociation energy of D_2 (~ 4.5 eV).

By artificially changing the initial molecular state of D_2, we can increase the resonant $dd\mu$ formation rate and thus enhance the overall fusion cycling rate [2]. One of such methods is to change the initial rotational level, K_i, of D_2, which can be achieved by changing the ortho to para ratio of D_2. Ortho- and para-D_2 are dominantly in $K_i = 0$ and $K_i = 1$ states at low temperatures, respectively, because of the energy difference of 7.4 meV.

Our group experimentally investigated the resonant $dd\mu$ molecular formation while controlling the ortho-para ratio of D_2 [3–6]. We have successfully observed a clear difference in *d*-*d* fusion neutron spectra between ortho-, normal- and para-enriched D_2. Recently, in order to determine the nature of the condensed-matter effect, we observed the ortho-para dependent phenomena in different target densities at similar temperatures with low-density gas, $\phi \leq 0.17$ LHD (liquid hydrogen density: 4.25×10^{22} atoms/cc) and $T = 36.2$ K, and pressurized liquid, $\phi \geq 0.86$ LHD and $T \geq 35$ K. Such an experiment is not only a sensitive examination of the ortho-para effect predicted by the existing μCF theories [2] (Faifman, private communication), but also essential to understand a high-density effect in condensed matter [7, 8].

1.1 Experiment

Details of the experimental techniques to observe the ortho-para dependent phenomenon are elsewhere [5, 6, 9]. The measurement was performed at the TRIUMF M9B muon channel. We changed the μ^- beam momentum in the range of 48–50 MeV/c for different target densities. The coincidence signal of two muon beamline counters opens a 14-μs gate for data taking. Four NE-213 liquid scintillators (ϕ2”×L2”) were placed around the deuterium target to detect 2.5-MeV neutrons emitted from *d*-*d* fusion reactions. Muon-decay electrons were detected by four pairs of plastic scintillation counters.

Main background for fusion neutron detection was originating from γ-rays and the capture neutrons, which came from a negative muon captured by nucleus in surrounding materials. In order to distinguish between a neutron and a γ-ray signal, a signal-shape analyzer (Ortec Inc. Delay Line Amplifier 460, and Pulse-Shape Analyzer 552) was used. The background neutrons due to the muon nuclear capture reactions were strongly suppressed by requiring the muon-decay electron to be detected between 0.3 μs and 5 μs after the neutron signal (electron condition). The remaining background under the electron condition mainly came from ambient neutrons with no correlation to muon arrival. The time distribution of background neutrons was determined by using the observed distribution with the hydrogen target.

We used two types of bullet-shaped target cells made of oxygen-free high-conductivity (OFHC) copper for the gas (50 mm in diameter and 120 mm in length) and the high-temperature liquid (30 mm in diameter and 55 mm in length) targets, respectively. The cell was sufficient to sustain the maximum operating gas pressure of 12.2 bars.

In order to make an ortho-rich D_2 target, we hold the deuterium for about one day in the converter. The converter is a chamber filled with catalyst (Al_2O_3 + Cr_2O_3) cooled to a temperature at 10 K. We used the preferential adsorption method [10] for preparing para-enriched targets. An appropriate amount of ortho- or para-enriched gas is sent to the target cell and condensed into liquid. After closing the inlet line to the cell, we controlled the temperature to obtain our desired density. It was confirmed that the ortho-para ratio of the target was not changed during each measurement with rotational Raman spectroscopy method.

1.2 Results and discussion

We analyzed the emission-time distribution of *d-d* fusion neutrons from both ortho- and para-rich D_2 around 35 K on the density of $\phi = 0.17$ LHD and 0.085 LHD. Figure 1 shows observed emission time spectra of *d-d* fusion neutrons. The fusion neutrons are normalized by both the number of muons stopped in the target and the density ϕ. Because the reaction rates between $d\mu$ and D_2 are linearly proportional to the target density, this obvious density dependence is removed.

One can find obvious density dependence at a glance in Fig. 1. We note that it is difficult to avoid large systematic errors accompanying with the different target densities in the comparison of spectra between different densities only with normal-D_2 (ortho 67%). The dependence of the spectra on the ortho-para ratio can be compared among the different target densities without such systematic errors. That is a great advantage to conventional experiments only with normal D_2 for investigating the high-density effect.

A delayed bump structure was observed only in the spectra for gaseous ortho-D_2 overlapping the fast exponential disappearance component of fusion neutrons. The bump structure did not appear clearly in other spectra. Because of the bump structure, the resonant $dd\mu$ formation rate is not a simple parameter. In the conventional analysis, the rapid $d\mu$ thermalization ($\lambda_{therm} \sim 10^9 \phi$) are assumed, which results in an exponential time spectrum for the resonant *d-d* fusion neutrons. The structure indicates that the slow completion of the thermalization process of $d\mu$ and the significance of the transient $dd\mu$ formation from $d\mu$ atoms in the thermalizing stage, which was ignored in the static kinetics model of *d-d* μCF. One of the approaches to extract the resonant $dd\mu$ formation rates from the spectra considering the slow $d\mu$ thermalization is described in [6].

In order to compare the strength of the resonance for ortho- and normal-D_2, we compared the number of fusion neutrons in ortho- and para-enriched D_2. As shown in Fig. 1, the ortho-para effect on the fusion neutron yield showed the opposite tendency between gaseous and liquid D_2 even at the almost same temperatures. The fusion neutron yield in the prompt time region (e.g., 0–500 ns) for 36.2-K gas D_2 increase with an increase of the ortho concentration. Because the difference between the $d\mu$ deceleration process in ortho- and para-D_2 is negligible in the gas phase due to large D_2 thermal motion at these temperatures, the increase of the yield in ortho-rich deuterium would be ascribed to the existence of the stronger resonance in ortho-D_2 than that in normal-D_2. The stronger resonance in ortho-D_2 suggested by the present result is qualitatively consistent with the theoretical ones [2] (Faifman,

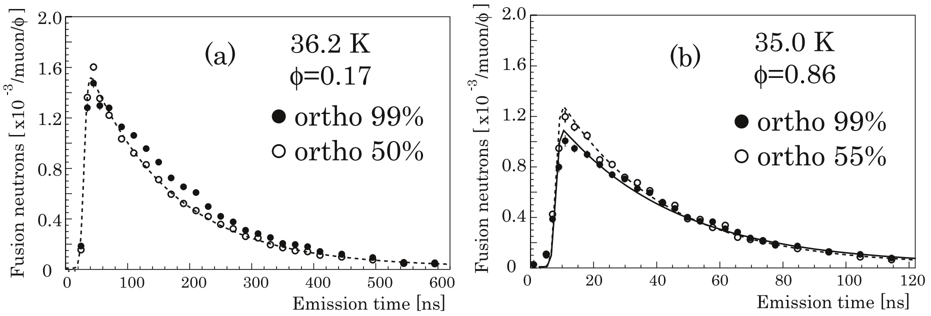

Fig. 1 Fusion neutrons emission time spectra for ortho- and para-enriched D_2 in 36.2-K gas (**a**) and 35.0-K liquid (**b**). The emission time from muon injection normalized by the target density is also shown. The *solid* and *dotted lines* are fitting results for ortho- and para-enriched D_2 with exponential functions derived from a static kinetics model in *d-d* μCF [11], respectively

private communication). For 35-K liquid D_2, the neutrons yield in the prompt region in ortho-rich D_2 is lower than that in normal-D_2, which is opposite to the theory and a similar tendency to that observed in 3.5–18-K solid and 19–23-K liquid [5]. The result in the liquid phase indicated that the resonant condition was modified from the theoretical calculations for isolated D_2.

In order to quantitatively understand the dependence of the observed structure dependence on the ortho-para ratio, theoretical studies with the Monte-Carlo method taking into account all *d-d* μCF processes that compete with $dd\mu$ formation are required. The difference in Fig. 1 provide us the strong motivation to observe the ortho-para effect at "middle" densities ($0.17<\phi<0.84$) to determine the nature of the density effect. The experimental and theoretical efforts for such study are continuing.

Acknowledgements The authors thank Profs. G. M. Marshall and J. M. Poutissou for their helpful support with the experiment. We thank Profs. A. Adamczak, L. I. Ponomarev and M. P. Faifman for their useful comments. Part of this study was supported by a Grant-in-Aid for Young Scientists (B)(16740154) from the Japanese Ministry of Education, Science, Sports and Culture, and by the Core-to-Core Program of JSPS (15005) and by a Grant-in-Aid for a JSPS fellowship.

References

1. Vesman, E.A.: Muon catalysis of nuclear fusion reactions. Sov. Phys. JETP Lett. **5**, 91 (1967)
2. Leon, M., Cohen, J.S.: Ortho- and paradeuterium effects in muon-catalyzed fusion. Phys. Rev. **A31**, 2680 (1985)
3. Toyoda, A., et al.: Measurements of an ortho-para effect in muon-catalyzed fusion in solid deutrium. Phys. Lett. **B509**, 30 (2001)
4. Toyoda, A., et al.: New insights in muon-catalyzed dd fusion by using ortho-para controlled solid deuterium. Phys. Rev. Lett. **90**, 243401 (2003)
5. Imao, H., et al.: Dependence of muon-catalyzed *d-d* fusion on the ortho-para ratio in solid and liquid deuterium. Phys. Lett. **B632**, 192 (2006)
6. Imao, H., et al.: Density effect in *d-d* muon-catalyzed fusion with ortho- and para-enriched D_2. Phys. Lett. **B658**, 120 (2008) (2005)
7. Adamczak, A., Faifman, M.P.: Resonant dd formation in condensed deuterium. Phys. Rev. **A64**, 052705 (2001)
8. Adamczak, A.: Differential cross sections for muonic atom scattering in solid hydrogenic targets. Phys. Rev. **A76**, 052512 (2007)

9. Imao, H., et al.: Preparation of ortho–para-ratio controlled D_2 gas for muon-catalyzed fusion. Rev. Sci. Instrum. **79**, 053502 (2008)
10. Silvera, I.F.: The solid molecular hydrogens in the condensed phase: fundamentals and static properties. Rev. Mod. Phys. **52**, 393 (1980)
11. Scrinzi, A., et al.: Muon-catalyzed dd fusion between 25 and 150 K: Theoretical analysis. Phys. Rev. **A47**, 4691 (1993)

PHYSICAL REVIEW B **81**, 014525 (2010)

Anisotropic superconducting order parameter in Li-intercalated layered superconductor Li_xZrNCl

M. Hiraishi,[1] R. Kadono,[1,2] M. Miyazaki,[1] S. Takeshita,[2] Y. Taguchi,[3] Y. Kasahara,[4] T. Takano,[4]
T. Kishiume,[4] and Y. Iwasa[4]
[1]*Department of Materials Structure Science, The Graduate University for Advanced Studies, Tsukuba, Ibaraki 305-0801, Japan*
[2]*Institute of Materials Structure Science, High Energy Accelerator Research Organization, Tsukuba, Ibaraki 305-0801, Japan*
[3]*Cross-Correlated Materials Research Group (CMRG), ASI, RIKEN, Wako 351-0198, Japan*
[4]*Institute for Materials Research, Tohoku University, Sendai 980-8577, Japan*
(Received 6 November 2009; published 27 January 2010)

In this study, it is shown that in a layered nitride superconductor, i.e., $\mathrm{Li}_x\mathrm{ZrNCl}(0.07 \leq x \leq 0.21)$, the superconducting order parameter is highly anisotropic in a sample with $x=0.12$, as inferred from both the temperature and the magnetic field dependences of the muon depolarization rate (σ_s, proportional to the superfluid density). Moreover, the tendency of strong anisotropy with an increase in x is indicated by the T dependence of σ_s. These observations are in good agreement with the recent theory that predicts the development of anisotropy in a $d+id'$ gap upon carrier filling to the bands with disconnected Fermi surfaces on a honeycomb lattice.

DOI: 10.1103/PhysRevB.81.014525 PACS number(s): 74.70.−b, 74.20.Rp, 76.75.+i

Layered nitrides such as β-MNCl (with $M=$ Zr, Hf) are attracting considerable attention since they exhibit superconductivity upon intercalating alkaline metals.[1,2] While these nitrides have relatively high superconducting transition temperatures [$T_c \simeq 15(25)$ K with $M=$ Zr (Hf)], the density of states at the Fermi level [$N(0)$] is reported to be considerably lower than that of other superconductors having similar T_c, as inferred from the results of the specific-heat measurement of $\mathrm{Li}_{0.12}$ZrNCl (Ref. 3) and magnetic susceptibility measurement of $\mathrm{Li}_{0.48}(\mathrm{THF})_y$HfNCl (where THF refers to tetrahydrofuran).[4] The small $N(0)$ is in excellent agreement with the prediction of the theoretical investigation.[5] Such situation naturally leads to the question of whether or not the superconductivity in layered nitrides is fully understood on the basis of the conventional BCS theory with electron-phonon coupling. Moreover, it has been shown that one of these nitrides, i.e., Li_xZrNCl, exhibits further anomalies that are not expected to be present in the simplest situation presumed by the BCS theory.

Li_xZrNCl has a lamellar structure consisting of alternating stacks of Zr-N double honeycomb layers and insulating Cl bilayers. Li atoms are intercalated into the van der Waals gap of the Cl bilayers to supply electrons to the conducting Zr-N layers. In addition to the above mentioned small $N(0)$, it has been also revealed that the electron-phonon interaction is too weak to explain its high T_c.[3,5,6] In general, in the case of two-dimensional electronic systems such as β-ZrNCl, $N(0)$ may be only weakly dependent on band filling. Therefore, provided that superconductivity is explained by the conventional BCS theory, T_c would not vary with the Li concentration (x). However, the fact is that while T_c is independent of doping for $x \gtrsim 0.15$, it increases steeply below $x \simeq 0.12$, reaching a maximum ($T_c=15.2$ K at $x=0.06$) and then suddenly transitioning into an insulating state for $x \lesssim 0.05$.[7] It might be worth noting that this tendency of T_c to be high at a low carrier density x is opposite to that of underdoped cuprates.

Another anomaly is reported in the magnetic field dependence of an electronic specific-heat (Sommerfeld) coefficient γ in the mixed state of $\mathrm{Li}_{0.12}$ZrNCl. While γ is expected to be approximately proportional to the number of flux lines, and accordingly to the magnetic field in conventional BCS superconductors (i.e., $\gamma \simeq \gamma_n H/H_{c2} \propto H/\Phi_0$, where γ_n is the electronic specific heat in the normal state, H is the magnetic field, H_{c2} is the upper critical field, and $\Phi_0=2.07 \times 10^{-15}$ T m^2 is the quantum flux), it increases with a gradient much steeper than γ_n/H_{c2} in $\mathrm{Li}_{0.12}$ZrNCl, approaching γ_n at $H \sim 0.4H_{c2}$.[3] This strongly suggests the occurrence of field-induced quasiparticle excitation that is not expected for the superconducting order parameter described by isotropic s-wave paring with a unique gap energy.

In this paper, we describe our muon spin rotation (μSR) study on Li_xZrNCl over a range of Li content near metal-to-insulator transition ($0.07 \leq x \leq 0.21$). We show that in a sample with $x=0.12$, the temperature and magnetic field dependences of the muon spin depolarization rate [$\sigma_s \equiv \sigma_s(T,H)$, which is proportional to the superfluid density n_s] is in complete agreement with the anomalies observed in the bulk properties, providing microscopic evidence for the anisotropic order parameter. Furthermore, a clear tendency of increasing anisotropy as a function of x is inferred from the magnitude of the gap ratio ($2\Delta/k_B T_c$). These observations support the recent theory that predicts the occurrence of anisotropic $d+id'$ pairing in Li_xZrNCl and the effect of electronic correlations on the Fermi surface specific to Li_xZrNCl, which develops with band filling.[8,9]

Conventional μSR measurements were performed on M15 and M20 beamlines of TRIUMF, Canada. A μSR apparatus with high time resolution was used to measure the time-dependent positron decay asymmetry under a transverse field (TF) up to 2 T. Li_xZrNCl samples, aligned along the c axis, were loaded on a He gas-flow cryostat, and they were field cooled to a target temperature to minimize the effect of flux pinning. Details of sample preparation are described in the earlier report, where special precaution was taken to maintain the homogeneity of samples.[7] The superconducting

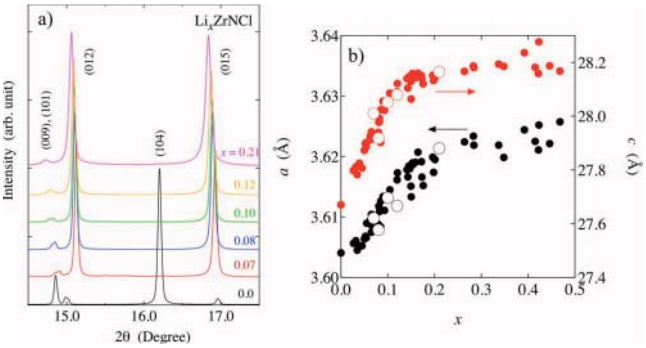

FIG. 1. (Color online) (a) x-ray diffraction spectra for the present samples obtained at SPring-8 (x-ray energy of 15.6 keV). The [104] line observed in the pristine compound is absent in Li-doped samples. (b) Lattice parameters (open circles show present data, and filled points are after Ref. 7).

volume fraction as well as T_c [=15.1 K (x=0.07), 14.0 K (x=0.08), 12.6 K (x=0.10), 12.5 K (x=0.12), and 11.6 K (x=0.21)] determined from magnetization measurements were in excellent agreement with the previous result.[7] The concentration of lithium was determined from inductively coupled plasma spectroscopy. As shown in Fig. 1, the homogeneity of samples was confirmed by carrying out high-resolution powder x-ray diffraction at SPring-8. The mean free path l of these samples were estimated to be 10–16 nm (increasing with x),[10] which is approximately equal to the coherence length (ξ=8–13 nm). Although this would not be in the clean limit, the condition $l > \xi$ is always satisfied, and thus, the situation is consistent with the observed influence of anisotropic gap on σ_s.

μSR is an effective microscopic technique for measuring the magnetic penetration depth (λ) in type-II superconductors. It is reasonably presumed that implanted muons are distributed randomly over the length scale of flux line lattice, probing local magnetic fields at their respective positions. Then the transverse muon spin precession signal consists of a random sampling of internal field distribution $B(\mathbf{r})$, such that

$$P_x^{\mathrm{v}}(t) = \int_{-\infty}^{\infty} \cos(\gamma_\mu B t + \phi) n(B) dB,$$

$$n(B) = \langle \delta[B(\mathbf{r}) - B] \rangle_{\mathbf{r}},$$

where $\gamma_\mu = 2\pi \times 135.53$ MHz/T is the muon gyromagnetic ratio, $n(B)$ is the spectral density for the internal field defined as a spatial average ($\langle\,\rangle_{\mathbf{r}}$) of the delta function, and ϕ is the initial phase of rotation. Hence, $n(B)$ can be obtained from the real amplitude of the Fourier transform of the TF-μSR signal. In the case of a relatively long magnetic penetration depth ($\lambda \geq 300$ nm), the Gaussian distribution is a good approximation for $n(B)$, yielding

$$P_x^{\mathrm{v}}(t) \simeq \exp(-\sigma_s^2 t^2/2) \cos(\omega_0 t + \phi),$$

where σ_s is obtained from a second moment of the field distribution $(=\gamma_\mu \sqrt{\langle [B(\mathbf{r}) - B]^2 \rangle})$ and $\omega_0 = \gamma_\mu B_0$ with $B_0 \simeq \mu_0 H$. Here, provided that the clean limit is achieved, λ is related to the superconducting carrier density n_s as follows:

$$\sigma_s \propto \frac{1}{\lambda^2} = \frac{n_s e^2}{m^* c^2}.$$

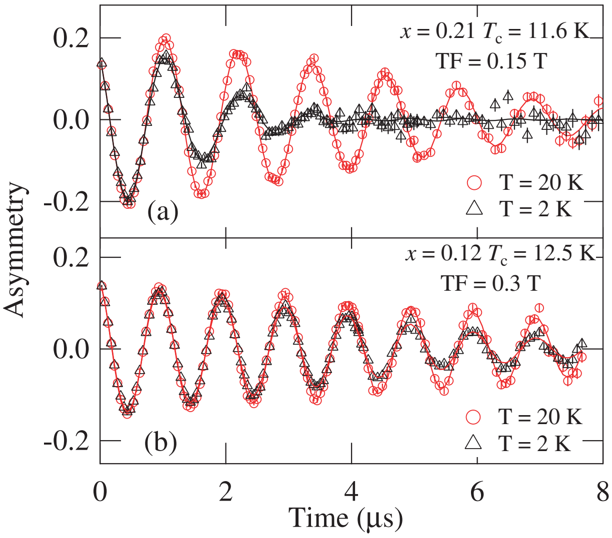

FIG. 2. (Color online) Examples of TF-μSR spectra with (a) x=0.21 and (b) 0.12 shown in a rotating reference frame frequency of 20 and 40 MHz, respectively. Circles represent the spectra above T_c, while triangles are those obtained below T_c. Solid lines are fits obtained using Eq. (1).

Figure 2 shows some examples of the TF-μSR time spectra observed in the samples with x=0.21 and 0.12 under a field of 0.15 and 0.3 T, respectively (shown in a rotating reference frame for visibility). While both spectra show a slow Gaussian damping above T_c because of random local fields from nuclear magnetic moments, further depolarization resulting from the formation of a flux line lattice is observed upon superconducting transition. A clear trend toward a high depolarization rate is observed for a high Li concentration x, which indicates an increase in n_s with x. We also note that an additional component that exhibits fast depolarization (~2 MHz) is observed in samples with x=0.08, 0.10, and 0.12. This observation is tentatively attributed to muonium (Mu) that may be formed when muons are stopped near the insulating Cl bilayers. Considering a background contribution from muons stopped in the sample holder, we used the following function for the analysis of the μSR time spectra by curve fitting:

$$A_0 P_x(t) = \exp(-\sigma_n^2 t^2)[A_s P_x^{\mathrm{v}}(t) + A_f e^{-\Lambda t} \cos(\omega_0 t + \phi)] + A_b \exp(-\sigma_b^2 t^2) \cos(\omega_b t + \phi), \quad (1)$$

where A_0 is the total positron decay asymmetry (~0.2), σ_n is the depolarization rate attributed to nuclear magnetic moments, A_s is the partial asymmetry of a superconducting fraction, A_f is that of the component related with Mu formation showing depolarization at a rate Λ, and $A_b(=A_0 - A_s - A_f \leq 0.01)$ and ω_b are the amplitude and central frequency of the background. It was found that A_f and Λ were mostly independent of temperature and magnetic field, and their fractional yield (A_f/A_0) was 0.26(1), 0.169(1), and 0.163(1) for x=0.08, 0.10, and 0.12, respectively. The influence of

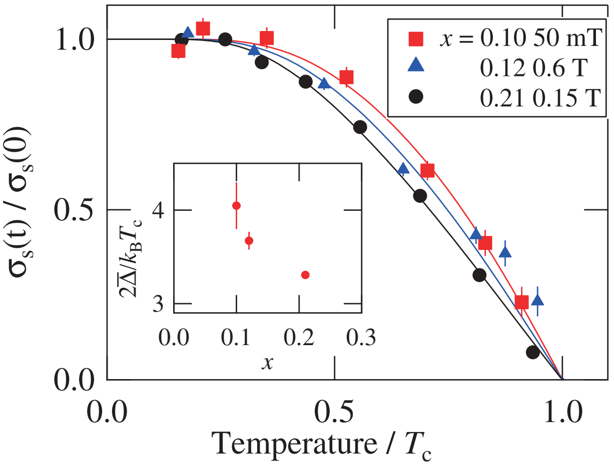

FIG. 3. (Color online) Temperature dependence of σ_s for samples with $x=0.10$, 0.12, and 0.21. Solid curves are fits obtained using the s-BCS theory as an *effective* model. Longitudinal and horizontal axes are normalized by $\sigma_s(0)$, T_c for comparison. Inset shows the x dependence of a fitting parameter $2\bar{\Delta}/k_BT_c$ with $\bar{\Delta}$ interpreted as a mean value.

flux pinning on σ_s was confirmed to be negligible for $x=0.10$ and 0.21, as inferred from the nearly field-independent σ_s at low magnetic induction (<0.2 T). This also confirms the formation of three-dimensional vortices as expected from relatively large coherence length ($\xi=8-13$ nm) over the Cl-bilayer thickness (~1 nm).

Figure 3 shows a plot of σ_s against temperature for the samples in which σ_s has been deduced with sufficient precision; it was found that n_s was too small for samples with $x<0.10$. Solid curves are the best fits obtained by applying the conventional BCS theory for s-wave symmetry with a single gap (s-BCS theory).[11] Here, assuming that electron-phonon coupling plays a minor role in Li$_x$ZrNCl, we use the s-BCS theory to determine the curve fit as an effective model extended to the case of anisotropic order parameters (having dips, nodes, or a secondary gap in multiple bands). This extension is achieved by allowing the gap ratio ($2\Delta/k_BT_c$) to vary freely, where the energy gap Δ is regarded as a mean value, $\bar{\Delta}$, averaged over the momentum space and relevant bands (while T_c is determined by the maximum of Δ). Then, we find that the deduced gap ratio ($2\bar{\Delta}/k_BT_c$, shown in the inset of Fig. 3) decreases with an increase in x. Assuming that T_c *decreases* with an increase in x, we find that the decrease in $\bar{\Delta}$ is steeper than that in decrease in T_c. While this tendency is not easily understood in the framework of electron-phonon coupling, it is understood in the extended model as an indication toward strong anisotropy with high Li content.

While we cannot distinguish the origin of anisotropy between one-band and multiband scenarios solely from the behavior of superfluid density, the presence of a secondary energy scale in the energy gap is inferred from the analysis using a phenomenological double-gap model for s-wave symmetry,[12] such that

$$\sigma_s(T) = \sigma_s(0)[1 - w\,\delta\sigma(\Delta_1,T) - (1-w)\,\delta\sigma(\Delta_2,T)],$$

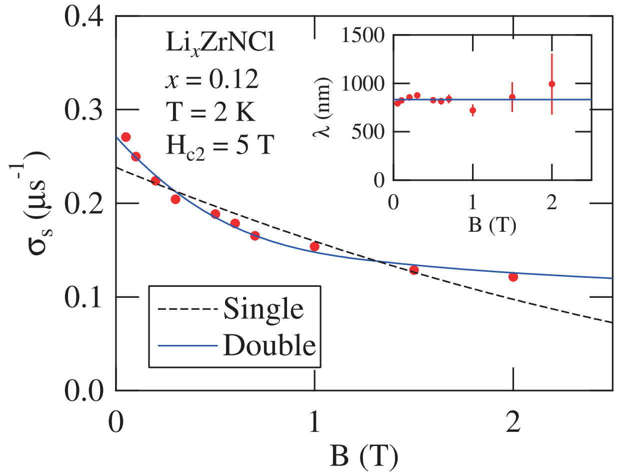

FIG. 4. (Color online) Field dependence of σ_s in Li$_x$ZrNCl with $x=0.12$. Solid curve represents the best fit obtained by Eq. (2) and the dashed curve corresponds to the case of $z=1$. Inset shows magnetic penetration depth deduced from the same analysis.

$$\delta\sigma(\delta,T) = \frac{2}{k_BT}\int_0^\infty f(\epsilon,T)[1-f(\epsilon,T)]d\epsilon,$$

$$f(\epsilon,T) = [1+\exp(\sqrt{\epsilon^2+\Delta(T)^2}/k_BT)]^{-1},$$

where $f(\epsilon,T)$ is the Fermi distribution function, $\Delta(T)$ is the standard BCS gap energy, and w is the fractional weight of the $i=1$ component. Although it is not easy to determine all the parameters using the curve fits of data shown in Fig. 3, Δ_2 for $x=0.12$ can be determined on the basis of an assumption that Δ_1 corresponds to $\Delta(T=0)$ determined by a jump in the specific heat near T_c (2.64 meV),[3] yielding excellent fit with the data obtained when $2\Delta_2/k_BT_c=2.4(4)$ [$\Delta_2=1.3(2)$ meV or $\Delta_1/\Delta_2=2.0(3)$] and $w=0.59(9)$.

The presence of a secondary energy scale in the order parameter is further suggested by the magnetic field dependence of σ_s measured at 2 K for the same sample in which an anomalous behavior of γ has been reported.[3] As shown in Fig. 4, it is observed that in the limit of $H/H_{c2}(\equiv h)\rightarrow 1$, σ_s exhibits a trend of asymptotic conversion to a value (σ_c). In the case of muonium formation, we attribute σ_c to an artifact resulting from an incomplete separation of A_s and A_f in the curve fit that might have led to residual depolarization, and we model the field dependence as follows:

$$\sigma_s(h) = z\sigma_0(h_1) + (1-z)\sigma_0(h_2) + \sigma_c, \tag{2}$$

$$\sigma_0(h_i) = 0.0274 \times \frac{\gamma_\mu\Phi_0}{\lambda^2}(1-h_i)[1+3.9(1-h_i)^2]^{1/2}, \tag{3}$$

where $h_i \equiv H/H_{c2}^{(i)}$, $H_{c2}^{(2)}$ is the secondary upper critical field (a parameter corresponding to Δ_2), z is the relative weight of $\sigma_s(h_1)$, and Eq. (3) is an approximated expression for the field dependence of σ_s for a single-gap case (with the Ginzburg-Landau parameter $\kappa \gg 1$).[13] In the curve fit, $H_{c2}^{(1)}$ was fixed to the reported value (5 T, determined by the specific heat[3]). This model reproduces our data excellently, yielding $z=0.22(3)$ and $H_{c2}^{(2)}=1.2(1)$ T. A good agreement between the ratios $H_{c2}^{(1)}/H_{c2}^{(2)}=4.2(2)$ and $(\Delta_1/\Delta_2)^2=4.1(5)$ is perfectly in line with the general relation $H_{c2}\propto\Delta^2$. (Note that the ratio Δ_1/Δ_2 is also in excellent agreement with that evaluated from the T dependence.) More interestingly, the value of H_{c2} corresponds to the field toward which γ exhibits a steep increase and then gradually saturates to γ_n for $H_{c2}^{(2)}\leq H\leq H_{c2}^{(1)}$.[3] This, together with the T dependence of σ_s, strongly suggests that the superconducting order parameter is highly anisotropic in the sample with $x=0.12$ that is characterized by a secondary energy scale $\Delta_2\simeq0.5\Delta_1$, where Δ_2 may result from dips in a single-band-gap or double-gap structure. Here, it would be worth quoting a prediction of band-structure calculation that carrier filling to the secondary band would not occur until x exceeds ~0.3, where a large increase in $N(0)$ is expected.[6,14] Absence of such an increase in the recent specific-heat measurement over the relevant range of x supports the one-band scenario,[15] suggesting that Δ_2 corresponds to the minimal gap energy (at the dips) in the order parameter.

According to a recent theory based on the Hubbard model considering disconnected Fermi surfaces on a honeycomb lattice,[8] spin fluctuation enhances T_c over a low x region. Since spin-fluctuation-mediated superconductivity needs to have sign change in the gap function, the structure of the relevant Fermi surface leads to the prediction of $d+id'$ pairing symmetry as the most probable candidate. The decrease in T_c with an increase in doping is explained by an increase in three dimensionality and associated reduction in the relative volume in the Brillouin zone, where the pairing interaction is strong (corresponding to wave vectors that bridge the opposite sides of each pieces of the Fermi surface). Moreover, the anisotropy attributed to the dips in the order parameter develops for $x\geq0.11$ and that the minimum of gap energy is reduced to $\Delta_{\min}\sim0.4\Delta_{\max}$ for $x=0.16$.[9] This behavior is in qualitative agreement with the tendency suggested by the x dependence of the gap ratio $2\bar{\Delta}/k_BT_c$ deduced from the T dependence of σ_s, where the secondary energy scale suggested in the case of $x=0.12$ $(\Delta_2\simeq0.5\Delta_1)$ may correspond to the minimal gap $(\Delta_{\min}\sim\Delta_2)$. Then, it is likely that the decrease in the gap ratio with an increase in x reflects a decrease in $\Delta_{\min}$ in the $d+id'$ gap.

Finally, we discuss the behavior of $\sigma_s(T\rightarrow0)$ as a function of T_c. As shown in Fig. 5(a), T_c increases with a decrease in σ_s. It is inferred from our data shown in Fig. 5(b) that σ_s is mostly proportional to x. Thus, the $\sigma_s(x)$ dependence of T_c is in excellent agreement with the earlier result that is shown in Fig. 5(c),[7] which strongly supports the high quality of the investigated samples. Meanwhile, this is in marked contrast with the σ_s dependence of T_c reported in an earlier literature,[16] where the authors maintain a linear relation common to that observed in underdoped cuprate superconductors (indicated by the area between dotted lines) based on their result obtained for $x=0.17$ and 0.4 (open triangles). In this regard, we point out the fact that the Li_xZrNCl samples studied in Ref. 16 do not follow the T_c versus x relation observed in our samples. In particular, their sample with $x=0.17$ seems to exhibit relatively high T_c corresponding to that of $x=0.07-0.08$ in our sample. Considering the difficulty associated with obtaining a uniform specimen for a low Li concentration,[7] one might speculate that their sample (particularly for $x=0.17$) might have had problems concerning homogeneity. The reported small μSR asymmetry [$\simeq0.1$ (Ref. 16)] might be further evidence for this speculation. In any case, our result shows that the n_s dependence of T_c is markedly different from that observed in the case of underdoped high T_c cuprates.

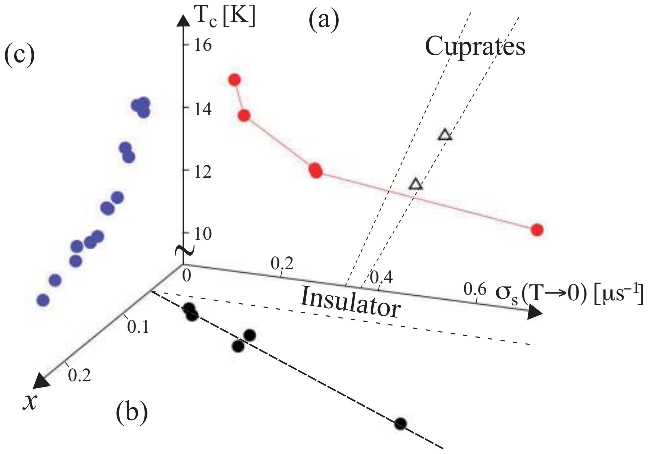

FIG. 5. (Color online) (a) T_c as a function of $\sigma_s(T\rightarrow0)$. Solid circles show the present data and open triangles are quoted from Ref. 16 (only for Li_xZrNCl with $x=0.17$ and 0.4, where the latter corresponds to the point with lower T_c). The hatched area represents the empirical linear relation found in underdoped cuprates (Ref. 16). (b) x dependence of σ_s (the present data) with the dashed line representing a linear relation. This line crosses zero at $x\simeq0.05$, where metal-insulator transition occurs. (c) x dependence of T_c (after Ref. 7).

In conclusion, it is microscopically shown by μSR measurements that the superconducting order parameter in Li_xZrNCl is strongly anisotropic in a sample with $x=0.12$, as inferred from the temperature and field dependence of σ_s. Therefore, the origin of anomalous behavior in the Sommerfeld coefficient observed in the specific-heat measurements is attributed to the strong anisotropy in the order parameter that might be characterized by a secondary energy scale Δ_2 (where $\Delta_2\simeq0.5\Delta_1$). The temperature dependence of σ_s over a range of x from 0.10 to 0.21 implies a tendency for the occurrence of a weak pairing interaction and strong anisotropy in the order parameter with an increase in x. The latter feature as well as the relatively high T_c at a low Li concentration supports the important role of electronic correlation for the mechanism of superconductivity in Li_xZrNCl predicted by the recent theory.

We thank the staff of TRIUMF for their technical support during the μSR experiment, and we appreciate the helpful discussion with K. Kuroki and H. Tou. This work was supported by the KEK-MSL Inter-University Program for Oversea Muon Facilities and a Grant-in-Aid for Scientific Research on Priority Areas by Ministry of Education, Culture, Sports, Science and Technology, Japan.

[1] S. Yamanaka, H. Kawaji, K. Hotehama, and M. Ohashi, Adv. Mater. (Weinheim, Ger.) **8**, 771 (1996).
[2] S. Yamanaka, K. Hotehama, and H. Kawaji, Nature (London) **392**, 580 (1998).
[3] Y. Taguchi, M. Hisakabe, and Y. Iwasa, Phys. Rev. Lett. **94**, 217002 (2005).
[4] H. Tou, Y. Maniwa, T. Koiwasaki, and S. Yamanaka, Phys. Rev. Lett. **86**, 5775 (2001).
[5] R. Weht, A. Filippetti, and W. E. Pickett, Europhys. Lett. **48**, 320 (1999).
[6] R. Heid and K.-P. Bohnen, Phys. Rev. B **72**, 134527 (2005).
[7] Y. Taguchi, A. Kitora, and Y. Iwasa, Phys. Rev. Lett. **97**, 107001 (2006).
[8] K. Kuroki, Sci. Technol. Adv. Mater. **9**, 044202 (2008).
[9] K. Kuroki, arXiv:1001.3167 (unpublished).
[10] T. Takano, A. Kitora, Y. Taguchi, and Y. Iwasa, Phys. Rev. B **77**, 104518 (2008).
[11] F. Bouquet, Y. Wang, R. A. Fisher, D. G. Hinks, J. D. Jorgensen, A. Junod, and N. E. Phillips, Europhys. Lett. **56**, 856 (2001).
[12] K. Ohishi, T. Muranaka, J. Akimitsu, A. Koda, W. Higemoto, and R. Kadono, J. Phys. Soc. Jpn. **72**, 29 (2003).
[13] E. H. Brandt, Phys. Rev. B **37**, 2349 (1988).
[14] C. Felser and R. Seshadri, J. Mater. Chem. **9**, 459 (1999).
[15] Y. Kasahara, T. Kishiume, T. Takano, K. Kobayashi, E. Matsuoka, H. Onodera, K. Kuroki, Y. Taguchi, and Y. Iwasa, Phys. Rev. Lett. **103**, 077004 (2009).
[16] T. Ito, Y. Fudamoto, A. Fukaya, I. M. Gat-Malureanu, M. I. Larkin, P. L. Russo, A. Savici, Y. J. Uemura, K. Groves, R. Breslow, K. Hotehama, S. Yamanaka, P. Kyriakou, M. Rovers, G. M. Luke, and K. M. Kojima, Phys. Rev. B **69**, 134522 (2004).